Università degli Studi di Torino
Scuola di Dottorato

UNIVERSITÀ
DI TORINO

Multiple (multi-)strange hadron production in proton-proton collisions at $\sqrt{s} = 5.02$ TeV with ALICE at the LHC

Sara Pucillo

Università degli Studi di Torino
Scuola di Dottorato

Dottorato in Fisica

Multiple (multi-)strange hadron production in proton-proton collisions at $\sqrt{s} = 5.02$ TeV with ALICE at the LHC

Author: **Sara Pucillo**

Reviewers: **Alberto Calivà, Roman Lietava**

Supervisor: **Livio Bianchi**

"I am enough of the artist to draw freely upon my imagination. Imagination is more important than knowledge. Knowledge is limited. Imagination encircles the world"

Albert Einstein

Abstract

The increased production of strange hadrons in heavy-ion collisions compared to minimum-bias pp collisions has historically been interpreted as one of the earliest signatures of the formation of a deconfined quark-gluon plasma. One of the most significant findings from Run 1 and Run 2 of the LHC is the observation by the ALICE Collaboration of an enhanced production of (multi-)strange to non-strange hadron yields, gradually rising from low-multiplicity to high-multiplicity pp and p–Pb collisions, reaching values close to those measured in peripheral Pb–Pb collisions [1]. Despite these observations, the origin of this phenomenon in small collision systems remains unclear. Furthermore, none of the current QCD-inspired Monte Carlo generators can quantitatively describe the observed behavior. This emphasizes the need for additional experimental data, new observables and theoretical advancements to uncover the microscopic mechanisms driving strangeness enhancement. A deeper understanding of the mechanisms behind strangeness production, and hadronization more in general, could be achieved by measuring the (multi-)strange particle multiplicity distribution ($\mathrm{P}(n_{\mathrm{S}})$). A novel method involving event-by-event counting of strange particles offers a promising approach. In this thesis, the first ALICE results of the multiplicity distributions for $\mathrm{K}^0_{\mathrm{S}}$, Λ, $\overline{\Lambda}$, Ξ^-, $\overline{\Xi}^+$, Ω^-, and $\overline{\Omega}^+$ in pp collisions at $\sqrt{s} = 5.02$ TeV are presented as a function of charged particle multiplicity. These results provide a unique perspective on the correlation between charged and strange particles' production. Furthermore, the measurement of $\mathrm{P}(n_{\mathrm{S}})$ enables the determination of the average yields of multiplets for each type of strange particle, widening the scope of strangeness production studies beyond average values and enabling the investigation of extreme cases where up to six strange quarks coalesce into hadrons in a single event. Additionally, by comparing hadron combinations with varying u and d quark compositions but identical total strange (s) quark content, it becomes possible to isolate the contributions to the enhancement pattern that arise from mechanisms unrelated to strangeness. These findings are compared with state-of-the-art phenomenological models implemented in commonly used Monte Carlo event generators, drastically enhancing the sensitivity to the different processes implemented in each approach.

This thesis also provides an overview of the data quality of the MUon IDentifier (MID) during pp and Pb–Pb collisions in Run 3 (2022–2024), with a focus on monitoring the asynchronous quality control.

Contents

Introduction **2**

1 High-energy nuclear physics **3**
1.1 An introduction to quantum chromodynamics . . . 3
1.1.1 Phase transition: QGP . . . 5
1.2 Heavy-ion collisions . . . 7
1.2.1 Space-time evolution of a collision . . . 9
1.2.2 QGP signatures . . . 9
1.3 Small hadronic collision systems . . . 20
1.4 Hadronization mechanisms . . . 26
1.4.1 Statistical models: canonical suppression . . . 26
1.4.2 Microscopic phenomenological models for pp collisions . . . 28
1.4.3 Core-corona models . . . 30

2 Strangeness production in high energy collisions **33**
2.1 Strangeness enhancement as a QGP signature . . . 34
2.2 Measurement of SE: energy hierarchy problem . . . 35
2.3 Strange hadron production across colliding systems . . . 37
2.3.1 ALICE recent results in small systems . . . 39

3 ALICE: A Large Ion Collider Experiment **47**
3.1 The Large Hadron Collider (LHC) . . . 47
3.2 ALICE in Run 1 and Run 2 . . . 49
3.2.1 ALICE sub-detectors . . . 49
3.2.2 Data acquisition and offline framework . . . 56
3.2.3 Track and vertex reconstruction . . . 58
3.2.4 Particle IDentification . . . 58
3.3 ALICE in Run 3 . . . 59
3.3.1 Data taking, processing and reconstruction upgrades . . . 60

4 (multi-)Strange particle multiplicity distribution **63**
4.1 Analysis strategy: summary . . . 64
4.2 Data and Monte Carlo samples . . . 65
4.3 Event selection and multiplicity categorization . . . 65
4.4 Candidate selection . . . 67
4.5 Signal extraction: raw multiplicity spectrum engineering . . . 73
4.6 Corrections: unfolding and trigger efficiency . . . 81

4.6.1 Monte Carlo choice . . . 84
4.6.2 Trigger efficiency . . . 88
4.7 Statistical and systematic uncertainties evaluation . . . 89
4.7.1 Cut variation . . . 90
4.7.2 Signal extraction . . . 92
4.7.3 Unfolding procedure . . . 93
4.7.4 Event efficiency . . . 95
4.7.5 Knowledge of the p_{T} distribution . . . 95
4.7.6 Effect of the cut on the OOB pile-up . . . 96
4.7.7 Feed-down correction . . . 96
4.7.8 Material budget . . . 96
4.7.9 Strangeness from material . . . 97
4.7.10 Hadronic interactions . . . 97
4.8 Average yield of strange hadron multiplets . . . 97

5 Results and discussion **99**
5.1 Strange particle multiplicity distribution: P(n_S) . . . 99
5.2 The strangeness-driven bias in charged-particle multiplicity . . . 103
5.3 Multiple strange hadron production yields . . . 105
5.4 Yield ratios with ΔS > 0: strangeness enhancement at its extremes . . . 107
5.5 Yield ratios with ΔS $= 0$: non-strangeness related effect . . . 109
5.6 Comparison with previous results . . . 112

6 Future directions **117**
6.1 Experimental Prospects . . . 117
6.1.1 Other colliding systems and/or centre-of-mass energies . . . 117
6.1.2 Run 3 and 4 . . . 121
6.2 Towards Refined Models . . . 124

7 Asynchronous quality control of the MID **145**
7.1 Muon Spectrometer . . . 145
7.2 Read-out architecture chain . . . 148
7.2.1 Quality control architecture chain . . . 149
7.3 Quality control objects for the MID . . . 153
7.3.1 Current status: statistics and issues . . . 156

8 Conclusions **167**

9 Appendices **171**
9.1 1D invariant mass fits . . . 171
9.2 Signal probability trends . . . 233
9.3 Analysis for different multiplicity classes . . . 241
9.4 Singular systematic source plots . . . 247
9.5 Convergence Plots . . . 260
9.6 Agreement between particle and anti-particle . . . 312
9.7 Fit to the (multi-)strange particle multiplicity distribution . . . 314

9.8 Strangeness-driven bias in the charged-particle multiplicity in Pythia 8 Monash and Epos LHC 316

Bibliography **319**

Introduction

Quantum chromodynamics (QCD) is the theory that describes strong interactions among quarks and gluons, the fundamental constituents of hadrons. A key feature of QCD is confinement: partons are bound within hadrons and cannot escape unless the system's energy density exceeds approximately 1 GeV/fm^3, at which point nuclear matter undergoes a phase transition to form a quark-gluon plasma (QGP). This state of matter, which characterized the early Universe, can be recreated in laboratory conditions. The A Large Ion Collider Experiment [2] (ALICE) at the Large Hadron Collider [3](LHC) is specifically designed to study relevant observables for the characterization of the QGP. Direct detection of the deconfined phase, whose lifetime is $\tau \sim 10^{-23}s$, is unfeasible; thus, QGP properties are inferred from final-state observables and their modifications.

Among several signatures of the QGP formation, the so-called Strangeness Enhancement (SE), i.e. the enhanced production of (multi-)strange particles in heavy-ion collisions compared to minimum-bias pp collisions, was one of the first proposed [4]. The SE phenomenon was first observed experimentally at the CERN SPS [5] and later confirmed at higher centre-of-mass energies at the BNL RHIC [6] and the CERN LHC [7]. However, the underlying origin of this phenomenon remains uncertain. Statistical hadronization models (SHM) have successfully reproduced strangeness production in heavy-ion collisions [8, 9, 10, 11], not necessarily requiring QGP formation. Instead, these models attribute SE to mechanisms such as the restoration of local flavor and charge conservation [12] or the incomplete equilibration of the strange quantum number [13]. At the LHC, beyond confirming SE at the highest centre-of-mass energies, the ALICE Collaboration has delivered a comprehensive set of measurements of strange-to-pion yield ratios as a function of the average charged-particle multiplicity density at mid-rapidity ($\langle \mathrm{d}N_{\mathrm{ch}}/\mathrm{d}\eta \rangle_{|\eta| < 0.5}$) across different collision systems and centre-of-mass energies. These include pp [1, 14, 15, 16], p–Pb [17, 18], and Pb–Pb [19] collisions. The results reveal an enhancement pattern that scales with the strangeness content of the hadron, independent of the collision system or centre-of-mass energy. This invariance of the SE pattern across different systems challenges the idea that the mechanisms governing high-multiplicity pp interactions are identical to those driving particle production in Pb–Pb collisions. Furthermore, phenomena traditionally associated with the creation of a partonic medium undergoing hydrodynamic expansion in A–A collisions have also been observed in high-multiplicity pp and p–Pb interactions.

Building on these observations, various phenomenological models implemented in widely used Monte Carlo (MC) event generators [20, 21] have been refined to better describe particle production in environments characterized by high parton densities [22, 23, 24].

Additionally, SHM fits have been extended to the low-multiplicity regimes of pp interactions [25, 26, 27]. While these refined models qualitatively reproduce the trends of SE, discrepancies remain when subjected to precise quantitative comparisons. These challenges have stimulated new experimental efforts to explore the relationships between strange particle production and both local and global event properties in pp interactions. In this context, studies have examined the link between strangeness production and jet activity [28, 29], the classification of events based on the isotropy of final-state charged-particle distributions [30] and the potential connection of SE with global event features such as effective energy [31]. Furthermore, two-particle correlation methods have been employed to investigate the conservation of the strange quantum number across both small and large collision systems [32, 33].

In previous studies, strange particle yields were determined by counting their total number in a given dataset — potentially dividing the sample based on topological or dynamical properties of the events or the strange particle candidates — and then normalizing the counts, corrected for acceptance and efficiency, to the total number of analyzed inelastic events in the dataset. In this sense, production rates represent the average of the multiplicity distribution of strange particles, providing insight into the underlying production mechanisms for a given particle species. This thesis presents an extension of these findings: for the first time, the multiplicity distribution of strange particles $\mathrm{P}(n_{\mathrm{S}})$ is measured for $\mathrm{K}^0_{\mathrm{S}}$, Λ, $\overline{\Lambda}$, Ξ^-, $\overline{\Xi}^+$, Ω^-, and $\overline{\Omega}^+$ in pp collisions at $\sqrt{s} = 5.02$ TeV. This analysis is performed across different classes of charged-particle multiplicity density, using an innovative event-by-event counting technique for strange particles. This approach has become feasible thanks to the recent release of transverse momentum (p_{T}) spectra of strange hadrons for each multiplicity class by the ALICE Collaboration [16], using the same dataset employed in this study. This novel technique allows the extraction of probabilities for scenarios such as observing events with very low overall charged-particle multiplicity density but featuring three or four cascades, or conversely, high-multiplicity events with a minimal (or even absent) presence of single-strange $\mathrm{K}^0_{\mathrm{S}}$ particles.

This thesis is organized as follows. In Chapter 1 the high-energy nuclear physics and the observables used to investigate the dynamic and thermal properties of the QGP are described. In Chapter 2 the strangeness production in high-energy collisions, presenting the state of the art and motivations underlying this work is reviewed. A detailed description of the ALICE detector, focusing on the Inner Tracking System (ITS), Time Projection Chamber (TPC) and V0 scintillator hodoscopes is provided in Chapter 3. The analysis strategy used in this thesis, including event selection, particle identification, signal extraction technique, applied corrections and systematic uncertainties are explained in Chapter 4. Results are presented, discussed and compared to phenomenological models in Chapter 5, while potential future developments of this analysis are discussed in Chapter 6, highlighting both experimental advancements and theoretical implications. Chapter 7 discusses the current status of the MID during Run 3, highlighting statistical insights and encountered issues while monitoring asynchronous quality control. Finally, the conclusions are summarized in Chapter 8.

Chapter 1

High-energy nuclear physics

Quantum chromodynamics (QCD) is the theory that describes the strong interactions between quarks and gluons, the fundamental constituents of hadrons. A key feature of QCD is confinement, which means that partons (quarks and gluons) cannot exist freely outside of hadrons unless the energy density of the system exceeds approximately 1 GeV/fm^3. At this point, nuclear matter undergoes a phase transition into a quark-gluon plasma (QGP), a state of matter where quarks and gluons are deconfined and can move over distances larger than the size of a hadron ($\sim$ 1 fm).
Both theoretical and experimental research explore the complex QCD phase diagram to investigate the nature of the phase transition, locate the critical point and understand the properties of the matter formed in these conditions. Experimentally, the QCD phase transition can be studied in laboratory through ultra-relativistic heavy-ion collisions, which recreate the high temperature, pressure and energy density conditions needed to form the QGP. After a short initial time, the system produced in these collisions thermalizes, forming a "fireball" in local thermal equilibrium that expands hydrodynamically as it cools. This fireball's evolution mirrors the early Universe's development, where deconfined partonic matter transitioned into confined hadrons just microseconds after the Big Bang.
In smaller systems, such as proton-proton (pp) collisions, the initial energy density and system size are significantly lower, making it harder to create and sustain a QGP-like state for a sufficient duration. However, the observation of phenomena reminiscent of heavy-ion collisions in these smaller systems has expanded the opportunity to deepen our understanding of high-energy hadronic collisions and the underlying QCD physics.

1.1 An introduction to quantum chromodynamics

The Standard Model (SM) [34] currently provides the most precise description of the Universe's fundamental forces and matter. It is a Yang-Mills theory based on the non-abelian group $U(1) \times SU(2) \times SU(3)$, which organizes matter into two main categories: fermions and bosons. Fermions consist of 12 elementary particles (along with their corresponding antiparticles) that have half-integer spin. These include 6 quarks and 6 leptons, each with distinct flavors. Bosons, in contrast, are particles with integer spin, most of which act as mediators of the fundamental forces. The photon mediates electromagnetic interactions, the $W^{\pm}$ and Z bosons mediate the weak force, and 8 gluons mediate the strong force. Figure 1.1 illustrates these particles, along with the Higgs boson, which plays a crucial

role in the SM by providing mass to elementary particles.

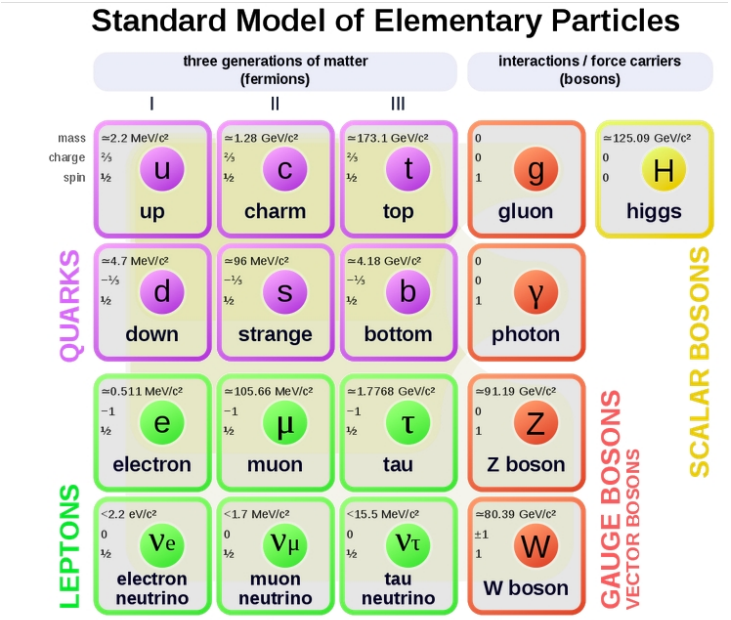

Figure 1.1: Overview of the elementary particles of the Standard Model.

The strong interaction is governed by quantum chromodynamics (QCD), a non-abelian quantum gauge field theory that is invariant under local SU(3) color group transformations. The symmetry of the QCD Lagrangian under SU(3) color transformations introduces a conserved charge known as color. The QCD Lagrangian density can be expressed as follows [35]:

$$\mathcal{L}_{\mathrm{QCD}} = \sum_{q} \overline{q_i}(i\gamma^{\mu}D_{\mu} - m_q)_{ij}q_j - \frac{1}{4}F^a_{\mu\nu}F^{\mu\nu}_a \tag{1.1}$$

where sums over repeated indices are implied. In the Lagrangian density, the first term in the sum represents the free quark field: q_i is the field of a quark with flavor q (which can be one of six flavors: up, down, strange, charm, bottom, and top), color i (which can be red, green, or blue) and mass $(m_q)_{ij} = m_q\delta_{ij}$. The quark field is described by a Dirac spinor, a four-component complex vector. γ^{μ} are the Dirac matrices and D_{μ} is the covariant derivative, which is defined as:

$$D_{\mu} = \partial_{\mu} - ig_s\frac{\lambda_a}{2}A^a_{\mu} \tag{1.2}$$

where g_s is the dimensionless coupling constant related to the strong coupling constant α_s by $\mathrm{g}_s = \sqrt{4\pi\alpha_s}$. The λ_a are the eight Gell-Mann matrices, which serve as the generators of the SU(3) color group, and A^a_{μ} represents the gluon field with a = 1,2,...,8 corresponding to the eight gluons. The kinematics and dynamics of gluons are described by the second term in the Lagrangian density through the gluon field tensor $F^{\mu\nu}_a$, which is defined as:

$$F^{\mu\nu}_a = \partial_{\mu}A^a_{\nu} - \partial_{\nu}A^a_{\mu} + f^a_{bc}A^b_{\mu}A^c_{\nu} \tag{1.3}$$

Here, f^a_{bc} are the structure constants of the SU(3) color group, a key feature of QCD's non-abelian nature. Unlike quantum electrodynamics (QED), which is based on the U(1) symmetry and where the photon does not interact with itself, the non-abelian SU(3) symmetry of QCD permits self-interactions between gluons due to non-zero structure constants. This leads to the possibility of three- and four-gluon interaction vertices, as shown in the corresponding Feynman diagrams in Fig. 1.2. These gluon self-interactions (bosonic loops) have profound implications for the strong force's behavior. Despite being massless, like photons, gluons mediate a short-range force, unlike the long-range electromagnetic force.

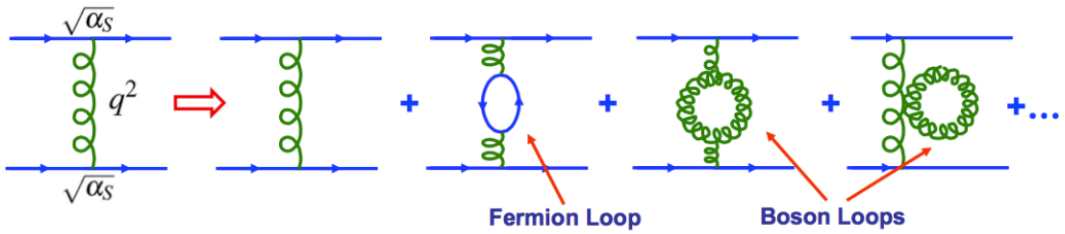

Figure 1.2: Feynman diagrams of the strong interaction with quark loops (charge screening) and gluon loops (charge anti-screening).

The self-interaction between gluons leads to a phenomenon known as "anti-screening", which causes the QCD coupling constant to depend on the momentum transfer Q strongly [36, 37]:

$$\alpha_s(|Q^2|) = \frac{\alpha_s(|\mu^2|)}{1 + \Big(\alpha_s(|\mu^2|)/12\pi\Big)\Big(33 - 2n_f\Big)\ln\Big(|Q^2|/\mu^2\Big)} \tag{1.4}$$

The variable n_f represents the number of quark flavors that contribute to the 1-loop corrections, specifically those for which $m_f < |Q|$, while μ refers to the renormalization mass scale, which is not determined by the theory itself. The dependence of α_s on Q^2 has been experimentally established, as shown in Fig. 1.3. At high Q values, corresponding to short distances, $\alpha_s(Q^2)$ decreases, allowing quarks to be treated as nearly free particles. This regime, called asymptotic freedom, arises due to the anti-screening effect of bosonic loops, which effectively increase the color charge at larger distances but reduce it at shorter distances. This behavior permits a perturbative approach to amplitude calculation, known as perturbative QCD (pQCD). On the other hand, at low Q values ($Q \leq 1$ GeV/c), the strong coupling constant increases significantly, leading to the confinement of quarks within hadrons. In this regime, referred to as confinement, quarks and gluons are bound inside hadrons and cannot exist as free particles. This feature is connected to the symmetry group that defines the theory itself, but its properties cannot be deduced from first principles (no perturbative methods) and have to be described using phenomenological models (e.g. string models parametrizing the QCD potential, see Section 1.4.2) or discretized phase-space calculations (Lattice-QCD, or LQCD).

1.1.1 Phase transition: QGP

As discussed earlier, the QCD coupling constant evolves with the energy scale of the process, leading to two distinct regimes. A perturbative approach to QCD is only feasible

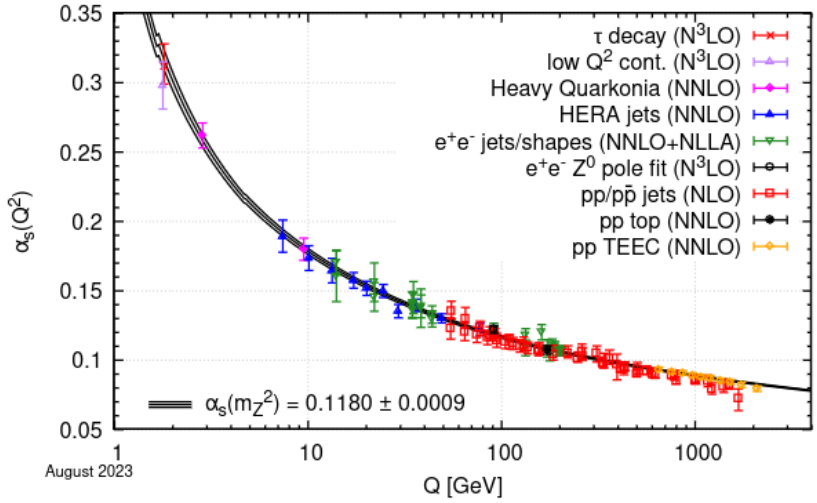

Figure 1.3: Trend of α_s as a function of the transferred momentum Q where the results of several experiments were considered [38].

when the coupling constant, α_s, is small enough. In the non-perturbative regime, however, alternative methods such as discretized phase-space calculations or phenomenological models must be employed to compute the QCD equation of state. These approaches study the properties of nuclear matter by analyzing macroscopic variables such as temperature T, energy density ϵ and baryon chemical potential μ_B. [1] Lattice QCD (LQCD) [39, 40] is a non-perturbative technique that uses a discretized Euclidean space-time lattice, where quark and gluon fields are simulated using Monte Carlo methods. As the lattice spacing approaches zero and the number of points becomes infinite, the description of QCD in continuous space-time is recovered. At sufficiently high temperatures ($T \sim 160$ MeV) and energy densities ($\epsilon \sim 0.3$ - 1.3 GeV/fm^3) [40], LQCD predicts that the strength of the color field weakens, preventing quarks and gluons from remaining confined within hadrons. In this scenario, nuclear matter undergoes a phase transition from a hadronic state to a quark-gluon plasma, a phase in which quarks and gluons are deconfined and can interact over distances on the order of 10-100 fm. This exotic state of strongly interacting QCD matter characterized the early Universe in the first microseconds following the Big Bang, according to the Big Bang theory [41].
The phase diagram of nuclear matter, depicted in Fig. 1.4, shows the relationship between temperature T and baryon chemical potential μ_B.
At $T = \mu_B = 0$ MeV, the system corresponds to the QCD vacuum. At low temperatures and baryonic densities ($T \sim 0$ MeV and $\mu_B \sim 940$ MeV), nuclear matter exists in its ordinary state, where quarks and gluons are confined within hadrons. As the temperature increases, the system enters a hadron gas (HG) phase, where nucleons interact with one another and form hadrons. Further increases in temperature and energy density lead to the deconfined QGP phase. At small values of T and large values of μ_B, a transition to a colour superconductor phase is expected. This exotic state of matter may exist in the

[1] The baryon chemical potential is defined as the energy required to increase the total number of baryons in a system by one: $\mu_B = \frac{\partial E}{\partial N_B}$, where N_B = N(B) - N($\overline{B}$). This potential provides insight into how the energy available in the initial state is redistributed to produce the observed particles in the final state.

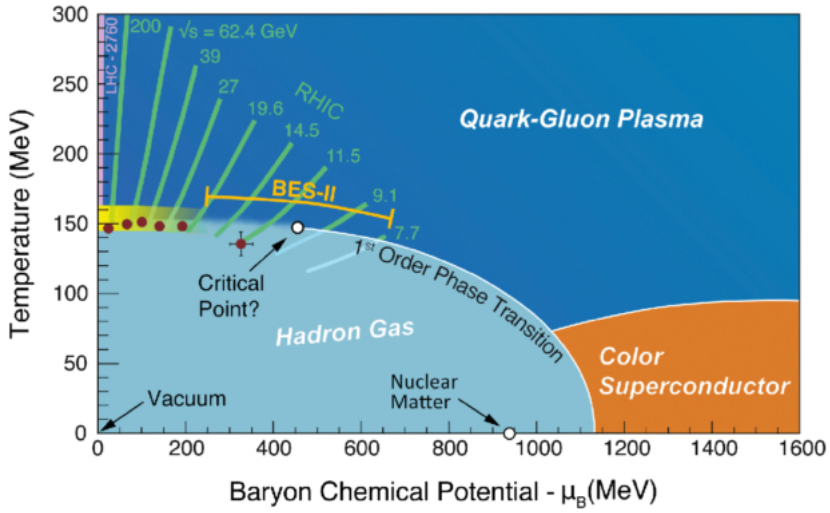

Figure 1.4: QCD phase diagram [42].

cores of neutron stars [43].
Phase transitions are traditionally classified based on discontinuities in the n-th derivative of the free energy with respect to a thermodynamic variable, such as temperature. A transition is said to be of order n if the n-th derivative is discontinuous. In contrast, a crossover occurs when the free energy and all its derivatives are continuous, meaning the system changes smoothly from one phase to another. At LHC energies, the region with $\mu_B \sim 0$ MeV is explored. According to lattice calculations, in this region the transition to QGP is expected to be a crossover at temperatures of $T \sim 154$ - 174 MeV [44]. For larger values of μ_B, the phase transition can be investigated at lower centre-of-mass energies, such as those studied at RHIC during the Beam Energy Scan (BES) program.

1.2 Heavy-ion collisions

The QGP can be studied in laboratory settings through ultra-relativistic heavy-ion collisions. The first experiments in this field began in the 1980s at the Super Proton Synchrotron (SPS) [45] at CERN and the Alternating Gradient Synchrotron (AGS) [46] at Brookhaven National Laboratory (BNL). These early fixed-target experiments explored collisions at centre-of-mass energies per nucleon pair ($\sqrt{s_{\mathrm{NN}}}$) in the range of approximately 5 to 20 GeV, probing the baryon chemical potential μ_B interval between 200 and 500 MeV. This energy range is referred to as the "stopping regime", where nucleons are halted in the collision region, resulting in a high net baryon density at mid-rapidity (see Eq. 1.5 for the definition of rapidity). Further studies of ultra-relativistic heavy-ion collisions have been conducted at the Relativistic Heavy Ion Collider (RHIC) [47] since 2000, and at the Large Hadron Collider (LHC) [48] at CERN since 2010. These facilities have achieved significantly higher centre-of-mass energies, with RHIC reaching $\sqrt{s_{\mathrm{NN}}} = 200$ GeV for Au–Au collisions, and the LHC reaching $\sqrt{s_{\mathrm{NN}}} = 5.36$ TeV for Pb–Pb collisions. At these higher energies, the colliding nuclei are no longer stopped at the collision point, leading to a very low net baryon density at mid-rapidity. This allows for the exploration of the $\mu_B \sim 0$ MeV region of the QCD phase diagram, known as the "Bjorken regime" or

"transparency regime."

Heavy-ion collisions are highly complex events in which two large, extended nuclei collide. Due to relativistic effects, these fast-moving nuclei undergo Lorentz contraction along the beam axis, making their transverse dimension larger than their longitudinal one. The energy carried by the individual nucleons is deposited within a very small spatial region and over a brief period of time. By generating such an incredibly hot and dense "fireball" of fundamental particles, the conditions (high temperature and energy density) for the formation of quark-gluon plasma can be reached. A schematic representation of a heavy-ion collision is shown in Fig. 1.5.

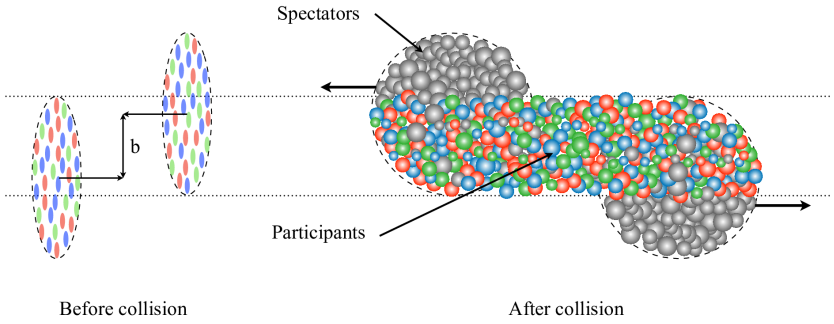

Figure 1.5: A schematic view of a heavy-ion collision. The two nuclei are Lorentz contracted; after the collision, a region containing the participating nucleons with high temperature and density is created, while the spectators continue their motion in the beam direction [49].

The geometry of a collision plays a significant role in determining the total energy released in the centre-of-mass frame, as the nuclei involved are extended objects in the transverse direction. The number of nucleons participating in the collision depends on how the beams interact. In nucleus-nucleus collisions, the impact parameter (b) is defined as the distance between the centers of the two colliding nuclei in the plane perpendicular to the collision axis. In proton-nucleus collisions, b is the distance between the center of the nucleus and the point where the proton strikes. Nucleons that take part in the collision are referred to as participants (N_{part}), while those that continue along their original trajectory without interacting are called spectators (N_{spec} = 2A - N_{part}). Collisions with a small impact parameter, where the nuclei collide nearly head-on, are known as central collisions, involving most of the nucleons and producing the highest particle multiplicity. Conversely, collisions with a large b are termed peripheral, involving fewer nucleons and leaving many spectators. In proton-proton interactions, the concept of centrality loses its significance, as only two nucleons are involved in a single collision.
Although the impact parameter cannot be measured directly, centrality information, which is closely related to b, can be inferred in two main ways:

- by measuring the number of spectator nucleons that escape the collision, using

calorimeters positioned along the beamline;

- by counting the number of charged-particles produced in the collision.

1.2.1 Space-time evolution of a collision

The evolution of the system created after a heavy-ion collision can be described in four main steps, as illustrated in Fig. 1.6 [48], considering that the collision starts at $\tau = 0$ fm/c:

- Pre-equilibrium ($\tau < 1$ fm/c): in the initial stages of the collision, parton-parton hard scatterings occur within the overlap region of the two nuclei, releasing a significant amount of energy. During this phase, particles with large masses or high transverse momentum are produced. These processes involve substantial momentum transfer, and the particle production can be described by perturbative QCD. At this point, however, the system has not yet reached thermal equilibrium.

- QCD phase/thermalization ($\tau \sim 1$ fm/c): the particles produced in the initial collisions continue to interact with each other, creating a region of high energy density that reaches thermal equilibrium, potentially leading to the formation of a QGP. As the system evolves, it undergoes expansion and cooling through inelastic and elastic collisions among its partonic constituents. During this phase, the relative abundances of quarks (u, d, s) and gluons shift. The rapid expansion of the QGP is typically modeled using relativistic hydrodynamics [50], which offers valuable insights for interpreting experimental data.

- Hadronization (6 fm/$c < \tau <$ 10 fm/c): during the expansion phase, as the temperature and energy density of the system decrease, the temperature eventually falls below a critical value, T_C. At this point, hadronization begins, where quarks and gluons become confined again within hadrons. The system transitions into a hadron gas, where the hadrons continue to interact through inelastic collisions.

- Freeze-out ($\tau \sim 10$ fm/c): when the energy density of the system drops low enough, inelastic interactions between particles cease, marking the point of *chemical freeze-out*. At this stage, the relative abundances of different hadron species are fixed, defining the system's hadrochemistry. However, elastic collisions that can modify the kinematic properties of the hadrons may still occur. These interactions continue until the hadrons are sufficiently spaced apart, beyond the range of their interactions, leading to *kinetic freeze-out*. At this point, the hadrons emerge and can be detected.

1.2.2 QGP signatures

The lifetime of the deconfined phase ($\tau \sim 10^{-23}$ s) is so brief that direct detection is impossible. Therefore, the characteristics of the QGP must be inferred through the study of final-state observables, referred to as "signatures". These observables are categorized based on the phase of the collision in which they are produced into three main types: electromagnetic, hard and soft probes.

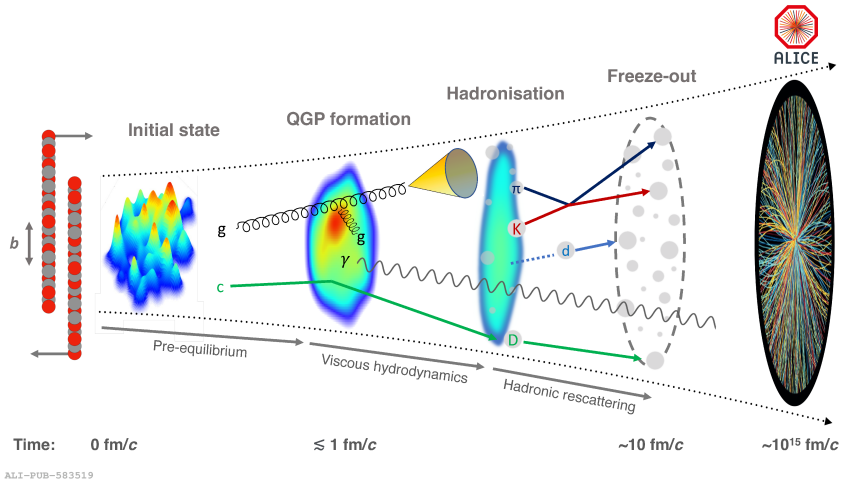

Figure 1.6: A schematic view of a space-time evolution of the strong interacting system created in ultra-relativistic heavy-ion collisions [48].

- Electromagnetic probes consist of photons emitted before and after the thermalization phase. These probes can be detected by identifying the lepton pairs they generate in the final state. However, isolating their signal from the background, particularly from photons produced in later stages of the medium evolution, is challenging.

- Hard probes involve processes with high momentum transfer, where particle production occurs over short time scales (such as partonic collisions). Since the strong coupling constant α_s is small in these processes (as shown in Fig. 1.3), their production rates can be calculated using perturbative QCD. Hard probes are produced only in the early stages of the collision, making them sensitive to the entire evolution of the medium. Examples include jets and the production of particles containing heavy quarks (c, b), such as in open charm/beauty and quarkonia (bound states of a quark and antiquark).

- Soft probes are characterized by low momentum transfer and cannot be treated with perturbative methods. Instead, non-perturbative models are necessary (see Fig. 1.3). These probes emerge from the later stages of the fireball's evolution and provide indirect information on the phase transition. They are primarily constituted by hadrons containing light quarks (u, d, s) with momenta below 2 GeV/c.

A selection of important observables and experimental results that have advanced our understanding of the properties of the QGP medium created in ultra-relativistic heavy-ion collisions is provided in the following.

Charged-particle multiplicity

The charged-particle multiplicity, denoted as N_{ch}, represents the number of charged-particles produced during a collision. When measuring particle production in the final state of the collision, it is crucial to introduce and define two kinematic variables:

- *rapidity*

$$y = \frac{1}{2} \ln \left(\frac{E + p_z c}{E - p_z c} \right) \tag{1.5}$$

  where E is the energy and $p_z c$ the longitudinal momentum.

- *pseudorapidity*

$$\eta = \frac{1}{2} \ln \left(\frac{|\mathbf{p}| + p_z c}{|\mathbf{p}| - p_z c} \right) = -\ln \left(\tan(\theta/2) \right) \tag{1.6}$$

  where θ is the angle between the momentum of the particle and the beam axis.

In the ultra-relativistic limit, rapidity may be approximated by pseudorapidity.
The charged-particle multiplicity is typically expressed per unit of pseudorapidity η as $\mathrm{d}N_{\mathrm{ch}}/\mathrm{d}\eta$ and serves as a global observable that is sensitive to the energy density during the pre-equilibrium phase of the collision, providing insights into the transition to the QGP phase. To facilitate comparisons of results obtained from different collision systems while accounting for the sizes of the colliding systems, the charged-particle multiplicity is generally normalized by the number of participant pairs, $\langle N_{part} \rangle / 2$.
The left panel of Fig. 1.7 depicts the charged-particle multiplicity at midrapidity as a function of the centre-of-mass energy per nucleon pair $\sqrt{s_{\mathrm{NN}}}$, as measured at the LHC by ATLAS [51] and CMS [52] at $\sqrt{s_{\mathrm{NN}}} = 2.76$ TeV, and at lower energies (in the range $\sqrt{s_{\mathrm{NN}}} = 9$ - 200 GeV) by experiments at the SPS [53] and RHIC [54, 55, 56, 57]. The charged-particle density shows a smooth increase with $\sqrt{s_{\mathrm{NN}}}$ for both pp and AA collisions. The dependence of $\frac{2}{\langle N_{part} \rangle} \cdot \langle \frac{dN_{ch}}{d\eta} \rangle$ on $\sqrt{s_{\mathrm{NN}}}$ follows a power-law behavior of the form $\mathrm{a} \cdot \mathrm{s}^b$, with b = 0.155 ± 0.004 for AA collisions and b = 0.103 ± 0.002 for pp collisions. This indicates that the charged-particle multiplicity increases more steeply with $\sqrt{s_{\mathrm{NN}}}$ in nucleus-nucleus collisions compared to proton-proton collisions. Additionally, the results from p–Pb and d–Au collisions align with the curve for pp collisions, implying that the significant increase seen in AA collisions cannot be solely attributed to multiple collisions among participants.
The right panel of Fig. 1.7 shows the relationship between $\frac{2}{\langle N_{part} \rangle} \cdot \langle \frac{dN_{ch}}{d\eta} \rangle$ and $\langle N_{part} \rangle$ as measured by ALICE in pp, p–Pb, and Pb–Pb collisions. According to the wounded nucleon model [58], the production of particles in soft processes, which occur more frequently than hard processes and are characterized by low momentum transfer, depends on the number of participant nucleons rather than the number of binary collisions. While a flat trend of $\frac{2}{\langle N_{part} \rangle} \cdot \langle \frac{dN_{ch}}{d\eta} \rangle$ would be expected as a function of $\langle N_{part} \rangle$, the charged-particle multiplicity shows a pronounced decreasing trend with $\langle N_{part} \rangle$ as one moves from central collisions (high $\langle N_{part} \rangle$) to peripheral collisions (low $\langle N_{part} \rangle$), exhibiting a slope of 1.8. In the context of soft probes, the wounded nucleon model predicts that their production should depend on N_{part}, suggesting no correlation with charged-particle multiplicity is expected. This trend is consistent across various colliding systems and centre-of-mass energies.

Identified hadron abundances: chemical freeze-out temperature

As detailed in Section 1.2.1, when the transition temperature is reached during the evolution of the heavy-ion collision, the system enters the hadronization phase. The microscopic

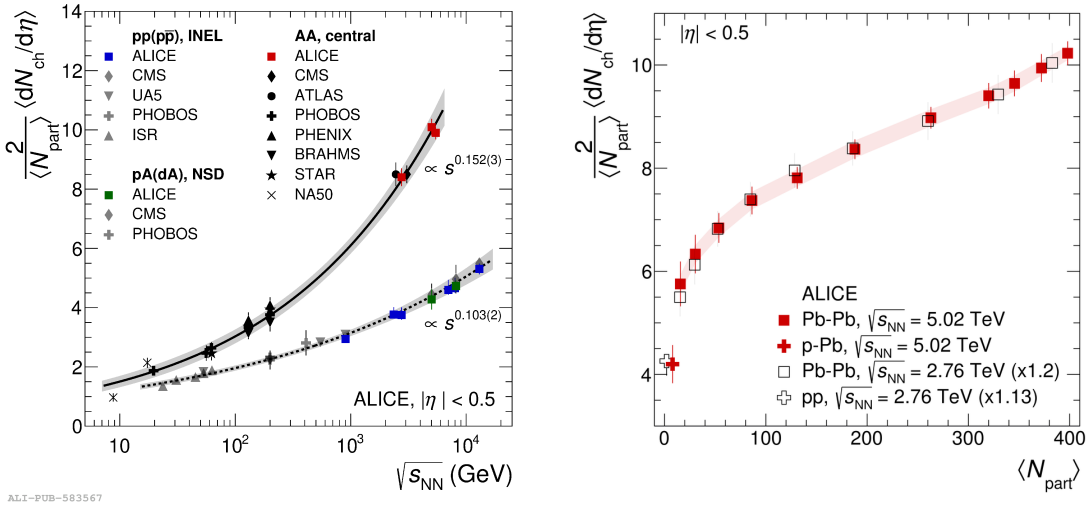

Figure 1.7: (*Left.*) Charged-particle multiplicity at midrapidity as a function of the centre-of-mass energy per nucleon pair $\sqrt{s_{\mathrm{NN}}}$ for various colliding systems. The lines are power-law fits to data, and the bands represent the uncertainties on the extracted dependencies [48]. (*Right.*) Charged-particle multiplicity at midrapidity as a function of $\langle N_{part} \rangle$ for various colliding systems [59].

description of this non-perturbative process, where numerous quarks and gluons combine to produce thousands of final-state hadrons, is highly complex. The relative abundances of various hadron species resulting from hadronic collisions are effectively described by the Statistical Hadronization Model (SHM). This model is founded on the premise that the system is in thermal and chemical equilibrium at the point of chemical freeze-out [10]. Particularly, the resulting hadrons are treated as a gas of non-interacting hadrons and resonances, described by a grand-canonical ensemble. In this framework, the energy and quantum numbers (baryon number, electric charge, and strangeness) of the system are conserved globally.

The SHM can determine the abundance N_i of different hadron species i in terms of the temperature T, volume V and chemical potential μ_i as:

$$N_i(T, V, \mu_i) = \frac{g_i V}{2\pi^2} \int_0^\infty \frac{p^2 dp}{e^{(E-\mu_i/T)} \pm 1} \tag{1.7}$$

where g_i denotes the spin degeneracy, the chemical potential $\mu_i = \mu_B + \mu_s + \mu_{I_3}$ is defined for each particle species as the sum of the quantum numbers multiplied by their respective chemical potentials and the $\pm$ sign is necessary to differentiate between Bose-Einstein and Fermi-Dirac statistics for bosons and fermions, respectively. Deviations from the grand-canonical description can be introduced by adding parameters to account for potential incomplete thermalization of the strange quarks (γ_s). In the context of proton-proton collisions, the γ_s parameter is typically found to be significantly less than one. More details on the SHM can be found in Section 1.4.1.

The yields of various identified hadron species measured by the ALICE Collaboration in the 10% most central Pb–Pb collisions at $\sqrt{s_{\mathrm{NN}}} = 5.02$ TeV are shown in Fig. 1.8. These data are compared with predictions from several versions of the SHM, including

THERMUS [60, 61], SHARE [62, 63, 64], Thermal-FIST [65, 11] and GSI-Heidelberg [66]. These models operate under different assumptions regarding the equilibrium conditions and/or conservation laws at the chemical freeze-out stage. By conducting a simultaneous fit to the observed yields, these models extract the values for the chemical freeze-out temperature T_{ch}, the volume V and the baryochemical potential μ_B, treating these as free parameters. Notably, these models successfully reproduce the measured particle abundances over a wide range, spanning nine orders of magnitude, with a resulting reduced χ^2 ranging from 2.4 to 0.9, depending on the model. Among the various parameters, the baryochemical potential μ_B has been set to approximately zero in most models, reflecting the nearly equal abundances of particles and antiparticles at LHC energies. An exception is the GSI-Heidelberg model, in which μ_B is treated as a free parameter and determined to be zero with an uncertainty of around 4 MeV. The chemical freeze-out temperature obtained from the fitting process is $T_{ch} \sim 156$ MeV, with uncertainties ranging between 2 to 3 MeV and minimal discrepancies ($\pm$ 1 MeV) across different implementations of the SHM. Another parameter estimated from the SHM fit is the fireball volume for one unit of rapidity at chemical freeze-out, which is approximately 4500 fm^3 according to the results from SHARE, Thermal-FIST, and GSI-Heidelberg. In contrast, the fits using THERMUS yield a significantly larger volume due to the inclusion of an excluded-volume (similar to Van der Waals) correction [67], which accounts for short-range repulsive interactions among hadrons, resulting in a lower particle density within the fireball.

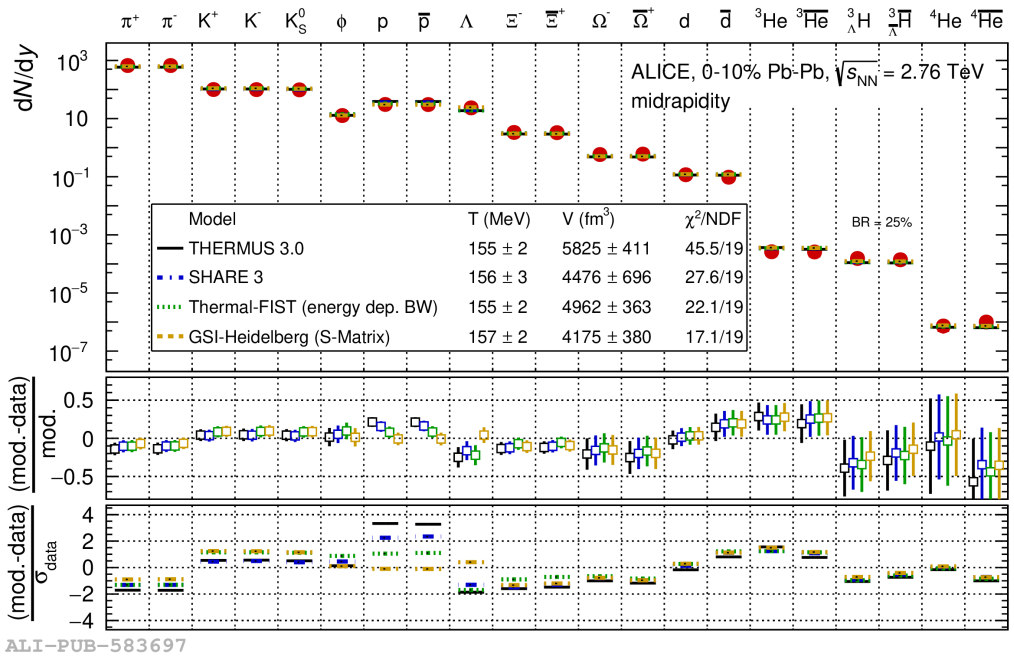

Figure 1.8: Measured multiplicity per unit of rapidity of different hadron species and light nuclei compared to SHM fits from THERMUS, SHARE, Thermal-FIST, and GSI-Heidelberg. Differences between the model calculations and the measured yields are shown in the bottom panels [48].

Hadrochemistry - Strangeness enhancement

Hadrochemistry refers to the measurement of the relative abundances of different particle species produced in collisions. The production of strange hadrons has always been crucial for studying QGP matter. Net strangeness is absent in the initial state of the nucleonic or nuclear collision, as the colliding beams consist of ordinary matter containing only valence u and d quarks, while s quarks exist only as sea quarks. Therefore, all valence strange quarks observed in the final-state hadrons are produced during the collision. Furthermore, since the s quark is the third lightest quark, with a mass between the two lighter quarks (u, d) and the three heavier ones (c, b, t), its production has a relatively low energy cost, leading to an abundant generation of strange quarks.
Starting from the fact that the bare mass of the s quark is approximately 100 MeV, which is well below the minimum temperature compatible with QGP existence ($T \gtrsim$ 160 MeV), Johann Rafelski and Berndt Müller [4] proposed that an increased relative production of strange hadrons in heavy-ion collisions compared to pp interactions could serve as a potential signature of QGP formation. During hadronization, the high density of strange quarks leads to an enhanced production of strange baryons, especially multi-strange baryons, relative to minimum bias pp collisions. This phenomenon, known as *Strangeness Enhancement* (SE), was first experimentally observed at the CERN SPS, as shown in Fig. 1.9 [5]. In this figure, the enhancements are defined as particle yields normalized by the number of participating nucleons in the collision and divided by the yields observed in proton-beryllium collisions. If the production were simply due to a superposition of nucleon-nucleon collisions, the yield would lie on a straight line at unity. However, the results show a clear strangeness enhancement pattern in Pb–Pb collisions, with the enhancement increasing with the number of s quarks in the hadron, reaching its peak for the triple-strange Ω^- baryon.
The topic of strangeness enhancement will be further discussed in Chapter 2.1.

Thermal freeze-out temperature and radial flow

At chemical freeze-out, the abundances of particles become fixed, but elastic scatterings between particles continue. These interactions only cease at thermal freeze-out, whose occurrence defines the momentum distribution of the primary particles. In the assumption that the fireball is a static thermal source in equilibrium, the low-p_{T} region of the transverse momentum spectra of produced particles can be well-described by a Maxwell-Boltzmann distribution. The slope parameter, T_{fo}, represents the thermal freeze-out temperature:

$$\frac{1}{p_{\mathrm{T}}}\frac{dN}{dp_{\mathrm{T}}} = \frac{1}{m_T}\frac{dN}{dm_T} \propto exp\big(-\frac{m_T}{T_{fo}}\big) \tag{1.8}$$

where $\mathrm{m}_T = \sqrt{p_{\mathrm{T}}^2 + m^2}$ is the transverse mass. Accordingly, the transverse mass spectra of different particle species follow an exponential law with the same slope parameter T_{fo}, a phenomenon referred to as m_T-scaling [69]. This scaling holds remarkably well in small systems at low p_{T} [48]. However, in AA collisions, deviations from m_T-scaling emerge due to pressure gradients in the fireball, which drive the collective expansion of the system. This collective motion, referred to as *radial flow*, means that particles experience both random motion (similar to proton-proton collisions) and collective movement caused by

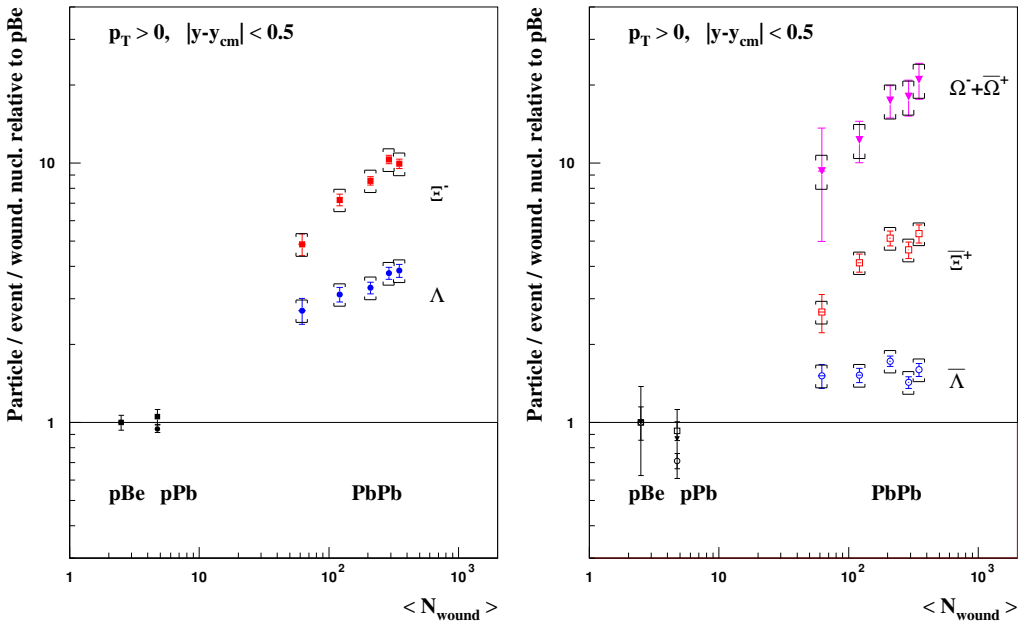

Figure 1.9: Particle yields normalized to the number of participating nucleons in the collision, and divided by the observed yield in proton-beryllium collisions as a function of the average number of participating nucleons [68].

the expanding fireball. As a result, the slope parameter T_{fo} must account for the effects of radial flow:

$$T_{fo} = T_{kin} + \frac{m}{2}\langle\beta_T\rangle^2 \tag{1.9}$$

In this equation, the second term represents the kinetic energy associated with radial flow, where $\langle\beta_T\rangle$ denotes the average transverse velocity of particles. Consequently, the average p_{T} of particles increases with their mass. Additionally, $\langle\beta_T\rangle$ varies across the transverse plane, defined as the plane perpendicular to the beam direction (z-axis): pressure gradients become stronger towards the periphery of the fireball, leading to a more pronounced radial flow. As a result, particles emitted from the outer regions exhibit steeper transverse mass spectra than those from the central region of the collision. The relationship between $\langle\beta_T\rangle$ and the transverse radius r of the fireball can be expressed as:

$$\beta_T(r) = \beta_s\left(\frac{r}{R}\right)^n \tag{1.10}$$

where R is the maximum radius of the fireball, β_s is the maximum radial flow velocity at the surface and n is the exponent of the flow velocity profile, typically found to be around 1 - 2 in the literature [70]. The p_{T} spectra of different particles can be accurately modeled by the Boltzmann-Gibbs Blast-Wave function [70], which accounts for both thermalization and radial expansion effects. This function allows calculations of p_{T} spectra based on parameters such as temperature, radial velocity and flow profile. Particles are assumed to be produced in a fluid element with a local temperature T_{kin} and then boosted radially with the velocity $\beta_T(r)$ of the fluid cell. However, it is important to note that the Blast-Wave model is an approximation. A more accurate description of the particle production spectra requires hydrodynamic calculations that account for the QGP phase

and the hadronization process.
The ALICE Collaboration measured the correlation between T_{kin} and $\langle\beta_T\rangle$ in Pb–Pb collisions at $\sqrt{s_{\rm NN}}$ = 2.76 [71] and $\sqrt{s_{\rm NN}}$ = 5.02 TeV [72]. The results in Fig. 1.10, are presented for various centrality classes. The values of $\langle\beta_T\rangle$ and T_{kin} are obtained by simultaneously fitting the $p_{\rm T}$ spectra of pions, kaons, and protons. The average transverse velocity, $\langle\beta_T\rangle$, increases with centrality, reaching a maximum value of $\langle\beta_T\rangle = 0.663 \pm 0.003$ in the 5% most central collisions. Conversely, the thermal freeze-out temperature, T_{kin}, decreases with centrality, dropping to a minimum of $T_{kin} = 0.090 \pm 0.003$ GeV in the 5% most central collisions. These findings suggest a faster expansion of the fireball in more central collisions, due to the larger system size, and a delayed thermal freeze-out occurring at lower temperatures. Notably, no significant differences were observed between the results for the two different LHC energies.

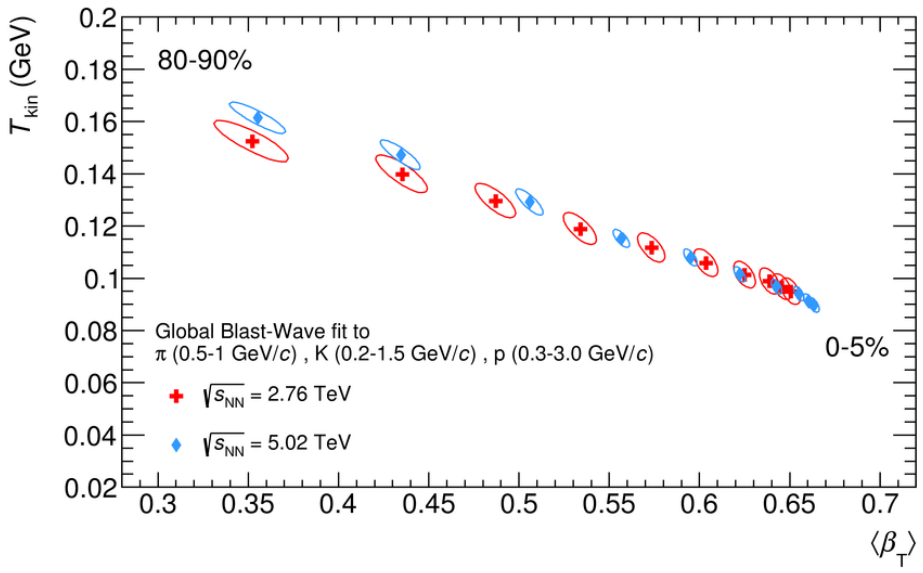

Figure 1.10: Average expansion velocity and kinetic freeze-out temperature T_{kin} obtained from the simultaneous Boltzmann-Gibbs Blast-Wave fit to pions, kaons, and protons spectra measured in Pb–Pb collisions at $\sqrt{s_{\rm NN}}$ = 2.76 and 5.02 TeV [72]. The correlated 1σ uncertainties, comprehensive of statistical and systematic uncertainty, are shown as ellipses.

Azimuthal anisotropy: elliptic flow

Radial flow is the dominant collective motion in central heavy-ion collisions. However, in non-central collisions, where two nuclei collide with a non-zero impact parameter, the overlapping region becomes asymmetric, leading to additional anisotropies in particle emission and momentum distribution. These anisotropies are formed before the system reaches the critical temperature and undergoes hadronization, making anisotropic flow sensitive to the early, hot phase of quark-gluon plasma evolution. The final azimuthal distribution of emitted particles can be expressed using the azimuthal Fourier coefficients of the transverse momentum spectrum [73]:

$$E\frac{d^3N}{dp^3} = \frac{1}{2\pi}\frac{d^2N}{p_{\mathrm{T}}dp_{\mathrm{T}}dy}\big(1 + 2\sum_{n=1}^{\infty} v_n cos[n(\phi - \Psi_n)]\big) \tag{1.11}$$

where p_{T} is the transverse momentum, y the rapidity, ϕ the azimuthal angle of the particle's momentum and Ψ_n is the symmetric plane of the n-th harmonic, which is an estimator of the reaction plane. The coefficients v_n

$$v_n = \langle cos[n(\phi - \Psi_n)]\rangle \tag{1.12}$$

are referred to as differential flow. The first coefficient, v_1, is known as *direct flow*. In central collisions (with zero impact parameter), the azimuthal distribution is isotropic, resulting in the v_n coefficients being equal to zero. In non-central collisions, the characteristic almond-shaped overlap region between the colliding nuclei creates a pressure gradient along the reaction plane. This collective motion is called *elliptic flow* and contributes to the v_2 coefficient. Thus, the measurement of these v_n coefficients is crucial, as they are connected to the initial geometric conditions and allow the characterization of the QGP in terms of viscosity.
The ALICE Collaboration measured the elliptic flow v_2 of identified charged-particles in Pb–Pb collisions at $\sqrt{s_{\mathrm{NN}}} = 5.02$ TeV in several centrality classes as reported in Fig. 1.11. The v_2 coefficient increases as centrality decreases, consistent with the expectation that the initial geometric anisotropy is more pronounced in peripheral collisions. This provides further evidence that the geometry of the collision primarily governs the development of flow coefficients. However, in very peripheral collisions (50–60% and 60–70% centrality), the shorter system lifetime and lower density constrain the development of v_2. For $p_{\mathrm{T}} <$ 2 GeV/c, the elliptic flow of $\pi^{\pm}$, $K^{\pm}$, $(p + \overline{p})$, ϕ, K^0_S, and $(\Lambda + \overline{\Lambda})$ shows a clear mass ordering, with lighter particles exhibiting a larger elliptic flow than heavier ones. This mass-ordering effect is attributed to the influence of radial flow which pushes higher-mass particles towards higher momenta. In the intermediate-p_{T} region (3 – 8 or 10 GeV/c), two distinct trends appear depending on whether the particles are mesons or baryons. Notably, baryons exhibit a larger v_2 than mesons. This supports the notion that hadron formation involves the combination of multiple quarks from the medium, with each quark contributing to the overall v_2 of the hadron [74]. Moreover, this suggests that the flow originates at the partonic level rather than during the hadronization stage.

High p_{T} hadrons and jet quenching

The dominant production mechanism for high-p_{T} hadrons, which include particles containing heavy quarks and other massive particles, is the fragmentation of high-p_{T} partons. These particles are particularly interesting to study because hard scatterings between quarks and gluons, occur only in the early stages of a collision. For high-p_{T} or high-mass particles to reach the detector, they must pass through the medium produced in the collision, losing energy along the way. As a result, they become sensitive probes of the properties of the QGP. One way to study the energy loss of partons as they propagate through the QGP is by measuring the *nuclear modification factor* R_{AA}, which is defined as the ratio of the p_{T}-differential yield in heavy-ion collisions to the yield in pp collisions, scaled by the average number of binary nucleon-nucleon collisions $\langle N_{coll}\rangle$:

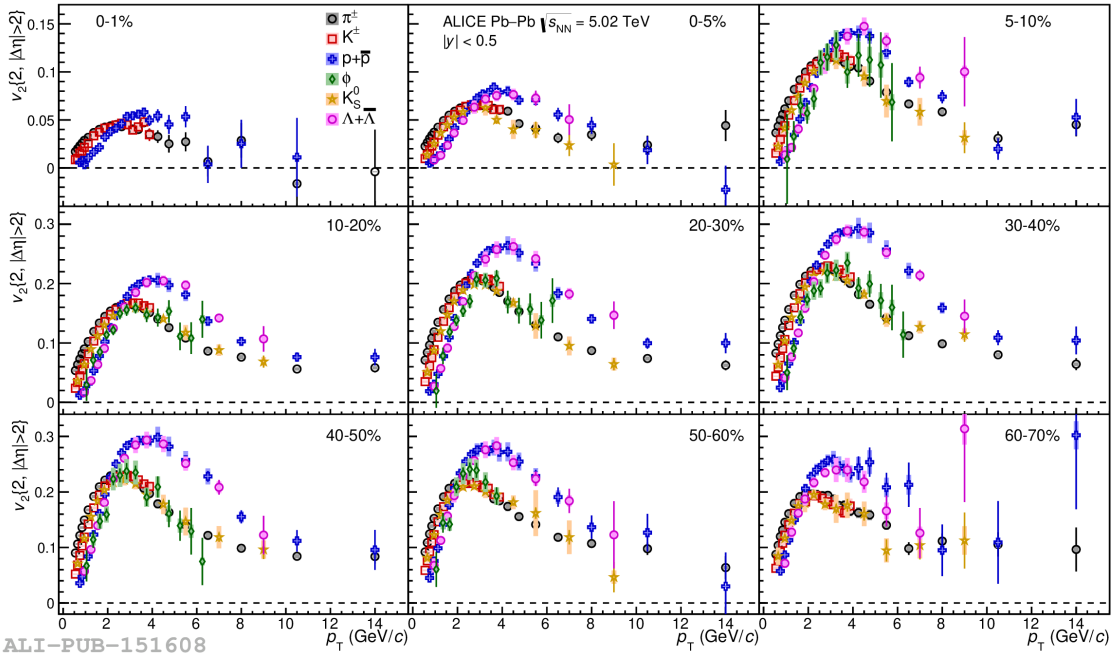

Figure 1.11: Elliptic flow coefficient v_2 of charged pions, charged and neutral kaons, protons, ϕ, mesons and hyperons as a function of p_{T} for several centrality classes in Pb–Pb collisions at $\sqrt{s_{\mathrm{NN}}} = 5.02$ TeV measured by the ALICE Collaboration [75].

$$R_{AA} = \frac{1}{\langle N_{coll} \rangle} \cdot \frac{d^2N^{AA}/dydp_{\mathrm{T}}}{d^2N^{pp}/dydp_{\mathrm{T}}} \tag{1.13}$$

In the absence of nuclear effects, where heavy-ion collisions can be treated as a simple superposition of nucleon-nucleon interactions, R_{AA} is expected to be 1. However, the energy loss in the QGP is expected to manifest as a suppression of high-p_{T} hadron yields relative to pp collisions, resulting in $R_{AA} < 1$ at high p_{T}. The left side of Fig. 1.12 shows the nuclear modification factor for various particle species in central Pb–Pb collisions at $\sqrt{s_{\mathrm{NN}}} = 5.02$ TeV, along with isolated photons as measured by the CMS experiment [48]. The plot indicates maximum suppression (a minimum) at p_{T} values around 6–7 GeV/c for all particle species, except for photons, which are "medium-blind probes" as they do not interact strongly with the QGP.

Another phenomenon that arises from parton energy loss in the QGP is known as *jet quenching*. Normally, in hadronization, jets are produced back-to-back in the transverse plane of the collision, forming what are called *di-jets*. However, the two parent partons that give rise to these jets may traverse different path lengths through the QGP, leading to varying degrees of energy loss. One parton may escape the medium and hadronize outside, producing a high-p_{T} jet, while the other parton loses significant energy while passing through the QGP, resulting in hadronization into lower-p_{T} particles as the medium absorbs the parton's energy.
The study of two-particle azimuthal correlation distributions can provide evidence for QGP formation in heavy-ion collisions. In each event, the hadron with the highest p_{T}

(likely produced near the surface of the QGP and directed outward) is considered the *trigger particle*, defining the position at $\phi = 0$. This trigger hadron undergoes a shorter path through the medium and experiences less suppression. Conversely, hadrons in the jets directed inward, through a longer path within the QGP, experience greater suppression. These are referred to as *associated particles* and their corresponding azimuthal angle, $\Delta\phi = \pi$, marks the away-side region. The suppression of the away-side peak is a clear signature of jet quenching. The right side of Fig. 1.12 shows the two-particle azimuthal correlations in pp, d–Au, and Au–Au collisions, as measured by the STAR Collaboration [76]. It highlights a significant suppression of the away-side peak in Au–Au collisions, an effect that is not observed in pp and d–Au collisions, where the creation of an extended QGP medium is not expected.

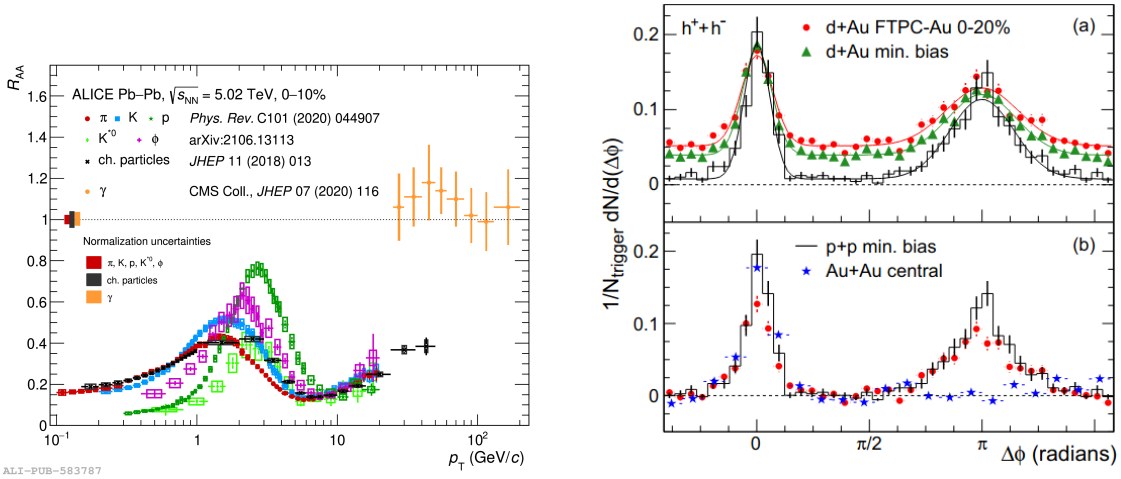

Figure 1.12: (*Left.*) Nuclear modification factor R_{AA} for various charged hadrons in central Pb–Pb collisions measured by ALICE. Isolated photons measured by CMS are also included for comparison [48]. (*Right.*) Top: Two-particle azimuthal correlations in pp and d–Au (minimum bias and central) collisions at $\sqrt{s_{\mathrm{NN}}} = 200$ GeV measured by the STAR Collaboration. Curves are fits. Bottom: Comparison of pedestal-subtracted yields in pp, d–Au, and Au–Au [76].

Quarkonium suppression

Due to their large mass, charm and beauty quarks are primarily produced in the hard scatterings between partons from the colliding hadrons. These processes occur on a timescale shorter than the typical formation time of the QGP, meaning that charm and beauty quarks endure through the medium's expansion, interacting with the free partons in the plasma. For this reason, the measurement of open heavy-flavor hadrons, which contain at least one heavy valence quark, and quarkonia, bound states of heavy quark-antiquark pairs $q\overline{q}$, serves as an excellent probe for studying the full space-time evolution of the QGP [77, 78]. The interaction potential between two quarks can be described by the Cornell potential:

$$V(r) = -\frac{\alpha}{r} + kr \tag{1.14}$$

where r is the radial distance between the quarks. The term $-\frac{\alpha}{r}$ represents the Coulomb interaction from gluon exchange between q and $\overline{q}$, while the term kr accounts for the confinement, based on a simple parametrization of non-perturbative effects. When quarkonium is in a color-charged medium like the QGP, the color charge responsible for binding the quark and antiquark is screened by the presence of free partons. This modifies the interaction potential: the confinement term vanishes, and the Coulomb part is "screened" by the high color density, resulting in:

$$V(r) = -\frac{\alpha}{r} \cdot e^{-\frac{r}{\lambda_d}} \tag{1.15}$$

where λ_d is the Debye screening radius, which represents the maximum distance over which two color charges can form a bound state in the QGP. The Debye screening length is inversely related to the temperature of the medium, and since the quarkonium radius is inversely proportional to its binding energy, quarkonium suppression is expected to increase as the temperature of the medium rises. Furthermore, excited quarkonium states (e.g., $\Psi(2S)$, $\Upsilon(1S)$, $\Upsilon(2S)$, and $\Upsilon(3S)$) have lower binding energies than the ground states (J/ψ and Υ(1S)), making them more susceptible to dissociation in the QGP. This leads to the concept of *sequential suppression* of quarkonium states in heavy-ion collisions [79, 80, 81, 82]. The dissociation of quarkonium manifests as a reduction in their production relative to pp collisions, quantified by the nuclear modification factor R_{AA}.
The left panel of Fig. 1.13 shows the R_{AA} for $\Upsilon(1S)$, $\Upsilon(2S)$ and $\Upsilon(3S)$ as a function of collision centrality, expressed in terms of the average number of participating nucleons $\langle N_{part} \rangle$, measured by the CMS experiment in Pb–Pb collisions at $\sqrt{s_{\mathrm{NN}}} = 5.02$ TeV [83]. The data indicate a clear pattern of ordered suppression, with stronger suppression from $\Upsilon(1S)$ to $\Upsilon(3S)$ as centrality increases, consistent with the sequential suppression model.
The right panel of Fig. 1.13 shows the R_{AA} of the J/ψ measured in heavy-ion collisions at different centre-of-mass energies as a function of charged-particle multiplicity. The data from NA50 [84] (green markers) and STAR [85] (light blue markers) show a clear decrease in R_{AA} with increasing multiplicity. However, the ALICE [48] results for Pb–Pb collisions at $\sqrt{s_{\mathrm{NN}}} = 5.02$ TeV (red markers) reveal that, at LHC energies, J/ψ suppression is less pronounced and its dependence on multiplicity is weaker. This is because, at higher energies, more heavy quarks are produced, increasing the likelihood of recombination between a quark from a dissociated $q\overline{q}$ pair and an antiquark from another dissociated pair. This phenomenon, known as *quarkonium regeneration* [48], suggests that a portion of charmonium production comes from the statistical recombination of charm and anti-charm quarks from unrelated hard scatterings. Quarkonium regeneration is expected to have a stronger impact on charmonium states compared to bottomonium, as it is driven by the number of heavy quark pairs produced in the collisions, which is smaller for bottom than for charm quarks.

1.3 Small hadronic collision systems

Other than Pb–Pb interactions, the LHC also provides proton-proton (pp) and proton-lead (p–Pb). These collisions are referred to as small systems due to the smaller size of the

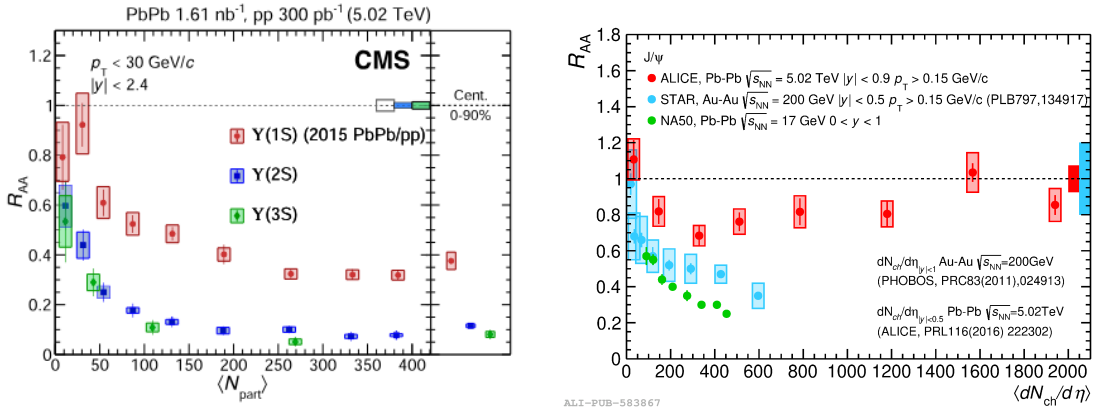

Figure 1.13: (*Left.*) Measured R_{AA} for Υ states as a function of $\langle N_{part} \rangle$ in Pb–Pb collisions at $\sqrt{s_{\mathrm{NN}}} = 5.02$ TeV by CMS [83]. (*Right.*) Measured nuclear modification factor R_{AA} for J/ψ as a function of the charged-particle multiplicity. The results of NA50 (SPS) [84], STAR (RHIC) [85] and ALICE (LHC) [48] are compared. For ALICE and STAR results, the selection $p_{\mathrm{T}} > 0.15$ GeV/c minimises the contribution of photoproduced J/ψ [48].

colliding objects (pp < p-A < AA) and the relatively limited size of the medium produced in these interactions. ALICE focuses on studying pp collisions because they serve as a reference point for comparisons in heavy-ion physics. Historically, it was believed that during pp collisions, partons would emerge without interacting with a dense, strongly interacting medium. Therefore, any differences observed between Pb–Pb and pp collisions could reveal the unique effects of the QGP medium present in heavy-ion collisions.
Recent surprising results from pp and p–Pb collisions, such as the observation of collective behaviors and a smooth transition in particle production from pp to Pb–Pb collisions, have obfuscated the lines between small and large systems. These findings have sparked a discussion about whether a unified explanation of particle production across all collision systems is possible, suggesting a continuous transition from microscopic QCD processes to the dynamics of an extended system as the QGP. Investigating these phenomena in small systems has now become a central aspect of the LHC physics program, particularly when comparing collisions that produce similar particle multiplicities to those seen in semi-central heavy-ion collisions.

Increased yield of strange hadrons

Historically, to estimate the strangeness enhancement effect, the production yields (per unit of rapidity) of hadron h in heavy-ion collisions were compared to those in pp interactions. To understand whether an increase in strange hadron production could also occur in small systems, it was recently decided to study the dependence of strange hadron production yields on charged-particle multiplicity, as it is an observable that can be defined across all colliding systems (pp, p–Pb, Pb–Pb).
The ALICE Collaboration observed that the ratios of strange hadron to charged pion yields increase with multiplicity, showing a smooth transition across different collision systems — starting unexpectedly in pp, continuing through p–Pb, and extending to Pb–Pb collisions — and different energy scales [1, 86, 72] as reported in Fig. 1.14. Further-

more, the steepness of this increase was found to correlate with the strangeness content of the hadron. This finding is remarkable, as different particle production mechanisms are expected to operate in each collision system. Historically, the enhanced production of strange hadrons in Pb–Pb compared to pp collisions was considered a signature of QGP formation. Since the analysis presented in this thesis aims to extend beyond the published results in pp collisions to better understand the mechanisms behind strangeness production, this topic will be detailed further in Section 2.1.

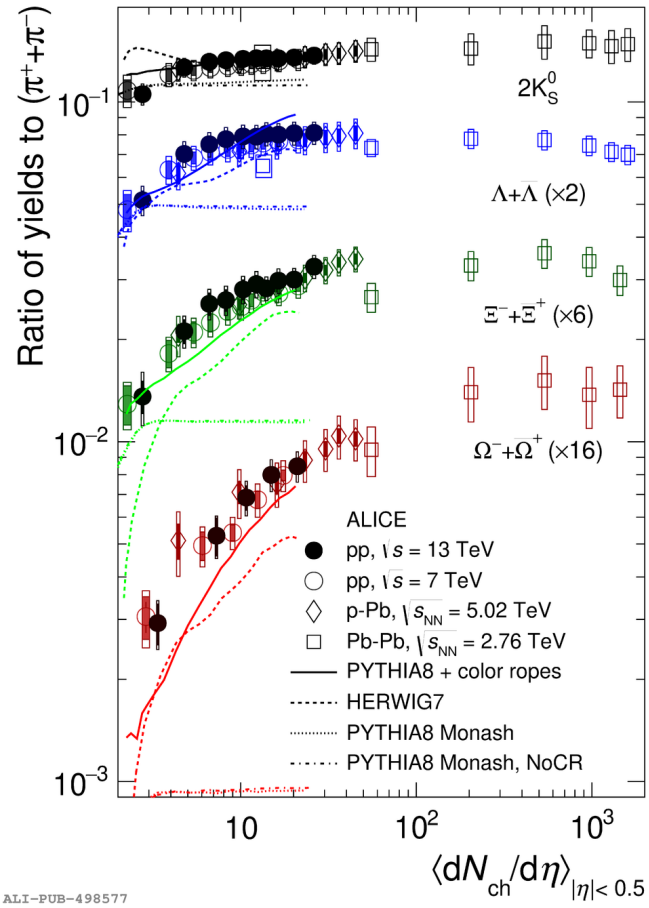

Figure 1.14: p_{T} integrated strange hadron yields ratios to charged pions ($\pi^+ + \pi^-$) as a function of $\langle dN_{ch}/d\eta \rangle$ measured in $|y| < 0.5$ [87].

Collectivity

In heavy-ion collisions, the development of collective behavior is linked to the formation of a strongly interacting QGP, where spatial anisotropies and correlations in the system are transferred into anisotropies in momentum space. Anisotropic flow coefficients have also been measured in small systems, revealing the presence of collective effects. Figure 1.15 presents measurements of the v_n coefficients using the two-particle cumulant method in pp, p–Pb, Xe–Xe and Pb–Pb collisions [88]. In large systems, a clear ordering of flow coefficients is observed, with $v_2 > v_3 > v_4$, along with a noticeable dependence of v_2 on multiplicity, reflecting the initial geometry of the colliding nuclei's overlapping region. At low multiplicities, the v_n values from Xe–Xe and Pb–Pb collisions align with those

from pp and p–Pb collisions, all showing a weak multiplicity dependence. Interestingly, a similar ordering of v_n is also observed in smaller collision systems, just like in the larger systems.

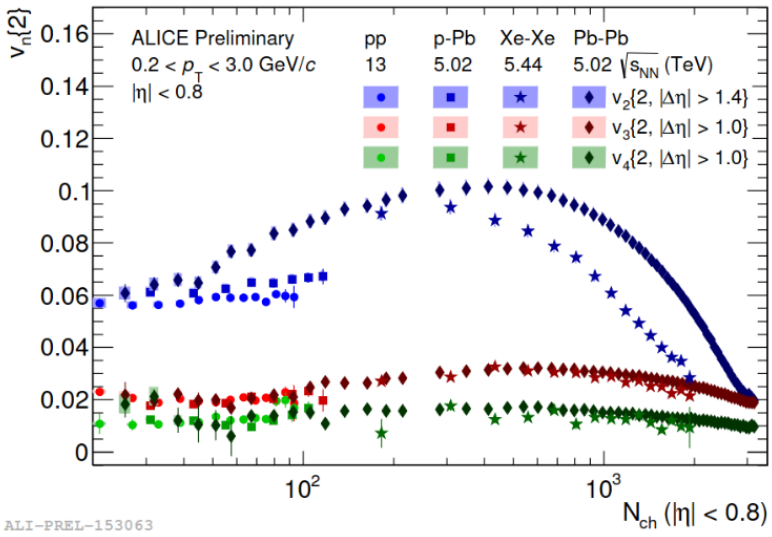

Figure 1.15: Multiplicity dependence of v_2, v_3 and v_4 measured using the two-particle cumulant method in small (pp and p–Pb) and large (Xe–Xe and Pb–Pb) collision systems by the ALICE Collaboration [88].

In addition to anisotropic flow coefficients, examining multi-particle correlations is essential for understanding the mechanisms behind particle production in high-energy collisions. Particles emitted from a collective system exhibit long-range correlations among multiple particles over a wide rapidity range, which result from their collective response to initial anisotropies. This phenomenon can be explored by analyzing azimuthal correlations, particularly the observed long-range structures in the two-dimensional $\Delta\eta$ - $\Delta\phi$ correlation functions. Here, $\Delta\eta$ and $\Delta\phi$ represent the differences in azimuthal angle ϕ and pseudorapidity η between the two particles. Figure 1.16 displays the two-dimensional two-particle correlation functions for (a) 2.76 TeV Pb–Pb collisions and (b) 5.02 TeV p–Pb collisions, as measured by the CMS experiment [89]. The peak located at ($\Delta\eta$, $\Delta\phi$) = (0,0) is attributed to particles produced within the same jet or arising from the decay of a common hadron. Long-range correlations are evident at $\Delta\phi \sim 0$ and $\Delta\phi \sim \pi$ (referred to as the double ridge), which stem from the elliptic flow generated by the hydrodynamic evolution in non-central nucleus-nucleus interactions. This contributes a $\cos(2\phi)$ modulation to the two-particle correlation function across a wide $|\eta|$ range, with the azimuthal structure reflecting the medium's response to the initial transverse geometry. Notably, similar collective effects have been observed in small collision systems, though their underlying causes may differ from those in heavy-ion collisions. For instance, a double-ridge structure was also detected in high-multiplicity pp collisions but not in minimum bias pp collisions [90]. The observation of the ridge across different collision systems, provided the multiplicity density is sufficiently high, indicates that a primordial collective evolution may already exist in smaller systems.

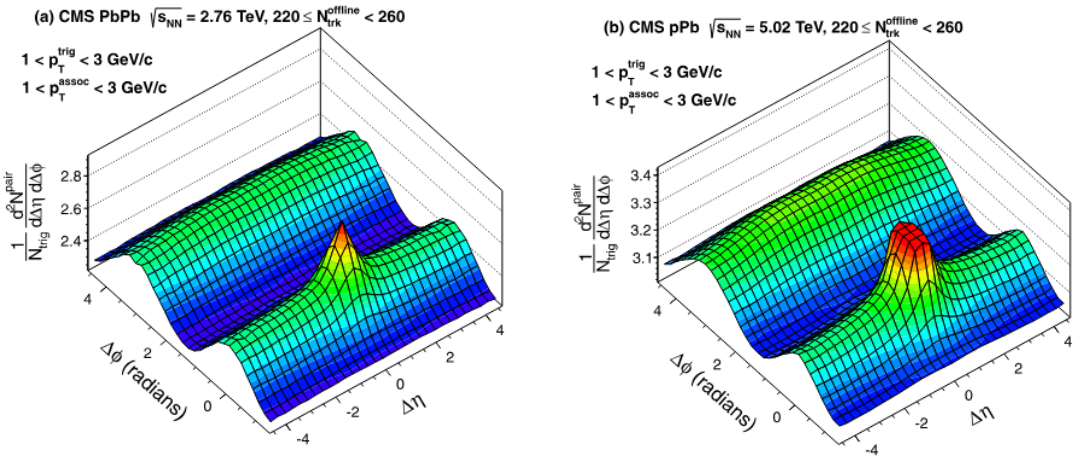

Figure 1.16: The 2D two-particle correlation functions for (a) 2.76 TeV Pb–Pb and (b) 5.02 TeV p–Pb collisions for pairs of charged-particles with $1 < p_{\mathrm{T}}{}^{trig} < 3$ GeV/c and $1 < p_{\mathrm{T}}{}_{ass} < 3$ GeV/c within the $220 < \mathrm{N}_{trk}^{offline} < 260$ multiplicity bin [89].

Dynamics of particle production: hardening of the p_{T} spectra with increasing multiplicity

In heavy-ion collisions, the average transverse momentum $\langle p_{\mathrm{T}} \rangle$ tends to increase with the centrality of the interaction, following a pattern of mass ordering. This phenomenon is attributed to the radial collective expansion of the strongly interacting medium produced during the collision, which accelerates the momenta of particles within a unified velocity field. Interestingly, a similar effect has been observed in pp and p–Pb collisions [91], where the increase in $\langle p_{\mathrm{T}} \rangle$ correlates with the multiplicity of charged-particles generated in the event, as illustrated in Fig. 1.17. The underlying mechanisms for this behavior in smaller collision systems remain to be fully clarified, particularly regarding whether the observed hardening of the spectra can be solely explained by radial flow or if alternative mechanisms might account for the mass-dependent rise of $\langle p_{\mathrm{T}} \rangle$ across different collision systems.

To further explore the dependence of the spectral shape on charged-particle multiplicity, the p_{T}-differential ratio between baryon and meson yields in small systems has been measured [14]. This is illustrated by the p/π and $\Lambda/\mathrm{K}^0_{\mathrm{S}}$ ratios, shown in Fig. 1.18 for pp (left), p–Pb (center) and Pb–Pb (right) collisions. In heavy-ion collisions, the enhancement observed is interpreted through a hydrodynamic model as a consequence of radial flow, which affects heavier particles more strongly, leading to an enhancement at intermediate p_{T} and a corresponding depletion at low p_{T}. Figure 1.18 shows that in all collision systems, these ratios exhibit an increase at intermediate p_{T} values ($\langle p_{\mathrm{T}} \rangle \sim 3$ GeV/c), which becomes more pronounced at higher charged-particle multiplicity. These results indicate that the production of identified strange particles is closely correlated with final-state charged-particle multiplicity and remains independent of the collision system and energy at the LHC.

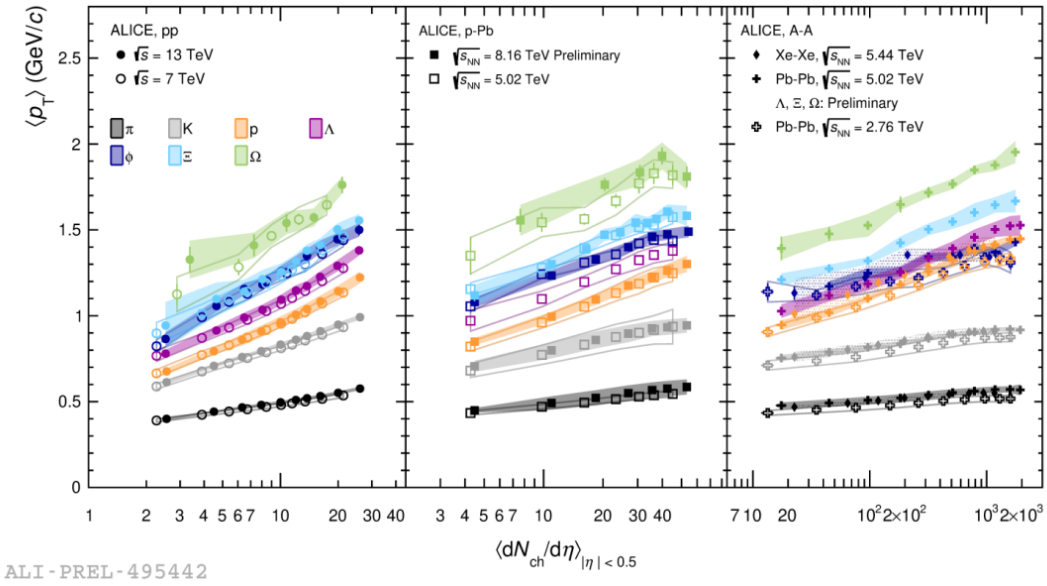

Figure 1.17: Average transverse momentum $\langle p_{\mathrm{T}} \rangle$ as a function of the charged-particle multiplicity at midrapidity $\langle dNch/d\eta \rangle$ in pp (left panel), p–Pb (central panel) and heavy-ion (Pb–Pb, Xe–Xe in the right panel) collisions.

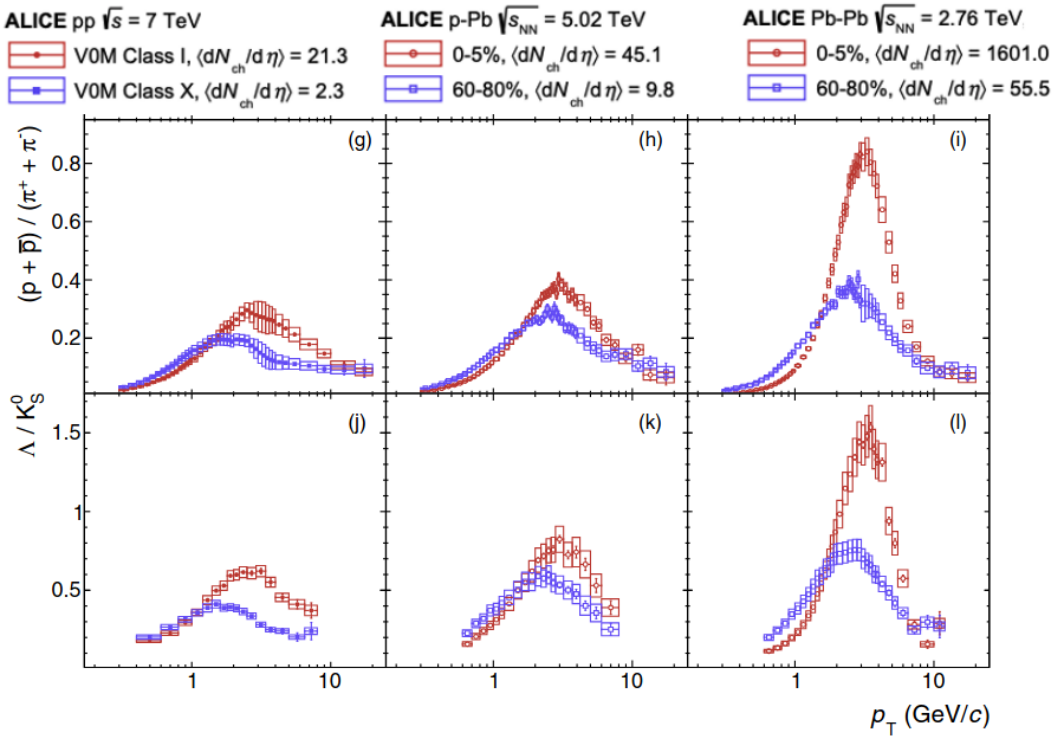

Figure 1.18: Transverse momentum dependence of p/π and $\Lambda/\mathrm{K}^0_{\mathrm{S}}$ ratio in pp (left), p–Pb (center) and Pb–Pb (right) collisions for high- and low- multiplicity classes (red and blue markers respectively) [14].

1.4 Hadronization mechanisms

The process leading a system of quarks to form the hadronic final state is called hadronization. As noted earlier (see Section 1.1), perturbative QCD is suitable for describing hard processes with large momentum transfer Q^2, but it is inadequate for modeling soft interactions (low Q^2). Consequently, low-p_{T} particle production is more effectively described using phenomenological models. Therefore, theoretically explaining hadron production in general requires a phenomenological modeling of the hadronization process, as its inherently non-perturbative nature prevents us from performing reliable quantum chromodynamics (QCD) ab initio calculations. Numerous models have been developed, which can be broadly categorized into macroscopic (statistical) models and microscopic (string, transport, etc.) models. Additionally, hybrid models exist, which apply different approaches — microscopic or macroscopic — depending on the specific regime being considered.
Currently, there is no single theoretical framework that comprehensively describes hadron-hadron and subsequent parton-parton interactions across all kinematic and energy ranges. Developing models that can provide a consistent and satisfactory explanation of all results from various collision systems is generally quite challenging.

This section will describe several models currently used in small systems, with a focus on the implementation of strangeness production, which is the main subject of this thesis.

1.4.1 Statistical models: canonical suppression

As discussed earlier in Section 1.2.2, hadron production in central ultra-relativistic heavy-ion collisions is successfully described by statistical hadronization models based on the grand-canonical ensemble. The primary concept behind these models is to utilize a minimal set of thermodynamic variables to define an ensemble of observables that best represents the chemical makeup of the system. For a statistically equilibrated system, the fundamental component is the partition function. Particle production within the large volume created by AA collisions can be described using a grand-canonical (GC) formalism. In this approach, the relative abundance of each hadron species in the final state is derived from the derivative of the system's partition function, as defined in Eq. 1.7.
The statistical hadronization framework can also be applied to smaller systems, such as pp or e^+e^-collisions. In these systems, the conservation of a quantum number, like strangeness, must be enforced locally following the canonical formulation.

$$\langle N_s \rangle - \langle N_{\bar{s}} \rangle = 0 \qquad N_s - N_{\bar{s}} = 0 \tag{1.16}$$

(*Left.*) Grand-Canonical strangeness conservation condition: the average is taken across an ensemble of physical systems, meaning across independent collisions. (*Right.*) The strangeness conservation law requires exact strangeness conservation in each individual collision.

Note that only in very large systems, such as central heavy-ion collisions, the grand-canonical conservation condition is satisfied, since the relative violation of the strangeness conservation law vanishes like $1/\sqrt{N_s}$ [92].

Canonical conservation of quantum numbers places substantial constraints on the phase space available for particle production, resulting in what is known as *canonical suppression* (CS). To capture deviations from the grand-canonical approach, which relies on the chemical freeze-out temperature (T_{ch}), baryochemical potential (μ_B) and correlation volume (V_c) — the volume within which strangeness is strictly conserved —, an additional parameter is introduced to account for the incomplete thermalization of strange quarks (γ_S). In non-equilibrium scenarios, this parameter typically has value below one.
A statistical hadronization model that combines grand-canonical conservation of the baryon quantum number with canonical conservation of strangeness successfully reproduces the primary characteristics of the strangeness enhancement factor, as discussed in Refs. [93, 94]. In this model, the observed decrease in the strangeness enhancement factor with lower $\langle N_{part} \rangle$ is interpreted as a suppression effect due to the canonical conservation of strangeness. The saturation value reached at higher $\langle N_{part} \rangle$ signals the thermodynamic limit, where the grand-canonical ensemble becomes valid. In this context, the dependencies of the strangeness enhancement factor on both energy and strangeness content largely arise from the reduced thermal phase space for strangeness production in pp collisions, which is more pronounced at lower collision energies and higher strangeness content. Furthermore, using the canonical ensemble, the SHM model is able to predict the yield of light-flavor particles across different collision systems with a precision exceeding 20% [26, 25]. Figure 1.19 illustrates the yield ratios of (a) p/π, (b) K/π, (c) ϕ/π, (d) Λ/π, (e) Ξ/π and (f) Ω/π as a function of charged-particle multiplicity $\langle dN_{ch}/d\eta \rangle$, calculated in the γ_SCSM with $V_c = 3dV/dy$, using thermal parameters determined for each multiplicity bin through χ^2 minimization. The γ_SCSM is an extension of the standard canonical statistical model (CSM) [26], which proposes that the chemical freeze-out temperature may vary with multiplicity, with smaller systems potentially exhibiting higher chemical freeze-out temperatures. This would imply earlier decoupling of inelastic hadronic reactions, possibly driven by stronger radial flow gradients in smaller collision systems [95]. Such behavior is also seen in the decoupling of (pseudo)elastic hadronic reactions, marked by the kinetic freeze-out temperatures extracted from blast-wave fits to the p_{T} spectra of pions, kaons, and protons [14, 96]. Higher T_{kin} values observed in pp collisions ($T_{kin} \approx 170$ MeV) compared to central Pb–Pb collisions ($T_{kin} \approx 100$ MeV) seem to suggest an earlier decoupling of these reactions in smaller systems, which typically corresponds to a shorter lifetime for the hadronic phase. The γ_SCSM incorporates the partial equilibration of strangeness into the CSM by introducing a strangeness saturation factor, γ_S. This model is used to perform thermal fits to the yields of π, K, $\mathrm{K^0_S}$, ϕ, p, Λ, Ξ and Ω particles, as measured by the ALICE Collaboration in different centrality bins in pp collisions at 7 TeV, p–Pb collisions at 5.02 TeV, and Pb–Pb collisions at 2.76 TeV. The fit parameters include temperature (T), volume per rapidity unit (dV/dy) and the strangeness saturation parameter γ_S. All conserved charges in the CSM fit are set to zero: $B = Q = S = 0$. The values of the extracted parameters are shown in Ref. [26] as a function of charged-particle multiplicity. The chemical freeze-out temperature obtained from the γ_SCSM model decreases as charged-particle multiplicity increases, with a maximum of approximately $T \sim 175$ MeV for the lowest multiplicity bins in pp collisions and a minimum of about $T \sim 155$ MeV for the highest multiplicities in Pb–Pb collisions. The strangeness saturation parameter γ_SCSM increases with multiplicity, approaching the equilibrium value of unity around $\langle \mathrm{d}N_{\mathrm{ch}}/\mathrm{d}\eta \rangle \sim 100$ - 200, suggesting that chemical equilibrium for strangeness is only

achieved in sufficiently large systems. Canonical suppression effects on hadron yields diminish significantly for higher multiplicities, becoming almost negligible when $\langle \mathrm{d}N_{\mathrm{ch}}/\mathrm{d}\eta \rangle \geq 50$. As shown in Fig. 1.19, the γ_SCSM effectively captures the trends observed in the data, with the exception of the p/π ratio, which is consistently overestimated at the 2σ level, and ϕ meson. In summary, the statistical model approach — incorporating exact conservation of baryon number, electric charge and strangeness, along with partial chemical equilibration of strangeness — offers a framework to describe strangeness enhancement as a function of multiplicity across various collision systems. However, it falls short in accurately capturing the proton-to-pion and ϕ-to-pion yield ratios across these systems, highlighting that a fully consistent description of all particle yield ratios has yet to be achieved.

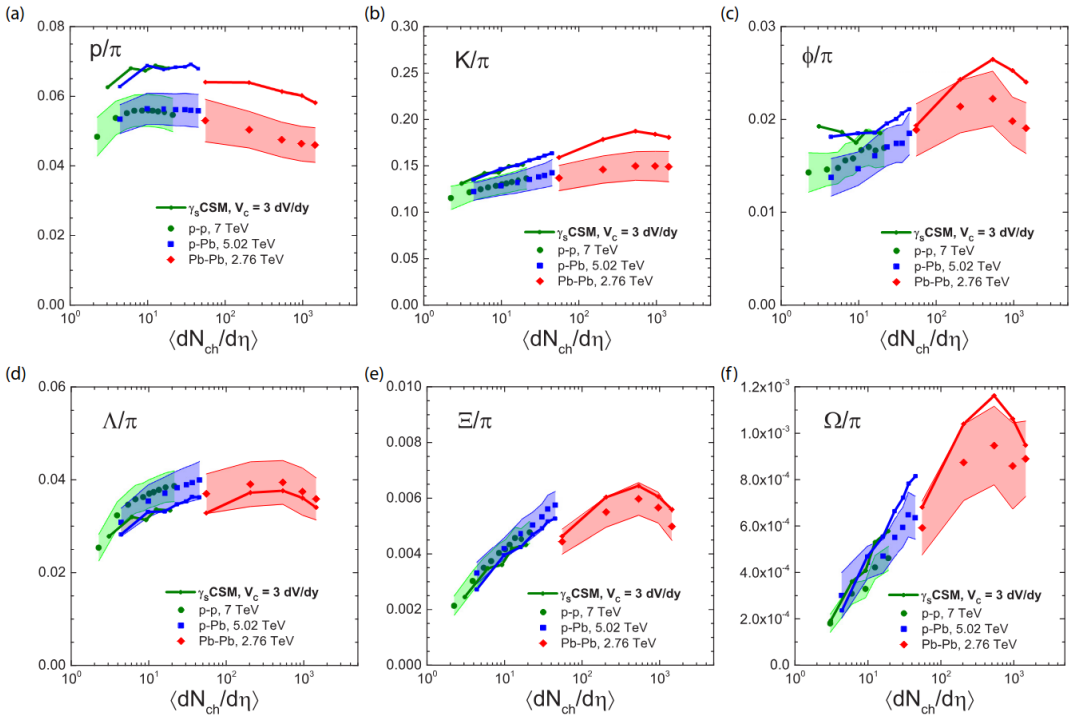

Figure 1.19: The yield ratios (a) p/π, (b) K/π, (c) ϕ/π, (d) Λ/π, (e) Ξ/π and (f) Ω/π are shown as a function of charged-particle multiplicity $\langle dN_{ch}/d\eta \rangle$, as calculated in the γ_SCSM with $V_c = 3dV/dy$, using thermal parameters obtained for each multiplicity bin via χ^2 minimization. The green circles, blue squares, and red diamonds represent the ratios measured by the ALICE Collaboration in pp (7 TeV), p–Pb (5.02 TeV) and Pb–Pb (2.76 TeV) collisions, respectively. Shaded bands correspond to the experimental uncertainties associated with each measurement [26].

1.4.2 Microscopic phenomenological models for pp collisions

Microscopic phenomenological models are constructed from a range of components that describe the physics from very short distance scales up to the characteristic scale of hadron formation and decay. PYTHIA8 [20, 97, 98] is the most widely used Monte Carlo particle generator at the LHC, employing a linear parametrization for the QCD interaction

potential at large distances, while using an approximate perturbative QCD approach for short - distance hard scattering processes. The model includes high-tension "strings" that represent a linearly growing potential with the separation between two quarks, simulating the gluon field between color charges. Beyond a certain distance, governed by the string tension ($k_0 \sim 1$ GeV/fm), it becomes energetically favorable to fragment the string into a quark-antiquark pair and subsequently into hadrons. To accurately model the multiplicity distribution observed in hadronic collisions, multiple parton-parton interactions (MPIs) are essential. In the original Lund string model [99], each MPI hadronizes independently from the others, leading to an increase in multiplicity without affecting the average transverse momentum or relative flavor composition. Although the model lacks dynamic interactions among different strings, color reconfiguration is handled through the color reconnection (CR) mechanism [22]. This mechanism, which occurs after the parton shower stage, reorganizes the resulting quarks according to all SU(3) - allowed configurations, reconnecting final-state partons in a way that minimizes the total string length.
This model does not accurately capture strangeness enhancement as a function of multiplicity, as illustrated in Fig. 1.14, which compares the evolution of (multi-)strange hadron-to-pion yield ratios with predictions from various phenomenological models for pp collisions at $\sqrt{s} = 13$ TeV. Specifically, the predictions from PYTHIA8.2 [98] (Monash 2013 tune [97]) underestimate these ratios and show no multiplicity dependence. The discrepancy increases with higher strangeness content, and no substantial improvement is observed even when allowing color reconnection [22] between partons. However, an improved description is achieved in PYTHIA8 when overlapping strings are allowed to interact, forming so-called "color ropes" [23]. This color-rope mechanism increases the effective string tension, enhancing the production rates of strange particles and baryons. As seen in Fig. 1.14, the inclusion of color ropes allows PYTHIA8 to qualitatively better describe strangeness enhancement with multiplicity. Yet, notable differences from the data remain, especially for the Ω/π ratio, which is underestimated at low multiplicities, and for the Λ/π ratio, which is overestimated in high-multiplicity pp collisions. While the color ropes approach provides a more realistic qualitative description of strangeness enhancement, it still falls short in predicting the multiplicity dependence of the proton-to-pion yield ratio, as shown in Fig. 1.20. In this case, PYTHIA8 with color ropes overestimates the ratio and predicts an increase with multiplicity, a trend that is not observed in the experimental data.
The results in Figures 1.14 and 1.20 are also compared with predictions from the HERWIG7 model [21, 100], which utilizes a clustering-based approach to hadronization that includes baryon ropes — a reconnection mechanism that increases the likelihood of baryon formation. HERWIG7 exhibits greater deviations from the data than PYTHIA8 with ropes, particularly for the Ξ/π ratio at low values of $\langle dN_{ch}/d\eta \rangle$. Additionally, it underpredicts the Ω/π ratio across the entire multiplicity range and overpredicts the $\mathrm{K}^0_\mathrm{S}/\pi$ ratio in the lowest multiplicity intervals ($\langle dN_{ch}/d\eta \rangle \leq 3$). However, unlike the implementations of PYTHIA8 presented, HERWIG7 successfully reproduces the p/π ratio (see Fig. 1.20). Overall, none of the presented Monte Carlo generators can consistently and quantitatively describe the multiplicity dependence of hadron-to-pion ratios, suggesting that our current understanding of particle production in pp collisions remains incomplete. The microscopic origins of strangeness enhancement in small collision systems thus remain an open question.

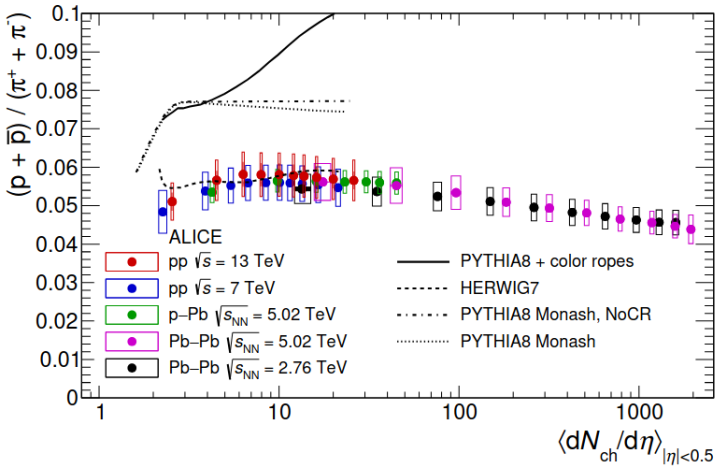

Figure 1.20: Proton-to-pion integrated yield ratios as a function of charged-particle multiplicity $\langle dN_{ch}/d\eta \rangle$ measured at midrapidity in pp, p–Pb, and Pb–Pb collisions at different centre-of-mass energies. Black lines represent predictions from different MC generators for pp collisions at $\sqrt{s} = 13$ TeV [87].

1.4.3 Core-corona models

The core-corona model was initially developed to describe collisions involving heavy nuclei [101]. In this framework, the system produced in a heavy-ion collision is divided into two distinct regions: a *core*, with high energy density where a deconfined medium forms, and a *corona*, a peripheral, lower-density region where nucleon-nucleon collisions occur. Hadronization in the core proceeds thermally, while in the corona, particles are produced via string breaking. In this model, the main mechanism of hadron production is thought to gradually shift from string fragmentation at low multiplicities to statistical hadronization at high multiplicities. For intermediate multiplicities, final hadron production results from a combination of both processes. As multiplicity rises, the high-density core region, where matter is largely thermalized, is expected to expand. Consequently, hadrons originating from thermalized matter come to dominate the final hadron yields. The core-corona model has also been applied to smaller collision systems, such as p–Pb and pp collisions, within the EPOS LHC event generator [102]. In small collision systems, strings located in low-density regions form the corona and undergo standard hadronization, whereas strings in high-density regions form the core and undergo collective hadronization. As demonstrated in Ref. [1], EPOS LHC provides a reasonable description of the K^0_S/π ratio but overestimates the strangeness enhancement with increasing multiplicity for the Λ, $\Xi^{\pm}$ and $\Omega^{\pm}$ baryons. The ratios of these baryons to pions are underestimated at lower multiplicities, specifically when $\langle dN_{ch}/d\eta \rangle$ is below 20, 15 and 7, respectively.

Recently, the core-corona model has been incorporated into the Dynamical Core-Corona Initialization (DCCI) framework [103, 104], which simultaneously addresses the dynamics of both the core (equilibrium) and corona (non-equilibrium) regions. In this model, initial partons are generated using PYTHIA8 or its heavy-ion extension, PYTHIA8 Angan-

tyr [105]. Partons that undergo sufficient interactions with others are likely to form thermally equilibrated matter, while those with limited interactions remain non-equilibrated, and their hadronization is simulated using the string fragmentation model in PYTHIA8. Within the DCCI framework, the multiplicity dependence of multi-strange baryon production in both small and large collision systems is attributed to a gradual shift in the proportions of core and corona components as multiplicity rises. Figure 1.21 presents the particle yield ratios to charged pions at midrapidity as a function of charged-particle multiplicity in both pp and Pb–Pb collisions, compared with experimental data from ALICE. Results from PYTHIA8 for pp collisions and PYTHIA8 Angantyr for Pb–Pb collisions are also included. The figure shows a gradual increase in (multi-)strange hadron-to-pion ratios, with values approaching those predicted by string fragmentation at low multiplicity and converging to hydrodynamic predictions at high multiplicity. Overall, the core-corona model offers a framework to describe strangeness enhancement in small collision systems, though it does not fully reproduce the experimental data quantitatively.

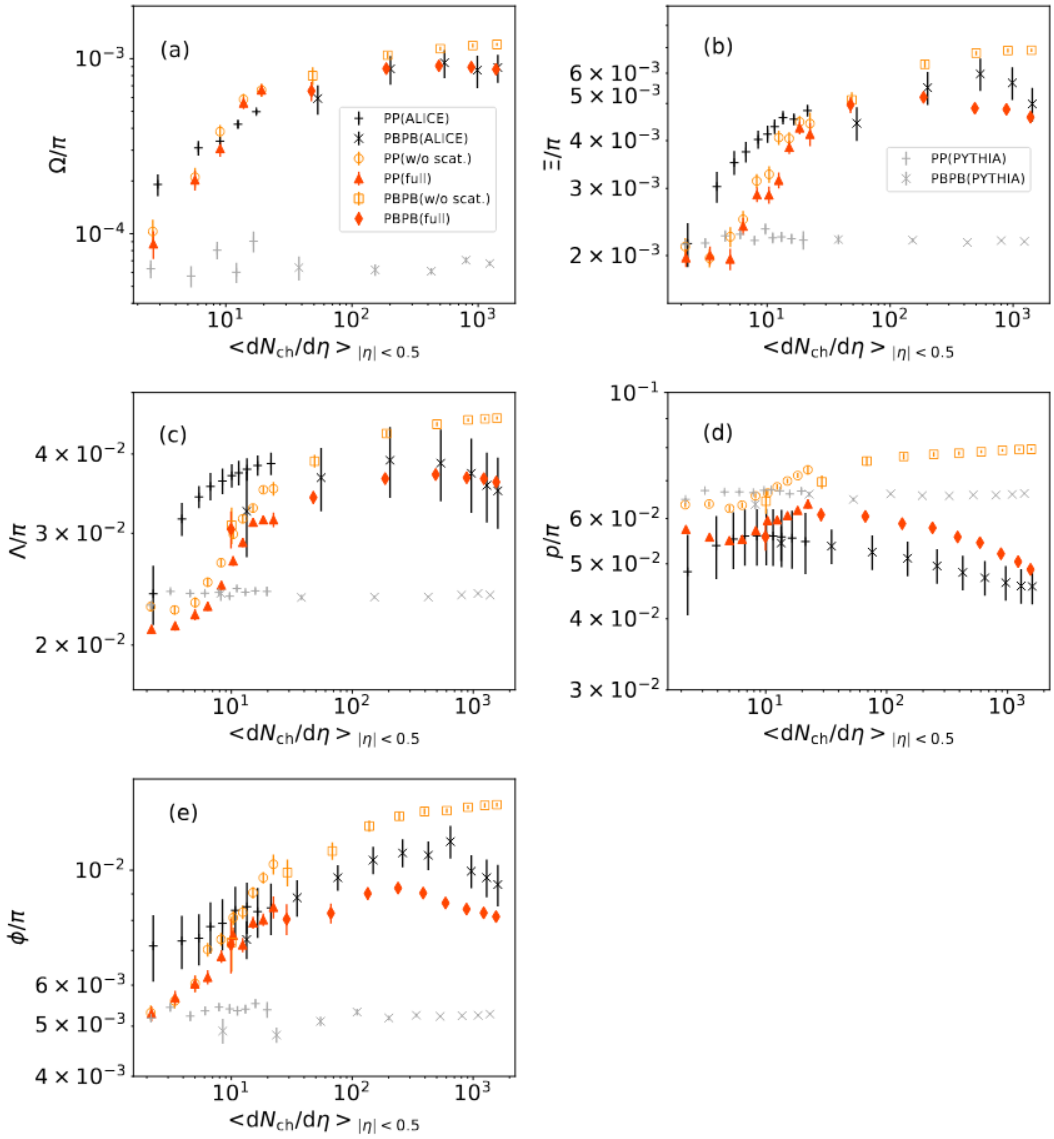

Figure 1.21: Particle yield ratios of (a) Ω ($\Omega^{\pm}$), (b) Ξ ($\Xi^{\pm}$), (c) Λ ($\Lambda+\overline{\Lambda}$), (d) protons (p + $\overline{p}$) and (e) ϕ to charged pions as a function of charged-particle multiplicity at midrapidity in pp and Pb–Pb collisions. The results from full DCCI2 simulations in pp collisions at $\sqrt{s}$ = 7 TeV (solid red triangles) and Pb–Pb collisions at $\sqrt{s_{\mathrm{NN}}}$ = 2.76 TeV (solid red diamonds) are compared with ALICE experimental data for pp (black plus signs) and Pb–Pb (black crosses) collisions. Results from PYTHIA8 in pp collisions (gray plus signs) and PYTHIA8 Angantyr in Pb–Pb collisions (gray crosses) are also shown for reference. Additionally, results without hadronic rescatterings are presented for pp (open orange circles) and Pb–Pb (open orange squares) collisions [104].

Chapter 2

Strangeness production in high energy collisions

This chapter aims to summarize the key concepts and findings related to the study of strange particle production in heavy-ion and hadronic collisions.

In the Standard Model [34], quarks are categorized into "light quarks" (up, down, strange) and "heavy quarks" (charm, bottom, top). Each particle is described by quantum numbers like spin, hypercharge, baryon number, strangeness and mass. The strangeness quantum number is defined as:

$$S = -(n_s - n_{\overline{s}}) \tag{2.1}$$

where n_s and $n_{\overline{s}}$ represent the number of strange quarks (s) and antiquarks ($\overline{s}$) in a hadron respectively. Since strangeness is conserved in strong and electromagnetic interactions but not in weak interactions, the lightest hadrons containing a strange quark cannot decay through the strong interaction and must instead decay via the much slower weak interaction. Hadrons that contain at least one strange quark but no heavier quarks are classified as kaons and hyperons. Kaons include the following states: $K^+(u\overline{s})$, $K^-(\overline{u}s)$, $K^0(d\overline{s})$ and $\overline{K^0}(\overline{d}\mathrm{s})$. Under the weak interaction, neutral kaons form two distinct physical eigenstates with significantly different lifetimes: K^0_S (short-lived, decays rapidly) and K^0_L (long-lived, decays more slowly), which are quantum combinations of K^0 and $\overline{K^0}$. Hyperons consist of: the Λ (uds), the triplet $\Sigma^+(uus)$, $\Sigma^0(uds)$ and $\Sigma^-(dds)$, the doublet Ξ^- (dss) and $\Xi^0(uss)$, the Ω^- (sss) and the corresponding antiparticles.
The study of strange hadrons production always played a pivotal role in the investigation of QGP matter [106]. Net strangeness is not present in the initial state of nucleonic or nuclear collision: two beams are constituted by ordinary matter only (u and d quarks) and s quarks exist as sea quarks. For this reason, all valence strange quarks contained in the detected final-state hadrons are created in the collision. Moreover, being the third lightest quark, the strange quark has a relatively low production energy cost, leading to its abundant generation.

2.1 Strangeness enhancement as a QGP signature

The motivation for studying strange particle production in the context of the QGP originates from an idea proposed by Johann Rafelski and Berndt Müller [4] in 1982. They suggested that an increase in strange hadron production in heavy-ion collisions, compared to pp interactions, could be a signature of QGP formation.
Strange hadron production can occur in two distinct environments:

- Hadron gas (HG): where quarks and gluons are confined and the degrees of freedom are hadronic.
- Quark-gluon plasma (QGP): where quarks and gluons are deconfined and the degrees of freedom are partonic.

Rafelski and Müller argued that in a partonic medium (QGP), the energy required to produce strange particle pairs is significantly lower than in a thermally equilibrated hadron gas. In an HG, strange hadron production comes primarily from pion reactions, but direct production ($\pi + \pi \rightarrow \pi + \pi$ + strange hadron + antiparticle) is limited by the strangeness and baryon number conservation. The reaction threshold, in this case, corresponds to two times the rest mass of the strange hadron: for the lightest strange mesons $K^{\pm} \sim 1$ GeV. On the other hand, indirect production mechanisms have lower thresholds but are still quite penalized by requiring two reactions in sequence: production of lighter hadrons ($\pi + N \rightarrow K + \Lambda$) followed by a reaction of these intermediate products to produce the heavier hadrons ($\pi + \Lambda \rightarrow K + \Xi$ and $\pi + \Xi \rightarrow K + \Omega$). In contrast, in a QGP, mechanisms such as gluon fusion dominate strange quark pair production. The Feynman diagrams corresponding to the lowest order in α_S for strangeness production are shown in Fig. 2.1: gluon fusion provides 80% of the $s\bar{s}$ pairs produced. In these reactions, the energy threshold, due to the partial chiral symmetry restoration, is roughly equal to twice the bare mass of the strange quark $\sim$ 200 MeV (see Fig. 1.1).

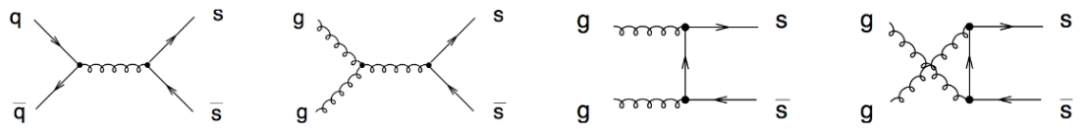

Figure 2.1: The lowest order Feynman diagrams for $s\bar{s}$ production in the QGP: the first is the fusion of two light quarks into a $s\bar{s}$ pair, while the other three are gluon fusion processes.

Another important factor is the equilibration time. Partonic reactions in a QGP equilibrate much faster than hadronic reactions. In an HG, equilibrium times for strange particles vary, taking around 30 fm for kaons and much longer for rare hyperons. In a QGP, typical temperatures of $\sim$ 200 MeV allow for equilibration times as short as $\sim$ 10 fm, comparable to the entire duration of a heavy-ion collision. However, this may not be enough to fully equilibrate the system.
Based on these considerations, multi-strange particles (Ξ^- and Ω^-) are much harder to produce in an HG than in a QGP, leading to higher production rates in the QGP. This

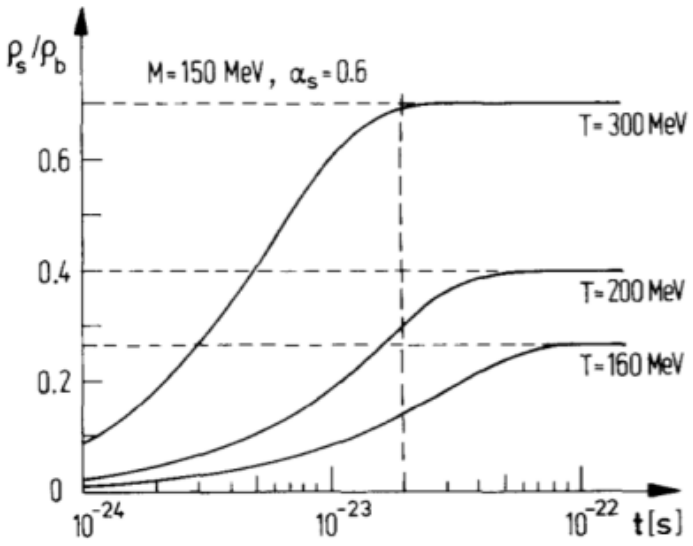

Figure 2.2: Time evolution of the relative strangeness to baryon density (ρ_s/ρ_b) produced in the plasma for various temperatures T, with $m_s = 150$ MeV and $\alpha_s = 0.6$. The vertical line corresponds to a time of ~ 6 fm/c [107].

phenomenon, known as *Strangeness Enhancement* (SE), was considered a key signature of QGP, marked by an overproduction of strange particles in heavy-ion collisions compared to pp collisions.

2.2 Measurement of SE: energy hierarchy problem

From an experimental perspective, it is important to establish how to compare production yields between HG and QGP scenarios, with the key challenge being the choice of an appropriate normalization method. Traditionally, yields have been normalized to the average number of participating nucleons in the collision ($\langle N_{part} \rangle$). Consequently, the experimental observable for strangeness enhancement in heavy-ion (AA) collisions, relative to pp interactions for a given hadron species h, is defined as:

$$E(h) = \frac{(dN^h/dy)^{AA}}{(dN^h/dy)^{pp}} \cdot \frac{N_{evt}^{pp}(\langle N_{part}^{pp} \rangle)}{N_{evt}^{AA}(\langle N_{part}^{AA} \rangle)} \tag{2.2}$$

where:

- $(dN^h/dy)^{AA}$ and $(dN^h/dy)^{pp}$ represent the production yields per rapidity unit of the hadron h in AA and pp collisions, respectively;
- N_{evt}^{AA} and N_{evt}^{pp} are the number of events for each colliding system;
- $\langle N_{part}^{AA} \rangle$ and $\langle N_{part}^{pp} \rangle$ are the average number of participating nucleons. This number is equal to two in the case of pp collisions and depends on the centrality in the AA collisions.

Strangeness enhancement has been experimentally observed across various heavy-ion systems and centre-of-mass energies, confirming the expectations mentioned earlier. Figure 2.3 compares measurements from different experiments: NA57 at CERN SPS (Pb–Pb and p–Pb collisions at $\sqrt{s_{\rm NN}} = 17.2$ GeV [5]), STAR at BNL RHIC (Au–Au collisions at $\sqrt{s_{\rm NN}} = 200$ GeV [6]) and ALICE at CERN LHC (Pb–Pb collisions at $\sqrt{s_{\rm NN}} = 2.76$ TeV [7]). The figure shows strangeness enhancement as a function of $\langle N_{part} \rangle$ for multi-strange hadrons $\Xi^{\pm}$ and $\Omega^{\pm}$. At all energy levels, the strangeness enhancement factor is greater than one and increases with $\langle N_{part} \rangle$, reaching saturation at LHC energies for $\langle N_{part} \rangle > 150 - 200$. The increase in the enhancement factor with $\langle N_{part} \rangle$ is more pronounced for the triple-strange $\Omega^{\pm}$ baryons compared to the double-strange $\Xi^{\pm}$ baryons, consistent to the interpretation of $s\bar{s}$ pair production in a deconfined medium.
Interestingly, the ratio of strange particle yields in heavy-ion collisions to those in elementary hadronic interactions appears unexpectedly higher at lower collision energies, a phenomenon referred to here as the *energy hierarchy problem*. If SE is driven by energy balance in a saturated medium, as previously described, one would not expect this enhancement to vary with $\sqrt{s}$, since the energy required to produce an $s\bar{s}$ pair (Q-value) remains constant across different $\sqrt{s}$ values. Conversely, if incomplete saturation at lower energies is responsible, one would anticipate greater enhancement with increasing $\sqrt{s_{\rm NN}}$. Thus, if strangeness production in elementary collisions is used as a baseline, different energies cannot be compared because strangeness production in low-energy pp collisions is much lower than that at higher energies.

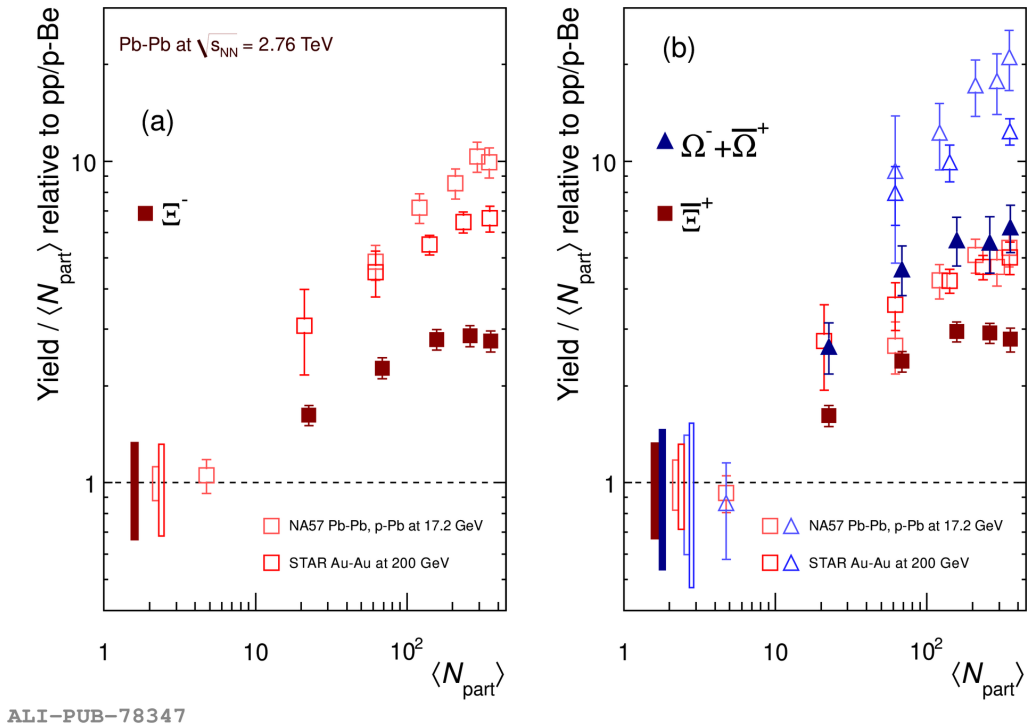

Figure 2.3: Normalized strange hadron yields in the rapidity range $|y| < 0.5$ as a function of the average number of participants to the collision $\langle N_{part} \rangle$, showing LHC (ALICE, full symbols), RHIC and SPS (open symbols) data [7].

This finding led to further investigations into strange particle production rates in elemen-

tary hadronic interactions over a range of centre-of-mass energies.
An improved observable would be the ratio of the yield of the particle under study to that of pions at the same centre-of-mass energy. Pion production serves as an effective baseline for soft-QCD activity within an event, enabling the comparison of relative strange particle yields across different $\sqrt{s_{\mathrm{NN}}}$ values. Figure 2.4 illustrates the hyperon-to-pion yield ratio as a function of $\langle N_{part} \rangle$ for various collision systems at both LHC and RHIC energies. The hyperon-to-pion ratios from pp to AA collisions increase by approximately 1.6 for $\Xi^{\pm}$ and 3.3 for $\Omega^{\pm}$, with no observable dependence on centre-of-mass energy. The saturation value reached at $\langle N_{part} \rangle > 150$ aligns well with predictions from thermal statistical models, as indicated by the solid line ($T_{ch} = 164$ MeV, [108]) and dashed line ($T_{ch} = 170$ MeV, [109]).

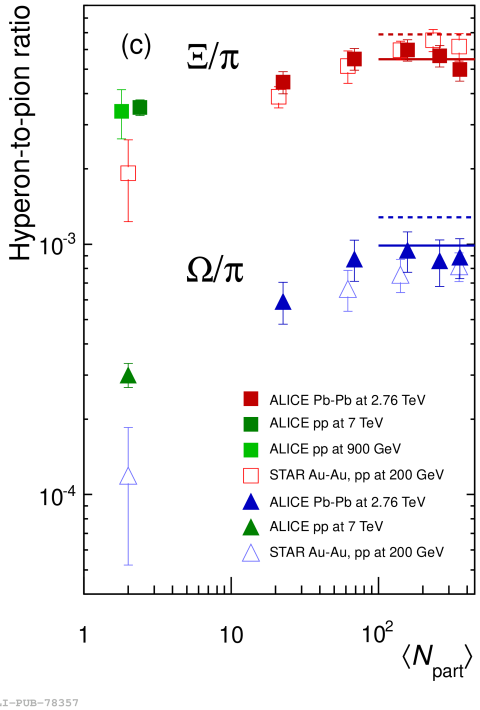

Figure 2.4: Hyperon-to-pion ratios as a function of $\langle N_{part} \rangle$ in for pp and AA collisions LHC and RHIC energies. The lines are predictions from statistical hadronization models with chemical freeze-out temperature $T_{ch} = 164$ MeV (full line, [108]) and $T_{ch} = 170$ MeV (dashed line, [109]) [7].

2.3 Strange hadron production across colliding systems

As discussed in Section 1.3, several effects in high-multiplicity pp and p–Pb collisions resemble those typically associated with the formation of a medium in thermal and kinematic equilibrium. In addition to confirming strangeness enhancement at the highest centre-of-mass energy [7, 17, 18], the ALICE Collaboration conducted a comprehensive study of strange hadron production relative to pions as a function of charged-particle multiplicity, defined as the total number of primary charged-particles in the central pseudorapidity range $|\eta| < 1$ [1, 86]. By examining this trend with respect to charged-particle

multiplicity, a quantity that can be measured across all collision systems, the Collaboration aimed to compare results from pp, p–Pb and Pb–Pb collisions, and to determine if SE occurs in pp collisions as well. Charged-particle multiplicity thus serves as a useful tool for comparing these systems, as it reflects both the final hadronic state and the initial energy involved in the collision.
Figure 2.5 displays the p_{T}-integrated yield ratios of strange hadron to pion ($\pi^+ + \pi^-$) yields as a function of charged-particle multiplicity at midrapidity for pp, p–Pb, Xe–Xe and Pb–Pb collisions over $5.02 < \sqrt{s_{\mathrm{NN}}} < 13$ TeV. A notable enhancement in strange-to-non-strange hadron production is observed with increasing particle multiplicity, beginning unexpectedly in pp collisions [1, 86, 14, 15], where it closely resembles the trend in p–Pb collisions in both absolute values and multiplicity-dependent behavior. At the highest multiplicities reached in pp, the yield ratios approach those observed in Pb–Pb collisions, where no significant change occurs beyond an initial modest increase. It is worth noting that the final-state average charged-particle multiplicity density varies over three orders of magnitude from low-multiplicity pp to central Pb–Pb collisions. Nevertheless, the particle ratios in pp and p–Pb collisions match closely at the same $\langle dN_{ch}/d\eta \rangle$, suggesting that in the LHC regime, strange particle production is independent of the colliding system or centre-of-mass energy; instead, charged-particle multiplicity appears to be strongly correlated to the measured ratios.

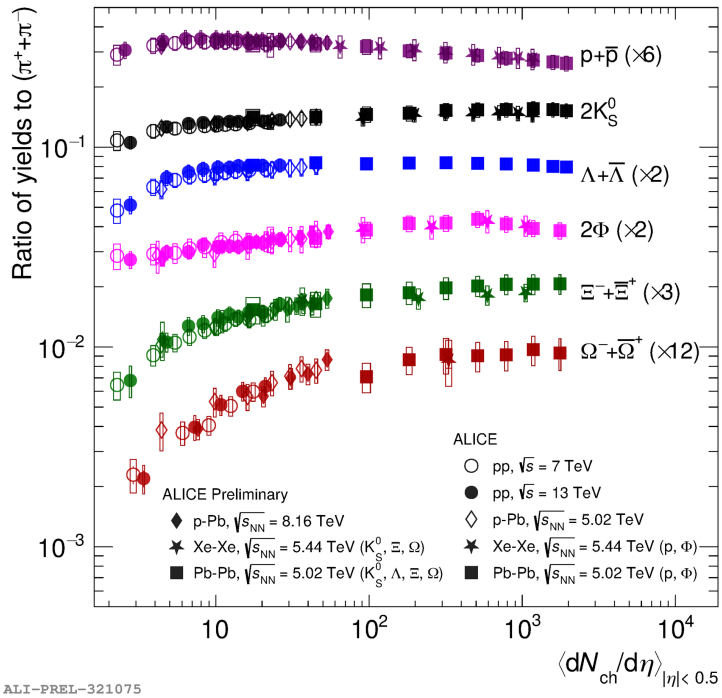

Figure 2.5: p_{T} integrated yields ratios to charged pions as a function of $\langle dN_{ch}/d\eta \rangle$ measured in $|y| < 0.5$ by ALICE in different colliding systems [110].

Notably, the relative production of the ϕ meson ($s\bar{s}$) rises with $\langle dN_{ch}/d\eta \rangle$ by an amount intermediate between that observed for $\mathrm{K}^0_{\mathrm{S}}$ and $\Xi^{\pm}$, behaving approximately as $S \sim 1.5$, indicating that ϕ production cannot be explained solely in terms of net strangeness or the number of strange quark constituents. In recent years, additional studies have been

conducted on ϕ meson production, some of which will be discussed in Section 2.3.1.
In addition, it is worth noting that the ratio between the yields of protons and pions (purple markers) decreases with multiplicity for $\langle dN_{ch}/d\eta \rangle \geq 20$, indicating that the increase of the strange hadron to pion yield ratios is not related to mass differences between numerator and denominator, but rather to the strangeness content in the hadron. A similar conclusion can be drawn looking at the left side of Fig. 2.6 that shows that the particle yield ratios $\Lambda/\mathrm{K}^0_\mathrm{S}$ and p/π do not change significantly with $\langle dN_{ch}/d\eta \rangle$, suggesting that the observed enhanced production rates of strange hadrons with respect to pions is predominantly not due to the difference in the masses of the hadrons nor to their meson/baryon nature.
Focusing on the yield ratios at low charged-particle multiplicity, the dependence on the strangeness content can be more clearly observed in Fig. 2.6, on the right, where the strange hadron to pion yields measured in pp collisions at $\sqrt{s} = 7$ TeV and in p–Pb collisions at $\sqrt{s_{\mathrm{NN}}} = 5.02$ TeV, divided by the values measured in the inclusive pp sample [1, 86] are shown. A significantly steeper increase with multiplicity for particles with larger strangeness content is observed.

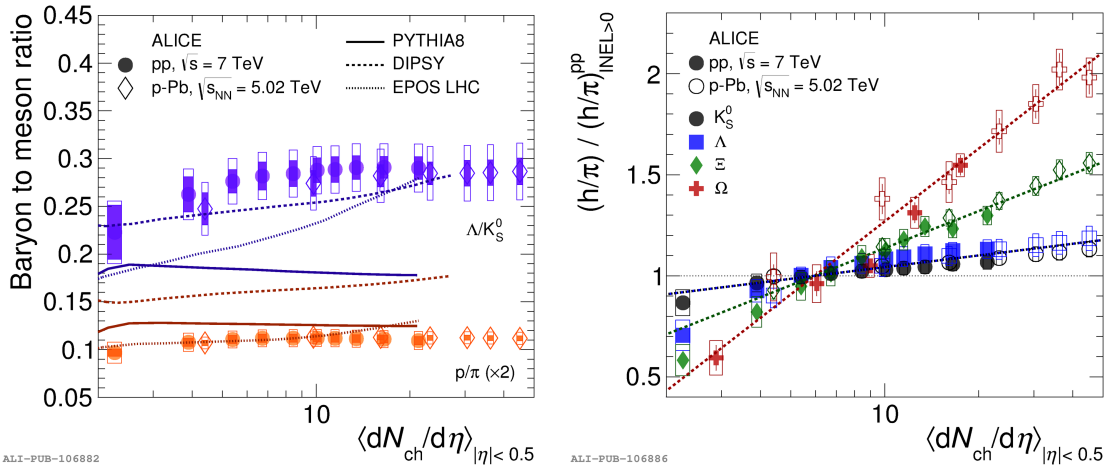

Figure 2.6: (*Left.*) Particle yield ratios $\Lambda/\mathrm{K}^0_\mathrm{S} = (\Lambda + \overline{\Lambda})/2\mathrm{K}^0_\mathrm{S}$ and $\mathrm{p}/\pi = (\mathrm{p}+\overline{\mathrm{p}})/(\pi^+ + \pi^-)$ as a function of $\langle dN_{ch}/d\eta \rangle$ [1, 86]. (*Right.*) Particle yield ratios to pions normalized to the values measured in the inclusive INEL$>$ 0 pp sample. The results are shown for pp and p–Pb collisions, both normalized to the inclusive INEL$>$ 0 pp sample [1, 86].

2.3.1 ALICE recent results in small systems

As discussed in the previous section, strangeness production increases with multiplicity across different energies and collision systems, starting unexpectedly with pp collisions, progressing through p–Pb, and reaching Pb–Pb collisions. Furthermore, this enhancement correlates with the hadron's strangeness content, being most pronounced for the triple-strange Ω. To explore the mechanisms of strangeness production in small collision systems, the ALICE Collaboration is conducting various studies on strange hadron production linked to either hard scattering processes or the underlying event (UE). Hard

processes are characterized by the formation of jets — streams of particles originating from a high momentum parton. In contrast, the underlying event comprises all processes aside from the primary partonic interaction. These include initial and final state radiation (ISR/FSR), where partons involved in scattering emit gluons before or after the interaction; Multi-Parton Interactions (MPI), which refer to additional partonic scatterings beyond the primary one; beam remnants, which are parts of the incoming beams that do not participate in any partonic scattering processes. The extent to which hard and soft processes contribute to strangeness production in pp collisions remains an open question. This can be explored using various techniques, including full-jet reconstruction and/or two-particle correlation methods.
The ALICE Collaboration has measured the yields of various (multi-)strange hadrons produced in jets, using jet-finding algorithms, and in the underlying event (UE) in pp collisions at $\sqrt{s} = 7$ and 13 TeV, as well as in p–Pb at $\sqrt{s_{\rm NN}} = 5.02$ TeV [28, 111]. Jet reconstruction is carried out using the anti-k_T algorithm [112, 113], which processes charged tracks with a jet resolution parameter of $\mathrm{R}_{res} = 0.4$ and requires $p_{\rm T}{}^{ch}_{jet} > 10$ GeV/c. Strange hadrons are considered to be within a jet cone if their distance from the jet axis in the $\eta - \phi$ plane is less than $\mathrm{R}_{cut} = \mathrm{R}_{res} = 0.4$. Strange hadrons not associated with hard scattering events, i.e., produced in the UE, are identified in a cone perpendicular to the jet cone with the same radius. The yield of strange hadrons produced in jets is then determined by subtracting the underlying event contribution from the yield measured within the jet cone. Figure 2.7 presents the density yields — i.e., yields normalized by the jet area $A = \pi R^2_{cut}$ — of $\mathrm{K}^0_{\rm S}$ and Λ ($\Lambda + \overline{\Lambda}$) on the left and right panels, respectively, measured within the jet cone (green markers), in the perpendicular cone (blue hollow markers) and in jets (red markers) as a function of transverse momentum in pp collisions at $\sqrt{s} = 7$ TeV. The plots also include the inclusive $\mathrm{K}^0_{\rm S}$ and Λ spectra (black markers), representing the spectra measured across all events, not limited to those with a reconstructed jet. For both particles, the yield spectrum in jets is harder than that observed in the perpendicular cone, as expected given the jet's association with hard scattering processes. Additionally, for $p_{\rm T} \geq 2$ GeV/c, the spectrum in jets aligns with that in the jet cone, suggesting that the underlying event's contribution to the jet cone diminishes as $p_{\rm T}$ increases.

In the past, it has been observed that if the ratio between baryon and meson spectra is calculated, an enhancement is present [1]. In this context, the same approach was applied, but dividing between jets, and the baryon-to-meson enhancement observed at intermediate $p_{\rm T}$ in pp collisions is examined by calculating the ratio of Λ to $\mathrm{K}^0_{\rm S}$ yields. Figure 2.8 shows that the ratio measured in the perpendicular cone (blue hollow markers) exhibits an enhancement around $p_{\rm T} \sim 3$ GeV/c, consistent with the one seen in the inclusive yield ratio (black markers). In contrast, the ratio in jets (red markers) does not display this enhancement. These findings suggest that jet fragmentation alone cannot fully account for strange particle production in hadronic collisions at LHC energies. Instead, they imply that the increase in the baryon-to-meson yield ratio at intermediate $p_{\rm T}$ values with multiplicity is likely driven by particle production within the underlying event.

These results do not provide insights into the multiplicity dependence of strange particle production inside and outside jets in pp collisions. However, the ALICE Collaboration

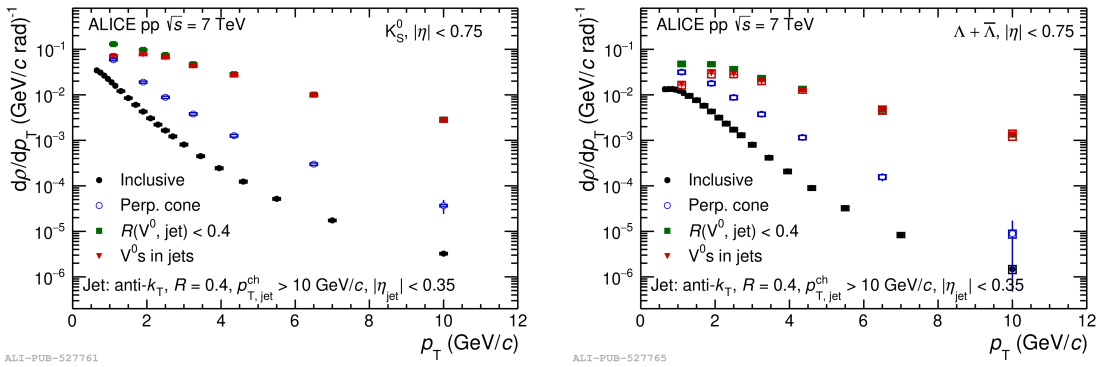

Figure 2.7: K^0_S (*left*) and $\Lambda + \overline{\Lambda}$ (*right*) density spectra as a function of the transverse momentum in pp collisions at $\sqrt{s} = 7$ TeV. The results are illustrated for inclusive K^0_S and Λ respectively in minimum bias events (black markers), in the underlying event (blue empty markers), in the jet cone (green markers) and in jets after the subtraction of the contribution from the underlying event (red markers) [28].

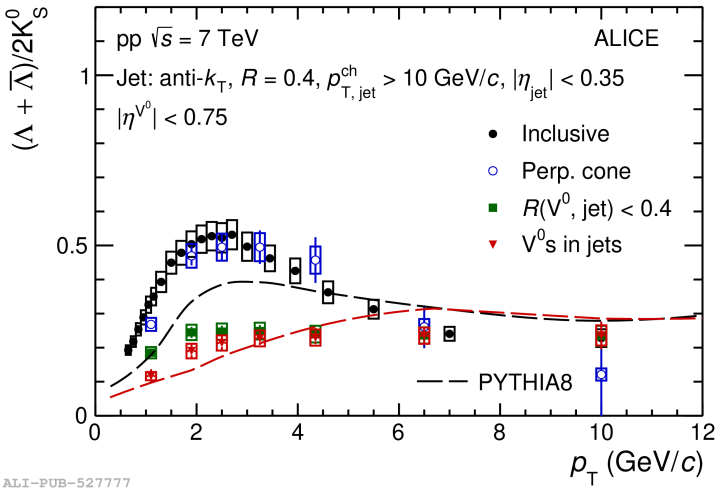

Figure 2.8: $(\Lambda + \overline{\Lambda})/K^0_S$ as a function of the transverse momentum in pp collisions at $\sqrt{s} = 7$ TeV. The results are illustrated for inclusive K^0_S and Λ respectively in minimum bias events (black markers), in the underlying event (blue empty markers), in the jet cone (green markers) and in jets after the subtraction of the contribution from the underlying event (red markers) [28].

recently measured Ξ and K^0_S yields in jets as a function of charged-particle multiplicity, using the angular correlation method [29]. This technique exploits the fact that particles produced in the near-side jet region have a small angular separation from the jet's trigger particle, identified as the particle with the highest transverse momentum in the event ($p_T > 3$ GeV/c). The angular distribution between the trigger particle and the associated strange hadron is analyzed in the ($\Delta\eta$, $\Delta\phi$) plane, which is divided into three regions: the *transverse-to-leading* region, representing out-of-jet production; the *toward-to-leading* region, serving as a proxy for near-side jet production; the *full inclusive* region, covering the entire angular correlation plane. The near-side jet contribution is determined

by subtracting the out-of-jet yield from the total yield in the toward-to-leading region. Figure 2.9 presents the K^0_S and Ξ yields per trigger particle and per unit of $\Delta\eta\Delta\phi$ on the left and right panels, respectively, as a function of charged-particle multiplicity at midrapidity. For both particles, the yields in the full region (blue markers) and in the transverse-to-leading region (green markers) increase with charged-particle multiplicity. Conversely, yields in the toward-to-leading region (red markers) exhibit only a slight dependence on multiplicity. Additionally, no energy dependence is observed, as results from pp collisions at $\sqrt{s} = 13$ TeV (open markers) and $\sqrt{s} = 5$ TeV (full markers) are consistent with each other.

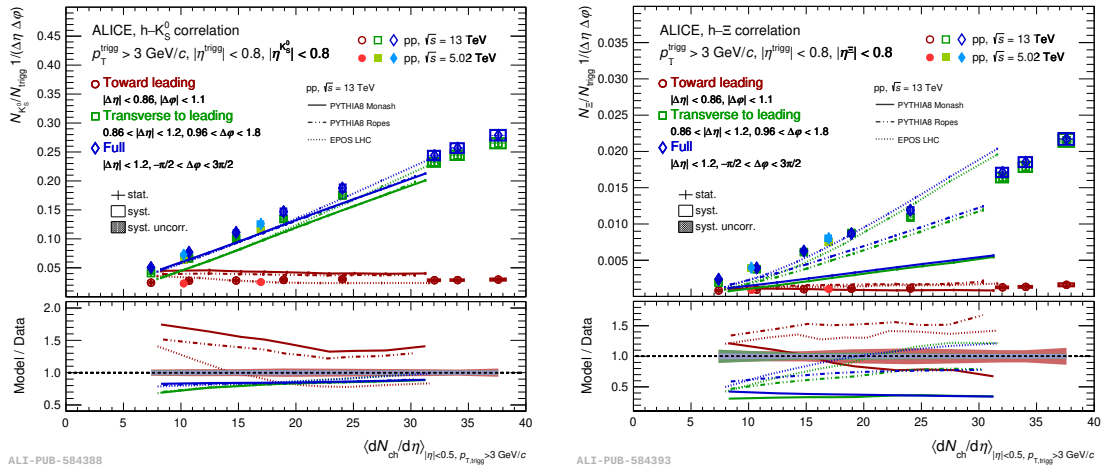

Figure 2.9: Upper panels: K^0_S (*left*) and Ξ (*right*) yields per trigger particle and per unit of $\Delta\eta\Delta\phi$ as a function of the charged-particle multiplicity produced at midrapidity. The yields are measured in the full (blue markets), toward-to-leading (red markers) and transverse-to-leading (green markers) regions for pp collisions at $\sqrt{s} = 13$ TeV and $\sqrt{s} = 5$ TeV respectively as open and full markers. Data are also compared with PYTHIA8 Monash (continuous line), PYTHIA8 Ropes (dashed line) and EPOS LHC (dotted line) models. Bottom panels: ratio between the model predictions and the cubic spline fitted to the data points [29].

Figure 2.10 presents the ratio of Ξ to K^0_S yields as a function of multiplicity. The ratios for full (blue markers) and transverse-to-leading (green markers) yields show an increase with multiplicity, consistent with the expected hierarchy of strangeness enhancement related to the hadron's strangeness content. Meanwhile, the toward-to-leading yield ratio (red markers) also exhibits an upward trend with multiplicity, though with large uncertainties, and is found to be lower compared to both the full and out-of-jet ratios. Both the toward- and transverse-to-leading ratios increase with multiplicity at proportional rates. These findings indicate that out-of-jet processes significantly contribute to the production of strange particles in pp collisions, although strangeness enhancement with multiplicity cannot be excluded in the jet.

The ALICE Collaboration also explores whether factors beyond differences in $\langle dN_{ch}/d\eta \rangle$ can explain the observed behaviors, classifying high-multiplicity (HM) in pp collisions at

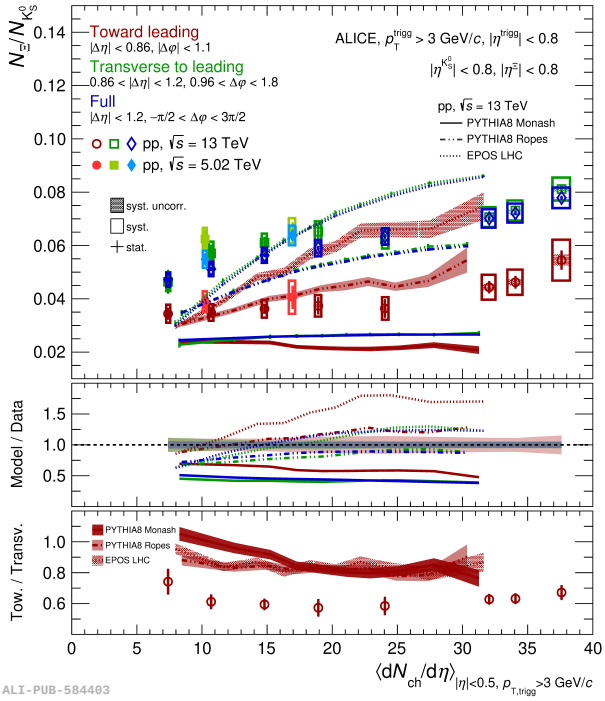

Figure 2.10: Top panel: full (blue), transverse-to-leading (green) and toward-to-leading (red) Ξ/K^0_S yields as a function of the charged-particle multiplicity. Data (markers) are also compared with PYTHIA8 Monash (continuous line), PYTHIA8 Ropes (dashed line) and EPOS LHC (dotted line) models. Central panel: ratio between the model predictions and the cubic spline fitted to the data points. Bottom panel: double ratio between the toward-to-leading and the transverse-to-leading Ξ/K^0_S ratios [29].

$\sqrt{s} = 13$ TeV events by event topology using transverse spherocity [30]. The unweighted transverse spherocity $S_0^{p_T=1}$ can be used to quantify the topology in the azimuthal plane and it is calculated as

$$S_0^{p_T=1} = \frac{\pi^2}{4} \min_{\hat{n}} \left(\frac{\sum_i |\hat{p_{T_i}} \times \hat{n}|}{N_{trks}} \right)^2 \tag{2.3}$$

The sum is taken over all charged-particles with $p_T > 0.15$ GeV/c, where $\hat{p_T}$ represents the transverse momentum unit vector, N_{trks} denotes the number of charged-particles in a given event and $\hat{n}$ is the unit vector that minimizes $S_0^{p_T=1}$. Unlike the conventional transverse spherocity estimator discussed in [114], in this study [30], the transverse momentum of each track is normalized to 1 ($p_T = 1$) when calculating $S_0^{p_T=1}$. This adjustment was necessary to achieve similar sensitivity for neutral and charged-particles; otherwise, significant discrepancies would arise in the production of neutral and charged kaons in jet-like events. Additionally, because $S_0^{p_T=1}$ is independent of particle p_T, it requires a high particle count to serve as a reliable indicator of event topology. Therefore, for events included in this study, the number of charged tracks must be at least 10, restricting the use of the unweighted spherocity estimator to only high-multiplicity (HM) pp collisions, where the average charged-particle multiplicity density $\langle dN_{ch}/d\eta \rangle$ exceeds 10. The values of $S_0^{p_T=1}$ are, by construction, constrained to lie between 0 and 1. Events with $S_0^{p_T=1} \approx 0$ imply that $|\hat{p_{T_i}} \times \hat{n}| \approx 0$ for all tracks, indicating that all tracks are aligned in the azimuthal

plane, characteristic of an event topology dominated by a pair of back-to-back jets. In this set of events particle production is primarily driven by hard processes (in-vacuum hadronization). In contrast, in events with $S_0^{p_T=1} \to 1$, tracks are uniformly distributed in the azimuthal plane, implying no preferred direction (symmetric azimuthal topology). In these cases, particle production is primarily driven by multiple softer collisions (hadronization in a medium).

By examining the p_T-differential particle-to-pion ratios, it is possible to detect QGP-like characteristics within the data. The p_T-differential relative yield of identified light-flavor hadrons compared to π mesons for the $N_{tracklets}^{|\eta|<0.8}$ 0-1% multiplicity events is shown for the top 10% $S_0^{p_T=1}$ percentile in Fig. 2.11, alongside predictions from PYTHIA 8.2. In the lower panels, the ratios to the $S_0^{p_T=1}$ integrated yield clearly indicate an enhancement of strangeness production in isotropic events (represented by blue markers) and a suppression in jet-like events (indicated by red markers). This suggests that the production of strange particles is favored in isotropic event topologies. By employing a narrower event selection, the effects of both enhancement and suppression become more pronounced. When comparing to models, the default Monash tune of PYTHIA 8.2 quantitatively predicts the interaction between the $S_0^{p_T=1}$-integrated high-multiplicity events and the $S_0^{p_T=1}$-differential event classes, though it shows significant quantitative deviations for most of the measured data. The rope tune performs somewhat better, especially for baryons, but both tunes exhibit substantial discrepancies for the ϕ meson. Additionally, both versions of PYTHIA 8.2 qualitatively capture the trends between isotropic and jet-like topologies for all particles shown in the lower panels. Interestingly, there is no observable difference between the Monash and Rope curves of PYTHIA 8.2, despite variations in the production rates of light-flavor hadrons.

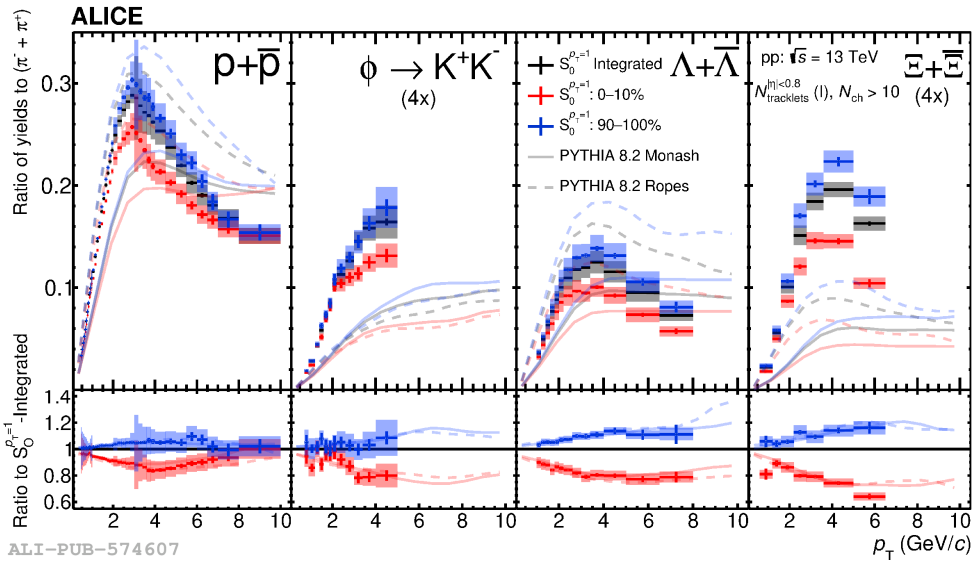

Figure 2.11: Top panels: p_T-differential relative yield of identified light-flavor hadrons to π mesons for the $N_{tracklets}^{|\eta|<0.8}$ 0-10% multiplicity events for the 10% $S_0^{p_T=1}$ percentile. Bottom panels: hadron-to-π double ratios of $S_0^{p_T=1}$ classes relative to $S_0^{p_T=1}$ integrated HM events. Experimental results are compared with predictions from PYTHIA 8.2 Monash and Ropes. [30].

The integrated particle ratios are shown on the left side of Fig. 2.12 for protons (p), lambda baryons (Λ) and xi baryons (Ξ) as a function of $S_0^{p_{\mathrm{T}}=1}$ for the $N_{tracklets}^{|\eta|<0.8}$ 0-10% multiplicity range. The results indicate that the yield of strange hadrons increases with $S_0^{p_{\mathrm{T}}=1}$, displaying a trend consistent with strangeness content (with protons showing little modification). Previous ALICE studies [86, 1, 110] demonstrated that in pp collisions at $\sqrt{s}$ = 13 TeV, the average charged-particle multiplicity density $\langle dN_{ch}/d\eta \rangle$ is a key observable correlated to the enhancement of strange hadrons. For the results presented in Fig. 2.12, the midrapidity $dN_{ch}/d\eta$ is restricted, allowing for a direct examination of whether $S_0^{p_{\mathrm{T}}=1}$ is sensitive to strangeness enhancement. Observations from the left side of Fig. 2.12 reveal that strange particle production is suppressed in events characterized by jet-like topologies, while it is slightly enhanced in softer, isotropic event topologies. In comparing models, the PYTHIA 8.2 Rope hadronization framework qualitatively captures the observed trends but fails to reproduce the strangeness ordering. In contrast, PYTHIA 8.2 Monash does not adequately describe the experimental results.

On the right side of Fig. 2.12, integrated yields of the ϕ meson are compared to those of the Ξ as a function of $S_0^{p_{\mathrm{T}}=1}$ for the $N_{tracklets}^{|\eta|<0.8}$ 0-10%, relative to the corresponding $\pi^+ + \pi^-$ yields. No significant modification of the relative ϕ meson yield is observed as a function of $S_0^{p_{\mathrm{T}}=1}$ within the limits of systematic uncertainties. This finding contrasts sharply with the behavior seen in the relative production of Ξ. Given the similarity of the proton curves on the left side of the figure, these results suggest that the ϕ meson behaves like particles with net-zero strangeness when analyzed in relation to $S_0^{p_{\mathrm{T}}=1}$. Consequently, the suppression or enhancement of relative hadron yields as a function of $S_0^{p_{\mathrm{T}}=1}$ is believed to be correlated more to the hadron mass than to its effective strangeness. The data are compared to predictions from PYTHIA 8.2 Ropes and EPOS-LHC, both of which can quantitatively predict the dynamics of the relative ϕ yields as a function of $S_0^{p_{\mathrm{T}}=1}$. However, in PYTHIA 8.2, one might naively expect the dynamics of the ϕ meson to follow the same trend as that of Ξ, as both are effectively double-strange particles. This observed discrepancy indicates that the enhancement of Ξ in the PYTHIA 8.2 rope model is largely attributed to the introduction of junction formations, which primarily enhances baryon production.

This study reveals that a similar strangeness enhancement observed in multiplicity differential analyses can be achieved by maintaining a fixed local charged-particle density while varying the azimuthal topology, rather than altering the charged-particle density itself. This finding suggests that particle production at high multiplicities is influenced by multiple sources, each with different strangeness-to-pion production rates. Specifically, jet-like events display levels of strangeness production typically linked to lower multiplicities. When analyzed alongside the p_{T} differential ratios, jet-like events are characterized by a notable decrease in relative production at intermediate p_{T}, along with a significant suppression of strangeness in total yields. In contrast, isotropic events exhibit an opposite trend, showing an increase in particle production at intermediate p_{T} and enhanced strangeness production in the p_{T}-integrated yields. These observations imply that the extent of QGP-like effects in small systems can be modulated by categorizing events based on their azimuthal topology. Furthermore, they indicate that $S_0^{p_{\mathrm{T}}=1}$-integrated high-multiplicity events are primarily governed by soft processes, offering important insights into the ALICE observation of universal scaling in strangeness enhancement relative to multiplicity.

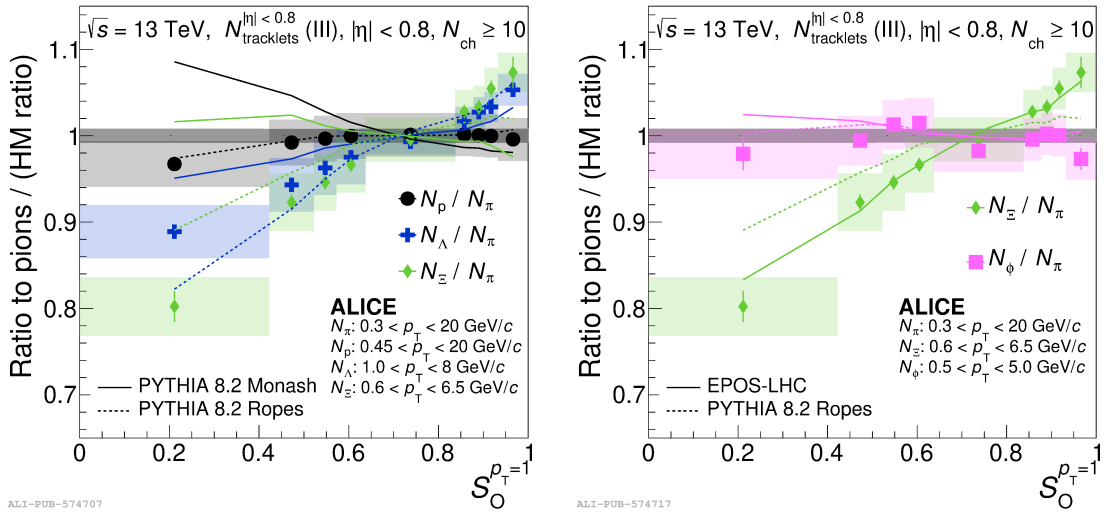

Figure 2.12: (*Left.*) Integrated yields of p, Λ and Ξ as a function of $S_0^{p_{\mathrm{T}}=1}$ for the $N_{tracklets}^{|\eta|<0.8}$ 0-10%, relative to the corresponding $\pi^+ + \pi^-$ yields. Model predictions have been reported for PYTHIA 8.2 Monash and Ropes as continuous and dotted lines respectively. (*Right.*) Integrated yields of the ϕ meson are compared to those of the Ξ as a function of $S_0^{p_{\mathrm{T}}=1}$ for the $N_{tracklets}^{|\eta|<0.8}$ 0-10%, relative to the corresponding $\pi^+ + \pi^-$ yields. Model predictions have been reported for PYTHIA 8.2 Ropes and EPOS-LHC as dotted and continuous lines respectively. [30]

Chapter 3

ALICE: A Large Ion Collider Experiment

The A Large Ion Collider Experiment [2, 115] (ALICE) is a general-purpose heavy-ion detector designed for heavy-ion physics, located at the Large Hadron Collider (LHC) [3] at the European Organization for Nuclear Research (CERN). Its aim is to investigate the physics of strongly interacting matter and the quark-gluon plasma, which emerges during high-energy collisions of heavy ions. ALICE focuses on exploring the extreme temperatures and energy densities released in Pb–Pb collisions, investigating the phase transition between hadronic matter and the QGP.
Beyond Pb–Pb collisions, the ALICE physics program encompasses collisions with lighter ions and at lower energies to vary energy densities and interaction volumes. Additionally, dedicated proton-nucleus and proton-proton collisions provide critical reference data for particle identification and help refine the heavy-ion program. The comparison of different collision systems is crucial for distinguishing the properties of QCD with and without medium effects.

3.1 The Large Hadron Collider (LHC)

The LHC [3] is the world's most powerful particle accelerator, located at CERN, under the Swiss-French border near Geneva, at depths ranging from 50 to 175 meters. The LHC features a 26.7 km circular tunnel, where two beams, either of protons or heavy ions (or one of protons and the other of heavy ions), travel in opposite directions. It is a synchrotron that accelerates the two counter-rotating beams in separate, parallel pipes inside superconducting dipoles ($\sim$ 1200 to bend the beams) and quadrupoles ($\sim$ 400 to focus the beams). The particle beams can be accelerated and collided at different center of mass energies, from less than one to more than 13 TeV, as detailed in Table 3.1.
The entire accelerator complex of CERN is reported in Fig. 3.1. The acceleration process consists of several stages. For pp collisions, protons are first obtained from a hydrogen gas bottle, where the hydrogen atoms are stripped of their electron using an electric field. The protons are then pre-accelerated by a linear accelerator (LINAC [116]) and grouped into bunches in the Proton Synchrotron (PS [117]), where their energy is increased. Afterward, the beams are sent to the Super Proton Synchrotron (SPS [118]) for further acceleration to 450 GeV. Once at this stage, the protons are ready to be injected into the LHC ring,

Table 3.1: Ultra-relativistic energies reached for different colliding systems at the LHC in Run 1, 2 and 3.

Colliding System	Centre-of-mass energy (TeV)
pp	0.9, 2.76, 5.02, 7, 8.16, 13, 13.6
p–Pb	5.02, 8.16
Pb–Pb	2.76, 5.02, 5.36
Xe–Xe	5.44

where they reach their maximum energy.

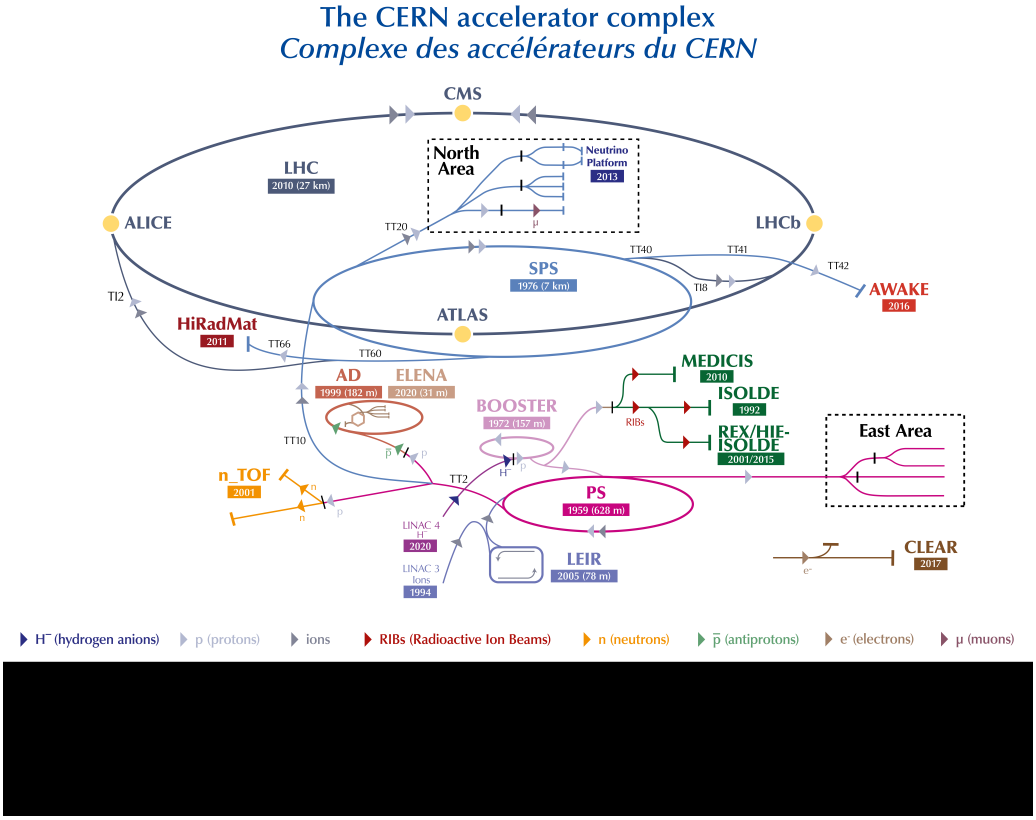

Figure 3.1: A schematic view of CERN accelerator complex [119].

The two counter-rotating beams can collide at four different interaction points (IPs), where the four largest detectors at CERN are located:

- LHCb (Large Hadron Collider beauty experiment) focuses on studying the physics of the b-quark, particularly the measurement of CP violation and rare decays of beauty and charm particles, to test the Standard Model and search for signs of new physics.
- CMS (Compact Muon Solenoid) is a general-purpose experiment designed to study the Higgs boson and explore physics beyond the Standard Model, such as new heavy particles predicted by supersymmetric theories.

- ATLAS (A Toroidal LHC ApparatuS) shares the same research goals as CMS.
- ALICE (A Large Ion Collider Experiment) is the only LHC experiment specifically designed to study heavy-ion collisions and investigate strongly interacting matter at extremely high energy densities, where the quark-gluon plasma phase is reached.

The physical goals and sub-detectors of ALICE, focusing on the main ones for this thesis, are described in the next sections.

3.2 ALICE in Run 1 and Run 2

The ALICE detector operated in the LHC Run 1 and Run 2 [2, 115], illustrated in Fig. 3.2, is a massive structure measuring 26 meters in length, 16 meters in height and 16 meters in width. It is located at the interaction point IP2 of the LHC and it is primarily dedicated to studying the physics of strongly interacting matter and the properties of the QGP at high temperatures and energy densities by analyzing modifications in final-state observables. The ALICE physics program includes data collection from various collision configurations:

- Pb–Pb collisions: to access the highest temperatures and energy densities ever achieved in a laboratory setting. They are used to explore the phase transition from hadronic matter to the quark-gluon plasma, as well as its phase diagram and properties, focusing on all relevant observables for QGP characterization.
- Lighter ion collisions: to extend the range of accessible energy densities and eccentricities.
- p–Pb collisions: to help disentangle cold nuclear matter effects from QGP effects.
- pp collisions: baseline for comparison with heavy-ion data, they offer interesting physics on their own, and help refine Monte Carlo models.

The detector must handle the high particle multiplicity associated with heavy-ion collisions (up to 2000 charged-particles per pseudorapidity unit at central pseudorapidity) while providing excellent Particle Identification (PID) and tracking performance. By combining a low magnetic field, excellent tracking and various PID techniques from various detectors, ALICE enables a comprehensive study of the particles produced in collisions, spanning a wide momentum range from 100 MeV/c to 100 GeV/c.

3.2.1 ALICE sub-detectors

ALICE is a complex apparatus composed of several detectors that can be categorized into three primary groups: the central barrel detectors, dedicated to tracking, vertexing and PID at central rapidity; the forward detectors, focusing on the determination of event properties from energy deposition at forward rapidity; the muon arm, which is specifically designed for muon reconstruction and identification. The reference coordinate system for ALICE is a right-handed orthogonal cartesian system, with the origin $(x, y, z) = 0$ located at the interaction point (IP). In this system, the z-axis aligns with the beam direction. The two sides of the detector along the z-axis are designated as A (counter-clockwise for positive z) and C (clockwise for negative z).

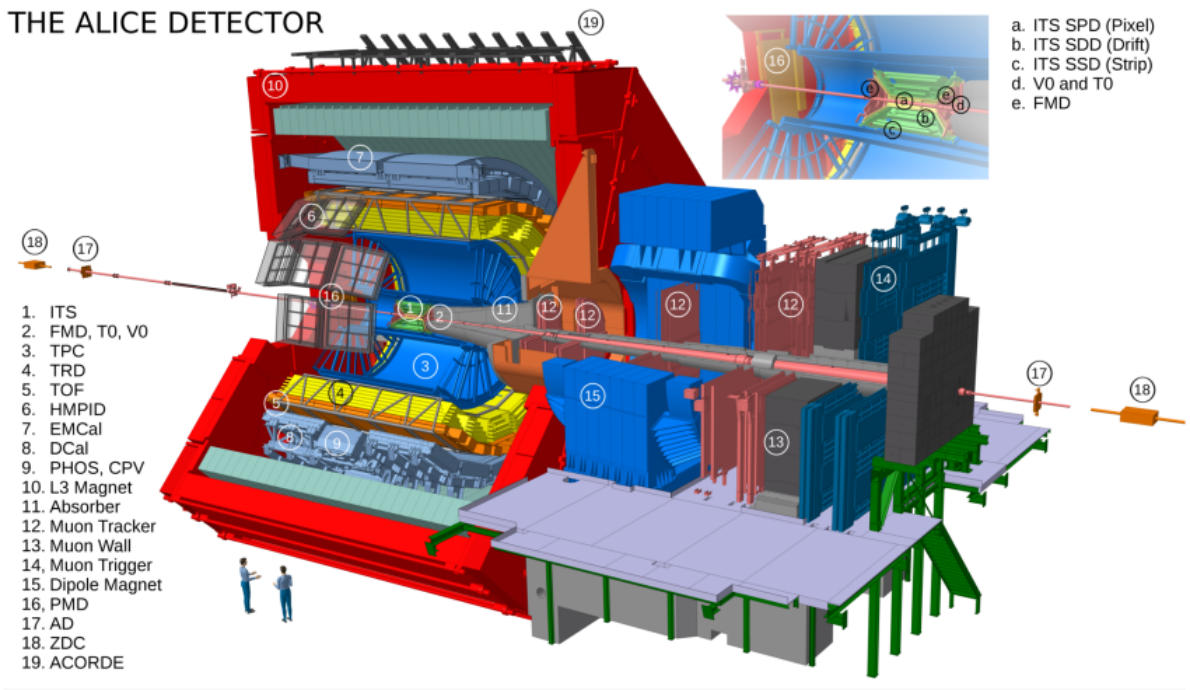

Figure 3.2: A schematic view of the ALICE detector. Figure from the ALICE figure repository.

- **Central barrel detectors**: they are enclosed in the L3 solenoid magnet, which provides a nominal magnetic field of 0.5 T. Starting from the interaction region and going outward one can identify:

  – Inner Tracking System (ITS);

  – Time Projection Chamber (TPC);

  – Transition Radiation Detector (TRD);

  – Time of Flight (TOF).

  They offer full azimuthal coverage ($0 \leq \phi \leq 2\pi$) with a pseudorapidity acceptance of $|\eta| < 0.9$ (corresponding to a polar acceptance of $\pi/4 < \theta < 3\pi/4$). In the mid-rapidity region, other detectors with limited acceptance can be found:

  – High-Momentum Particle Identification Detector (HMPID);

  – PHOton Spectrometer (PHOS);

  – ElectroMagnetic CALorimeter (EMCal).

- **Muon spectrometer**: it is located in the backward pseudorapidity region ($-4.0 \leq \eta \leq -2.5$) and is composed of a dipole magnet along with tracking and trigger chambers. This system is optimized to reconstruct heavy quark resonances via their decay channel into $\mu^+\mu^-$ pairs and for detecting single muons originating from open charm and bottom hadrons.

- **Forward detectors**: they are situated in the high pseudorapidity region (at small angles relative to the beam pipe) and have varying acceptances. They are small and specialized detector systems, which include:
  - Forward Multiplicity Detector (FMD) ($-3.4 < \eta < -1.7$ and $1.7 < \eta < 5.0$);
  - Photon Multiplicity Detector (PMD) ($2.3 < \eta < 3.7$);
  - Zero Degree Calorimeters (ZDC) ($\eta > 8.7$);
  - V0 Detectors ($2.8 < \eta < 5.1$ for V0A and $-3.7 < \eta < -1.7$ for V0C) ;
  - T0 Detectors ($4.61 < \eta < 4.92$ for T0-A and $-3.28 < \eta < -2.97$ for T0-C).

In addition to the detectors mentioned above, an array of scintillators known as ACORDE is installed above the L3 magnet and is dedicated to triggering on cosmic rays.
Table 3.2 shows a summary of the ALICE sub-detectors.

Table 3.2: Summary of the ALICE detector sub-systems [115].

Detector	**Acceptance: Polar**	**Acceptance: Azimuthal**	**Technology**	**Main purpose**
ITS layer 1: SPD	$\|\eta\| < 2.0$	$full$	Si pixel	tracking, vertex
ITS layer 2: SPD	$\|\eta\| < 1.4$	$full$	Si pixel	tracking, vertex
ITS layer 3: SDD	$\|\eta\| < 0.9$	$full$	Si drift	tracking, PID
ITS layer 4: SDD	$\|\eta\| < 0.9$	$full$	Si drift	tracking, PID
ITS layer 5: SSD	$\|\eta\| < 1.0$	$full$	Si strip	tracking, PID
ITS layer 6: SSD	$\|\eta\| < 1.0$	$full$	Si strip	tracking, PID
TPC	$\|\eta\| < 0.9$	$full$	Ne drift+MWPC	tracking, PID
TRD	$\|\eta\| < 0.8$	$full$	TR+Xe drift+MWPC	tracking, $e^{\pm}$ id
TOF	$\|\eta\| < 0.9$	$full$	MRPC	PID
HMPID	$\|\eta\| < 0.6$	$1^\circ < \phi < 59^\circ$	$C_6F_{14}RHIC + MWPC$	PID
PHOS	$\|\eta\| < 0.12$	$220^\circ < \phi < 320^\circ$	$PbWO_4$	photons
EMCal	$\|\eta\| < 0.7$	$80^\circ < \phi < 187^\circ$	Pb+scint.	photons and jets
Muon Spectometer: MCH	$-4.0 < \eta < -2.5$	$full$	MWPC	muon tracking
Muon spectometer: MTR	$-4.0 < \eta < -2.5$	$full$	RPC	muon trigger
FMD: disc1	$3.6 < \eta < 5.0$	$full$	Si strip	charged-particles
FMD: disc2	$1.7 < \eta < 3.7$	$full$	Si strip	charged-particles
FMD: disc3	$-3.4 < \eta < -1.7$	$full$	Si strip	charged-particles
PMD	$2.3 < \eta < 3.9$	$full$	Pb+PC	photons
ZDC: ZN	$\|\eta\| > 8.8$	$full$	W+quartz	forward neutrons
ZDC: ZP	$6.5 < \|\eta\| < 7.5$	$\|\phi\| < 10^\circ$	brass+quartz	forward protons
ZDC: ZEM	$4.8 < \eta < 5.7$	$\|2\phi\| < 32^\circ$	Pb+quartz	photons
V0-A	$2.8 < \eta < 5.1$	$full$	scint.	charged-particles
V0-C	$-3.7 < \eta < -1.7$	$full$	scint.	charged-particles
T0-A	$4.6 < \eta < 4.9$	$full$	quartz	time, vertex
T0-C	$-3.3 < \eta < -3.0$	$full$	quartz	time, vertex
ACORDE	$\|\eta\| < 1.3$	$30^\circ < \phi < 150^\circ$	scint.	cosmics

The following sub-paragraphs provide details about some of these sub-detectors, concentrating on those utilized to acquire the data analyzed in this thesis work.

Inner Tracking System (ITS)

The ITS [120, 121] (see Fig. 3.3) is the detector situated closest to the beam pipe. Its primary purposes are:

- to locate the primary vertex with a resolution better than 100 μm;

- to reconstruct secondary vertices from the decays of heavy-flavor and strange particles;
- to track and identify particles with low transverse momentum (50 MeV/c < p_{T} < 100 MeV/c), which are too deflected to be reconstructed by the TPC;
- to enhance the performance in momentum, impact parameter, and angle resolution for high p_{T} particles tracked in the TPC;
- to reconstruct particles that pass through dead regions of the TPC.

This detector comprises six cylindrical layers of silicon detectors, positioned at radii ranging from 3.9 cm to 43 cm.

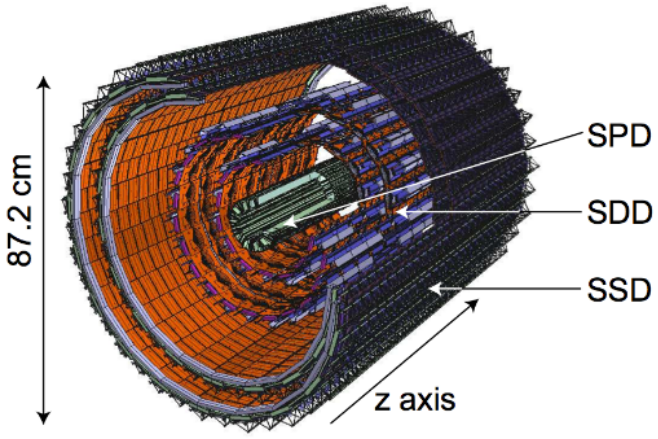

Figure 3.3: A schematic view of the ITS detector [122].

Due to the high track density, the two innermost layers consist of Silicon Pixel Detectors (SPD), which ensure high granularity. This high granularity is crucial for accurately determining the position of the primary vertex and measuring the impact parameters of secondary tracks that arise from the weak decays of strange, charm, and beauty particles. The SPD is constructed from hybrid silicon pixels, featuring a two-dimensional matrix of reverse-biased silicon detector diodes connected to the readout chip, which corresponds to an electronic readout cell input. The SPD output is digital, providing the hit information, with no measurement of the energy loss.
Following the SPD, two layers of Silicon Drift Detectors (SDD) and two outermost layers of double-sided Silicon Micro-Strip Detectors (SSD) feature analog readout. This allows for PID through the measurement of dE/dx for low-momentum particles. To minimize the effects of multiple scattering on momentum and impact parameter resolutions for low-momentum particles, the amount of material in the active volume has been kept to a minimum. Each SDD is made from a silicon wafer that has a diameter of 12.7 cm and a thickness of 0.3 cm. When a particle passes through the SDD, it releases electrons, which drift toward an array of anodes under the influence of an applied electric field. The y coordinate of the particle is determined by measuring the drift time, while the x coordinate is derived from the centroid of the electrons along the anodes.

Figure 3.4 illustrates the resolution of the transverse distance to the primary vertex, demonstrating an impact parameter resolution better than 100 μm in the transverse plane for $p_{\mathrm{T}} > 1$ GeV/c for identified particle global tracks and better than 70 μm for all charged tracks.

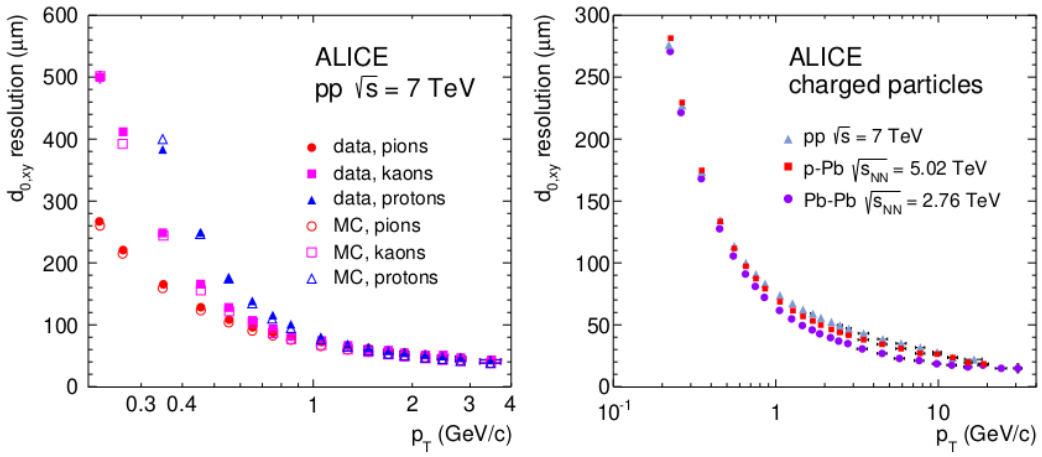

Figure 3.4: Resolution of the transverse distance to the primary vertex for identified particle global ITS –TPC tracks (*Left*) and for all charged ITS –TPC tracks (*Right*) [115].

Time Projection Chamber (TPC)

The TPC [123] (see Fig. 3.5) serves as the primary tracking detector within the central barrel of ALICE. Its main objectives are:

- to provide charged-particle momentum measurements, in conjunction with the other central barrel detectors, covering a range from approximately $p_{\mathrm{T}} \sim 0.1$ GeV/c to $p_{\mathrm{T}} \sim 100$ GeV/c, while ensuring good two-track separation;
- to enable particle identification and vertex determination with adequate momentum resolution;
- to deliver excellent tracking performance in the high-multiplicity environment characteristic of Pb–Pb collisions.

To achieve these goals, the TPC is designed as a drift chamber, consisting of two drift regions separated by a central electrode. It has a cylindrical shape, measuring 5 m in length and encompassing an internal volume of 88 m^3, filled with a mixture of Ar and CO_2 during the Run 2 data taking campaign (2015 - 2018). As charged-particles pass through the TPC volume, they ionize the gas along their trajectory, generating free electrons and ions that migrate towards the end-plates due to a drift electric field of 400 V/cm.
The readout end-plates are divided into 18 sectors, each containing Multi-Wire Proportional Chambers (MWPC) with cathode pad readout. In the high electric fields near the anode wires, an avalanche of electrons is produced, amplifying the primary ionization signal. The electrical signal induced by the positive space charge on a segmented pad plane

is shaped, amplified, digitized, processed and then read out from each pad by the data acquisition system. The drift time for electrons over the entire path is approximately 95 μs. Although the TPC is a relatively slow detector, it effectively manages the minimum bias collision rate in Pb–Pb collisions, which is around 8 kHz at nominal luminosity.

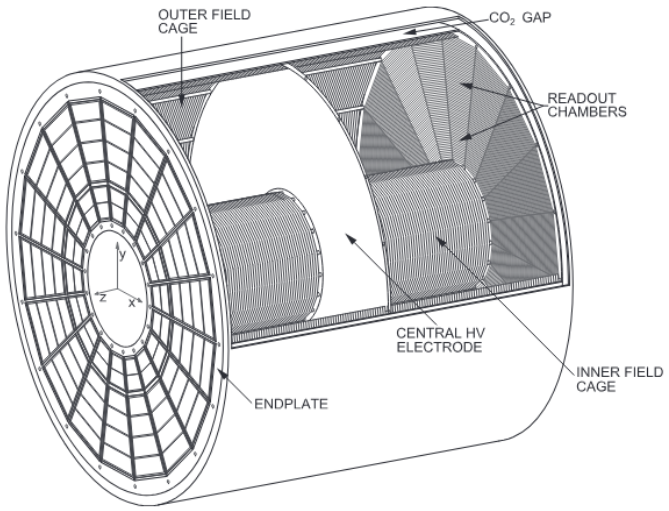

Figure 3.5: A schematic view of the TPC detector [124].

The inner radius of the TPC (85 cm) is determined by the maximum allowable track density, while the outer radius (250 cm) is dictated by the minimum track length necessary to achieve a resolution of less than 10% in the energy loss ($\mathrm{d}E/\mathrm{d}x$) determination for particle identification. Due to its excellent $\mathrm{d}E/\mathrm{d}x$ resolution, the TPC can identify particles with $p_{\mathrm{T}} < 1$ GeV/c on a track-by-track basis.
Figure 3.6 (left) illustrates the tracking efficiency, defined as the ratio of reconstructed tracks to generated primary particles in the simulation, as a function of transverse momentum. Additionally, Fig. 3.6 (right) presents the transverse momentum resolution for both standalone TPC tracks and combined ITS – TPC tracks, which is extracted from the track covariance matrix. The inverse p_{T} resolution depicted in this figure is related to the relative transverse momentum resolution through the equation

$$\frac{\sigma_{p_{\mathrm{T}}}}{p_{\mathrm{T}}} = p_{\mathrm{T}} \cdot \sigma_{1/p_{\mathrm{T}}} \tag{3.1}$$

The plot illustrates the most sophisticated reconstruction scheme applied to the data collected during the most recent p–Pb run. In central Pb–Pb collisions, the p_{T} resolution is anticipated to degrade by approximately 10–15 % at high p_{T} due to the loss (or reduction) of clusters on ion tails, overlap of clusters, and the presence of fake clusters associated with the tracks.

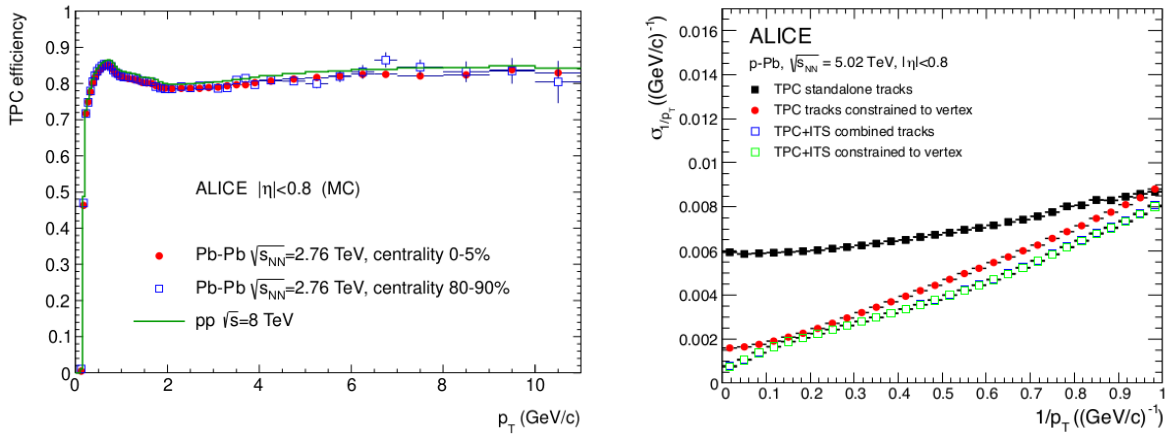

Figure 3.6: (*Left.*) TPC track finding efficiency for primary particles in pp and Pb–Pb collisions (simulation) [115]. (*Right.*) The p_{T} resolution for standalone TPC and ITS – TPC matched tracks with and without constraint to the vertex. The vertex constrain significantly improves the resolution of TPC standalone tracks. For ITS – TPC tracks, it has no effect (green and blue squares overlap) [115].

V0 Detectors

The V0 detector [125] is a small-angle device composed of two segmented arrays of 32 plastic scintillator counters, known as V0A and V0C, positioned on either side of the interaction point around the beam pipe. V0A is located along the positive z-axis, 329 cm from the interaction point, and covers the pseudorapidity range $2.8 < \eta < 5.1$. V0C is positioned on the opposite side, along the negative z-axis, at Z = -88 cm, with pseudorapidity coverage of $-3.7 < \eta < -1.7$. Each V0 array is divided into four concentric rings, with each ring further segmented into eight 45° sectors in the azimuthal plane as shown in Fig. 3.7. The scintillator counters contain wavelength-shifting fibers, as illustrated in Fig. 3.8. Clear fibers collect the signals and transport them to photomultiplier tubes located 3 to 5 meters away inside the L3 magnet. The counters have a time resolution of better than 1 ns, and their responses are recorded within a 25 ns time window around the nominal beam crossing time.

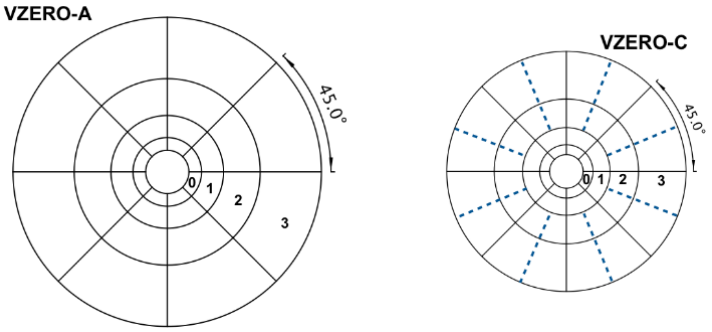

Figure 3.7: Segmentation of the VZERO-A/VZERO-C arrays [125].

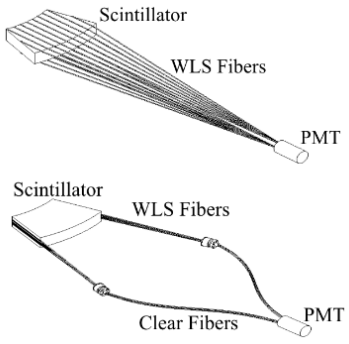

Figure 3.8: Schematic design of the V0A (*Top*) and V0C (*Bottom*) detection elements [2].

The V0 detector serves as a trigger system, providing both minimum-bias (MB) and high-multiplicity (HM) triggers for the central barrel detectors across all collision systems. In the early data-taking periods (starting from 2009), the ALICE MB trigger was set up to require a hit in the SPD or in either of the V0 arrays (V0A or V0C). However, due to increasing LHC luminosity and beam-related backgrounds, the trigger criteria have become stricter in recent data-taking periods, requiring a coincidence between both V0 arrays and the LHC bunch crossing signals.
The V0 detector plays a crucial role in background suppression, particularly in rejecting beam-gas collisions. This is achieved through a time-of-flight comparison between the two arrays: when a beam-gas interaction occurs outside the region between the arrays, particles will arrive 6 ns before or after the expected time of a beam-beam collision. If the beam-gas interaction takes place within the region between the two arrays, the event cannot be rejected immediately and requires an offline trigger to be applied.
In addition to its triggering and background suppression functions, the V0 detector is vital for measuring charged-particle multiplicity, based on the energy deposited in its scintillators. Since the amplitude of the signal registered by the V0 arrays correlates monotonically with the number of primary particles emitted in the collision, which in turn correlates to the number of charged-particles emitted in central rapidity, the V0 is used as a multiplicity estimator by recording the analogic signal's amplitude. Through detailed simulations of the detector, the relationship between the total charge collected in a V0 ring and the number of primary charged-particles emitted into the corresponding pseudorapidity range can be determined. Figure 3.9 shows a typical distribution of V0 amplitudes for minimum-bias and high-multiplicity triggers in pp collisions at $\sqrt{s} = 13$ TeV (see Section 4.3 for further details on the ALICE multiplicity measurement).

3.2.2 Data acquisition and offline framework

During Run 1 and 2, ALICE's data-taking operations were managed by several key online systems. The Detector Control System (DCS) oversaw the operation of the detector hardware through a centralized interface. The Data Acquisition (DAQ) system managed the configuration of detectors during data collection and the Trigger (TRG) system was responsible for selecting events with a specific physics interest. The ALICE trigger system consisted of a low-level hardware trigger, managed by the Central Trigger Processor

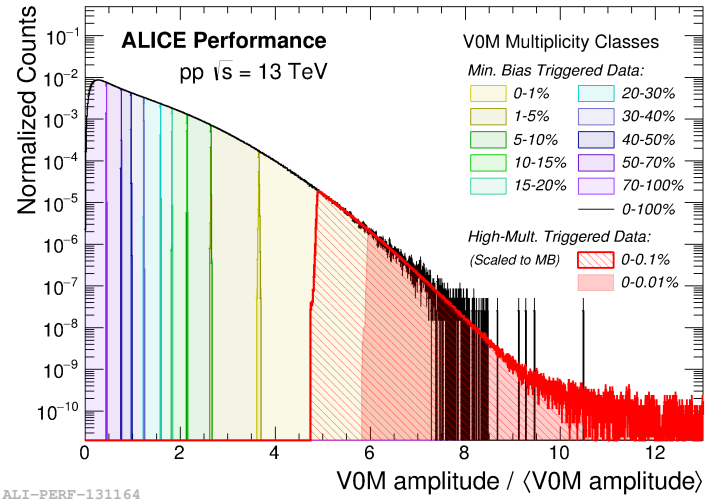

Figure 3.9: Distribution of the self-normalized sum of signal amplitudes recorded by the V0 detector for minimum-bias and high-multiplicity triggers in pp collisions at $\sqrt{s} = 13$ TeV. V0 multiplicity classes are defined based on this distribution. [126].

(CTP) and a High-Level software Trigger (HLT). The CTP made trigger decisions by combining input from various detectors, which had different readout times. The trigger process was divided into three stages: L0, L1 and L2. The initial trigger decision (L0) occurred approximately 0.9 μs after a collision. If successful, the event moved to Level 1 (L1), where the decision was made about 6.5 μs after L0 to account for signal propagation and more complex algorithm times. Events passing L1 progressed to Level 2 (L2), which took around 100 μs to ensure full ionization charge drift in the TPC. Events passing all hardware trigger levels were then processed to the DAQ system. The DAQ system interfaced with the HLT, which performed rapid event reconstruction and further data reduction to minimize file sizes without losing critical physics information. The finalized data were stored at CERN's computing center. Given the immense volume of data produced by ALICE, data processing was distributed across multiple global computing centres, coordinated by the Worldwide LHC Computing Grid (WLCG) [127]. This infrastructure is organized hierarchically: Tier-0 at CERN is the primary hub, supported by large Tier-1 centres responsible for storing raw data, and smaller Tier-2 centres, which handle additional tasks like calibration, reconstruction, simulation and analysis.
The ALICE Collaboration has developed a service called ALICE Environment (AliEn) [128] that provides researchers to access the data stored on the Grid, facilitates job submissions to computing centres, and allows for monitoring of analysis and simulation progress. After raw data is reconstructed, the output is stored in Event Summary Data (ESD) files. These contain detailed information such as reconstructed tracks, vertices and detector signals, which are primarily used for calibration and validation. For final physics analyses, the ESD files are filtered into more compact Analysis Oriented Data (AOD) files. These AOD files are based on the ROOT data format, a flexible, object-oriented framework in C++ used for data storage and analysis. ALICE's offline framework, built on ROOT, consists of two main components: AliRoot [129] and AliPhysics [130]. AliRoot provides the necessary tools for alignment, calibration and data reconstruction, while also supporting

Monte Carlo simulations using event generators like PYTHIA [20] for pp collisions and HIJING [131] for heavy-ion collisions. Particle transport through the detector is simulated using GEANT3 [132] and GEANT4 [133], offering detailed models of detector and beam conditions. AliPhysics, on the other hand, contains the tools for data analysis and is updated regularly by the ALICE Collaboration to support ongoing research.

3.2.3 Track and vertex reconstruction

The reconstruction of tracks and primary vertices in ALICE follows a systematic workflow [115]. First, detector hits are grouped into clusters — sets of hits produced by the same particle. These clusters contain information about position, signal amplitude and timing, and this clustering process is done independently for each detector. The interaction vertex is initially estimated by determining the point where the maximum number of tracklets (track segments formed by linking clusters in the two SPD layers) converge. The track reconstruction process follows a three-step inward-outward-inward approach, as shown in Fig. 3.10. In the TPC, the process begins at the outermost radius, where track seeds are created using two clusters from the outermost TPC pad rows along with the estimated vertex position. Additional seeds are then formed without relying on the vertex constraint, using three clusters. These seeds are iteratively propagated inward, incorporating nearby clusters at each step using the Kalman filter technique [134]. Since clusters may be shared by multiple seeds, a specialized algorithm identifies and eliminates duplicate tracks by removing the lower-quality one. Only tracks with a minimum of 20 clusters (out of a maximum of 159) are retained.
After reconstructing the TPC tracks, they are propagated inward to the outermost ITS layer to begin track reconstruction in the ITS. Here, TPC tracks serve as the starting points, and candidate tracks are updated at each ITS layer by considering nearby clusters that satisfy a proximity threshold. This reconstruction is performed both with and without a vertex constraint, as in the TPC. High-quality tracks are then selected based on the Kalman-filter χ^2 result. Once ITS reconstruction is finished, tracks are propagated toward the preliminary interaction vertex. A second outward propagation follows, where tracks are refitted using the Kalman filter, matching clusters from the TRD and TOF detectors, as well as signals from HMPID and calorimeters. Although no further kinematic updates are made during this stage, information required for particle identification is attached to the tracks.
Finally, in the last step, tracks are propagated back inward from the outer TPC radius toward the interaction point, with a final refitting to calculate the track parameters and their covariance matrix. After this step, the position of the primary vertex is recalculated using global tracks (from both TPC and ITS) and the final vertex is determined by extrapolating these tracks to the beam-line. The tracks are then propagated to this reconstructed vertex.

3.2.4 Particle IDentification

The goal of Particle Identification (PID) is to determine the mass associated to each reconstructed track, which, combined with its charge, allows for the identification of the particle. The ALICE experiment features unique PID capabilities through the combined

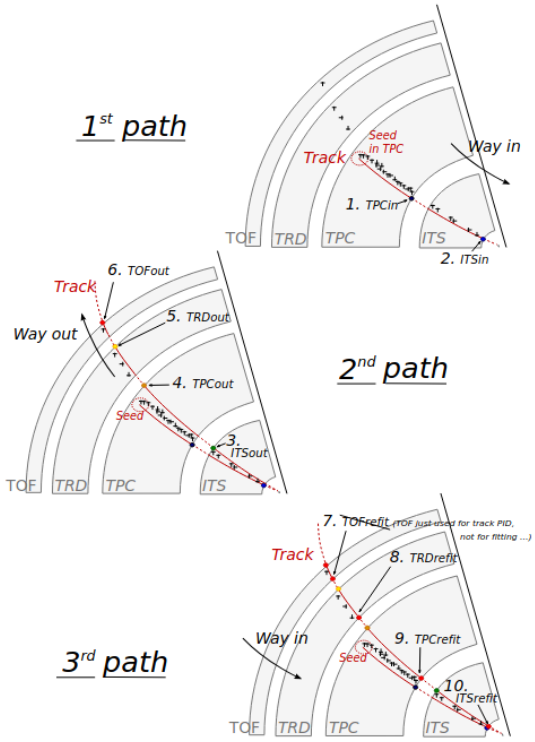

Figure 3.10: Workflow of the track reconstruction in ALICE [135].

use of the ITS, TPC and TOF detectors [115]. Each of these detectors employs a different PID method: the ITS and TPC measure the specific energy loss ($\mathrm{d}E/\mathrm{d}x$) of particles, while the TOF detector measures their velocity. These techniques complement each other and are used together to optimize PID performance across a wide range of particle momenta. Additionally, the HMPID detector enhances PID capabilities at high p_{T} by accurately measuring the Cherenkov angle of photons emitted when a particle crosses the detector material. Electrons are also identified using the TRD, which detects the radiation emitted as particles pass through different dielectric layers. The PHOS and EMCal calorimeters further assist in electron identification by measuring the energy released in the calorimeters and comparing it to the particles' momentum. Some examples of PID performance can be seen in Fig. 3.11.

3.3 ALICE in Run 3

During the LHC Long Shutdown 2 (LS2), ALICE underwent several critical upgrades, marking a new chapter in its operations, now in Run 3 [136]. ALICE aims to address key physics questions with the Run 3 data-taking, focusing on the measurement of heavy-flavour hadrons, quarkonia and low-mass di-leptons, particularly at low transverse momenta. These measurements are particularly challenging due to their very low signal-to-background ratio, requiring large data samples and the development of innovative, physics-driven triggering techniques. Additionally, improving the pointing resolution and tracking efficiency, while maintaining the excellent particle identification capabilities

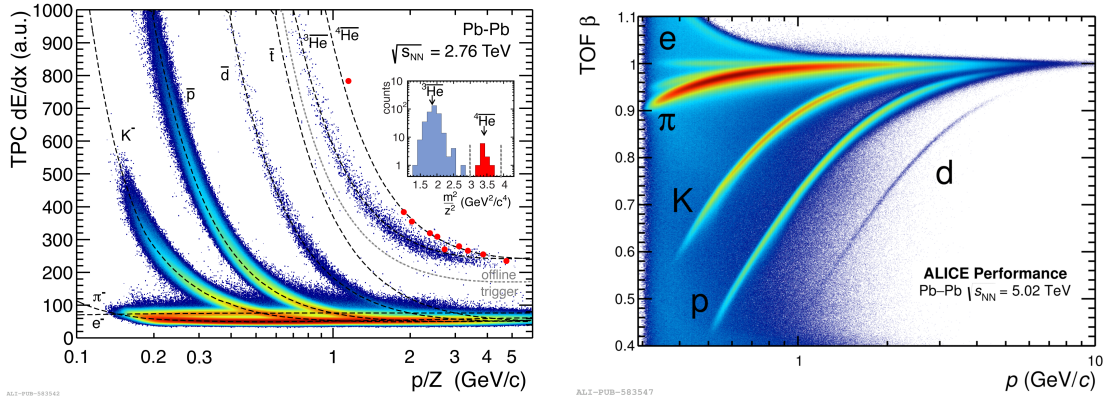

Figure 3.11: PID performance of TPC and TOF. (*Left.*) Specific energy-loss measured by the TPC as a function of the and rigidity (p/Z) in Pb–Pb collisions at $\sqrt{s_{\mathrm{NN}}} = 2.76$ TeV [48]. (*Right.*) The β parameter, measured by the TOF, as a function of p, measured by the TPC, in Pb–Pb collisions at $\sqrt{s_{\mathrm{NN}}} = 5.02$ TeV [48].

of the previous ALICE detector, is crucial.
With the LHC now providing Pb–Pb collisions at rates up to $L = 6 \cdot 10^{27} cm^{-2} s^{-1}$, corresponding to an interaction rate of 50 kHz, the upgraded ALICE detector must also handle these higher rates. The key upgrades implemented during LS2, can be summarized as follows:

- a new beam pipe with smaller diameter;
- a brand-new high-resolution ITS;
- an upgraded TPC;
- upgrade of the ALICE readout electronics to handle high rate operations;
- upgrade of the forward trigger detectors;
- upgrade of the readout electronics and a complete update of the timing and trigger system;
- implementation of a new online system capable of receiving and processing the full detector information;
- new offline reconstruction and analysis framework.

3.3.1 Data taking, processing and reconstruction upgrades

In Run 3 operations of ALICE, the traditional event trigger system has been replaced by continuous data readout from detectors, resulting in significantly higher data capacity — over 1 TB/s for Pb–Pb events, which is about 100 times more than in Run 1 [137]. To manage this increased data volume, the ALICE computing model aims to reduce the amount of data read out as early as possible in the data flow. This is achieved through synchronous data reconstruction during data collection, particularly with the TPC, where

raw data is quickly reconstructed to eliminate irrelevant clusters using initial tracking algorithms and early calibrations.
Data processing occurs in a continuous mode, where the data is split into short Sub-Time Frames ($\sim$ 10 ms) by the First Level Processors (FLP), where initial compression (zero suppression) takes place. These Sub-Time Frames are then sent to Event Processing Nodes (EPN), where data from different detectors is assembled into complete timeframes and a synchronous reconstruction of events is performed. Compressed Time Frames (CTF) are generated and stored on a disk buffer. In the asynchronous stage, a second reconstruction, incorporating final calibrations, is performed on the EPN farm or GRID nodes, generating Analysis Object Data (AO2D) for permanent storage.
Event selection now occurs at the software level rather than through hardware triggers, allowing for refined analysis of specific events. Specific triggers utilizing the full reconstruction of each event are implemented to study rare probes with high precision [138]. More details on the software-based trigger in the light-flavor sector, with a focus on strangeness, are discussed in Section 6.1.2. Following this event selection, the original CTFs are deleted from the disk buffer to make room for new data. Skimming procedures are applied exclusively to pp collisions to reduce the amount of data stored on tape, while all recorded Pb–Pb data is saved. Quality control procedures are performed in real time to validate detector data on the EPNs and FLPs. With the integration of online and offline computing systems into the unified O^2 project, offline Quality Assurance (QA) and online Data Quality Monitoring (DQM) have been merged into a single Quality Control (QC) system. This integrated QC framework is crucial for promptly identifying and resolving potential issues during data taking, ensuring that calibration and reconstruction processes operate as expected in both synchronous and asynchronous modes. More details regarding the QC of the MID during Run 3 will be discussed in Section 7.

Chapter 4

(multi-)Strange particle multiplicity distribution

Chapter 2 introduces the concept of strangeness enhancement (SE), defined as the increased production of strange hadrons in heavy-ion collisions compared to minimum-bias pp collisions. The ALICE experiment at the LHC has shown that small collision systems exhibit remarkable similarities to Pb–Pb collisions when studied as a function of multiplicity. Specifically, the ratio of strange hadron yields to pions increases with charged-particle multiplicity, starting from pp and p–Pb collisions and progressing smoothly across different collision systems and energies until reaching Pb–Pb collisions. As discussed in Section 2.3.1, to investigate the origins of strangeness production in small collision systems, the ALICE Collaboration is conducting a variety of studies on strange hadron production, though this remains a major challenge in high-energy hadron physics. Notably, in all previous studies, strange particle yields have typically been obtained by counting their total sum in a given data set — potentially dividing the sample based on topological or dynamic properties of the events or strange particle candidates — and then normalizing, after acceptance and efficiency corrections, to the total number of inelastic events analyzed in the sample. In this approach, production rates represent the average multiplicity distribution of strange particles, reflecting the underlying production mechanism for each particle species. This thesis extends these results by presenting, for the first time, a measurement of the multiplicity distribution $\mathrm{P}(n_{\mathrm{S}})$ for strange particles $\mathrm{K}^0_{\mathrm{S}}$, Λ, $\overline{\Lambda}$, Ξ^-, $\overline{\Xi}^+$, Ω^- and $\overline{\Omega}^+$ in pp collisions at $\sqrt{s} = 5.02$ TeV, thus advancing the study of strangeness production beyond the distribution average yields. This is achieved within various charged-particle multiplicity density classes, using an analysis technique based on counting the number of strange particles on an event-by-event basis. This novel technique makes it possible to determine the probability of observing, for example, events with a very low overall charged-particle multiplicity density but containing three or four cascades, or conversely, high-multiplicity events with few or no $\mathrm{K}^0_{\mathrm{S}}$ particles. Additionally, the measurement of $\mathrm{P}(n_{\mathrm{S}})$ enables calculation of the average yield of multiplets for each strange particle type. This approach provides a way to explore strangeness enhancement at its extremes, not limited to the Ω/π ratio but extending to configurations with six s-quarks in Ω doublets or Ξ triplets. At the same time, this technique allows for a clearer identification of the non-strangeness component in SE patterns, by examining the ratio of Λ and $\mathrm{K}^0_{\mathrm{S}}$ multiplets as a function of multiplicity. More generally, it enables the study

of the relative hadronization probability into various final-state strange hadron multiplets in events characterized by a specific number of s-quarks created in the collision.

4.1 Analysis strategy: summary

The initial step of the analysis involves selecting a minimum-bias pp collisions data set that is optimally suited to the analysis at hand. This sample needs to contain a large number of events to effectively study the particle multiplicity distribution, including its low-probability tail. Additionally, each event must meet standard selection criteria to minimize contributions from overlapping events (pile-up) and beam-gas interactions, which should be excluded. The selected events are subsequently divided into various percentile classes, based on the information from the V0 detectors, which use the total charge deposited in the forward region. A detailed description of all the applied selection criteria and the method of categorizing multiplicity is provided in Section 4.3.
The next phase involves identifying candidates for K^0_S, Λ, $\overline{\Lambda}$, Ξ^-, $\overline{\Xi}^+$, Ω^- or $\overline{\Omega}^+$ particles from the reconstructed tracks on an event-by-event basis. This selection process is based on track quality and the topology of the weak decay, as detailed in Section 4.4. Once the candidate particles of interest have been identified, signal extraction is carried out using a procedure that assigns signal/background weights derived from the data, as discussed in Section 4.5. The likelihood for each candidate of being signal or background is determined by fitting the invariant mass distribution in several p_T bins across all multiplicity classes. For Λ and $\overline{\Lambda}$ candidates, the feed-down contribution from the decay of Ξ^- ($\overline{\Xi}^+$) and Ξ^0 is accounted for by evaluating the ratio between reconstructed primary and inclusive Λ in MC simulations, after adjusting the p_T distributions of Ξ and Λ at the generated level to match those measured in Ref. [16]. All events are then re-analyzed, assigning to each candidate its probability of being signal or background, and all product combinations of these probabilities across candidates are calculated and grouped by the total signal yield. This makes it possible to evaluate scenarios where all candidates are signal, all are background, or intermediate situations, resulting in a complete raw probability spectrum for each event, ranging from 0 to N. By summing across all analyzed events and normalizing by the total number of triggered events, a full reconstructed spectrum is obtained for each multiplicity class. Additional details on the signal extraction procedure are provided in Section 4.5.
The reconstructed spectra still reflect the inefficiencies and acceptance limitations of the detector and thus require corrections for these effects and normalization to the number of events to yield the so-called corrected spectra. This correction for detector response is achieved through a one-dimensional Bayesian unfolding procedure [139], using a Monte Carlo simulation that includes realistic transverse momentum distributions for strange particles and accurately represents detector conditions. Additionally, trigger inefficiencies affecting the measurement are accounted for, as discussed alongside the unfolding procedure in Section 4.6.
Finally, a comprehensive description of the statistical and systematic uncertainties evaluation is provided in Section 4.7.

4.2 Data and Monte Carlo samples

The work presented in this thesis is based on data collected in 2017 during the LHC Run 2 operations with pp collisions at $\sqrt{s} = 5.02$ TeV [140]. This dataset features large statistics (approximately $1.1 \cdot 10^9$ MB events, corresponding to an integrated luminosity of ~ 2.3 nb^{-1}) and stable detector conditions ensured by the relatively short acquisition period (less than one month). The accelerator settings were optimized to meet the ALICE experiment requirements, comprising sparsely populated proton bunches along the full orbit and a beam focusing strategy aligned with ALICE's rate capabilities ($\beta^* = 10$ m). These factors make this dataset particularly suitable for the present study. Two distinct detector readout strategies were implemented, referred to as CENT and FAST. In the CENT configuration, the SDD was employed in the reconstruction process, whereas in the FAST configuration, the SDD was excluded. The SDD, being the slowest detector in terms of readout time (~ 1 ms), was omitted in FAST to enhance the data acquisition rate, thereby increasing the statistics. However, the inclusion of the SDD in CENT improves vertexing, particularly in determining the z-coordinate of the vertex. Since the compatibility of the results obtained from the FAST and CENT samples was confirmed during preliminary studies, it was decided to combine the FAST and CENT data (excluding SDD), instead of performing separate analyses and merging them at a later stage to derive the final results. To account for the detector response, Monte Carlo simulations are essential. As a first step, the MC samples used in this study were generated using the Pythia 8 Monash 2013 [20] event generator, with particle propagation through the detector material simulated via GEANT4 [133]. These were general-purpose productions anchored to the data samples, replicating the detector configuration during data acquisition. However, due to the limited statistics available ($\sim 3.4 \cdot 10^8$), it was decided to perform simulations injecting strange particles (with realistic p_{T} distributions measured in [16]) inside Pythia 8 Monash events, which serve as templates for the underlying event. Particles were injected separately for strange (V^0s) and multi-strange (cascades) species, as detailed in Tables 4.1 and 4.2, respectively. This process was carried out for both the FAST and CENT configurations, resulting in a total available statistics of approximately $1.9 \cdot 10^9$ events for V^0s and $\sim 2.2 \cdot 10^7$ events for cascades. For Λ, Ξ and Ω, equal quantities of particles and anti-particles were injected. For all MC events, the reconstruction was carried out using the same techniques applied to real data, with the detector conditions aligned to those of the runs under investigation. More details about the MC simulations are discussed in Section 4.6.1.

4.3 Event selection and multiplicity categorization

In this analysis, basic event selection criteria are applied, following the standard ALICE procedure for pp analyses. The data were collected using a MB event trigger (internally referred to as kINT7), which requires signals from both V0A and V0C in coincidence with the arrival of a proton bunch from each LHC beam direction. To ensure roughly uniform detector acceptance and to reduce contamination from beam-gas collisions, only events with a primary vertex (PV) located within $\pm$ 10 cm of the nominal interaction point are considered, with the z-coordinate measured along the beam axis. Beam-gas interactions are removed offline by using the timing information from the V0 detectors

Table 4.1: Injected V^0 particles (K^0_S on the left and $\Lambda/\overline{\Lambda}$ in the center) with the corresponding number of requested events in the right column. To ensure a balanced injection rate, a low number of K^0_S and a high number of $\Lambda/\overline{\Lambda}$ were used, and vice versa. Equal quantities of particles and anti-particles were injected for Λ and $\overline{\Lambda}$.

n-particle gen K^0_S	n-particle gen Λ ($\overline{\Lambda}$)	#events requested
1	7	10^6
2	6	10^6
3	5	10^6
4	4	10^6
5	3	10^6
6	2	10^6
7	1	10^6
8	11	10^7
9	10	10^7
10	9	10^7
11	8	10^7
12	11	10^7
13	10	10^7
14	9	10^7
15	8	10^7

and by exploiting the correlation between the number of hits and tracks detected by the standalone SPD [115]. Events with multiple reconstructed primary interaction vertices (in-bunch pile-up), identified through the SPD, are marked as pile-up and excluded from the analysis [115]. Furthermore, events with pile-up occurring during the drift time of the TPC are rejected based on the correlation between the number of SDD and SSD clusters and the total number of clusters in the TPC. To further reduce pile-up contamination, primarily from out-of-bunch (OOB) collisions, it is required that at least one of the tracks among the decay products of the (multi-)strange hadron under study be matched to either the ITS or the TOF detectors. The results presented correspond to an event class (INEL$>$ 0) where at least one reconstructed SPD tracklet is produced within the pseudorapidity range $|\eta| < 1$ with respect to the beam axis, which corresponds to about 75% of the total inelastic cross-section. After applying these selection criteria, a total of approximately $\sim 1.1 \cdot 10^9$ minimum-bias events were retained.

The collisions that successfully meet these quality criteria are classified into event categories using the V0M estimator at forward rapidity. The V0A and V0C detectors, collectively referred to as V0M, are plastic scintillators, and the signal they produce is linearly proportional to the number of charged-particles that interact with them. This, in turn, is directly correlated with the mid-rapidity multiplicity. Charged-particle multiplicity, often simply referred to as multiplicity, is defined as the total number of primary charged-particles — those with a mean proper lifetime of at least 1 cm/c, either directly produced in the interaction or originating from the decay of particles with a lifetime shorter than 1 cm/c — within a defined kinematic region (in this case, $|y| < 0.5$). This forward rapidity estimator has been shown to be unbiased in terms of charged-to-neutral particle

Table 4.2: Injected cascade particles ($\Xi^{\pm}$ on the left and $\Omega^{\pm}$ in the center) with the corresponding number of requested events in the right column. To maintain a balanced injection rate, a low number of $\Xi^{\pm}$ and a high number of $\Omega^{\pm}$ were used, and vice versa. Equal quantities of particles and anti-particles were injected for both cascade types.

n-particle gen $\Xi^{\pm}$	n-particle gen $\Omega^{\pm}$	#events requested
1	10	10^6
2	9	10^6
3	8	10^6
4	7	10^6
5	6	10^6
6	5	10^6
7	4	10^6
8	3	10^6
9	2	10^6
10	1	10^6

ratios [14], as it is correlated to the global event activity rather than to local fluctuations in mid-rapidity particle production. The signals measured by the V0 detectors are grouped into percentile classes, which represent the fraction of events within each range relative to the total number of events. For example, the V0M class 0-1% corresponds to the 1% of events with the highest V0 amplitude, and this applies to the other percentile classes as well. Each event in a given percentile class is associated with a corresponding number of charged-particles produced at mid-rapidity, which can be determined by counting the number of tracks. Therefore, for each percentile class, it is possible to construct a corresponding distribution of mid-rapidity multiplicity. The average of this distribution, fully corrected for acceptance, tracking and vertexing efficiencies, as well as for contamination from secondary particles and combinatorial background, and normalized by the pseudorapidity range $|\eta| < 0.5$, gives the mid-rapidity charged-particle multiplicity density corresponding to the V0M percentile under study ($\langle \mathrm{d}N_{\mathrm{ch}}/\mathrm{d}\eta \rangle_{|\eta| < 0.5}$), often referred to simply as "multiplicity". In this thesis, we will refer to this quantity as "$\langle \mathrm{d}N_{\mathrm{ch}}/\mathrm{d}\eta \rangle_{|\eta| < 0.5}$ (V0M class)". Table 4.3 reports $\langle \mathrm{d}N_{\mathrm{ch}}/\mathrm{d}\eta \rangle_{|\eta| < 0.5}$ (V0M class) for all the multiplicity classes used in this study. Each V0M class corresponds to a broad mid-rapidity multiplicity distribution, with the relative RMS varying from 70% in the lowest multiplicity classes to 30% in the highest. Further discussion on the implications of multiplicity variability for this specific study can be found in Section 5.2, where multiplicity fluctuations and the strangeness-induced charged-particle multiplicity bias are addressed.

4.4 Candidate selection

The ALICE experiment identifies strange hadrons by reconstructing their weak decays topologically in the central pseudorapidity region. After their creation, these particles travel a few centimeters before undergoing weak decay. The decay length is determined by the particle's momentum and mean lifetime, represented by the product $c\tau$. To enhance the signal-to-background ratio, geometrical and kinematic selections are applied

Table 4.3: List of event multiplicity classes (first column), percentile intervals (second column) and corresponding charged-particle pseudorapidity densities ($|\eta| < 0.5$) in pp collisions at $\sqrt{s} = 5.02$ TeV [141] for the different particles under study (K^0_S and Λ in third, Ξ and Ω in fourth column). Class names and percentile boundaries are chosen to match those defined in Ref. [16].

Class	Multiplicity (%)	$\langle dN_{ch}/d\eta \rangle_{\|\eta\|<0.5}$ (V0M class)	
		K^0_S, Λ	Ξ, Ω
I+II+III	$0 - 0.9152$	18.50 ± 0.17	18.50 ± 0.17
IV	$0.9152 - 4.5770$	14.51 ± 0.18	14.51 ± 0.18
V	$4.5770 - 9.1560$	11.93 ± 0.11	11.24 ± 0.13
VI	$9.1560 - 13.740$	9.70 ± 0.13	
VII	$13.740 - 18.320$		8.38 ± 0.12
VIII	$18.320 - 27.510$	7.76 ± 0.11	
IX	$27.510 - 36.760$	6.34 ± 0.08	5.78 ± 0.08
X	$36.760 - 46.110$	5.22 ± 0.07	
XI	$46.110 - 65.450$	3.94 ± 0.06	3.94 ± 0.06
XII	$65.450 - 100$	2.42 ± 0.04	2.42 ± 0.04
INEL > 0	$0 - 100$	5.48 ± 0.07	

to the reconstructed candidates, targeting specific decay topologies. Strange hadrons are classified into two categories: V^0s and *Cascades*. Single-strange hadrons (K^0_S, Λ, $\overline{\Lambda}$) are referred to as V^0s due to their V-shaped decay topology, whereas multi-strange hadrons (Ξ^-, $\overline{\Xi}^+$, Ω^-, $\overline{\Omega}^+$) are known as *Cascades* because of their characteristic double-step weak decay. A summary of the properties of all particles studied can be found in Table 4.4.

The reconstruction of strange hadrons begins with the V^0 finding procedure. Since V^0s are neutral particles, they cannot be directly detected by the charge-sensitive tracking detectors (ITS and TPC, which are the primary detectors for reconstructing strange hadrons). Instead, the reconstruction relies on tracking their charged decay products. The decay vertices of V^0s are identified using ALICE's offline reconstruction algorithms, which pair oppositely charged tracks that meet basic topological criteria. To ensure that the tracks originate from secondary particles, two separate cuts are applied to the minimum values of their impact parameters relative to the primary vertex. Additionally, V^0 candidates are retained only if the Distance of Closest Approach (DCA) between the decay products is below a specified threshold and if the decay vertex falls within a predefined fiducial radius. Finally, the V^0 finding algorithm checks whether the candidate's momentum vector ($\mathbf{p}$) is consistent with originating from the primary vertex. This is achieved by applying a cut on the cosine of the angle between $\mathbf{p}$ and the vector connecting the primary vertex to the V^0 decay position, ensuring the particle trajectory does not directly point back to the primary vertex (pointing angle).

After applying selective cuts on the topological features of the weak decay, particle identification is performed based on the specific energy loss measured in the gas volume of the TPC. As charged-particles traverse the TPC, they ionize the detector's gas, and the measurement of this energy loss is used to identify the particle. The energy loss per unit length, dE/dx, is a key physics observable governed by the Bethe–Bloch equation (see Eq.

Table 4.4: Properties of strange K^0_S, Λ and $\overline{\Lambda}$ and multi-strange Ξ^-, $\overline{\Xi}^+$, Ω^- and $\overline{\Omega}^+$ hadrons. Values are taken from [142].

Particle	Quarks	S	I(J^P)	Mass (MeV/c^2)	Decay channel	B.R.(Γ_i/Γ)	$c\tau$ (cm)
K^0_S	$\frac{d\bar{s}-s\bar{d}}{\sqrt{2}}$	$-$	$\frac{1}{2}(0^-)$	497.611 ± 0.013	$\pi^0\pi^0$ $\pi^+\pi^-$	$(30.69 \pm 0.5)\%$ $(69.20 \pm 0.5)\%$	2.68
Λ	uds	-1	$0(\frac{1}{2}^+)$	1115.683 ± 0.006	$p\pi^-$ $n\pi^0$	$(63.9 \pm 0.5)\%$ $(35.8 \pm 0.5)\%$	7.89
$\overline{\Lambda}$	$\overline{u}\overline{d}\overline{s}$	$+1$	$0(\frac{1}{2}^+)$	1115.683 ± 0.006	$\overline{p}\pi^+$ $n\pi^0$	$(63.9 \pm 0.5)\%$ $(35.8 \pm 0.5)\%$	7.89
Ξ^-	dss	-2	$\frac{1}{2}(\frac{1}{2}^+)$	1321.71 ± 0.07	$\Lambda\pi^-$	$(99.887 \pm 0.035)\%$	4.91
$\overline{\Xi}^+$	$\overline{d}\overline{s}\overline{s}$	$+2$	$\frac{1}{2}(\frac{1}{2}^+)$	1321.71 ± 0.07	$\overline{\Lambda}\pi^+$	$(99.887 \pm 0.035)\%$	4.91
Ω^-	sss	-3	$0(\frac{3}{2}^+)$	1672.45 ± 0.29	ΛK^- $\Xi^0\pi^-$	$(67.7 \pm 0.7)\%$ $(24.3 \pm 0.7)\%$	2.461
$\overline{\Omega}^+$	$\overline{s}\overline{s}\overline{s}$	$+3$	$0(\frac{3}{2}^+)$	1672.45 ± 0.29	$\overline{\Lambda}K^+$ $\Xi^0\pi^+$	$(67.7 \pm 0.7)\%$ $(24.3 \pm 0.7)\%$	2.461

(4.1)), which depends on the particle's charge, mass and velocity (β). Since the charge is typically unitary and β is related to momentum — estimated from the curvature of the particle's track — the PID process infers the mass of the ionizing particle from the $\mathrm{d}E/\mathrm{d}x$ measurement. The Bethe–Bloch equation is given as:

$$-\langle \mathrm{d}E/\mathrm{d}x \rangle = k_1 \cdot z^2 \frac{Z}{A} \cdot \frac{1}{\beta^2} [\frac{1}{2} \ln(k_2 \cdot m_e c^2 \cdot \beta^2\gamma^2) - \beta^2 + k_3] \tag{4.1}$$

where

- Z and A are the atomic and the mass number of the ionized gas;
- z is the electric charge of the ionizing particle in unit of electron charge e;
- β is the velocity, normalized to the light velocity c, of the ionizing particle;
- $\gamma = 1/\sqrt{1-\beta^2}$ is the Lorentz factor ($\beta\gamma = p/Mc$, where p is the momentum and M the mass of the ionizing particle);
- m_e is the mass of the electron;
- k_1, k_2, k_3 are constants depending on the ionized medium.

Figure 3.11 in Section 3.2.4 illustrates the specific energy loss measured in the TPC as a function of rigidity (p/Z) for Pb–Pb collisions at $\sqrt{s_{\mathrm{NN}}} = 2.76$ TeV [48]. The statistical distribution of the measured $\mathrm{d}E/\mathrm{d}x$ values is centered around the expected mean, which matches the Bethe–Bloch prediction. For a given mass hypothesis and momentum of an ionizing particle, the total charge deposited along the track is subject to statistical fluctuations, which are well-described by a Landau distribution. To perform PID, the difference between the measured $\mathrm{d}E/\mathrm{d}x$ and the corresponding value predicted by the Bethe–Bloch parametrization for a given momentum is evaluated. This difference can be normalized by the TPC resolution in $\mathrm{d}E/\mathrm{d}x$ measurement, yielding a number of σ deviations from the assumed mass hypothesis:

$$n_\sigma = \frac{[(dE/dx)_{measured} - (dE/dx)_{BB}]}{\sigma_{TPC}} \tag{4.2}$$

This approach quantitatively assesses the validity of the particle's mass hypothesis. By applying a cut on the n_σ value, it is possible to reduce combinatorial background arising from misidentified decay products.
After identifying V^0 candidates, the reconstruction of cascade decays is performed by searching for V-shaped decays involving a Λ ($\overline{\Lambda}$) daughter and an additional charged pion or kaon. The association between the V^0 and the bachelor particle is established if the distance of closest approach (DCA) between the bachelor track and the V^0 trajectory falls below a specified threshold. Bachelor tracks are identified as charged pions or kaons using the TPC for PID. The cascade candidate is retained if its reconstructed momentum aligns with the primary vertex, as determined by the cosine of the cascade pointing angle. The process of locating secondary vertices from particle decays is illustrated in Fig. 4.1, with examples provided for K^0_S and Ξ^- decays. Additional details on the track reconstruction procedure can be found in [143].

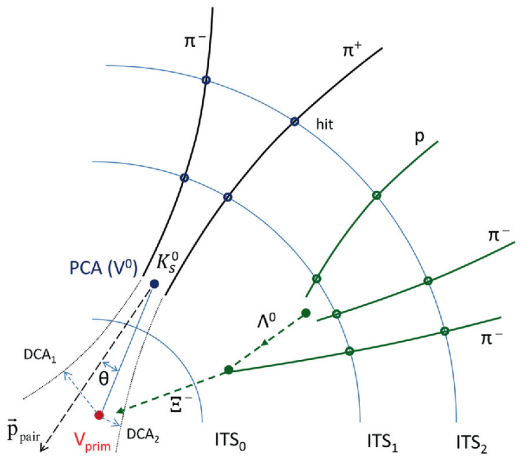

Figure 4.1: Secondary vertex reconstruction principle. Solid lines represent the reconstructed charged-particle tracks, extrapolated to the secondary vertex candidates. Extrapolations to the primary vertex and auxiliary vectors are shown with dashed lines.

All selections used in this study were optimized through detailed studies of MC simulations and are described in detail below (for further information, see Ref. [144]). The specific

values for the selections are reported in Table 4.5. It is important to note that the same criteria were applied to both data and MC samples, as well as to particles and antiparticles.

- **Kinematic selections**: strange particles are reconstructed within the mid-rapidity range ($|y| < 0.5$), while the pseudorapidity of the daughter tracks must lie within the range $|\eta| < 0.8$ to minimize acceptance losses near the edges of the TPC. A selection based on the proper lifetime is applied, which is calculated using the formula mL/p, where m is the expected mass according to the current hypothesis, L is the 3D distance between the primary vertex and the V^0 decay vertex and p is the total momentum of the candidate.

- **Topological Selections**: geometrical requirements are imposed to ensure that the tracks are spatially constrained according to the decay topology of the particle of interest:

  - *Minimum DCA (Negative/Positive) to Primary Vertex (PV):* these variables represent the impact parameters between the daughters (positive/negative) and the PV. They are applied to prevent tracks originating from the PV from being incorrectly identified as V^0 or Cascade daughters.
  - *Maximum DCA between V^0 Daughters:* the distance of closest approach (DCA) between the two tracks associated with a V^0 must be smaller than a specific number of standard deviations of the resolution to ensure they originated from the decay of a K^0_S or a Λ ($\overline{\Lambda}$).
  - *Minimum DCA Bachelor Track to PV:* this refers to the DCA between the bachelor track and the primary vertex.
  - *Minimum DCA V^0 Track to PV:* this refers to the DCA between the V^0 track and the primary vertex.
  - *Maximum DCA between Cascade Daughters:* the DCA between the two tracks associated with a Cascade must be smaller than a certain number of standard deviations of the resolution to confirm they originated from the decay of a Ξ^- ($\overline{\Xi}^+$) or Ω^- ($\overline{\Omega}^+$).
  - *Minimum V^0/Cascade Transverse Decay Radius:* A cut on the minimum transverse decay radius is applied to reduce background from random pairing of primary tracks.
  - *Minimum V^0/Cascade Pointing Angle:* this is the angle between the decay path of the V^0/Cascade (connecting the primary vertex to the decay point) and the reconstructed momentum of the V^0/Cascade. A cut on this variable ensures that the theoretical direction of the V^0/Cascade aligns with the direction of its reconstructed momentum.

- **PID selection**: for a track to be identified as a particular particle species, its ($\mathrm{d}E/\mathrm{d}x$) must be compatible within a specified n_σ range with the expected value for that species.

- **Daughter track quality selections:** these selections ensure that only high-quality daughter tracks are considered:

  - *Minimum Number of Crossed Rows:* each track must have at least a certain number of hits or clusters in the TPC. This ensures good transverse momentum (p_{T}) resolution and stable PID using $\mathrm{d}E/\mathrm{d}x$ in the TPC.
  - *Minimum Crossed Rows Over Findable:* the ratio of the number of crossed rows (clusters reconstructed) to the number of findable clusters (clusters that should have been reconstructed) must be at least 0.8. This criterion helps exclude tracks that passed through the dead zones of the TPC.

- **OOB pile-up rejection**: to reduce the effects of out-of-bunch pile-up, it is required that at least one daughter track from the decay products of the strange hadron has a hit in the TOF detector or it is reconstructed by both the ITS and TPC detectors. Out-of-bunch pile-up occurs when additional pp collisions take place in bunch crossings immediately before or after the collision of interest. This requirement helps mitigate pile-up effects, as the read-out time frames for the TOF and ITS detectors (less than 10 bunch crossings) are much shorter than the time frame of the TPC (one full LHC orbit).

- **Primary selection and MC association**: these criteria, applied to the MC truth, ensure that both the daughter and mother candidates belong to the correct species by associating the appropriate Particle Data Group [38] code with the track. Only primary candidates are retained for further analysis.

Table 4.5: List of selection criteria applied to V^0 and cascade candidates. The same criteria have been applied to both particles and antiparticles for Λ, Ξ^-, and Ω^-.

Daughter track selection	$\mathrm{K}^0_{\mathrm{S}}$ (Λ)	Ξ (Ω)
pseudorapidity	$\lvert\eta\rvert < 0.8$	$\lvert\eta\rvert < 0.8$
N_{x-rows}	$> 69(70)$	$> 69(67)$
$N_{x-rows}/N_{findable}$	≥ 0.8	≥ 0.8
TPC $\mathrm{d}E/\mathrm{d}x$	$< 5(4)\sigma_{dE/dx}$	$< 5(5.5)\sigma_{dE/dx}$
N_{trk} with (TOF || ITS)	≥ 1	≥ 1
Candidate selection	$\mathrm{K}^0_{\mathrm{S}}$ (Λ)	Ξ (Ω)
rapidity	$\lvert y\rvert < 0.5$	$\lvert y\rvert < 0.5$
DCA V^0 daughter to PV	$> 0.035(0.06)$ cm	> 0.11cm
DCA V^0 daughters	$< 0.5(0.6)\sigma$	$< 0.8(0.7)\sigma$
DCA V^0 to PV	–	> 0.04 cm
DCA bachelor to PV	–	$> 0.03(0.02)$ cm
DCA cascade daughters	–	$< 0.8(0.7)$ cm
$R_{xy}V^0$	$> 0.35(0.5)$ cm	> 0.6 cm
R_{xy} cascade	–	$> 0.4(0.35)$ cm
Proper Lifetime ($m\mathrm{L}/p$)	$< 40(30)$ cm	$< 17(10)$ cm
V^0 cosθ_{PA}	$> 0.99(0.996)$	$> 0.985(0.98)$
cascade cosθ_{PA}	–	$> 0.985(0.98)$
Primary selection (MC only)	`AliStack::IsPhysicalPrimary`	`AliStack::IsPhysicalPrimary`
MC association (MC only)	`PDGcode`	`PDGcode`

After applying these selection criteria, the (multi-)strange particle candidates are grouped into intervals based on their transverse momentum (p_{T} range [0, 10] GeV/c). The subse-

quent steps are then carried out independently for each p_{T} interval and for each multiplicity class, as defined in Table 4.3).

- p_{T} $^{\mathrm{K}^0_{\mathrm{S}}}$ intervals: [0-0.5), [0.5-1), [1-1.25), [1.25-1.75), [1.75-2), [2-3), [3-4), [4-5), [5-6), [6-7), [7-8), [8-9), [9-10) GeV/c;
- p_{T} $^{\Lambda}$ (p_{T} $^{\overline{\Lambda}}$) intervals: [0-1), [1-2], [2-3), [3-4), [4-5), [5-6), [6-7), [7-8), [8-10) GeV/c;
- p_{T} $^{\Xi^-}$ (p_{T} $^{\overline{\Xi}^+}$) intervals: [0-1), [1-2), [2-3), [3-4), [4-5), [5-6), [6-10) GeV/c;
- p_{T} $^{\Omega^-}$ (p_{T} $^{\overline{\Omega}^+}$) intervals: [0-1), [1-2), [2-3), [3-4), [4-10) GeV/c;

Examining the invariant mass spectra shown in Fig. 4.2 for the particles under study before and after applying the selection criteria listed in Table 4.5 for integrated multiplicity within a specific p_{T} bin, the impact of the cuts can be clearly observed. Similarly, Fig. 4.3 presents the corresponding plots for the antiparticles under investigation.

4.5 Signal extraction: raw multiplicity spectrum engineering

The raw multiplicity spectra were determined by applying the selection criteria outlined in the previous section and performing signal extraction. In this analysis, the signal extraction was carried out using a data-driven weighting procedure that assigns a probability to each candidate, indicating the likelihood of being signal or background.
The first step involved fitting the one-dimensional invariant mass spectrum in each p_{T} bin and across all multiplicity classes using a combination of two functions: one modeling the signal and the other representing the background. For the signal, to model peak distributions with asymmetric tails, a double-sided Crystal Ball function (dsCB [145]) was employed

$$f(x;\overline{x},\sigma,\alpha_L,n_L,\alpha_H,n_H) = \begin{cases} \left(\frac{n_L}{|\alpha_L|}\right)^{n_L}\cdot e^{-\frac{|\alpha_L|^2}{2}}\cdot\left(\frac{n_L}{|\alpha_L|}-|\alpha_L|-\frac{x-\overline{x}}{\sigma}\right)^{-n_L} & \left(\frac{x-\overline{x}}{\sigma}\right)<-\alpha_L, \\ e^{-\frac{1}{2}\left(\frac{x-\overline{x}}{\sigma}\right)^2} & -\alpha_L\leq\left(\frac{x-\overline{x}}{\sigma}\right)<\alpha_H, \\ \left(\frac{n_H}{|\alpha_H|}\right)^{n_H}\cdot e^{-\frac{|\alpha_H|^2}{2}}\cdot\left(\frac{n_H}{|\alpha_H|}-|\alpha_H|-\frac{x-\overline{x}}{\sigma}\right)^{-n_H} & \left(\frac{x-\overline{x}}{\sigma}\right)\geq\alpha_H. \end{cases} \tag{4.3}$$

where $\overline{x}$ represents the central value of the distribution or the position of the main peak, σ defines the width of the Gaussian part of the distribution, α_L and α_H control the transition points where the distribution changes from Gaussian to power-law behavior and n_L and n_H define the power-law behavior of the left and right tails respectively. For the background, a first-degree polynomial was used for all particles analyzed, except for Ω particles, where a Gaussian function was selected.

$$f(x;a,b)=a\cdot x+b \qquad f(x;\overline{x},\sigma)=\frac{1}{\sqrt{2\pi\sigma^2}}e^{\frac{(x-\overline{x})^2}{2\sigma^2}} \tag{4.4}$$

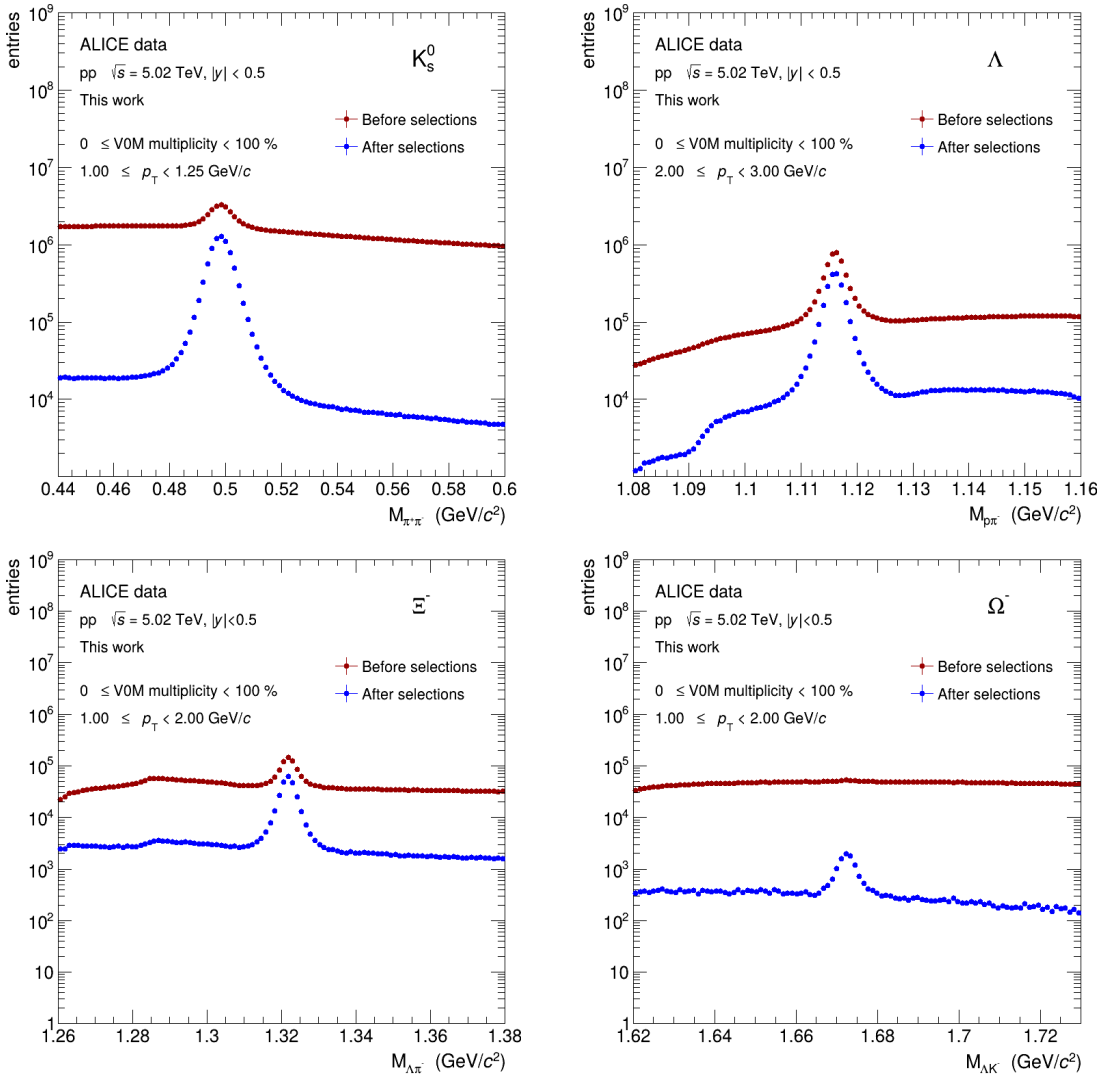

Figure 4.2: Invariant mass distributions for all particles under study are shown before (red) and after (blue) applying the selection criteria for INEL > 0 within a specific p_{T} bin. The first row presents the comparisons for $\mathrm{K}^0_{\mathrm{S}}$ and Λ, while the second row displays those for Ξ^- and Ω^-.

Figure 4.4 presents examples of invariant mass distributions for strange and multi-strange particles in the INEL > 0 event class. The top panels show distributions for strange particles, while the bottom panels display those for multi-strange particles. Data points for a low p_{T} interval (around 1 GeV/c) are shown in red, while those for a high p_{T} interval (up to 10 GeV/c) are shown in blue. The dashed lines represent the total fits, obtained as the sum of a double-sided Crystal Ball function for the signal and a first-degree polynomial (or a Gaussian for Ω) for the background. All the 1D invariant mass distributions, along with the corresponding fits, are provided in Appendix 9.1 for each particle and antiparticle across all p_{T} bins considered, organized by multiplicity class.

This procedure enables the assignment of weights to each candidate, reflecting its likelihood of being signal or background based on its p_{T}, invariant mass and the event's

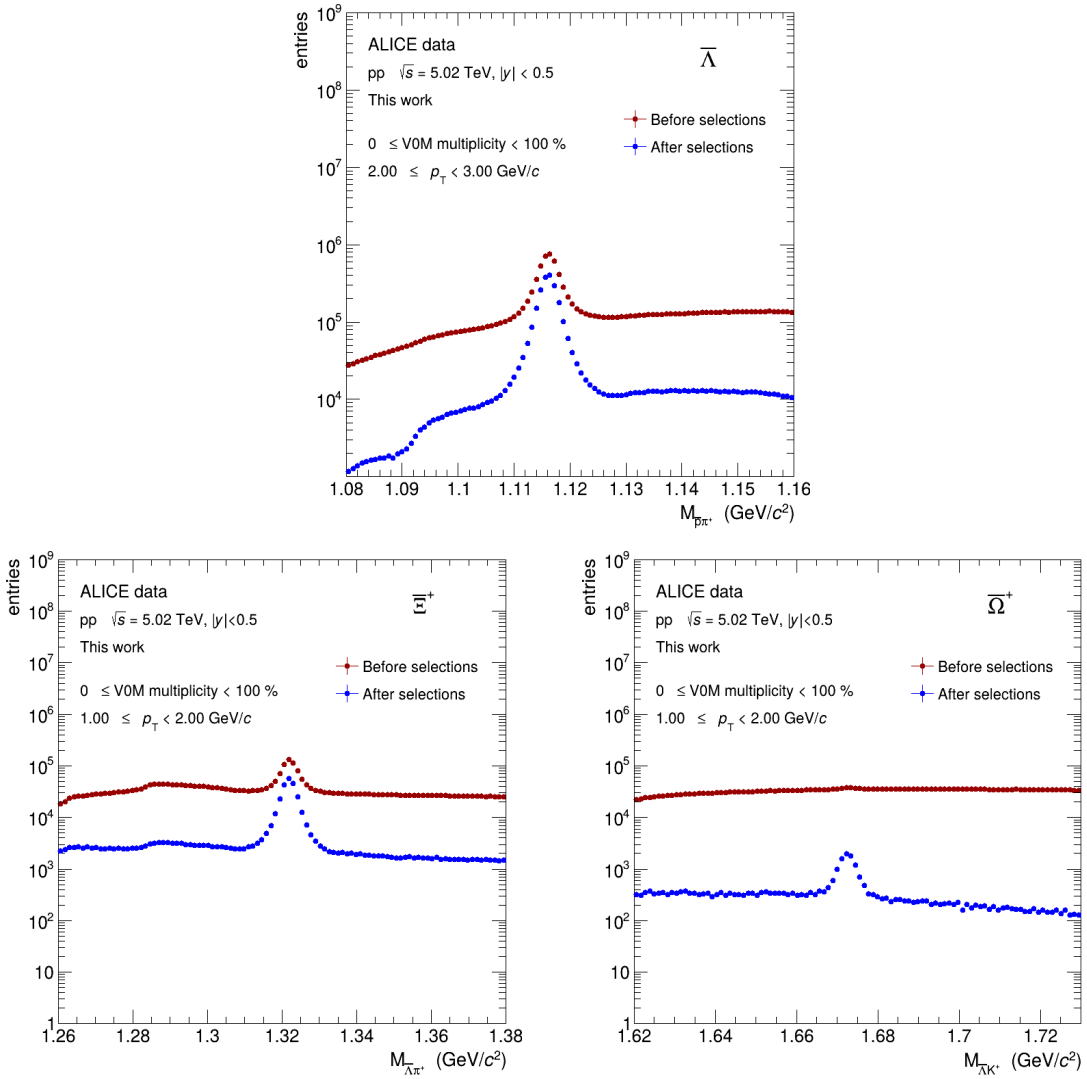

Figure 4.3: Invariant mass distributions for all antiparticles under study are displayed before (red) and after (blue) applying the selection criteria for INEL > 0 within a specific p_{T} bin. The first row shows the comparison for $\overline{\Lambda}$, while the second row includes $\overline{\Xi}^+$ and $\overline{\Omega}^+$.

measured multiplicity. The weights are defined as follows:

$$w_S\left(p_{\mathrm{T}}, m_{\mathrm{inv}}; \mathrm{V0M}\right) = \frac{\mathrm{dsCB}\ \left(p_{\mathrm{T}}, m_{\mathrm{inv}}; \mathrm{V0M}\right)}{\mathrm{Total}\ \left(p_{\mathrm{T}}, m_{\mathrm{inv}}; \mathrm{V0M}\right)} \left\{ \cdot\, w_{FD}(p_{\mathrm{T}}; \mathrm{V0M}) \right\} \quad , \; w_B \;=\; 1 - w_{\mathrm{S}} \quad (4.5)$$

Here, w_S represents the signal weight and w_B the background weight. The factor $w_{FD}(p_{\mathrm{T}}; \mathrm{V0M})$ is specifically included in the Λ ($\overline{\Lambda}$) analysis to account for the feed-down contribution from the decays of Ξ^- ($\overline{\Xi}^+$) and Ξ^0. The factor w_{FD} is evaluated as the ratio between reconstructed primary and inclusive Λ in the MC simulation, once the p_{T} distributions of both Ξ and Λ have been corrected at the generated level to match those measured in Ref. [16]. For the Ξ^0, its p_{T} shape is assumed to match the shape measured for charged Ξ. This approach, differing from the method used in previous analyses —

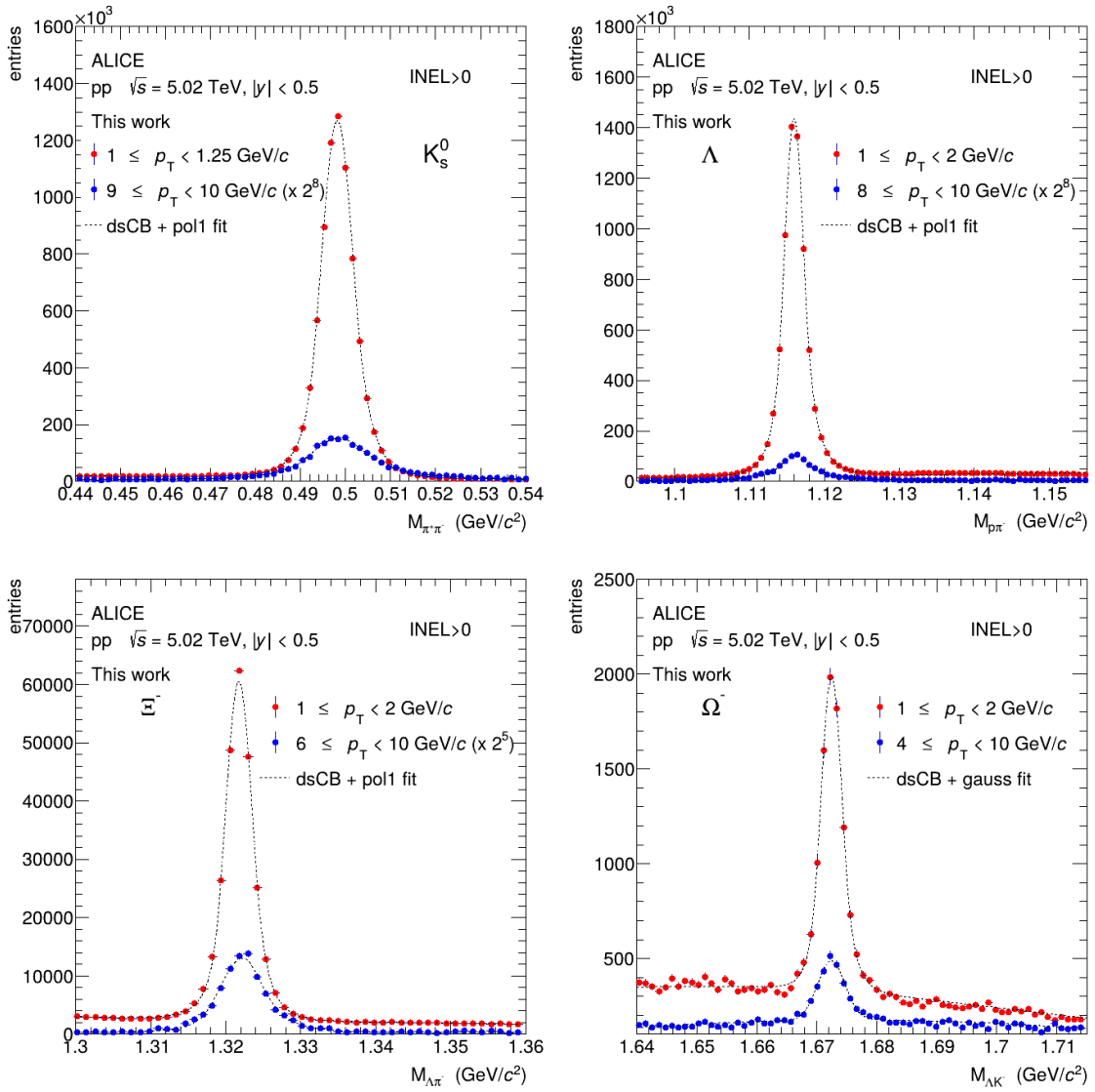

Figure 4.4: Invariant mass distributions for K^0_S (top, left), Λ (top, right), Ξ^- (bottom, left) and Ω^- (bottom, right), at low ($\sim$ 1 GeV/c, red circles) and high transverse momentum (blue circles) for the INEL > 0 event class. The dashed lines illustrate the total fits, obtained as the sum of a double-sided Crystal Ball function for the signal and a first-degree polynomial (or a Gaussian for Ω) for the background.

which relied on constructing a feed-down matrix [1]— utilizes the prior determination of the p_{T} distribution for the particles under study. The comparison between the feed-down fractions determined with the two techniques shows very good agreement. Figure 4.5 illustrates the feed-down fraction removed as a function of p_{T} for Λ and $\overline{\Lambda}$, represented by full and open markers, respectively. The left panel shows the fraction for integrated multiplicity, while the right panel displays the fractions across all considered multiplicity

[1]The feed-down matrix represents the probability or the quantitative contribution with which mother particles of a certain type decay into observed daughter particles. Thus, each element M_{ij} of the matrix describes the fraction of the contribution of the mother particle i to the daughter particle j.

classes. To achieve finer granularity, each fraction was fit using a fifth-degree polynomial. The feed-down correction applied during signal extraction was then determined as the value of the fitted function at the p_{T} of each candidate.

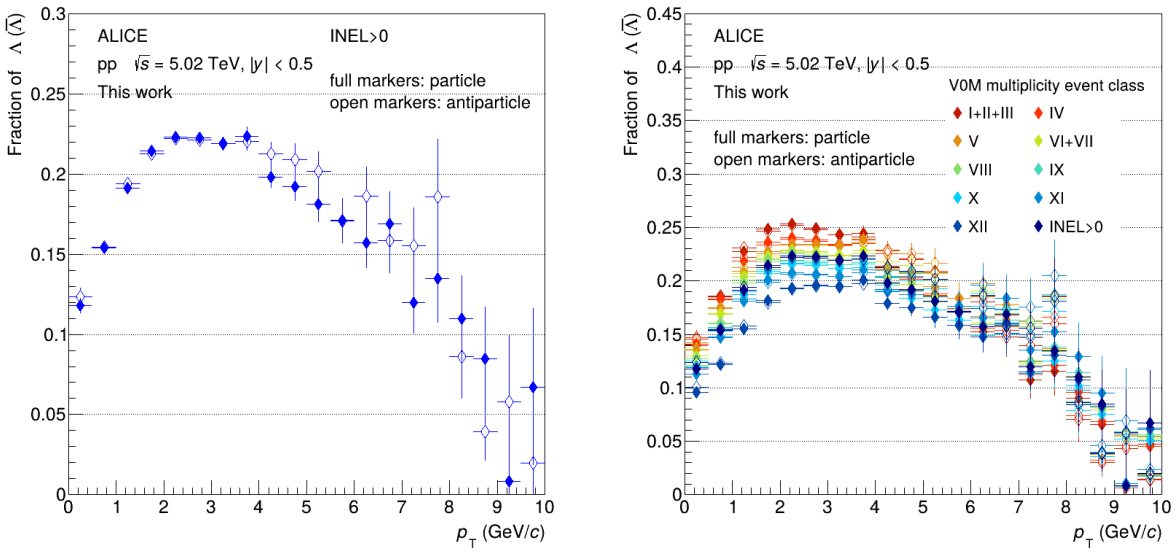

Figure 4.5: The fraction removed as a function of p_{T} for Λ and $\overline{\Lambda}$ particles as full and open markers respectively for INEL > 0 (*Left*) and for all the multiplicity classes (*Right*).

To ensure the signal weights were correctly implemented, the trend of the signal probability as a function of the invariant mass was analyzed across various p_{T} bins for each multiplicity class under study. Figure 4.6 illustrates these trends, with the first row showing results for V^0 particles ($\mathrm{K}^0_{\mathrm{S}}$ and Λ) and the second row displaying cascades (Ξ^- and Ω^-), all corresponding to INEL > 0. Similar trends were observed for the respective antiparticles, and these, along with the results for all other multiplicity classes, are included in Appendix 9.2.

Furthermore, the signal probability was also studied as a function of the candidate's p_{T}, as shown in the left panel of Fig. 4.7. In this case two distinct regions of the invariant mass distribution were considered: at the peak (round markers) and at a distance of -$1\sigma_{dsCB}$ from the peak position (square markers). At the peak, w_S is generally very high, exceeding 0.9 even at $1\sigma_{dsCB}$ for most particles, except for Ω^-, where the lower signal-to-background ratio results in smaller signal probabilities. Notably, w_S evolves smoothly with p_{T}, indicating that the chosen p_{T} granularity is sufficiently fine to avoid rapid variations of w_S within the p_{T} bins.

After this first step, each of the N candidates in every event is considered with its corresponding w_S and the combined probability for all candidates to be signal, background and all intermediate $\frac{N!}{M!(N-M)!}$ combinations with M signals and $N-M$ backgrounds are evaluated and summed. In this way, for each event with N candidates a full reconstructed probability spectrum spanning from 0 to N is extracted. As an example, with three V^0 candidates in the event i, the reconstructed spectrum R_i is composed by four bins, whose contents are calculated as:

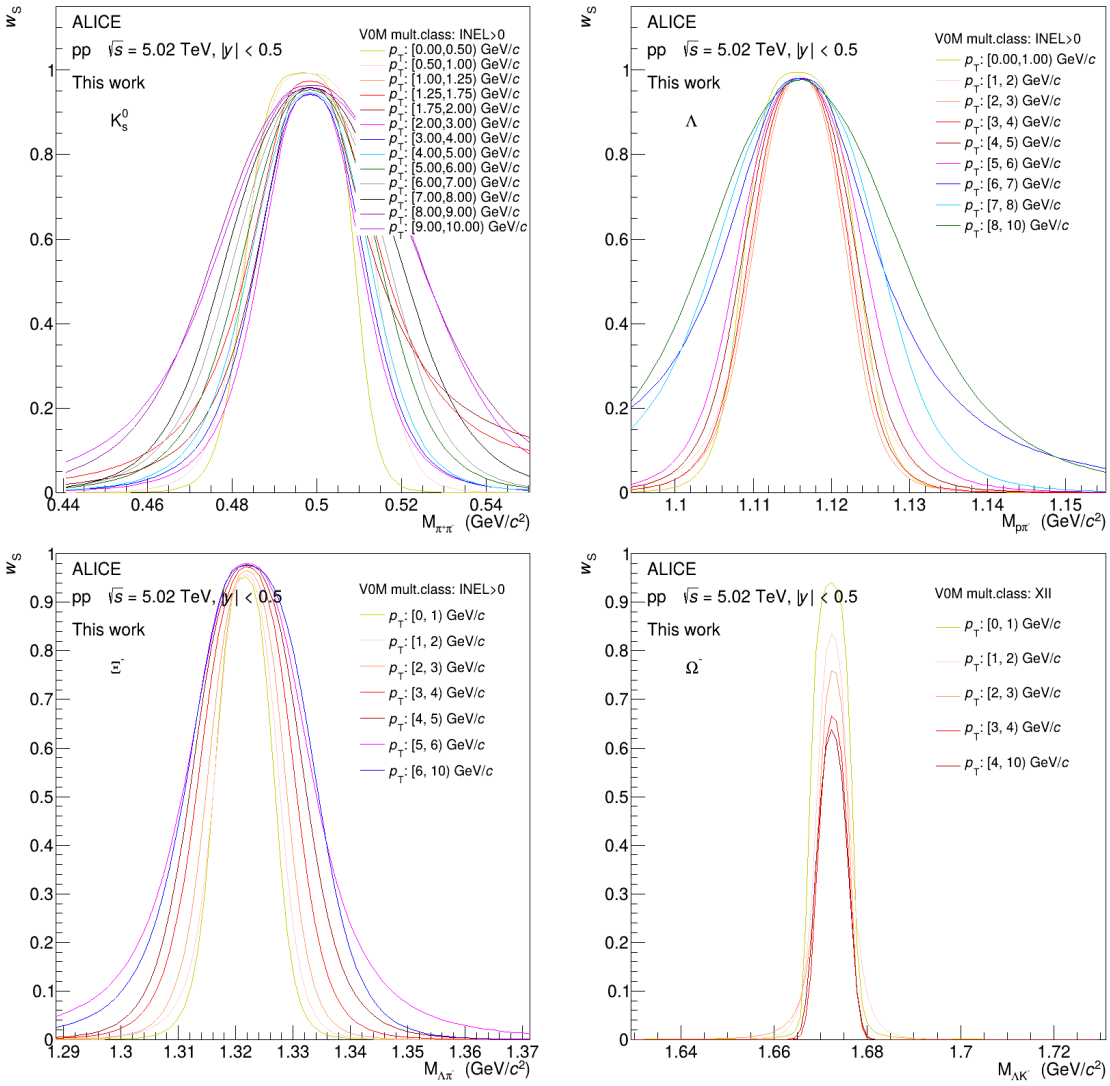

Figure 4.6: Signal probability trend as a function of invariant mass, accounting for the p_{T} dependence for INEL > 0. The first row shows the results for $\mathrm{K}^0_{\mathrm{S}}$ and Λ, while the second row presents the results for Ξ^- and Ω^-.

$$
\begin{aligned}
R_i[0] &= w_B(1) \cdot w_B(2) \cdot w_B(3) \\
R_i[1] &= w_S(1) \cdot w_B(2) \cdot w_B(3) + w_B(1) \cdot w_S(2) \cdot w_B(3) + w_B(1) \cdot w_B(2) \cdot w_S(3) \\
R_i[2] &= w_S(1) \cdot w_S(2) \cdot w_B(3) + w_S(1) \cdot w_B(2) \cdot w_S(3) + w_B(1) \cdot w_S(2) \cdot w_S(3) \\
R_i[3] &= w_S(1) \cdot w_S(2) \cdot w_S(3).
\end{aligned}
$$

Summing over all the analyzed events (over all i in the example above) and normalizing to the total number of triggered events, the full reconstructed spectrum is extracted. The procedure is carried out for the INEL > 0 event class and in every V0M multiplicity class. A special note should be made regarding events with zero particles of a given species per event. These events can originate from two distinct scenarios: either no candidates passed the applied selection criteria despite being present, or no reconstructed candidates were

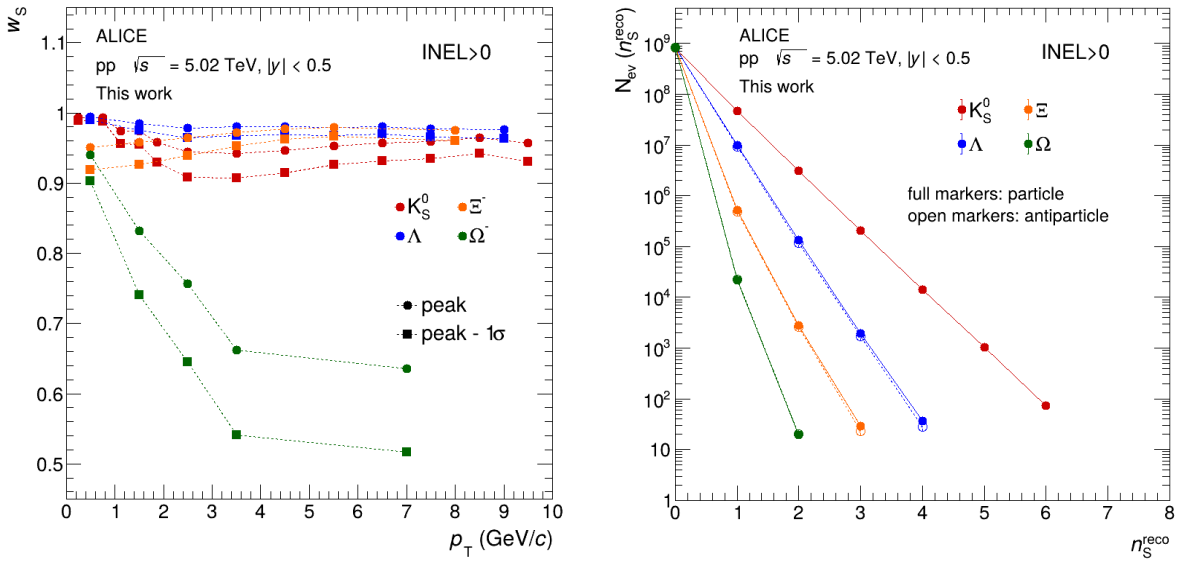

Figure 4.7: (*Left.*) Signal weights at the signal peak position (circles) and at 1σ distance from the peak (square markers) for all particles under study as a function of p_{T} in the INEL > 0 event class. Dashed lines are shown to guide the eye. (*Right.*) Un-corrected multiplicity spectrum for all particles under study in the INEL > 0 event class. Particles correspond to full markers, anti-particles to hollow markers.

produced in the event. Both cases are appropriately accounted for and summed together in the analysis.
The right panel of Fig. 4.7 reports the reconstructed multiplicity spectrum for all particles (full circles) and antiparticles (open circles) for INEL > 0, where statistical errors have been evaluated using sub-samples method (see Section 4.7). The spectrum is truncated (to enhance visibility) at an n_S^{reco} which features at least 10 occurrences in the analyzed sample. The uncorrected spectra for all other multiplicity classes are presented in Appendix 9.3, separately for V^0s and cascades.

To ensure the correct implementation of the weights procedure, a formal validation was carried out for the $\mathrm{K}^0_{\mathrm{S}}$ case, exploring the two-dimensional scenario where a 2D fit is feasible. A toy Monte Carlo simulation with 10^9 events was generated, where for each event, the mass values m_1 and m_2 were randomly sampled from the one-dimensional invariant mass spectrum. This produced the 2D plot of m_1 vs m_2, shown on the left in Fig. 4.8. A 2D fit was then performed using the sum of a double-sided Crystal Ball function for the signal and a linear function for the background in each dimension. The resulting fit is displayed on the right in Fig. 4.8.
The total function components corresponding to double, single and zero signals were extracted, as shown in Fig. 4.9. These components were obtained, respectively, by:

- Multiplying two double-sided Crystal Ball functions for the double-signal case (*Left*)
- Considering one double-sided Crystal Ball function for the single-signal contribution (*Center*)

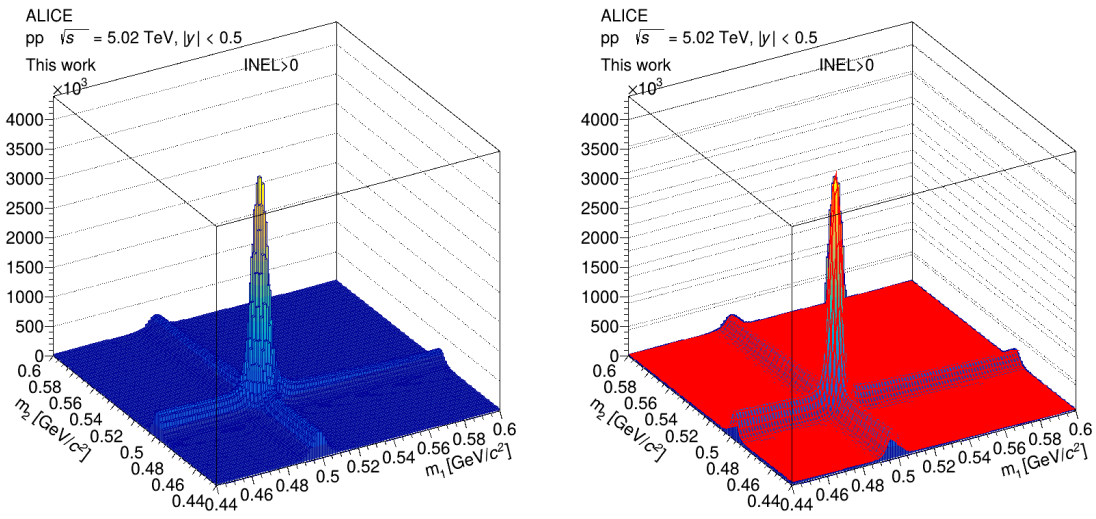

Figure 4.8: *Left:* The two-dimensional invariant mass spectrum obtained from a toy Monte Carlo simulation with 10^9 events, where for each event, the mass values m_1 and m_2 were randomly sampled from the one-dimensional invariant mass spectrum for the integrated multiplicity. *Right:* The 2D fit consisting of the sum of a double-sided Crystal Ball function for the signal and a linear function for the background in each dimension.

- Multiplying two linear functions for the zero-signal case (*Right*).

Integrating these components yielded the number of events containing two, one or zero signals.

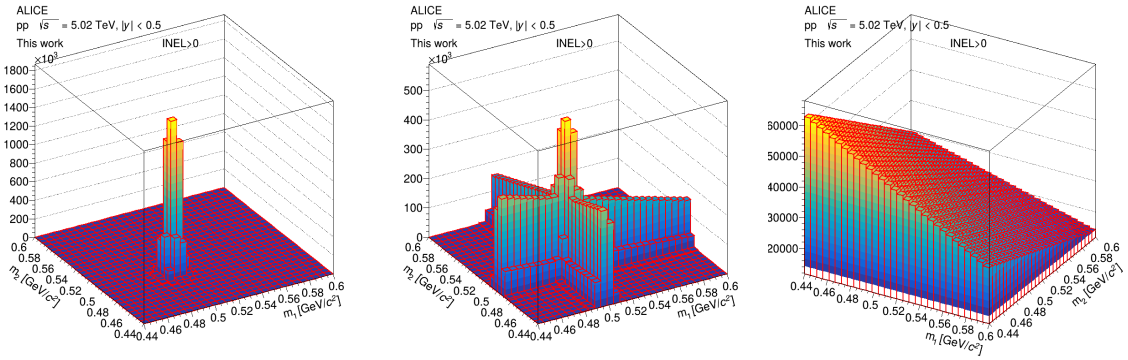

Figure 4.9: The total function components for K^0_S are shown. (*Left:*) The component associated with the double signal, obtained by multiplying two double-sided Crystal Ball functions. (*Center:*) The component corresponding to a single signal, given by the sum of the product of a double-sided Crystal Ball function for m_1 and a linear function for m_2, and the product of a linear function for m_1 and a double-sided Crystal Ball function for m_2. (*Right:*) The component associated with zero signal, obtained by multiplying two linear functions.

To extend the weights procedure to the two-dimensional case, the relative weights of the signal and background were multiplied by the total number of signals of interest.

The comparison between the two methods shows excellent agreement, as illustrated in Fig. 4.10. Here, the results obtained with the weights procedure are shown in blue, while those from the 2D fit are shown in red, with a slight shift applied for better visualization. Following this successful validation, the weights procedure was applied to the full dataset, extending it to the n-dimensional case.

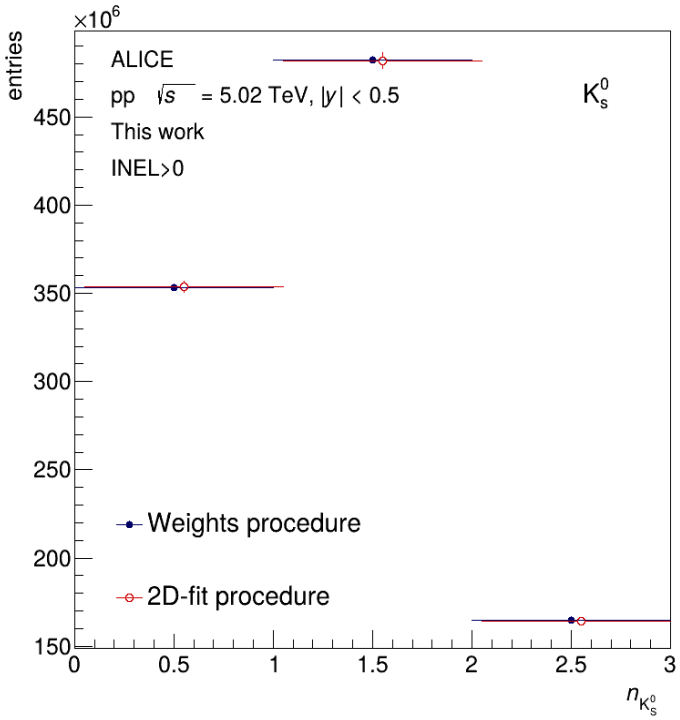

Figure 4.10: Formal check in 2D: comparison between the two-dimensional results obtained using the 2D fit and the weights procedure, shown in red and blue, respectively for INEL > 0 event class. The results from the 2D fit were slightly shifted for better visualization.

4.6 Corrections: unfolding and trigger efficiency

Two different types of corrections have been considered and applied to the number of strange particles per event (n_S): one accounting for the detector response and the other for trigger efficiency.

To evaluate the detector response, the analysis must be performed on MC simulated data, applying the same set of selections as those used for real data. However, the analysis of MC events offers the advantage of an additional selection criterion unavailable in real data: PDG association. In simulations, the correspondence between a reconstructed candidate and its originating generated particle type is explicitly known. This information can be used to refine the analysis, limiting it to pure signal candidates.

In traditional statistical analyses of particle production across a given number of events, the correction for detector effects is typically achieved through the *Acceptance* × *Efficiency*

method ($A\times\varepsilon$). For each p_{T} bin and across all multiplicity classes, the $A\times\varepsilon$ is calculated as the ratio between the number of reconstructed particles ($N^{MC}_{reconstructed}$) and the number of generated particles ($N^{MC}_{generated}$):

$$A\times\varepsilon = \frac{N^{MC}_{reconstructed}}{N^{MC}_{generated}} \tag{4.6}$$

However, this analysis requires a different approach, specifically the use of the *unfolding* technique. While the $A\times\varepsilon$ method is suitable for correcting the number of signal candidates (i.e., the yield), this analysis focuses on correcting the number of events containing a specific number of particles of a given species.
Starting from the MC production, one can select events with a given number of simulated particles and calculate conditional probabilities as follows:

P(R0|G0) = probability of reconstructing 0 particles given that 0 particles were generated
P(R1|G0) = probability of reconstructing 1 particle given that 0 particles were generated
...
P(R0|G1) = probability of reconstructing 0 particles given that 1 particle was generated
...

By organizing these conditional probabilities appropriately, one constructs the detector response matrix, which maps generated events to reconstructed ones. This is represented as:

$$\begin{pmatrix} R0 \\ R1 \\ R2 \\ \dots \\ \dots \\ Rn \end{pmatrix} = \begin{pmatrix} P(R0|G0) & P(R0|G1) & P(R0|G2) & \dots & \dots & P(R0|Gn) \\ P(R1|G0) & P(R1|G1) & P(R1|G2) & \dots & \dots & \dots \\ P(R2|G0) & \dots & \dots & \dots & \dots & \dots \\ \dots & \dots & \dots & \dots & \dots & \dots \\ \dots & \dots & \dots & \dots & \dots & \dots \\ P(Rn|G0) & \dots & \dots & \dots & \dots & P(Rn|Gn) \end{pmatrix} \cdot \begin{pmatrix} G0 \\ G1 \\ G2 \\ \dots \\ \dots \\ Gn \end{pmatrix} \tag{4.7}$$

Ideally, if both the square detector response matrix R and the true distribution T are known, the measured distribution M can be written as:

$$M = R \cdot T \tag{4.8}$$

Thus, in principle, if M and R are available, the true distribution T can be obtained by inverting the response matrix:

$$T = R^{-1} \cdot M \tag{4.9}$$

However, this straightforward procedure can lead to complications. First, the response matrix may be singular, making it impossible to invert. Even if it is non-singular, the resolution of the spectrum may introduce non-physical fluctuations into the result, as discussed in [146]. There are two main sources of uncertainties:

- Statistical uncertainties: these arise from the Monte Carlo events used to populate the matrix M. These uncertainties are bin-to-bin independent. These statistical errors propagate through the unfolding formalism.

- Systematic uncertainties: these are typically described by a variation $M \rightarrow M+\delta M$, representing changes in experimental conditions.

Such uncertainties can cause instabilities in the unfolding procedure. This effect can be illustrated schematically in Fig. 4.11. Assuming that the true distribution T is known and that the response matrix R is non-singular, the derivation of M is straightforward ($M = R \cdot T$). From the measured distribution M, a sample of N events, denoted $\tilde{M}$, is produced. When attempting to derive $\tilde{T} = R^{-1}\tilde{M}$, oscillations due to the resolution of $\tilde{M}$ appear, as shown in Fig. 4.12. It is evident that $\tilde{T}$ is not the true distribution.

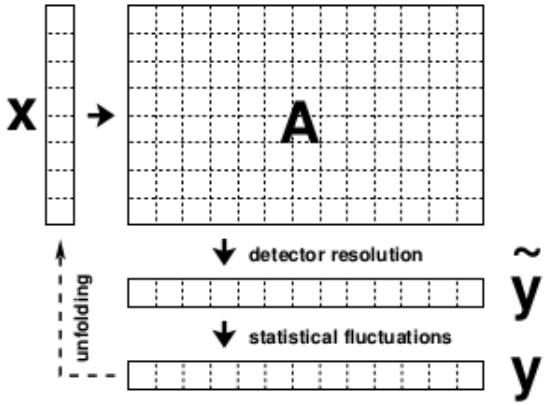

Figure 4.11: Schematic representation of migration effects and statistical fluctuations [146].

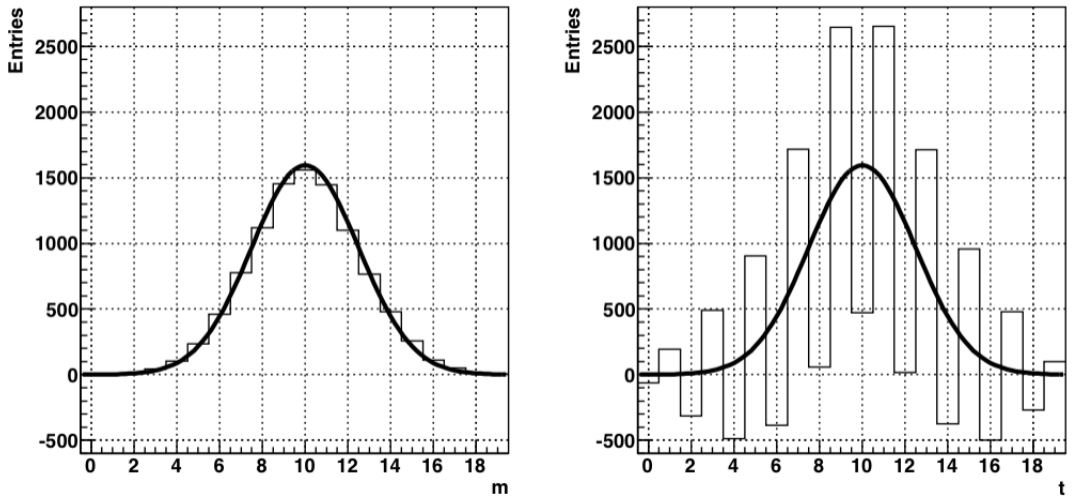

Figure 4.12: (*Left:*) The measured distribution and the binned sample produced from it. (*Right:*) The initially known true distribution and the binned histogram with $\tilde{T}$ derived from the inversion of the response matrix [147].

To mitigate such fluctuations, smoothness conditions are often imposed through a specific procedure known as regularization.
Specific tools interfaced with the ROOT analysis framework [148], such as TUnfold [146],

are available for handling migration and background effects in high-energy physics, especially for multi-dimensional distributions. An attempt was made to use TUnfold in this analysis; however, due to the limited statistics in the MC simulation, which led to many zero entries and caused the determinant to vanish, the inversion procedure could not be applied.
In addition to matrix inversion, other techniques for unfolding are available. One such method, tested in this analysis, is Bayesian unfolding [139], which relies on an iterative process. This procedure is based on Bayes' theorem:

$$P(G_j|R_i) \propto P(R_i|G_j) \cdot P(G_j) \tag{4.10}$$

where

- $P(G_j|R_i)$ is the *posterior probability*, representing the likelihood that the theory (corrected distribution) is valid given the new data (reconstructed yield).
- $P(G_j)$ is the *prior probability*, reflecting the validity of the theory before the measurement. This is a subjective assessment based on prior knowledge and is calibrated using available information.
- $P(R_i|G_j)$ is the *likelihood*, representing the probability of observing the data R_i given the theory distribution G_j.

The probabilities $P(R_i|G_j)$ can be derived from MC simulations, while the posterior probabilities $P(G_j|R_i)$ depend on the initial distribution and the unknown prior probability $P(G_j)$. The iterative procedure involves selecting a prior distribution, which is used in Bayes' theorem to compute a posterior probability matrix. This matrix is then applied to the raw spectrum, providing a first estimate of the corrected spectrum. In the next iteration, the corrected probability distribution from the previous step becomes the new prior probability, and the process is repeated. This continues until the unfolding procedure converges to a stable result. It is important to note that, like with matrix inversion, a regularization procedure must be applied to the posterior probability before it can be used as the prior in the next iteration.

A specialized framework, *RooUnfold* [149], implements various unfolding techniques and was used to correct the reconstructed spectra.

4.6.1 Monte Carlo choice

To properly account for the detector response, MC simulations are essential. In this study, the MC samples were initially generated using the Pythia 8 Monash 2013 event generator [20], with particle propagation through the detector material simulated via GEANT4 [133]. These samples were general-purpose (GP) productions, anchored to the data samples and designed to replicate the detector configuration during data acquisition. A preliminary closure test was performed: the response matrix was constructed using a fraction of the MC statistics, while the remaining fraction was treated as "data." However, due to the limited available statistics ($\sim 3.4 \cdot 10^8$), the closure test was successful only for events with a low number of particles. To address this limitation, it was decided to

use a first-injected MC production incorporating realistic p_{T} distributions, as recently measured in Ref. [16]. This approach efficiently populates events with a high number of generated particles. A second closure test was performed, this time constructing the response matrix using the first-injected MC production while treating the GP productions as "data." However, the closure test did not yield perfect agreement. The discrepancy was traced back to the difference in the p_{T} distributions implemented in Pythia 8 Monash 2013 and the first-injected MC production. Specifically, the response matrix constructed with the first-injected MC production revealed two distinct regions:

- A low-particle region, dominated by candidates with the Pythia 8 Monash 2013-based p_{T} distribution.
- A high-particle region, dominated by the realistic p_{T} distribution, where Pythia 8 Monash 2013 events are insignificant.

To confirm that the observed discrepancy was caused by the differing p_{T} distributions, a third closure test was performed using only the first-injected MC production. In this test, 70% of the statistics was used to construct the response matrix, while the remaining 30% served as "data." The results showed excellent agreement between the generated spectra and the unfolded distributions, demonstrating the success of the closure test. This confirmed that the issue with the GP productions and the first-injected MC production was indeed the difference in the p_{T} distributions. When the p_{T} distributions differ, the $A \times \varepsilon$ behaves differently, leading to mismatches between the reconstructed spectra and the response matrix. Since realistic p_{T} distributions are necessary to accurately correct the reconstructed spectra, a new MC-injected production with higher statistics was requested for all particles under study. This production allows particle injection even in the low-particle region, ensuring a consistent p_{T} distribution across all multiplicities. In summary, the focus was shifted entirely to MC samples with particle injection.

At the end, a dedicated MC simulation was carried out, featuring Pythia 8 Monash 2013 events combined with injected strange particles, sorted according to their measured p_{T} distributions from Ref. [16] as described in Section 4.2. It is important to note that strange hadrons originally simulated by Pythia 8 Monash 2013 were removed a posteriori. Their p_{T} distributions differ from those observed in real data, and their inclusion would introduce a bias, as discussed earlier. Figure 4.13 shows the response matrices in the INEL > 0 class for $\mathrm{K}^0_{\mathrm{S}}$, Λ, Ξ^- and Ω^-. As this is a counting measurement, the errors associated to the detector response matrices are considered to be Poissonian, and therefore given by the square root of the counts.

Note that strange particles were injected following a sub-sample scheme designed to ensure similar statistics in events with varying strange particle multiplicities. This approach results in a flat distribution of the number of events as a function of the generated strange particle multiplicity. However, as shown in Fig. 4.14, the generated distributions obtained from the projection of the response matrices in the INEL > 0 class for $\mathrm{K}^0_{\mathrm{S}}$, Λ, Ξ^- and Ω^- exhibit deviations from the expected trend. This discrepancy primarily arises because two different rapidity ranges were considered in MC ($|y| < 0.6$) and data ($|y| < 0.5$) to avoid border effects, leading to a loss of approximately 1/6 of the candidates. For $\mathrm{K}^0_{\mathrm{S}}$, the requested injection scheme (see Table 4.1) anticipated a flat distribution at 10^6 events

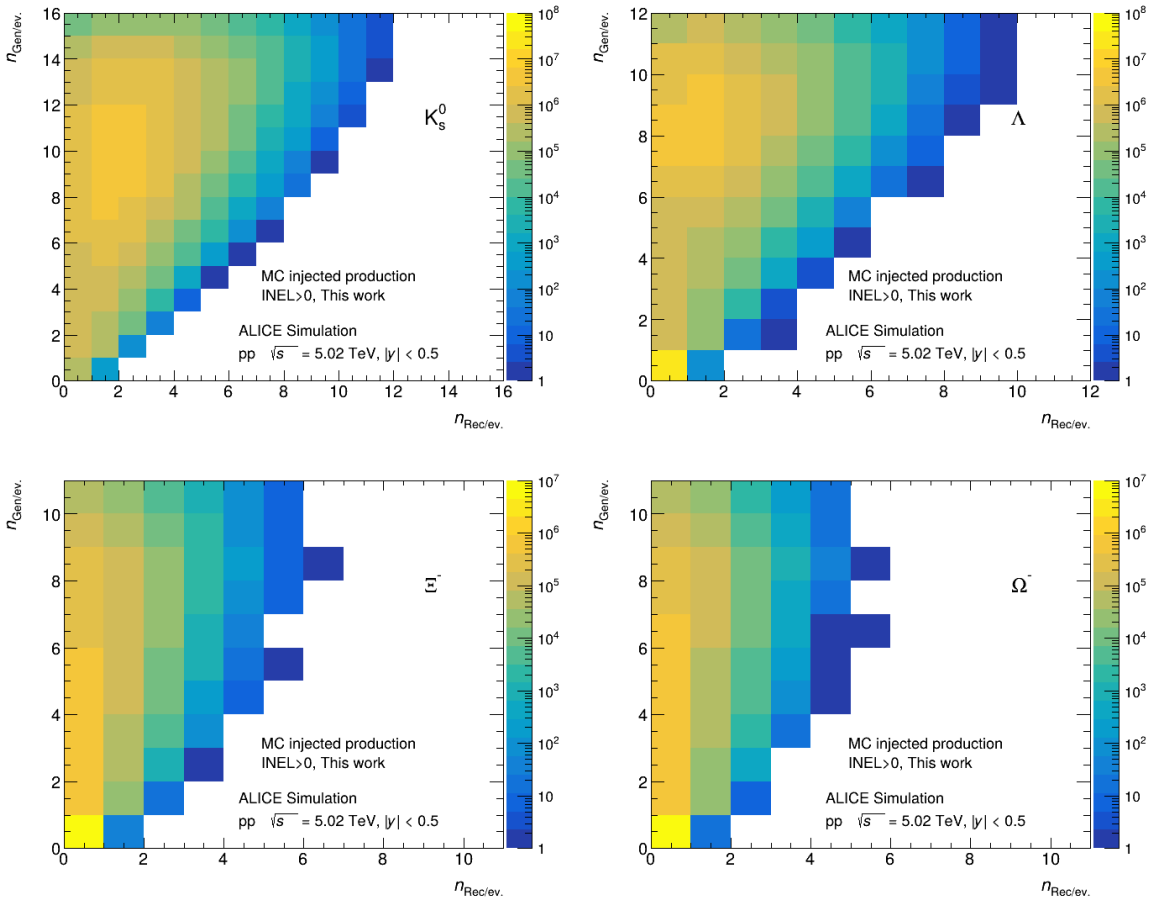

Figure 4.13: Response matrices obtained considering a dedicated MC simulation including the measured p_{T} distributions from Ref. [16] of $\mathrm{K}^0_{\mathrm{S}}$ (top left), Λ (top right), Ξ^- (bottom left) and Ω^- (bottom right) in pp collisions at $\sqrt{s} = 5.02$ TeV for the INEL > 0 event class.

between 1 and 7 candidates/event, and at 10^7 events between 8 and 15 candidates/event. Instead, at 0 candidates/event, we observe all events without candidates in the rapidity acceptance. Between 4 and 7 candidates/event, and between 12 and 15 candidates/event, a progressive increase and decrease are observed instead of a flat distribution, caused by migration from bins with higher candidate multiplicities, again due to the rapidity acceptance. For Λ (and $\overline{\Lambda}$), particles were injected from 1 to 11 candidates/event with varying statistics (see Table 4.1). The injection scheme expected a flat distribution at 10^6 events between 1 and 7 candidates/event and at $2 \cdot 10^7$ events between 8 and 11 candidates/event. However, at 0 candidates/event, we observe two contributions: events without candidates in the rapidity acceptance and events where only the antiparticle ($\overline{\Lambda}$) was injected, not the particle (Λ). The reverse trend is observed for the $\overline{\Lambda}$ distribution. Between 4 and 7 candidates/event, and between 8 and 11 candidates/event, there is again a progressive increase and decrease due to both rapidity acceptance effects and the fact that only the particle or antiparticle was injected. Additionally, between 1 and 3 candidates/event, we observe an almost flat distribution at $5 \cdot 10^5$ events, corresponding to half the required

statistics because either the particle or the antiparticle was injected (10^6 total events for both), and there is minimal migration from bins with higher candidate multiplicities. For cascade particles (Ξ^- and Ω^-), the injection scheme involved generating between 1 and 10 candidates/event (see Table 4.2), with an expected flat distribution at 10^6 events across this range. Instead, at 0 candidates/event, the distribution includes events without candidates in the rapidity acceptance and those where only antiparticles ($\overline{\Xi}^+$ and $\overline{\Omega}^+$) were injected, but not the particles (Ξ^- and Ω^-). The reverse trend is seen for the antiparticle distributions. Between 1 and 6 candidates/event, the distributions are nearly flat at $5 \cdot 10^5$ events, again corresponding to half the required statistics because either the particle or the antiparticle was injected (10^6 total events for both), with minimal migration effects. However, between 7 and 10 candidates/event, the distributions show a progressive decrease instead of being flat, due to rapidity acceptance effects and the injection of only the particle or the antiparticle.

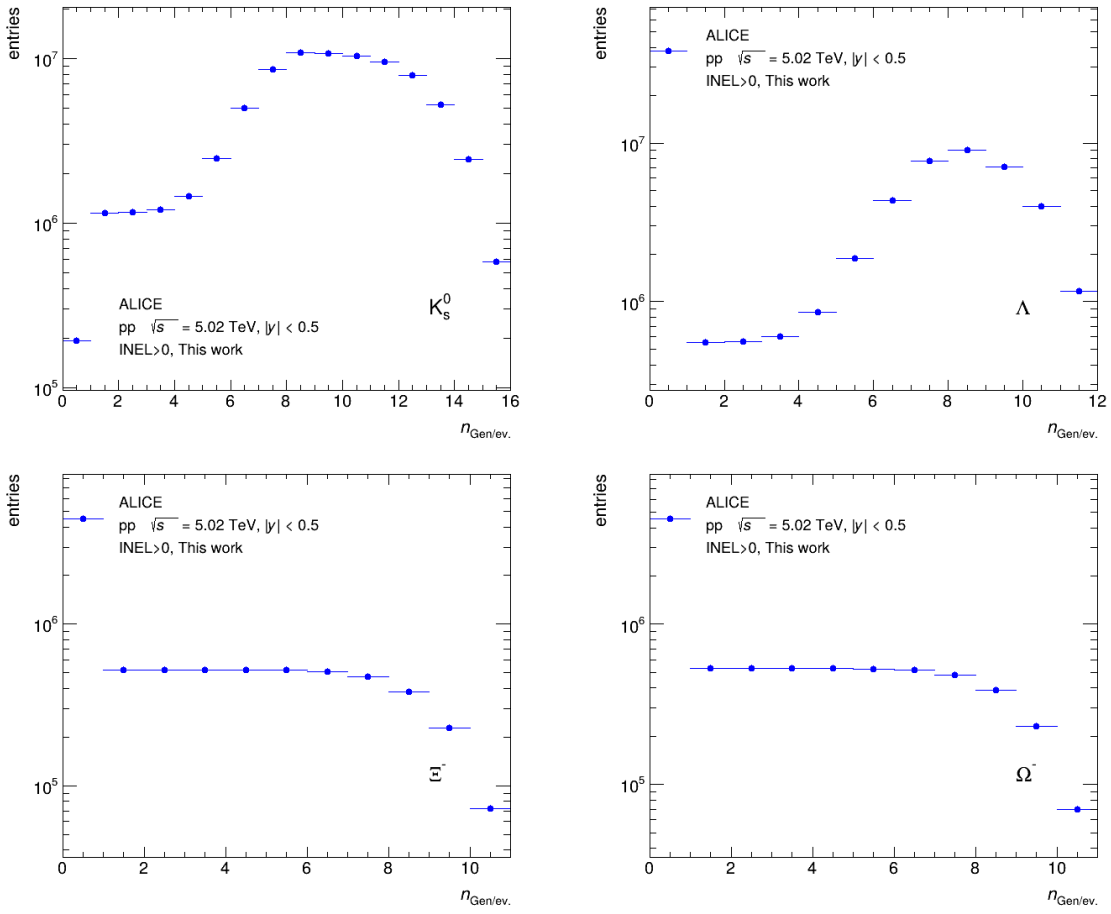

Figure 4.14: Generated distribution obtained by the projection of the response matrices of K^0_S (top left), Λ (top right), Ξ^- (bottom left) and Ω^- (bottom right) in pp collisions at $\sqrt{s} = 5.02$ TeV for the INEL > 0 event class.

The p_T-averaged $A \times \varepsilon$ associated with the applied cuts is generally below 10% for all particles, leading to a response matrix (Fig. 4.13) that significantly limits the number of

reconstructed particles, particularly for cascades. This results in large correction factors for the high tail of the multiplicity distribution, requiring careful stability studies. In the Bayesian unfolding procedure, the regularization parameter corresponds to the number of iterations needed to stabilize the corrected spectrum. During the initial $\sim$ 10 iterations, the unfolded spectrum undergoes substantial changes, as the starting point in the response matrix is a flat generated distribution, while the unfolding process converges toward a steeply declining spectrum. Beyond 10 iterations, fluctuations in the corrected spectrum are generally below $\sim 1\%$ with further iterations. Consequently, after the first 10 iterations, a preliminary unfolded spectrum is fitted with a negative binomial distribution (NBD, [150]), which reproduces the data well (see Section 5). A new unfolding procedure is then performed, using the generated distribution in the response matrix reweighted to match the extracted preliminary NBD. Figure 4.15 shows the response matrices in the INEL > 0 class for K^0_S, Λ, Ξ^- and Ω^- obtained after the reweighting with NBD weights in 2 steps. The errors associated to the weighted response matrices and to the weighted generated and reconstructed distributions are simply given by the product of the previous error times the weight applied. In this configuration, the Bayesian procedure requires a smaller regularization parameter to achieve convergence, and the MC closure test confirms the validity of this approach, starting from different generated multiplicity distributions, with an accuracy of approximately 2% for all particles.
It has been previously demonstrated [16] that the p_T-differential $A \times \varepsilon$ is independent of event multiplicity for all particles studied in pp collisions. However, the evolution of the p_T distribution with multiplicity for strange particle production results, when integrated over p_T, in a different average $A \times \varepsilon$ as the V0M class varies. Therefore, the detector response for different multiplicity classes was obtained from the same MC simulation by applying the appropriate weights to each candidate. These weights adjust the p_T distribution to match the one measured in the specific V0M class under study. The resulting response matrices, obtained after reweighting, are shown in Appendix 9.3 for each multiplicity class. Specifically, Figures 9.73, 9.74, 9.75, 9.76, 9.77, 9.78 and 9.79 correspond to K^0_S, Λ, $\overline{\Lambda}$, Ξ^-, $\overline{\Xi}^+$, Ω^- and $\overline{\Omega}^+$, respectively, for INEL > 0.

4.6.2 Trigger efficiency

After correcting for the detector response, it is necessary to account for event trigger efficiency corrections, as these impact the measurement in two distinct ways. First, the normalization of the strange particle multiplicity spectrum to the total number of analyzed events must include the trigger efficiency factor (ε_{trigg}), as estimated and reported in Ref. [141]. ε_{trigg} is applied to the whole multiplicity spectrum equally as it affects all bins proportionally in the same way. Secondly, lost events may include strange particle candidates. To address this, a correction factor that accounts for the number of lost candidates (ε_{part}) in lost events is derived from MC simulations. In this case, the p_T-differential factor evaluated in Ref. [16] is averaged using the appropriate p_T distribution for all particles in each multiplicity class. The factor ε_{part} is applied to each bin n of the multiplicity spectrum, raised to the n-th power as illustrated in Equations 4.11 and 4.12.

$$P_{ev}^{true}(1_{part}) \cdot \varepsilon_{part} = P_{ev}^{obs}(1_{part}) \qquad P_{ev}^{true}(2_{part}) \cdot (\varepsilon_{part})^2 = P_{ev}^{obs}(2_{part}) \tag{4.11}$$

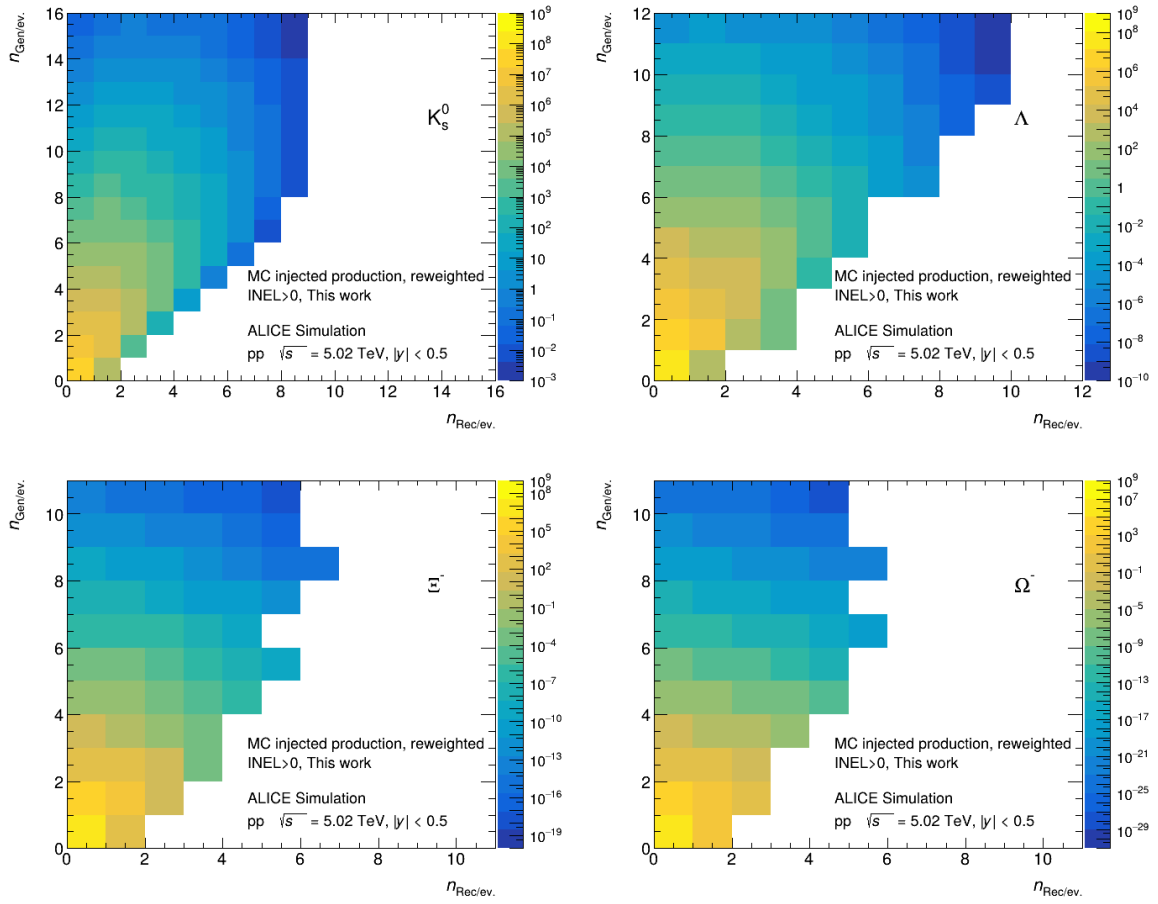

Figure 4.15: Response matrices obtained after the reweighting of K^0_S (top left), Λ (top right), Ξ^- (bottom left) and Ω^- (bottom right) in pp collisions at $\sqrt{s} = 5.02$ TeV for the INEL > 0 event class.

$$\#events = \frac{P^{obs}_{ev}(n_{part})}{(\varepsilon_{part})^n} \tag{4.12}$$

As a result, the multiplicity spectrum for the strange particle (S) production is obtained as:

$$\mathrm{P}(n_{\mathrm{S}}) = \frac{\varepsilon_{trig}}{\varepsilon^n_{part}} \cdot \left\{ \frac{\sum_{i=1}^{N_{tot}} R_i[n]}{N_{tot}} \right\}_{Unfolded}, \tag{4.13}$$

where N_{tot} is the total number of analyzed events.

4.7 Statistical and systematic uncertainties evaluation

The statistical uncertainties associated with the uncorrected spectrum and the particle multiplicity distribution are estimated using the sub-sample method [151]. The dataset is divided into 20 sub-samples for V^0 particles and 15 for cascades, each of equal size. For each sub-sample, the observable under study is calculated following the previously

outlined procedure. The central value and the statistical uncertainty for each bin of the multiplicity spectrum are determined as the mean and standard deviation of the 20 (or 15) obtained values:

$$\overline{C} = \frac{\sum_{i=0}^{k} C_i^2}{k} \tag{4.14}$$

$$\delta C = \sqrt{\frac{\sum_{i=0}^{k} (C_i - \overline{C})^2}{k(k-1)}} \tag{4.15}$$

where $\sum_{i=0}^{k}$ represents the summation over all k sub-samples.

To ensure consistency, the method is also applied to the average of the distribution. In this case, the mean and its statistical uncertainty are computed using the analogous formulas:

$$\overline{X} = \frac{\sum_{i=0}^{k} X_i^2}{k} \tag{4.16}$$

$$\delta X = \sqrt{\frac{\sum_{i=0}^{k} (X_i - \overline{X})^2}{k(k-1)}} \tag{4.17}$$

The relative statistical uncertainties obtained for the average of the distribution across all multiplicity classes for each particle are presented in Fig. 4.16. The slight deviation from the trend observed for one point corresponds to the integrated multiplicity.
This procedure also provides an important check on the stability of the overall method. The distribution of the 20 (or 15) values is centered at the mean value, rapidly falling symmetrically, indicating the absence of outliers. This confirms the stability of the unfolding procedure.

Regarding systematic uncertainties, various sources are considered, and their impact on the final results is evaluated. A comprehensive explanation of how these uncertainties are handled is presented in this section. Table 4.6 lists the relative systematic uncertainties estimated in the INEL > 0 event class for all studied particles, across three representative cases: the lowest (zero), an intermediate and the highest n_S considered. Figure 4.17 illustrates the comparison of relative systematic uncertainties evaluated for the integrated multiplicity of all particles, with similar trends observed for their corresponding anti-particles. The general trend shows that systematic uncertainty increases significantly with n_S, as the influence of potential biases becomes more pronounced at higher n_S. In the zero bin of n_S, the systematic uncertainties are consistently below 4%, whereas they rise to tens of percent in the highest bin.
Furthermore, Fig. 4.18 compares the statistical and total systematic relative uncertainties, demonstrating that this analysis is predominantly affected by systematic uncertainties.

4.7.1 Cut variation

Potential differences in the distribution of selection variables in MC and real data can impact the final result. To study this, a multi-trial procedure is followed. For each selection variable, a range around the default value is established by identifying two boundary

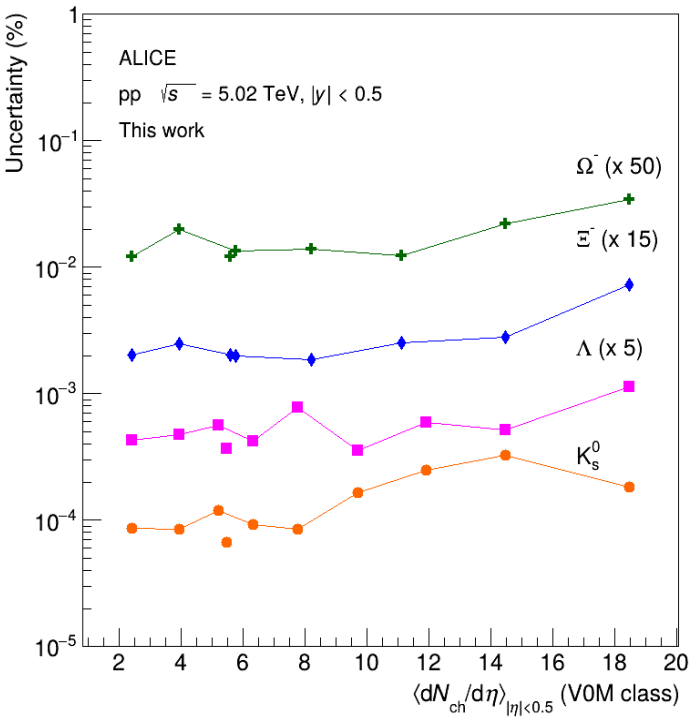

Figure 4.16: Relative statistical uncertainties for the average of the distribution across all investigated multiplicity classes are shown for all particles: orange represents K^0_S, magenta represents Λ, blue represents Ξ^- and green represents Ω^-.

values that result in a raw signal variation of no more than 10% compared to the default. These values are listed in Table 4.7. Afterward, 500 different combinations of selection criteria are randomly chosen inside their respective variability window and the full analysis chain is performed for every trial, from signal extraction to raw spectrum determination, unfolding and trigger efficiency corrections.

For the Λ and $\overline{\Lambda}$ analyses the feed-down weight is also re-evaluated for each trial, as the correction is applied at the reconstructed candidate level. Figure 4.19 illustrates two key aspects of the feed-down correction. On the left, the discrepancy between the feed-down correction calculated using the default set of criteria and that obtained for each trial is shown as a function of p_{T}. On the right, the fraction removed as a function of p_{T} is displayed for Λ and $\overline{\Lambda}$ particles, represented by full and open markers, respectively, for the INEL > 0 event class in each trial.

For each bin of $\mathrm{P}(n_{\mathrm{S}})$, the procedure leads to 500 values which are Gaussian distributed around the default as can be noticed in Figures 9.80, 9.81, 9.82 and 9.83 for K^0_S, Λ, Ξ^- and Ω^- respectively in Appendix 9.4. The standard deviation of the distribution defines the systematic uncertainty that is illustrated in Fig. 9.84 in Appendix 9.4 for all the analyzed particles. Similar results have been obtained also for anti-particles.
Given the complex and resource-consuming procedure, this systematic uncertainty is evaluated on the INEL > 0 spectrum and then applied to all the $\mathrm{P}(n_{\mathrm{S}})$ in the different V0M classes.

Table 4.6: Systematic uncertainty sources and corresponding values (%) in three different n_S (zero, intermediate and highest) of the INEL > 0 multiplicity distribution of all strange hadrons under study. The last two sources are evaluated separately for particles and antiparticles, with only the highest value reported in the table (in brackets if it is the one corresponding to antimatter).

	Systematic uncertainty (%)											
Hadron	K^0_S			Λ			Ξ^-			Ω^-		
n_S	0	3	7	0	2	5	0	2	4	0	1	2
Cut variation	0.3	5.6	21	0.07	5.7	38	0	6.3	38	0	4.4	10
Signal extraction	0.09	0.4	0.6	0	0.17	0.9	0	0.19	0.23	0.01	0.04	0.07
Unfolding procedure	1.6	17.8	22.5	0.4	16.8	65	0.2	15.1	65	0	10.7	24
ε_{part}	0.9	6.3	15.8	0.2	3.7	9.5	0.04	7.3	14	0	2.95	5.9
p_{T} distribution	0.4	11.9	12.5	3.5	4.9	45	3	3.3	5.6	0	5.4	13
OOB pile-up cut	0.09	8.5	16.5	0.4	9.8	26	0.01	2.6	5	0	0.43	0.85
Feed-down correction	-	-	-	0.15	3.01	7.8	-	-	-	-	-	-
Material budget	0.6	1.6	3.7	1.1	2.2	5.4	1.2	2.3	4.7	1	1.1	2
Strangeness from material	0.15	0.38	0.9	0.4	0.7	1.7	0.48	0.9	1.8	0.25	0.31	0.44
Hadronic interaction	-	-	-	(0.17)	(0.31)	(0.8)	(0.2)	(0.36)	(0.72)	(0.2)	(0.28)	(0.36)
Total	2	23.5	37	3.7	21.5	90	3.3	17.6	66	1.1	14.4	30

Table 4.7: List of interval for each selection criteria applied to V^0 and cascade candidates. The same criteria have been applied to both particles and antiparticles for Λ, Ξ^- and Ω^-.

Daughter track selection	range K^0_S	range Λ ($\overline{\Lambda}$)	range Ξ^- ($\overline{\Xi}^+$)	range Ω^- ($\overline{\Omega}^+$)
N_{x-rows}	$67-71$	$68-72$	$67-71$	$65-69$
TPC dE/dx	$(3-7)\sigma_{dE/dx}$	$(2-6)\sigma_{dE/dx}$	$(3-7)\sigma_{dE/dx}$	$(3.5-7.5)\sigma_{dE/dx}$
Candidate selection	**range K^0_S**	**range Λ ($\overline{\Lambda}$)**	**range Ξ^- ($\overline{\Xi}^+$)**	**range Ω^- ($\overline{\Omega}^+$)**
DCA V^0 daughter to PV	$(0.01-0.06)$ cm	$(0.035-0.085)$ cm	$(0.085-0.135)$ cm	$(0.085-0.135)$ cm
DCA V^0 daughters	$(0.3-1.0)\sigma$	$(0.4-1.0)\sigma$	$(0.4-1.0)\sigma$	$(0.5-1.0)\sigma$
DCA V^0 to PV	–	–	$0.02-0.06$	$0.02-0.06$
DCA bachelor to PV	–	–	$0.02-0.04$	$0.01-0.03$
DCA cascade daughters	–	–	$(0.4-1.0)$ cm	$(0.5-0.9)$ cm
$R_{xy}V^0$	$(0.15-0.55)$ cm	$(0.3-0.7)$ cm	$(0.4-0.8)$ cm	$(0.4-0.8)$ cm
R_{xy} cascade	–	–	$(0.2-0.6)$ cm	$(0.15-0.55)$ cm
Proper Lifetime (mL/p)	$(30-50)$ cm	$(20-40)$ cm	$(12-22)$ cm	$(5-15)$ cm
V^0 cosθ_{PA}	$0.97-0.999$	$0.993-0.999$	$0.965-0.999$	$0.96-0.999$
cascade cosθ_{PA}	–	–	$0.965-0.999$	$0.96-0.999$

4.7.2 Signal extraction

The systematic uncertainty associated with the signal extraction procedure is assessed by varying the p_{T} granularity used in the determination of w_S. These weights depend on p_{T} (as shown in Fig. 4.7(*Left.*)) because the selection variables are p_{T}-dependent, and the combinatorial background evolves with transverse momentum. The default p_{T} binning is selected to ensure sufficient statistics in each invariant mass distribution, enabling a reliable fit. The systematic uncertainty is estimated by slightly modifying the number of p_{T} bins (12, 11, 11 and 9 for K^0_S, Λ, Ξ and Ω, respectively) and repeating the full analysis procedure with the adjusted binning configuration. The difference between the resulting spectrum and the default spectrum is taken as the systematic uncertainty and is reported for the INEL > 0 class in Fig. 9.85 in Appendix 9.4 for all analyzed particles. Comparable results have also been observed for their corresponding anti-particles. This

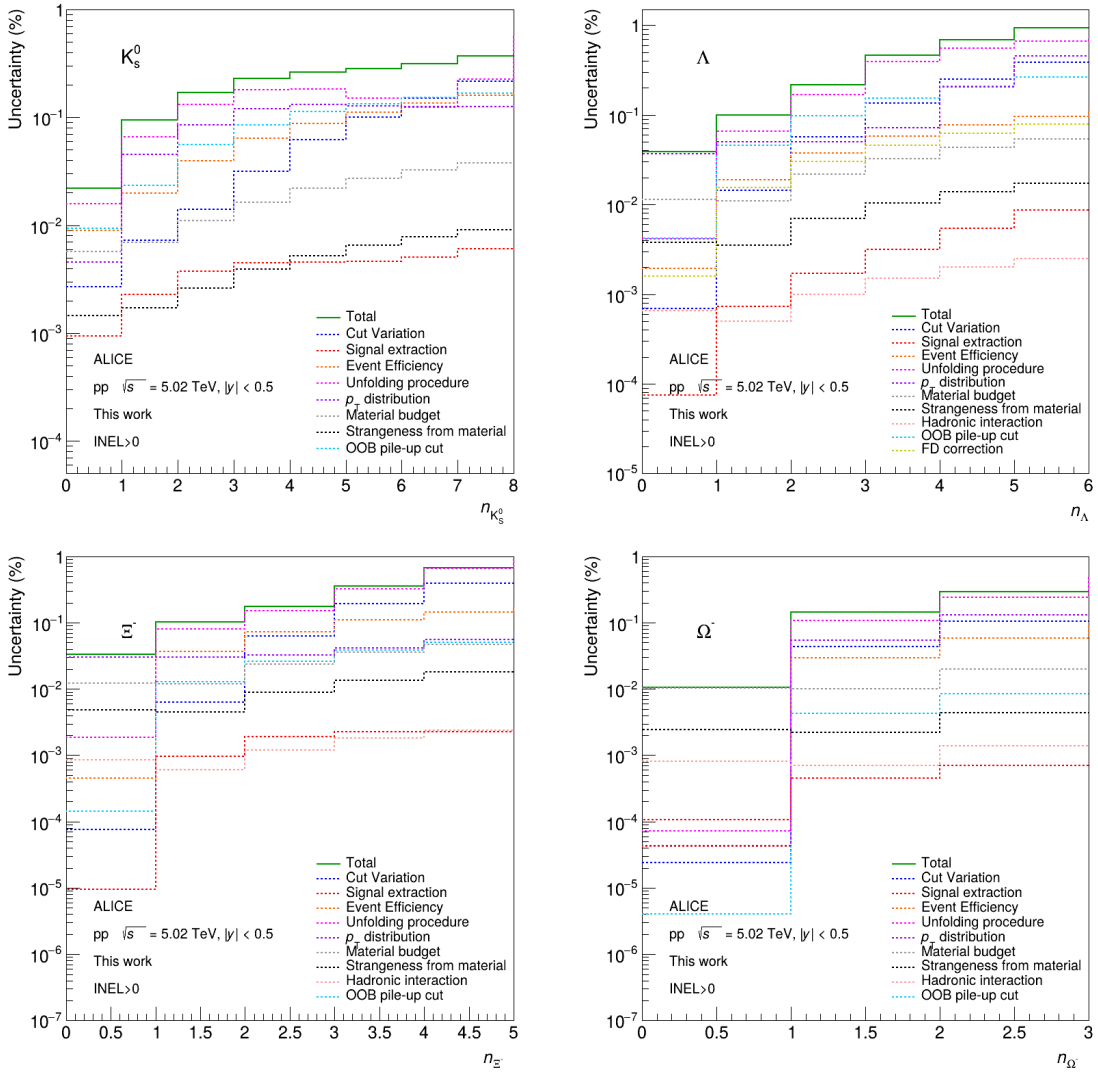

Figure 4.17: Comparison of relative systematic uncertainties evaluated for the integrated multiplicity of all particles. The first row shows the results for K^0_S and Λ, while the second row presents the results for Ξ^- and Ω^-.

effect is subdominant, never exceeding 1% for any n_S, indicating that the p_T granularity used in the default analysis is sufficient to ensure robust w_S determination.
Due to the resource-intensive nature of the procedure, this systematic uncertainty is evaluated for the INEL > 0 spectrum and subsequently applied to all P(n_S) across the different V0M classes.

4.7.3 Unfolding procedure

As previously discussed, the stability of the unfolding procedure is rigorously tested. In this context, a systematic uncertainty may arise from variations in the starting point of the generated distribution used as input for the response matrix. In the default procedure, the starting point is the NBD obtained from a fit to the unfolded spectrum after 10 initial iterations. To evaluate the impact of this choice, two alternative functions are

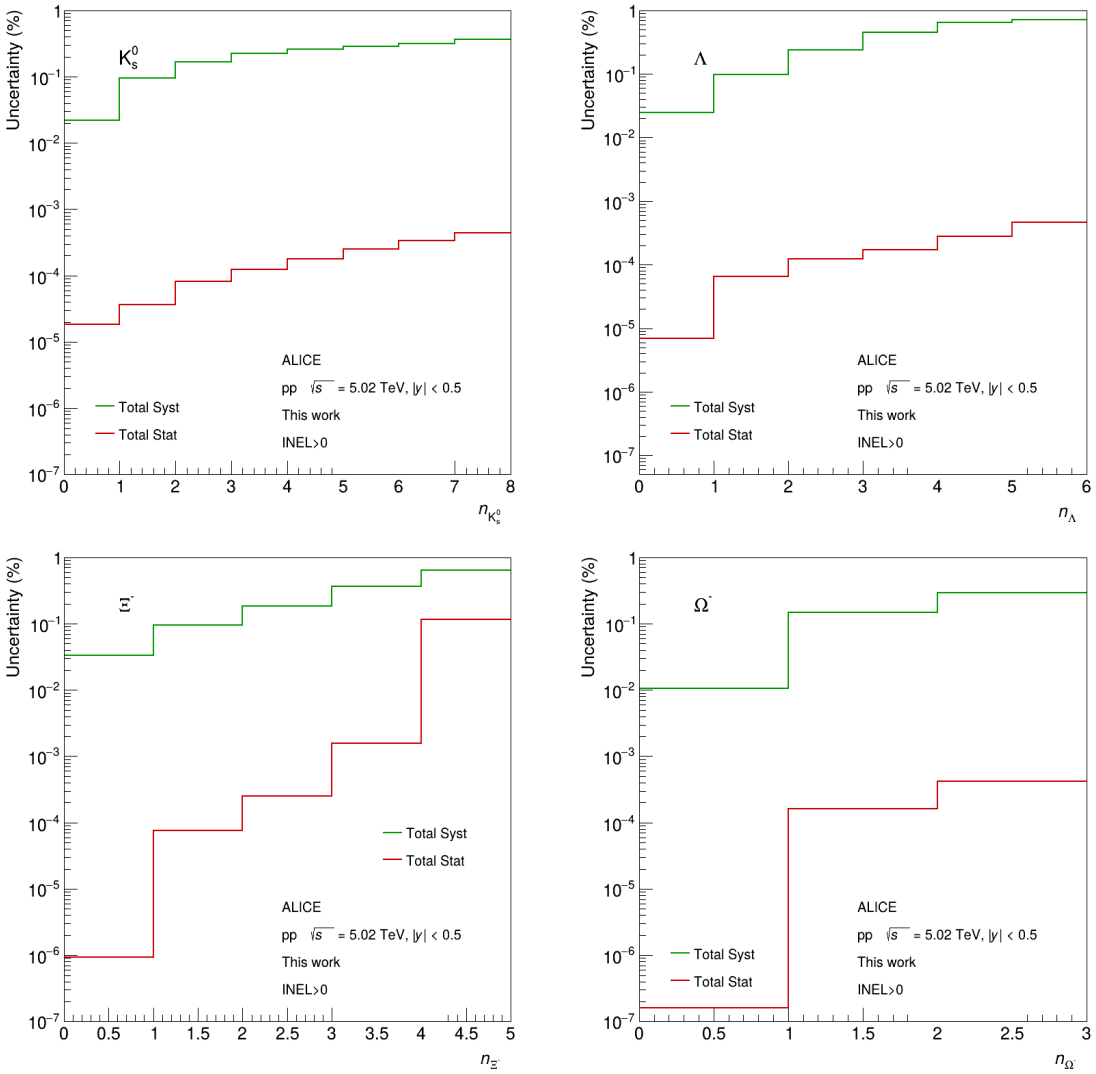

Figure 4.18: Comparison of the relative statistical (red) and total systematic (green) uncertainties evaluated for the integrated multiplicity of all particles. The first row shows the results for K^0_S and Λ, while the second row presents the results for Ξ^- and Ω^-.

considered for each V0M class i: the preliminary NBD fit corresponding to classes $i-1$ and $i+1$. For the lowest (highest) V0M class, where $i-1$ ($i+1$) is unavailable, the $i+2$ ($i-2$) case is used. In the INEL > 0 case, the adjacent classes V and VI serve as alternatives. In more detail, each bin of the distributions was analyzed as a function of the number of iterations for three different NBD-weights. Appendix 9.5 presents a comparison of the unfolded distributions across all multiplicity classes: results using NBD-weights specific to each class are shown in dark red, while those obtained using weights from classes $i-1$ and $i+1$ are depicted in pink and azure, respectively. These comparisons, performed for both particles and antiparticles, demonstrate that the unfolding procedure achieves good convergence for all bins, all particles, and across all multiplicity classes. After choosing the iteration number, the largest deviation between the results obtained with the default starting point and the two alternative configurations is taken as the systematic uncertainty. The relative errors associated with the unfolding procedure across

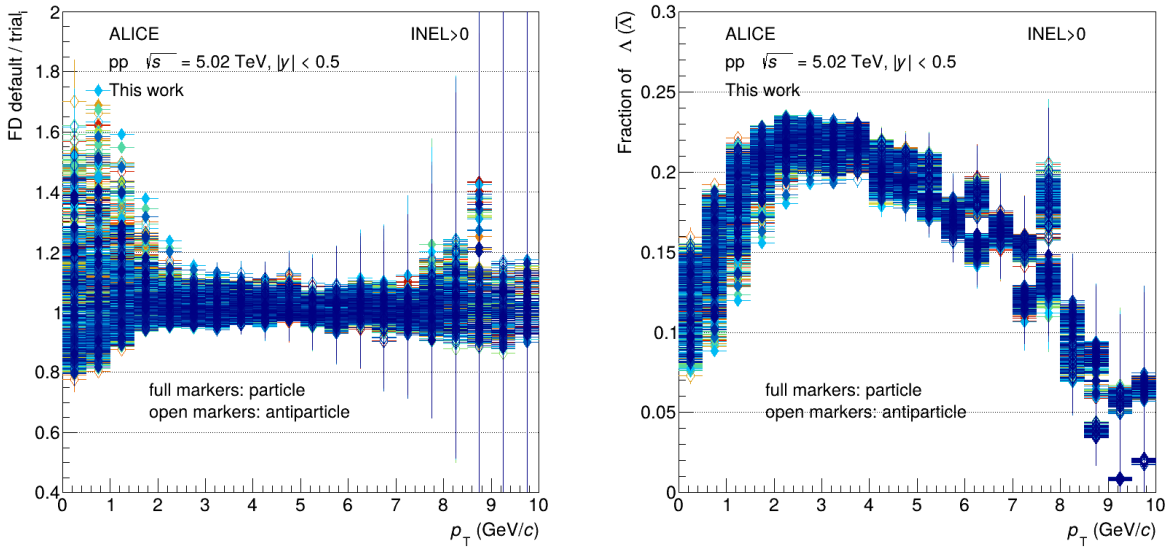

Figure 4.19: (*Left:*) Discrepancy between the feed-down correction calculated for the default set of criteria and the one evaluated for each trial as a function of p_{T}. (*Right:*) Fraction removed as a function of p_{T} for Λ and $\overline{\Lambda}$ particles as full and open markers respectively for INEL > 0 for each trial.

all the investigated multiplicity classes are shown in Fig. 9.86 in Appendix 9.4 for all analyzed particles. Similar results have also been observed for their corresponding anti-particles. At low n_S, the relative uncertainty is minimal but increases substantially at higher n_S, becoming the dominant contribution for the highest n_S values across all particle types. Interestingly, the effect is most pronounced in low-multiplicity classes, while the uncertainty decreases in high-multiplicity classes.

4.7.4 Event efficiency

Corrections for trigger inefficiencies can also contribute to systematic uncertainties. While ε_{trig} is determined with very high precision [141] and thus does not introduce significant systematics, ε_{part} is model-dependent. To account for this, different Monte Carlo simulations are used to estimate variations in this correction factor. This approach follows the methodology outlined in Ref. [16], resulting in a p_{T}-dependent uncertainty ($\delta\varepsilon_{part}$). This uncertainty is used to evaluate its impact on the determination of the strange particle multiplicity spectrum. By applying two adjusted ε_{part} factors, corresponding to $\varepsilon_{part} \pm \delta\varepsilon_{part}$, two corrected multiplicity spectra are obtained for each V0M class. The maximum deviation from the default spectrum is then taken as the systematic uncertainty and is shown in Fig. 9.87 in Appendix 9.4 for all analyzed particles across all the investigated multiplicity classes. Similar results have also been observed for their corresponding anti-particles.

4.7.5 Knowledge of the p_{T} distribution

A critical aspect of the analysis presented here, which enables the use of a one-dimensional unfolding procedure, is the prior determination of the p_{T} distribution for all hadrons under

study ([16]). The transverse momentum spectra are measured with a certain experimental precision, and their shape in the unmeasured low-p_{T} region is extrapolated. Consequently, a systematic uncertainty may arise from using different p_{T} parameterizations. To address this, the INEL > 0 p_{T} spectrum is extrapolated at low p_{T} by re-scaling two functional forms associated with different V0M classes — one resulting in larger and the other in smaller extrapolation fractions. The response matrix is then re-weighted using these alternative p_{T} parameterizations, and the full analysis is repeated for both cases. The maximum deviation from the default procedure is taken as the systematic uncertainty and is reported for the INEL > 0 class in Fig. 9.88 in Appendix 9.4 for all analyzed particles. Similar results have also been observed for their corresponding anti-particles.

4.7.6 Effect of the cut on the OOB pile-up

The systematic uncertainty arising from the out-of-bunch (OOB) pileup rejection is evaluated by tightening the selection criteria. Specifically, the number of daughter tracks required to satisfy the (TOF||ITS) condition (see Table 4.5) is increased to at least two, compared to the default requirement. The resulting difference in the final outcome, which is significant only for the highest n_S in the V^0 analysis, is taken as the systematic uncertainty. The relative systematic errors associated with this effect are shown in Fig. 9.89 in Appendix 9.4 for all analyzed particles, across all the investigated multiplicity classes. Similar results have also been observed for their corresponding anti-particles.

4.7.7 Feed-down correction

The Λ and $\overline{\Lambda}$ spectra are subject to a systematic bias arising from the feed-down evaluation, primarily due to uncertainties in the p_{T} distributions of Ξ particles. To quantify this effect, the feed-down fraction is recalculated by varying the measured cascade p_{T} spectra within their respective systematic uncertainties. This variation results in slightly different w_{FD} factors, which are then applied during the signal extraction process. The full analysis is repeated using these modified reconstructed distributions, and the relative systematic uncertainty is determined as the maximum deviation from the default case. The relative systematic errors associated with the feed-down correction across all the investigated multiplicity classes are shown in Fig. 9.90 in Appendix 9.4 for Λ and $\overline{\Lambda}$ respectively on the left and on the right.

4.7.8 Material budget

The imperfect reproduction of the detector material budget in the MC is also considered. The uncertainty in the material budget determination, as discussed in Ref. [115], is estimated at $\pm 4.5\%$. Previous analyses [15, 14, 19] have investigated the impact of this uncertainty on the $A \times \varepsilon$ for strange particle measurements. To propagate this systematic effect to the multiplicity spectrum determination, the p_{T}-dependent uncertainty is weighted by the measured p_{T} distribution, resulting in a δ_{mat} factor that accounts for the efficiency bias associated with each reconstructed candidate. Consequently, the systematic uncertainty related to the material budget determination is evaluated as $(1 - \delta_{mat})^{n_S}$ and is presented in Fig. 9.91 in Appendix 9.4 for all analyzed particles for the integrated

multiplicity. Similar results have also been observed for their corresponding anti-particles. Note that initially, the systematic uncertainty was evaluated for each multiplicity class. However, as no significant dependence on multiplicity was found, it was decided to apply the systematic uncertainty derived from the INEL > 0 spectrum uniformly to all $\mathrm{P}(n_{\mathrm{S}})$ in the various V0M classes.

4.7.9 Strangeness from material

A minor source of systematic uncertainty arises from the limited knowledge of the cross-section for strange particle production through interactions of primary hadrons with the detector material. Using the ratio of secondary to total strange particles reported in Ref. [19] and weighting it by the measured p_{T} distribution, an f^{sec} fraction is derived and applied on a candidate-by-candidate basis. Accordingly, the systematic uncertainty due to strange particle production from hadron-material interactions is estimated as $(f^{sec})^{n_S}$ and is reported for the integrated multiplicity in Fig. 9.92 in Appendix 9.4 for all analyzed particles. It is important to note that the systematic uncertainty was first assessed for the different multiplicity classes also for this source. Yet, due to the lack of any noticeable dependence on multiplicity, the uncertainty from the INEL > 0 spectrum was applied consistently across all $\mathrm{P}(n_{\mathrm{S}})$ in the different V0M classes.

4.7.10 Hadronic interactions

A minor source of systematic uncertainty also originates from the limited knowledge of the cross-section for the annihilation of strange antiparticles in interactions with the detector material. Using results reported in Ref. [152] and weighting by the measured p_{T} distribution, a δ_{had} factor is derived and applied on a candidate-by-candidate basis. Consequently, the systematic uncertainty associated with hadronic interactions is evaluated as $(1 - \delta_{had})^{n_S}$ and is shown for Λ, Ξ^- and Ω^- (blue) together with the results for the respective anti-particle (red) for the integrated multiplicity in Fig. 9.93 in Appendix 9.4. It is worth noting that while the systematic uncertainty was initially considered for each multiplicity class, no substantial multiplicity dependence was observed. Consequently, the uncertainty from the INEL > 0 spectrum was chosen and applied uniformly to all $\mathrm{P}(n_{\mathrm{S}})$ across the different V0M classes.

4.8 Average yield of strange hadron multiplets

The quantity $\mathrm{P}(n_{\mathrm{S}})$ represents the probability of observing n particles of type S in the final state. From this strange particle multiplicity distribution, the average production yield of n particles per event is calculated using:

$$\langle \mathrm{Y_{nS}} \rangle = \sum_{\mathrm{i=n}}^{\mathrm{n_S^{max}}} \frac{\mathrm{i!}}{\mathrm{n!(i-n)!}} \cdot \mathrm{P(i_S)}, \tag{4.18}$$

where n_S^{max} is the highest measured bin of the multiplicity spectrum for particle S. The value $\langle \mathrm{Y_{1S}} \rangle$ represents the mean of the multiplicity distribution, providing the average production rate of hadron S. This measure is equivalent to the "yield" or "$\mathrm{d}N/\mathrm{d}y$ "

terminology used in previous studies [1, 14, 15, 16]. As such, this approach enables direct comparison with earlier results (see Section 5.6), thereby verifying the reliability of this analysis method. In contrast, $\langle Y_{n>1S} \rangle$ describes the average production yield of multiplets (such as doublets or triplets) of the particle. Statistical and systematic uncertainties associated with each bin in the multiplicity distribution are treated as fully uncorrelated and are propagated accordingly in Eq. 4.18. Uncertainties for $\langle Y_{n>1S} \rangle$ are also consistent with previous findings, further demonstrating excellent agreement.

It is important to highlight that Eq. 4.18 is, in principle, defined over an infinite range, as the probability of multiplet formation theoretically considers the entire multiplicity distribution. However, as discussed in Chapter 5, $P(n_S)$ distributions decrease steeply, with probabilities differing by several orders of magnitude between consecutive bins. Consequently, truncating the summation at n_S^{max} introduces only a minimal bias in the calculation of $\langle Y_{nS} \rangle$. As a general guideline, n-tuplets are computed only up to $n = n_S^{max} - 1$ for all particles, except for Ω, where the calculation is extended to $n = n_\Omega^{max}$. To account for the bias introduced by this truncation, a systematic uncertainty is added. This is estimated by extrapolating the tail of the multiplicity distribution using an exponential fit to the last three bins. The summation in Eq. 4.18 is then extended up to $n = 100$, using the extrapolated probabilities $P(n_S > n^{max})$ for the additional terms. The relative difference between this extended calculation and the default approach is taken as a one-sided systematic uncertainty, which affects the yields in the upward direction. Table 4.8 presents the relative systematic uncertainty from sum truncation for all average n-tuplet yields in the INEL > 0 event class. This procedure is repeated for each V0M class. As shown in the table, this uncertainty grows significantly with increasing n, due to the rapid decrease in $P(n_S)$ being counterbalanced by the larger combinatorial factor in Eq. 4.18. Consequently, the calculation of $\langle Y_{6K^0_S} \rangle$ is omitted.

Table 4.8: Relative systematic uncertainty related to the sum truncation of Eq. 4.18 in the $\langle Y_{nS} \rangle$ determination for the INEL > 0 event class.

hadron	Sum truncation systematic uncertainty (%)				
	$\langle Y_{1S} \rangle$	$\langle Y_{2S} \rangle$	$\langle Y_{3S} \rangle$	$\langle Y_{4S} \rangle$	$\langle Y_{5S} \rangle$
K^0_S	<1	1.3	6.6	23.7	79.0
Λ	<1	<1	1.5	6.1	-
Ξ	<1	<1	<1	-	-
Ω	<1	<1	-	-	-

Chapter 5

Results and discussion

This chapter presents the first measurement of the multiplicity distribution, $P(n_S)$, for strange particles (K^0_S, Λ, Ξ^- and Ω^-) and their antiparticles ($\overline{\Lambda}$, $\overline{\Xi}^+$ and $\overline{\Omega}^+$) in pp collisions at $\sqrt{s}$ = 5.02 TeV. This analysis advances the understanding of strangeness production by extending the study beyond the average probability. The results are categorized according to different classes of charged-particle multiplicity density. From these multiplicity distributions, the average production yield of n particles per event is extracted as a function of the charged-particle multiplicity at midrapidity for all particles and antiparticles. Additionally, by measuring the production yields of multiple strange hadrons, various yield ratios are examined to investigate the relative probability of s-quarks hadronizing into different types of final-state hadrons. Specifically, the analysis examines yield ratios with perfect strangeness balance ($\Delta S = 0$) as well as ratios probing extreme scenarios of strangeness enhancement ($\Delta S > 0$), both evaluated as function of charged-particle multiplicity. These results are compared to previous measurements and theoretical predictions, including those from the Pythia 8 event generator with different configurations (Pythia 8 Monash [98] and Pythia 8 QCD-CR Ropes [23]) and the hybrid Epos LHC model [102].
Some of the results presented in this chapter have been approved by the ALICE Collaboration and were shared at several international conferences [153, 154, 155].

5.1 Strange particle multiplicity distribution: P(n_S)

The multiplicity distributions of strange particles ($P(n_S)$) measured in pp collisions at $\sqrt{s}$ = 5.02 TeV are presented in Fig. 5.1. These distributions display, for each studied hadron species, the probability of producing n particles per event across various V0M multiplicity classes. As expected at LHC energies, the distributions for particles and antiparticles are compatible within systematic uncertainties across all multiplicity classes, from the highest to the lowest. This compatibility, illustrated in Figures 9.156, 9.157 and 9.158 in Appendix 9.6, aligns with previous observations for average production probabilities [1, 14, 15]. Consequently, in the following discussion, Λ, Ξ and Ω will be used interchangeably to refer to both particles and antiparticles.
The dataset under analysis allows the measurement of $P(n_S)$ up to 7 K^0_S, 5 Λ, 4 Ξ (3 in the lowest multiplicity bin) and 2 Ω particles per event. This represents a unique opportunity to probe the relationship between charged and strange particle production under extreme

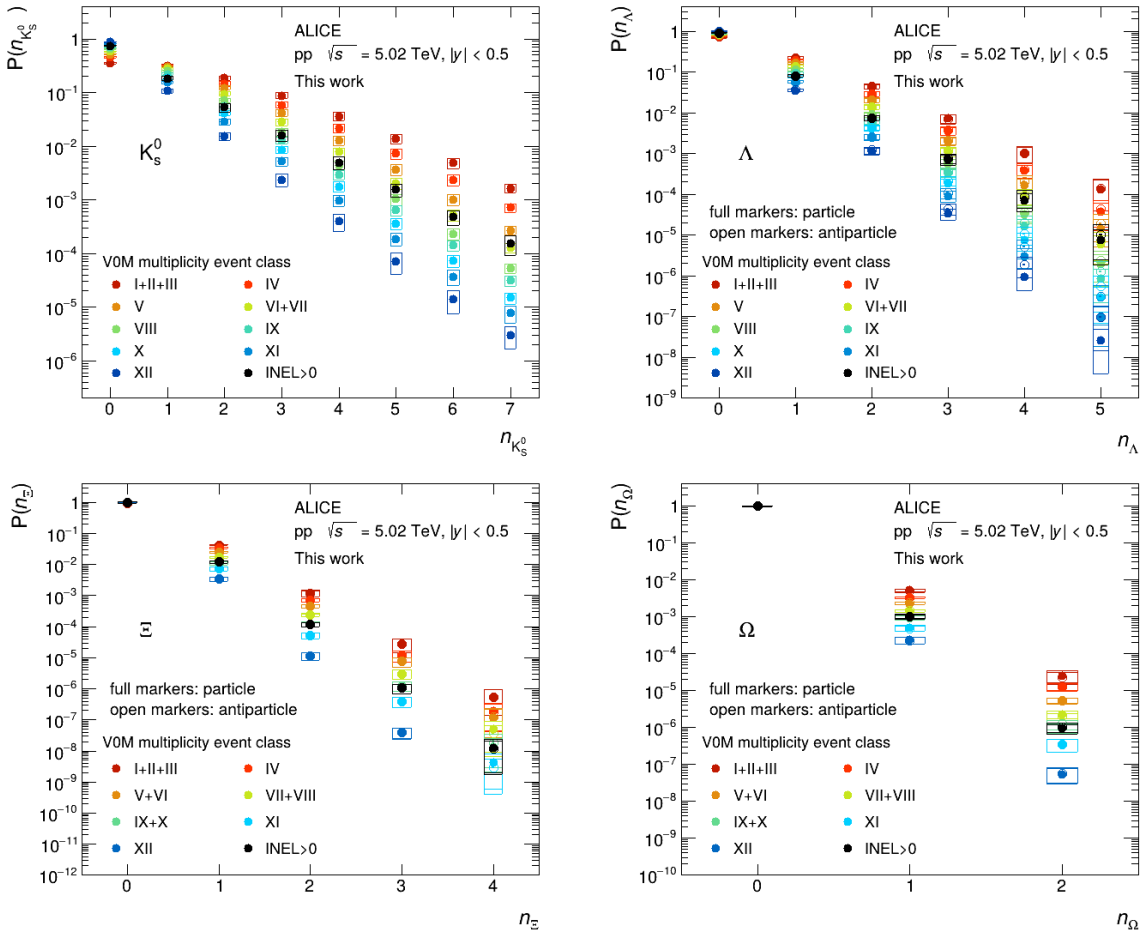

Figure 5.1: (multi-)Strange particle multiplicity distributions for K^0_S (top-left), Λ and $\overline{\Lambda}$ (top-right), Ξ^- and $\overline{\Xi}^+$ (bottom-left) and Ω^- and $\overline{\Omega}^+$ (bottom-right) for several V0M multiplicity classes.

conditions — for instance, spanning from events with 7 K^0_S in low-multiplicity scenarios ($\langle dN_{ch}/d\eta \rangle \sim 3$) to events with 0 K^0_S in high-multiplicity scenarios ($\langle dN_{ch}/d\eta \rangle \sim 20$). Furthermore, the probability $P(n_S)$ for $n > 0$ increases with multiplicity, consistent with previous observations of average production [16] for all the studied hadrons. Notably, this increase is steeper for higher n, as evidenced by the larger separation between blue and red points in the high-n tail of the logarithmically scaled distributions.

Figure 5.1 also reports the multiplicity-integrated (INEL > 0) result, represented by black markers (see also Fig. 5.2). It is noteworthy that the INEL > 0 multiplicity distribution decreases less steeply at high n_S compared to the multiplicity-differential distributions. This is particularly evident for K^0_S and Λ, whose multiplicity spectra extend to larger n_S. This characteristic is crucial for the proper interpretation of the results discussed in this study (see the Section 5.2).

Various functional forms have been explored to fit the obtained distributions. Naively,

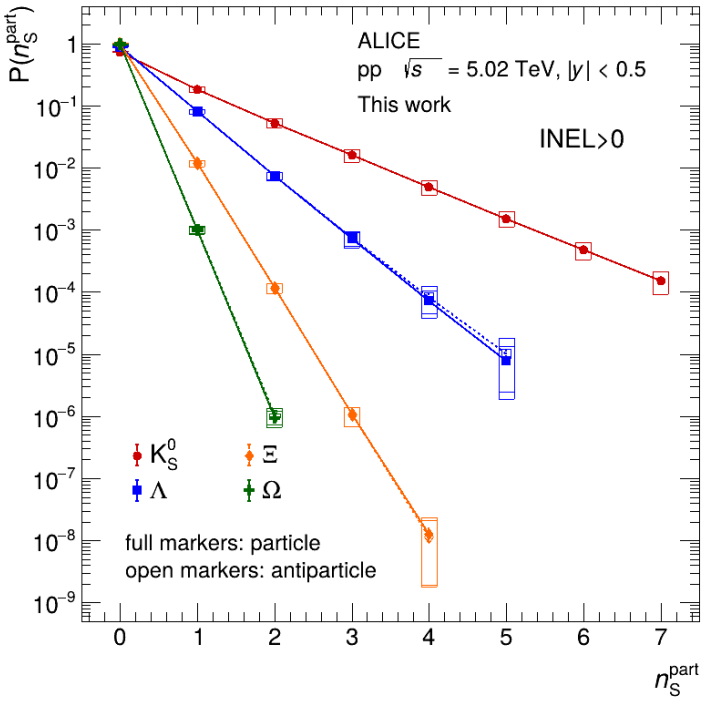

Figure 5.2: (multi-)Strange particle multiplicity distributions for K^0_S (red), Λ and $\overline{\Lambda}$ (blue), Ξ^- and $\overline{\Xi}^+$ (orange) and Ω^- and $\overline{\Omega}^+$ (dark green) for INEL > 0. Results obtained for particles have been reported as full points, while for the antiparticles as open ones. Lines are not fit, they connect only data points.

considering strangeness production as a rare process, one might expect the distributions to follow a Poissonian behavior, with an average being equal to the $\mathrm{d}N/\mathrm{d}y$ value previously determined in [16]. Figure 9.159 in Appendix 9.7 shows Poisson fits applied to the multiplicity distributions, with the mean fixed to the $\mathrm{d}N/\mathrm{d}y$ values [16]. However, it is clear that this assumption fails to adequately describe the measurements, particularly for the V^0 particles. To further investigate whether the $\mathrm{P}(n_S)$ follow a Poissonian distribution, the results were also fitted with a Poisson distribution without fixing the mean. As shown in Fig. 9.160 in Appendix 9.7, this approach shows better agreement with the data, particularly at higher multiplicities. Nevertheless, for events with a high number of strange particles per event, this functional form still fails to fully capture the observed results. This discrepancy can be attributed to the presence of multiple physics processes leading to strangeness production: the sum of several Poissonian processes with different averages could lead to a non-Poissonian pattern. At low multiplicities, the conservation of quantum numbers, including strangeness, must occur locally within a limited phase-space volume, leading to correlations in particle production. At higher multiplicities, where conservation becomes less stringent, these correlations may weaken (see Section 6.2 for further investigations in this direction). It should be noted that for cascades we are unable to conclusively determine whether their distributions follow a Poissonian pattern.
Finally, the $\mathrm{P}(n_S)$ were fitted using a Negative Binomial Distribution (NBD), following the methodology used in the analysis of charged-particle multiplicity distributions [156, 147], which is defined as:

$$P_{n,p}(k) = \frac{(k+n-1)!}{k!(n-1)!} p^n (1-p)^k \tag{5.1}$$

The NBD gives the probability of $n-1$ successes and k failures in $k+n-1$ trilas, and success on the $(k+n)$th trial. In Fig. 5.3, the NBD [150] fit to all multiplicity distributions is shown. The NBD discrete distribution is able to accommodate all the data, similarly to what previously observed for the charged-particle multiplicity distribution [156, 147], with χ^2 lower than 1 for V^0s and lower than 3 for Cascades.

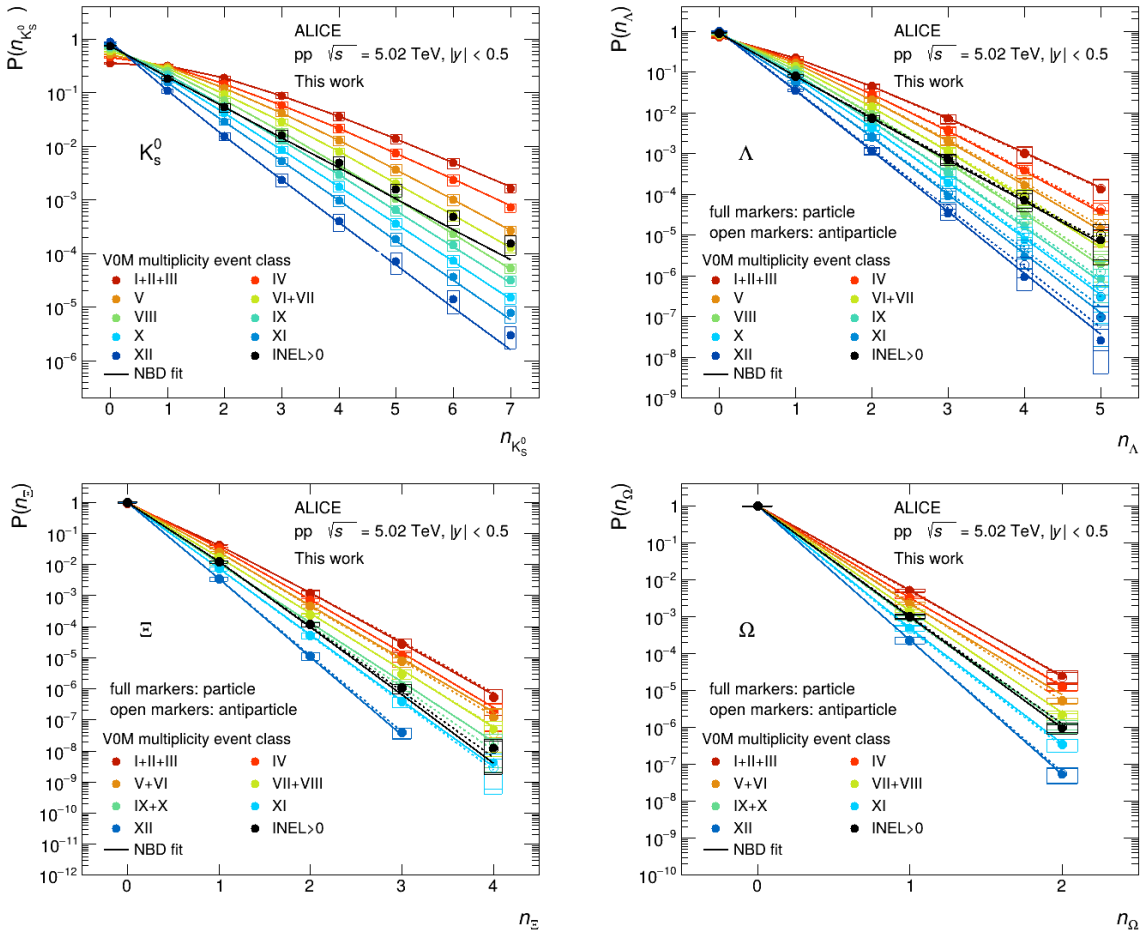

Figure 5.3: (multi-)Strange particle multiplicity distributions for K^0_S (top-left), Λ and $\overline{\Lambda}$ (top-right), Ξ^- and $\overline{\Xi}^+$ (bottom-left) and Ω^- and $\overline{\Omega}^+$ (bottom-right) for several V0M multiplicity classes. Continuous (dashed) lines represent Negative Binomial Distribution fits to the multiplicity distributions ([150]).

5.2 The strangeness-driven bias in charged-particle multiplicity

The charged-particle multiplicity distribution at midrapidity covers a wide range, from 0 to over 50 charged-particles per event, as reported in Refs. [147, 157]. Within the INEL > 0 class, events with high n_{S} exhibit a midrapidity multiplicity distribution that is shifted towards higher values compared to the unbiased distribution, resulting in a higher $\langle \mathrm{d}N_{\mathrm{ch}}/\mathrm{d}\eta \rangle$. Conversely, events with low n_{S} correspond to a charged-particle multiplicity distribution skewed towards lower values. Consequently, the INEL > 0 measurements shown in Fig. 5.1 (top-left) align more closely with those of V0M classes X-XI (azure) on the left side of the distribution, while tending towards class VI (yellow-orange) on the right tail. Even within narrower V0M classes, the associated $\mathrm{d}N_{\mathrm{ch}}/\mathrm{d}\eta$ distributions at midrapidity still exhibit significant relative RMS values, as discussed in Ref. [16]. This demonstrates that the "multiplicity bias" effect persists, although with varying intensity, even when analyzing multiplicity-differential distributions. To quantify this effect, a MC study was conducted using the Pythia 8 QCD-CR Ropes model, with results shown in Fig. 5.4.

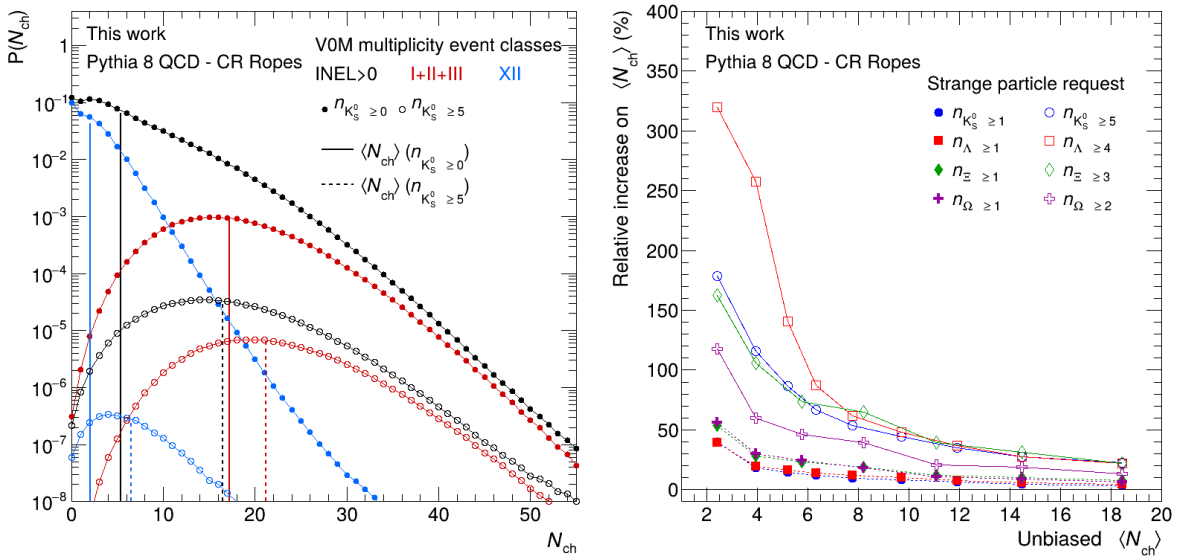

Figure 5.4: Illustration of the strangeness-induced charged-particle multiplicity bias effect observed in Pythia 8 QCD-CR Ropes simulations. (*Left.*) The $\mathrm{d}N_{\mathrm{ch}}/\mathrm{d}\eta|_{|\eta| < 0.5}$ distribution is presented for the INEL > 0 (black markers), V0M-(I+II+III) and V0M-XII event classes (red and light blue points, respectively). Open markers indicate the corresponding $\mathrm{d}N_{\mathrm{ch}}/\mathrm{d}\eta|_{|\eta| < 0.5}$ distributions obtained when requiring at least five $\mathrm{K}^0_{\mathrm{S}}$ particles per event. Continuous and dashed lines represent the averages of the unbiased and biased multiplicity distributions, respectively. (*Right.*) The relative shift in $\langle \mathrm{d}N_{\mathrm{ch}}/\mathrm{d}\eta \rangle$ is shown for all V0M event classes, with a requirement of at least one (solid markers) or more than one (open markers) strange particle per event. Lines are included to guide the eye.

In the left panel of Fig. 5.4, the un-biased $\mathrm{d}N_{\mathrm{ch}}/\mathrm{d}\eta$ distributions for INEL > 0, V0M-

(I+II+III) and V0M-XII event classes are compared to the corresponding distributions obtained when imposing a minimum of 5 K^0_S per event. This comparison highlights that, while the biased and un-biased distributions share a qualitatively similar shape, they are systematically shifted on average (indicated by the dashed lines). The extent of this shift depends both on the specific requirement for the number of strange particles and on the type of strange particle being analyzed. This dependence is illustrated in the right panel of the figure, where the relative shift in $\langle \mathrm{d}N_{\mathrm{ch}}/\mathrm{d}\eta \rangle$ is plotted against the un-biased $\langle \mathrm{d}N_{\mathrm{ch}}/\mathrm{d}\eta \rangle$ for all V0M classes under different biasing conditions on n_{S}. Solid markers represent minimal biasing ($n_{\mathrm{S}} \geq 1$), while open markers correspond to increasingly stringent conditions ($n_{\mathrm{S}} \geq 5, 4, 3, 2$ for K^0_S, Λ, Ξ, and Ω, respectively, reflecting the available statistics). The results show that the bias is stronger under more stringent requirements for n_{S}. Additionally, the bias varies by particle species, with a stronger effect observed for multi-strange hadrons. For instance, imposing a minimum of 3 Ξ^- leads to a similar relative bias as requiring 5 K^0_S. Notably, the relative shift in $\langle \mathrm{d}N_{\mathrm{ch}}/\mathrm{d}\eta \rangle$ is more pronounced in low-multiplicity classes but decreases to below 50% for all particles and n_{S} in the highest-multiplicity class.

Similar qualitative trends are observed when using the Epos LHC and Pythia 8 Monash models, though the magnitude of the bias varies significantly across the different approaches. For example, in the lowest multiplicity class, a requirement of $n_\Lambda \geq 4$ induces a relative shift in $\langle \mathrm{d}N_{\mathrm{ch}}/\mathrm{d}\eta \rangle$ of 320%, 215% and 500% for the Pythia 8 QCD-CR Ropes, Pythia 8 Monash and Epos LHC models, respectively. For a more detailed analysis of the observed trends, refer to Figures 9.162 and 9.161 in Appendix 9.8, which correspond to the Pythia 8 Monash and Epos LHC models, respectively. These variations reflect differences in how the models implement the microscopic mechanisms governing strange particle production and their correlations with non-strange hadron formation. In this sense, the strangeness-induced charged-particle multiplicity bias provides a complementary perspective on the strangeness enhancement puzzle: models that accurately reproduce this bias also tend to correctly describe strangeness enhancement.

However, this feature can introduce complications when analyzing particle ratios as a function of multiplicity. For instance, in the computation of the Ω/π ratio, as shown in Ref. [1], the average charged-particle multiplicity of events containing at least one Ω is 50% higher than the un-biased average (see Fig. 5.5). Consequently, the ratio is effectively evaluated at slightly different multiplicities. This issue becomes even more pronounced when ratios involving multi-strange particles, such as the production probability of multi-strange hadrons relative to single K^0_S, are considered, as the multiplicity bias can differ significantly between numerator and denominator. Despite this, when comparing results with Monte Carlo generators, the exact multiplicity at which the ratio is calculated for a given V0M class is not critical. The agreement or disagreement with the data is primarily determined by the model's ability to reproduce the relative production probabilities of particles with different strangeness content (see Section 6.2). For this reason, particle ratios as a function of multiplicity are reported at the un-biased $\langle \mathrm{d}N_{\mathrm{ch}}/\mathrm{d}\eta \rangle$ value, denoted as $\langle \mathrm{d}N_{\mathrm{ch}}/\mathrm{d}\eta \rangle_{|\eta| < 0.5}$ (V0M class). This represents the ratio measured for a set of collisions corresponding to a given V0M class and is consistent with the methodology adopted in previous ALICE publications for ratio-to-pion measurements.

5.3 Multiple strange hadron production yields

From the measurement of $P(n_S)$, Eq. 4.18 enables the calculation of the average yield $\langle Y_{nS} \rangle$, which represents the production of n particles of type S per event. This includes the dN/dy for $n = 1$ (the mean of the strange particle multiplicity distribution) as well as the yields for multiple production events (from pairs of particles up to the maximum $P(n_S)$ measurement range). Specifically, to compute $\langle Y_{2S} \rangle$ ($\langle Y_{2S} \rangle = P(2) + 3P(3) + 6P(4) + ...$), it is necessary to account for all possible combinations that result in a doublet. For instance, if there are 2 candidates, there is only one possible doublet configuration (combinatorial factor of 1). If there are 3 candidates (labeled A, B and C), several combinations yield a pair of particles (e.g., AB, AC, BC), resulting in a combinatorial factor of 3, and so on.
As discussed in Section 4.8, it is important to note that Eq. 4.18 theoretically extends to infinity, as all possible multiplicities contribute to the determination of the probabilities for higher-order multiplets. However, in practice, the calculation of n-tuplets is performed only up to $n = n_S^{max} - 1$ for all particles except Ω, where it is extended to $n = n_\Omega^{max}$.

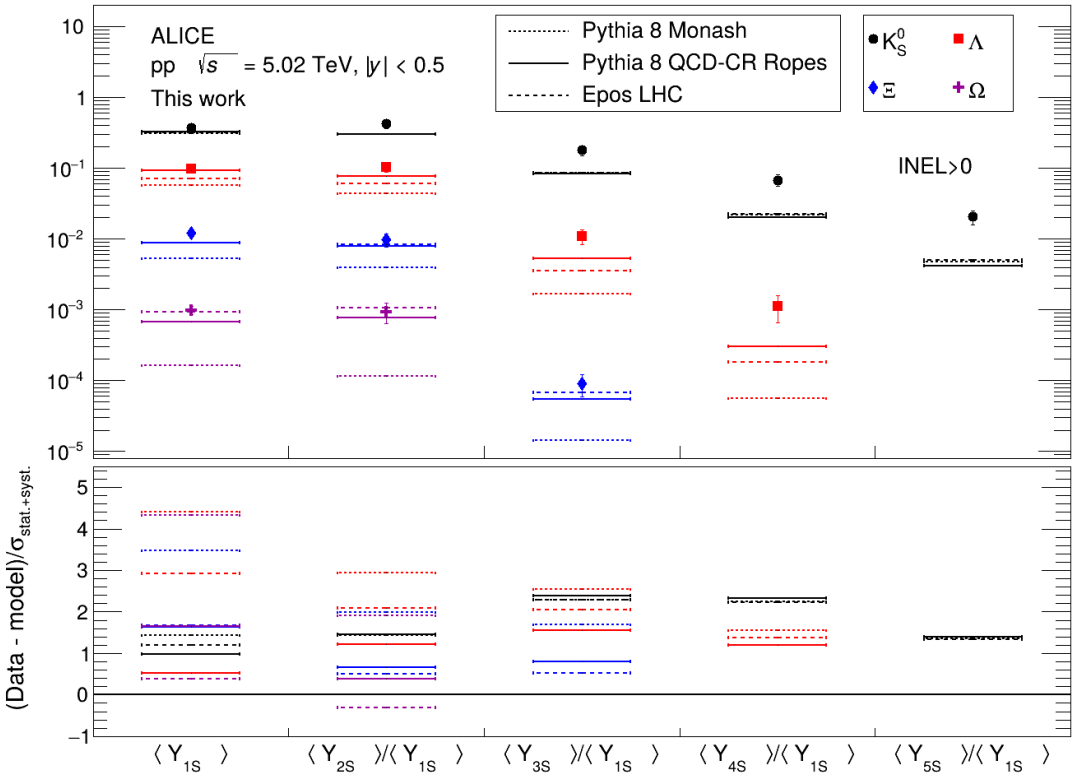

Figure 5.5: $\langle Y_{1S} \rangle$ and $\langle Y_{n>1S} \rangle / \langle Y_{1S} \rangle$ in the INEL > 0 event class. Results obtained for K^0_S, Λ, Ξ and Ω are reported as black circles, red squares, blue diamonds and purple crosses respectively. Model predictions by Pythia 8 Monash, Pythia 8 QCD-CR Ropes and Epos LHC are shown as dotted, continuous and dashed lines respectively.

Figure 5.5 presents $\langle Y_{1S} \rangle$ and various yield ratios normalized to $\langle Y_{1S} \rangle$ for all the hadrons studied in the INEL > 0 event class. These ratios serve as a tool to assess the performance

of MC generators in reproducing the higher moments of the strange particle multiplicity distribution. Normalizing to $\langle Y_{1S} \rangle$ effectively removes potential discrepancies in the average strange particle production rates, focusing the comparison on the higher-order features of the distribution. The bottom panel of the figure displays the pulls, normalized to the quadratic sum of statistical and systematic uncertainties from the data. The comparison reveals that the Pythia 8 QCD-CR Ropes and Epos LHC models reproduce the average distribution ($n = 1$, first column) within 2 - 3σ for all particles, whereas Pythia 8 Monash exhibits larger deviations. This highlights the significant advancements in the Pythia generator achieved with the inclusion of QCD-inspired CR mechanisms and color ropes hadronization. These improvements are particularly evident in the description of baryon yields, while the K^0_S yield remains largely unaffected. When examining the ratios $\langle Y_{n>1S} \rangle / \langle Y_{1S} \rangle$, the comparison with model predictions indicates discrepancies not exceeding 2.5σ across different n values and particle species.

Multiple production yields are also calculated across different V0M multiplicity classes, as shown in Fig. 5.6. The results are presented for V^0 particles and cascades in the first and second row, respectively, displaying both matter (full markers) and anti-matter (open markers) yields. As previously discussed, the x-axis positions of the data points correspond to the average of the un-biased charged-particle multiplicity distribution for the respective V0M class. However, for events involving multiple strange particle production, a bias is expected that shifts the averages to higher values. It is important to note that this bias would further emphasize the observed yield enhancement with increasing multiplicity, as the strongest effects are anticipated at low multiplicity (see Fig. 5.4).

As previously mentioned, $\langle Y_{1S} \rangle$ corresponds to the familiar $\mathrm{d}N/\mathrm{d}y$ trend with multiplicity, consistent with prior measurements. In fact, a comparison of these results with those in Ref. [16] reveals perfect agreement, further validating this novel technique for measuring strange particle yields. Additional details regarding this comparison will be reported in Section 5.6. The increase in yields with multiplicity is more than linear for the production of multiple strange particles, becoming progressively steeper as the number of produced hadrons grows. Specifically, $\langle Y_{5K^0_S} \rangle$, $\langle Y_{4\Lambda} \rangle$, $\langle Y_{3\Xi} \rangle$ and $\langle Y_{2\Omega} \rangle$ increase by approximately $2 - 3$ orders of magnitude from the lowest to the highest charged-particle multiplicity classes.
In Fig. 5.6, a comparison with phenomenological models is also shown. Among the models tested, Pythia 8 Monash exhibits the poorest agreement with the data, with significant discrepancies even for $\langle Y_{1S} \rangle$ in baryon production, which grows larger as the number of strange hadrons increases, reaching up to 2 orders of magnitude in the worst cases. The situation improves notably with the Pythia 8 QCD-CR Ropes model for baryons, although it remains unchanged for K^0_S, indicating that strange quark production, rather than strange baryon formation, remains a challenge in Pythia. The Epos LHC model exhibits better agreement with the data at high multiplicities for baryons, but it underestimates the yields at low multiplicities, suggesting that the model performs best in the region dominated by the core (in-medium hadronization) effects. For K^0_S, no significant difference among the three tested models is observed.

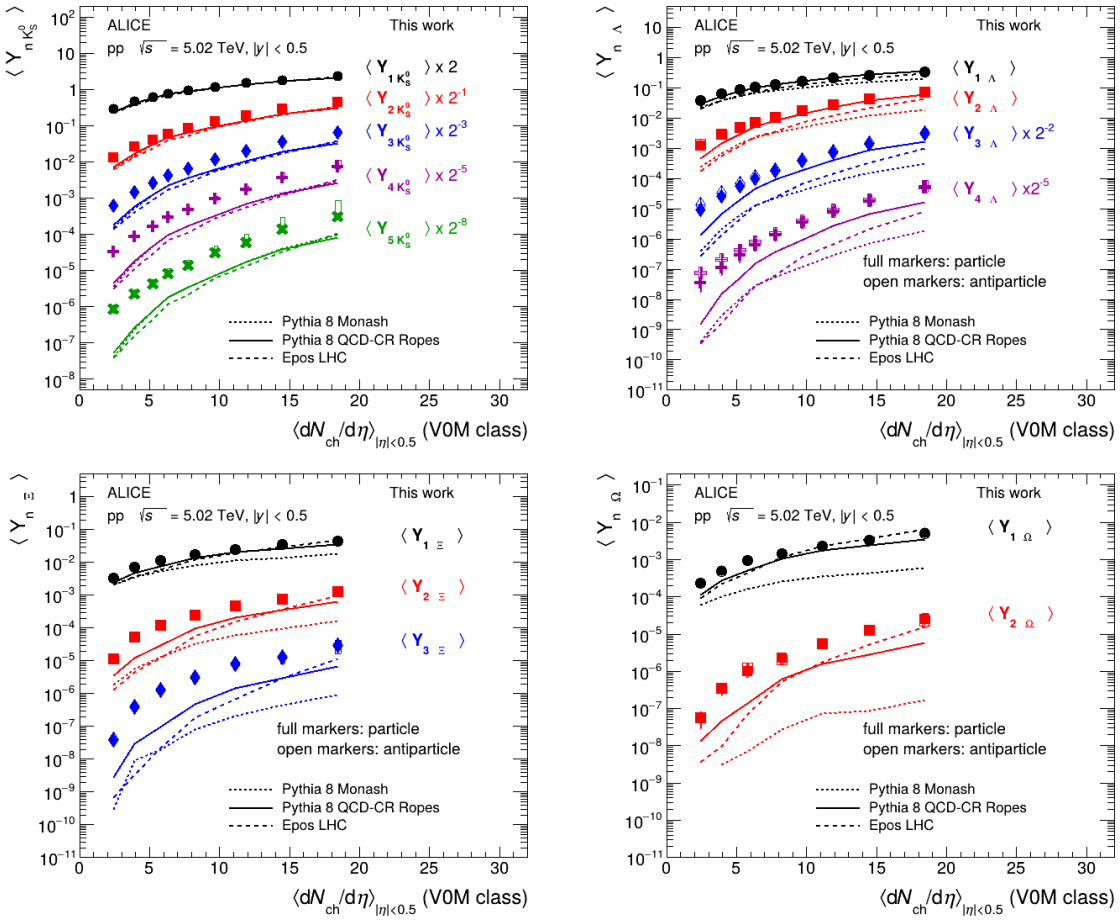

Figure 5.6: Multiple strange hadron production yields as a function of the un-biased average charged-particle multiplicity $\langle dN_{ch}/d\eta \rangle_{|\eta|<0.5}$ (V0M class) for K^0_S (top-left), Λ (top-right), Ξ (bottom-left) and Ω (bottom-right). Matter corresponds to full markers, anti-matter to open markers. Model predictions are reported for Pythia 8 Monash, Pythia 8 QCD-CR Ropes and Epos LHC as dotted, continuous and dashed lines respectively.

5.4 Yield ratios with $\Delta S > 0$: strangeness enhancement at its extremes

Strangeness enhancement is typically studied by taking the ratio of production yields of particles with differing strangeness content. The reference can be either pions (as in Ref. [1]) or hadrons with limited strangeness content, such as K^0_S (as in Ref. [15]). In previous studies, the maximum difference in strange quark content (ΔS) between the numerator and denominator was limited to three, corresponding to the comparison of single-particle yields, where the maximum strangeness content of a single hadron is three, as in the case of Ω.

The measurement of multiple strange hadron production yields now allows the exploration of strangeness enhancement with larger ΔS. This is presented in Fig. 5.7, which shows

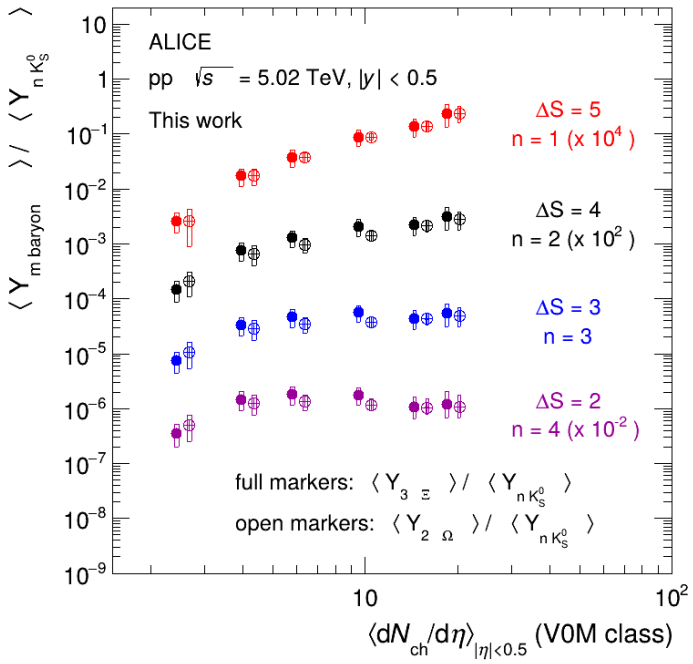

Figure 5.7: $\langle Y_{3\Xi}\rangle/\langle Y_{nK^0_S}\rangle$ (full markers) and $\langle Y_{2\Omega}\rangle/\langle Y_{nK^0_S}\rangle$ (open markers) as a function of the unbiased average charged-particle multiplicity at midrapidity. n runs from 1 to 4, corresponding to red, black, blue and purple markers respectively. Open markers are shifted to the right by 10% to enhance visibility.

the ratios $\langle Y_{3\Xi}\rangle/\langle Y_{nK^0_S}\rangle$ and $\langle Y_{2\Omega}\rangle/\langle Y_{nK^0_S}\rangle$ as function of the unbiased average charged-particle multiplicity at midrapidity. For the first time, a maximum ΔS of 5 is achieved, corresponding to an extraordinary enhancement of two orders of magnitude between the lowest and highest V0M multiplicity classes. Ratios for smaller ΔS are also reported, showing progressively lower enhancement factors, as expected. The relative increases observed for $\Delta S = 3$ and 2 are consistent, within systematic uncertainties, with those previously reported for the Ξ/π and Ω/π ratios [1]. Additional details about this comparison will be provided in Section 5.6.
It is notable that the trends observed for $\langle Y_{3\Xi}\rangle$ and $\langle Y_{2\Omega}\rangle$ are consistent for each n, both in terms of relative increase and absolute values (with the $\langle Y_{2\Omega}\rangle$ ratios slightly shifted to the right by 10% for clarity). This consistency indicates that the enhancement pattern is primarily driven by the strangeness content of the hadron, rather than by other factors such as the number of baryons formed, the total mass generated, or the involvement of light quarks. Further insights into this will be discussed later in the context of ratios with $\Delta S = 0$ (see Section 5.5).

The comparison with MC generators is shown in Fig. 5.8. The Epos LHC model demonstrates a very good agreement with the data at high $\langle dN_{ch}/d\eta\rangle_{|\eta|<0.5}$ (V0M class) values, but the multiplicity trend does not align with the observed behavior, underestimating the ratio by two orders of magnitude at very low multiplicity for the $\Delta S = 5$ case. This suggests that while the model successfully describes relative strangeness pro-

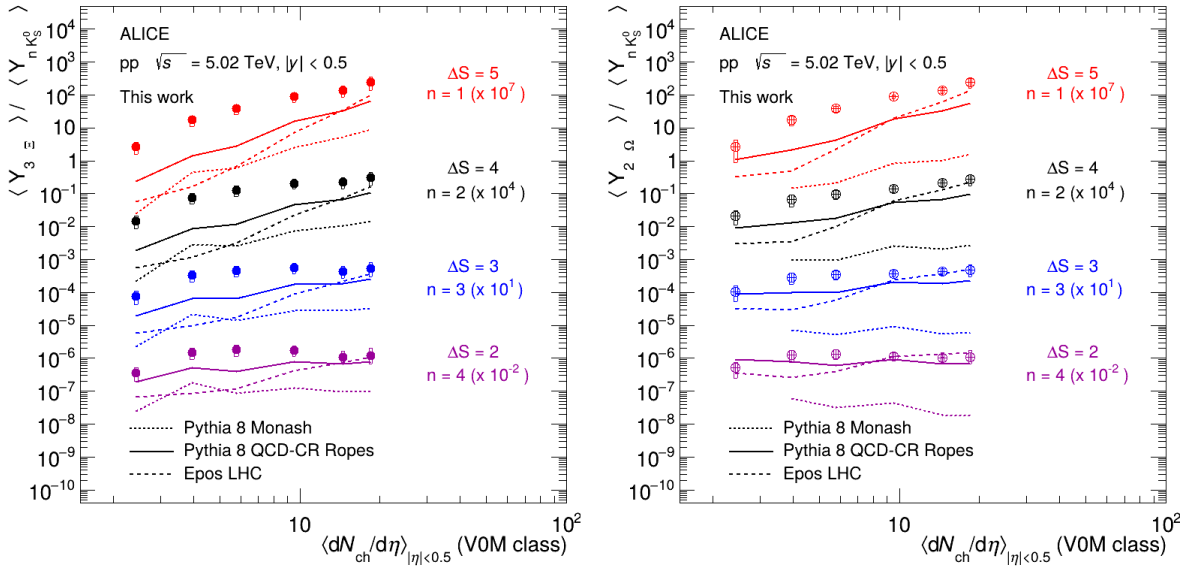

Figure 5.8: $\langle Y_{3\Xi}\rangle/\langle Y_{nK^0_S}\rangle$ (*Left.*) and $\langle Y_{2\Omega}\rangle/\langle Y_{nK^0_S}\rangle$ (*Right.*) as a function of the unbiased charged-particle multiplicity density compared with MC generators: Pythia 8 Monash (dotted line), Pythia 8 QCD-CR Ropes (continuous line) and Epos LHC (dashed line).

duction in the core (modeled as statistical production), it fails to capture the transition to a corona-dominated system at low multiplicity, which severely underestimates the production of multiple multi-strange baryons. On the other hand, Pythia 8 QCD-CR Ropes shows better agreement with the data at high multiplicity, though it still deviates from the measured trend, underestimating the data at low multiplicity, but to a lesser extent than Epos LHC. It is also important to note that, although the data show consistency between $\langle Y_{3\Xi}\rangle/\langle Y_{nK^0_S}\rangle$ and $\langle Y_{2\Omega}\rangle/\langle Y_{nK^0_S}\rangle$, both MC generators exhibit different multiplicity dependencies. Specifically, both models show a steeper increase in multiplicity when a larger number of baryons is involved (e.g., $\langle Y_{3\Xi}\rangle$). This indicates that the multiplicity increase in these two models is significantly influenced by the number of baryons in the numerator (3Ξ or 2Ω), a trend not observed in the data.

5.5 Yield ratios with $\Delta S = 0$: non-strangeness related effect

The observed enhancement pattern in the strange-to-pion ratio as a function of multiplicity is typically attributed to the strangeness content of the hadrons. This hypothesis is supported by the fact that no such enhancement has been observed in ratios where the numerator and denominator contain an equal number of strange quarks, such as in the Λ/K^0_S and p/π ratios, which show no clear enhancement pattern in the multiplicity range from ~ 5 to ~ 50 [1]. While a notable depletion in these ratios was observed at lower multiplicities, this effect was confined to a single data point in each case. To further investigate the potential presence of a non-strangeness-related influence on the evolution of particle ratios with multiplicity, the relative production of different multiplets with

$\Delta S = 0$ is calculated and presented in Figures 5.9 and 5.10.

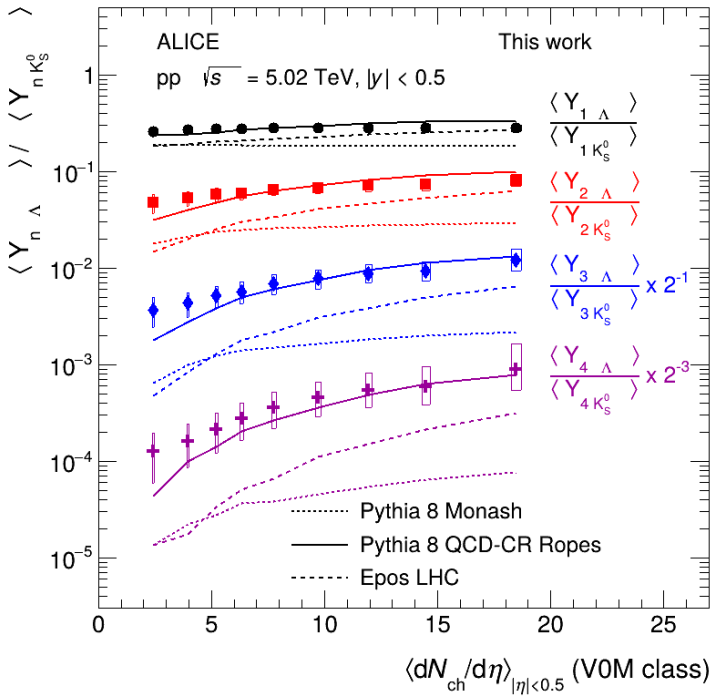

Figure 5.9: $\langle Y_{n\Lambda} \rangle / \langle Y_{nK^0_S} \rangle$ as a function of the un-biased average charged-particle multiplicity at midrapidity. Black, red, blue and purple points correspond to $n = 1$, 2, 3 and 4 respectively. MC predictions from Pythia 8 Monash (dotted lines), Pythia 8 QCD-CR Ropes (continuous lines) and Epos LHC (dashed lines) are also shown.

In Fig. 5.9, the $\langle Y_{n\Lambda} \rangle / \langle Y_{nK^0_S} \rangle$ ratio shows, for the first time, an increase with $\langle dN_{ch}/d\eta \rangle_{|\eta|<0.5}$ (V0M class) for $n > 1$, indicating that the evolution of multi-particle yield ratios with multiplicity is not solely due to the strangeness imbalance between the numerator and denominator. For $n = 1$, the ratio aligns with the results reported in Refs. [1, 15] (see Section 5.6 for additional details), confirming that the enhancement observed at $\Delta S = 0$ is sub-leading with respect to the strangeness-related effect. However, it is not possible to conclusively determine whether the observed enhancement in the $\langle Y_{n\Lambda} \rangle / \langle Y_{nK^0_S} \rangle$ ratio with multiplicity is related to a baryon effect, the larger total mass in the numerator, or the number of u and d quarks required to form a Λ or a K^0_S, based solely on the data shown in Fig. 5.9.

In order to further investigate the relative probability of s-quarks hadronizing into different types of final-state hadrons, Fig. 5.10 presents additional examples of $\Delta S = 0$ multiplet ratios as a function of the un-biased average charged-particle multiplicity at midrapidity. The left panel shows the ratios $\langle Y_{1\Xi} \rangle / \langle Y_{2K^0_S} \rangle$, $\langle Y_{1\Omega} \rangle / \langle Y_{3K^0_S} \rangle$ and $\langle Y_{2\Xi} \rangle / \langle Y_{4K^0_S} \rangle$. In all these cases, the numerator involves a higher overall mass and baryon content compared to the denominator, yet the ratios exhibit a decreasing trend with increasing multiplicity. This observation suggests that mass and baryon numbers alone do not drive the enhancement with multiplicity. On the other hand, the trends in Fig. 5.9 and the left panel of Fig. 5.10

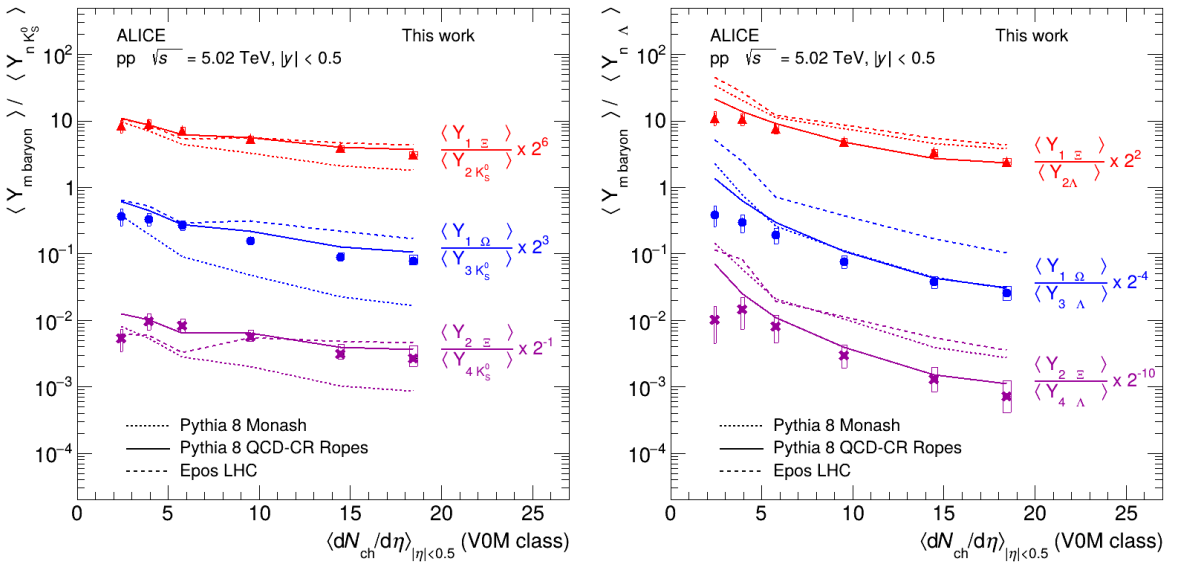

Figure 5.10: $\Delta S = 0$ multiple-particle yield ratios as a function of $\langle dN_{ch}/d\eta\rangle_{|\eta|<0.5}$ (V0M class), compared to MC predictions from Pythia 8 Monash (dotted lines), Pythia 8 QCD-CR Ropes (continuous lines) and Epos LHC (dashed lines). (*Left.*) $\langle Y_{1\Xi}\rangle/\langle Y_{2K^0_S}\rangle$ (red), $\langle Y_{1\Omega}\rangle/\langle Y_{3K^0_S}\rangle$ (blue) and $\langle Y_{2\Xi}\rangle/\langle Y_{4K^0_S}\rangle$ (purple). (*Right.*) $\langle Y_{1\Xi}\rangle/\langle Y_{2\Lambda}\rangle$ (red), $\langle Y_{1\Omega}\rangle/\langle Y_{3\Lambda}\rangle$ (blue) and $\langle Y_{2\Xi}\rangle/\langle Y_{4\Lambda}\rangle$ (purple).

can be qualitatively explained within a naïve quark coalescence framework. Taking the $\langle Y_{1\Omega}\rangle/\langle Y_{3K^0_S}\rangle$ ratio as an example, the requirement of one Ω or three K^0_S fixes the minimum number of strange quarks at 3. Forming an Ω requires no additional u or d quarks, whereas forming three K^0_S requires three light quarks. In low-multiplicity environments, the scarcity of light quarks increases the likelihood of the three strange quarks coalescing into an Ω rather than forming three K^0_S. Conversely, in high-multiplicity environments, the abundance of light quarks facilitates pairing with strange quarks, favoring the production of three K^0_S.
A qualitatively similar behavior is observed in the right panel of Fig. 5.10, which displays the ratios $\langle Y_{1\Xi}\rangle/\langle Y_{2\Lambda}\rangle$, $\langle Y_{1\Omega}\rangle/\langle Y_{3\Lambda}\rangle$ and $\langle Y_{2\Xi}\rangle/\langle Y_{4\Lambda}\rangle$. When comparing ratios normalized to K^0_S versus Λ while keeping the numerator fixed (Ξ or Ω), the decreasing trend with multiplicity is more pronounced when a baryon is present in the denominator. This can be understood by noting that a Λ baryon contains two light quarks, whereas a K^0_S meson contains only one. Although this explanation is simplistic, it provides a consistent interpretation for the observed trends in all ratios reported in Figures 5.9 and 5.10, offering insight into the interplay of light and strange quark availability across different multiplicity environments.

The comparison with models offers valuable insights. Pythia 8 Monash underestimates all particle ratios relative to K^0_S (Fig. 5.9 and the left panel of Fig. 5.10) while overestimating ratios relative to Λ (right panel of Fig. 5.10), with the sole exception of $\langle Y_{1\Omega}\rangle/\langle Y_{3\Lambda}\rangle$. Additionally, it fails to reproduce the observed increasing or decreasing trends. In contrast, Pythia 8 QCD-CR Ropes provides an excellent description of all trends, both qualita-

tively and quantitatively, demonstrating that the QCD-CR mechanism implemented in the model effectively captures the reconnection of strange and light quarks as a function of multiplicity. Epos LHC qualitatively captures the multiplicity trend for all ratios relative to K^0_S, but systematically underestimates their values. For ratios relative to Λ (right panel of Fig. 5.10), Epos LHC consistently overestimates the observed values.

5.6 Comparison with previous results

To verify the consistency of the results obtained with the new analysis technique presented in this thesis, several comparisons with previous findings have been conducted.

As previously mentioned, $\langle Y_{1S} \rangle$ corresponds to the standard dN/dy trend with multiplicity. As a first step, a comparison was made with the results presented in Ref. [16]. Figure 5.11 illustrates this comparison: on the left for K^0_S and on the right for $\Lambda + \overline{\Lambda}$. The blue markers represent the dN/dy progression with multiplicity for pp at $\sqrt{s} = 5.02$ TeV, obtained using a standard analysis ([16]). The errors shown here are the sum of statistical and systematic uncertainties. In contrast, the dark green markers indicate the mean values extracted in this analysis. The plots also include continuous lines representing linear fits to the results reported in [16]. As shown, there is very good agreement with the published distributions, both in terms of the values and the systematic uncertainties, for both hadron species. It is worth noting that, for Λ particles, the comparison with previous results (blue points [16]) — which account for the dN/dy progression of $\Lambda + \overline{\Lambda}$ — was performed by summing the values obtained in this analysis for particles and antiparticles separately.

For cascade particles, similar results are shown in Fig. 5.12, where $\Xi^- + \overline{\Xi}^+$ and $\Omega^- + \overline{\Omega}^+$ are presented on the left and right, respectively. The plots include both data and fit lines: linear fits for Ξ and quadratic fits for Ω, performed on the results from [16], represented as continuous lines. Once again, very good agreement with the published results is observed. Also in this case, to compare the results with previous ones (blue points [16]), the values obtained in this analysis for particles and antiparticles separately have been summed.

To better examine the comparison between the previous results and those obtained in this analysis, the ratio between the data and the fit was calculated. Figure 5.13 displays these ratios, calculated as the ratio between the data points and the linear or quadratic fit: blue markers represent the ratios for the previous results ([16]), while green squares represent the ratios for this analysis. The first row shows the results for K^0_S and $\Lambda + \overline{\Lambda}$, and the second row shows those for $\Xi^- + \overline{\Xi}^+$ and $\Omega^- + \overline{\Omega}^+$. The uncertainties associated with the ratios were calculated using the error propagation formula. Observing the ratios, it is evident that, within the uncertainties, the results from this thesis are consistent with the previous findings for all particle species, as was already observed for the dN/dy progression with $\langle dN_{ch}/d\eta \rangle$. Furthermore, the uncertainties achieved in this analysis are smaller compared to those from earlier studies. This difference can be attributed to the method used for estimating systematics on the set of cuts: in this work, a multi-trial approach was employed, whereas previous analyses repeated the process by varying individual variables within defined ranges. The multi-trial method results in smaller errors as it provides a

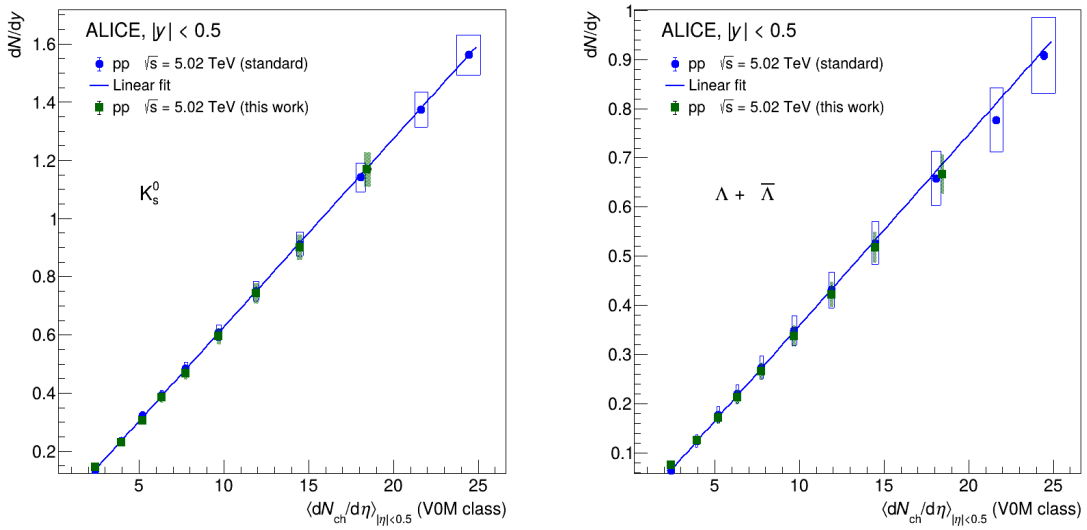

Figure 5.11: Comparison of the $\mathrm{d}N/\mathrm{d}y$ progression with multiplicity between the results obtained in Ref. [16] and those from this analysis, shown for K^0_S on the left and $\Lambda + \overline{\Lambda}$ on the right. The blue markers represent the $\mathrm{d}N/\mathrm{d}y$ progression with multiplicity for pp collisions at $\sqrt{s} = 5.02$ TeV from the standard analysis in Ref. [16], while the dark green markers indicate the mean values derived in this analysis using tighter cuts. The continuous line corresponds to linear fits to the results reported in Ref. [16].

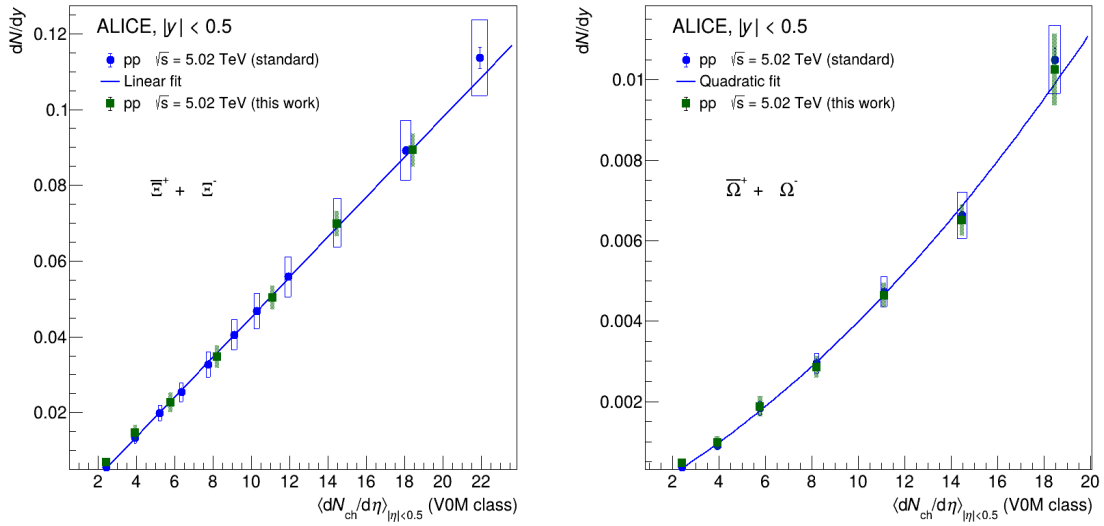

Figure 5.12: Comparison of the $\mathrm{d}N/\mathrm{d}y$ progression with multiplicity between the results obtained in Ref. [16] and those from this analysis, shown for $\Xi^- + \overline{\Xi}^+$ on the left and $\Omega^- + \overline{\Omega}^+$ on the right. The blue markers represent the $\mathrm{d}N/\mathrm{d}y$ progression with multiplicity for pp collisions at $\sqrt{s} = 5.02$ TeV from the standard analysis in Ref. [16], while the dark green markers indicate the mean values derived in this analysis using tighter cuts. The continuous line corresponds to linear (for $\Xi^- + \overline{\Xi}^+$) and quadratic (for $\Omega^- + \overline{\Omega}^+$) fits to the results reported in Ref. [16].

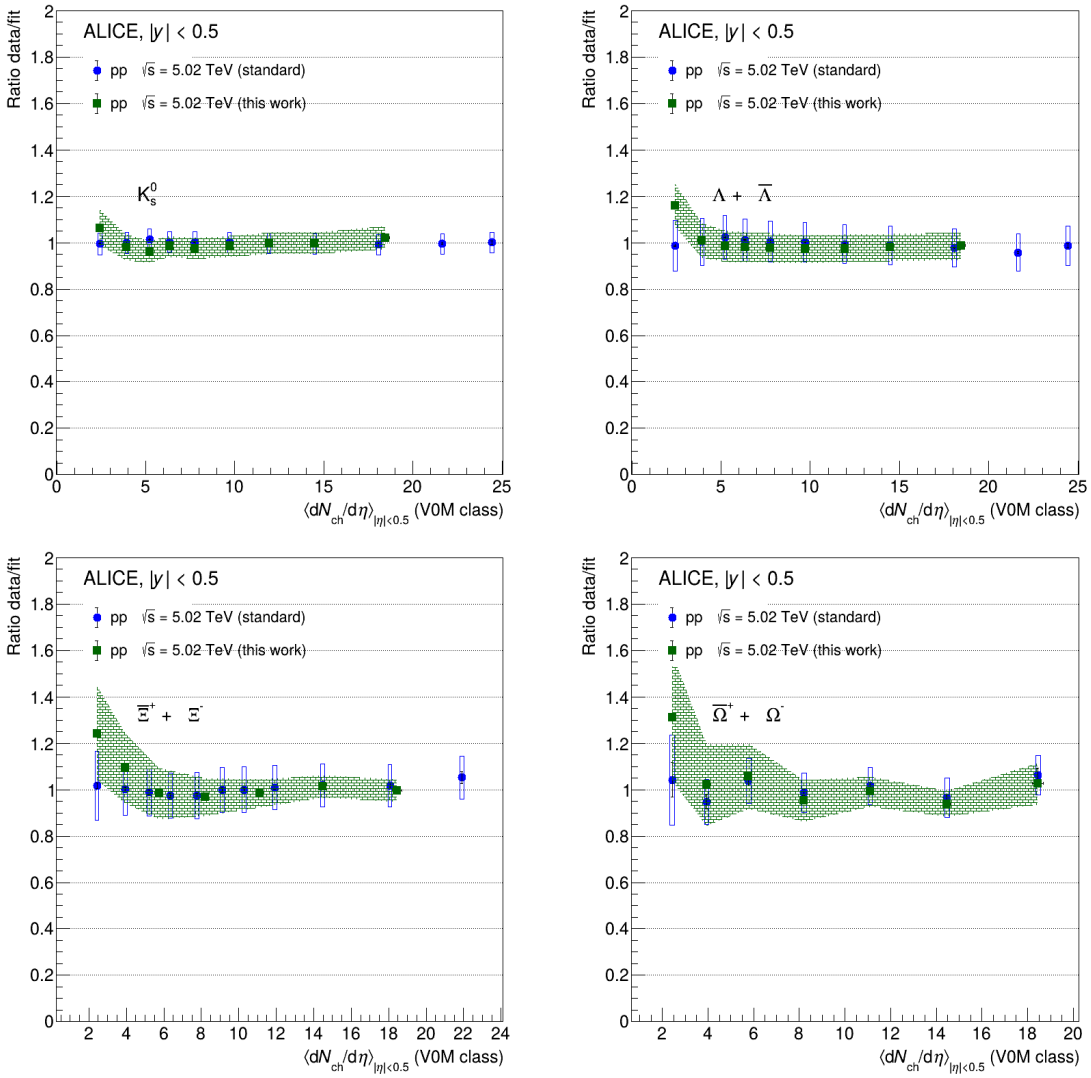

Figure 5.13: The ratios between the data and the fits are reported: the first row presents the results for K^0_S and $\Lambda + \overline{\Lambda}$, while the second row shows the results for $\Xi^- + \overline{\Xi}^+$ and $\Omega^- + \overline{\Omega}^+$. The ratios are computed by dividing the data points by the corresponding linear or quadratic fit. Blue markers represent the ratios for the previous results ([16]), while green squares correspond to the ratios obtained in this analysis.

more uniform and comprehensive exploration of the variable space, reducing variance and accounting for potential correlations between variables.

Beyond validating the new analysis technique applied in this thesis, the obtained results and systematic uncertainties were used to evaluate the ratios $\langle Y_{1\Lambda} \rangle / \langle Y_{1K^0_S} \rangle$, $\langle Y_{1\Xi} \rangle / \langle Y_{1K^0_S} \rangle$ and $\langle Y_{1\Omega} \rangle / \langle Y_{1K^0_S} \rangle$. These ratios were then compared with previously reported results from pp collisions at $\sqrt{s} = 13$ TeV [15]. Figure 5.14 presents the comparisons: $\langle Y_{1\Lambda} \rangle / \langle Y_{1K^0_S} \rangle$ on the left, $\langle Y_{1\Xi} \rangle / \langle Y_{1K^0_S} \rangle$ in the center, and $\langle Y_{1\Omega} \rangle / \langle Y_{1K^0_S} \rangle$ on the right. The blue markers represent values obtained for pp at $\sqrt{s} = 13$ TeV using a standard analysis [15], while the dark green markers show the ratios derived in this thesis. For cascades, the results were

calculated by summing the values for particles and antiparticles obtained in this analysis. As shown, there is a good consistency with the published distributions. This agreement is observed not only for the values but also for the systematic uncertainties of all the considered ratios, further confirming the validity of the novel technique developed in this thesis.

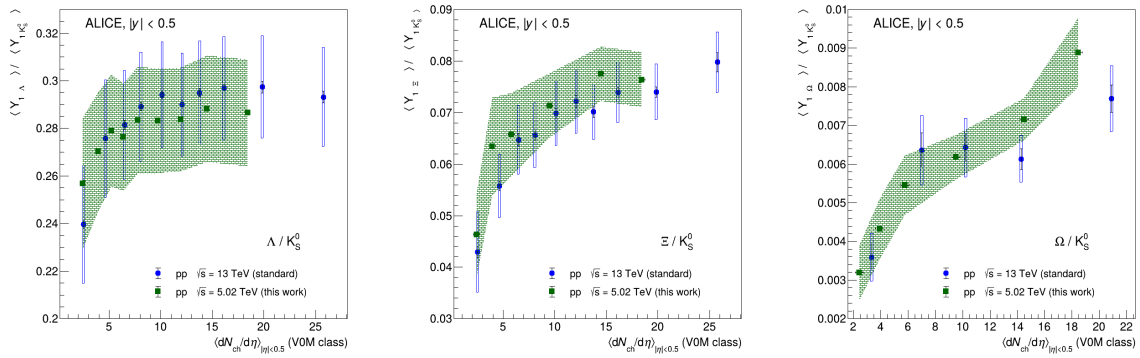

Figure 5.14: Comparison of the $\langle Y_{1\Lambda}\rangle/\langle Y_{1K^0_S}\rangle$, $\langle Y_{1\Xi}\rangle/\langle Y_{1K^0_S}\rangle$ and $\langle Y_{1\Omega}\rangle/\langle Y_{1K^0_S}\rangle$ ratios as a function of charged-particle multiplicity. Blue markers represent the values obtained in pp collisions at $\sqrt{s} = 13$ TeV ([15]), with statistical uncertainties shown as error bars and systematic uncertainties as empty boxes. Dark green markers show the values from this analysis, with statistical uncertainties indicated by error bars and systematic uncertainties by a shaded color band.

Another check was performed in order to corroborate further the analysis technique, the obtained results and the conclusions drawn from them. As discussed in Section 5.4, studying the strangeness enhancement at its extremes revealed that the enhancement pattern is primarily influenced by the strangeness content of the hadron, rather than other factors such as the number of baryons produced, the total mass generated, or the involvement of light quarks. To further test this conclusion, (multiple-)yield ratios with the same ΔS but involving different numbers of light quarks were compared with previous results at different energies ([1, 15]). Specifically, ratios with $\Delta S = 3$ ($\langle Y_{3\Xi}\rangle/\langle Y_{3K^0_S}\rangle$ and $\langle Y_{2\Omega}\rangle/\langle Y_{3K^0_S}\rangle$) were compared to the d$N$/d$y$ ratio Ω/π measured in pp collisions at $\sqrt{s} =$ 7 TeV (Ref. [1]). Ratios with $\Delta S = 2$ ($\langle Y_{3\Xi}\rangle/\langle Y_{4K^0_S}\rangle$ and $\langle Y_{2\Omega}\rangle/\langle Y_{4K^0_S}\rangle$) were compared to the d$N$/d$y$ ratio Ξ/π measured in pp collisions at $\sqrt{s} = 7$ TeV (Ref. [1]) and the dN/dy ratio Ω/K^0_S measured in pp collisions at $\sqrt{s} = 13$ TeV (Ref. [15]). Please note that in this study, particles and antiparticles were analyzed separately, so all dN/dy ratios were divided by two. The left panel of Fig. 5.15 compares (multiple-)yield ratios with the same ΔS, involving different numbers of light quarks, across various energies: ratios with $\Delta S = 3$ are shown in blue, while those with $\Delta S = 2$ are in magenta. However, yield ratios with the same ΔS do not agree because of differing normalizations. To enable a consistent comparison of results across different centre-of-mass energies and analysis strategies, all (multiple-)yield ratios were normalized to the INEL > 0 value in pp collisions at $\sqrt{s} =$ 5.02 TeV. For previously published results (Refs. [1, 15]), the yield ratios were divided by the fit value corresponding to the MB at this energy. Previous studies collected in Ref. [158] demonstrated that the measured yields of strange particles generally exhibit an

approximately linear dependence on the charged-particle multiplicity, except for Ω, which follows a quadratic trend. After verifying this behavior, Ω/π, $\Omega/\mathrm{K}^0_\mathrm{S}$ and Ξ/π ratios were fitted using appropriate functional forms: quadratic over linear for Ω/π and $\Omega/\mathrm{K}^0_\mathrm{S}$, and linear over linear for Ξ/π. Using these fits, the value at $\langle \mathrm{d}N_\mathrm{ch}/\mathrm{d}\eta \rangle = 5.49$ ($\langle \mathrm{d}N_\mathrm{ch}/\mathrm{d}\eta \rangle$ associated to the MB in pp at $\sqrt{s} = 5.02$ TeV) was extracted and the results are shown in the right panel of Fig. 5.15. The comparison of (multiple-)yield ratios with the same ΔS, normalized to the same value, reveals good agreement among the results of this study and previous works (Refs. [1, 15]). Moreover, this finding not only confirms the validity of the analysis technique and the results obtained, but also provides additional evidence that the enhancement pattern observed in the strange sector is mainly driven by the strangeness content of the hadrons.

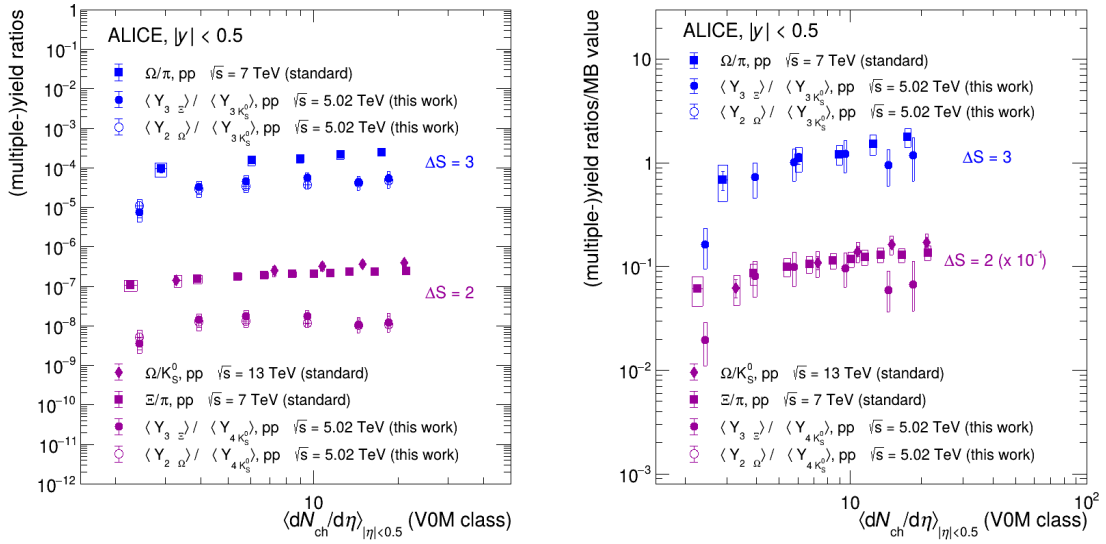

Figure 5.15: (*Left.*) Comparison of (multiple-)yield ratios with the same ΔS, involving different numbers of light quarks, at various energies. (*Right.*) Comparison of (multiple-)yield ratios normalized to the MB value in pp collisions at $\sqrt{s} = 5.02$ TeV. In both plots, (multiple-)yield ratios with $\Delta\mathrm{S} = 3$ are shown in blue: the $\mathrm{d}N/\mathrm{d}y$ ratio Ω/π measured in pp collisions at $\sqrt{s} = 7$ TeV (Ref. [1]) is represented as full squares, $\langle \mathrm{Y}_{3\Xi} \rangle / \langle \mathrm{Y}_{3\mathrm{K}^0_\mathrm{S}} \rangle$ from this work as full circles, and $\langle \mathrm{Y}_{2\Omega} \rangle / \langle \mathrm{Y}_{3\mathrm{K}^0_\mathrm{S}} \rangle$ from this work as open circles. Conversely, (multiple-)yield ratios with $\Delta\mathrm{S} = 2$ are displayed in magenta: the $\mathrm{d}N/\mathrm{d}y$ ratio $\Omega/\mathrm{K}^0_\mathrm{S}$ measured in pp collisions at $\sqrt{s} = 13$ TeV (Ref. [15]) is displayed as full diamonds, Ξ/π measured in pp collisions at $\sqrt{s} = 7$ TeV (Ref. [1]) as full squares, $\langle \mathrm{Y}_{3\Xi} \rangle / \langle \mathrm{Y}_{4\mathrm{K}^0_\mathrm{S}} \rangle$ from this work as full circles, and $\langle \mathrm{Y}_{2\Omega} \rangle / \langle \mathrm{Y}_{4\mathrm{K}^0_\mathrm{S}} \rangle$ from this work as open circles.

Chapter 6

Future directions

After successfully obtaining and validating the first measurement of the multiplicity distribution, $P(n_S)$, for strange particles (K^0_S, Λ, Ξ^- and Ω^-) and their antiparticles ($\overline{\Lambda}$, $\overline{\Xi}^+$ and $\overline{\Omega}^+$) in pp collisions at $\sqrt{s} = 5.02$ TeV, this chapter explores potential future directions, addressing both experimental advancements and phenomenological implications.

6.1 Experimental Prospects

The results presented in this thesis were obtained using the complete pp data sample collected during Run 2 at $\sqrt{s} = 5.02$ TeV. In addition to pp collisions, ALICE also collected data at the same energy for two other collision systems during the Run 1 and Run 2 campaigns: p–Pb and Pb–Pb. For these systems, the p_T distributions and dN/dy values of (multi-)strange particles were measured as a function of charged-particle multiplicity ([17, 18, 19]). ALICE also explored pp collisions at higher energies ($\sqrt{s} = 7$ and 13 TeV), where similar measurements of p_T distributions and dN/dy values were performed ([14, 15]). Section 6.1.1 discusses the relevance of investigating (multi-)strange particle multiplicity distributions across different collision systems and/or centre-of-mass energies. In addition, in July 2022, the LHC resumed operations (Run 3) with ALICE collecting data in pp collisions at both lower ($\sqrt{s} = 900$ GeV) and higher ($\sqrt{s} = 13.6$ TeV) centre-of-mass energies, and in Pb–Pb at $\sqrt{s} = 5.36$ TeV. ALICE also plans to explore exotic collision systems, such as proton-oxygen (p-O) and oxygen-oxygen (O-O). As briefly mentioned in Section 3.3, to cope with the higher luminosity of Run 3, the ALICE apparatus underwent a significant upgrade ([159, 160]). Key improvements include the replacement of the traditional event trigger system with a continuous data readout from detectors. Section 6.1.2 examines potential improvements and extensions in the measurement of $P(n_S)$ enabled by this new data-taking era.

6.1.1 Other colliding systems and/or centre-of-mass energies

During Run 1 and Run 2, ALICE collected data at $\sqrt{s} = 5.02$ TeV for three colliding systems: pp, p–Pb and Pb–Pb. In these systems, the p_T distributions and dN/dy values of (multi-)strange particles were measured as a function of charged-particle multiplicity [16, 17, 18, 19]. Figure 6.1 illustrates the dN/dy progression with multiplicity for pp, p–Pb and Pb–Pb collisions at $\sqrt{s} = 5.02$ TeV, represented by black, red and blue markers,

respectively. The results indicate that for all analyzed particles, the progression with multiplicity across different collision systems at the same centre-of-mass energy exhibits a smooth, nearly linear trend ([158]).

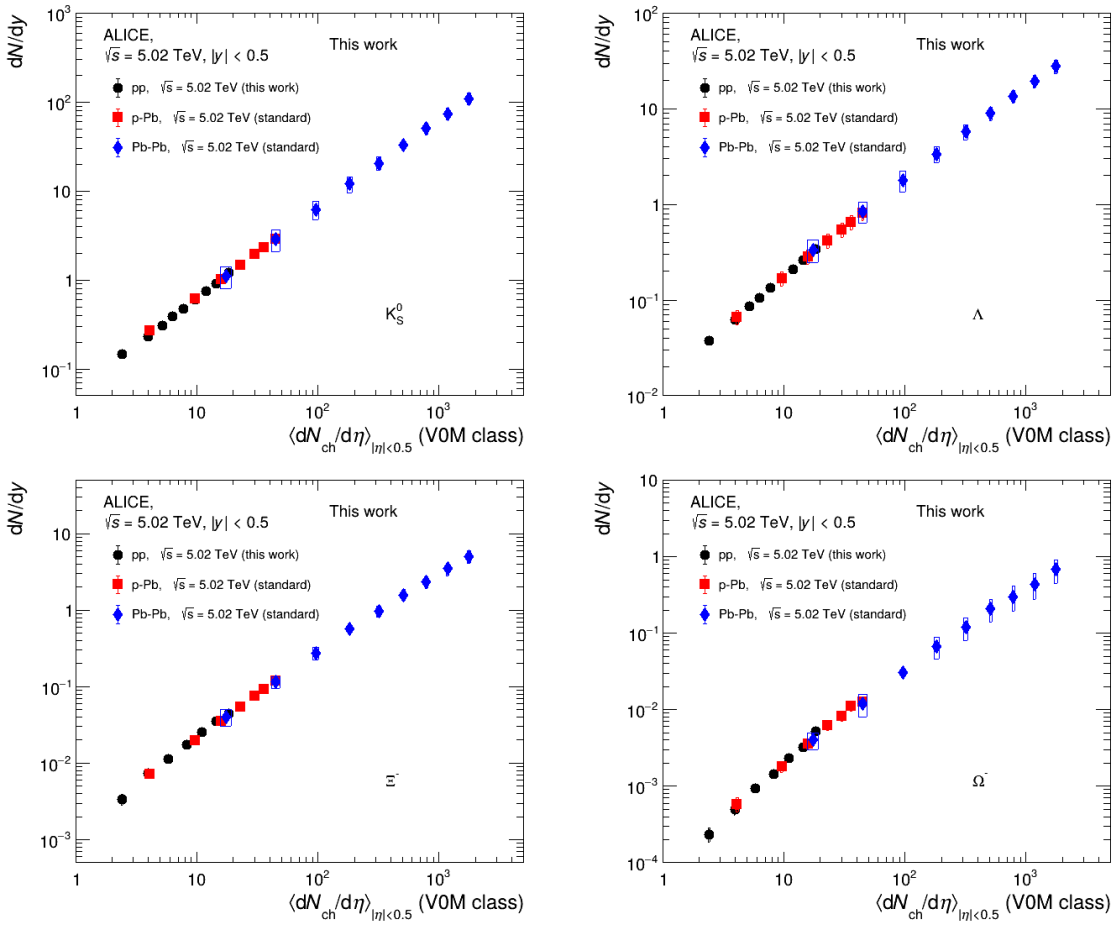

Figure 6.1: Comparison of the $\mathrm{d}N/\mathrm{d}y$ progression with multiplicity is presented for pp, p–Pb and Pb–Pb collisions at $\sqrt{s} = 5.02$ TeV, displayed respectively by black, red, and blue markers. The pp results are derived from this thesis, whereas the p–Pb outcomes are drawn from previous studies ([17, 18]), and the Pb–Pb results are based on findings reported in ([19]). The results are displayed for the strange particles K^0_S (top-left), Λ (top-right), Ξ^- (bottom-left) and Ω^- (bottom-right).

This thesis demonstrates that by measuring the multiplicity distribution of (multi-)strange particles, it is possible to determine multiple production yields of these hadrons as a function of charged-particle multiplicity. Figure 6.2 presents the production yields of multiple strange hadrons obtained in this thesis, together with the $\mathrm{d}N/\mathrm{d}y$ progression with multiplicity measured in Pb–Pb collisions at $\sqrt{s} = 5.02$ TeV ([19]). Polynomial fits of order n are also shown across the multiplicity range from pp to Pb–Pb collisions. Consistent with the trends observed in Fig. 6.1, the progression of $\langle \mathrm{Y}_{1\mathrm{S}} \rangle$ with multiplicity appears to follow a linear behavior from pp to Pb–Pb collisions. For $\langle \mathrm{Y}_{>1\mathrm{S}} \rangle$, the evolution is suggested to diverge at high multiplicity. It is worth noting that the results shown in

the plots were obtained by assuming the behavior in pp collisions and extrapolating to high multiplicity. If the same trend continues in other colliding systems, there would be a significant increase in events where the multiple production of strange particles is favored. Measuring the multiplicity distribution of (multi-)strange particles offers valuable insights to further understand these processes.

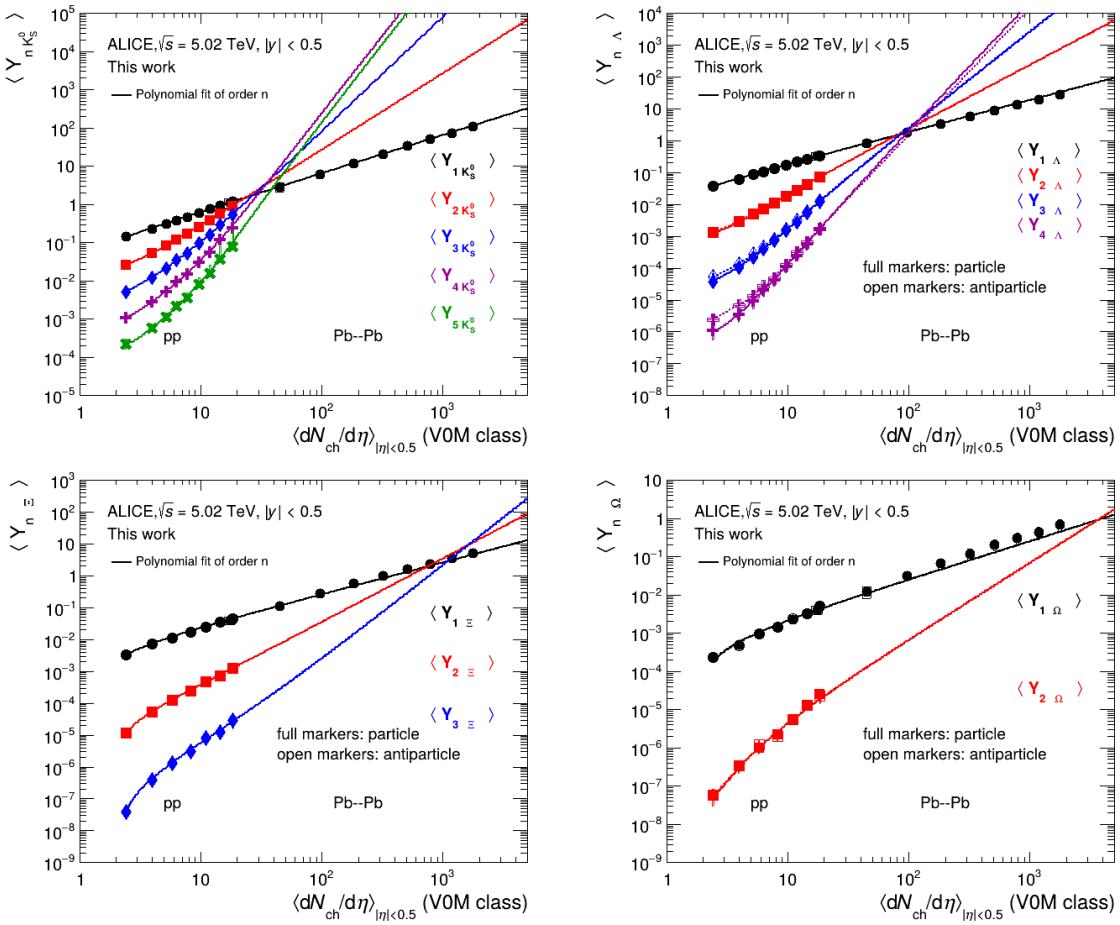

Figure 6.2: The production yields of multiple strange hadrons are presented as a function of the un-biased average charged-particle multiplicity for K^0_S (top-left), Λ (top-right), Ξ^- (bottom-left) and Ω^- (bottom-right), as analyzed in this thesis. Additionally, the trend of the $\langle Y_{1S} \rangle$ (familiar dN/dy) with multiplicity is included for Pb–Pb collisions at $\sqrt{s} = 5.02$ TeV (see [19]). Full markers represent matter, while open markers represent anti-matter. Continuous and dashed lines indicate the results of a polynomial fit of order n performed across the multiplicity range from pp to Pb–Pb collisions.

To further explore the extension of this analysis to Pb–Pb collisions, certain yield ratios have been fitted using the ratio of the polynomial functions previously employed to describe the production of multiple yields. Figure 6.3 illustrates the simplest yield ratio at $\Delta S = 0$: $\langle Y_{n\Lambda} \rangle / \langle Y_{nK^0_S} \rangle$, plotted as a function of the charged-particle multiplicity. The figure also includes lines representing the trends obtained from the fit ratio, extrapolated to the multiplicity range of Pb–Pb collisions. It is evident that the ratio increases with multiplicity until reaching a plateau at high multiplicities. This observation suggests that

the naïve quark coalescence framework can account for the observed behavior: in high-multiplicity environments, the greater abundance of light quarks promotes pairing with strange quarks.

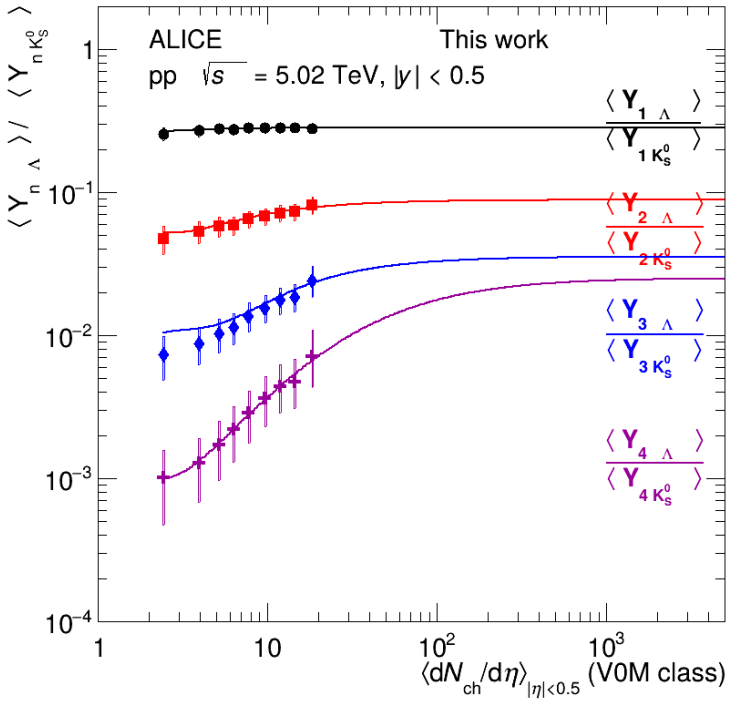

Figure 6.3: $\langle Y_{n\Lambda} \rangle / \langle Y_{nK^0_S} \rangle$ as a function of the un-biased average charged-particle multiplicity at midrapidity. Black, red, blue and purple points correspond to $n = 1$, 2, 3 and 4 respectively. Lines represent the trends obtained by performing the fit ratio, extended to the multiplicity range of Pb–Pb collisions.

Figure 6.4 displays the ratios $\langle Y_{3\Xi} \rangle / \langle Y_{nK^0_S} \rangle$ and $\langle Y_{2\Omega} \rangle / \langle Y_{nK^0_S} \rangle$ as a function of the charged-particle multiplicity. Continuous and dashed lines in the figure indicate the trends obtained from the fit ratios for Ξ and Ω, respectively, extended to the multiplicity range of Pb–Pb collisions. In the left panel, $\langle Y_{n\Omega} \rangle$ is fitted using a polynomial function of order n, while in the right panel, the fit employs a polynomial function of order $n + 1$. The choice of different polynomial orders for describing the progression of Ω with multiplicity reflects the distinct behavior observed in different colliding systems. When only pp collisions are considered, the results are better described by a quadratic function. However, including Pb–Pb data necessitates using a linear function to account for yields across the full multiplicity range. A comparison of the left and right panels highlights that different functional forms for the yield fits produce varying yield ratios at Pb–Pb multiplicity. This emphasizes that studying the multiplicity distribution of (multi-)strange particles across different collision systems provides valuable insights into the mechanisms of strangeness production under diverse environmental conditions.

Additionally, during Run 1 and Run 2, ALICE investigated pp collisions at higher energies ($\sqrt{s} = 7$ and 13 TeV), where similar measurements of p_{T} distributions and $\mathrm{d}N/\mathrm{d}y$ values

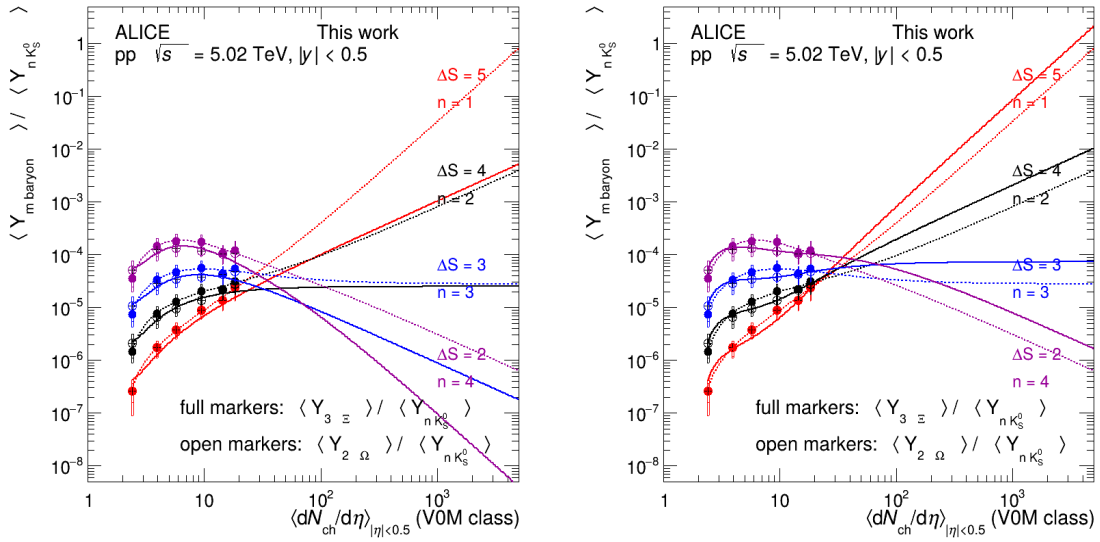

Figure 6.4: $\langle Y_{3\Xi}\rangle/\langle Y_{nK^0_S}\rangle$ (full markers) and $\langle Y_{2\Omega}\rangle/\langle Y_{nK^0_S}\rangle$ (open markers) as a function of the unbiased average charged-particle multiplicity at midrapidity. n runs from 1 to 4, corresponding to red, black, blue and purple markers respectively. Continuous and dashed lines indicate the trends obtained from the fit ratio for Ξ and Ω, respectively, extended to the multiplicity range of Pb–Pb collisions. (*Left.*) For Ω, $\langle Y_{n\Omega}\rangle$ were fitted using a polynomial function of order n. (*Right.*) For Ω, $\langle Y_{n\Omega}\rangle$ were fitted using a polynomial function of order $n+1$.

were carried out ([14, 15]). Ref. [16] reported that both the average transverse momentum ($\langle p_T\rangle$) and the integrated yields as a function of multiplicity remain consistent across all centre-of-mass energies studied ($\sqrt{s}$ = 5.02, 7 and 13 TeV). Furthermore, as observed when fixing $\sqrt{s}$ and varying collision systems, measuring P(n_S) across different centre-of-mass energies enhances the analysis beyond average distributions, offering deeper insights into the mechanisms underlying strangeness production.

6.1.2 Run 3 and 4

As detailed in Section 3.3, the ALICE detector underwent significant upgrades for the Run 3 and Run 4 campaigns, enhancing its readout speed to handle the higher interaction rates delivered by the LHC. These improvements enable a substantial increase in the number of recorded proton-proton collisions compared to Run 2. Specifically, the integrated luminosity for pp collisions at $\sqrt{s} = 13.6$ TeV during Run 3 and Run 4 is expected to reach $L_{int} \sim 200\ pb^{-1}$, corresponding to approximately 14×10^{12} inelastic collisions. This represents an increase of three orders of magnitude in integrated luminosity for measurements based on the minimum bias sample collected during Run 2, and a factor of 5 to 20 for measurements utilizing dedicated triggers for rare events [138]. Figure 6.5 illustrates the total integrated luminosity for pp collisions at $\sqrt{s} = 13.6$ TeV and $\sqrt{s} = 5.36$ TeV during various data-taking periods in 2024. The left panel compares the integrated luminosity for $\sqrt{s} = 13.6$ TeV data collected in 2024 (magenta) with that from 2022 (red) and 2023 (blue). In the right panel, the integrated luminosity is shown for the $\sqrt{s} = 5.36$ TeV pp reference data collected in 2024, representing approximately $\sim 4 \cdot 10^{11}$ events.

Notably, for $\sqrt{s} = 13.6$ TeV, only about 1.3 pb^{-1} of luminosity was dedicated to unfiltered minimum-bias events, corresponding to roughly $1.3 \cdot 10^{11}$ events.

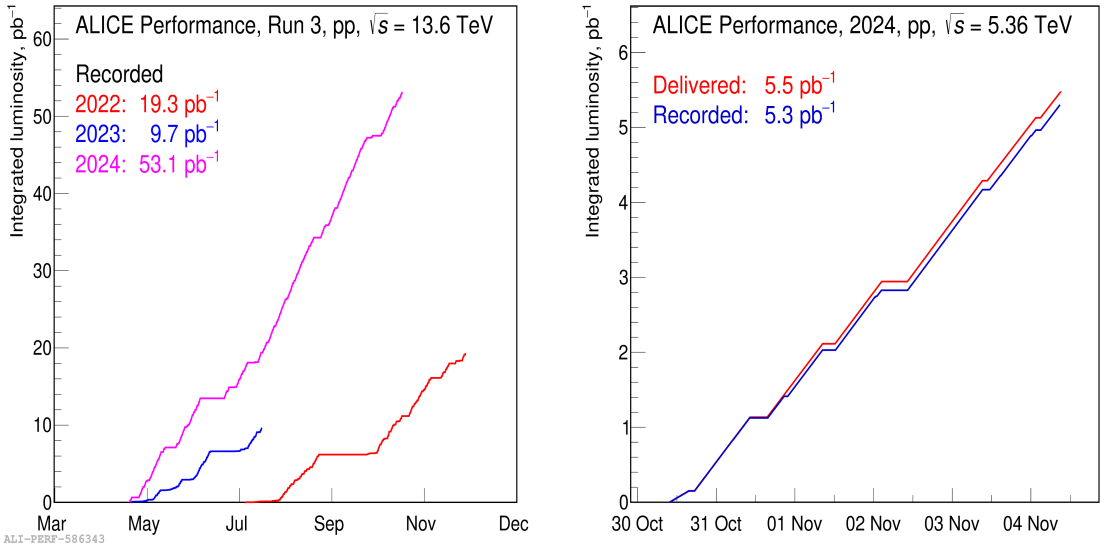

Figure 6.5: (*Left.*) Total integrated luminosity for pp data taken in 2024 (magenta) compared with 2022 (red) and 2023 (blue) data taking periods at $\sqrt{s} = 13.6$ TeV. (*Right.*) Total integrated luminosity for pp reference ($\sqrt{s} = 5.36$ TeV) data taken in 2024 [161].

Given the vast amount of data recorded, only a fraction of events — approximately 0.1% — can be retained to cope with the available computing resources. Unlike previous runs, where event selection relied on hardware triggers, the continuous readout mode implemented in Run 3 enables software-based event selection. This approach uses advanced software triggers, leveraging full event reconstruction to identify and retain events of interest. Within the ALICE Collaboration, various software filters have been developed to facilitate high-precision studies of rare probes. During the final six months of my PhD, I contributed to this effort as Trigger Coordinator within the light-flavor group. My responsibilities included assessing the selectivity of filters designed for multi-differential studies of strangeness production and performing quality checks to validate their performance. These filters allow for the selection of the following types of events:

1. Events with at least one Ω baryon: with an integrated luminosity of 200 pb^{-1}, approximately 10^9 Ω baryons are expected, providing a dataset three orders of magnitude larger than Run 2. This will enable studies of Ω yields as a function of midrapidity charged-particle multiplicity up to $\sim$ 100, comparable to peripheral Pb–Pb collisions. Additionally, the large sample will allow for angular correlation studies of transverse-to-leading and toward-leading Ω production versus multiplicity, which were not feasible in Run 2.

2. Events with Ω tracked with the strangeness tracking: thanks to the innermost ITS layer, Ω particles can be tracked using a novel reconstruction technique called strangeness tracking [162]. The strangeness tracking algorithm improves DCA resolution, reduces background and allows distinguishing between primary and secondary Ω.

3. Events with a high-p_{T} charged hadron and at least one Ξ baryon candidate: these events facilitate studies of strange hadron production in- and out-of-jets. The increased collision statistics in Run 3 will permit raising the trigger particle's minimum p_{T} threshold above 3 GeV/c, reducing contamination from soft processes.

4. Events with a high-p_{T} charged hadron and at least one Ω baryon candidate: these events are essential for hadron-Ω correlation studies, exploring toward-leading (jet-like) and transverse-to-leading (underlying event) production as a function of multiplicity. Run 3 data will support increasing the trigger particle's minimum p_{T} to over 5 GeV/c, providing better proxies for the jet axis.

5. Events with a Ξ baryon candidate with large decay radius: this sample will improve measurements of the Ξ-nucleon elastic cross-section, extending the low-statistics results for $p_{\mathrm{T}} < 1$ GeV/c [163]. To resolve the scattering angle θ, the Ξ momentum before and after scattering must be determined. Post-scattering momentum can be reconstructed topologically while pre-scattering momentum can be measured via strangeness tracking [162], provided the Ξ traverses at least four ITS layers.

6. Events with two or more Ξ baryons: these events enable studies of exotic states decaying into two Ξ baryons and correlations in space and momentum between Ξ baryons produced in the same event.

7. Events with two or more Ω baryons: such events are suitable for investigating exotic states decaying into two Ω baryons, as well as same-sign and opposite-sign Ω correlation studies

8. Events with at least one Ω and one Ξ baryons: this sample allows for the study of same-sign and opposite-sign Ω-Ξ correlations, expanding on previous measurements

It is worth noting that some of these filters were employed exclusively during the 2022, 2023 or 2024 data-taking periods. In particular, triggers 1, 6, 7 and 8 would be especially helpful for enhancing the physics outcomes of the analyses discussed in this thesis. In Ref. [164] a summary of the configuration of strangeness triggers and relevant correction factors is reported. As highlighted in Chapter 5, with the Run 2 dataset collected in pp collisions at $\sqrt{s} = 5.02$ TeV, it was possible to measure up to 7 $\mathrm{K}^0_{\mathrm{S}}$, 5 Λ ($\overline{\Lambda}$), 4 Ξ^- ($\overline{\Xi}^+$) and 2 Ω^- ($\overline{\Omega}^+$) particles per event, respectively. Even considering only the minimum-bias events collected in pp collisions at 13.6 TeV during Run 3, this analysis would benefit from a factor of 10^2 increase in statistics for each bin of the reconstructed particle distributions. Furthermore, as previously mentioned, many of the implemented triggers are of primary interest for extending this work to events with a larger number of particles.
In addition, thanks to the increased statistics and the online trigger implementation, another important outcome of this analysis would be the extraction of the combined multi-species PDF. The idea behind this study is that if (e.g.) a Ξ^- particle is produced in one event, then the double s quarks contained in the baryon have to be balanced by the production of other $\overline{s}$-flavored particles, which might be mesons or baryons. Additionally, the conservation of the baryonic number limits the phase space for particles formation. As an example, the probability of producing associated Ξ^- and $\overline{\Xi}^+$ pairs compared to the probability of producing a Ξ^- and associated double $\mathrm{K}^0_{\mathrm{S}}$ (or double Λ) would be of

primary interest in understanding the mechanism for multi-strange particle formation, both in small and large colliding systems. The analysis technique in this case would be very similar to the one utilized for the 1-D PDF, with the complication that unfolding would not be uni-dimensional (even in its easiest implementation), but at least 2-D, with a four-dimensional response matrix which includes marginal probabilities of the type: $P(R0_{\Xi^-}, R2_{\overline{\Xi}^+} | G1_{\Xi^-}, G3_{\overline{\Xi}^+})$ = probability of reconstructing 0 Ξ^- and 2 $\overline{\Xi}^+$ given that 1 Ξ^- and 3 $\overline{\Xi}^+$ were generated.

6.2 Towards Refined Models

As introduced in Section 5.1, the measurement of the (multi-)strange particle multiplicity distribution provides a unique opportunity to examine the connection between charged and strange particle multiplicity production, even in extreme scenarios that span wide ranges of strangeness and multiplicity variations. In each V0M bin, the charged-particle multiplicity measured at mid-rapidity exhibits a wide distribution, leading to significant event-by-event variations in multiplicity. This highlights that multiplicity fluctuations impact individual events and that this effect is partially correlated with fluctuations in the number of strange particles. Under the assumption that strangeness production is linked to local multiplicity at mid-rapidity, the shape of the strange particle multiplicity distribution can be inferred either from the probability distribution at fixed local multiplicity or from the variation of local multiplicity within a given V0M class. Addressing this issue involves exploring whether it is possible to remove the "trivial" effect of multiplicity in strange particle fluctuations and evaluating whether such a correction is important. Considering the nature and the target of the analysis presented in this thesis, this is viewed not as a limitation, but as a significant challenge posed by the measurement to MC models. Nonetheless, additional investigation into this topic has been conducted.

To understand the impact of multiplicity fluctuations on the measured strange particle multiplicity distributions, the initial approach involved combining a specific distribution (e.g. Poisson) for strange particle production (at fixed multiplicity) with the experimentally measured charged-particle multiplicity distribution $P(N_{ch})$ ([157]). The resulting distributions are then compared to the measured $P(n_S)$. The so-called composition procedure incorporates two main steps: for each N_{ch} (with high granularity), generate $P(N_{ch}) \cdot N_{evts}$ strange particles of a given species according to a Poisson distribution (Poisson(n_S; dN/dy (N_{ch})) $\circ$ $P(N_{ch})$). Note that the average of the Poisson distribution is tuned to the dN/dy trend with multiplicity. Subsequently, the spectra of strange particles for each N_{ch} are summed, correctly weighting for the multiplicity distribution, at least to the first order.
Figure 6.6 illustrates the comparison between the measured $P(n_S)$ and the distributions obtained via the composition procedure for all particles analyzed in this thesis for INEL > 0. It is observed that the two trends show good agreement for V^0s, whereas for cascades, the agreement deteriorates as n increases.

It is noteworthy that applying the composition procedure to determine multiplicity distributions corresponding to specific V0M selections would be of significant interest. However,

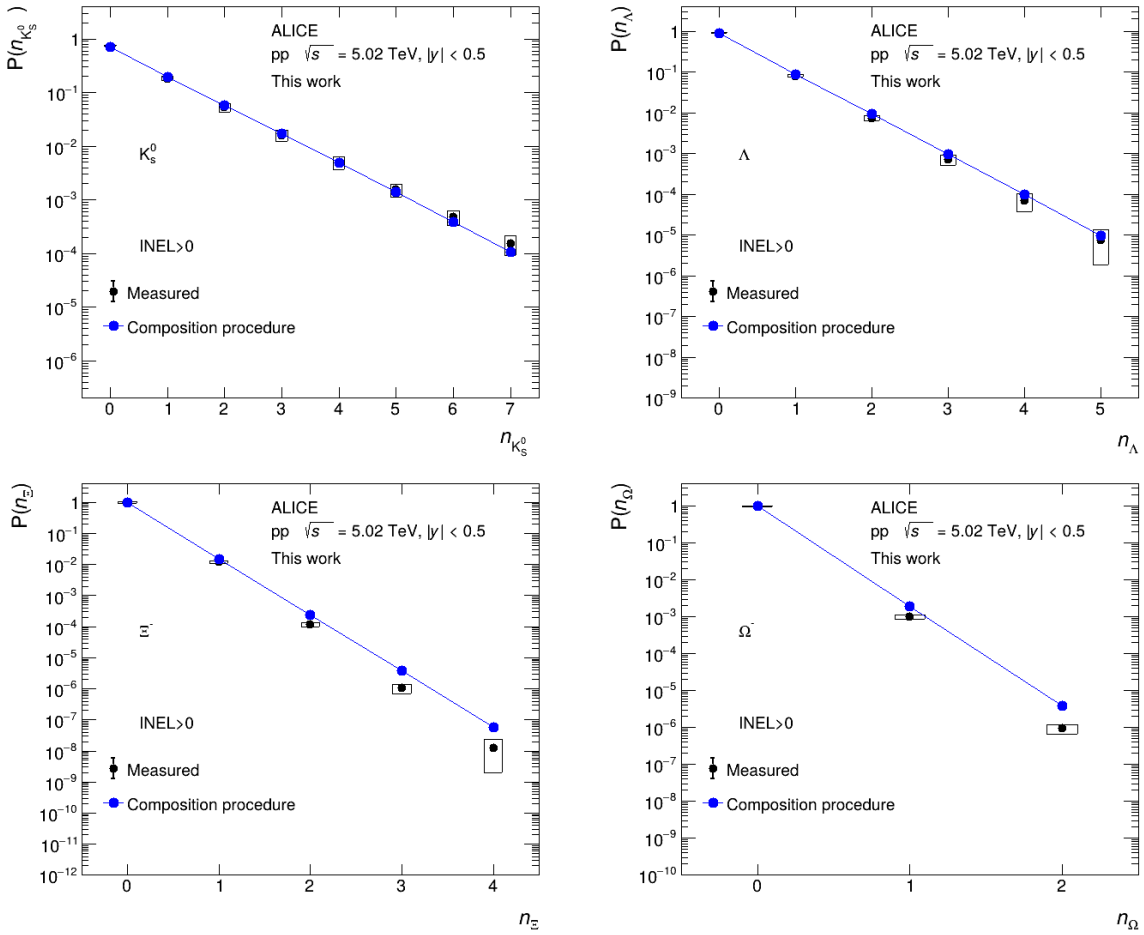

Figure 6.6: Measured (multi-)strange particle multiplicity distributions (black markers) for K^0_S (top-left), Λ (top-right), Ξ^- (bottom-left) and Ω^- (bottom-right) compared with the distributions obtained via the composition procedure composing a Poisson distribution with the measured $P(N_{ch})$ ([157]) (blue markers and line) for INEL > 0.

the ALICE Collaboration has only measured the charged-particle multiplicity distribution $P(N_{ch})$ for INEL > 0 [157]. Additionally, $P(N_{ch})$ was measured within $|\eta| < 0.8$, whereas the analysis discussed in this thesis is based on event multiplicity classes and the corresponding charged-particle pseudorapidity densities in $|\eta| < 0.5$. Since the models (Pythia 8 Monash and Pythia 8 QCD-CR Ropes) provide $P(N_{ch})$ for both $|\eta| < 0.8$ and $|\eta| < 0.5$, and for all multiplicity classes, the strategy is to extract model-dependent weights and apply them to the measured charged-particle multiplicity distribution $P(N_{ch})$ in $|\eta| < 0.8$ for INEL > 0 ([157]). This allows the derivation of the corresponding $P(N_{ch})$ in $|\eta| < 0.5$ for INEL > 0 and for all multiplicity classes considered in this thesis in data.
Figure 6.7 shows, in the upper panel, a comparison of $P(N_{ch})$ between $|\eta| < 0.8$ and < 0.5, as obtained from Pythia 8 Monash (dotted line) and Pythia 8 QCD-CR Ropes (continuous line) for INEL > 0. The lower panel displays the ratios of $P(N_{ch})$ in $|\eta| < 0.5$ to $P(N_{ch})$ in $|\eta| < 0.8$, representing the extracted weights. Using these model-dependent weights, $P(N_{ch})$ in $|\eta| < 0.5$ for INEL > 0 can be derived by applying the weights to the

measured P(N_{ch}) in $|\eta| < 0.8$ ([157]).

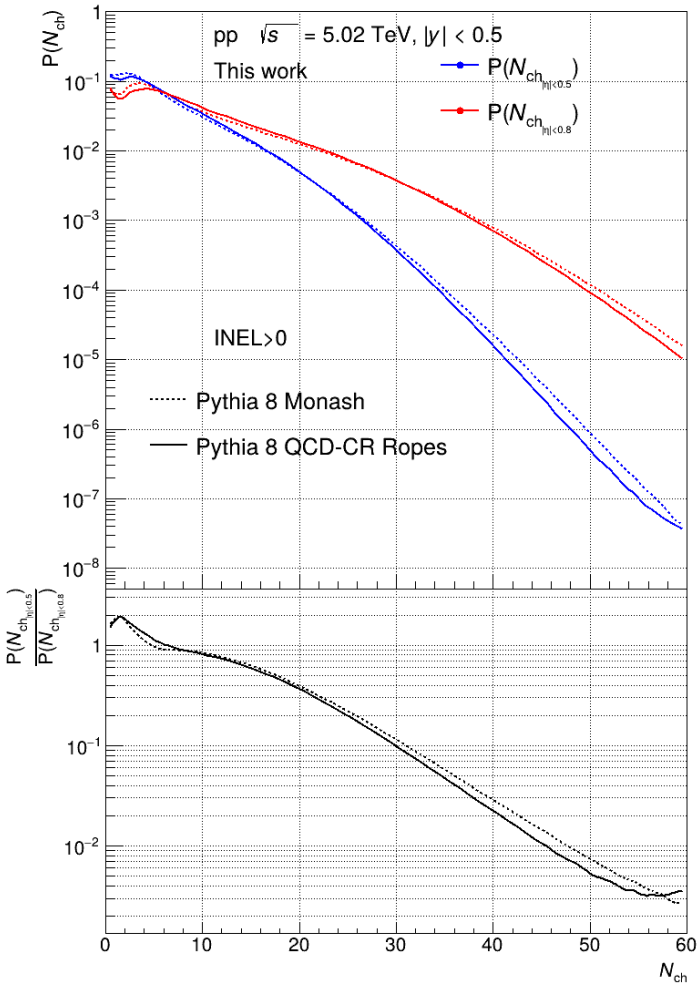

Figure 6.7: (*Upper panel.*) Comparison of P(N_{ch}) between $|\eta| < 0.8$ and < 0.5, as obtained from Pythia 8 Monash (dotted line) and Pythia 8 QCD-CR Ropes (continuous line) for INEL > 0. (*Bottom panel.*) Ratios of P(N_{ch}) in $|\eta| < 0.5$ to P(N_{ch}) in $|\eta| < 0.8$.

Figure 6.8 presents the comparison between the measured P(N_{ch}) in $|\eta| < 0.8$ ([157]) and the resulting P(N_{ch}) in $|\eta| < 0.5$, obtained using the weights extracted from Pythia 8 Monash (left panel) and Pythia 8 QCD-CR Ropes (right panel) for INEL > 0. In these plots, the average values of the distributions are also shown alongside the measured ones ([141]). This provides a straightforward method to validate the procedure for deriving P(N_{ch}) in $|\eta| < 0.5$ from data using model-dependent weights. By comparing the average of the extracted P(N_{ch}) distribution in $|\eta| < 0.5$ with the measured value ([141]), it can be concluded that the procedure is able to catch, at least to first order, the change in multiplicity distribution for different pseudorapidity intervals.

Figure 6.9 compares the measured P(N_{ch}) in $|\eta| < 0.8$ ([157]) with the charged-particle multiplicity distributions predicted by Pythia 8 Monash (left) and Pythia 8 QCD-CR

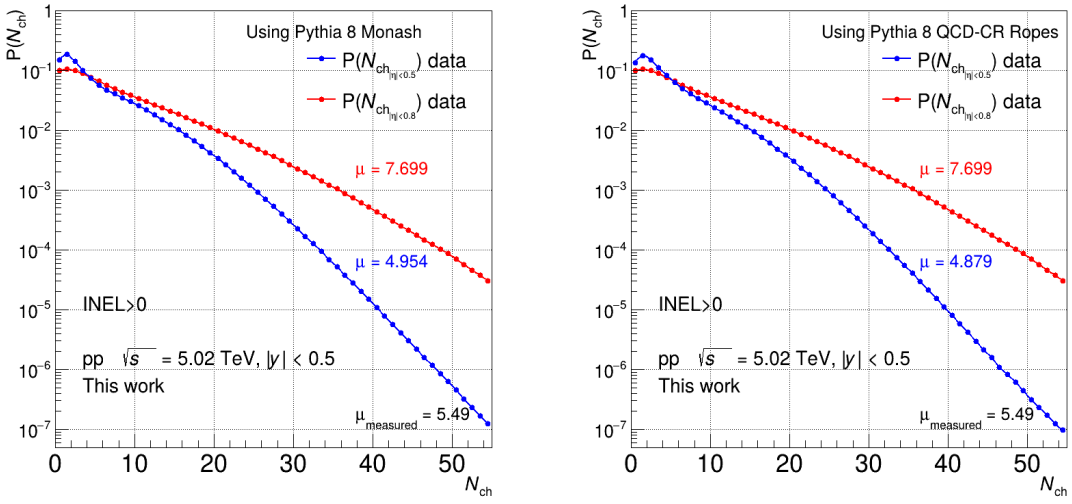

Figure 6.8: Comparison between the measured $P(N_{ch})$ in $|\eta| < 0.8$ ([157]) and the resulting $P(N_{ch})$ in $|\eta| < 0.5$, obtained using the weights extracted from Pythia 8 Monash (*Left*) and Pythia 8 QCD-CR Ropes (*Right*) for INEL > 0. In these plots, the average values of the distributions are also shown alongside the measured ones ([141]).

Ropes (right) for INEL > 0. The lower panels illustrate the ratios of the model predictions to the measured $P(N_{ch})$ in $|\eta| < 0.8$. Similarly, Fig. 6.10 presents a comparison between the extracted $P(N_{ch})$ in $|\eta| < 0.5$ — derived using weights from Pythia 8 Monash (left) and Pythia 8 QCD-CR Ropes (right) — and the multiplicity distributions predicted by models for INEL > 0. The lower panels again display the ratios of model predictions to the extracted $P(N_{ch})$ in data for $|\eta| < 0.5$. A comparable level of agreement between models and data is observed in both $|\eta|$ intervals.

After validating the procedure for INEL > 0, a similar approach was employed to determine $P(N_{ch})$ in $|\eta| < 0.5$ for all multiplicity classes. In this case, the weights are defined as the ratio between $P(N_{ch})$ obtained from models for the class under consideration and $P(N_{ch})$ obtained from models for INEL > 0. These weights are then applied to the extracted $P(N_{ch})$ in $|\eta| < 0.5$ for data, using the model-dependent weights in INEL > 0 (distributions shown in Fig. 6.8 in blue). Figure 6.11 illustrates, on the left, $P(N_{ch})$ for all multiplicity classes considered for V^0s and, on the right, for cascades in $|\eta| < 0.5$ using weights extracted from the Pythia 8 Monash model. To validate the extension of the procedure to several multiplicity classes, the discrepancy between the published mean values ([141]) and those extracted via our procedure was investigated. These discrepancies are shown in Fig. 6.12. Since the ratio remains below 20% in all cases, it can again be concluded that the procedure is effective and can be applied. The same analysis was performed using the Pythia 8 QCD-CR Ropes model, yielding similar conclusions. The $P(N_{ch})$ distributions obtained for all multiplicity classes are shown in Fig. 6.13, while the discrepancies between the averages are illustrated in Fig. 6.14.

At this stage, with the $P(N_{ch})$ distributions in $|\eta| < 0.5$ obtained from data using model-dependent weights for both INEL > 0 and the multiplicity classes, the composition pro-

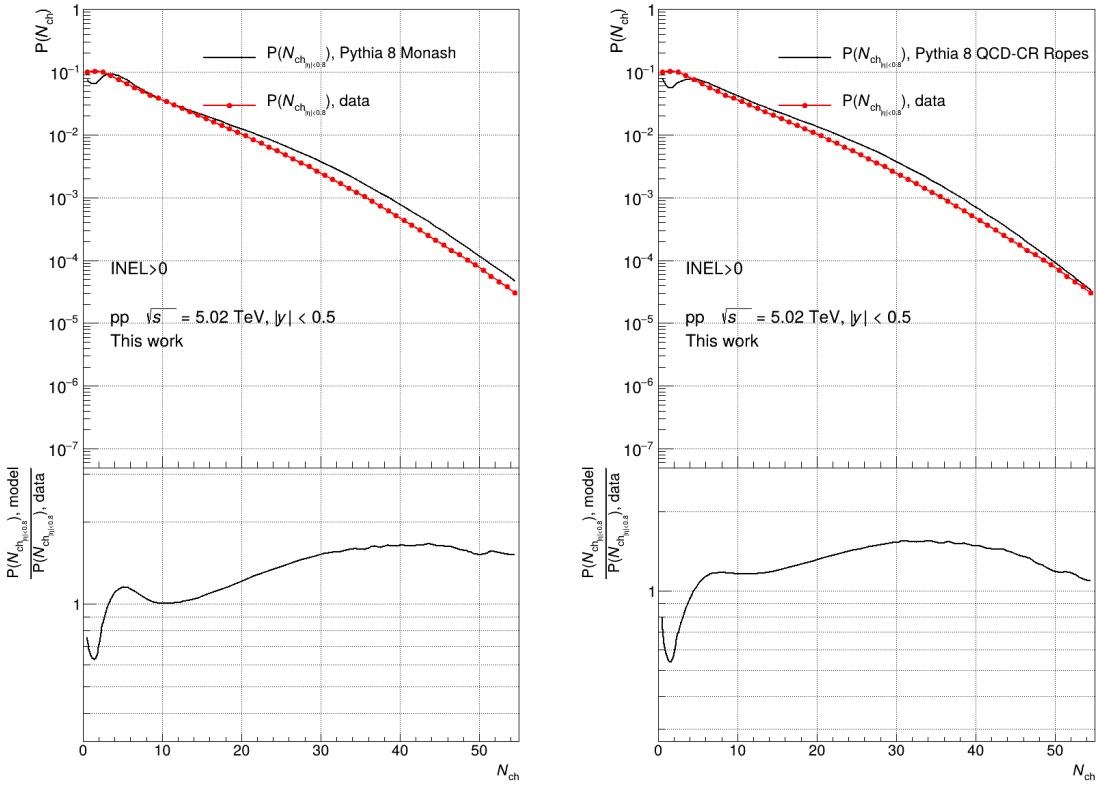

Figure 6.9: Comparison between the measured $P(N_{ch})$ in $|\eta| < 0.8$ ([157]) and charged-particle multiplicity distributions obtained from Pythia 8 Monash (*Left*) and form Pythia 8 QCD-CR Ropes (*Right*) for INEL > 0. The lower panels display the ratios between the $P(N_{ch})$ predicted by models and the measured $P(N_{ch})$ in $|\eta| < 0.8$.

cedure can be applied. This involves the composition Poisson(n_S; dN/dy (N_{ch})) $\circ$ $P(N_{ch})$ in $|\eta| < 0.5$. Figure 6.15 shows a comparison between the measured $P(n_S)$ reported in this thesis and the distributions derived via the composition procedure for all particles analyzed in INEL > 0. These include the distributions obtained by combining a Poisson distribution with the measured $P(N_{ch})$ ([157]) (blue markers and lines), by combining a Poisson distribution with the extracted $P(N_{ch})$ in $|\eta| < 0.5$ using Pythia 8 Monash weights (red markers and lines) and by combining a Poisson distribution with the extracted $P(N_{ch})$ in $|\eta| < 0.5$ using Pythia 8 QCD-CR Ropes weights (green markers and lines).

To better understand the level of agreement between the results, Fig. 6.16 illustrates the ratios between the measured $P(n_S)$ in this thesis and the distributions obtained through the composition procedure. The results indicate a disagreement between the distributions derived using the composition procedure with $P(N_{ch})$ measured in $|\eta| < 0.8$ ([157]) and those extracted in $|\eta| < 0.5$. For V^0 particles, the distributions obtained using $P(N_{ch})$ measured in $|\eta| < 0.8$ via the composition procedure are consistent with the measured $P(n_S)$ within uncertainties. However, the distributions derived using $P(N_{ch})$ extracted in $|\eta| < 0.5$ deviate increasingly from the measured $P(n_S)$ as n grows. Conversely, for cascades, the agreement with the measured $P(n_S)$ improves when $P(N_{ch})$ extracted in $|\eta| < 0.5$ is used.

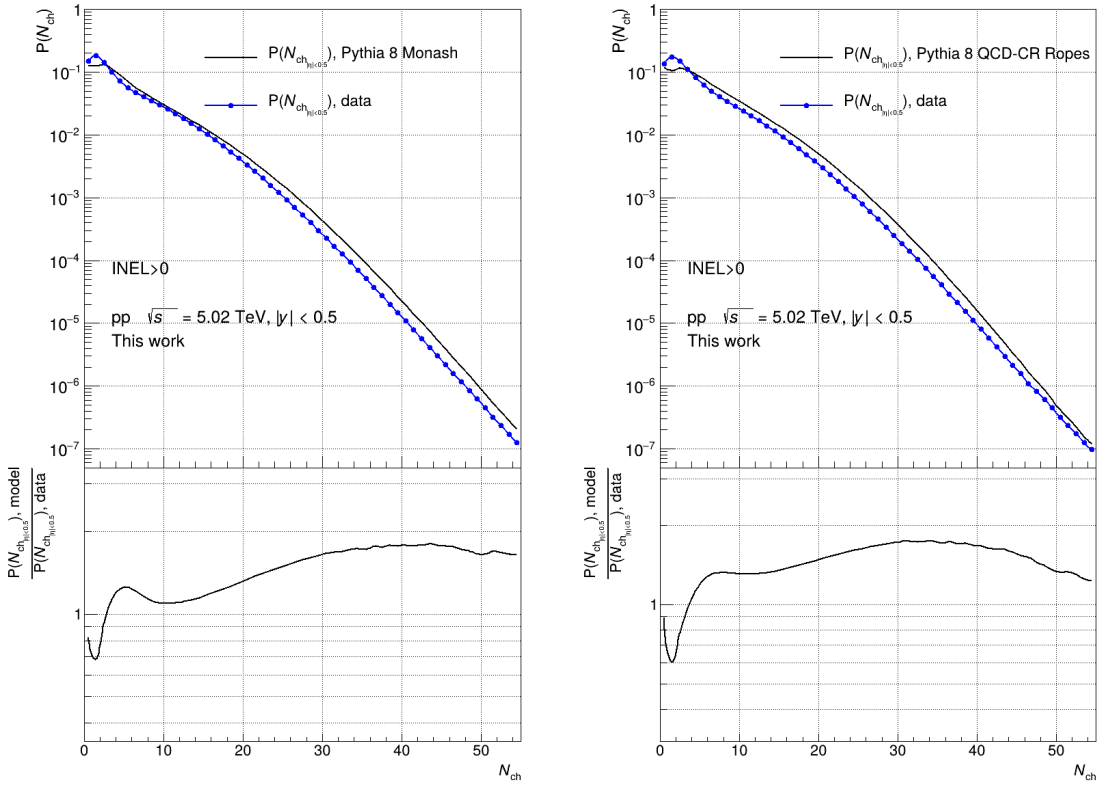

Figure 6.10: Comparison between the extracted $\mathrm{P}(N_{ch})$ in $|\eta| < 0.5$, obtained using the weights extracted from Pythia 8 Monash (left panel) and Pythia 8 QCD-CR Ropes (right panel), and the charged-particle multiplicity distributions predicted by models for INEL > 0. The lower panels display the ratios between the $\mathrm{P}(N_{ch})$ predicted by models and the extracted $\mathrm{P}(N_{ch})$ in data in $|\eta| < 0.5$.

Figure 6.17 provides a comparison between the measured $\mathrm{P}(n_{\mathrm{S}})$ reported in this thesis and the distributions obtained via the composition procedure for all particles across several multiplicity classes. The analysis uses $\mathrm{P}(N_{ch})$ extracted in $|\eta| < 0.5$ from the Pythia 8 Monash (dotted lines) and Pythia 8 QCD-CR Ropes (continuous lines) models.

To further evaluate the agreement, Fig. 6.18 illustrates the ratios between the measured $\mathrm{P}(n_{\mathrm{S}})$ and the composition procedure results. Overall, a disagreement is observed between the measured $\mathrm{P}(n_{\mathrm{S}})$ and the distributions obtained via the composition procedure using $\mathrm{P}(N_{ch})$ extracted in $|\eta| < 0.5$ with both Pythia models for all particles, except for some classes for baryons. In addition, for $\mathrm{K}^0_{\mathrm{S}}$, the agreement worsens as n increases and as the analysis shifts from high- to low-multiplicity classes.

To analyze in more detail whether the observed disagreement arises from the choice of a Poisson distribution as the baseline for strange particle production or from the method used to extract $\mathrm{P}(N_{ch})$ in the corrected $|\eta|$ interval (potentially introducing artifacts), an alternative composition was considered. This approach utilizes $\mathrm{P}(N_{ch})$ measured in models instead of data: $\mathrm{Poisson}(n_S;\, \mathrm{d}N/\mathrm{d}y\ (N_{ch})) \circ \mathrm{P}(N_{ch})$ from models. Figure 6.19 shows

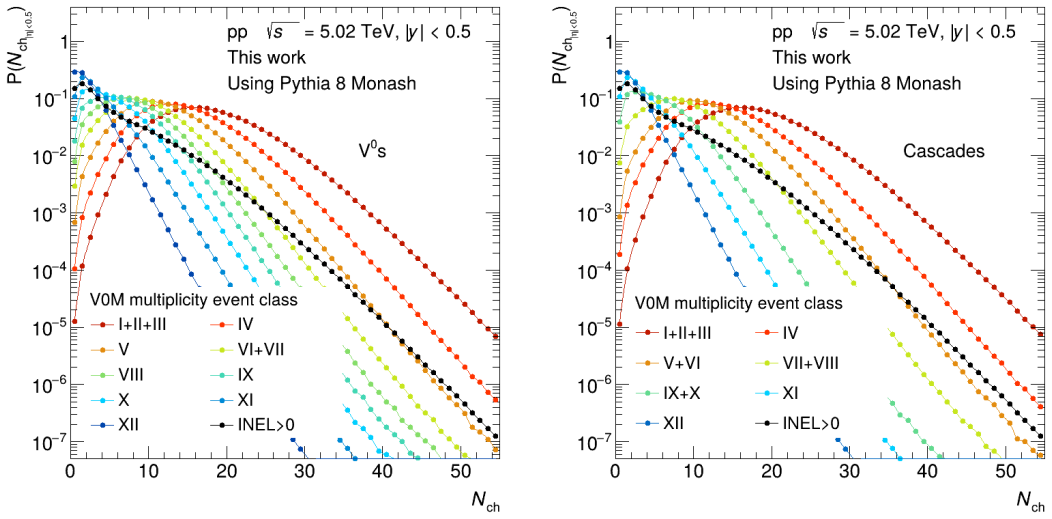

Figure 6.11: (*Left.*) $P(N_{ch})$ distributions for all multiplicity classes corresponding to V^0s in $|\eta| < 0.5$, derived using weights from the Pythia 8 Monash model. (*Right.*) $P(N_{ch})$ distributions for all multiplicity classes corresponding to cascades in $|\eta| < 0.5$, derived using weights from the Pythia 8 Monash model.

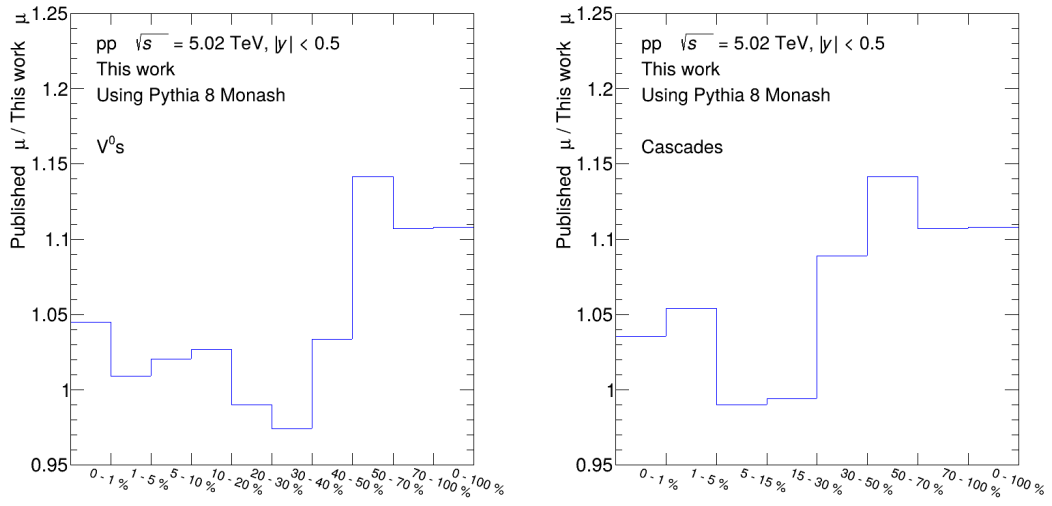

Figure 6.12: Discrepancy between the published mean values of the charged-particle multiplicity distribution ([141]) and those extracted in this work using weights from the Pythia 8 Monash model, shown for each multiplicity class (*Left*: V^0s, *Right*: cascades).

a comparison between the measured $P(n_S)$ reported in this thesis and the distributions derived using the composition procedure. These include $P(N_{ch})$ predicted in $|\eta| < 0.5$ from the Pythia 8 Monash (red markers and lines) and Pythia 8 QCD-CR Ropes (green markers and lines) models for all particles analyzed in INEL > 0. The differences in the charged-particle multiplicity distributions across these models do not result in significant changes to the final state $P(n_S)$.

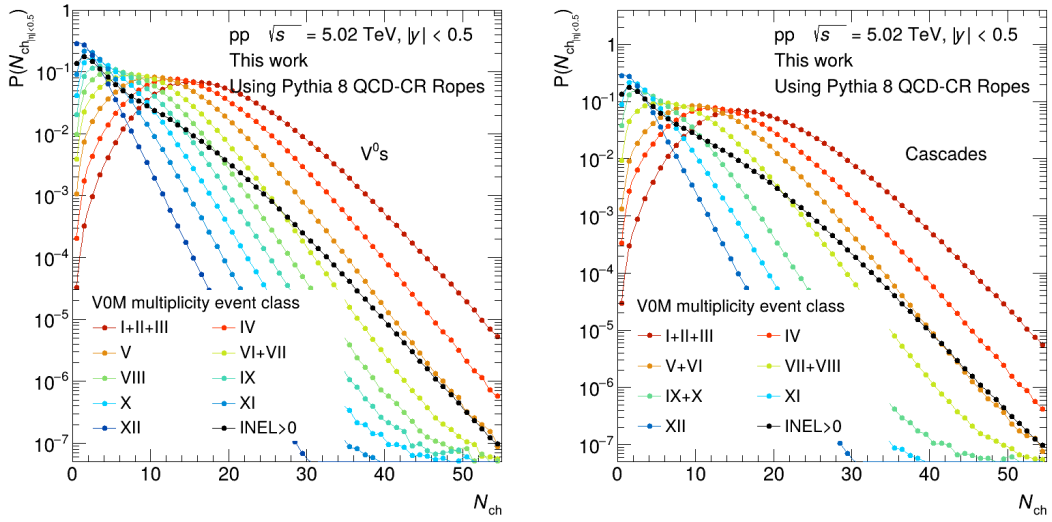

Figure 6.13: (*Left.*) $\mathrm{P}(N_{ch})$ distributions for all multiplicity classes corresponding to V^0s in $|\eta| < 0.5$, derived using weights from the Pythia 8 QCD-CR Ropes model. (*Right.*) $\mathrm{P}(N_{ch})$ distributions for all multiplicity classes corresponding to cascades in $|\eta| < 0.5$, derived using weights from the Pythia 8 QCD-CR Ropes model.

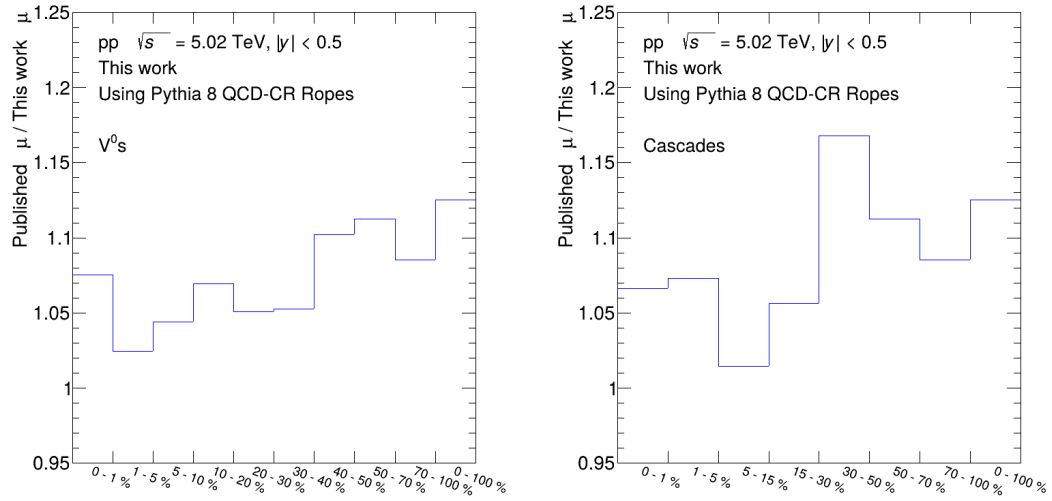

Figure 6.14: Discrepancy between the published mean values of the charged-particle multiplicity distribution ([141]) and those extracted in this work using weights from the Pythia 8 QCD-CR Ropes model, shown for each multiplicity class (*Left*: V^0s, *Right*: cascades).

To better assess the impact of using $\mathrm{P}(N_{ch})$ from models versus $\mathrm{P}(N_{ch})$ extracted from data with model-dependent weights, Figures 6.20 and 6.21 compare the measured $\mathrm{P}(n_{\mathrm{S}})$ presented in this thesis with the results of the composition procedure incorporating both sources of $\mathrm{P}(N_{ch})$. Specifically, in Fig. 6.20, red markers and lines represent the distribu-

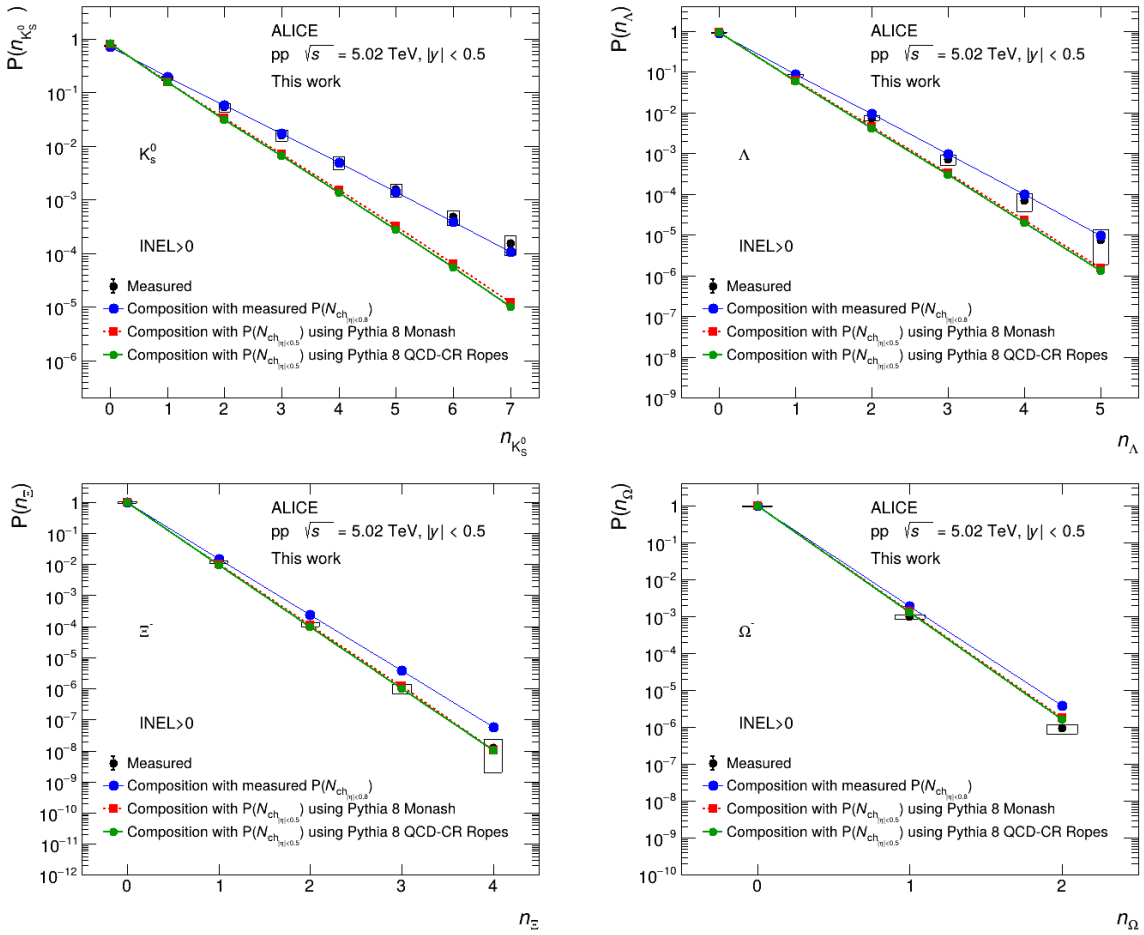

Figure 6.15: Measured (multi-)strange particle multiplicity distributions (markers) for K^0_S (top-left), Λ (top-right), Ξ^- (bottom-left) and Ω^- (bottom-right) are shown in comparison with the distributions derived via the composition procedure for INEL > 0. Blue markers and lines represent the distributions obtained by combining a Poisson distribution with the measured P(N_{ch}) ([157]). Red markers and lines depict the distributions derived by combining a Poisson distribution with the extracted P(N_{ch}) in $|\eta| < 0.5$ using Pythia 8 Monash weights, while green markers and lines correspond to those obtained by combining a Poisson distribution with the extracted P(N_{ch}) in $|\eta| < 0.5$ using Pythia 8 QCD-CR Ropes weights.

tions obtained by combining a Poisson distribution with the P(N_{ch}) predicted by Pythia 8 Monash in $|\eta| < 0.5$, while magenta markers and lines correspond to those derived by combining a Poisson distribution with the P(N_{ch}) extracted in $|\eta| < 0.5$ using Pythia 8 Monash weights. Similarly, in Fig. 6.21, green markers and lines illustrate the distributions obtained by combining a Poisson distribution with the P(N_{ch}) predicted by Pythia 8 QCD-CR Ropes in $|\eta| < 0.5$, whereas orange markers and lines represent those obtained by combining a Poisson distribution with the P(N_{ch}) extracted in $|\eta| < 0.5$ using Pythia 8 QCD-CR Ropes weights.

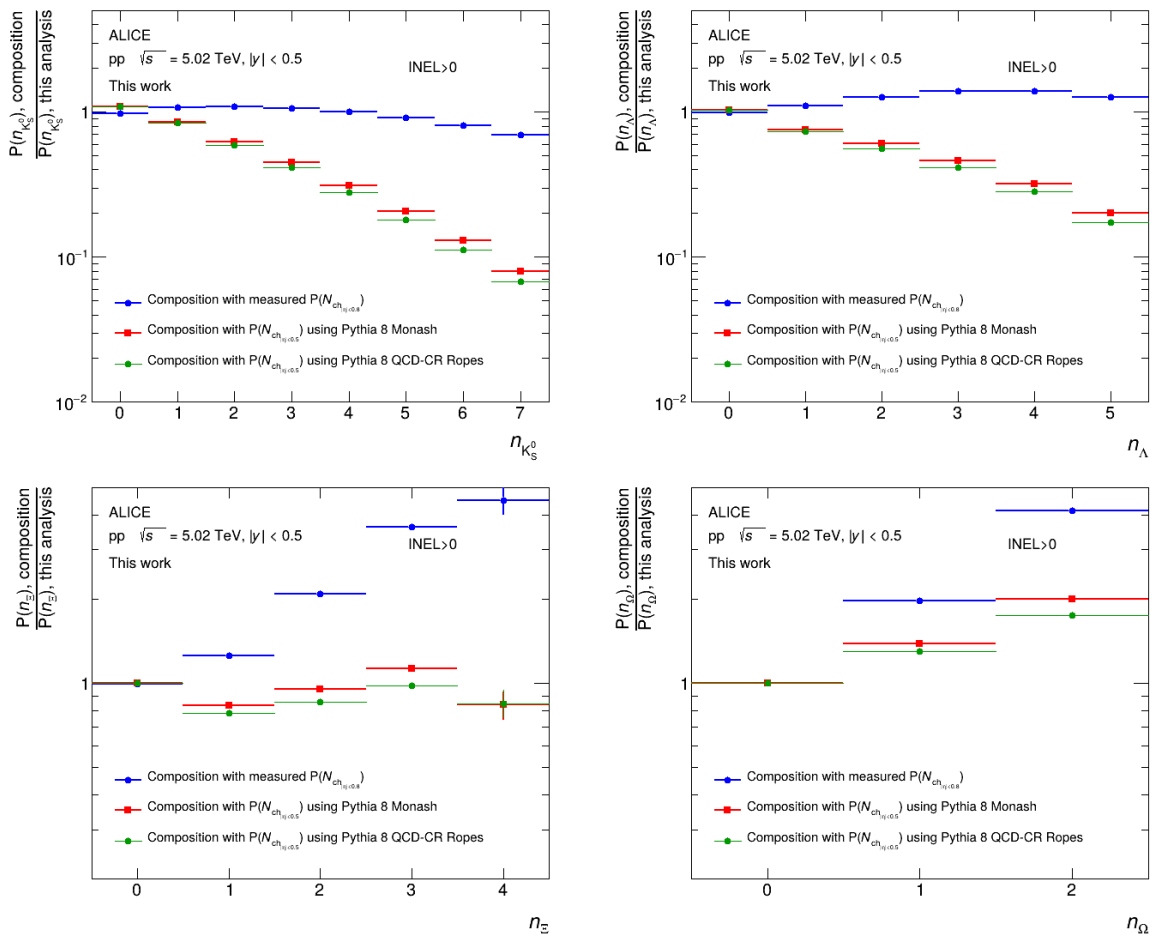

Figure 6.16: Ratios between the measured (multi-)strange particle multiplicity distributions for K^0_S (top-left), Λ (top-right), Ξ^- (bottom-left) and Ω^- (bottom-right) and the distributions derived via the composition procedure for INEL > 0. Blue markers represent the ratios with respect to the distributions obtained by combining a Poisson distribution with the measured P(N_{ch}) ([157]). Red markers depict the ratios with respect to the distributions derived by combining a Poisson distribution with the extracted P(N_{ch}) in $|\eta| < 0.5$ using Pythia 8 Monash weights, while green markers correspond to those obtained by combining a Poisson distribution with the extracted P(N_{ch}) in $|\eta| < 0.5$ using Pythia 8 QCD-CR Ropes weights.

To perform a deeper evaluation of these differences, Fig. 6.22 presents the ratios between the measured P(n_S) and the composition procedure results considering both P(N_{ch}) predicted by models and extracted using model-dependent weights. It is evident that when using the same Poisson distribution as the starting point for strange particle production but different sources for P(N_{ch}), the output is essentially identical. The ratios obtained with P(N_{ch}) from models (squares markers) align with those obtained with P(N_{ch}) from data (dots points). This observation suggests that P(N_{ch}) is not the cause of the disagreement. Consequently, it may be necessary to explore alternative distributions as the starting point for strange particle production.

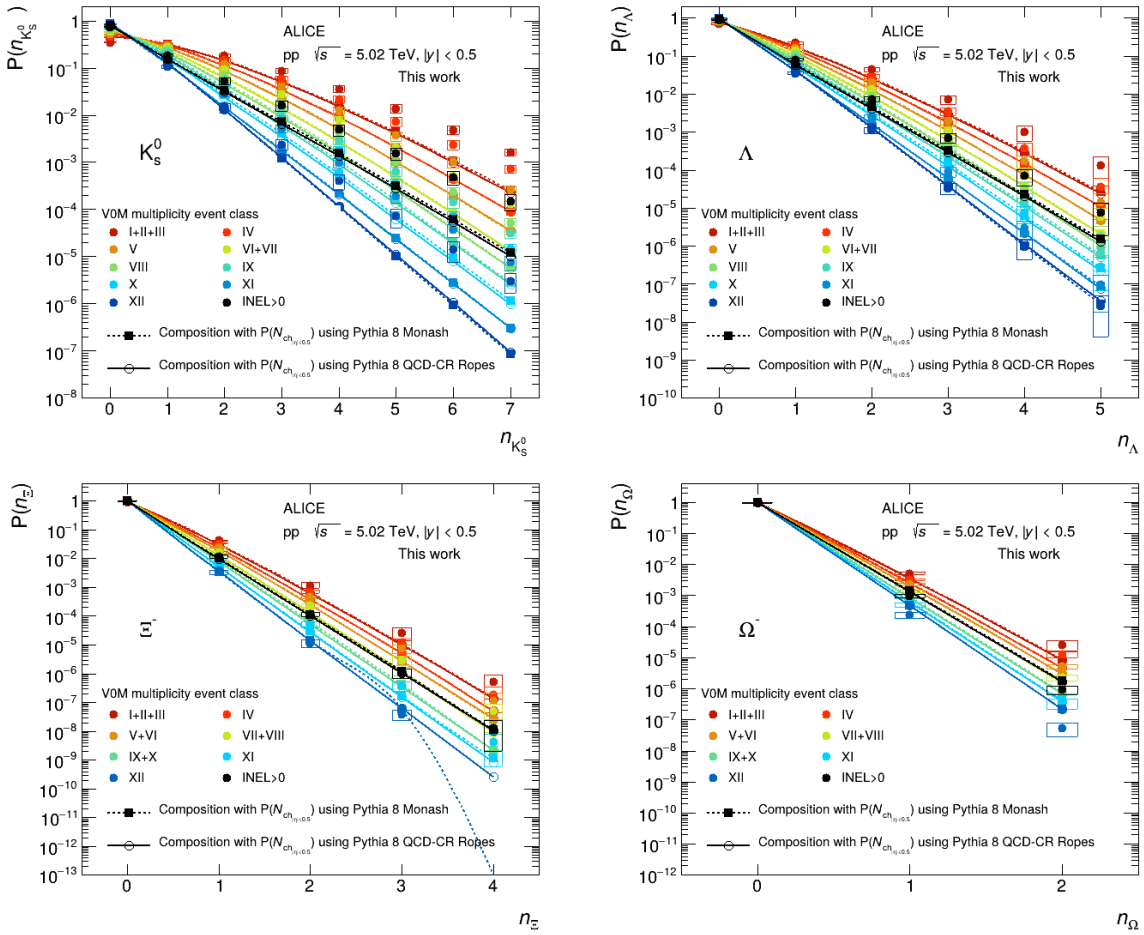

Figure 6.17: Measured (multi-)strange particle multiplicity distributions (markers) for K^0_S (top-left), Λ (top-right), Ξ^- (bottom-left), and Ω^- (bottom-right) are shown in comparison with the distributions derived via the composition procedure for all multiplicity classes. Dotted lines depict the distributions derived by combining a Poisson distribution with the extracted $P(N_{ch})$ in $|\eta| < 0.5$ using Pythia 8 Monash weights, while continuous lines correspond to those obtained by combining a Poisson distribution with the extracted $P(N_{ch})$ in $|\eta| < 0.5$ using Pythia 8 QCD-CR Ropes weights.

Figure 6.23 presents a comparison between the (multi-)strange particle multiplicity distributions measured in this thesis (shown as points) and the predictions from Pythia 8 Monash (dotted lines) and Pythia 8 QCD-CR Ropes (continuous lines) models across all multiplicity classes in $|\eta| < 0.5$. It is observed that for all considered models and particles, the agreement worsens with increasing n, but shows slight improvement at higher multiplicities. Furthermore, for K^0_S, no significant differences are evident between Pythia 8 Monash and Pythia 8 QCD-CR Ropes, whereas for baryons, the comparison slightly improves with Pythia 8 QCD-CR Ropes.

To investigate whether the disagreement between data and models arises from incorrect

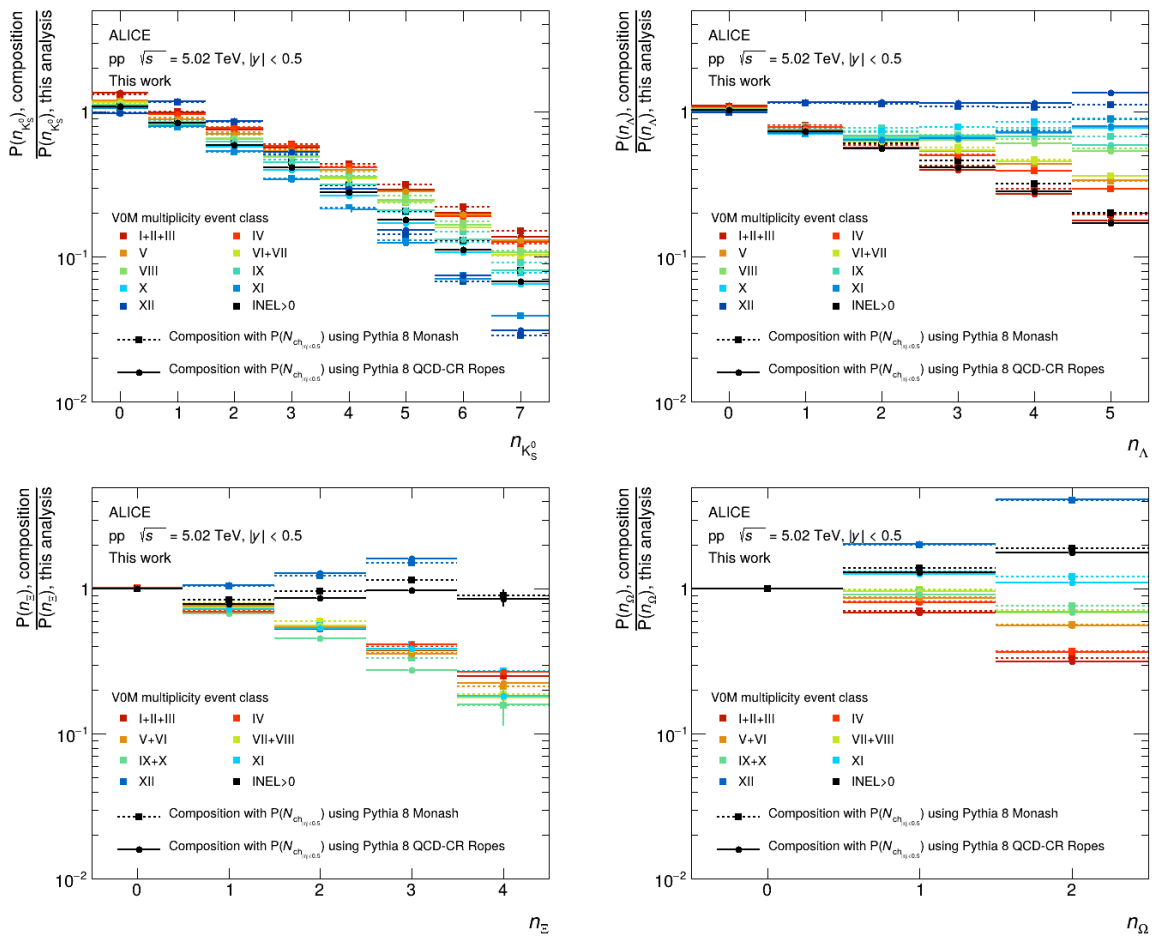

Figure 6.18: Ratios between the measured (multi-)strange particle multiplicity distributions for K^0_S (top-left), Λ (top-right), Ξ^- (bottom-left), and Ω^- (bottom-right) and the distributions derived via the composition procedure for all multiplicity classes. Squares markers depict the ratios with respect to the distributions derived by combining a Poisson distribution with the extracted P(N_{ch}) in $|\eta| < 0.5$ using Pythia 8 Monash weights, while dots points correspond to those obtained by combining a Poisson distribution with the extracted P(N_{ch}) in $|\eta| < 0.5$ using Pythia 8 QCD-CR Ropes weights.

implementation of strangeness production mechanisms in the models or from an otherwise accurate implementation paired with incorrect reweighting for P(N_{ch}), a composition procedure was employed. This procedure involves combining P(n_S) at fixed multiplicity from models (representing events at specific local multiplicities) with P(N_{ch}) extracted from data in $|\eta| < 0.5$. Specifically, the composition process consists of the following steps:

- Selecting events at fixed multiplicity in midrapidity to extract P(n_S) from models for specific N_{ch} values.
- Multiplying each bin of P(n_S) at fixed multiplicity by the corresponding P(N_{ch}) extracted from data.
- Summing the P(n_S) across all fixed multiplicity values to obtain a composite dis-

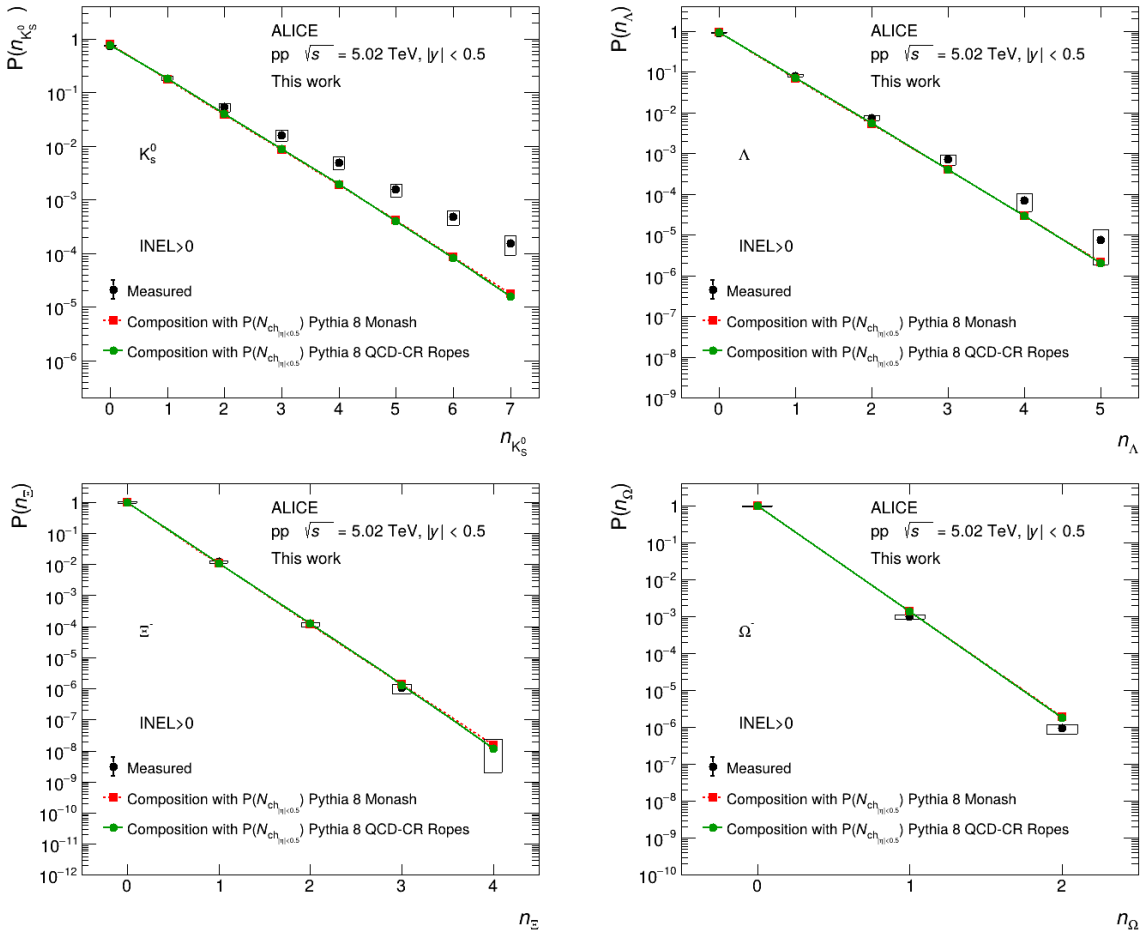

Figure 6.19: Measured (multi-)strange particle multiplicity distributions (markers) for K^0_S (top-left), Λ (top-right), Ξ^- (bottom-left) and Ω^- (bottom-right) are shown in comparison with the distributions derived via the composition procedure for INEL > 0. Red markers and lines depict the distributions derived by combining a Poisson distribution with the predicted P(N_{ch}) by Pythia 8 Monash in $|\eta| < 0.5$, while green markers and lines correspond to those obtained by combining a Poisson distribution with the predicted P(N_{ch}) by Pythia 8 QCD-CR Ropes in $|\eta| < 0.5$.

tribution representing the strange particle spectra derived using model-based P(n_S) and data-driven P(N_{ch}).

Figure 6.24 presents a comparison between the measured (multi-)strange particle multiplicity distributions (points) and those obtained through the composition procedure. The composition was performed using P(n_S) predicted by Pythia 8 Monash (dotted lines) and Pythia 8 QCD-CR Ropes (continuous lines), combined with P(N_{ch}) extracted from data. Additionally, Figures 6.25 and 6.26 provide a detailed comparison of model predictions and distributions obtained via the composition procedure. For all particles and multiplicity classes, the comparison reveals excellent agreement between the trends derived from composition and the model predictions, indicating that the observed disagreement between data and models (Fig. 6.21) is not attributable to a correct implementation of

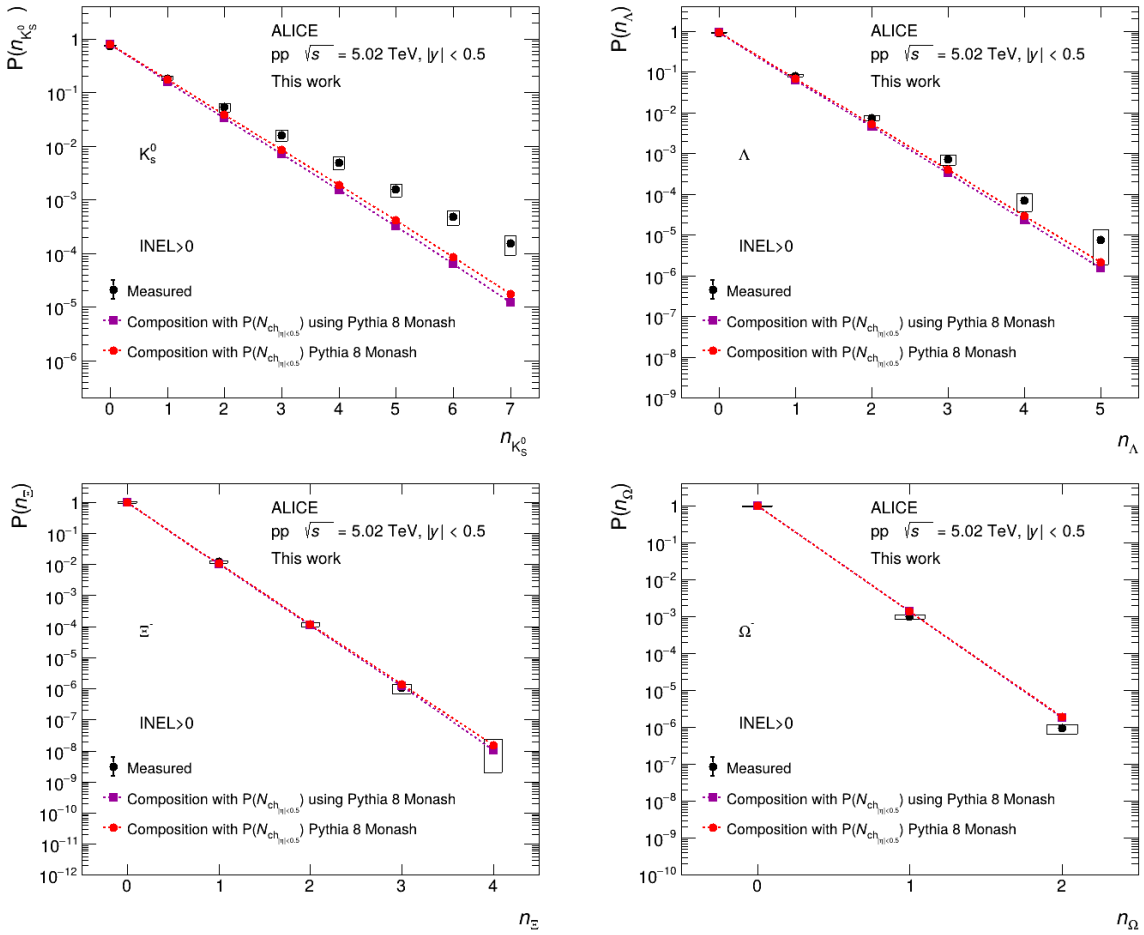

Figure 6.20: Measured (multi-)strange particle multiplicity distributions (markers) for K^0_S (top-left), Λ (top-right), Ξ^- (bottom-left) and Ω^- (bottom-right) are shown in comparison with the distributions derived via the composition procedure for INEL > 0. Red markers and lines depict the distributions derived by combining a Poisson distribution with the predicted P(N_{ch}) by Pythia 8 Monash in $|\eta| < 0.5$, while magenta markers and lines correspond to those obtained by combining a Poisson distribution with the extracted P(N_{ch}) in $|\eta| < 0.5$ using Pythia 8 Monash weights.

strangeness production followed by incorrect reweighting for P(N_{ch}) (i.e., due to multiplicity fluctuations). Instead, the disagreement arises from deficiencies in the models' implementation of the underlying strangeness production mechanisms. As discussed in Section 5.2 regarding the strangeness-driven bias in charged-particle multiplicity, we conclude that the alignment or misalignment with data primarily depends on the models' capability to accurately reproduce the relative production probabilities of particles with varying strangeness content.

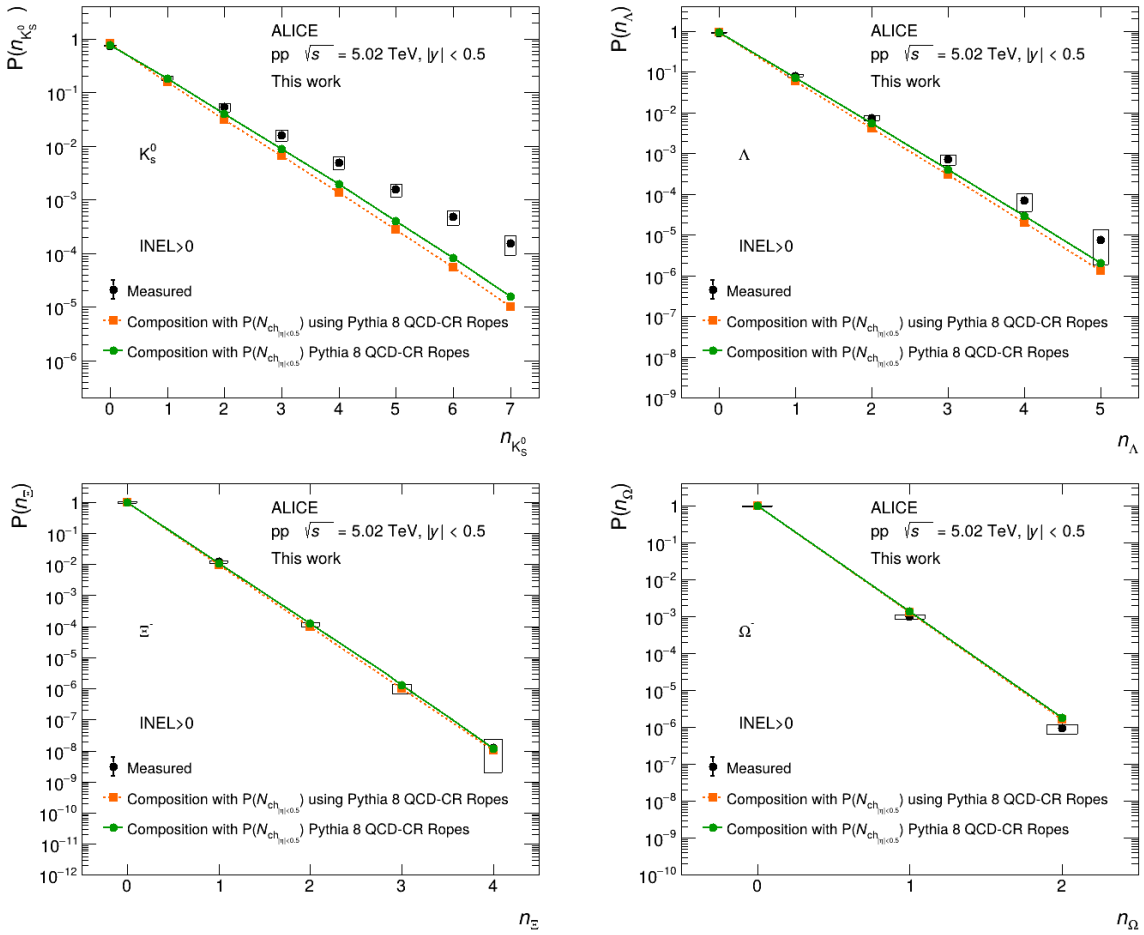

Figure 6.21: Measured (multi-)strange particle multiplicity distributions (markers) for K^0_S (top-left), Λ (top-right), Ξ^- (bottom-left) and Ω^- (bottom-right) are shown in comparison with the distributions derived via the composition procedure for INEL > 0. Green markers and lines depict the distributions derived by combining a Poisson distribution with the predicted P(N_{ch}) by Pythia 8 QCD-CR Ropes in $|\eta| < 0.5$, while orange markers and lines correspond to those obtained by combining a Poisson distribution with the extracted P(N_{ch}) in $|\eta| < 0.5$ using Pythia 8 QCD-CR Ropes weights.

A potential next step could involve exploring statistical models, such as FIST [11], instead of relying on phenomenological models like Pythia, to extract $P(N_{ch})$ or P(n_S). With FIST, directly comparing the measured P(n_S) to model predictions is challenging due to volume fluctuations, as the measurements in this thesis refer to particles rather than net-particles. However, as illustrated in Fig. 6.27, a correlation exists between the volume per unit rapidity dV/dy and the charged-particle multiplicity $\langle dN_{ch}/d\eta \rangle$. This correlation reflects the average relationship, while a scatter plot would reveal the multiplicity fluctuations for a fixed volume. Using this information, it may be possible to determine the N_{ch} dependence of the distribution associated with a specific volume (on average, at least). Investigating whether the first moments of the multiplicity distribution for a given particle at a specific volume can be extracted would be particularly interest-

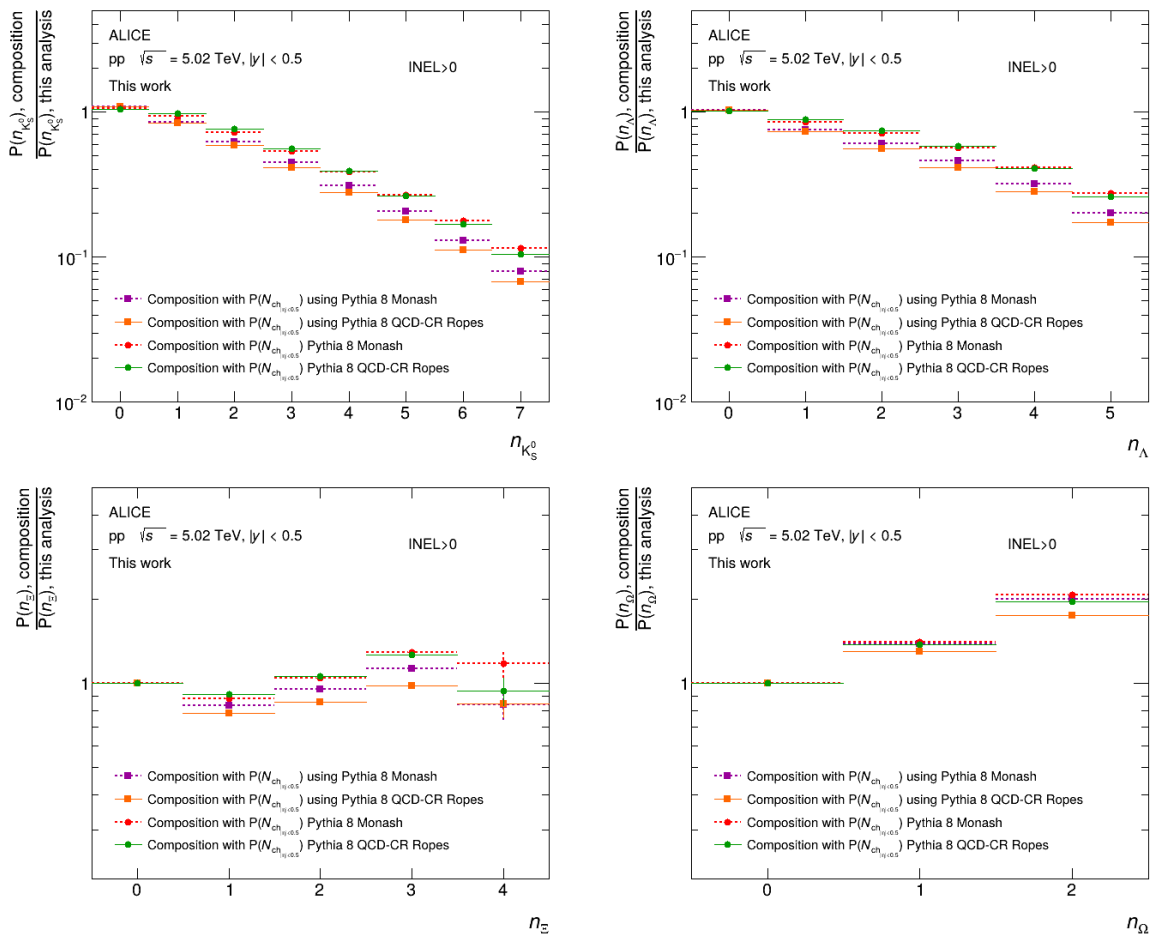

Figure 6.22: Ratios of the measured (multi-)strange particle multiplicity distributions for K^0_S (top-left), Λ (top-right), Ξ^- (bottom-left) and Ω^- (bottom-right) to the distributions obtained via the composition procedure for INEL > 0. Magenta and orange square markers represent the ratios derived using a Poisson distribution combined with the predicted P(N_{ch}) from Pythia 8 Monash and Pythia 8 QCD-CR Ropes in $|\eta| < 0.5$, respectively, while red and green dots correspond to the ratios obtained using a Poisson distribution combined with the P(N_{ch}) extracted in $|\eta| < 0.5$ with Pythia 8 Monash and Pythia 8 QCD-CR Ropes weights, respectively.

ing. If feasible, these moments could be converted into an approximate $P(N_{ch})$, enabling the application of the composition procedure to assess the agreement with the measured P(n_S) presented in this thesis.

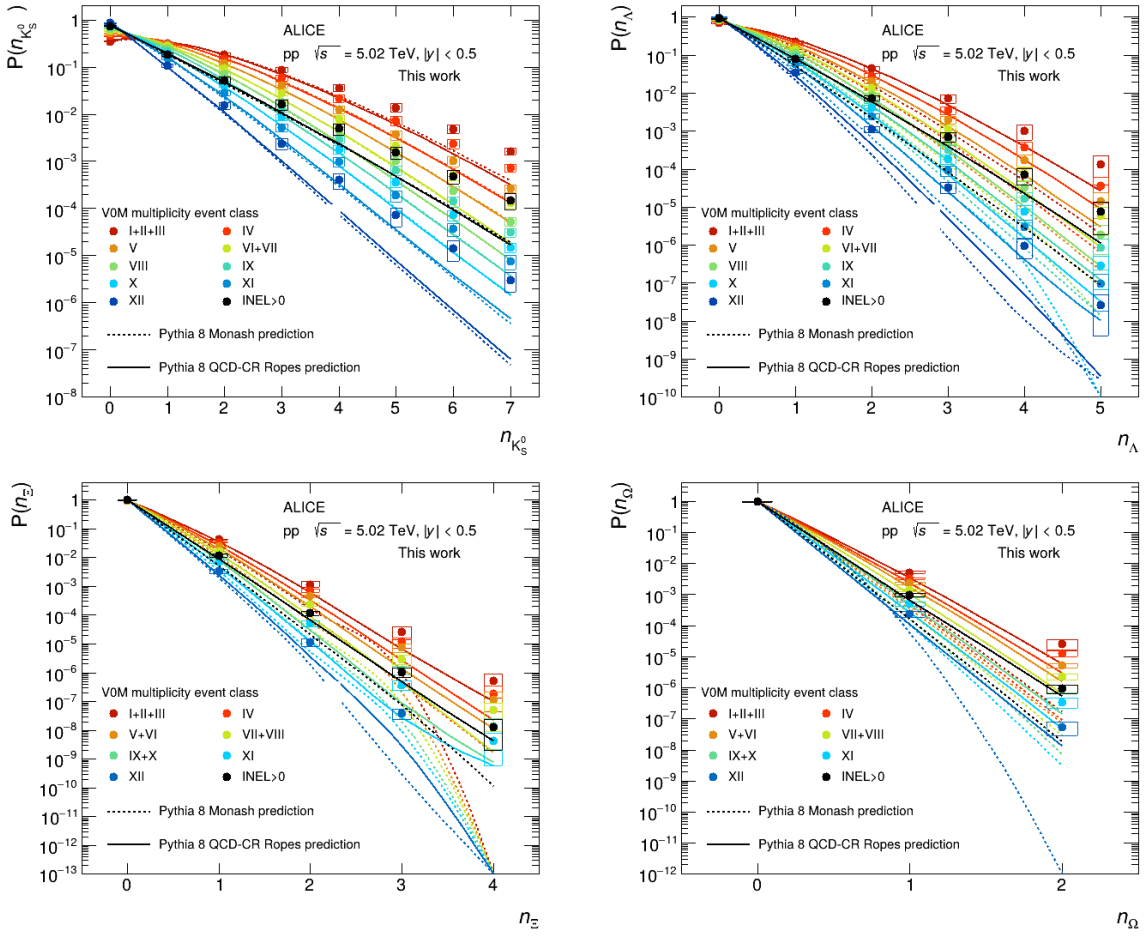

Figure 6.23: Measured (multi-)strange particle multiplicity distributions (markers) for K^0_S (top-left), Λ (top-right), Ξ^- (bottom-left) and Ω^- (bottom-right) are shown with the predictions from Pythia 8 Monash (dotted lines) and Pythia 8 QCD-CR Ropes (continuous lines) for all the multiplicity classes.

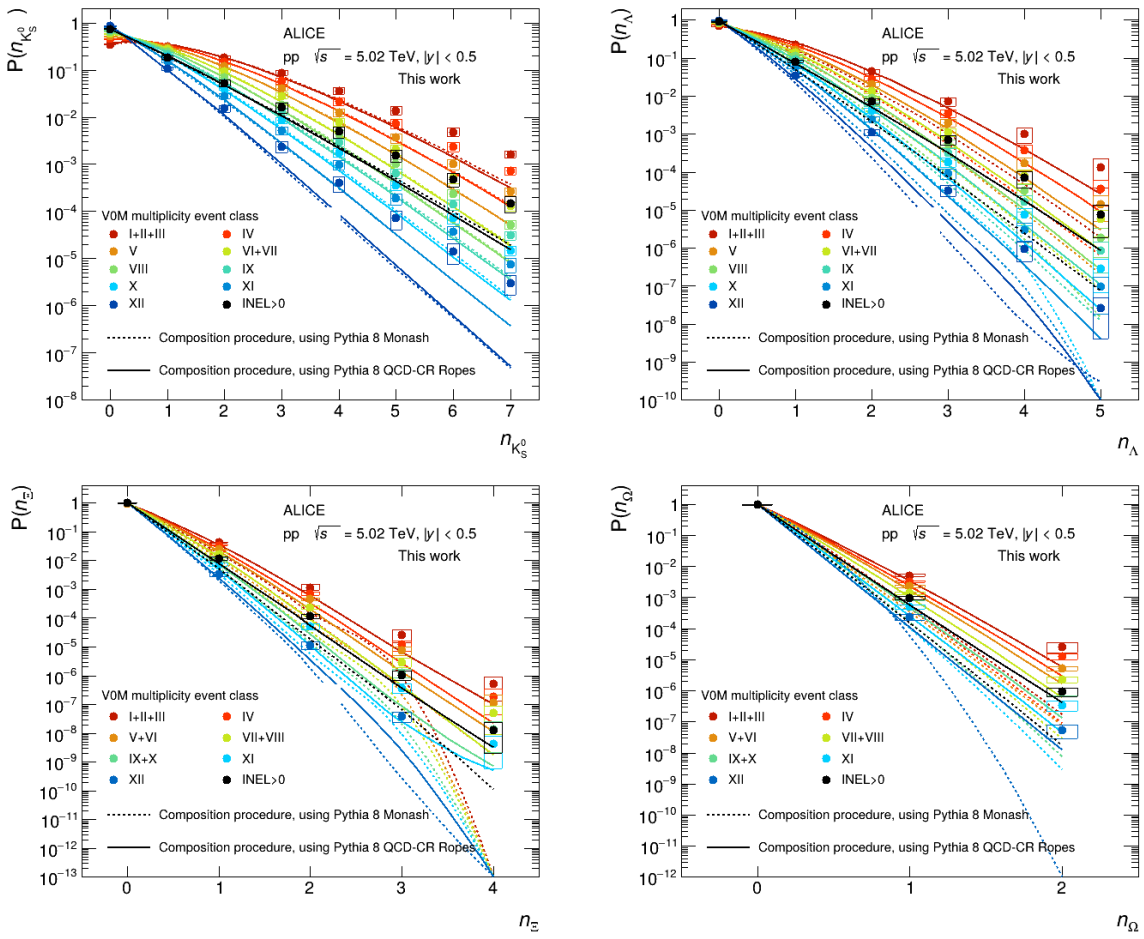

Figure 6.24: Measured (multi-)strange particle multiplicity distributions (markers) for K^0_S (top-left), Λ (top-right), Ξ^- (bottom-left) and Ω^- (bottom-right) are shown with the distributions obtained via the composition procedure for all the multiplicity classes. Dotted and continuous lines depict the distributions derived by combining $P(n_S)$ predicted by Pythia 8 Monash and Pythia 8 QCD-CR Ropes respectively with the extracted $P(N_{ch})$ for data using model-dependent weights.

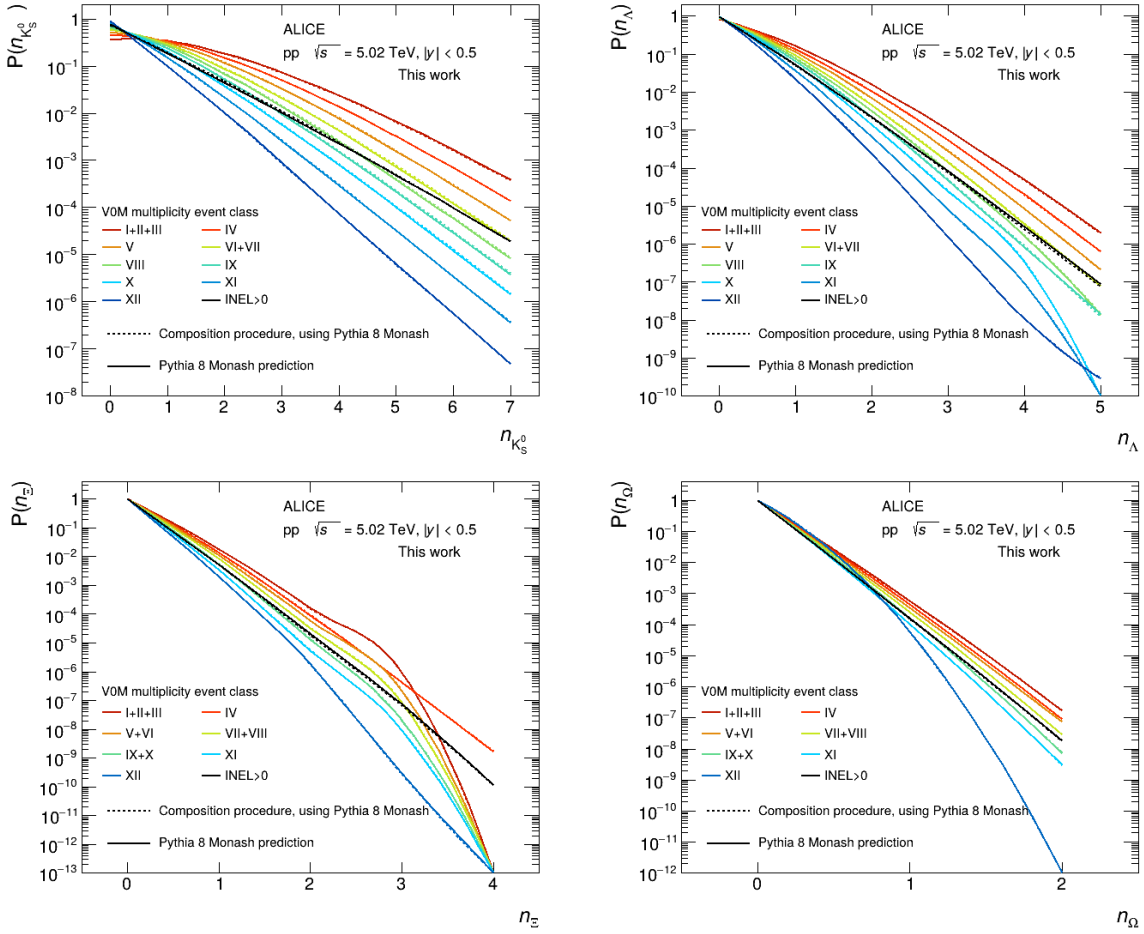

Figure 6.25: K^0_S (top-left), Λ (top-right), Ξ^- (bottom-left) and Ω^- (bottom-right) particle multiplicity distributions predicted by Pythia 8 Monash (continuous lines) and obtained via the composition procedure (dotted lines) for all multiplicity classes. The dotted lines represent distributions derived by combining $P(n_S)$ predicted by Pythia 8 Monash with the $P(N_{ch})$ extracted from data using model-dependent weights.

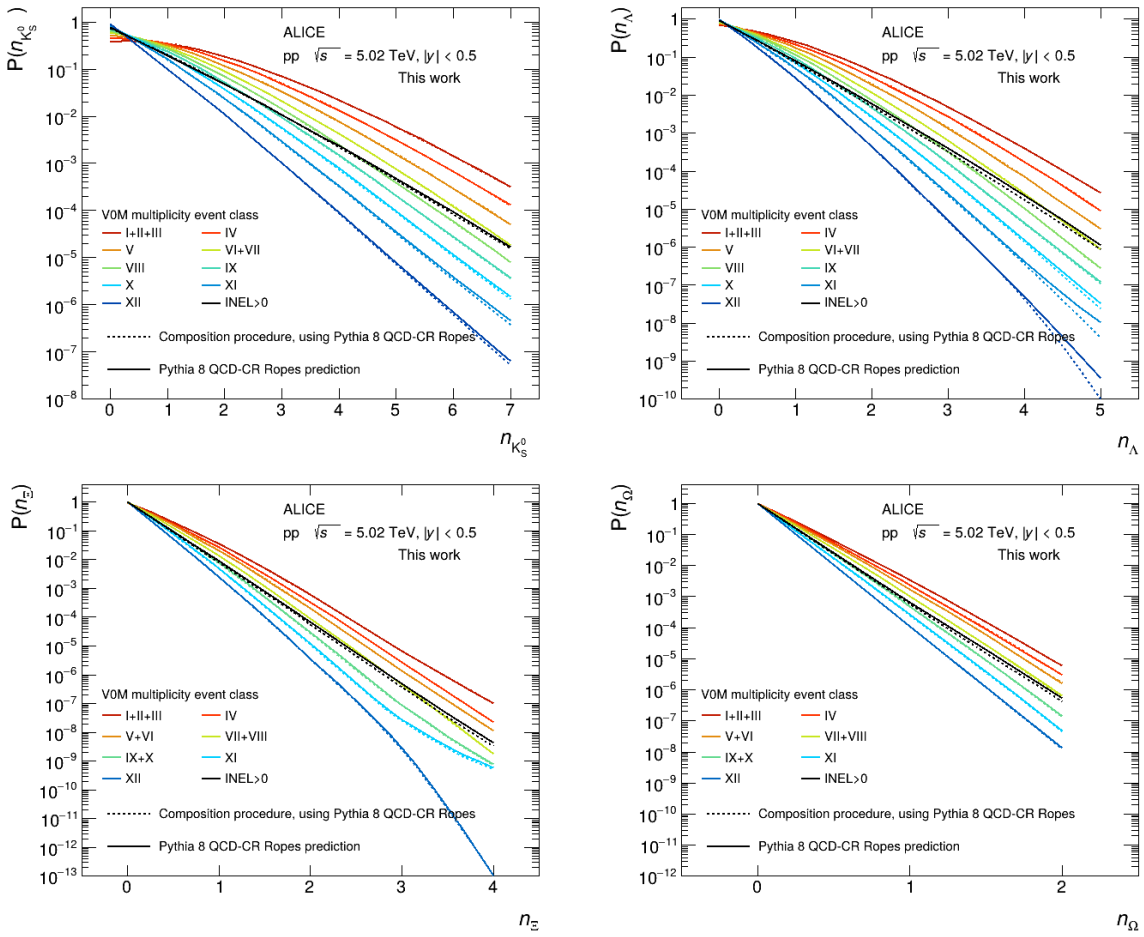

Figure 6.26: K^0_S (top-left), Λ (top-right), Ξ^- (bottom-left) and Ω^- (bottom-right) particle multiplicity distributions predicted by Pythia 8 QCD-CR Ropes (continuous lines) and obtained via the composition procedure (dotted lines) for all multiplicity classes. The dotted lines represent distributions derived by combining $P(n_S)$ predicted by Pythia 8 QCD-CR Ropes with the $P(N_{ch})$ extracted from data using model-dependent weights.

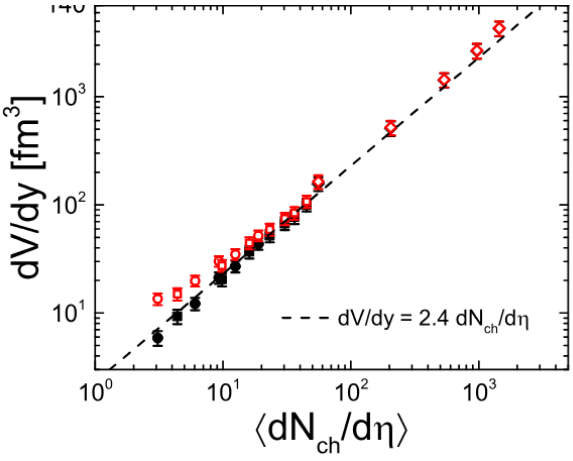

Figure 6.27: Results of the thermal fits to pp (circles), p–Pb (squares), and Pb–Pb (diamonds) data of the ALICE Collaboration within the CSM with $V_C = 3\ d\mathrm{V}/dy$ (full black symbols) and in the grand-canonical limit $V_C \to \infty$ (open red symbols). The dependence of the volume per unit rapidity $d\mathrm{V}/dy$ on the charged-particle multiplicity $\langle \mathrm{d}N_{\mathrm{ch}}/\mathrm{d}\eta \rangle$ is depicted [26].

Chapter 7

Asynchronous quality control of the MID

Alongside my analysis work, during my PhD, I acted as a quality control (QC) expert for the MUon IDentifier (MID). My role involved monitoring the detector's performance and data quality during pp and Pb–Pb collisions in Run 3 (2022–2024). This chapter offers an overview of the Muon Spectrometer in Run 3, with a particular emphasis on the MID. It then delves into the read-out architecture, including a comprehensive examination of the QC architecture. The chapter continues with an overview of the QC objects, focusing specifically on the Asynchronous QC. It provides details on its current status, statistical analysis and the issues encountered. The chapter concludes by discussing potential improvements for the QC of the MID, aiming to enable a more thorough investigation of the detector's performance.

7.1 Muon Spectrometer

In ALICE (see Chapter 3), the Muon Spectrometer [165] is positioned in the forward pseudorapidity region and, during Run 2, consisted of a dipole magnet along with tracking and trigger chambers. The spectrometer spans a pseudorapidity range of $-4.0 < \eta < -2.5$ and comprises several components: a passive front absorber to filter out charged hadrons and decay muons from π/K mesons, a high-granularity tracking system with ten detection planes, a 3T dipole magnet for vertical track bending, a passive muon filter wall followed by four Resistive Plate Chamber (RPC) layers for triggering, and inner beam shielding to protect the detection chambers from particles produced at large rapidities. These components are illustrated in Fig. 7.1. This system was specifically designed to reconstruct light mesons (e.g., ρ, η and ϕ) and heavy vector mesons (e.g., the J/Ψ and Υ families) through their $\mu^+\mu^-$ decay channels. It also detects single muons originating from heavy-flavor hadron decays and $W^{\pm}$ boson decays. Key features of the spectrometer include excellent J/Ψ acceptance down to $p_T = 0$ and high readout granularity, ensuring only 2% occupancy even in central Pb–Pb collisions. With a mass resolution of approximately 100 MeV/c^2 at 10 GeV/c^2, it effectively resolves the various Υ resonances, even in the high-background environment of central Pb–Pb collisions.

In Run 3, the Muon Spectrometer was upgraded with the addition of a new Muon For-

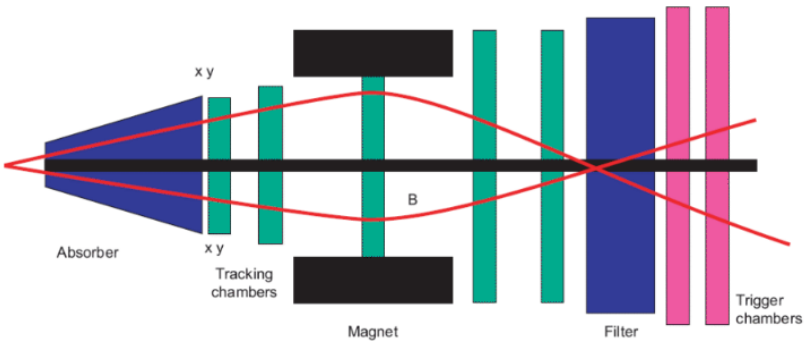

Figure 7.1: A schematic side view of the Muon Spectrometer during Run 1 and Run 2.

ward Tracker (MFT) [166] positioned upstream of the first absorber. Additionally, the Muon Trigger system (MTR) [167] was transformed into the Muon IDentifier (MID) to accommodate the new triggerless operation mode adopted by ALICE (see Fig. 7.2).

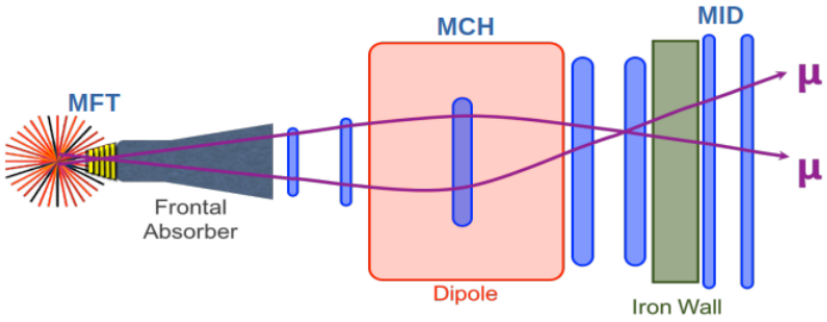

Figure 7.2: A schematic side view of the Muon Spectrometer during Run 3.

The MFT has been installed in order to improve the resolution of the secondary vertex and to allow new physics measurements. It consists of two half-cones, each containing five detection half-disks, positioned along the beam axis at distances between -460 mm and -768 mm from the IP, covering a pseudorapidity range of -3.6 $< \eta <$ -2.5. These detection planes are made of ALPIDE Silicon pixel sensors [168], which are based on Monolithic Active Pixel Sensors (MAPS), also used in the upgraded ALICE Inner Tracking System. Each ALPIDE chip contains about half a million pixels in a 4.5 cm^2 active area, and the entire MFT is composed of 936 sensors arranged on 280 ladders with 2 to 5 sensors per ladder. The sensors have dimensions of 15 $\times$ 30 mm^2, with individual pixel sizes of 27 μm $\times$ 29 μm. This high pixel density provides precise track measurements, giving the MFT a spatial resolution better than 5 μm.

To handle the increased collision rate, the Muon Chambers (MCH) [169] have also been upgraded. Both the Cathode Pad Chambers (CPC) and Cathode Strip Chambers (CSC) now feature new front-end electronics and an updated readout chain. The upgraded boards are designed to amplify, digitize, filter, and compress the signals.

To meet the demands of high-luminosity LHC runs, ALICE adopted a continuous readout mode (i.e., without a trigger) and the Muon Trigger system was reconfigured into the Muon Identifier (MID). The MID consists of 72 single-gap bakelite RPCs arranged in two stations, MT1 and MT2, separated by one meter and located 16.1 m and 17.1 m from the IP, respectively. Each station contains two planes, covering a total area of 5.5 × 6.5 m^2, with each plane comprising 18 RPCs. Figure 7.3 presents a schematic representation of the entire MID system, highlighting the two stations (MT1, MT2), each divided into two planes (MT11, MT12 for MT1 and MT21, MT22 for MT2) and further split into two half-planes (INSIDE and OUTSIDE relative to the LHC ring).

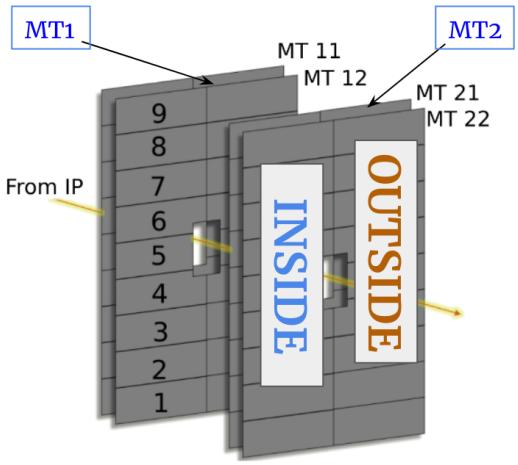

Figure 7.3: Sketch of the whole MID system during Run 3.

The RPCs feature a 2 mm single gas gap and electrodes made from 2 mm thick, low-resistivity bakelite coated with a double layer of linseed oil (see Fig. 7.4, left). Each RPC measures approximately 70 × 270 cm^2. To accommodate the LHC beam pipe, three types of RPCs were implemented: "long" (rectangular, ∼ 274 × 72 cm^2), "cut" (trapezoidal with dimensions similar to the "long" type) and "short" (rectangular, 223 × 72 cm^2), as illustrated in the right panel of Fig. 7.4. The RPCs are read out on both sides using perpendicular copper strips, providing spatial information in the x (vertical strips, non-bending plane) and y (horizontal strips, bending plane) directions within the plane perpendicular to the z-axis of the beam pipe. This arrangement, totaling approximately 21k readout channels, enables three-dimensional reconstruction of muon track hits. Strip pitches of 1, 2 and 4 cm were implemented based on the expected occupancy, as detailed in Ref. [170].
The readout architecture used in Runs 1 and 2 was no longer sufficient for the increased Pb–Pb collision rate in Run 3, which is 5 – 10 times higher, raising the maximum counting rate from ∼10 Hz/cm^2 to ∼90 Hz/cm^2. This increase introduced limitations in readout speed and aging effects on the MTR's RPC detectors. To address these challenges, the same gas mixture was retained (89.7% R134a, 10% i-C4H10, 0.3% SF_6), but the detectors were operated at a lower gain, transitioning from maxi-avalanche to avalanche mode. A new front-end electronics system (FEERIC) was implemented, including a signal pre-

amplification stage upstream of the front-end discriminators.
Further details on the MID's performance and data quality during Run 3 are discussed in Section 7.3.1.

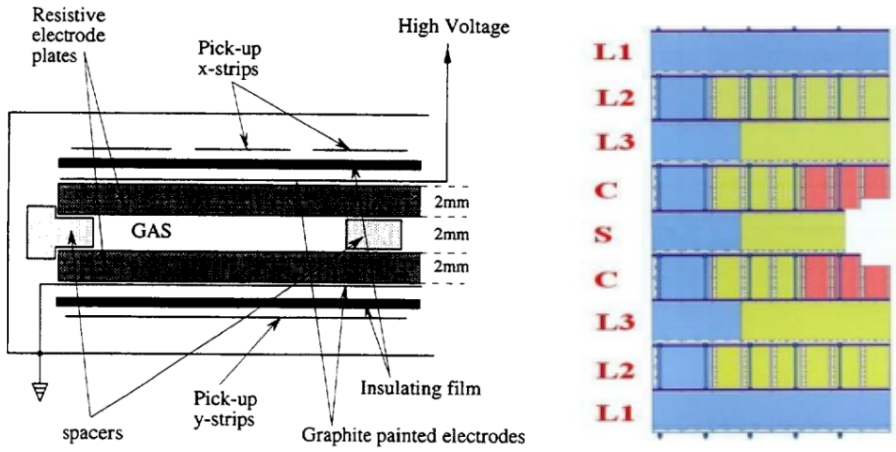

Figure 7.4: (*Left.*) Scheme of the mechanical construction for the ALICE RPCs. (*Right.*) Schematic view of a MID's half-plane composition.

7.2 Read-out architecture chain

To adapt to the new triggerless operating mode, the transition from the MTR to the MID required the implementation of a completely new readout architecture, which is described in this section.
In Runs 1 and 2, the primary objectives of the MTR readout electronics were to execute the local trigger algorithm. Specifically, it needed to generate the Level-0 muon trigger for heavy-quark and quarkonia measurements in the forward region by applying a transverse momentum cut to individual tracks. Additionally, it was responsible for determining the trigger decision for single tracks, storing strip bit patterns and trigger decisions in a pipeline memory, which was subsequently read out whenever an ALICE trigger sequence occurred. With the shift to ALICE's continuous readout mode, all readout electronics cards previously used in Runs 1 and 2 had to be replaced. The new MID readout system [171] is composed of 16 identical *regional crates* for the entire setup. Each crate contains 16 *local cards*, 1 *regional card* and 1 *J2 bus*. In total, the system includes 234 local boards/cards (with up to 16 per VME crate), 16 regional FPGA-based cards connected to the ALICE Common Readout Unit (CRU) via 2 GBTx links each and 16 J2 buses that connect the local cards to their corresponding regional card. A schematic representation of the electronics is provided in Fig. 7.5.

The local cards process Low Voltage Differential Signaling (LVDS) chamber signals from FEERIC, which encode the x and y fired strip patterns of the four detection planes for each bunch crossing. Each local card handles signals from the same xy area across all four MID planes. A schematic view of one of the four MID planes, displaying the 18

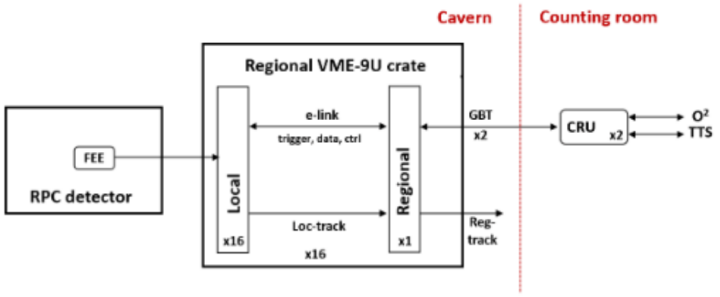

Figure 7.5: Schematic representation of the read-out chain for the MID during Run 3.

RPCs and the 234 local boards, is shown in Fig. 7.6. Notably, the distribution of the local boards corresponds to the strip segmentation, which is finer in regions closer to the beam pipe due to the higher particle density in that area. In both the bending plane (BP, horizontal strips) and non-bending plane (NBP, vertical strips), each local board collects information from either 8 or 16 strips, depending on the strip pitch and the board width. Specifically, the local boards typically group 16 strips with a 1 cm pitch or 8 strips with a 2 cm or 4 cm pitch, with some exceptions.
Then, each of the 16 regional crates is managed by a regional card, which collects data from the local boards through 16 serial links (J2 buses) and compiles the raw events into their final format. The regional card is equipped with two bi-directional optical GBTx links, each operating at 3.2 Gbit/s, to transmit data to 2 CRUs. Each CRU processes data from one half of the MID — either the inside or the outside region. Subsequently, the CRUs forward all the MID data to a single DAQ First Level Processor (FLP) located in the counting rooms above the ALICE cavern. For the MID, each regional card is connected to one GBTx link.
In the data acquisition system, a track is accepted and processed by the read-out architecture if at least 3 out of the 4 detection planes are triggered. This 3/4 condition was selected to account for potential detector inefficiencies or dead channels.

7.2.1 Quality control architecture chain

As already discussed briefly in Section 3.3, in Run 3 data processing is conducted in continuous mode, where the data is divided into short Sub-Time Frames by the FLP, which handle initial compression (zero suppression). These Sub-Time Frames are then transmitted to the Event Processing Nodes (EPN), where data from different detectors are combined into complete timeframes and a synchronous event reconstruction is performed. Compressed Time Frames (CTF) are generated and stored in a disk buffer. During the asynchronous phase, a second reconstruction with final calibrations is carried out on the EPN farm or GRID nodes, producing Analysis Object Data (AO2D) for permanent storage.
Event selection is conducted at the software level, replacing hardware triggers, which allows for a more detailed analysis of specific events. After this event selection process, the original CTFs are removed from the disk buffer to make space for new data. Skimming procedures are applied to pp collisions in order to reduce the amount of data stored on tape, while all recorded Pb–Pb data are preserved. Real-time quality control procedures

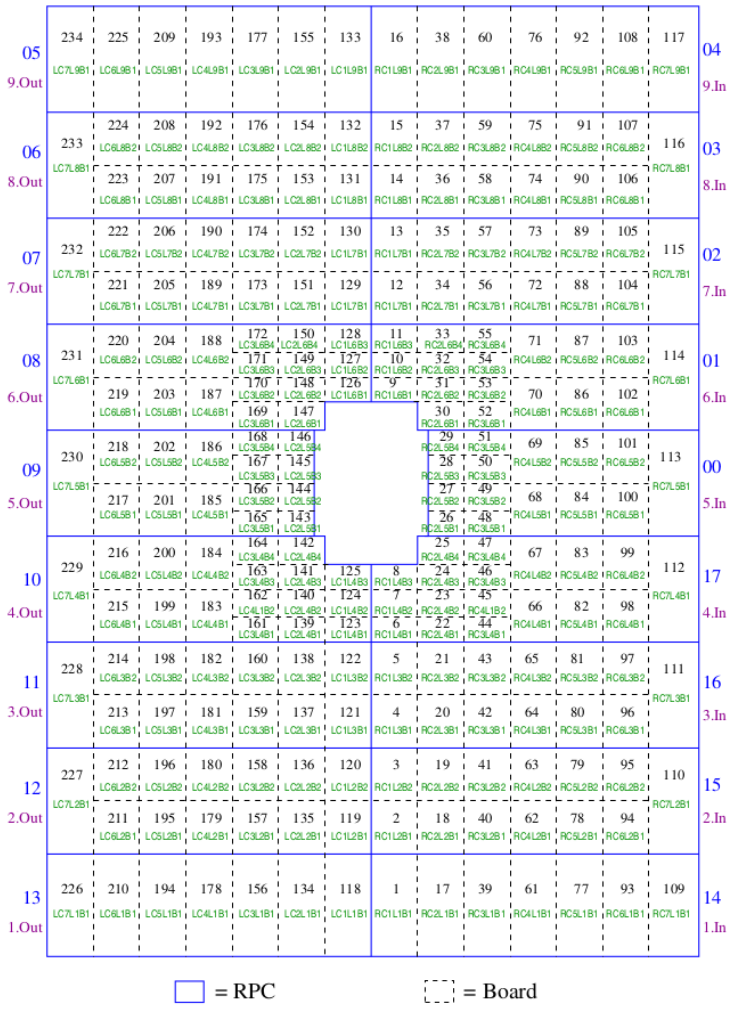

Figure 7.6: Schematic view of one of the MID planes (looking from the IP) showing the 18 RPCs and the 234 local boards. The board enumeration, both in labels and numbers, is also shown.

are carried out to validate detector data on the EPNs and FLPs. With the integration of online and offline computing systems into the unified O^2 project, offline Quality Assurance (QA) and online Data Quality Monitoring (DQM) have been combined into a single quality control (QC) system. This integrated QC framework plays a crucial role in quickly identifying and addressing potential issues during data acquisition, ensuring that calibration and reconstruction processes function as expected in both synchronous and asynchronous modes.

Figure 7.7 shows a schematic representation of the quality control architecture chain during Run 3 [172]. The main data flow is displayed in blue. Data samples, selected by the Data Sampling process, are forwarded to the QC tasks, which can run on the same machines or separate ones. These tasks generate TObjects, typically histograms, which are encapsulated in a MonitorObject. These MonitorObjects are then merged (if necessary)

and reviewed. The checkers [1] output a QualityObject along with the MonitorObjects, which may have been altered. Both the MonitorObjects and QualityObjects are stored in the repository. Additionally, the QualityObjects can be optionally aggregated by the Aggregators [2] to create further QualityObjects, which are also saved in the database. In parallel, the Post-processing phase can retrieve MonitorObjects from the database when certain events occur (such as the release of a new version of an object or a new run) and generate new TObjects, like trending plots.

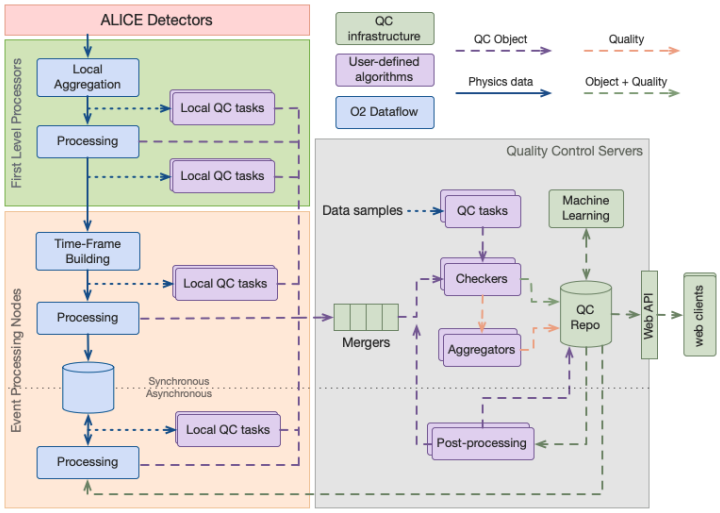

Figure 7.7: Schematic representation of the quality control architecture chain during Run 3 [172].

MonitorObjects and QualityObjects, which represent the results of the QC, are stored in a repository commonly referred to as the QCDB. This repository is built on the same underlying technology as the CCDB (Condition and Calibration DataBase). For testing and development purposes, the test instance of the CCDB is utilized. However, in the production environment, a separate and distinct instance from the CCDB is employed.
Note that before beginning code development, it is essential to create a new module if one does not already exist. Typically, each detector team is responsible for preparing their own module.
Lastly, Aggregators can gather the QualityObjects generated by Checks or other Aggregators to produce new QualityObjects. This functionality is particularly valuable for assessing the overall quality of an individual detector or a group of detectors (refer to Fig. 7.8 for an example).

Data quality control workflow

Data quality is assessed using two complementary approaches:

[1] A Check is a function that determines the quality of the MonitorObjects produced in the Task.
[2] The Aggregators are software components used to collect, combine and group data, making the analysis of large amounts of information more efficient and manageable.

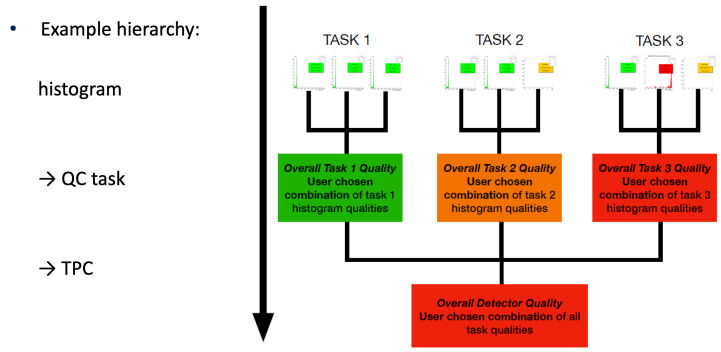

Figure 7.8: An example of the functionality provided by aggregators [172].

- Automated Checks: the quality control framework executes automated Checks that may generate quality Flags.
- Manual Review: detector experts examine the data through the Run Condition Table (RCT [173]) and can modify or add Flags as needed.

Both approaches rely on the same data format for *Flags*. During both synchronous and asynchronous processing, Checks produce quality evaluations and assign them corresponding Flags. The quality control framework subsequently communicates these Flags to the Run Condition Table using a Google Remote Procedure Call (gRPC) interface [3]. Detector experts can then review and, if necessary, adjust or supplement the automatically generated Flags directly within the RCT. A quality control Flag includes the following components:

- Flag Type identifies the specific issue the flag represents (details provided below).
- Time Range specifies the time period affected by the flag.
- Comment (Optional) provides a human-readable explanation for the flag assignment.
- Source String indicates the origin of the flag, such as a person or software module.

Regarding the Flag Type, 13 types are currently available, as detailed in [174]. For the MID, three types are particularly relevant:

- *Good*: it indicates that no issues were detected by a Check or an expert for the specified time interval.
- *Limited Acceptance (MC Reproducible)*: it indicates that part of the detector did not acquire quality data, but the condition can be reproduced in Monte Carlo simulations.

[3]The gRPC interface is a powerful remote communication framework that allows distributed systems to interact efficiently and at scale, using remote procedure calls (RPC) and leveraging modern technologies such as Protocol Buffers for data serialization.

- *Bad Tracking*: it signifies that analyses requiring accurate track reconstruction should exclude this data.

Additionally, it is now possible to assign Flag Types dynamically over time if the detector's performance changes within a single run. In the context of Asynchronous QC, the RCT offers a comprehensive QC summary with detailed comments for each run and detector. Figure 7.9 presents an example from the pp data taking in 2024, where a time-dependent flag was applied to the MID.

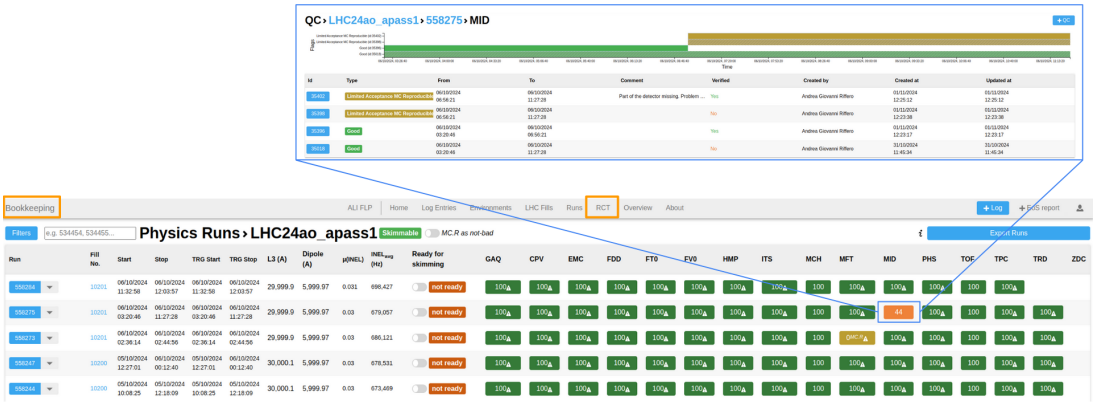

Figure 7.9: Example run where a time-dependent flag was applied to the MID [173].

For further information on the data quality control workflow, refer to the Data Preparation Group (DPG) TWiki page [175]. Furthermore, it is important to monitor the Asynchronous QC throughout the various phases of reconstruction. This process begins with **cpass0**, the initial reconstruction pass on 10% of the statistics used for calibration. It then progresses from **apass*1*** to **apass*n***, representing the first and subsequent (n-th) full reconstruction passes on 100% of the statistics, during which trigger extraction is performed. Additionally, experts must ensure that the skimmed outputs are thoroughly checked.

7.3 Quality control objects for the MID

Various tasks and checks have been developed to monitor the MID QC both online and offline (asynchronously). These tasks are grouped into five categories, each focusing on specific trends to assist experts and QC shifters in thoroughly assessing the MID QC:

- Digits: the task includes strips occupancies for each plane (bending and non-bending), bending AND non-bending plane local boards occupancy for each plane, strip multiplicities per plane for bending and non-bending planes, along with a quality message.

- Clusters: the task contains tracks cluster multiplicity and cluster maps for each plane, as well as the mean number of clusters per bunch crossing. [4]

[4] A cluster is defined as the group of adjacent strips on which a signal is induced in the same event.

- Tracks: the task incorporates features track maps (XY) and deviations, track efficiency per local board, RPC, and globally for each plane (bending, non-bending, and bending AND non-bending planes), along with θ, η, and p_{T} track distributions and the mean number of tracks per bunch crossing.

- Raw: the task examines the mean size of the data transferred per bunch crossing and identifies the busy local boards.

- Calibration: the task identifies the number of dead strips and their location within the detector, strip noise multiplicity and maps, and combined noisy+dead (bad) maps, which are used for masking.

For online quality control, plots are analyzed either as a function of time or, for cases where this is not feasible, updated at fixed intervals (e.g., every 10 minutes). In contrast, offline quality control integrates the plots over the entire duration of the run [5]. In ALICE, each run is uniquely identified by an increasing number (*run number*), and the entire data-taking process is divided into periods labeled *LHCxxyy*, where each period corresponds to a change in external conditions (e.g., magnet polarity). It is important to highlight that Digits, Clusters, Tracks and Raw tasks (along with their Checks) are analyzed during specific types of runs: Physics runs (data-taking with pp or Pb–Pb collisions), Cosmics runs (cosmic ray data-taking during periods without collisions), Technical runs (dedicated to testing detector readout) and Synthetic runs (designed to test the entire readout chain by injecting simulated data into the FLPs, bypassing the detectors). In contrast, Calibration tasks are assessed exclusively during calibration runs.

Focusing on the Asynchronous QC, it is important to highlight that the RPCs are read out from both sides using perpendicular strips, which provide spatial information in the x direction (vertical strips, non-bending plane) and y direction (horizontal strips, bending plane) of the muon impact point within the plane perpendicular to the z-axis of the beam pipe. Four distinct types of plots are analyzed in detail:

- strips occupancies for each plane (bending and non-bending, 2 different sets of plots)

- bending AND non-bending plane local boards occupancy for each plane

- mean number of tracks per bunch crossing

- bending AND non-bending plane track efficiency per RPC for each plane

Figures 7.10, 7.11, 7.12, 7.13 and 7.14 present the plots of interest for a sample run (run 552403, period LHC24aj, apass1) recorded during the pp data taking at $\sqrt{s} = 13.6$ TeV in 2024, which was flagged as *Good* for the MID. In detail, Figures 7.10 and 7.11 show the strips occupancy for the bending and non-bending plane, respectively, for MT11 (top-left), MT12 (top-right), MT21 (bottom-left) and MT22 (bottom-right). Each plane is further divided into two half-planes: OUTSIDE on the left (negative x axis) and INSIDE on the right (positive x axis). The y axis ranges from 0 to 9 to distinguish the RPCs, while the x axis spans from -7 to +7 (-7 to 0 for the OUTSIDE section and 0 to +7 for

[5] A run is a set of data collected within a start and a stop of the data acquisition

the INSIDE section), as the local boards are distributed across 7 columns. As previously discussed, each local board collects data from either 8 or 16 strips, depending on the strip pitch and board width. Consequently, finer bins are observed in the horizontal direction for bending plane (BP) plots and in the vertical direction for non-bending plane (NBP) plots. The quality of these plots is considered *Good* when the maps exhibit uniformity, as is the case for the run under consideration. Similar observations apply to Fig. 7.12, which displays the bending AND non-bending plane local board occupancies for MT11 (top-left), MT12 (top-right), MT21 (bottom-left) and MT22 (bottom-right). Once again, each plane is divided into OUTSIDE (negative x axis) and INSIDE (positive x axis) half-planes, and the plots are classified as *Good* if the maps show uniformity, as observed in this example run. Transitioning from Digits to Tracks, Fig. 7.13 shows the mean number of tracks per bunch crossing (BC). The x axis ranges from 0 to 3564, that is the maximum number of bunches of LHC, while the y axis displays the normalized mean number of tracks reconstructed by the MID per BC. This plot naturally varies based on the LHC's filling scheme, and its quality is classified as *Good* if the observations from the MID align with those from filling scheme itself and other detectors. Any inconsistency between the detectors indicates a misassociation of events and bunch crossings, leading to incorrect track reconstruction. Finally, Fig. 7.14 illustrates the bending AND non-bending plane RPCs track efficiency for MT11 (top-left), MT12 (top-right), MT21 (bottom-left) and MT22 (bottom-right). The tracking efficiency is calculated as the ratio of tracks firing all four RPC planes (4/4) to the total number of tracks (3/4 + 4/4). Similar to the occupancy plots, each plane is divided into two half-planes: OUTSIDE on the left and INSIDE on the right. The y axis ranges from 0 to 9, distinguishing the RPCs, while the x axis spans from -7 to +7 (-7 to 0 for the OUTSIDE half-plane and 0 to +7 for the INSIDE half-plane), corresponding to the 7 columns of local boards. These plots are considered as *Good* if the efficiency is higher than 80% for all RPCs, as observed in this example run.

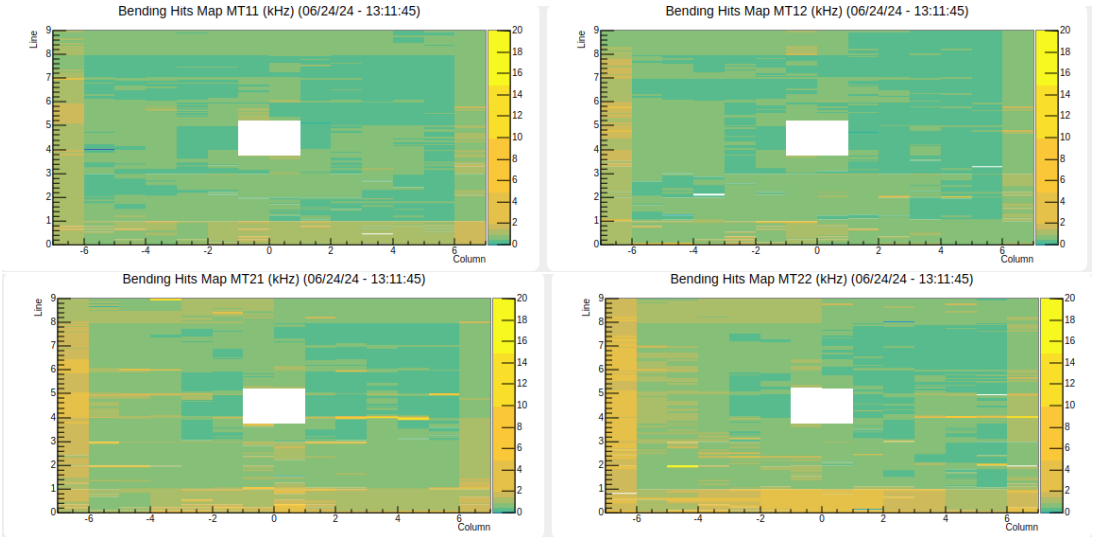

Figure 7.10: Bending plane strips occupancies plots for MT11 (top-left), MT12 (top-right), MT21 (bottom-left) and MT22 (bottom-right) for an example run (run 552403, period LHC24aj, apass1) where the quality is *Good* [176].

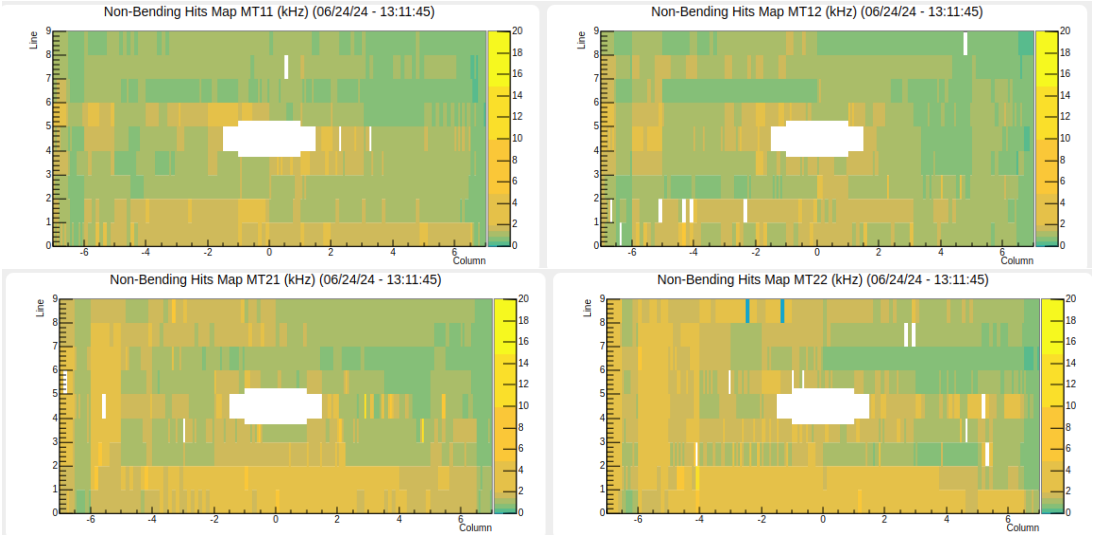

Figure 7.11: Non-Bending plane strips occupancies plots for MT11 (top-left), MT12 (top-right), MT21 (bottom-left) and MT22 (bottom-right) for an example run (run 552403, period LHC24aj, apass1) where the quality is *Good* [176].

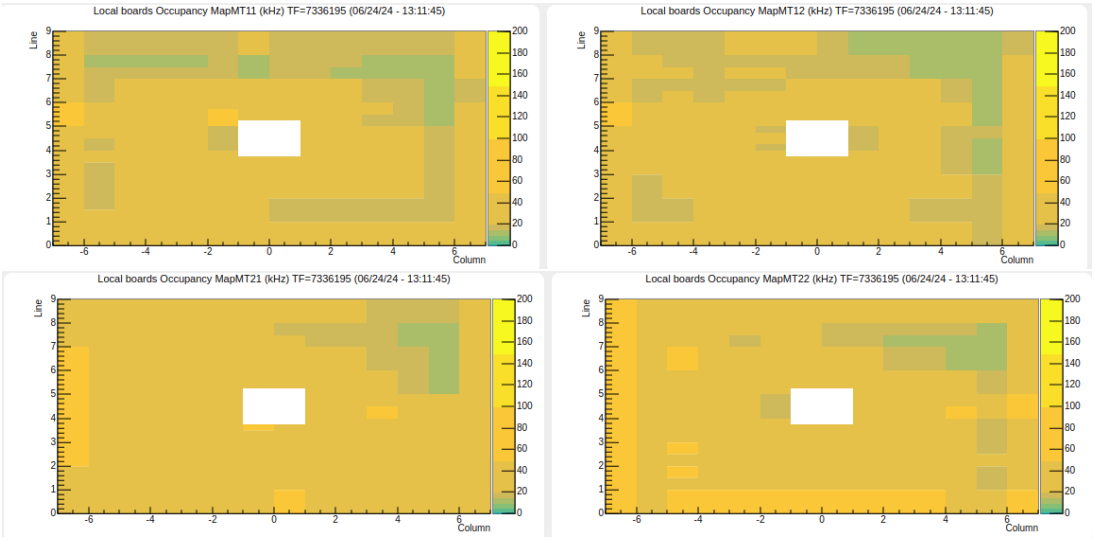

Figure 7.12: Bending AND Non-Bending plane local boards occupancies plots for MT11 (top-left), MT12 (top-right), MT21 (bottom-left) and MT22 (bottom-right) for an example run (run 552403, period LHC24aj, apass1) where the quality is *Good* [176].

7.3.1 Current status: statistics and issues

Since 2022, the ALICE Collaboration has collected data across various collision systems at different centre-of-mass energies. Specifically, during 2022 and 2023, data were collected for pp collisions at $\sqrt{s} = 900$ GeV and 13.6 TeV, as well as for Pb–Pb collisions at $\sqrt{s} = 5.36$ GeV. In 2024, additional data were acquired for pp collisions at $\sqrt{s} = 900$ GeV, 5.36 TeV and 13.6 TeV, along with Pb–Pb collisions at $\sqrt{s} = 5.36$ GeV. Utilizing all the data collected and reconstructed to date, summary plots can be produced for each data-taking

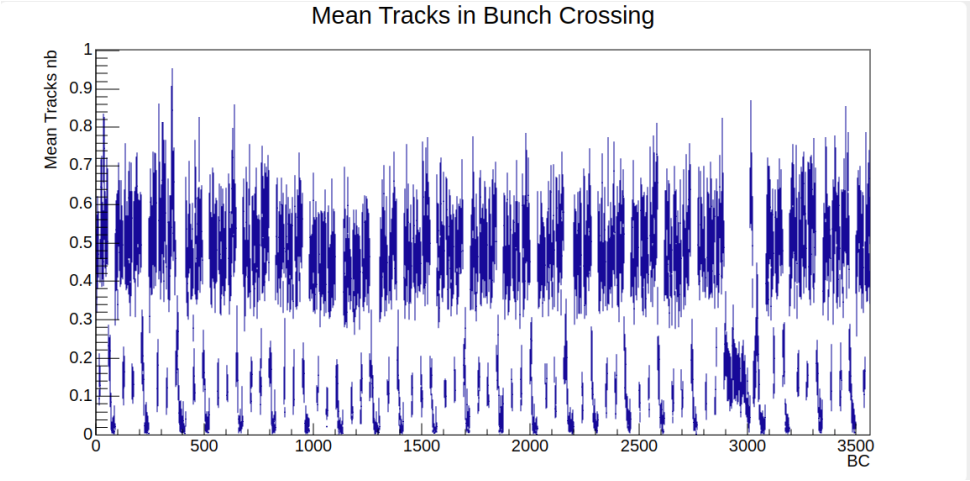

Figure 7.13: Mean number of tracks per bunch crossing for an example run (run 552403, period LHC24aj, apass1) where the quality is *Good* [177].

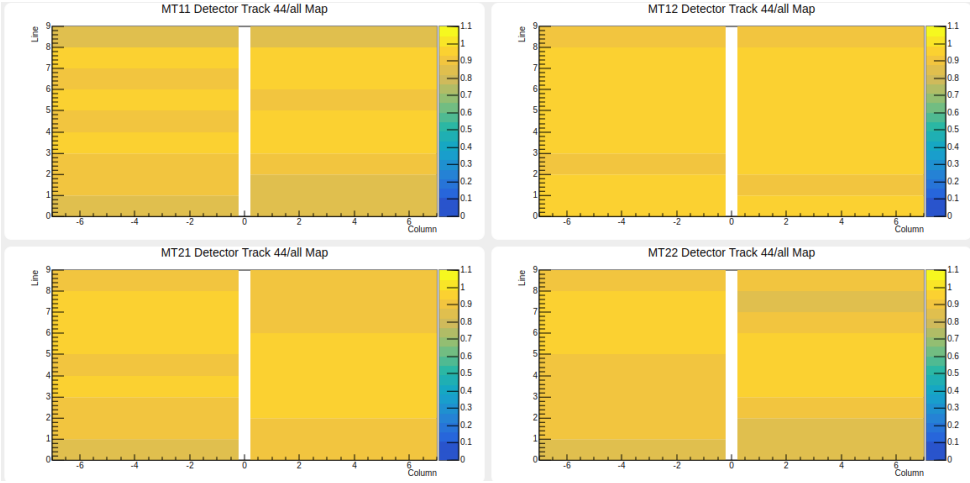

Figure 7.14: Bending AND Non-Bending plane RPCs track efficiency for MT11 (top-left), MT12 (top-right), MT21 (bottom-left) and MT22 (bottom-right) for an example run (run 552403, period LHC24aj, apass1) where the quality is *Good* [177].

scenario to assess the performance of the MID in the context of asynchronous QC during Run 3 operations. Figure 7.15 demonstrates that the asynchronous QC status for the MID during Run 3, analyzed by the number of runs, has generally been flagged as *Good* for both pp and Pb–Pb collisions, with the exception of pp at $\sqrt{s} = 900$ GeV.
Furthermore, as outlined in Section 7.2.1, time-dependent flags became feasible in 2024. Figure 7.16 presents the performance of the MID in the context of asynchronous QC during 2024, analyzed over time. Notably, examining QC as a function of the run duration confirms that the status of asynchronous QC for the MID generally remains *Good* for both pp and Pb–Pb collisions in 2024, with the exception of pp at $\sqrt{s} = 900$ GeV.

Although the MID performed well during data taking in the context of asynchronous QC,

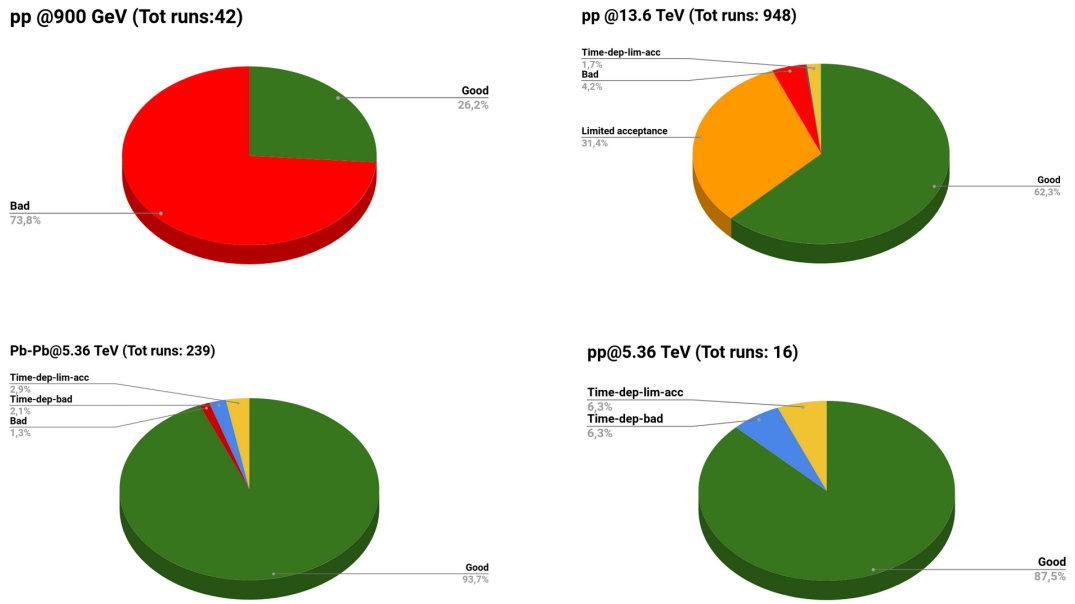

Figure 7.15: Performance of the MID in the context of asynchronous QC during Run 3 operations, analyzed by the number of runs: (top-left) pp collisions at $\sqrt{s} = 900$ GeV, (top-right) pp collisions at $\sqrt{s} = 13.6$ TeV, (bottom-left) Pb–Pb collisions at $\sqrt{s} = 5.36$ TeV and (bottom-right) pp collisions at $\sqrt{s} = 5.36$ TeV.

some issues were encountered.
In particular, during 2022, pp collision runs were flagged as *Bad tracking* for three different reasons: very low RPCs track efficiency, endpoint loss and few local boards counting. Figure 7.17 shows the BP AND NBP RPCs track efficiency for each of the four planes for a sample run (run 517679, period LHC22c, apass4), where very low RPCs track efficiency was recorded. On the other hand, Fig. 7.18 displays the local boards occupancy plots for BP AND NBP for each of the four planes in a sample run (run 526938, period LHC22o, apass4) where an endpoint loss occurred in the INSIDE section of the MID. This can happen when one or more GBTx links stop transmitting data. Finally, Fig. 7.19 shows similar plots for a sample run (run 529690, period LHC22t, apass4), where few strips/local boards were counting.

During 2023, all pp runs flagged as *Limited acceptance (MC reproducible)* were affected by inverted HV polarity in MT22 INSIDE1 and MT22 INSIDE2, resulting in very low track efficiency. Figure 7.20 illustrates the BP AND NBP RPCs track efficiency for each of the four planes in a sample run (run 539220, period LHC23zk, apass4), where the inverted HV polarity in MT22IN1 and MT22IN2 caused significantly reduced efficiency. Notably, this issue was resolved for Pb–Pb data taking.
Additionally, pp runs in 2023 were flagged as *Bad tracking* for two reasons: parts of the detector were unresponsive and endpoint loss. Figure 7.21 presents the local boards occupancies plots for BP AND NBP across the four planes in a sample run (run 535725, period LHC23zh, apass4), where RPCs 7, 8 and 9 in all four planes failed to respond, resulting in a *Bad tracking* quality flag. Conversely, Fig. 7.22 shows similar plots for a

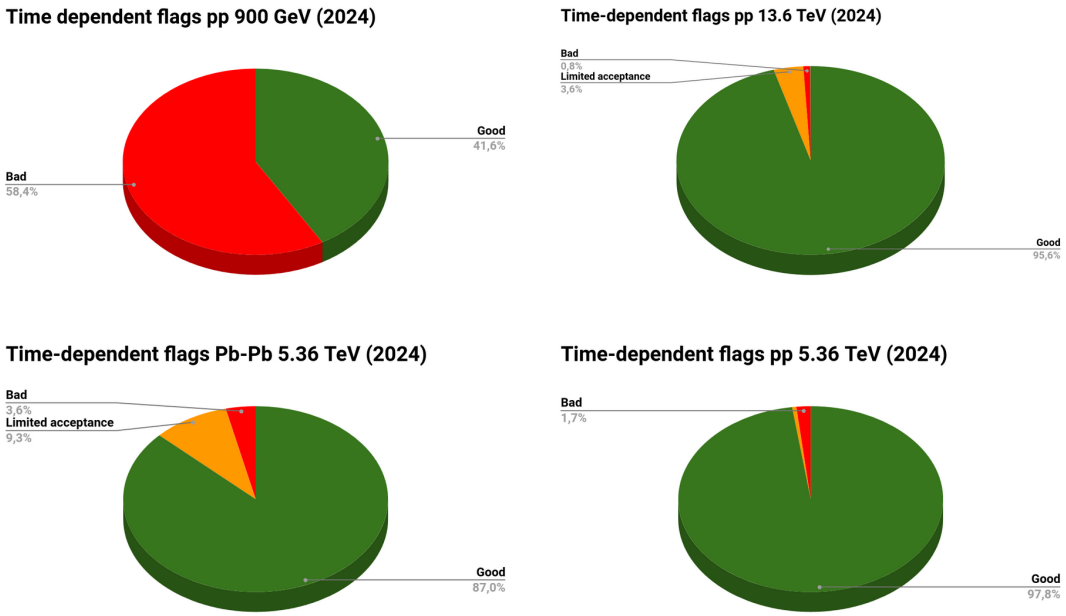

Figure 7.16: Performance of the MID in the context of asynchronous QC during Run 3 operations, analyzed over time: (top-left) pp collisions at $\sqrt{s} = 900$ GeV, (top-right) pp collisions at $\sqrt{s} = 13.6$ TeV, (bottom-left) Pb–Pb collisions at $\sqrt{s} = 5.36$ TeV and (bottom-right) pp collisions at $\sqrt{s} = 5.36$ TeV.

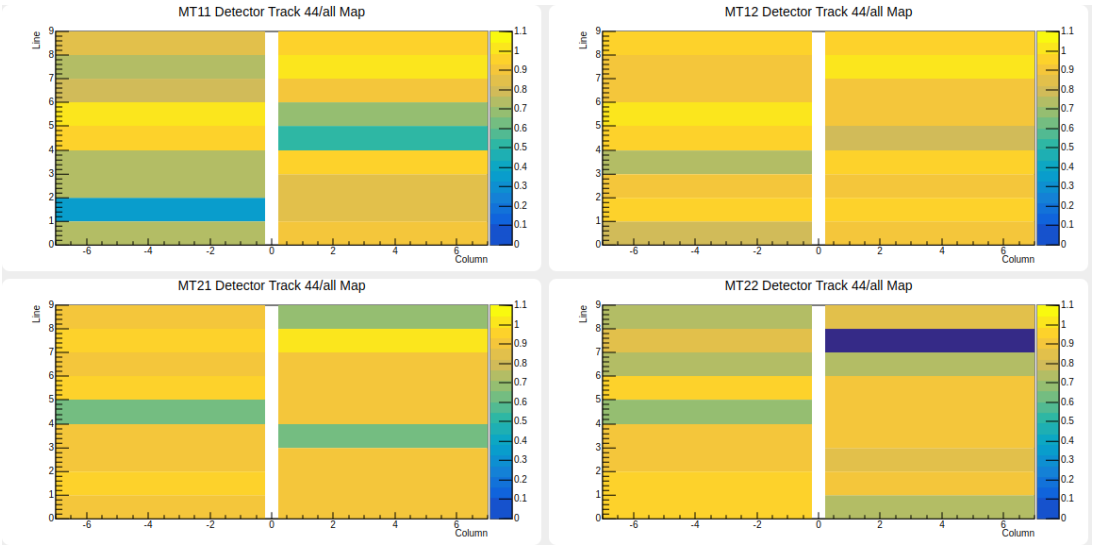

Figure 7.17: Bending AND Non-Bending plane RPCs track efficiency for MT11 (top-left), MT12 (top-right), MT21 (bottom-left) and MT22 (bottom-right) for an example run (run 517679, period LHC22c, apass4) where very low local boards track efficiency was recorded [177].

sample run (run 536489, period LHC23q, apass4) where an endpoint loss occurred, this time in the OUTSIDE section of the detector.

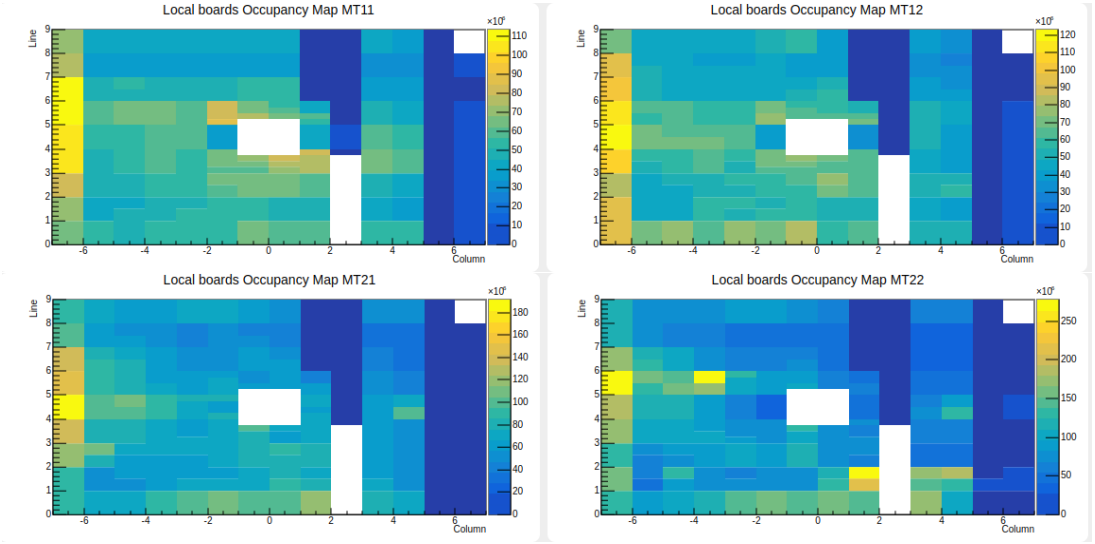

Figure 7.18: Bending AND Non-Bending plane local boards occupancies plots for MT11 (top-left), MT12 (top-right), MT21 (bottom-left) and MT22 (bottom-right) for an example run (run 526938, period LHC22o, apass4) where an endpoint loss occurred [176].

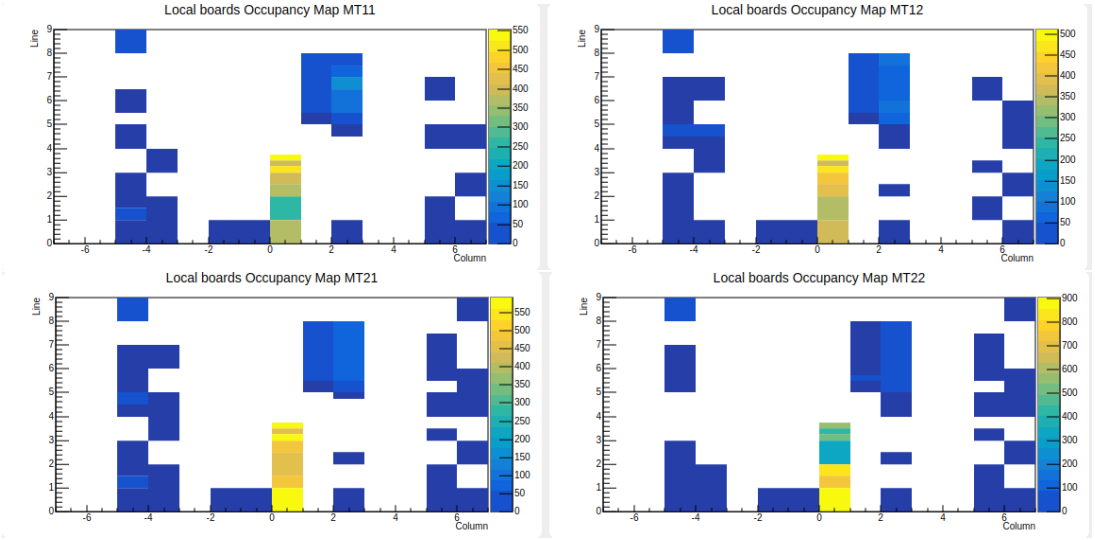

Figure 7.19: Bending AND Non-Bending plane local boards occupancies plots for MT11 (top-left), MT12 (top-right), MT21 (bottom-left) and MT22 (bottom-right) for an example run (run 526938, period LHC22o, apass4) where few strips/local boards were counting [176].

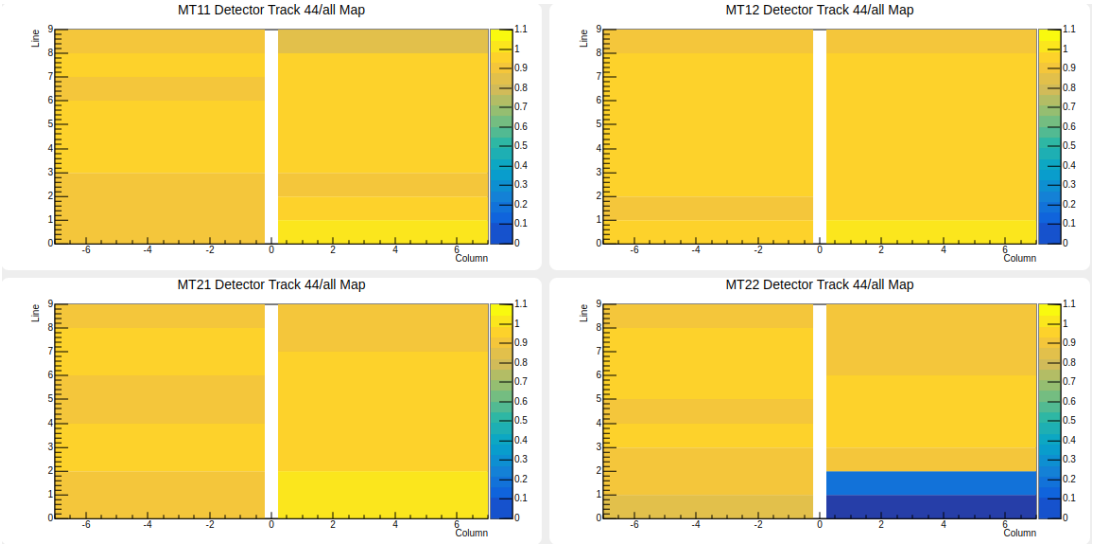

Figure 7.20: Bending AND Non-Bending plane RPCs track efficiency for MT11 (top-left), MT12 (top-right), MT21 (bottom-left) and MT22 (bottom-right) for an example run (run 539220, period LHC23zk, apass4), where the inverted HV polarity in MT22IN1 and MT22IN2 caused significantly reduced efficiency [177].

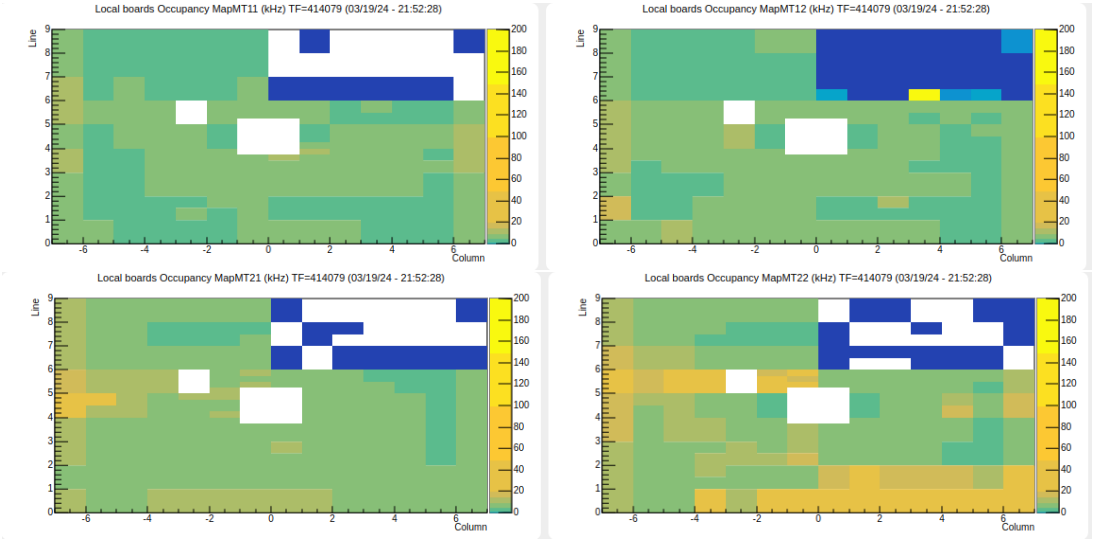

Figure 7.21: Bending AND Non-Bending plane local boards occupancies plots for MT11 (top-left), MT12 (top-right), MT21 (bottom-left) and MT22 (bottom-right) for an example run (run 535725, period LHC23zh, apass4), where RPCs 7, 8, and 9 in all four planes failed to respond [176].

Regarding Pb–Pb data taking in 2023, only 2 out of 141 runs were flagged as *Bad tracking* for the MID in the context of asynchronous QC, both due to endpoint loss. This, as in the pp case, caused entire columns in the hit maps to display low occupancy.

Finally, for 2024, it is preferable to address the experienced issues by considering the

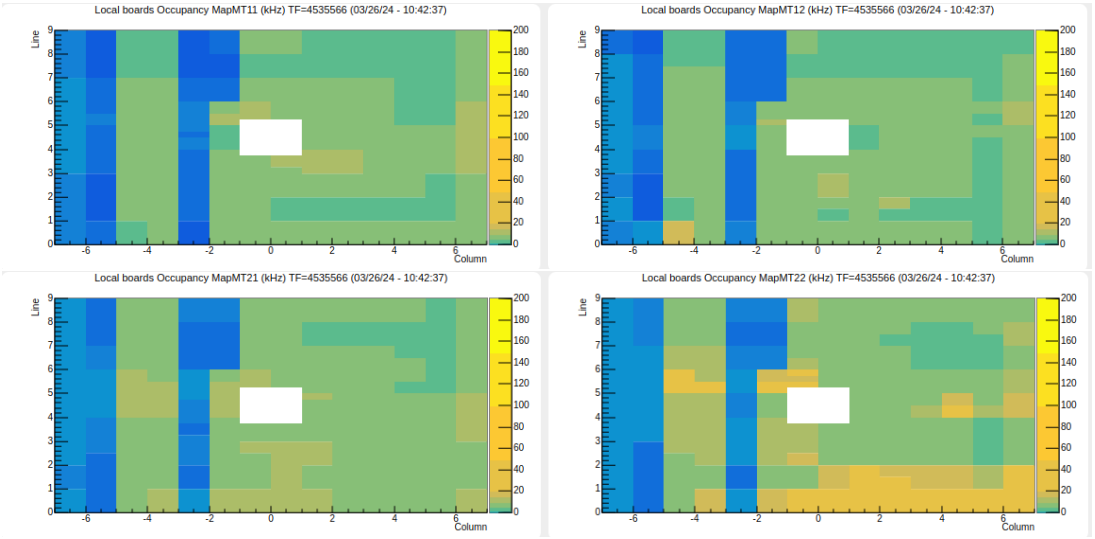

Figure 7.22: Bending AND Non-Bending plane local boards occupancies plots for MT11 (top-left), MT12 (top-right), MT21 (bottom-left) and MT22 (bottom-right) for an example run (run 536489, period LHC23q, apass4) where an endpoint loss occurred [176].

different centre-of-mass energies separately. Beginning with pp collisions at $\sqrt{s} = 900$ GeV, some runs were flagged as *Bad tracking* due to significant discrepancies between the RPCs track efficiency plots observed online and those in the asynchronous QC both in the **cpass0** and in the **apass1**. Figure 7.23 presents a comparison between the asynchronous (upper) and online (lower) QC plots, showing the RPCs track efficiency for both Bending and Non-Bending planes in the MT11 (top-left), MT12 (top-right), MT21 (bottom-left) and MT22 (bottom-right) for an example run (run 548707, period LHC24aa, cpass0), where discrepancies are observed for the MID. These differences could originate from variations in statistics between the online and asynchronous QC or from using different versions of the code (O^2Physics). To investigate whether the issue is related to statistics, the merging procedure in the asynchronous QC was examined by comparing the number of entries in several plots (e.g., ϕ, η distributions) for individual CTFs and the entire run. It was found that the statistics for the entire run were approximately 10 times greater than those for an individual CTF, which is consistent with expectations if the merging was successful. However, since the CTFs are filled over time, it may be useful to study how the graphs evolve. On the other hand, to determine if the differences are due to the code version, the `configuration files` were first compared, revealing no significant differences that could explain the issue. The versions of the code were also examined; although these differ between online and asynchronous, the same versions have been used for some time without any unusual results. Finally, a test was performed by running the same version of the code in the asynchronous QC as in the online QC, and the plots obtained were similar to those from the asynchronous QC. Therefore, it can be concluded that the issue is not related to the code version, but appears to be specific to the online QC, which could not be reproduced. However, the exact cause of this problem is still under investigation, although it is considered of low priority since it only occurs in a few runs and not in subsequent ones.

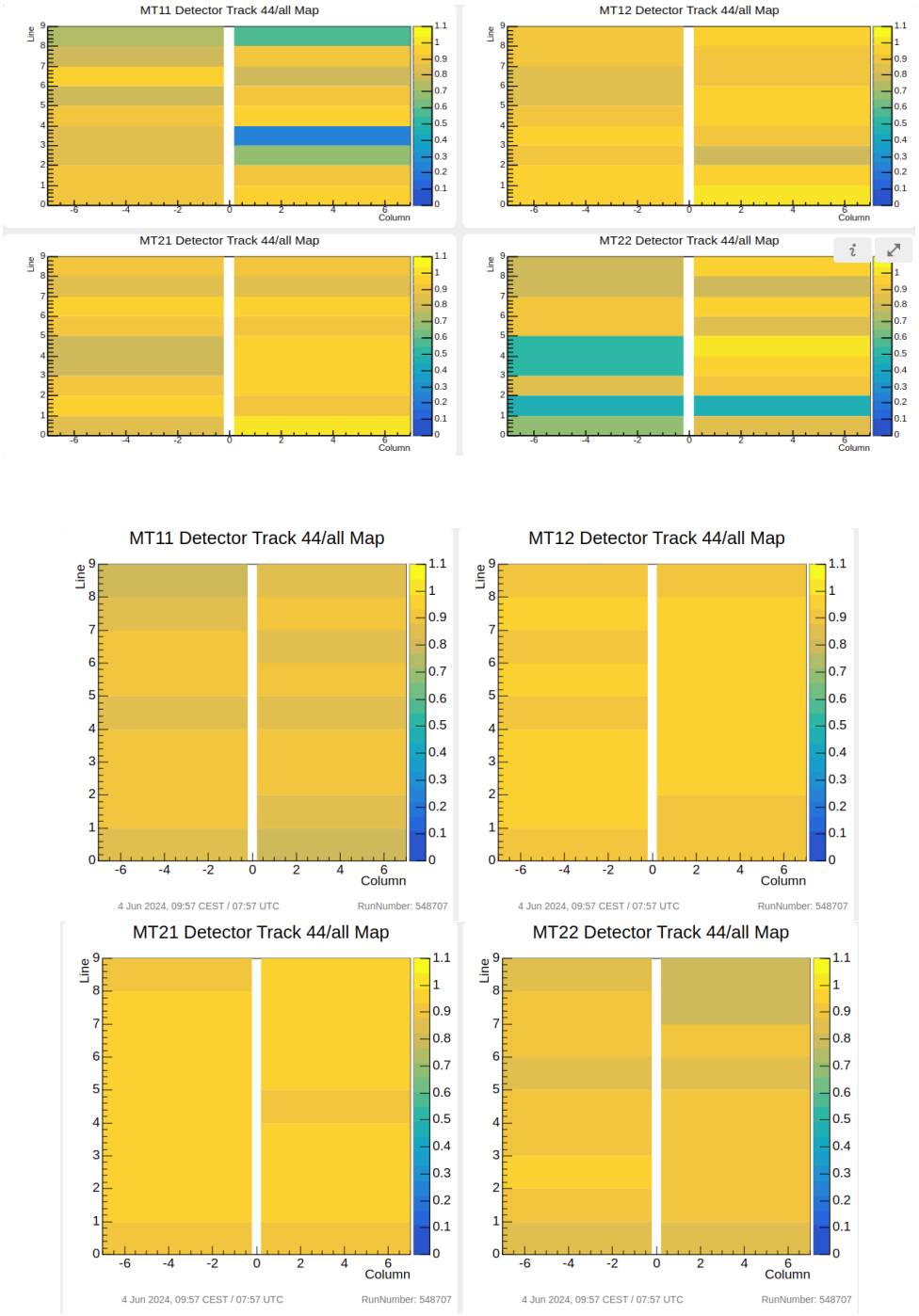

Figure 7.23: Comparison between the asynchronous (upper, [177]) and the online (lower, [178]) QC plots showing the RPCs track efficiency for both Bending and Non-Bending planes in the MT11 (top-left), MT12 (top-right), MT21 (bottom-left) and MT22 (bottom-right) for an example run (run 548707, period LHC24aa, cpass0), where differences are observed for the MID.

After pp collisions at $\sqrt{s} = 900$ GeV, ALICE collected data at $\sqrt{s} = 13.6$ TeV in 2024. At

this energy, two common issues were observed for the MID at the asynchronous QC level: missing local boards or entire columns and some GBTx links going down. For many runs, these issues appeared only during part of the run duration, allowing for flags that were time-dependent and partially marked as *Good*, *Bad tracking*, or *Limited acceptance (MC reproducible)*. Figure 7.24 shows the local board occupancies plots for BP AND NBP across the four planes in a sample run (run 556641, period LHC24an, apass1), where entire columns are missing, leading to a *Bad tracking* quality flag. On the other hand, the issue related to GBTx links, which went down towards the end of some runs, is visible in the expert interface (the asynchronous QC provides integrated information about the run). Figure 7.25 displays similar plots for an example run (run 551890, period LHC24aj, apass1), where half of a column is empty due to a GBTx link failure during the second interval of the run.

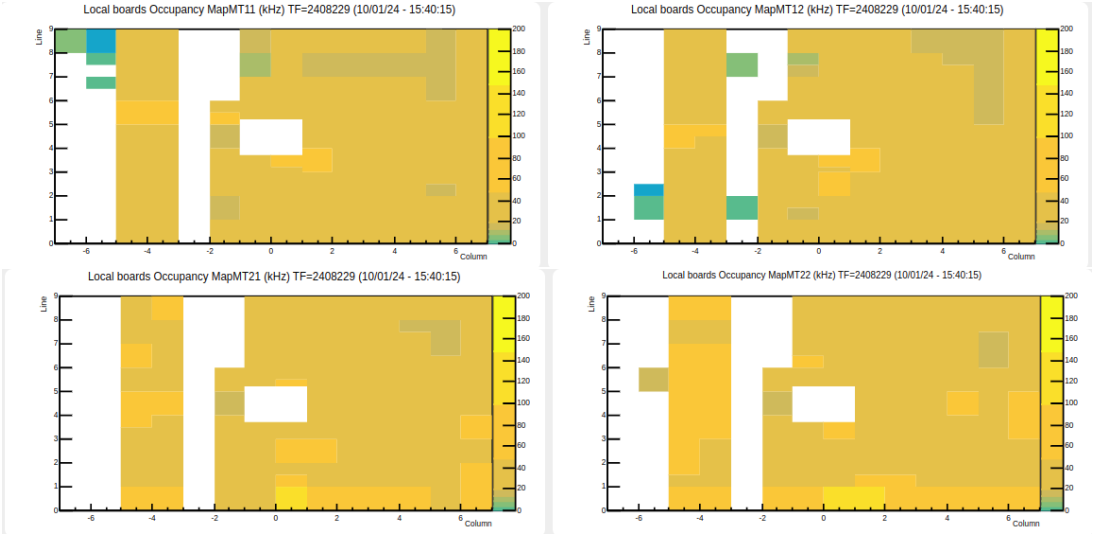

Figure 7.24: Bending AND Non-Bending plane local boards occupancies plots for MT11 (top-left), MT12 (top-right), MT21 (bottom-left) and MT22 (bottom-right) for an example run (run 556641, period LHC24an, apass1) where entire columns are missing [176].

For pp collisions at $\sqrt{s} = 5.36$ TeV, only two runs were not flagged as entirely *Good*. These runs were marked as time-dependent *Limited acceptance (MC reproducible)* due to a half-column missing (run 559408, period LHC24aq, apass1), and as time-dependent *Bad tracking* because some local boards were out-of-sync (run 559361, period LHC24ap, apass1).

Regarding Pb–Pb collisions in 2024, similar issues to those previously discussed were encountered, particularly endpoint losses and local boards being out-of-sync. Additionally, due to a significant increase in the interaction rate during 2024 (up to $\sim$ 50 kHz), the occupancy of strips and local boards in some runs exceeded the threshold previously set by the MID expert. As a result, the threshold was adjusted from 800 to 1050 kHz. Moreover, during Pb–Pb data taking, an issue with the pressure sensor led to a drop in the MID's HV. This problem caused a *Bad tracking* quality flag for run 559802 (period LHC24ar) from the asynchronous QC perspective.

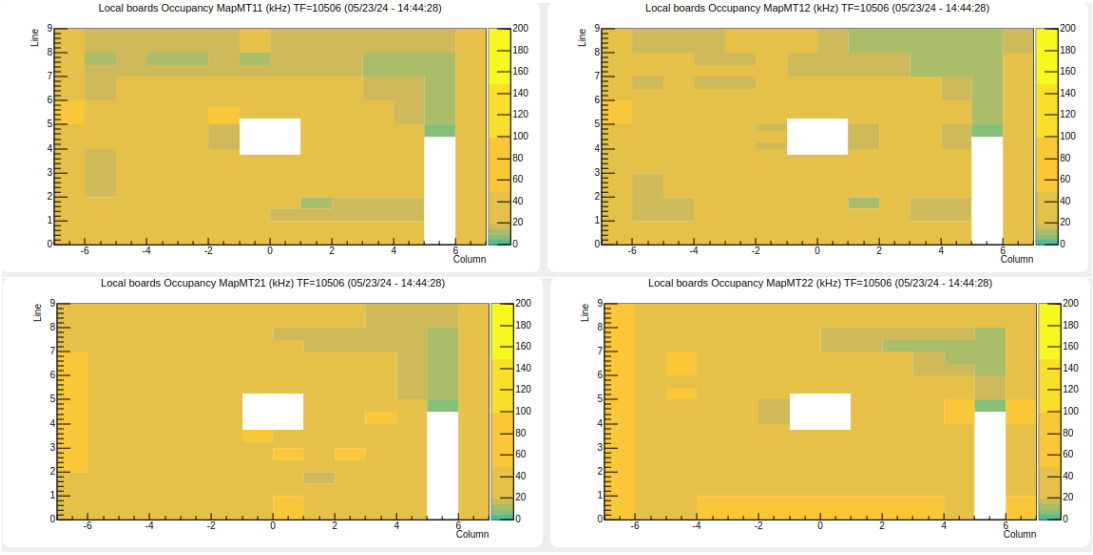

Figure 7.25: Bending AND Non-Bending plane local boards occupancies plots for MT11 (top-left), MT12 (top-right), MT21 (bottom-left) and MT22 (bottom-right) for an example run (run 551890, period LHC24aj, apass1) where one half of a column is empty due to a GBTx link down [179].

Possible improvements

As discussed previously and illustrated in Figures 7.15 and 7.16, the asynchronous QC status for the MID during Run 3, analyzed both by the number of runs and, in 2024, also as a function of run duration, has generally been flagged as *Good* for both pp and Pb–Pb collisions, with the exception of pp at $\sqrt{s} = 900$ GeV. Nevertheless, there are potential improvements for the MID QC that could enable a more thorough investigation of the detector's performance. For example, it could be useful not only to produce RPC track efficiency for both the Bending and Non-Bending planes but also to assess the efficiency of local boards and possibly strip tracks, in order to better understand where the detector is less efficient. Additionally, investigating when the MID fails could be valuable: identifying spikes in the number of channels activated in a given bunch crossing and examining how the number of channels touched per BC varies over time (at the online level) could provide useful insights.

Expanding the scope of potential improvements, it could be interesting to study the matching of tracks between MCH and MID, as well as between MFT and MCH, and MCH and MID (MFT, MCH, MID), considering other detectors in the Muon Spectrometer alongside the MID. Currently, quality evaluation is conducted for individual detectors, although studies aimed at achieving this goal are ongoing.

Chapter 8

Conclusions

This chapter is dedicated to briefly summarizing the studies presented in this thesis, with a focus on the originality of the work.

The study of strange hadron production in various hadronic collisions (pp, p–Pb, Pb–Pb) at LHC energies has shown a smooth increase in the ratios of strange to non-strange hadron yields as a function of the charged-particle multiplicity produced in the collision. This behavior, known as strangeness enhancement, is particularly notable since different particle production mechanisms are expected to be involved in the different collision systems. In particular, the higher ratio of (multi-)strange hadron to pion yields observed in central Pb–Pb collisions compared to minimum bias pp collisions has traditionally been interpreted as a signature of quark-gluon plasma formation, a phenomenon not expected to occur in small collision systems. Moreover, the inability of current QCD-inspired Monte Carlo generators to quantitatively describe the observed behavior emphasizes the need for further experimental data and theoretical advancements. Such progress is essential to reveal the microscopic mechanisms underlying strangeness enhancement. A more comprehensive understanding of strangeness production can be achieved through precise measurements of (multi-)strange particle multiplicity distributions ($\mathrm{P}(n_{\mathrm{S}})$).

This thesis presents the first measurement of the production probability of multiple strange particles ($\mathrm{K}^0_{\mathrm{S}}$, Λ, Ξ^- and Ω^-) and their antiparticles ($\overline{\Lambda}$, $\overline{\Xi}^+$ and $\overline{\Omega}^+$) in pp collisions at $\sqrt{s} = 5.02$ TeV at midrapidity. Results are categorized by charged-particle multiplicity density classes. The analysis adopts an innovative approach that counts strange particles on an event-by-event basis and applies a one-dimensional Bayesian unfolding procedure to correct the raw multiplicity spectrum. This novel technique enables a more detailed investigation of strangeness production beyond the mean multiplicity, providing a new benchmark for Monte Carlo generator testing.
The dataset allows measurements of $\mathrm{P}(n_{\mathrm{S}})$ up to 7 $\mathrm{K}^0_{\mathrm{S}}$, 5 Λ, 4 Ξ (3 in the lowest multiplicity bin) and 2 Ω particles per event. This offers a unique opportunity to explore the interplay between charged and strange particle production under extreme conditions. For example, events with very low charged-particle multiplicity can still feature several cascades, while high-multiplicity events may exhibit limited single-strange $\mathrm{K}^0_{\mathrm{S}}$ production. Furthermore, results show that the probability of producing multiple strange particles of a given species increases non-linearly with charged-particle multiplicity. At high n_S values,

$P(n_S)$ in the INEL > 0 class develops a tail that approaches the probabilities observed in high-multiplicity V0M classes. This behavior reflects a charged-particle multiplicity bias introduced by selecting events with a high number of strange particles. Examining this bias in MC generators offers valuable insights into the mechanisms driving strange and non-strange particle production.

From the measured $P(n_S)$, the average production yield of n particles per event (multiplets, $\langle Y_{nS} \rangle$) is calculated as a function of the charged-particle multiplicity at midrapidity for all particles and antiparticles. Results indicate an enhancement with increasing multiplicity, with steeper growth for higher n. Comparisons with the Pythia8 MC generator reveal significant improvements in the Pythia 8 QCD-CR Ropes tune for baryons, though no substantial improvements are observed for K^0_S mesons. In contrast, the Epos LHC hybrid model shows better agreement at high multiplicity but significantly underestimates $\langle Y_{nS} \rangle$ at low multiplicity.

Additionally, by measuring multiplets, various yield ratios are analyzed to investigate the relative probability of s-quarks hadronizing into different types of hadrons. Ratios with perfect strangeness balance ($\Delta S = 0$) and those probing extreme scenarios of strangeness enhancement ($\Delta S > 0$) are studied as functions of charged-particle multiplicity. The analysis reveals unprecedented levels of strangeness enhancement by examining the ratios of cascade multiplets to single K^0_S yields, with strangeness imbalances (ΔS) reaching as high as 5. A consistent agreement between $\langle Y_{3\Xi} \rangle / \langle Y_{nK^0_S} \rangle$ and $\langle Y_{2\Omega} \rangle / \langle Y_{nK^0_S} \rangle$ confirms that the enhancement primarily stems from the strange content imbalance. Conversely,
$\Delta S = 0$ ratios exhibit distinct trends, indicating a secondary role for light u and d quarks. For instance, $\langle Y_{n\Lambda} \rangle / \langle Y_{nK^0_S} \rangle$ shows a clear enhancement at high multiplicity for the first time, while other baryon-to-meson ratios decrease. These findings can be qualitatively explained by a simple coalescence scenario, where the likelihood of combining light quarks with s-quarks evolves with event multiplicity. Notably, $\Delta S = 0$ ratios are well-reproduced by the Pythia 8 QCD-CR Ropes model, underscoring the relevance of its QCD-color reconnection mechanism for strange baryons.

The findings presented in this thesis establish the first step for a new generation of strange particle yield measurements, enabling the study of the relative probabilities for a given number of strange quarks in a pp event to hadronize into different combinations of strange hadrons. Several potential future directions, focusing on experimental progress and phenomenological implications, have already been explored and discussed. By assuming that strangeness production is linked to local multiplicity at mid-rapidity, the shape of the strange particle multiplicity distribution can be deduced either from the probability distribution at fixed local multiplicity or from the variation in local multiplicity within a specific V0M class. Further studies have been conducted to assess how multiplicity fluctuations impact the measured strange particle multiplicity distributions. The comparison between the measured $P(n_S)$, model predictions and the resulting distributions obtained by combining a specific distribution for strange particle production ($P(n_S)$ predicted by models at fixed multiplicity) with the experimental charged-particle multiplicity distribution $P(N_{ch})$ has shown excellent agreement between the trends derived from composition and the model predictions for all particles and multiplicity classes. This indicates that

the observed discrepancies in $P(n_S)$ between data and models are not due to a correct implementation of strangeness production followed by incorrect reweighting for $P(N_{ch})$ (e.g., due to multiplicity fluctuations), but rather stem from limitations in the models' representation of the underlying strangeness production mechanisms.
Larger datasets from the LHC Run 3 campaign will extend the presented measurements to even higher strange particle multiplicities and enable investigations of the simultaneous production of multiple strange hadron species.

Additionally, this thesis provides an in-depth discussion of the asynchronous quality control (QC) of the MID, detailing its current status, statistical analysis and the challenges encountered. Overall, the asynchronous QC performance for the MID during Run 3 has been generally flagged as *Good* for both pp and Pb–Pb collisions, with the exception of pp collisions at $\sqrt{s} = 900$ GeV. This conclusion is based on analyses conducted by the number of runs and, in 2024, also as a function of run duration.

Chapter 9

Appendices

9.1 1D invariant mass fits

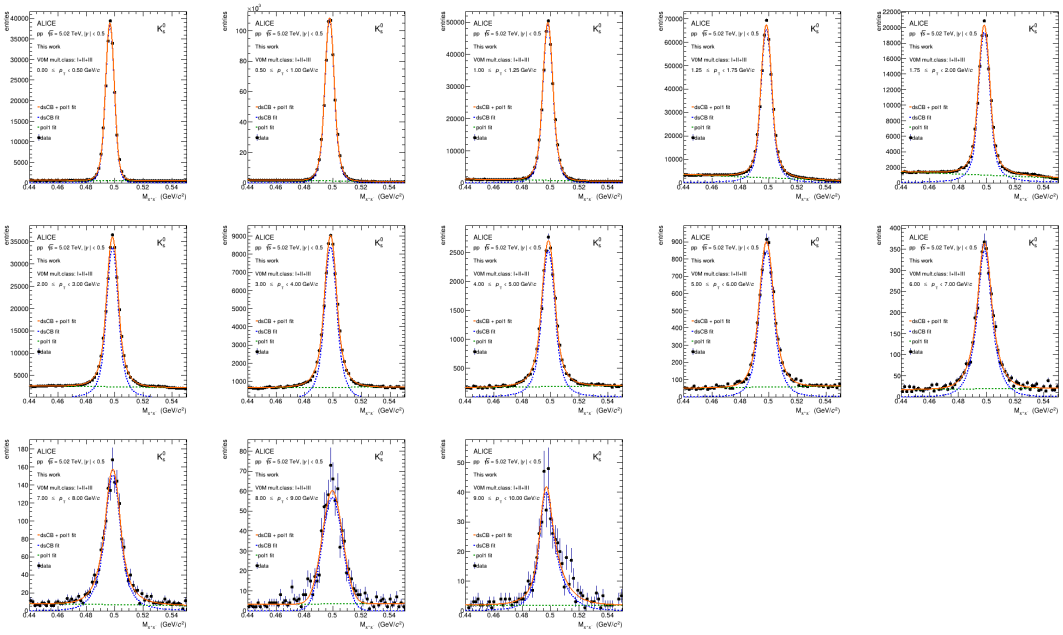

Figure 9.1: K^0_S 1D invariant mass spectra fit for different p_T bins in the range [0,10] GeV/c for $0 \leq V0M < 1\%$. In the first line, starting on the left there are the 1D invariant mass spectra for p_T intervals [0,0.5) GeV/c, [0.5,1) GeV/c, [1,1.25) GeV/c, [1.25,1.75) GeV/c, [1.75,2) GeV/c, in the second line there are the 1D invariant mass spectra for p_T intervals [2,3) GeV/c, [3,4) GeV/c, [4,5) GeV/c, [5,6) GeV/c, [6,7) GeV/c and in the third line there are the 1D invariant mass spectra for p_T intervals [7,8) GeV/c, [8,9) GeV/c and [9,10) GeV/c.

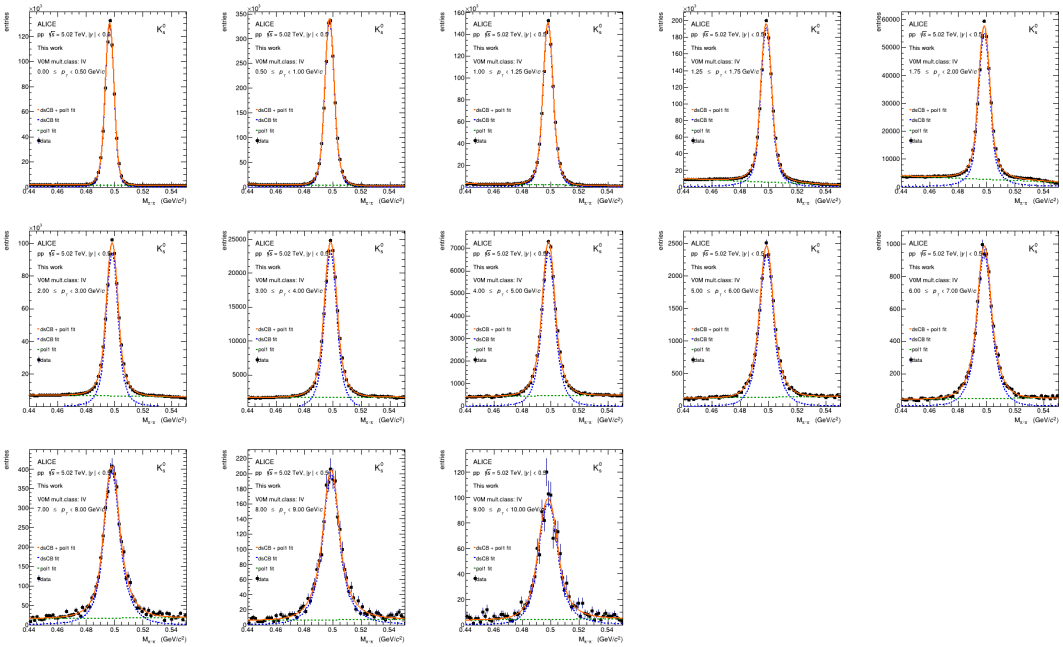

Figure 9.2: K^0_S 1D invariant mass spectra fit for different p_T bins in the range [0,10] GeV/c for $1 \leq V0M < 5\%$. In the first line, starting on the left there are the 1D invariant mass spectra for p_T intervals [0,0.5) GeV/c, [0.5,1) GeV/c, [1,1.25) GeV/c, [1.25,1.75) GeV/c, [1.75,2) GeV/c, in the second line there are the 1D invariant mass spectra for p_T intervals [2,3) GeV/c, [3,4) GeV/c, [4,5) GeV/c, [5,6) GeV/c, [6,7) GeV/c and in the third line there are the 1D invariant mass spectra for p_T intervals [7,8) GeV/c, [8,9) GeV/c and [9,10) GeV/c.

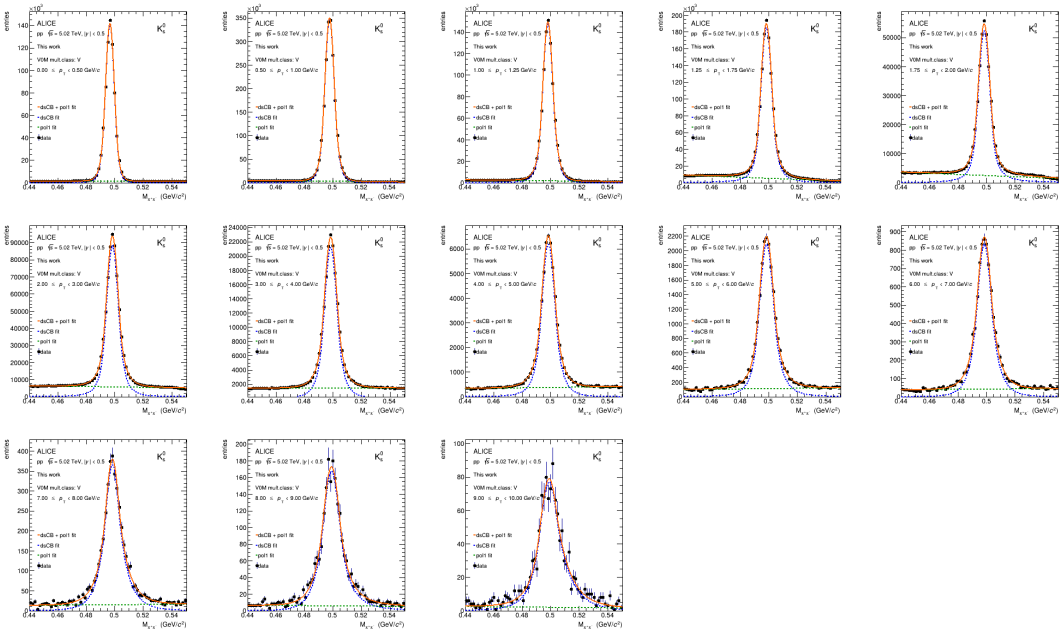

Figure 9.3: K^0_S 1D invariant mass spectra fit for different p_T bins in the range [0,10] GeV/c for $5 \leq V0M < 10\%$. In the first line, starting on the left there are the 1D invariant mass spectra for p_T intervals [0,0.5) GeV/c, [0.5,1) GeV/c, [1,1.25) GeV/c, [1.25,1.75) GeV/c, [1.75,2) GeV/c, in the second line there are the 1D invariant mass spectra for p_T intervals [2,3) GeV/c, [3,4) GeV/c, [4,5) GeV/c, [5,6) GeV/c, [6,7) GeV/c and in the third line there are the 1D invariant mass spectra for p_T intervals [7,8) GeV/c, [8,9) GeV/c and [9,10) GeV/c.

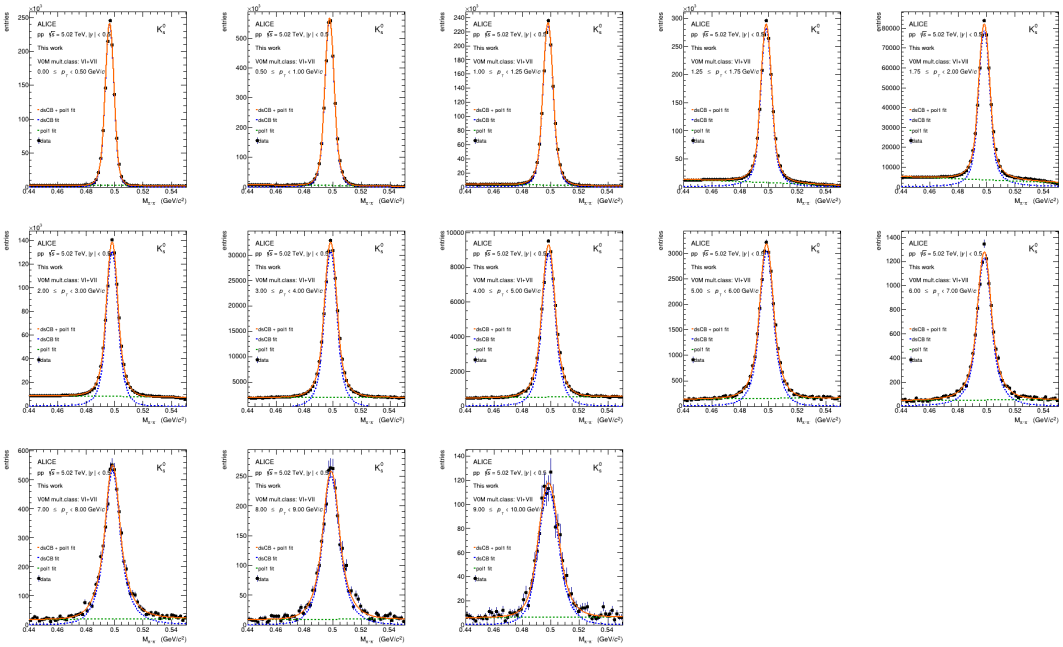

Figure 9.4: K^0_S 1D invariant mass spectra fit for different p_T bins in the range [0,10] GeV/c for $10 \leq V0M < 20\%$. In the first line, starting on the left there are the 1D invariant mass spectra for p_T intervals [0,0.5) GeV/c, [0.5,1) GeV/c, [1,1.25) GeV/c, [1.25,1.75) GeV/c, [1.75,2) GeV/c, in the second line there are the 1D invariant mass spectra for p_T intervals [2,3) GeV/c, [3,4) GeV/c, [4,5) GeV/c, [5,6) GeV/c, [6,7) GeV/c and in the third line there are the 1D invariant mass spectra for p_T intervals [7,8) GeV/c, [8,9) GeV/c and [9,10) GeV/c.

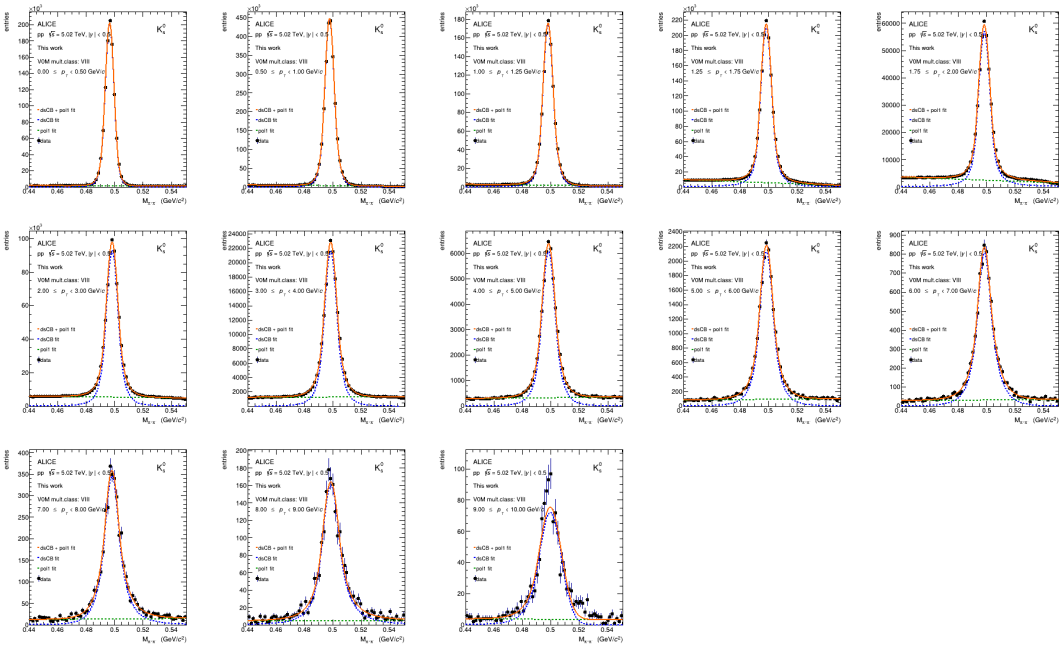

Figure 9.5: K^0_S 1D invariant mass spectra fit for different p_T bins in the range [0,10] GeV/c for $20 \leq V0M < 30\%$. In the first line, starting on the left there are the 1D invariant mass spectra for p_T intervals [0,0.5) GeV/c, [0.5,1) GeV/c, [1,1.25) GeV/c, [1.25,1.75) GeV/c, [1.75,2) GeV/c, in the second line there are the 1D invariant mass spectra for p_T intervals [2,3) GeV/c, [3,4) GeV/c, [4,5) GeV/c, [5,6) GeV/c, [6,7) GeV/c and in the third line there are the 1D invariant mass spectra for p_T intervals [7,8) GeV/c, [8,9) GeV/c and [9,10) GeV/c.

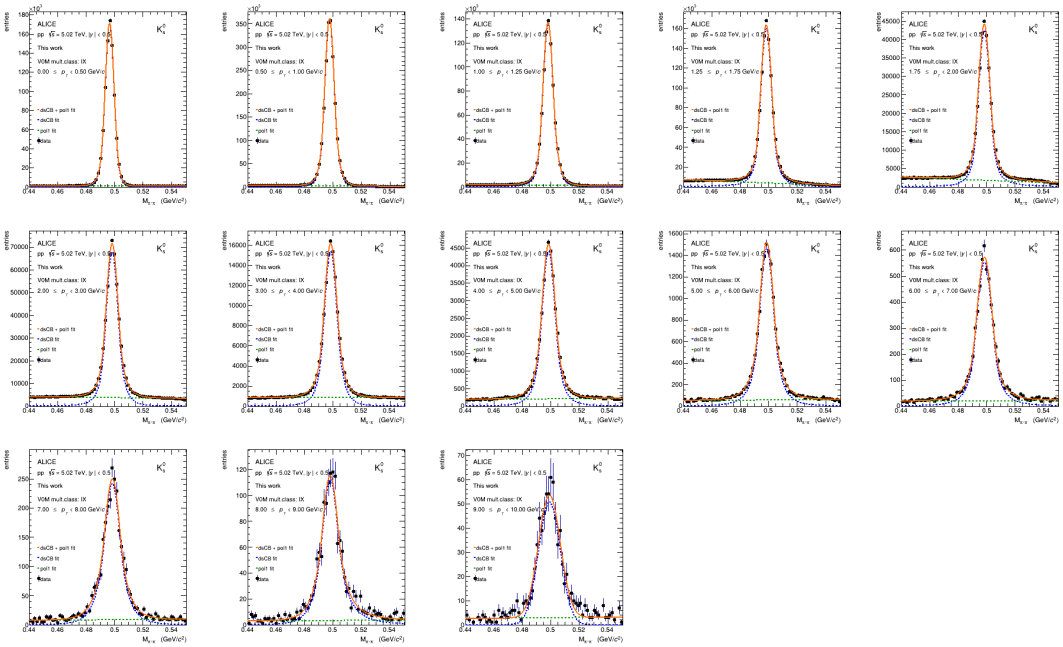

Figure 9.6: K^0_S 1D invariant mass spectra fit for different p_T bins in the range [0,10] GeV/c for $30 \leq V0M < 40\%$. In the first line, starting on the left there are the 1D invariant mass spectra for p_T intervals [0,0.5) GeV/c, [0.5,1) GeV/c, [1,1.25) GeV/c, [1.25,1.75) GeV/c, [1.75,2) GeV/c, in the second line there are the 1D invariant mass spectra for p_T intervals [2,3) GeV/c, [3,4) GeV/c, [4,5) GeV/c, [5,6) GeV/c, [6,7) GeV/c and in the third line there are the 1D invariant mass spectra for p_T intervals [7,8) GeV/c, [8,9) GeV/c and [9,10) GeV/c.

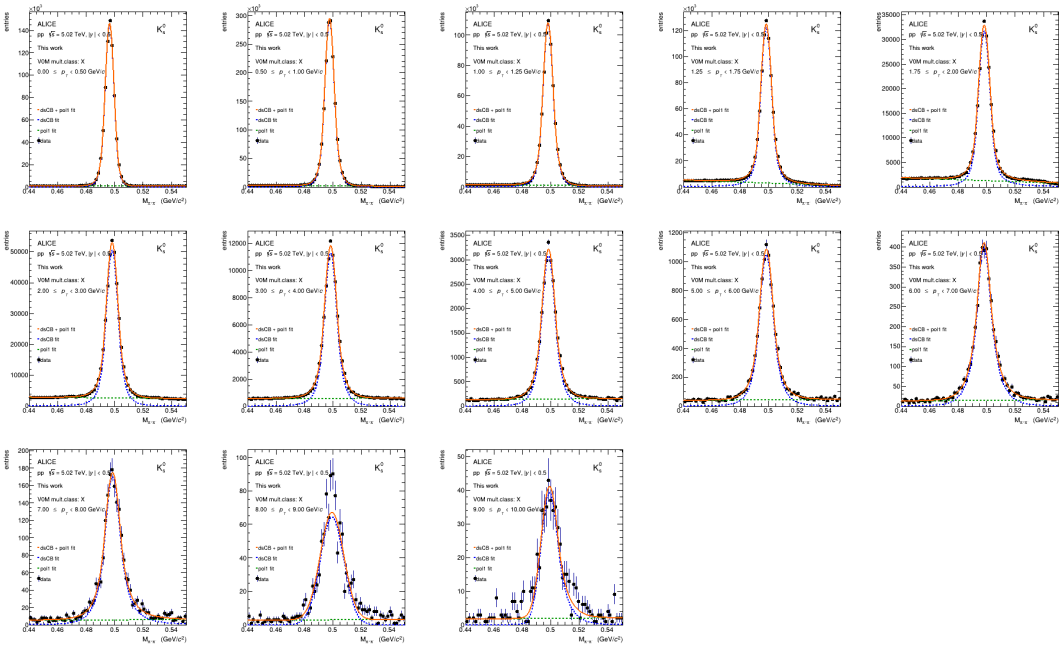

Figure 9.7: K^0_S 1D invariant mass spectra fit for different p_T bins in the range [0,10] GeV/c for $40 \leq V0M < 50\%$. In the first line, starting on the left there are the 1D invariant mass spectra for p_T intervals [0,0.5) GeV/c, [0.5,1) GeV/c, [1,1.25) GeV/c, [1.25,1.75) GeV/c, [1.75,2) GeV/c, in the second line there are the 1D invariant mass spectra for p_T intervals [2,3) GeV/c, [3,4) GeV/c, [4,5) GeV/c, [5,6) GeV/c, [6,7) GeV/c and in the third line there are the 1D invariant mass spectra for p_T intervals [7,8) GeV/c, [8,9) GeV/c and [9,10) GeV/c.

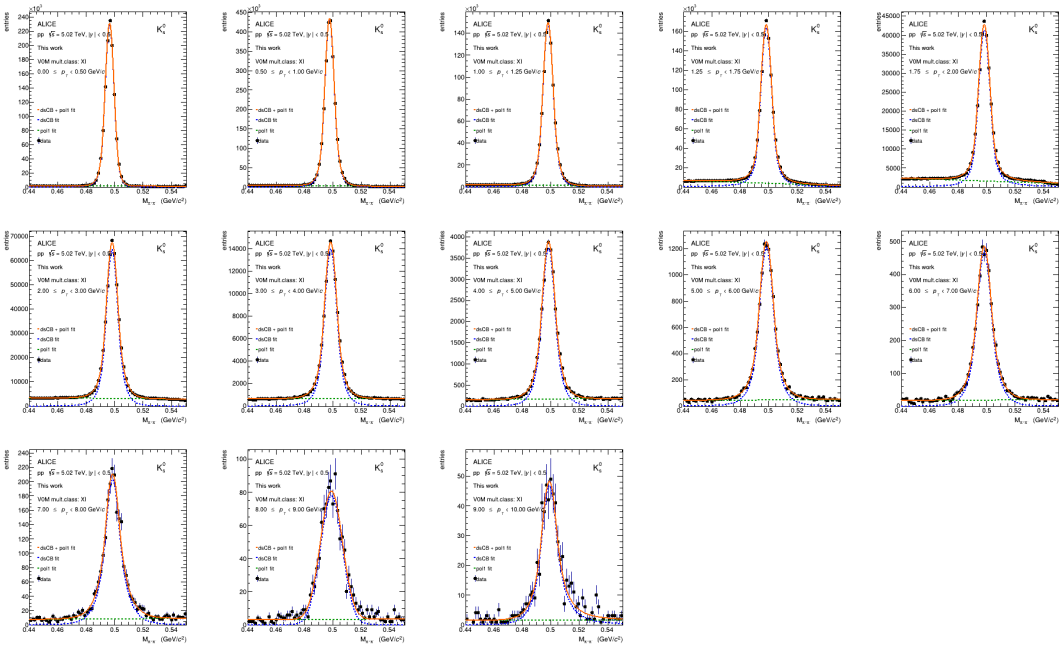

Figure 9.8: K^0_S 1D invariant mass spectra fit for different p_T bins in the range [0,10] GeV/c for $50 \leq V0M < 70\%$. In the first line, starting on the left there are the 1D invariant mass spectra for p_T intervals [0,0.5) GeV/c, [0.5,1) GeV/c, [1,1.25) GeV/c, [1.25,1.75) GeV/c, [1.75,2) GeV/c, in the second line there are the 1D invariant mass spectra for p_T intervals [2,3) GeV/c, [3,4) GeV/c, [4,5) GeV/c, [5,6) GeV/c, [6,7) GeV/c and in the third line there are the 1D invariant mass spectra for p_T intervals [7,8) GeV/c, [8,9) GeV/c and [9,10) GeV/c.

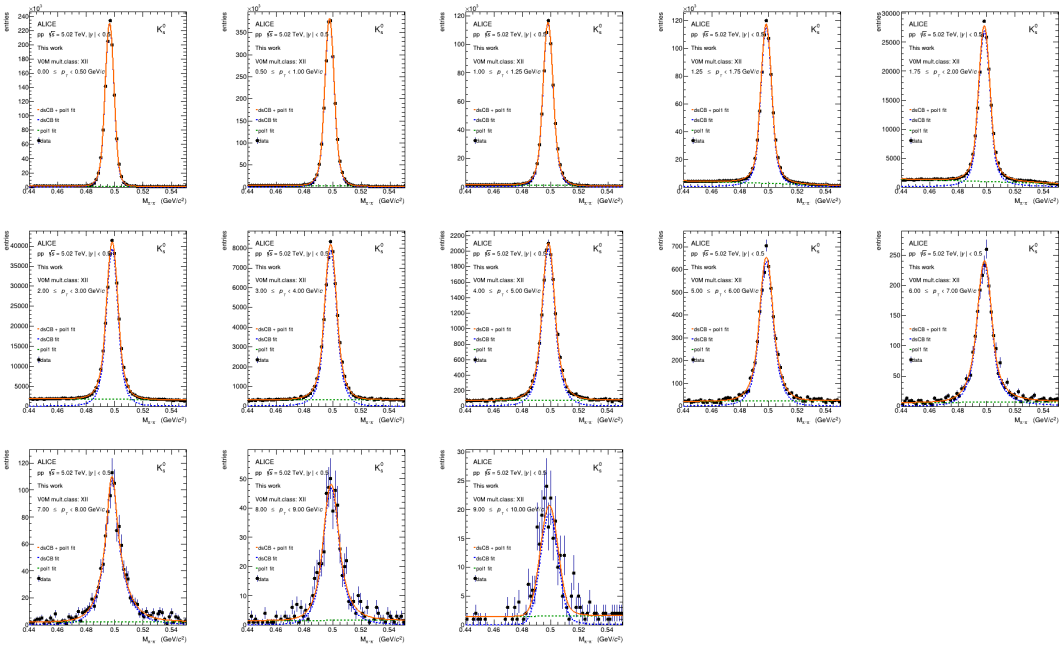

Figure 9.9: K^0_S 1D invariant mass spectra fit for different p_T bins in the range [0,10] GeV/c for $70 \leq V0M < 100\%$. In the first line, starting on the left there are the 1D invariant mass spectra for p_T intervals [0,0.5) GeV/c, [0.5,1) GeV/c, [1,1.25) GeV/c, [1.25,1.75) GeV/c, [1.75,2) GeV/c, in the second line there are the 1D invariant mass spectra for p_T intervals [2,3) GeV/c, [3,4) GeV/c, [4,5) GeV/c, [5,6) GeV/c, [6,7) GeV/c and in the third line there are the 1D invariant mass spectra for p_T intervals [7,8) GeV/c, [8,9) GeV/c and [9,10) GeV/c.

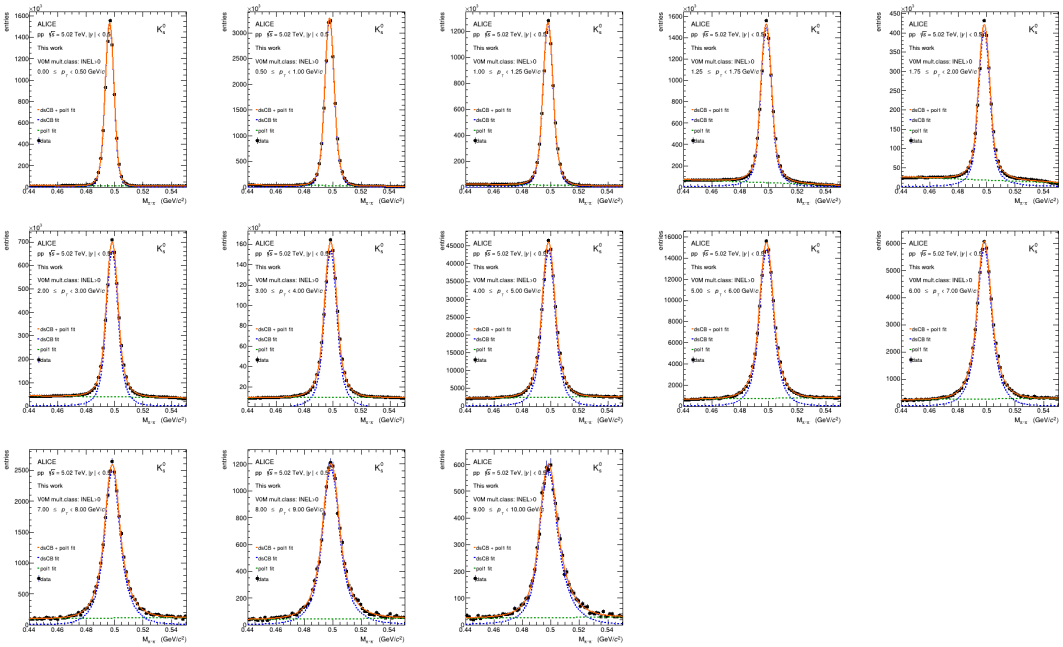

Figure 9.10: K^0_S 1D invariant mass spectra fit for different p_T bins in the range [0,10] GeV/c for $0 \leq V0M < 100\%$. In the first line, starting on the left there are the 1D invariant mass spectra for p_T intervals [0,0.5) GeV/c, [0.5,1) GeV/c, [1,1.25) GeV/c, [1.25,1.75) GeV/c, [1.75,2) GeV/c, in the second line there are the 1D invariant mass spectra for p_T intervals [2,3) GeV/c, [3,4) GeV/c, [4,5) GeV/c, [5,6) GeV/c, [6,7) GeV/c and in the third line there are the 1D invariant mass spectra for p_T intervals [7,8) GeV/c, [8,9) GeV/c and [9,10) GeV/c.

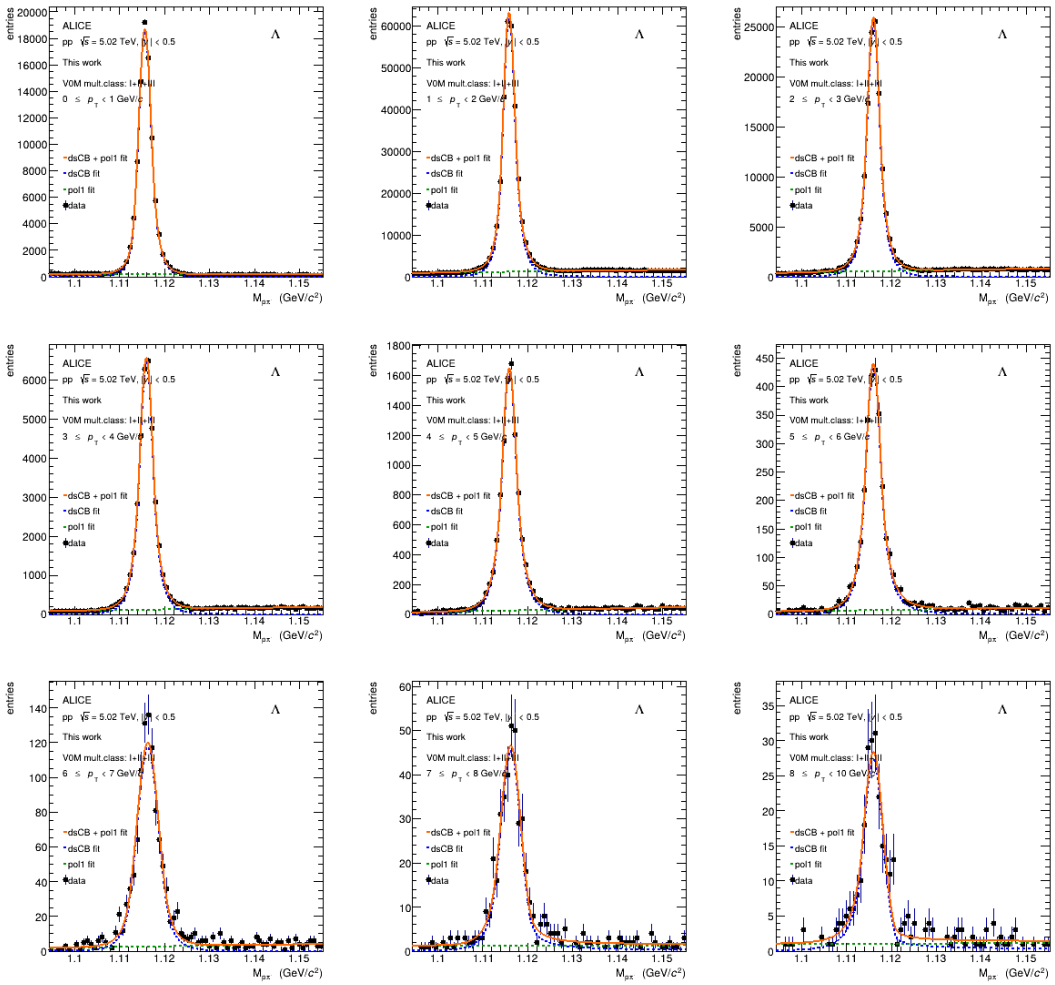

Figure 9.11: Λ 1D invariant mass spectra fit for different p_{T} bins in the range [0,10] GeV/c for $0 \leq V0M < 1\%$. In the first line, starting on the left there are the 1D invariant mass spectra for p_{T} intervals [0,1) GeV/c, [1,2) GeV/c, [2,3) GeV/c, in the second line there are the 1D invariant mass spectra for p_{T} intervals [3,4) GeV/c, [4,5) GeV/c, [5,6) GeV/c, and in the third line there are the 1D invariant mass spectra for p_{T} intervals [6,7) GeV/c, [7,8) GeV/c and [8,10) GeV/c.

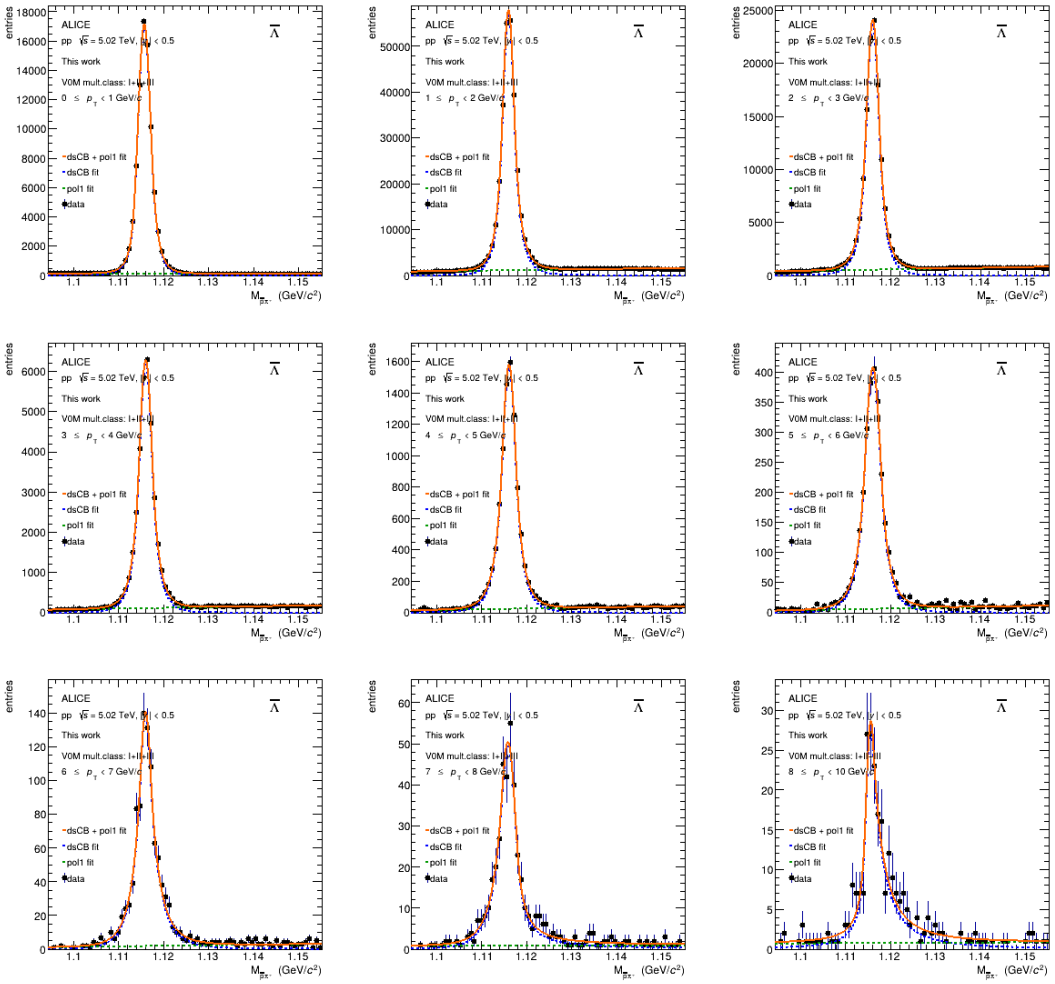

Figure 9.12: $\overline{\Lambda}$ 1D invariant mass spectra fit for different p_{T} bins in the range [0,10] GeV/c for $0 \leq V0M < 1\%$. In the first line, starting on the left there are the 1D invariant mass spectra for p_{T} intervals [0,1) GeV/c, [1,2) GeV/c, [2,3) GeV/c, in the second line there are the 1D invariant mass spectra for p_{T} intervals [3,4) GeV/c, [4,5) GeV/c, [5,6) GeV/c, and in the third line there are the 1D invariant mass spectra for p_{T} intervals [6,7) GeV/c, [7,8) GeV/c and [8,10) GeV/c.

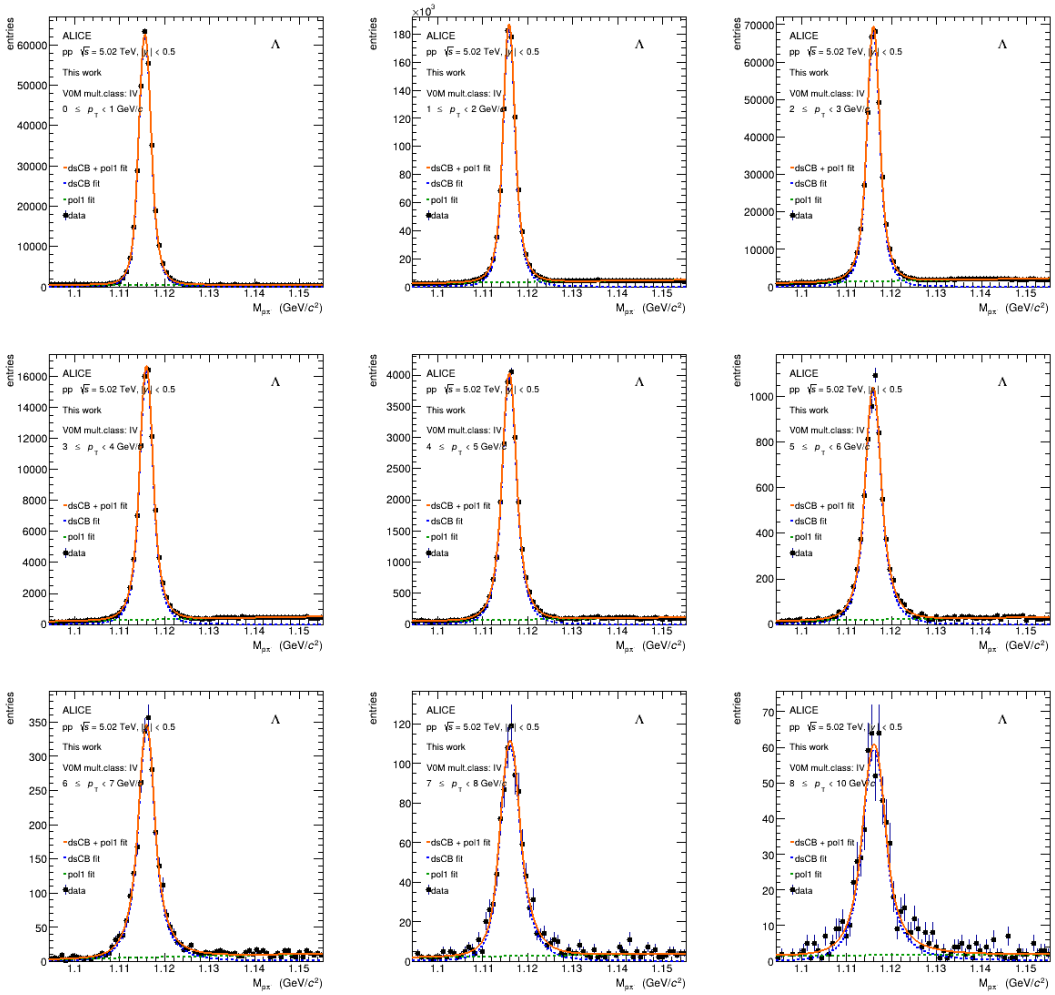

Figure 9.13: Λ 1D invariant mass spectra fit for different p_{T} bins in the range [0,10] GeV/c for $1 \leq V0M < 5\%$. In the first line, starting on the left there are the 1D invariant mass spectra for p_{T} intervals [0,1) GeV/c, [1,2) GeV/c, [2,3) GeV/c, in the second line there are the 1D invariant mass spectra for p_{T} intervals [3,4) GeV/c, [4,5) GeV/c, [5,6) GeV/c, and in the third line there are the 1D invariant mass spectra for p_{T} intervals [6,7) GeV/c, [7,8) GeV/c and [8,10) GeV/c.

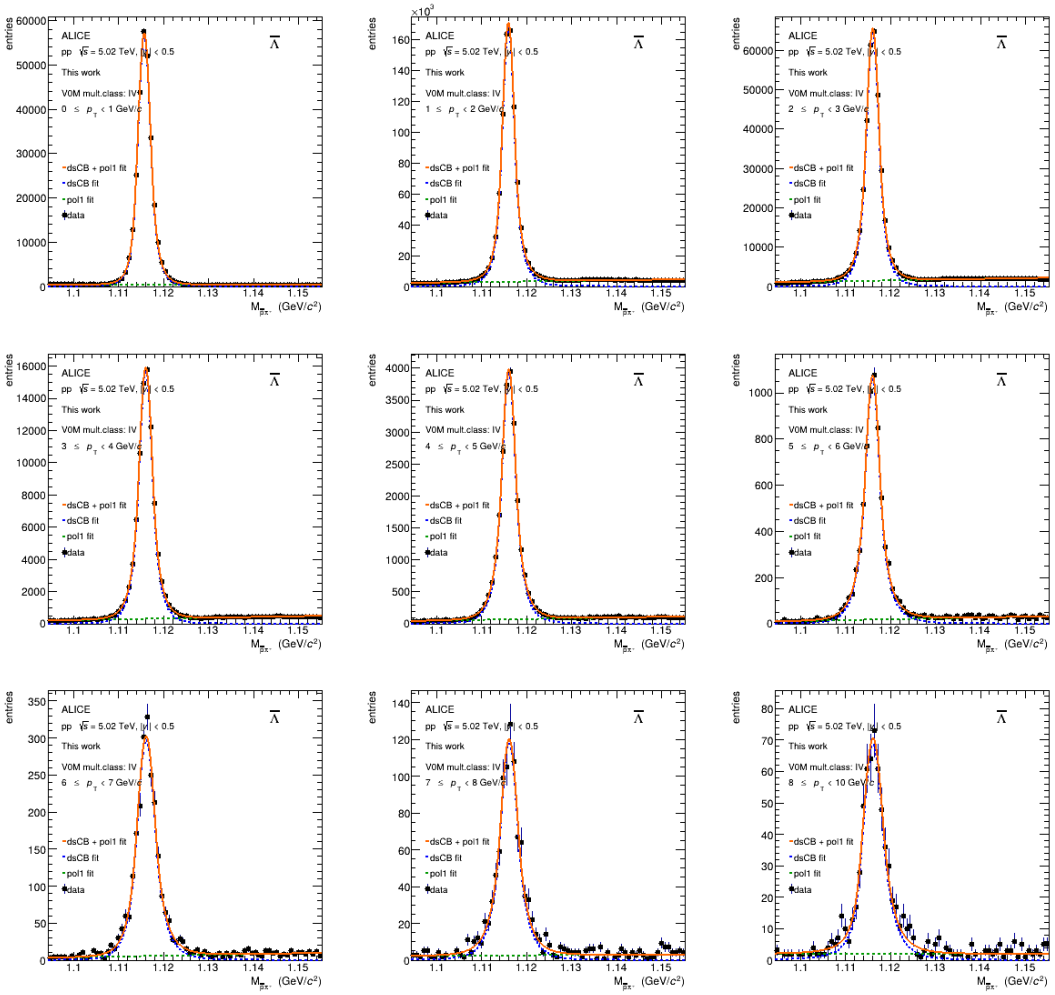

Figure 9.14: $\overline{\Lambda}$ 1D invariant mass spectra fit for different p_{T} bins in the range [0,10] GeV/c for $1 \leq V0M < 5\%$. In the first line, starting on the left there are the 1D invariant mass spectra for p_{T} intervals [0,1) GeV/c, [1,2) GeV/c, [2,3) GeV/c, in the second line there are the 1D invariant mass spectra for p_{T} intervals [3,4) GeV/c, [4,5) GeV/c, [5,6) GeV/c, and in the third line there are the 1D invariant mass spectra for p_{T} intervals [6,7) GeV/c, [7,8) GeV/c and [8,10) GeV/c.

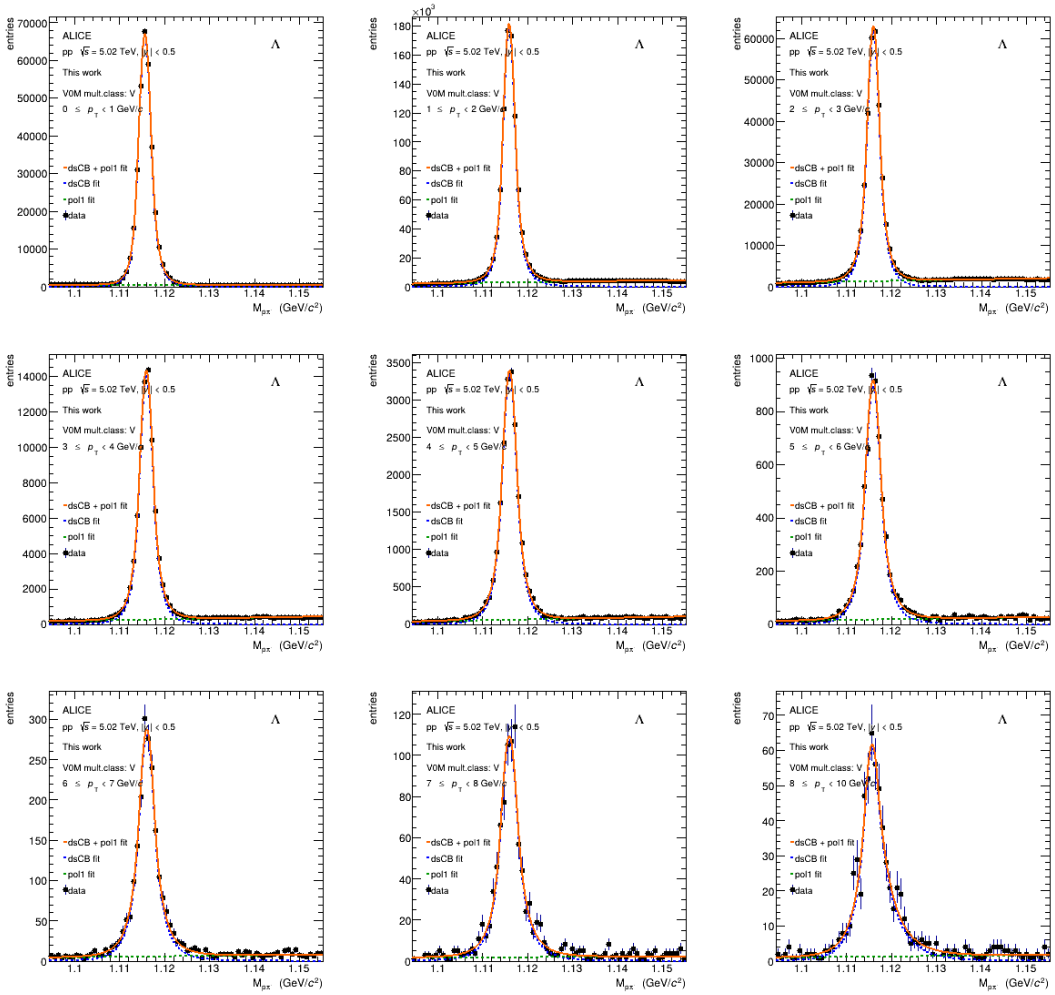

Figure 9.15: Λ 1D invariant mass spectra fit for different p_{T} bins in the range [0,10] GeV/c for $5 \leq V0M < 10\%$. In the first line, starting on the left there are the 1D invariant mass spectra for p_{T} intervals [0,1) GeV/c, [1,2) GeV/c, [2,3) GeV/c, in the second line there are the 1D invariant mass spectra for p_{T} intervals [3,4) GeV/c, [4,5) GeV/c, [5,6) GeV/c, and in the third line there are the 1D invariant mass spectra for p_{T} intervals [6,7) GeV/c, [7,8) GeV/c and [8,10) GeV/c.

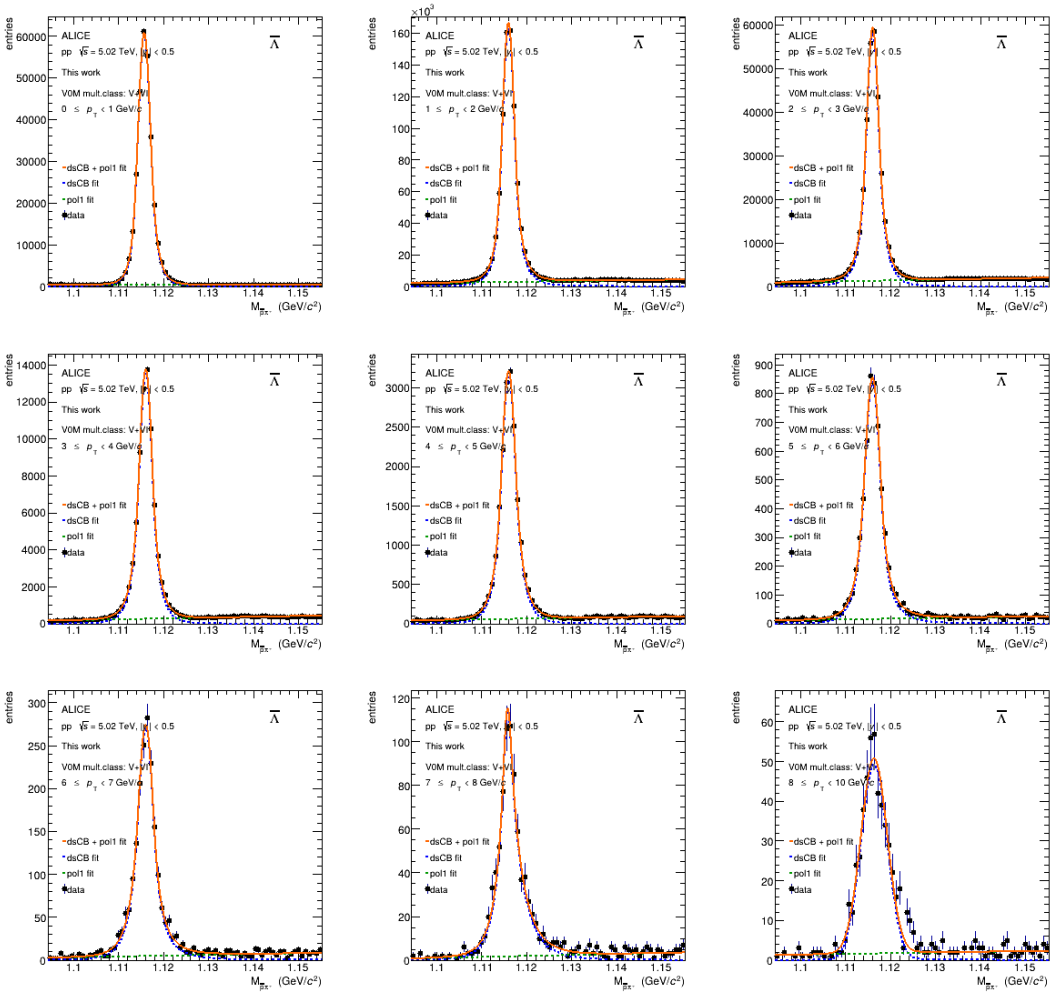

Figure 9.16: $\overline{\Lambda}$ 1D invariant mass spectra fit for different p_{T} bins in the range [0,10] GeV/c for $5 \leq V0M < 10\%$. In the first line, starting on the left there are the 1D invariant mass spectra for p_{T} intervals [0,1) GeV/c, [1,2) GeV/c, [2,3) GeV/c, in the second line there are the 1D invariant mass spectra for p_{T} intervals [3,4) GeV/c, [4,5) GeV/c, [5,6) GeV/c, and in the third line there are the 1D invariant mass spectra for p_{T} intervals [6,7) GeV/c, [7,8) GeV/c and [8,10) GeV/c.

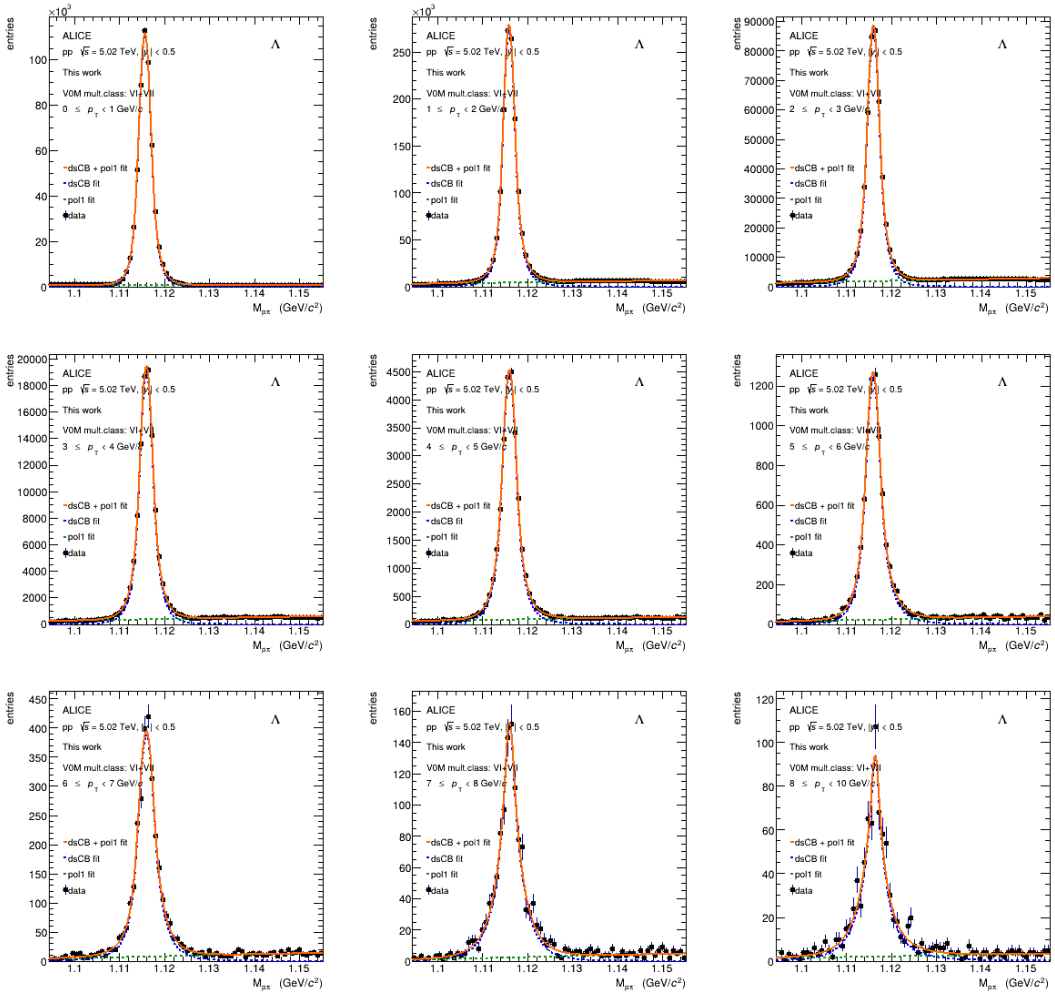

Figure 9.17: Λ 1D invariant mass spectra fit for different p_{T} bins in the range [0,10] GeV/c for $10 \leq V0M < 20\%$. In the first line, starting on the left there are the 1D invariant mass spectra for p_{T} intervals [0,1) GeV/c, [1,2) GeV/c, [2,3) GeV/c, in the second line there are the 1D invariant mass spectra for p_{T} intervals [3,4) GeV/c, [4,5) GeV/c, [5,6) GeV/c, and in the third line there are the 1D invariant mass spectra for p_{T} intervals [6,7) GeV/c, [7,8) GeV/c and [8,10) GeV/c.

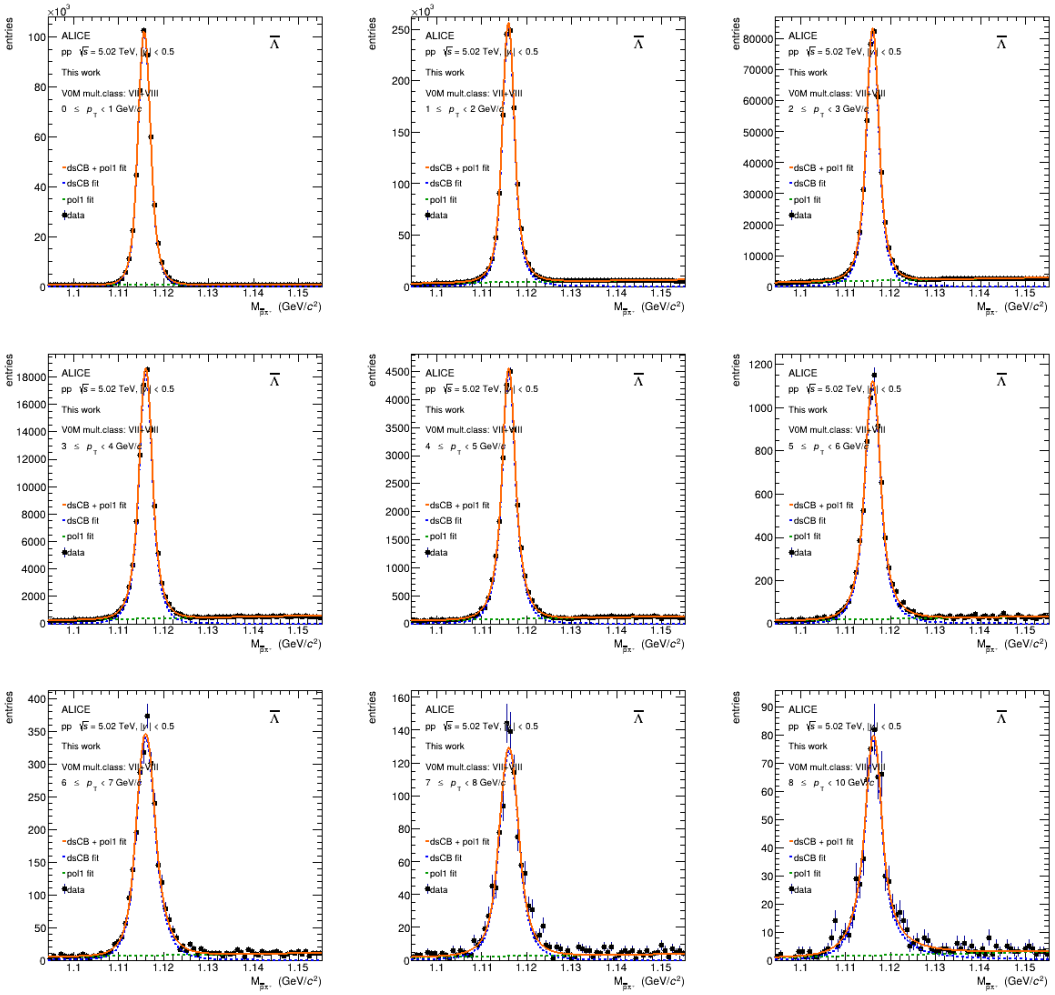

Figure 9.18: $\overline{\Lambda}$ 1D invariant mass spectra fit for different p_{T} bins in the range [0,10] GeV/c for $10 \leq V0M < 20\%$. In the first line, starting on the left there are the 1D invariant mass spectra for p_{T} intervals [0,1) GeV/c, [1,2) GeV/c, [2,3) GeV/c, in the second line there are the 1D invariant mass spectra for p_{T} intervals [3,4) GeV/c, [4,5) GeV/c, [5,6) GeV/c, and in the third line there are the 1D invariant mass spectra for p_{T} intervals [6,7) GeV/c, [7,8) GeV/c and [8,10) GeV/c.

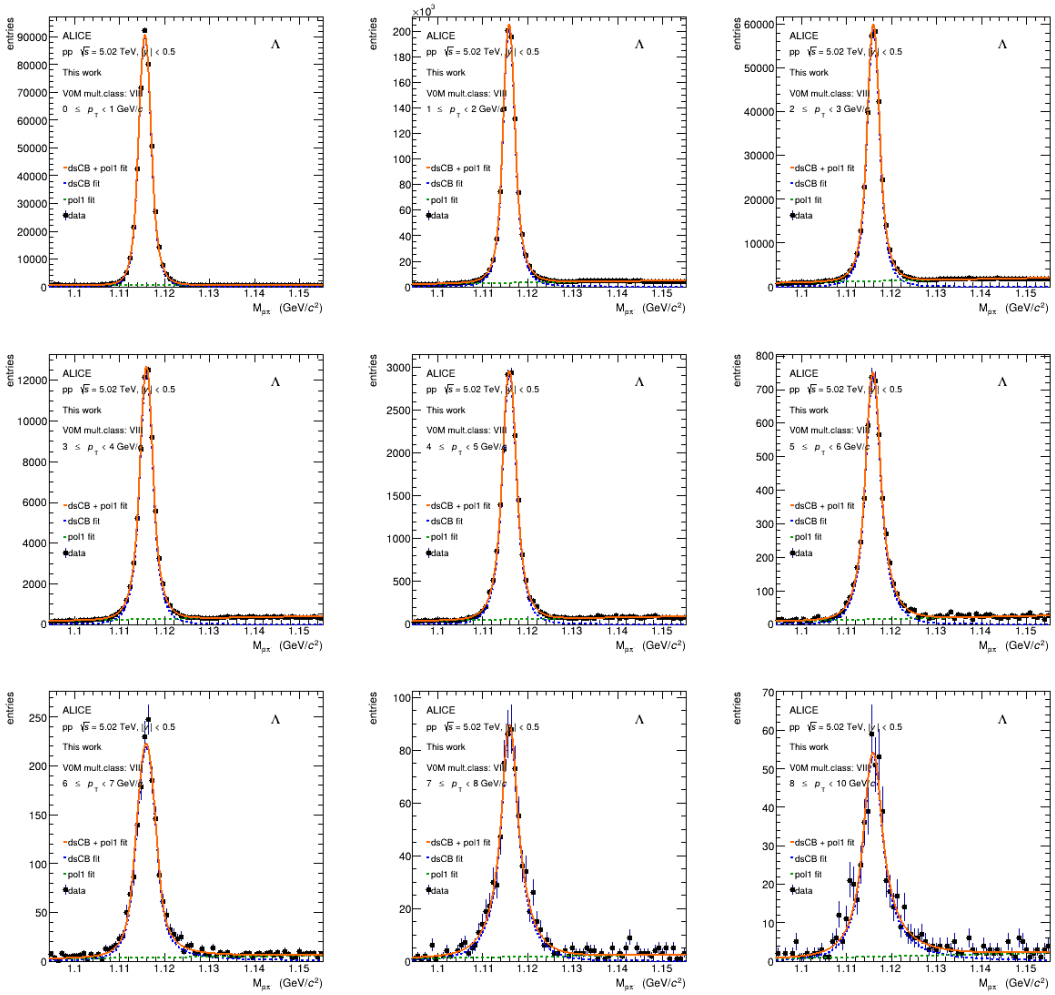

Figure 9.19: Λ 1D invariant mass spectra fit for different p_{T} bins in the range [0,10] GeV/c for $20 \leq V0M < 30\%$. In the first line, starting on the left there are the 1D invariant mass spectra for p_{T} intervals [0,1) GeV/c, [1,2) GeV/c, [2,3) GeV/c, in the second line there are the 1D invariant mass spectra for p_{T} intervals [3,4) GeV/c, [4,5) GeV/c, [5,6) GeV/c, and in the third line there are the 1D invariant mass spectra for p_{T} intervals [6,7) GeV/c, [7,8) GeV/c and [8,10) GeV/c.

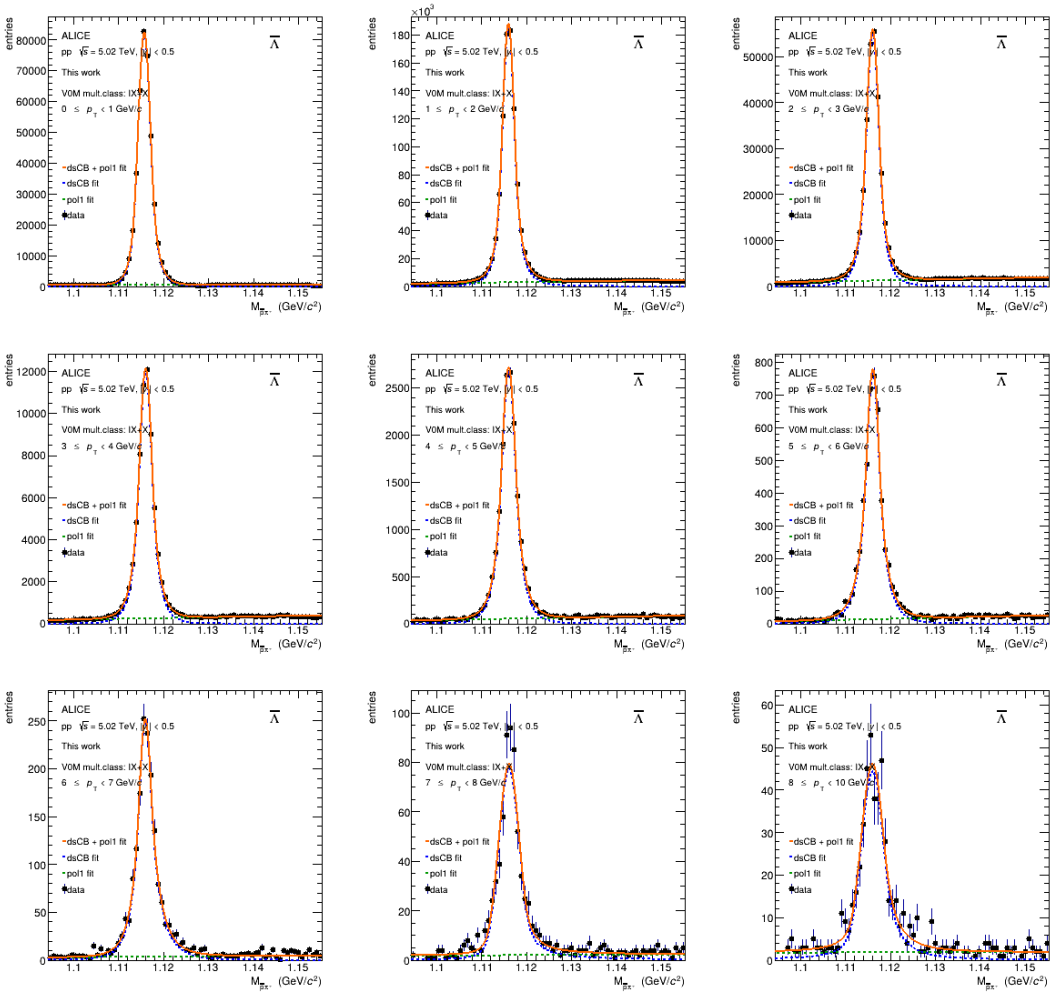

Figure 9.20: $\overline{\Lambda}$ 1D invariant mass spectra fit for different p_{T} bins in the range [0,10] GeV/c for $20 \leq V0M < 30\%$. In the first line, starting on the left there are the 1D invariant mass spectra for p_{T} intervals [0,1) GeV/c, [1,2) GeV/c, [2,3) GeV/c, in the second line there are the 1D invariant mass spectra for p_{T} intervals [3,4) GeV/c, [4,5) GeV/c, [5,6) GeV/c, and in the third line there are the 1D invariant mass spectra for p_{T} intervals [6,7) GeV/c, [7,8) GeV/c and [8,10) GeV/c.

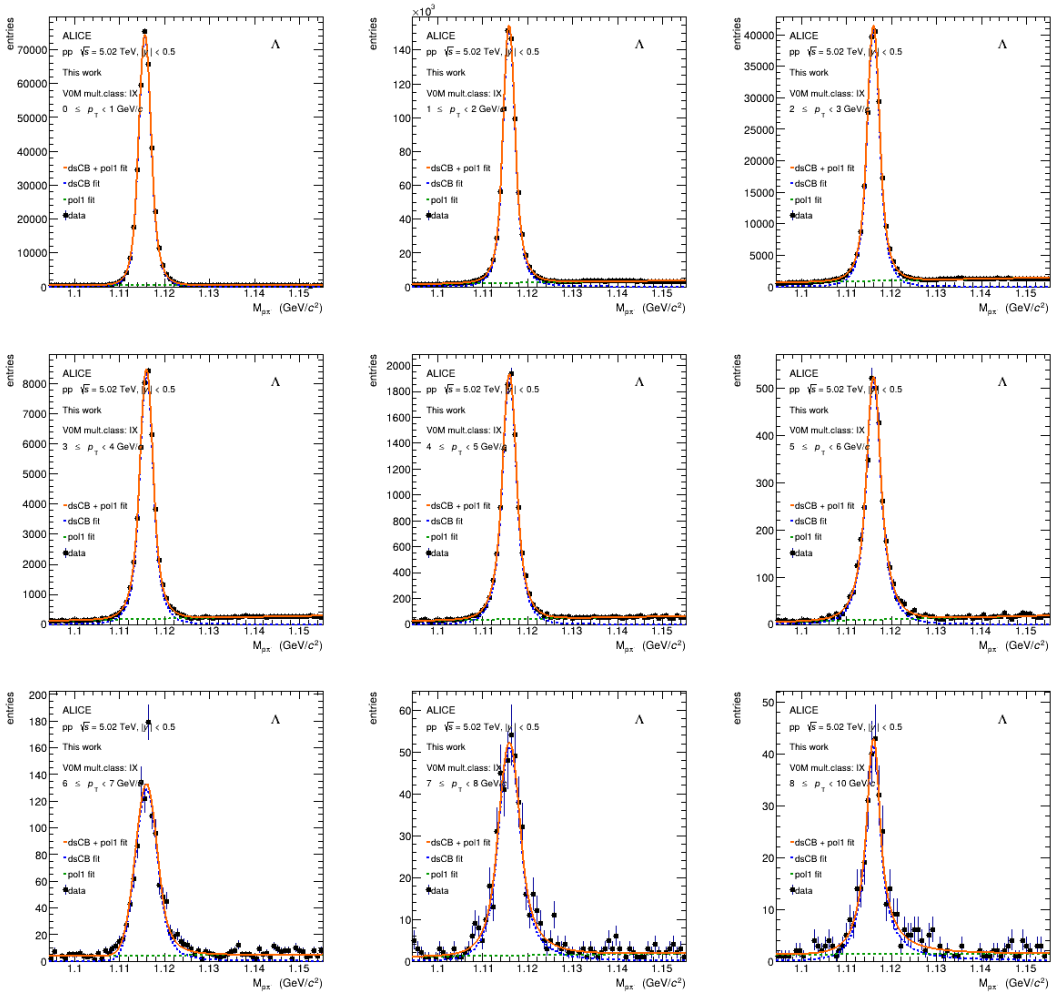

Figure 9.21: Λ 1D invariant mass spectra fit for different p_{T} bins in the range [0,10] GeV/c for $30 \leq V0M < 40\%$. In the first line, starting on the left there are the 1D invariant mass spectra for p_{T} intervals [0,1) GeV/c, [1,2) GeV/c, [2,3) GeV/c, in the second line there are the 1D invariant mass spectra for p_{T} intervals [3,4) GeV/c, [4,5) GeV/c, [5,6) GeV/c, and in the third line there are the 1D invariant mass spectra for p_{T} intervals [6,7) GeV/c, [7,8) GeV/c and [8,10) GeV/c.

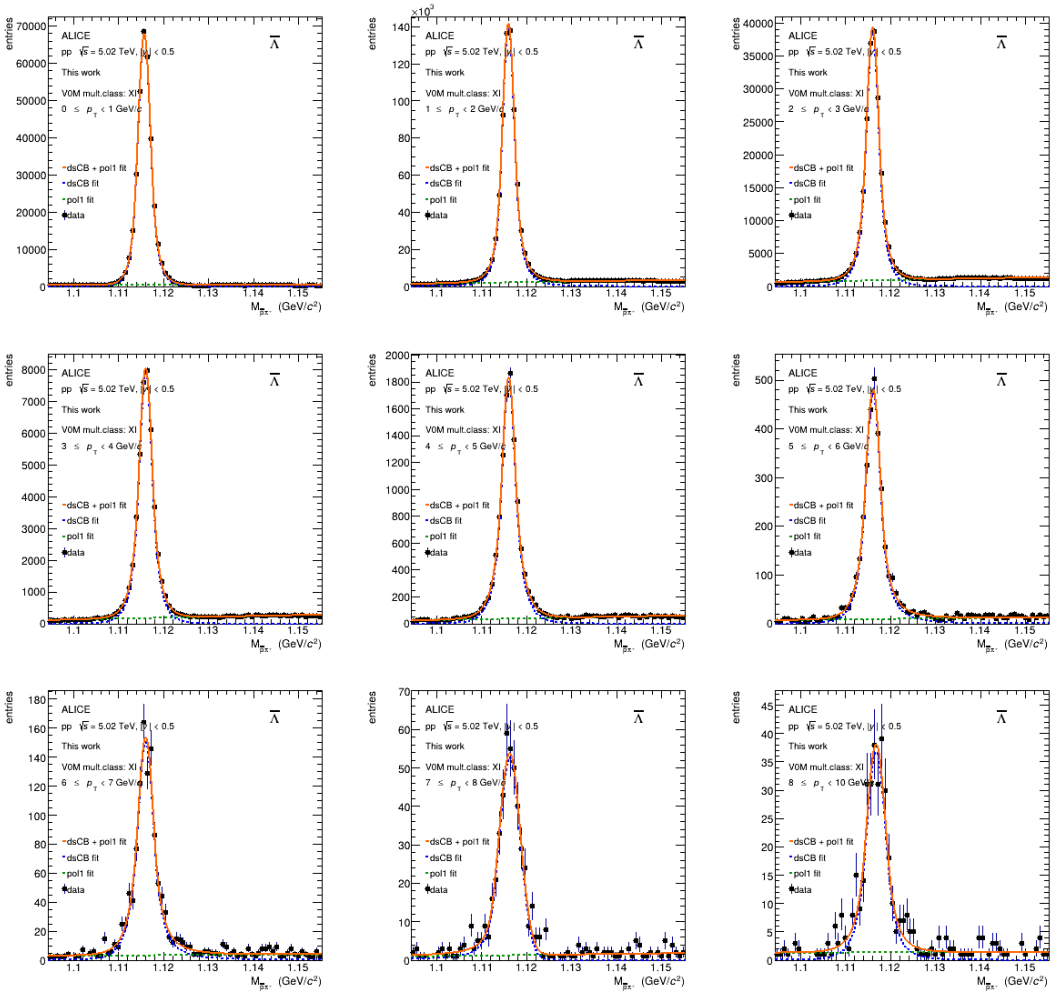

Figure 9.22: $\overline{\Lambda}$ 1D invariant mass spectra fit for different p_{T} bins in the range [0,10] GeV/c for $30 \leq V0M < 40\%$. In the first line, starting on the left there are the 1D invariant mass spectra for p_{T} intervals [0,1) GeV/c, [1,2) GeV/c, [2,3) GeV/c, in the second line there are the 1D invariant mass spectra for p_{T} intervals [3,4) GeV/c, [4,5) GeV/c, [5,6) GeV/c, and in the third line there are the 1D invariant mass spectra for p_{T} intervals [6,7) GeV/c, [7,8) GeV/c and [8,10) GeV/c.

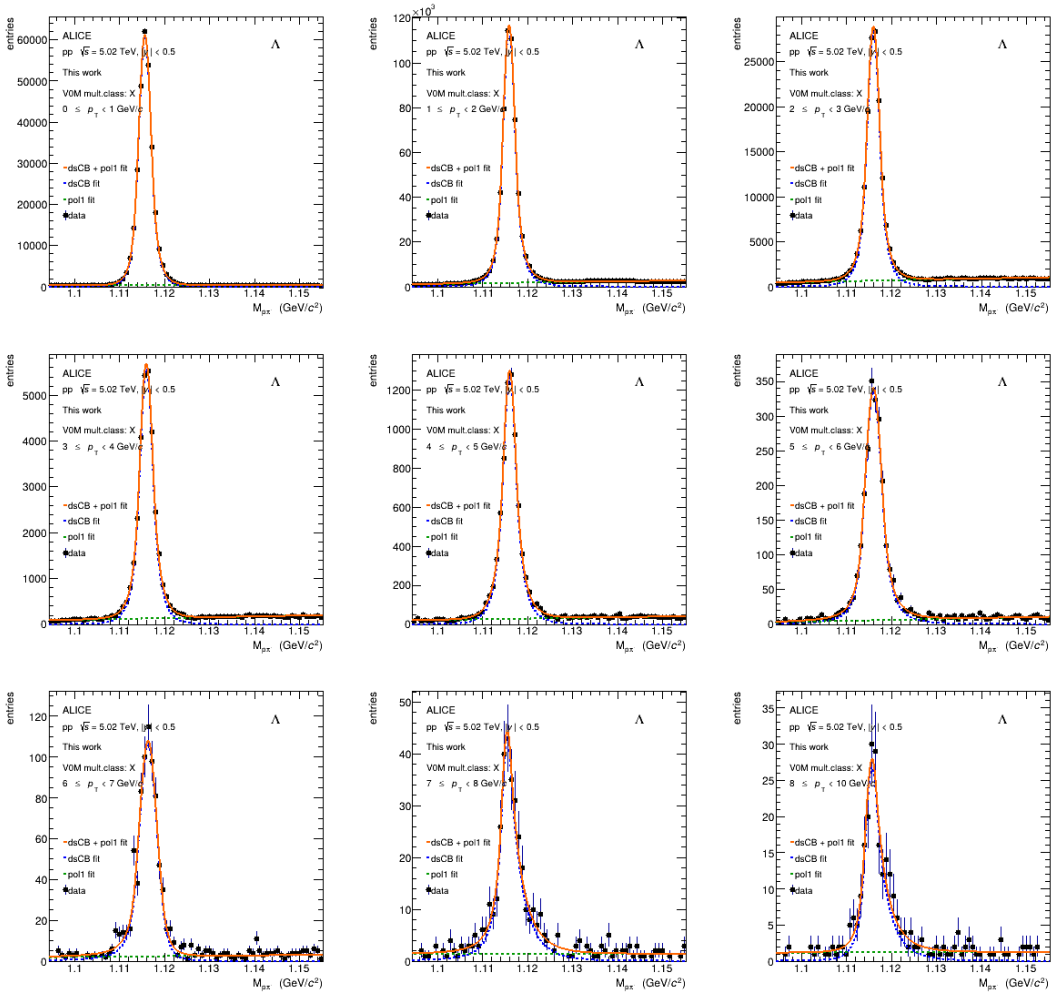

Figure 9.23: Λ 1D invariant mass spectra fit for different p_{T} bins in the range [0,10] GeV/c for $40 \leq V0M < 50\%$. In the first line, starting on the left there are the 1D invariant mass spectra for p_{T} intervals [0,1) GeV/c, [1,2) GeV/c, [2,3) GeV/c, in the second line there are the 1D invariant mass spectra for p_{T} intervals [3,4) GeV/c, [4,5) GeV/c, [5,6) GeV/c, and in the third line there are the 1D invariant mass spectra for p_{T} intervals [6,7) GeV/c, [7,8) GeV/c and [8,10) GeV/c.

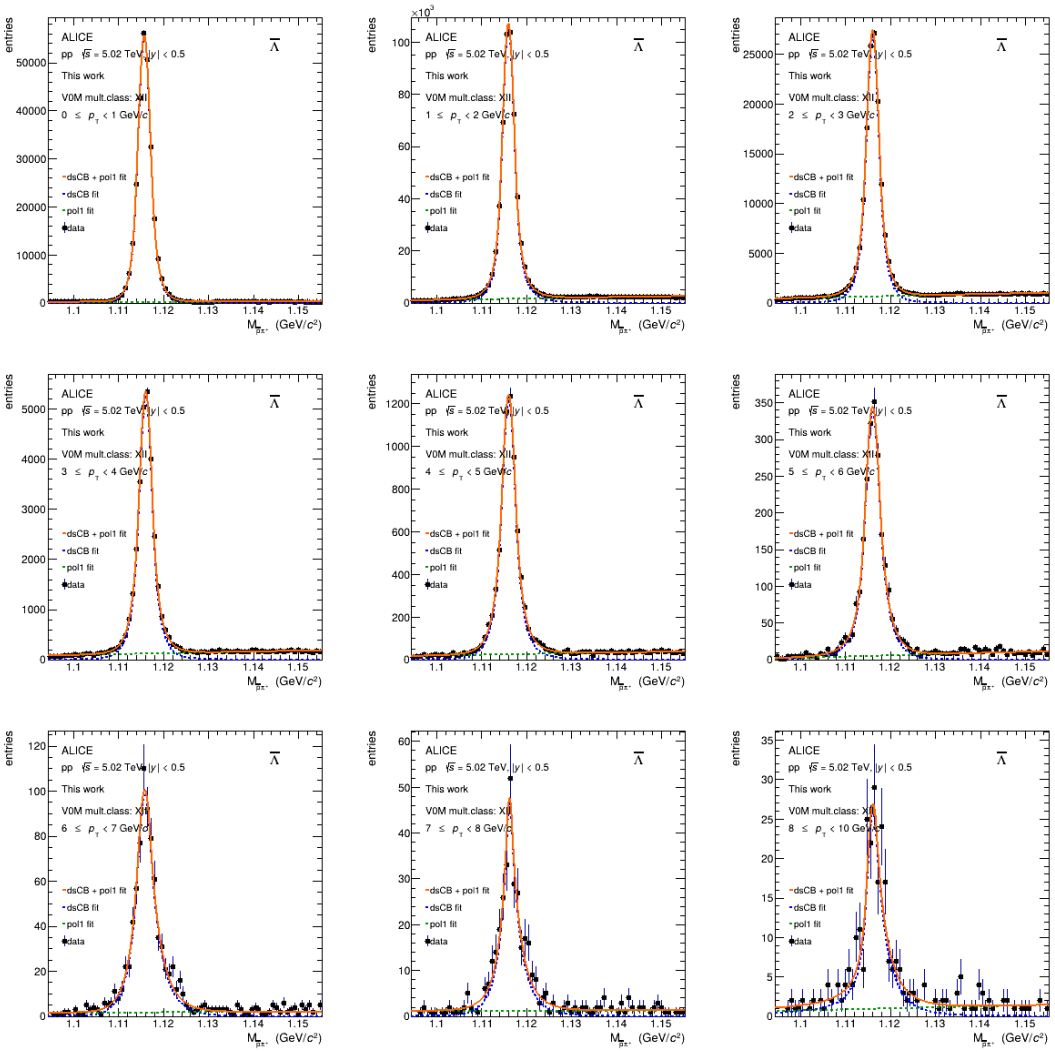

Figure 9.24: $\overline{\Lambda}$ 1D invariant mass spectra fit for different p_{T} bins in the range [0,10] GeV/c for $40 \leq V0M < 50\%$. In the first line, starting on the left there are the 1D invariant mass spectra for p_{T} intervals [0,1) GeV/c, [1,2) GeV/c, [2,3) GeV/c, in the second line there are the 1D invariant mass spectra for p_{T} intervals [3,4) GeV/c, [4,5) GeV/c, [5,6) GeV/c, and in the third line there are the 1D invariant mass spectra for p_{T} intervals [6,7) GeV/c, [7,8) GeV/c and [8,10) GeV/c.

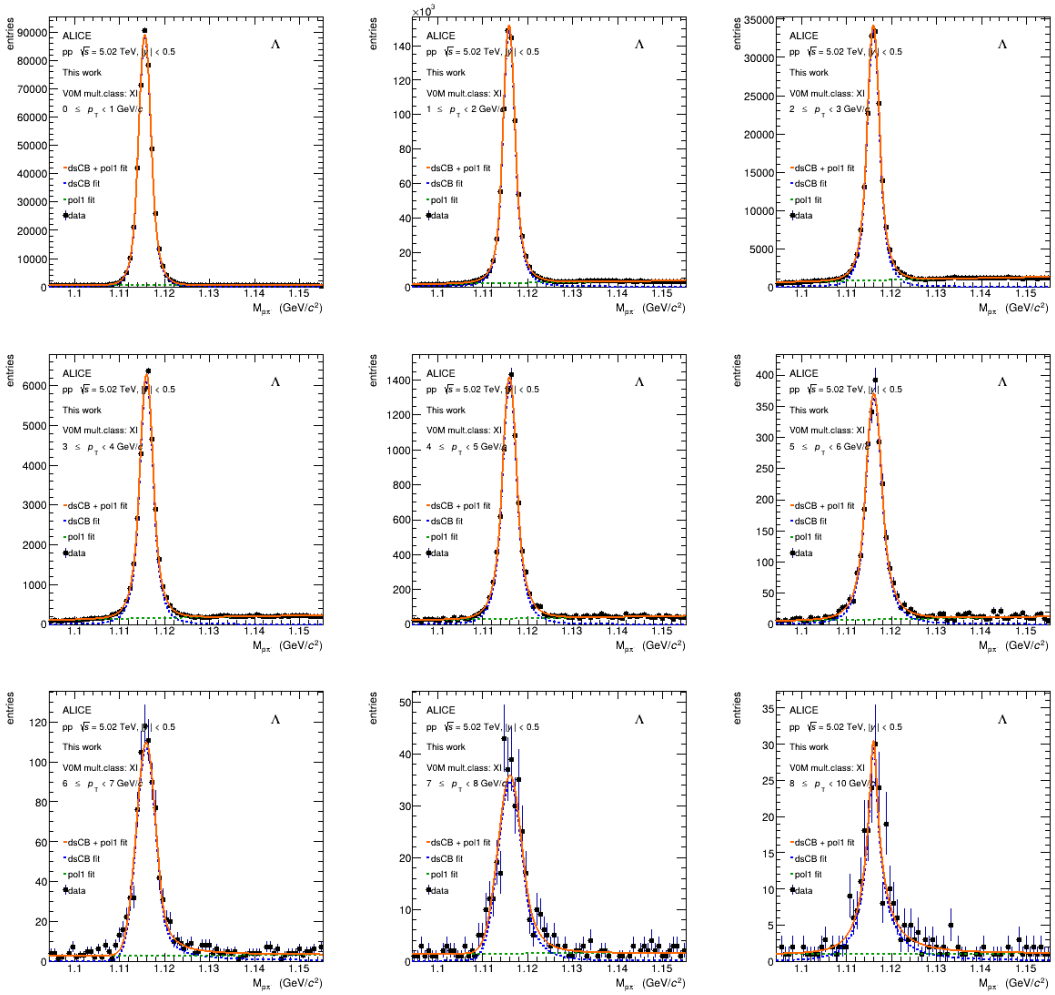

Figure 9.25: Λ 1D invariant mass spectra fit for different p_{T} bins in the range [0,10] GeV/c for $50 \leq V0M < 70\%$. In the first line, starting on the left there are the 1D invariant mass spectra for p_{T} intervals [0,1) GeV/c, [1,2) GeV/c, [2,3) GeV/c, in the second line there are the 1D invariant mass spectra for p_{T} intervals [3,4) GeV/c, [4,5) GeV/c, [5,6) GeV/c, and in the third line there are the 1D invariant mass spectra for p_{T} intervals [6,7) GeV/c, [7,8) GeV/c and [8,10) GeV/c.

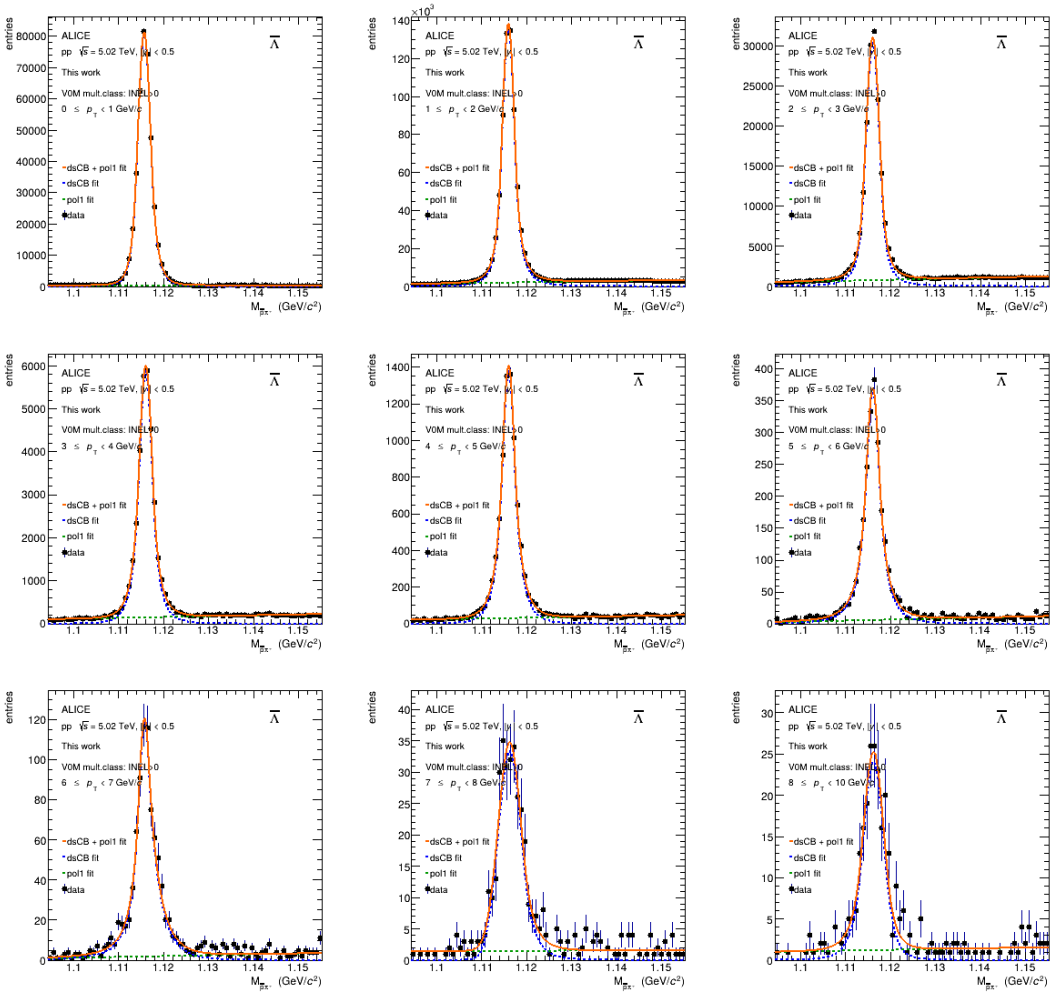

Figure 9.26: $\overline{\Lambda}$ 1D invariant mass spectra fit for different p_{T} bins in the range [0,10] GeV/c for $50 \leq V0M < 70\%$. In the first line, starting on the left there are the 1D invariant mass spectra for p_{T} intervals [0,1) GeV/c, [1,2) GeV/c, [2,3) GeV/c, in the second line there are the 1D invariant mass spectra for p_{T} intervals [3,4) GeV/c, [4,5) GeV/c, [5,6) GeV/c, and in the third line there are the 1D invariant mass spectra for p_{T} intervals [6,7) GeV/c, [7,8) GeV/c and [8,10) GeV/c.

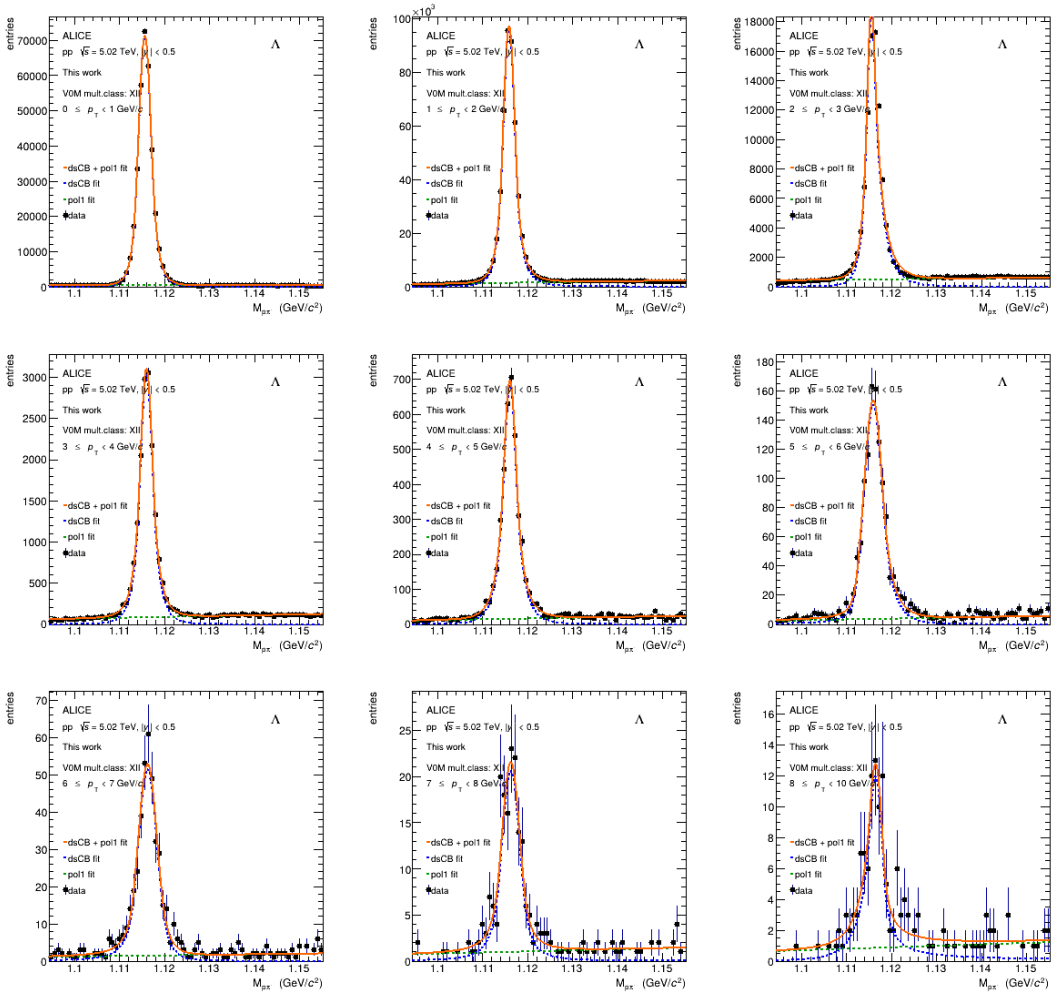

Figure 9.27: Λ 1D invariant mass spectra fit for different p_{T} bins in the range [0,10] GeV/c for $70 \leq V0M < 100\%$. In the first line, starting on the left there are the 1D invariant mass spectra for p_{T} intervals [0,1) GeV/c, [1,2) GeV/c, [2,3) GeV/c, in the second line there are the 1D invariant mass spectra for p_{T} intervals [3,4) GeV/c, [4,5) GeV/c, [5,6) GeV/c, and in the third line there are the 1D invariant mass spectra for p_{T} intervals [6,7) GeV/c, [7,8) GeV/c and [8,10) GeV/c.

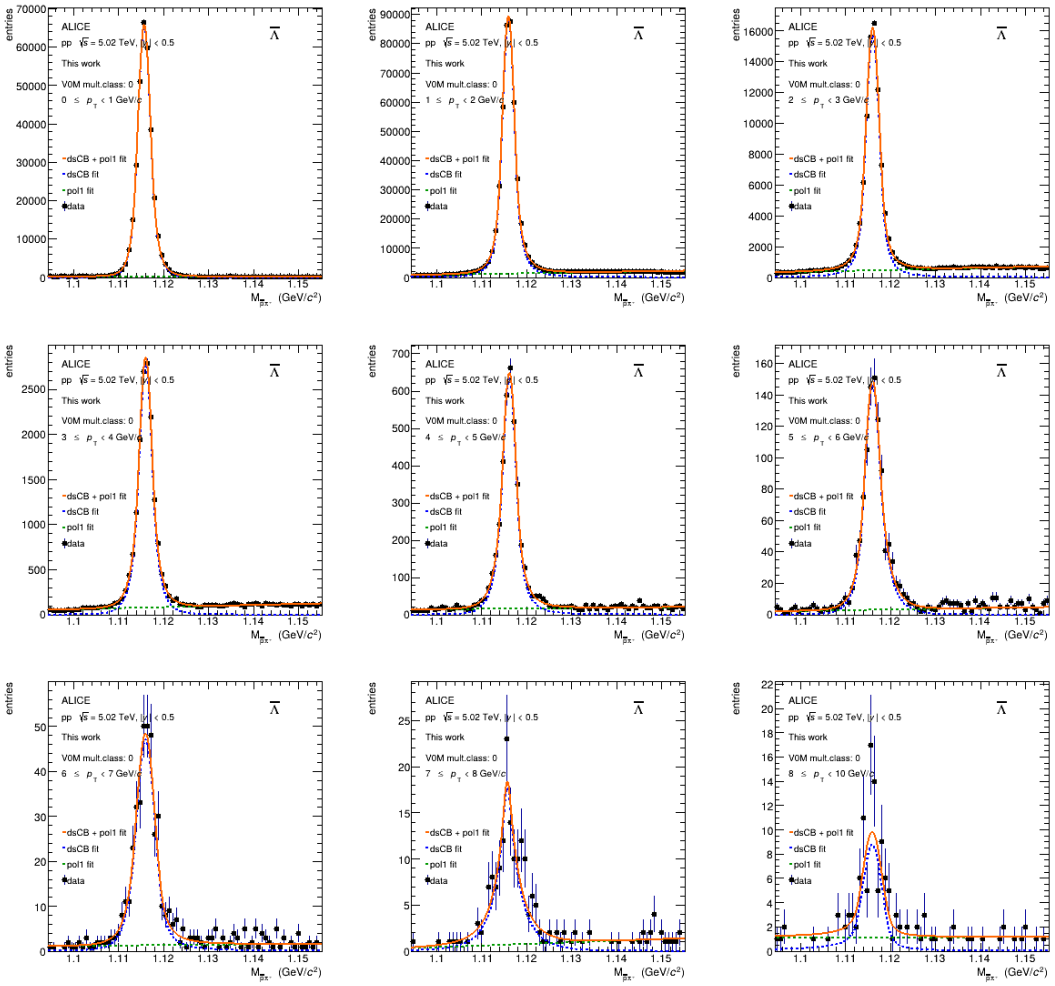

Figure 9.28: $\overline{\Lambda}$ 1D invariant mass spectra fit for different p_{T} bins in the range [0,10] GeV/c for $70 \leq V0M < 100\%$. In the first line, starting on the left there are the 1D invariant mass spectra for p_{T} intervals [0,1) GeV/c, [1,2) GeV/c, [2,3) GeV/c, in the second line there are the 1D invariant mass spectra for p_{T} intervals [3,4) GeV/c, [4,5) GeV/c, [5,6) GeV/c, and in the third line there are the 1D invariant mass spectra for p_{T} intervals [6,7) GeV/c, [7,8) GeV/c and [8,10) GeV/c.

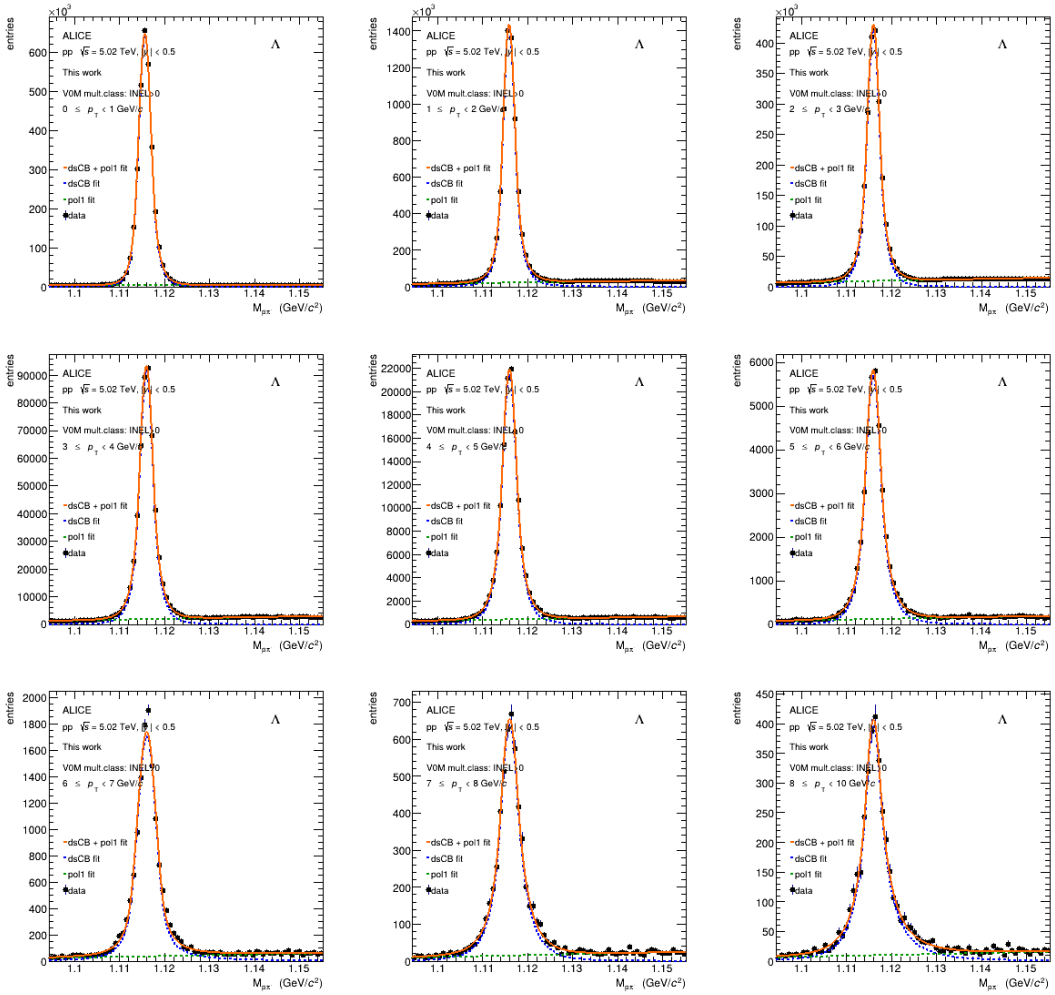

Figure 9.29: Λ 1D invariant mass spectra fit for different p_{T} bins in the range [0,10] GeV/c for $0 \leq V0M < 100\%$. In the first line, starting on the left there are the 1D invariant mass spectra for p_{T} intervals [0,1) GeV/c, [1,2) GeV/c, [2,3) GeV/c, in the second line there are the 1D invariant mass spectra for p_{T} intervals [3,4) GeV/c, [4,5) GeV/c, [5,6) GeV/c, and in the third line there are the 1D invariant mass spectra for p_{T} intervals [6,7) GeV/c, [7,8) GeV/c and [8,10) GeV/c.

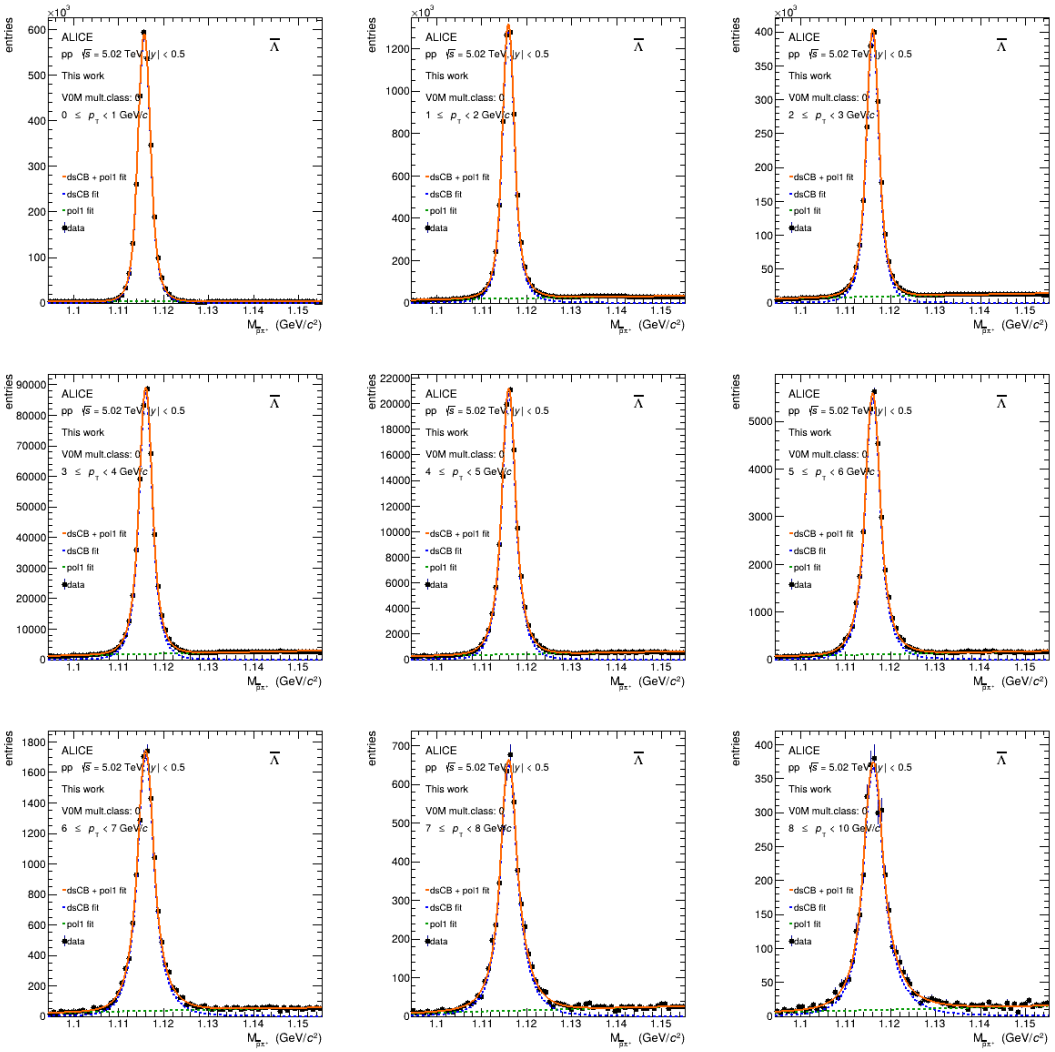

Figure 9.30: $\overline{\Lambda}$ 1D invariant mass spectra fit for different p_{T} bins in the range [0,10] GeV/c for $0 \leq V0M < 100\%$. In the first line, starting on the left there are the 1D invariant mass spectra for p_{T} intervals [0,1) GeV/c, [1,2) GeV/c, [2,3) GeV/c, in the second line there are the 1D invariant mass spectra for p_{T} intervals [3,4) GeV/c, [4,5) GeV/c, [5,6) GeV/c, and in the third line there are the 1D invariant mass spectra for p_{T} intervals [6,7) GeV/c, [7,8) GeV/c and [8,10) GeV/c.

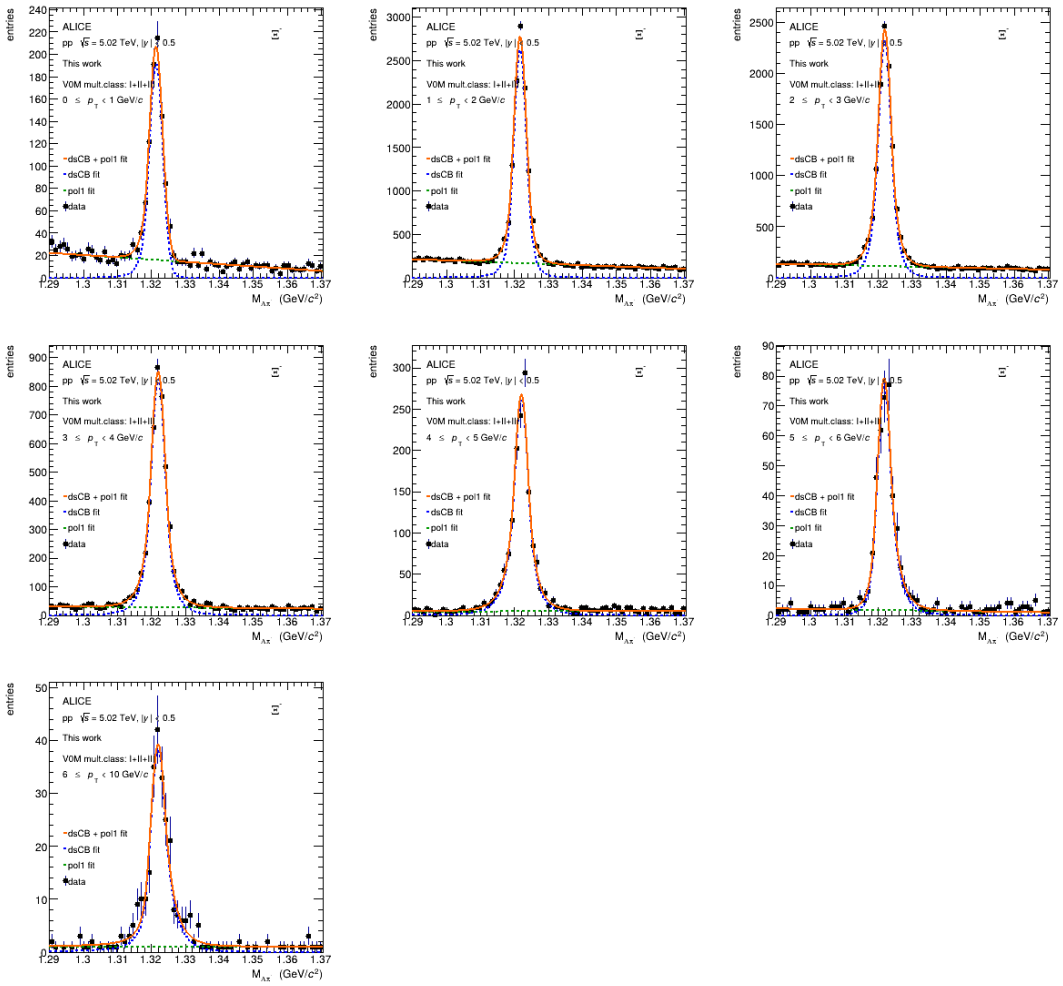

Figure 9.31: Ξ^- 1D invariant mass spectra fit for different p_{T} bins in the range [0,10] GeV/c for $0 \leq V0M < 1\%$. In the first line, starting on the left there are the 1D invariant mass spectra for p_{T} intervals [0,1) GeV/c, [1,2) GeV/c, [2,3) GeV/c, in the second line there are the 1D invariant mass spectra for p_{T} intervals [3,4) GeV/c, [4,5) GeV/c, [5,6) GeV/c and in the third line there is the 1D invariant mass spectra for p_{T} interval [6,10) GeV/c.

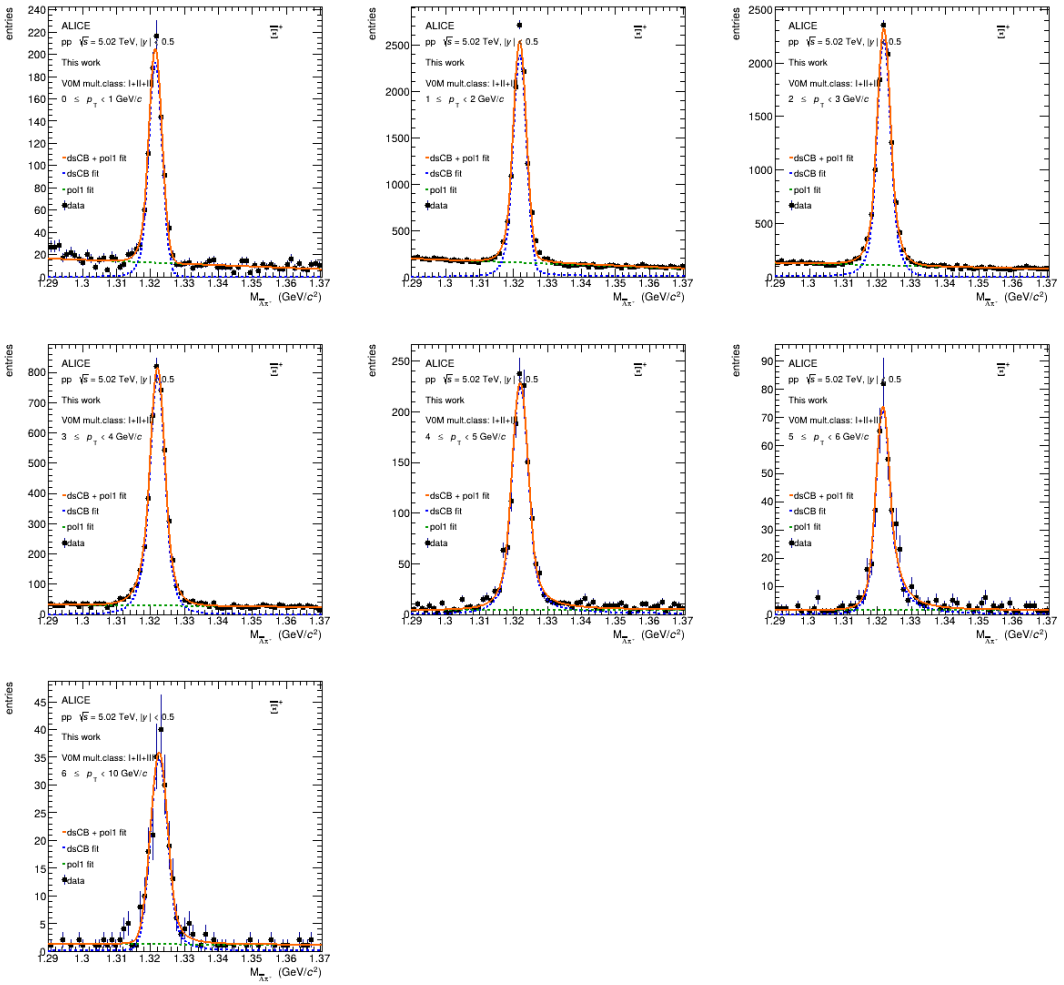

Figure 9.32: $\overline{\Xi}^{+}$ 1D invariant mass spectra fit for different p_{T} bins in the range [0,10] GeV/c for $0 \leq V0M < 1\%$. In the first line, starting on the left there are the 1D invariant mass spectra for p_{T} intervals [0,1) GeV/c, [1,2) GeV/c, [2,3) GeV/c, in the second line there are the 1D invariant mass spectra for p_{T} intervals [3,4) GeV/c, [4,5) GeV/c, [5,6) GeV/c and in the third line there is the 1D invariant mass spectra for p_{T} interval [6,10) GeV/c.

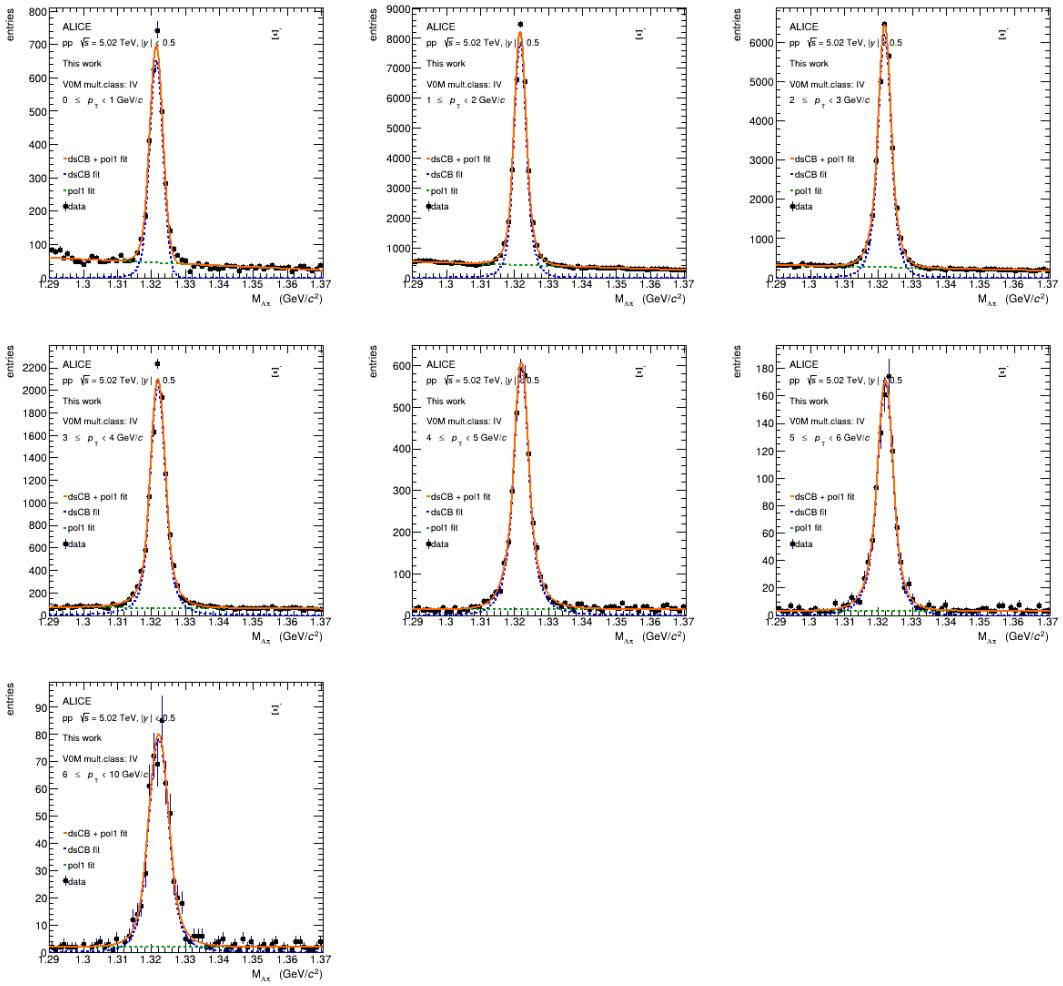

Figure 9.33: Ξ^- 1D invariant mass spectra fit for different p_{T} bins in the range [0,10] GeV/c for $1 \leq V0M < 5\%$. In the first line, starting on the left there are the 1D invariant mass spectra for p_{T} intervals [0,1) GeV/c, [1,2) GeV/c, [2,3) GeV/c, in the second line there are the 1D invariant mass spectra for p_{T} intervals [3,4) GeV/c, [4,5) GeV/c, [5,6) GeV/c and in the third line there is the 1D invariant mass spectra for p_{T} interval [6,10) GeV/c.

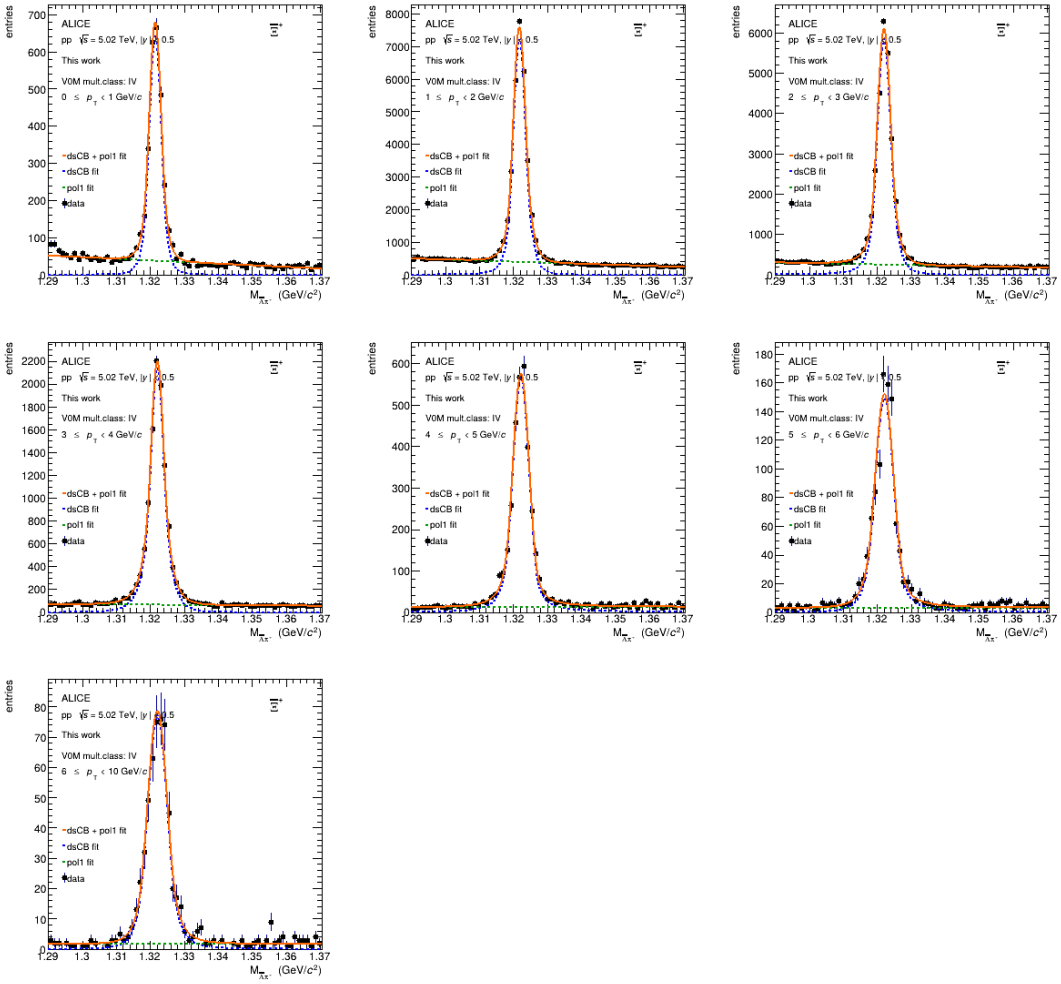

Figure 9.34: $\overline{\Xi}^+$ 1D invariant mass spectra fit for different p_{T} bins in the range [0,10] GeV/c for $1 \leq V0M < 5\%$. In the first line, starting on the left there are the 1D invariant mass spectra for p_{T} intervals [0,1) GeV/c, [1,2) GeV/c, [2,3) GeV/c, in the second line there are the 1D invariant mass spectra for p_{T} intervals [3,4) GeV/c, [4,5) GeV/c, [5,6) GeV/c and in the third line there is the 1D invariant mass spectra for p_{T} interval [6,10) GeV/c.

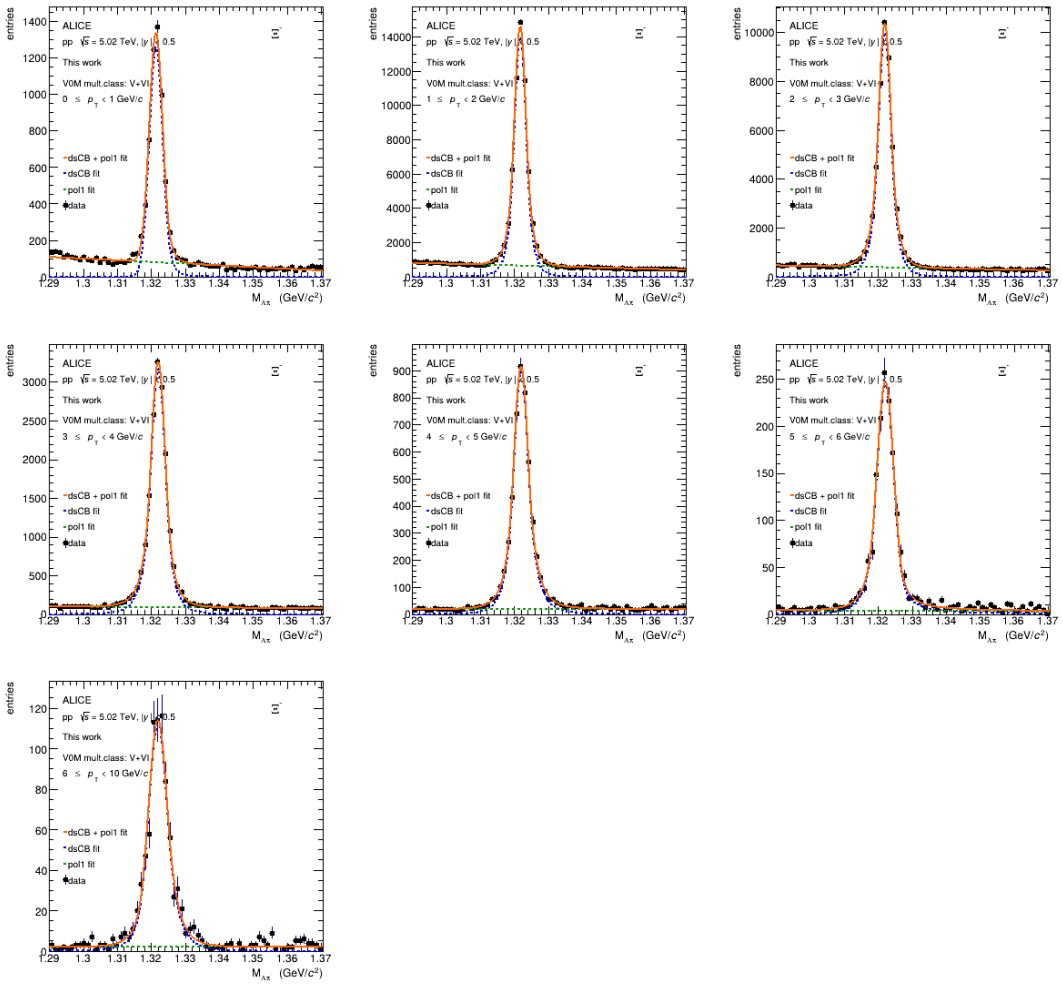

Figure 9.35: Ξ^- 1D invariant mass spectra fit for different p_{T} bins in the range [0,10] GeV/c for $5 \leq V0M < 15\%$. In the first line, starting on the left there are the 1D invariant mass spectra for p_{T} intervals [0,1) GeV/c, [1,2) GeV/c, [2,3) GeV/c, in the second line there are the 1D invariant mass spectra for p_{T} intervals [3,4) GeV/c, [4,5) GeV/c, [5,6) GeV/c and in the third line there is the 1D invariant mass spectra for p_{T} interval [6,10) GeV/c.

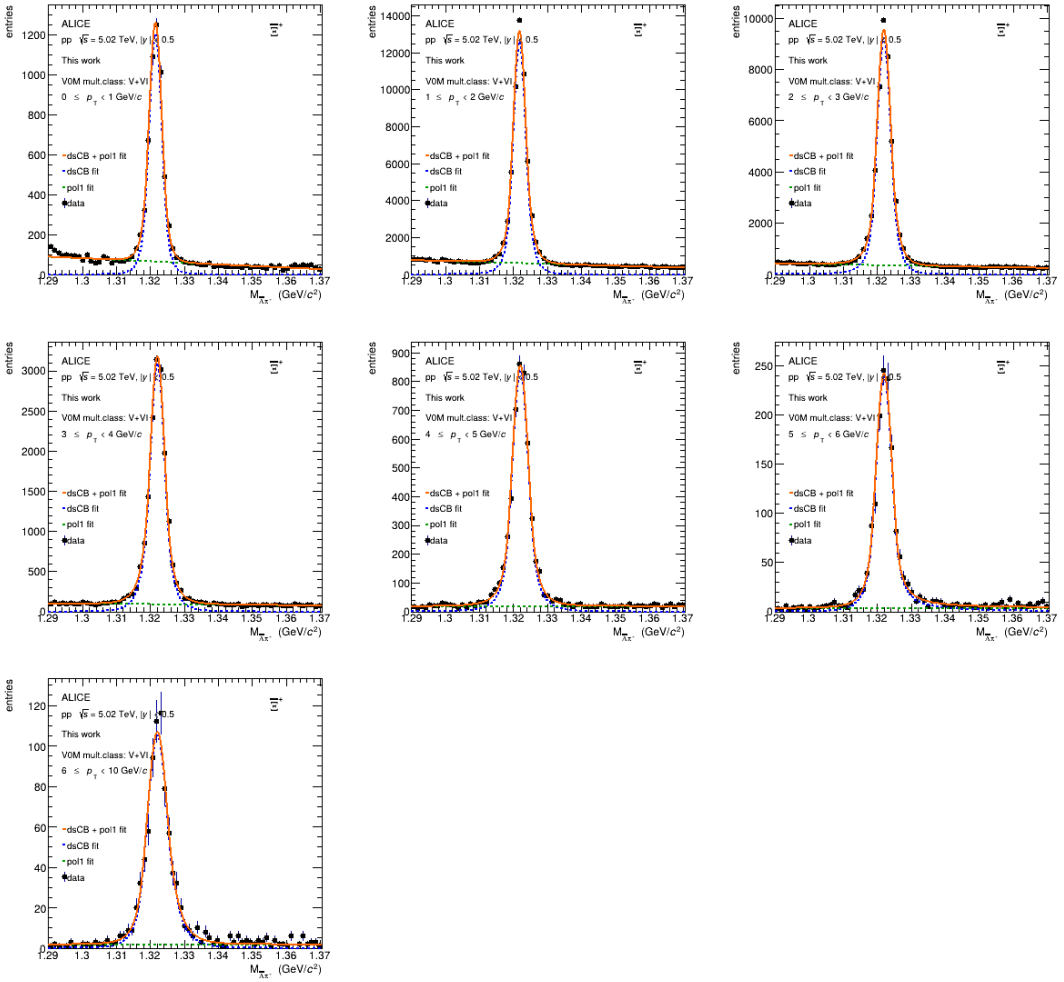

Figure 9.36: $\overline{\Xi}^{+}$ 1D invariant mass spectra fit for different p_{T} bins in the range [0,10] GeV/c for $5 \leq V0M < 15\%$. In the first line, starting on the left there are the 1D invariant mass spectra for p_{T} intervals [0,1) GeV/c, [1,2) GeV/c, [2,3) GeV/c, in the second line there are the 1D invariant mass spectra for p_{T} intervals [3,4) GeV/c, [4,5) GeV/c, [5,6) GeV/c and in the third line there is the 1D invariant mass spectra for p_{T} interval [6,10) GeV/c.

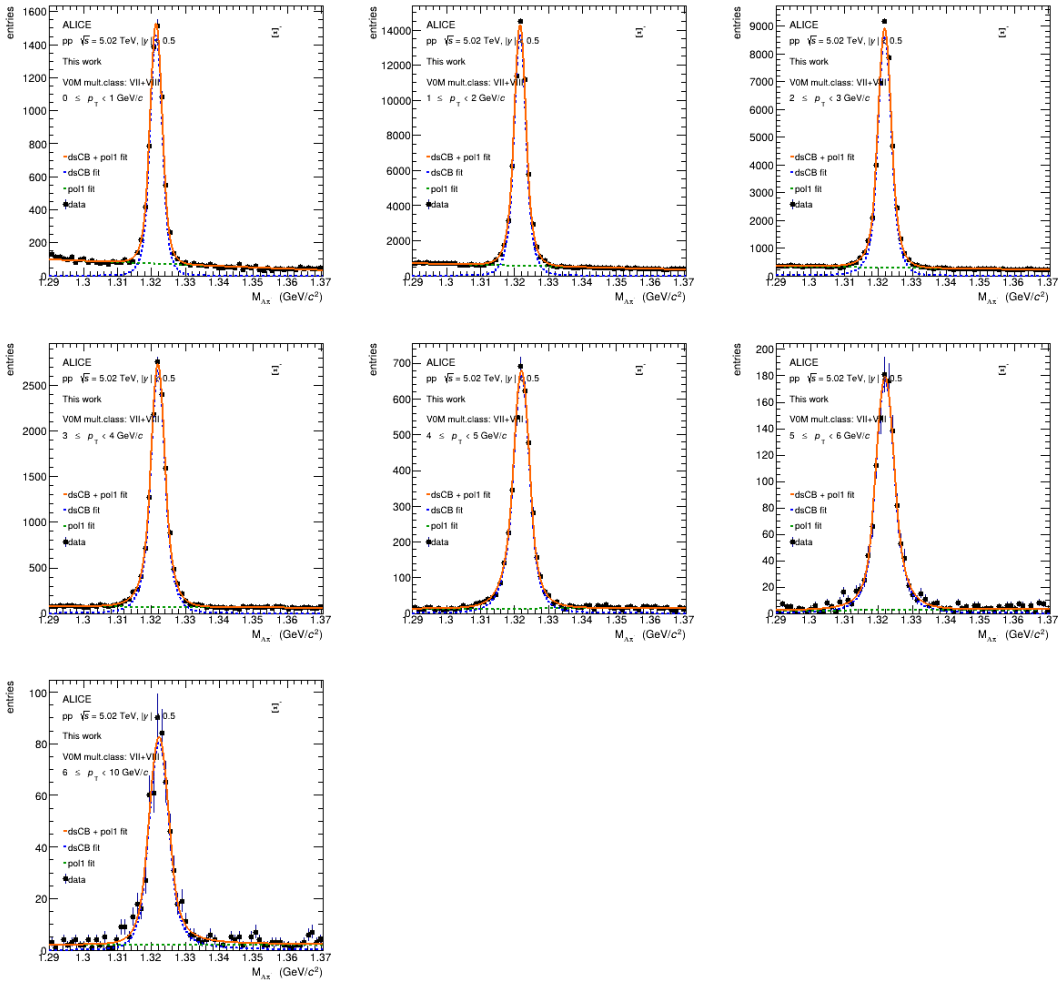

Figure 9.37: Ξ^- 1D invariant mass spectra fit for different p_{T} bins in the range [0,10] GeV/c for $15 \leq V0M < 30\%$. In the first line, starting on the left there are the 1D invariant mass spectra for p_{T} intervals [0,1) GeV/c, [1,2) GeV/c, [2,3) GeV/c, in the second line there are the 1D invariant mass spectra for p_{T} intervals [3,4) GeV/c, [4,5) GeV/c, [5,6) GeV/c and in the third line there is the 1D invariant mass spectra for p_{T} interval [6,10) GeV/c.

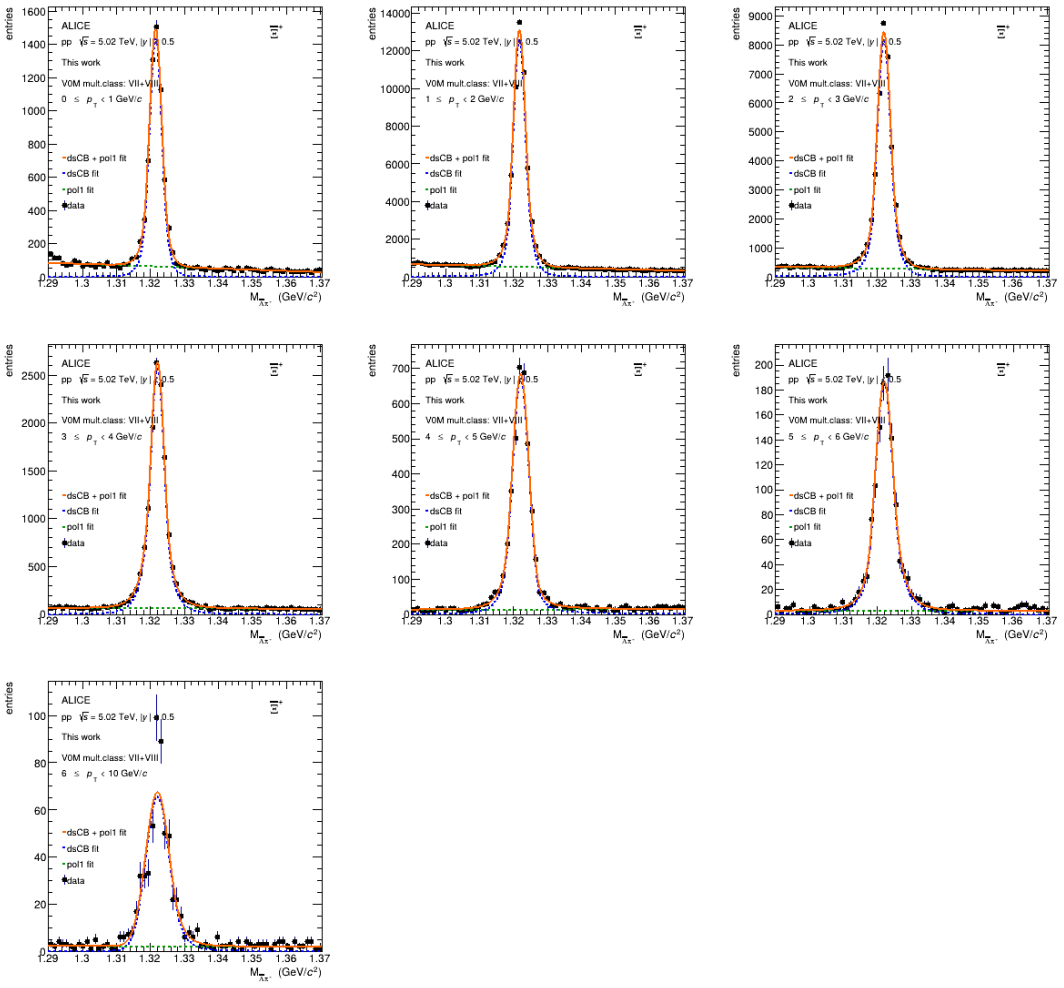

Figure 9.38: $\overline{\Xi}^+$ 1D invariant mass spectra fit for different p_{T} bins in the range [0,10] GeV/c for $15 \leq V0M < 30\%$. In the first line, starting on the left there are the 1D invariant mass spectra for p_{T} intervals [0,1) GeV/c, [1,2) GeV/c, [2,3) GeV/c, in the second line there are the 1D invariant mass spectra for p_{T} intervals [3,4) GeV/c, [4,5) GeV/c, [5,6) GeV/c and in the third line there is the 1D invariant mass spectra for p_{T} interval [6,10) GeV/c.

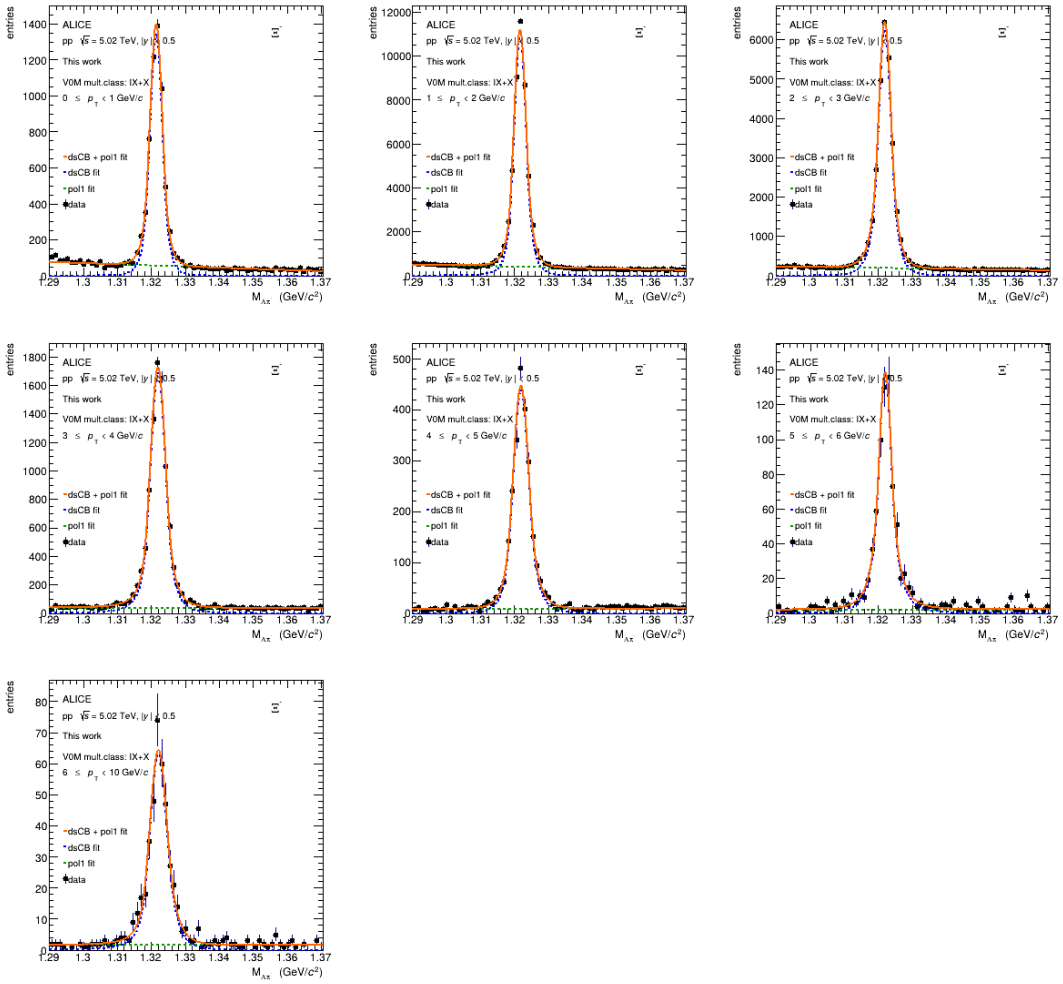

Figure 9.39: Ξ^- 1D invariant mass spectra fit for different p_{T} bins in the range [0,10] GeV/c for $30 \leq V0M < 50\%$. In the first line, starting on the left there are the 1D invariant mass spectra for p_{T} intervals [0,1) GeV/c, [1,2) GeV/c, [2,3) GeV/c, in the second line there are the 1D invariant mass spectra for p_{T} intervals [3,4) GeV/c, [4,5) GeV/c, [5,6) GeV/c and in the third line there is the 1D invariant mass spectra for p_{T} interval [6,10) GeV/c.

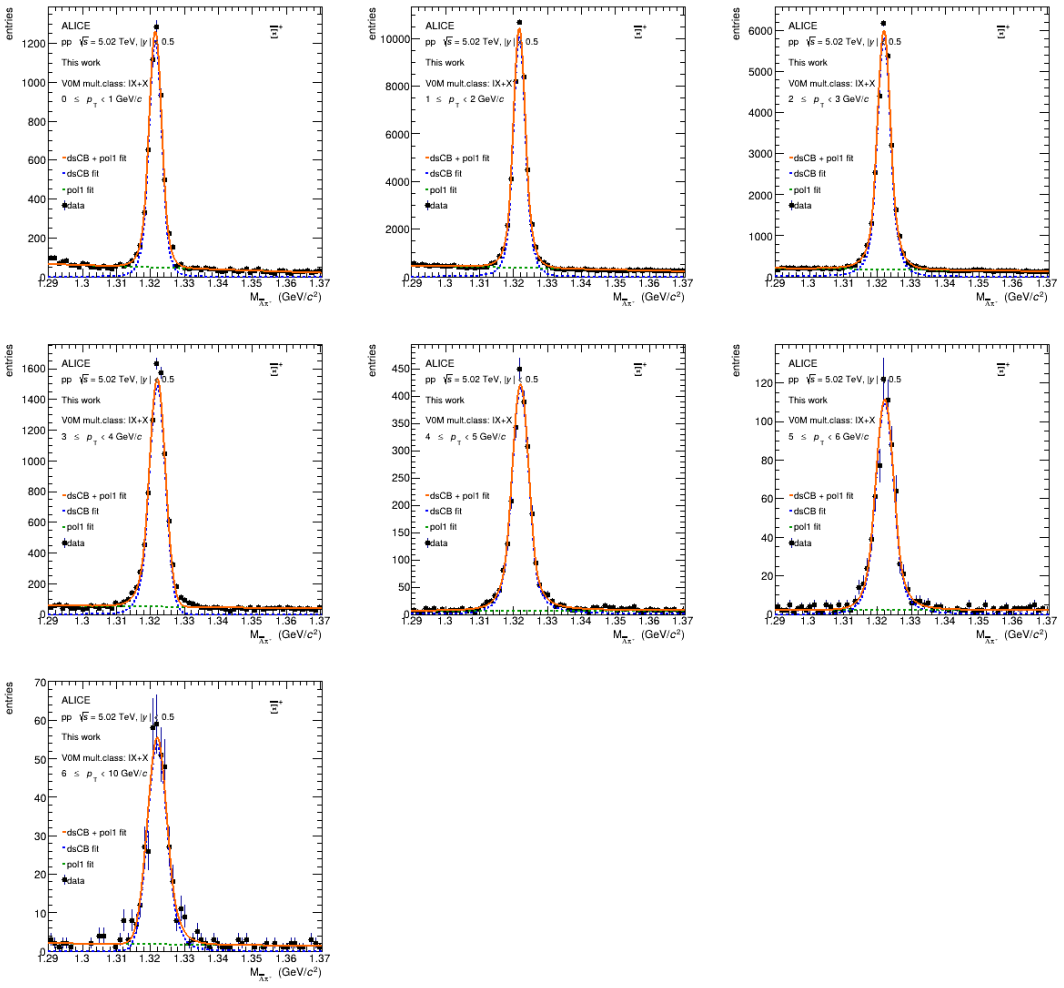

Figure 9.40: $\overline{\Xi}^+$ 1D invariant mass spectra fit for different p_{T} bins in the range [0,10] GeV/c for $30 \leq V0M < 50\%$. In the first line, starting on the left there are the 1D invariant mass spectra for p_{T} intervals [0,1) GeV/c, [1,2) GeV/c, [2,3) GeV/c, in the second line there are the 1D invariant mass spectra for p_{T} intervals [3,4) GeV/c, [4,5) GeV/c, [5,6) GeV/c and in the third line there is the 1D invariant mass spectra for p_{T} interval [6,10) GeV/c.

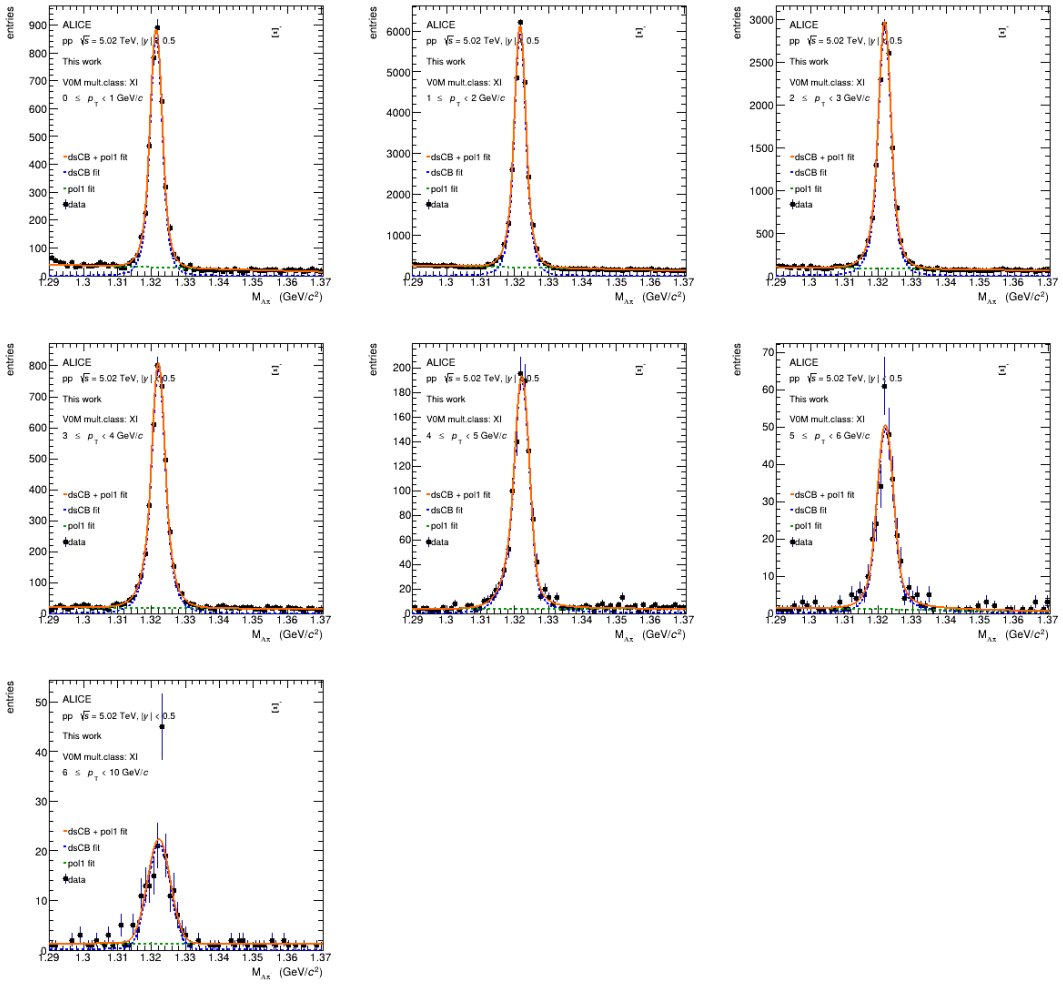

Figure 9.41: Ξ^- 1D invariant mass spectra fit for different p_{T} bins in the range [0,10] GeV/c for $50 \leq V0M < 70\%$. In the first line, starting on the left there are the 1D invariant mass spectra for p_{T} intervals [0,1) GeV/c, [1,2) GeV/c, [2,3) GeV/c, in the second line there are the 1D invariant mass spectra for p_{T} intervals [3,4) GeV/c, [4,5) GeV/c, [5,6) GeV/c and in the third line there is the 1D invariant mass spectra for p_{T} interval [6,10) GeV/c.

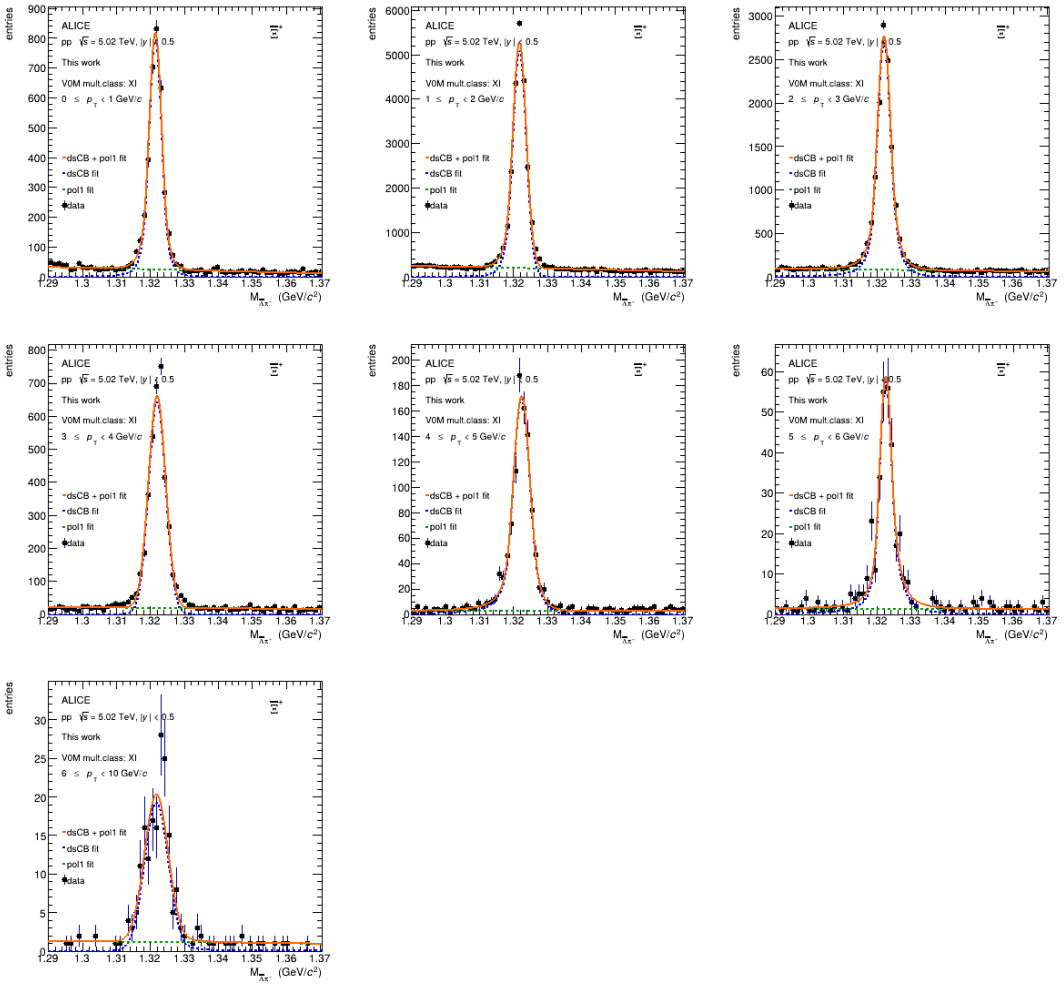

Figure 9.42: $\overline{\Xi}^+$ 1D invariant mass spectra fit for different p_{T} bins in the range [0,10] GeV/c for $50 \leq V0M < 70\%$. In the first line, starting on the left there are the 1D invariant mass spectra for p_{T} intervals [0,1) GeV/c, [1,2) GeV/c, [2,3) GeV/c, in the second line there are the 1D invariant mass spectra for p_{T} intervals [3,4) GeV/c, [4,5) GeV/c, [5,6) GeV/c and in the third line there is the 1D invariant mass spectra for p_{T} interval [6,10) GeV/c.

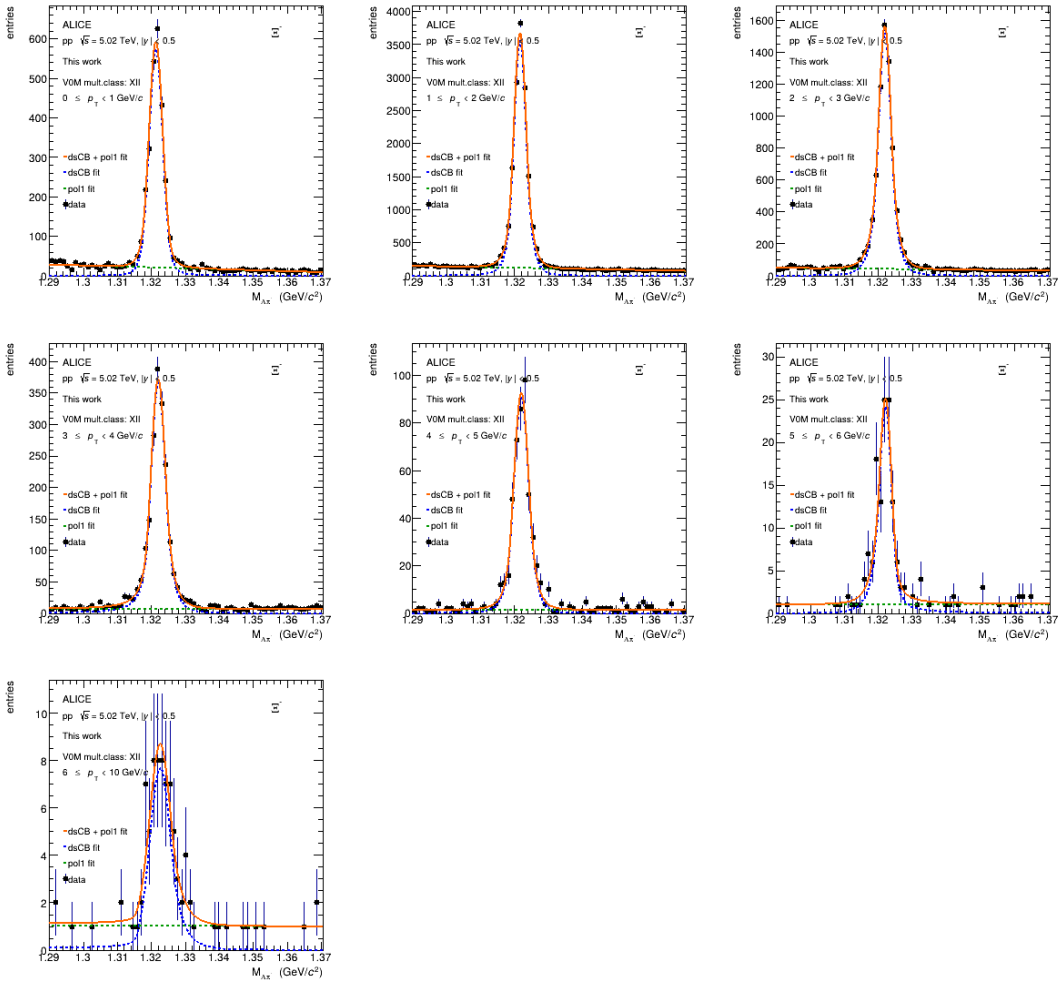

Figure 9.43: Ξ^- 1D invariant mass spectra fit for different p_{T} bins in the range [0,10] GeV/c for $70 \leq V0M < 100\%$. In the first line, starting on the left there are the 1D invariant mass spectra for p_{T} intervals [0,1) GeV/c, [1,2) GeV/c, [2,3) GeV/c, in the second line there are the 1D invariant mass spectra for p_{T} intervals [3,4) GeV/c, [4,5) GeV/c, [5,6) GeV/c and in the third line there is the 1D invariant mass spectra for p_{T} interval [6,10) GeV/c.

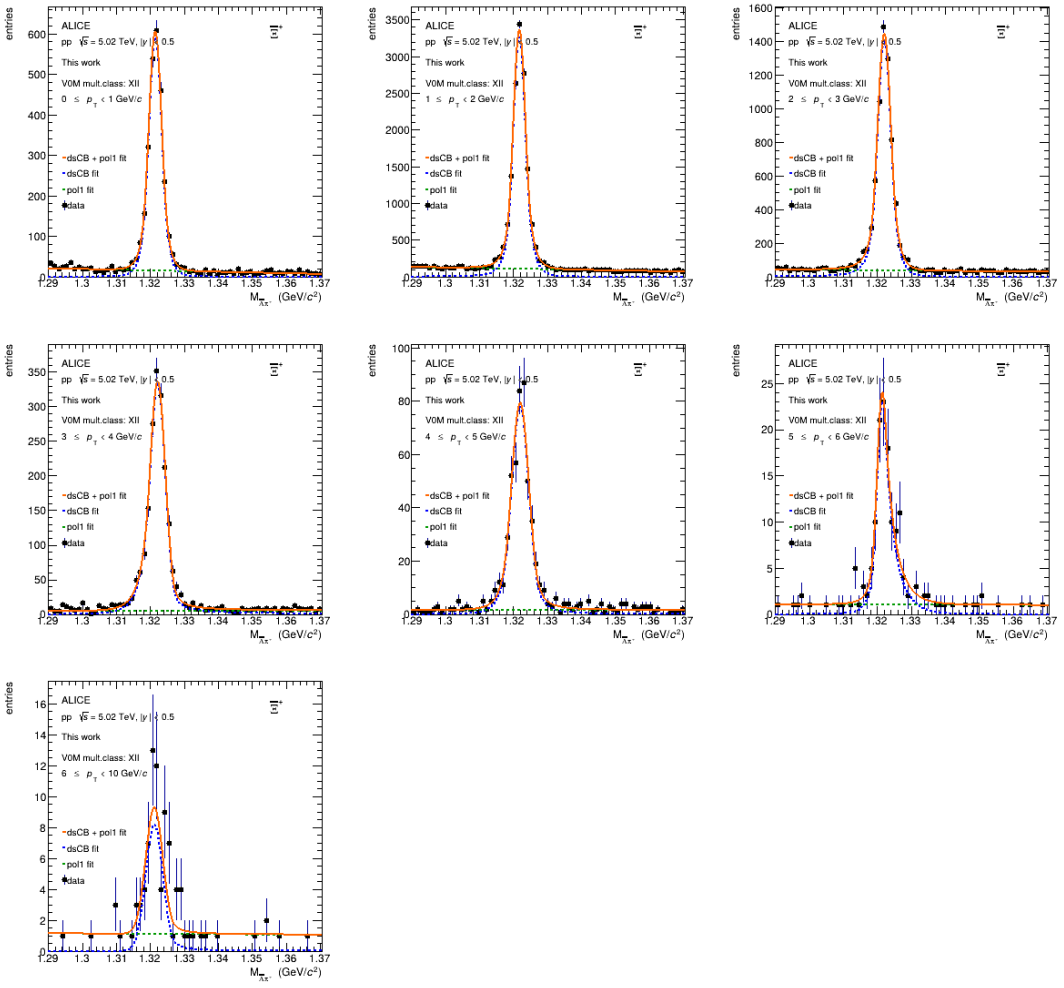

Figure 9.44: $\overline{\Xi}^+$ 1D invariant mass spectra fit for different p_{T} bins in the range [0,10] GeV/c for $70 \leq V0M < 100\%$. In the first line, starting on the left there are the 1D invariant mass spectra for p_{T} intervals [0,1) GeV/c, [1,2) GeV/c, [2,3) GeV/c, in the second line there are the 1D invariant mass spectra for p_{T} intervals [3,4) GeV/c, [4,5) GeV/c, [5,6) GeV/c and in the third line there is the 1D invariant mass spectra for p_{T} interval [6,10) GeV/c.

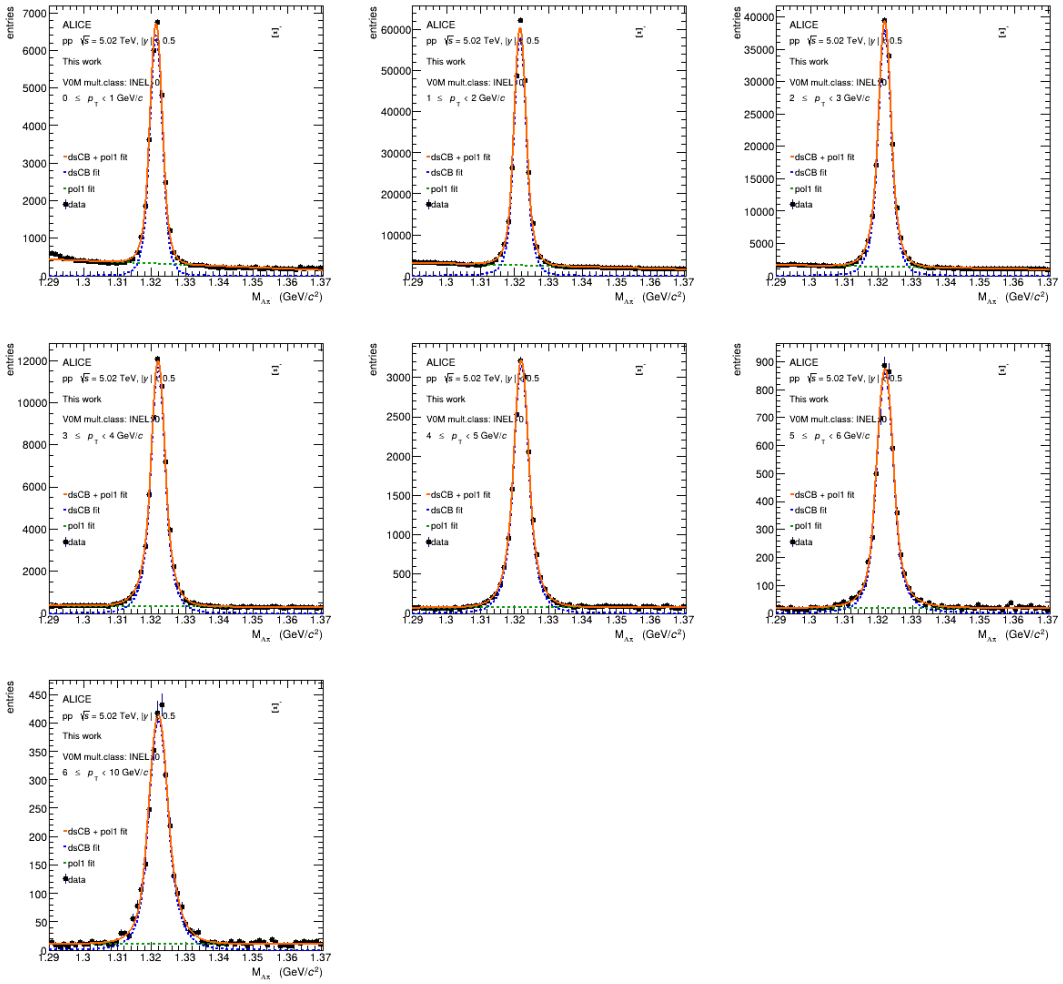

Figure 9.45: Ξ^- 1D invariant mass spectra fit for different p_{T} bins in the range [0,10] GeV/c for $0 \leq V0M < 100\%$. In the first line, starting on the left there are the 1D invariant mass spectra for p_{T} intervals [0,1) GeV/c, [1,2) GeV/c, [2,3) GeV/c, in the second line there are the 1D invariant mass spectra for p_{T} intervals [3,4) GeV/c, [4,5) GeV/c, [5,6) GeV/c and in the third line there is the 1D invariant mass spectra for p_{T} interval [6,10) GeV/c.

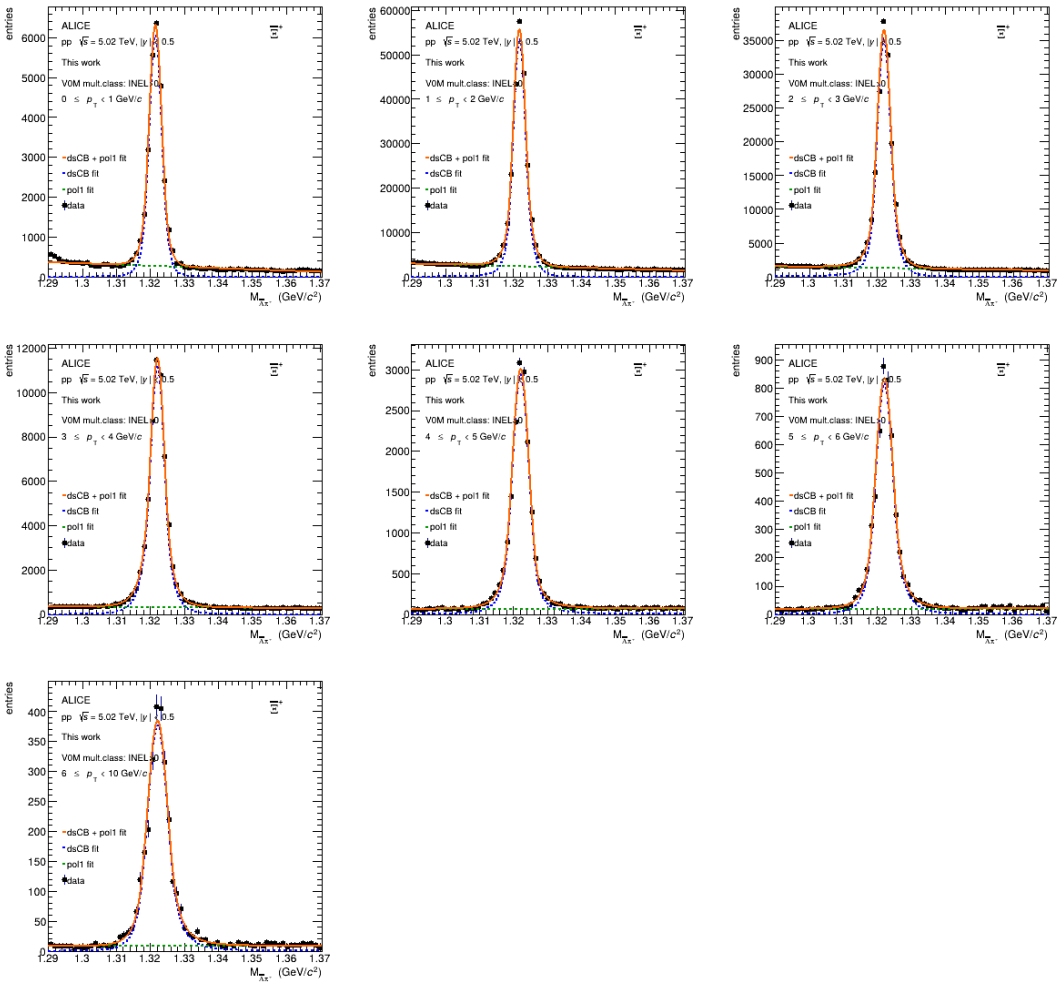

Figure 9.46: $\overline{\Xi}^+$ 1D invariant mass spectra fit for different p_{T} bins in the range [0,10] GeV/c for $0 \leq V0M < 100\%$. In the first line, starting on the left there are the 1D invariant mass spectra for p_{T} intervals [0,1) GeV/c, [1,2) GeV/c, [2,3) GeV/c, in the second line there are the 1D invariant mass spectra for p_{T} intervals [3,4) GeV/c, [4,5) GeV/c, [5,6) GeV/c and in the third line there is the 1D invariant mass spectra for p_{T} interval [6,10) GeV/c.

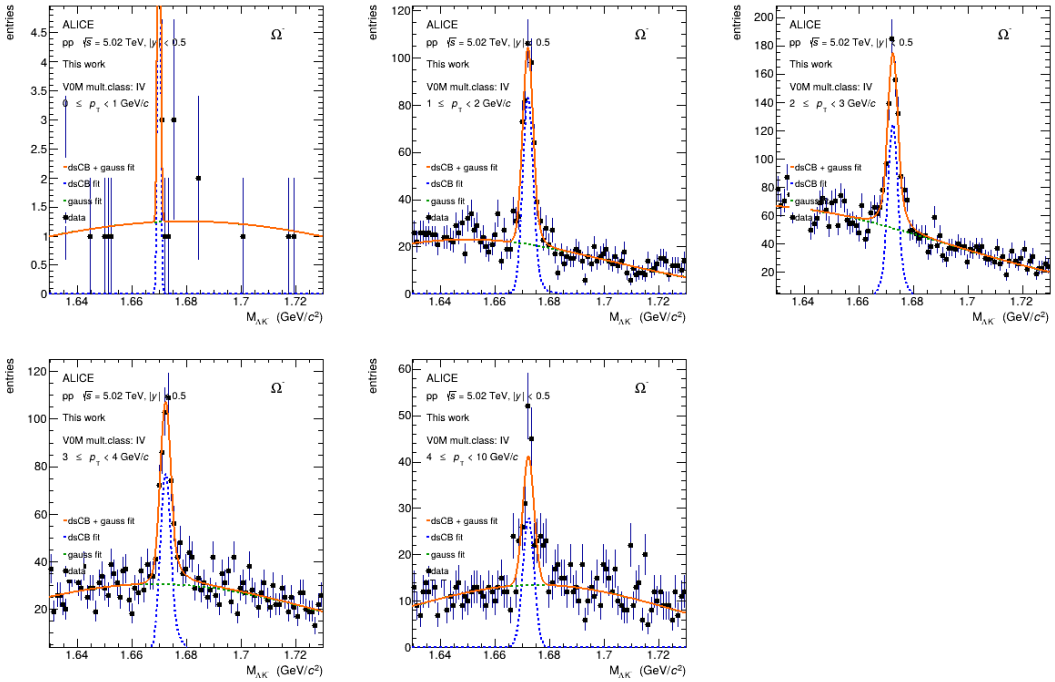

Figure 9.47: Ω^- 1D invariant mass spectra fit for different p_{T} bins in the range [0,10] GeV/c for $0 \leq V0M < 1\%$. In the first line, starting on the left there are the 1D invariant mass spectra for p_{T} intervals [0,1) GeV/c, [1,2) GeV/c, [2,3) GeV/c, in the second line there are the 1D invariant mass spectra for p_{T} intervals [3,4) GeV/c and [4,10) GeV/c. Note that due to the insufficient amount of statistical data, accurate fit cannot be performed in the p_{T} interval [0,1) GeV/c.

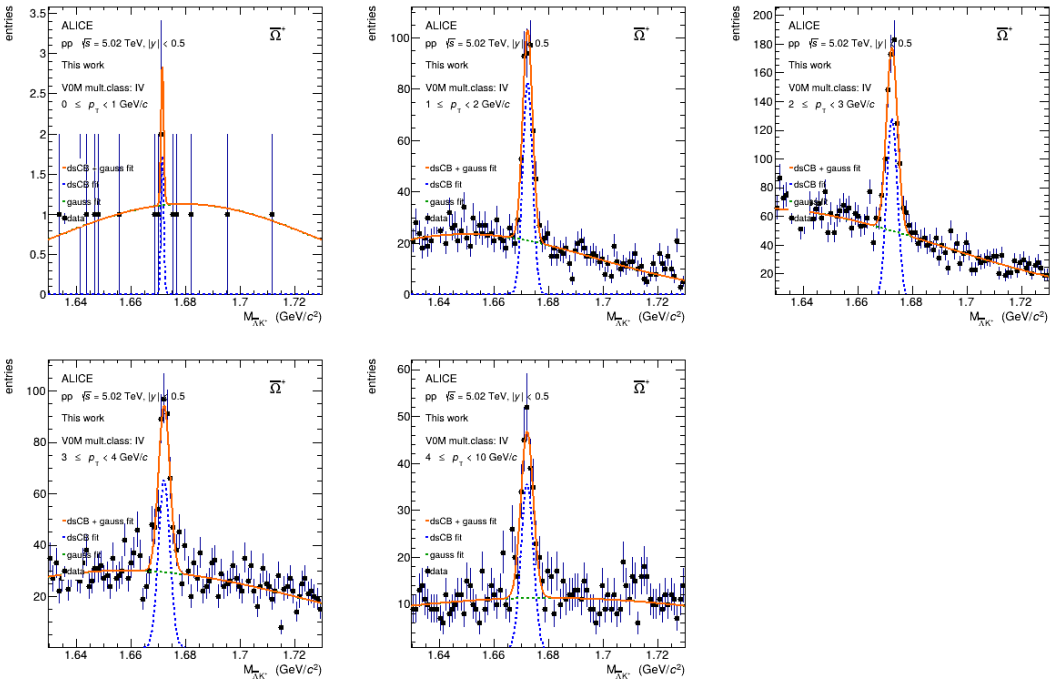

Figure 9.48: $\overline{\Omega}^+$ 1D invariant mass spectra fit for different p_{T} bins in the range [0,10] GeV/c for $0 \leq V0M < 1\%$. In the first line, starting on the left there are the 1D invariant mass spectra for p_{T} intervals [0,1) GeV/c, [1,2) GeV/c, [2,3) GeV/c, in the second line there are the 1D invariant mass spectra for p_{T} intervals [3,4) GeV/c and [4,10) GeV/c. Note that due to the insufficient amount of statistical data, accurate fit cannot be performed in the p_{T} interval [0,1) GeV/c.

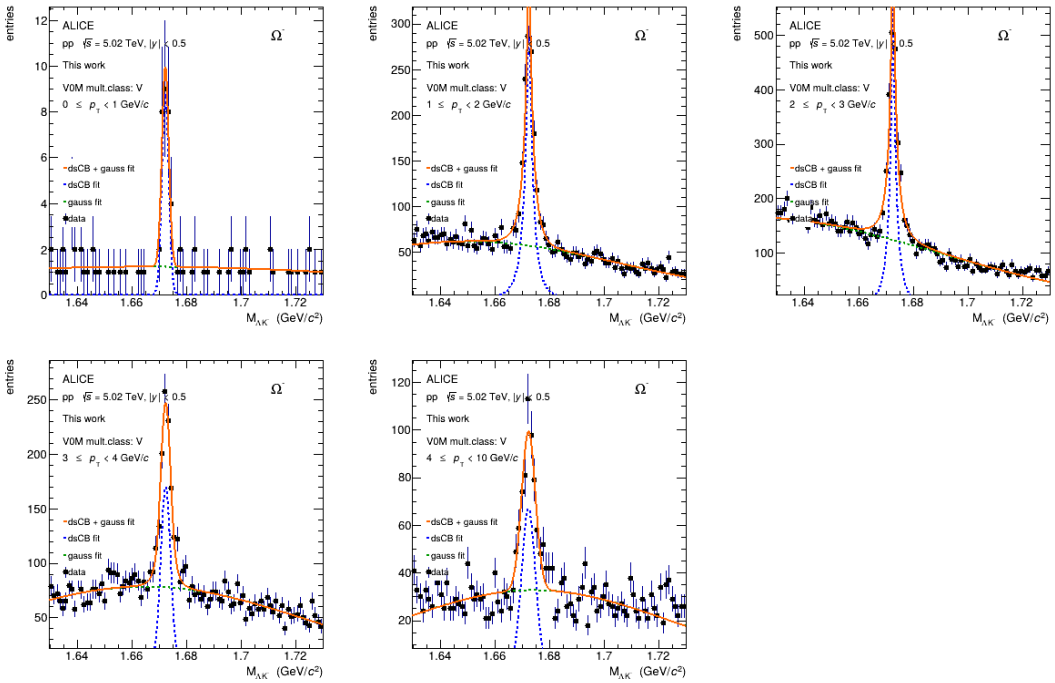

Figure 9.49: Ω^- 1D invariant mass spectra fit for different p_{T} bins in the range [0,10] GeV/c for $1 \leq V0M < 5\%$. In the first line, starting on the left there are the 1D invariant mass spectra for p_{T} intervals [0,1) GeV/c, [1,2) GeV/c, [2,3) GeV/c, in the second line there are the 1D invariant mass spectra for p_{T} intervals [3,4) GeV/c and [4,10) GeV/c.

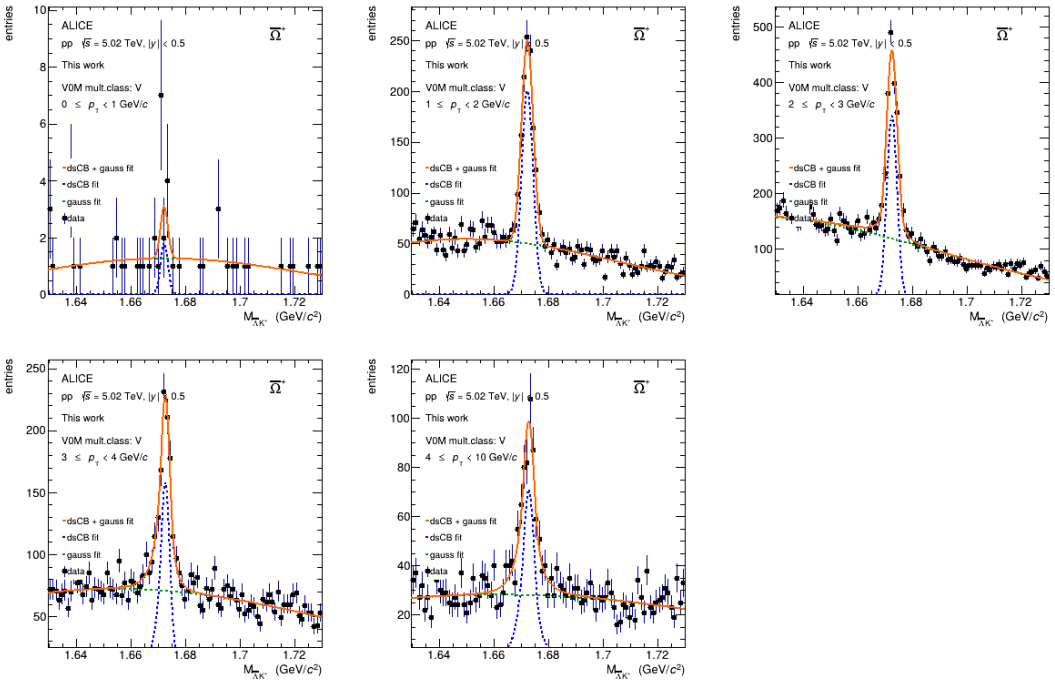

Figure 9.50: $\overline{\Omega}^{+}$ 1D invariant mass spectra fit for different p_{T} bins in the range [0,10] GeV/c for $1 \leq V0M < 5\%$. In the first line, starting on the left there are the 1D invariant mass spectra for p_{T} intervals [0,1) GeV/c, [1,2) GeV/c, [2,3) GeV/c, in the second line there are the 1D invariant mass spectra for p_{T} intervals [3,4) GeV/c and [4,10) GeV/c. Note that due to the insufficient amount of statistical data, accurate fit cannot be performed in the p_{T} interval [0,1) GeV/c.

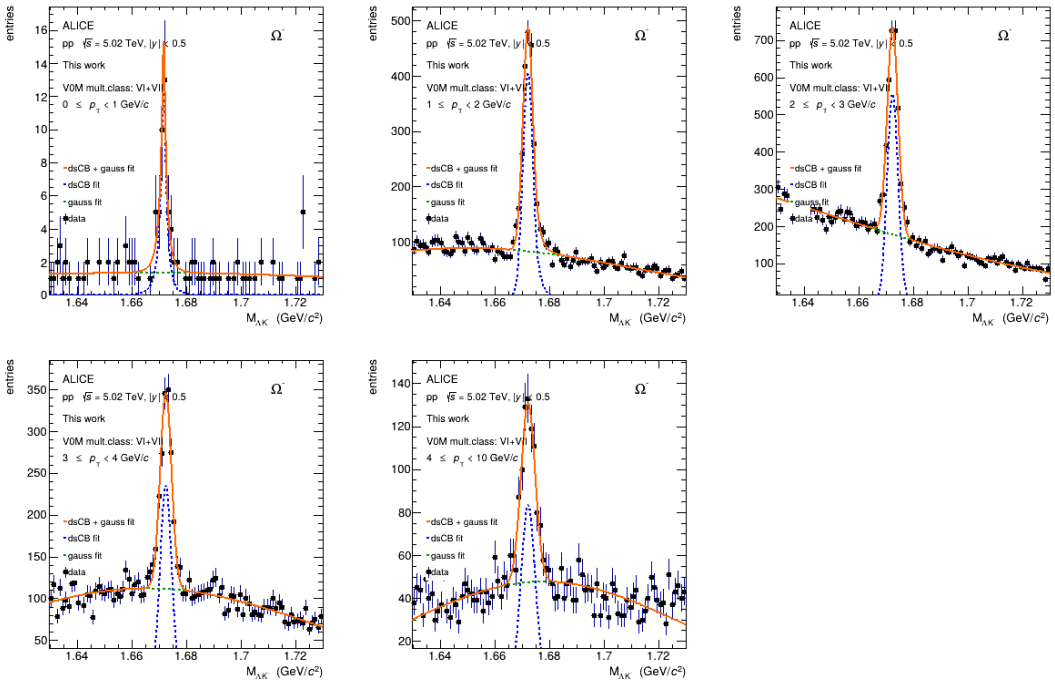

Figure 9.51: Ω^- 1D invariant mass spectra fit for different p_{T} bins in the range [0,10] GeV/c for $5 \leq V0M < 15\%$. In the first line, starting on the left there are the 1D invariant mass spectra for p_{T} intervals [0,1) GeV/c, [1,2) GeV/c, [2,3) GeV/c, in the second line there are the 1D invariant mass spectra for p_{T} intervals [3,4) GeV/c and [4,10) GeV/c.

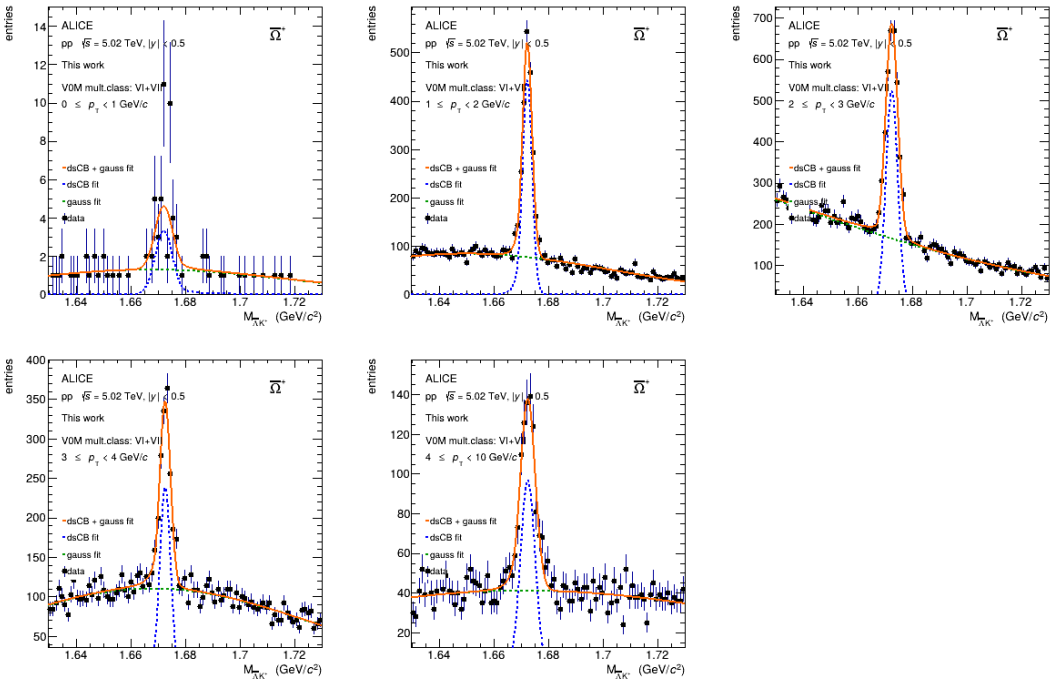

Figure 9.52: $\overline{\Omega}^+$ 1D invariant mass spectra fit for different p_{T} bins in the range [0,10] GeV/c for $5 \leq V0M < 15\%$. In the first line, starting on the left there are the 1D invariant mass spectra for p_{T} intervals [0,1) GeV/c, [1,2) GeV/c, [2,3) GeV/c, in the second line there are the 1D invariant mass spectra for p_{T} intervals [3,4) GeV/c and [4,10) GeV/c. Note that due to the insufficient amount of statistical data, accurate fit cannot be performed in the p_{T} interval [0,1) GeV/c.

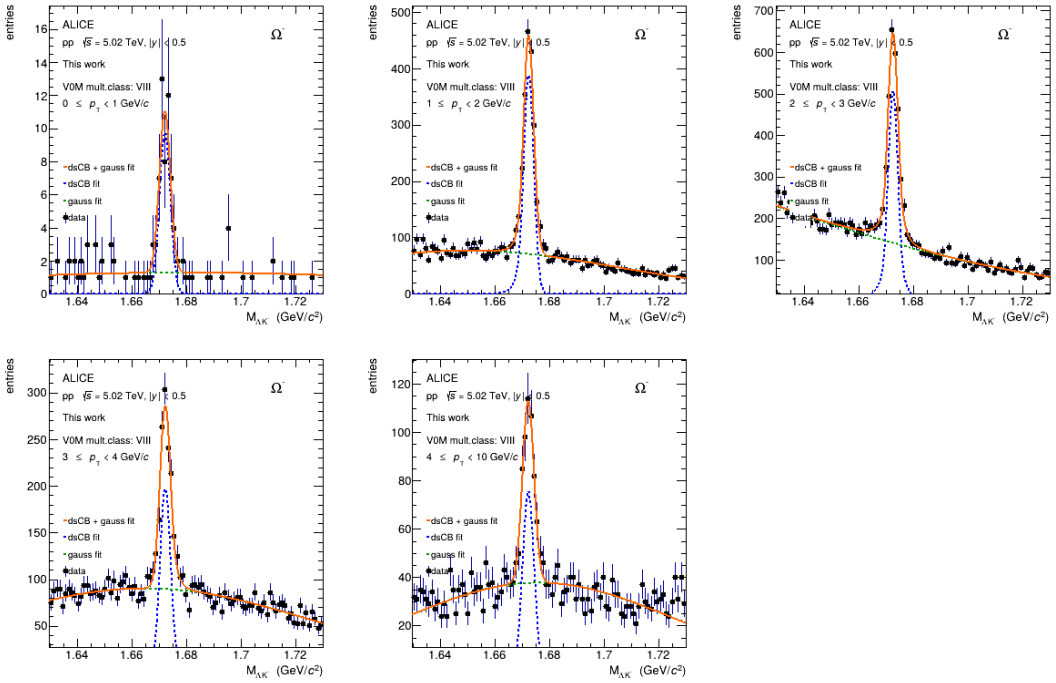

Figure 9.53: Ω^- 1D invariant mass spectra fit for different p_{T} bins in the range [0,10] GeV/c for $15 \leq V0M < 30\%$. In the first line, starting on the left there are the 1D invariant mass spectra for p_{T} intervals [0,1) GeV/c, [1,2) GeV/c, [2,3) GeV/c, in the second line there are the 1D invariant mass spectra for p_{T} intervals [3,4) GeV/c and [4,10) GeV/c.

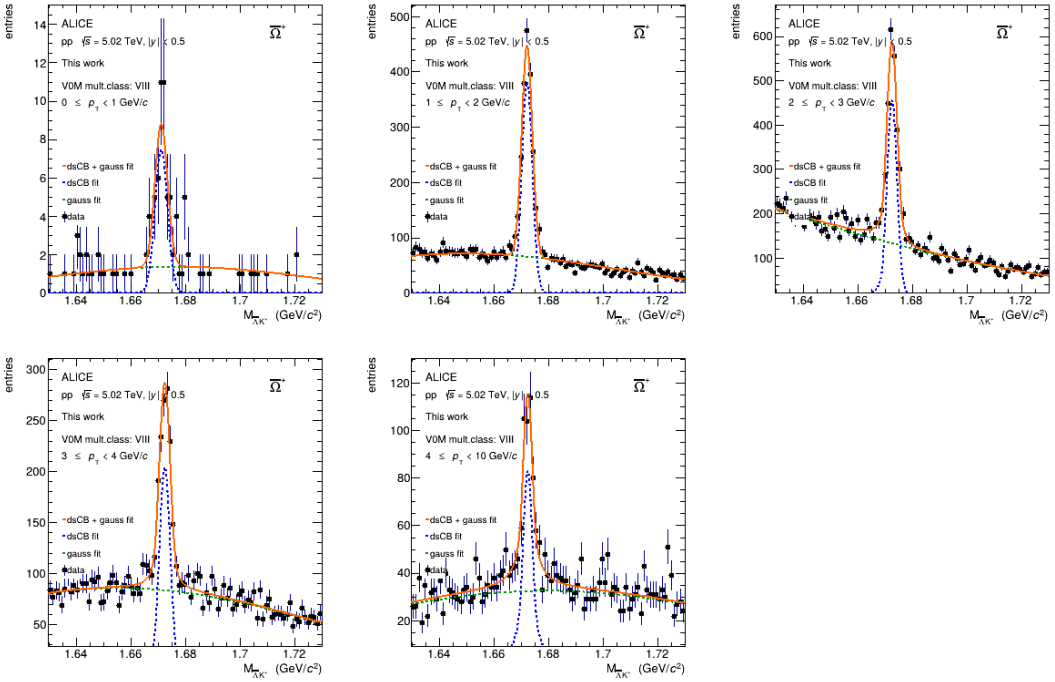

Figure 9.54: $\overline{\Omega}^+$ 1D invariant mass spectra fit for different p_{T} bins in the range [0,10] GeV/c for $15 \leq V0M < 30\%$. In the first line, starting on the left there are the 1D invariant mass spectra for p_{T} intervals [0,1) GeV/c, [1,2) GeV/c, [2,3) GeV/c, in the second line there are the 1D invariant mass spectra for p_{T} intervals [3,4) GeV/c and [4,10) GeV/c.

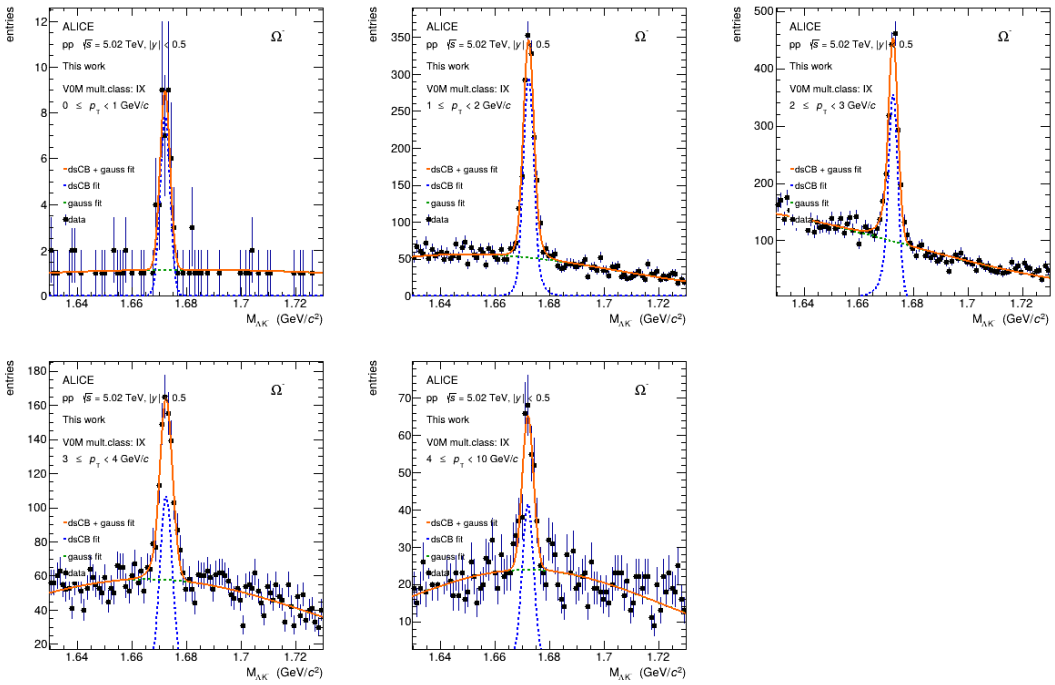

Figure 9.55: Ω^- 1D invariant mass spectra fit for different p_{T} bins in the range [0,10] GeV/c for $30 \leq V0M < 50\%$. In the first line, starting on the left there are the 1D invariant mass spectra for p_{T} intervals [0,1) GeV/c, [1,2) GeV/c, [2,3) GeV/c, in the second line there are the 1D invariant mass spectra for p_{T} intervals [3,4) GeV/c and [4,10) GeV/c.

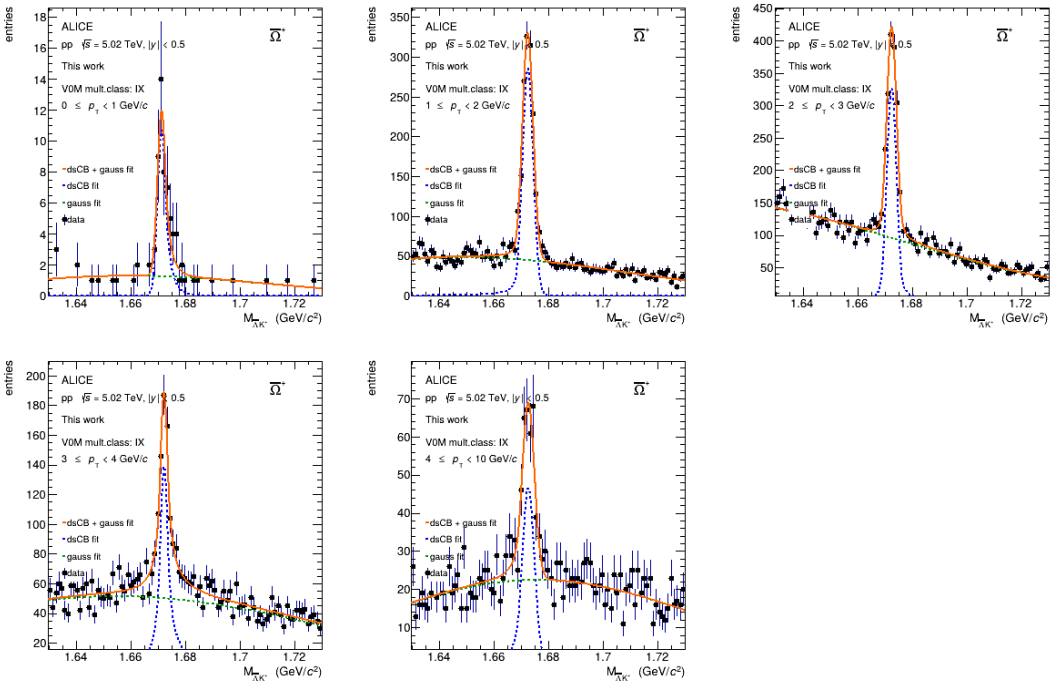

Figure 9.56: $\overline{\Omega}^+$ 1D invariant mass spectra fit for different p_{T} bins in the range [0,10] GeV/c for $30 \leq V0M < 50\%$. In the first line, starting on the left there are the 1D invariant mass spectra for p_{T} intervals [0,1) GeV/c, [1,2) GeV/c, [2,3) GeV/c, in the second line there are the 1D invariant mass spectra for p_{T} intervals [3,4) GeV/c and [4,10) GeV/c.

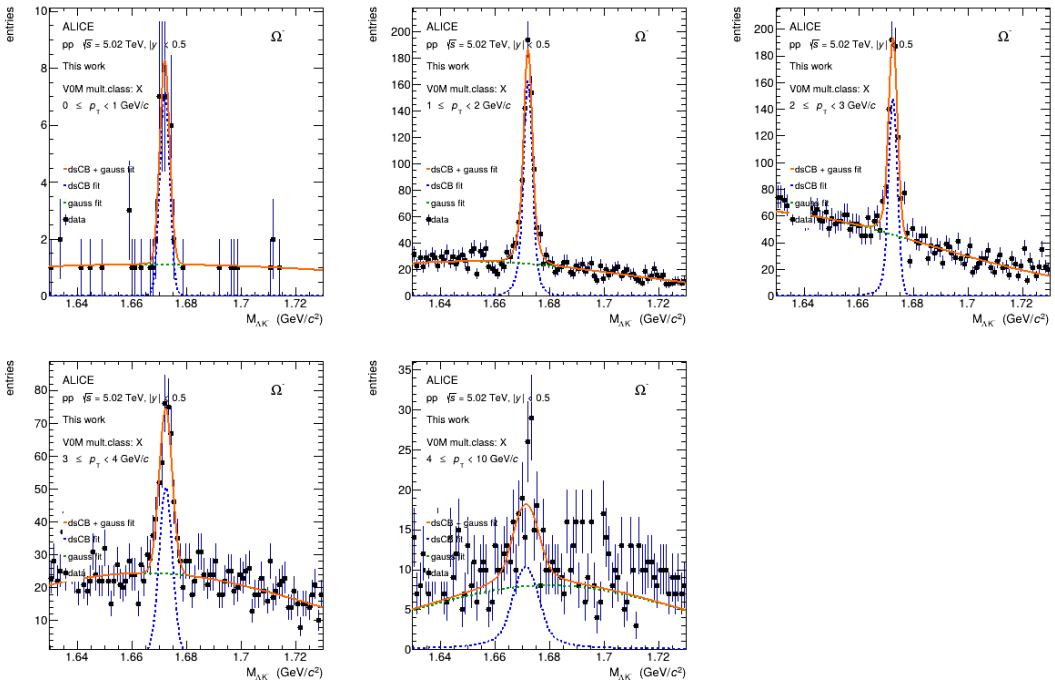

Figure 9.57: Ω^- 1D invariant mass spectra fit for different p_{T} bins in the range [0,10] GeV/c for $50 \leq V0M < 70\%$. In the first line, starting on the left there are the 1D invariant mass spectra for p_{T} intervals [0,1) GeV/c, [1,2) GeV/c, [2,3) GeV/c, in the second line there are the 1D invariant mass spectra for p_{T} intervals [3,4) GeV/c and [4,10) GeV/c.

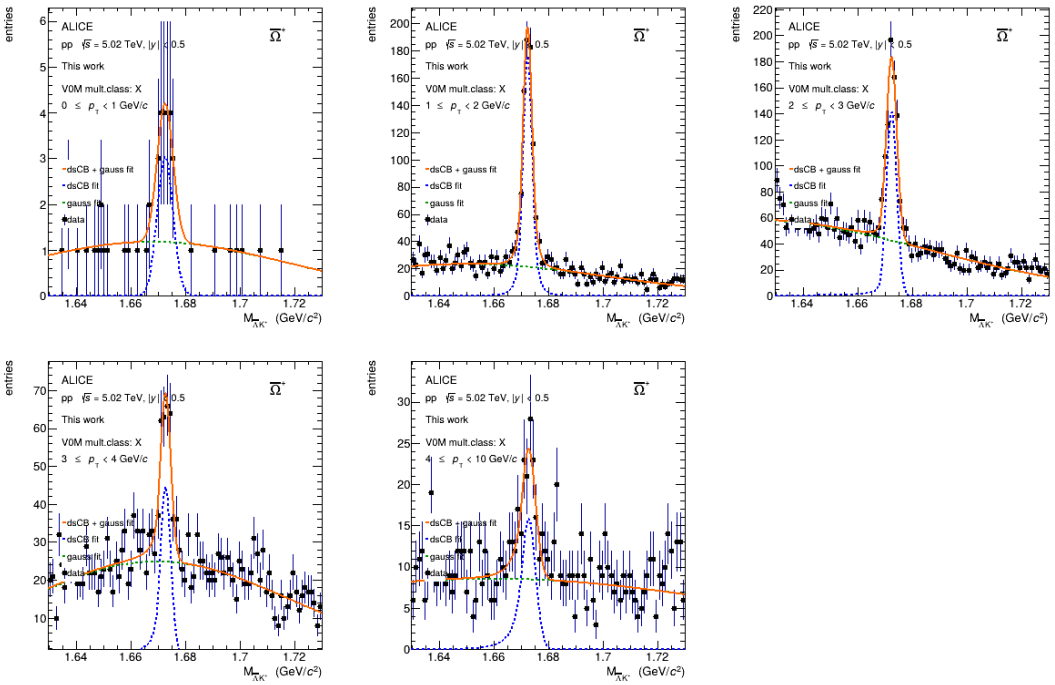

Figure 9.58: $\overline{\Omega}^+$ 1D invariant mass spectra fit for different p_{T} bins in the range [0,10] GeV/c for $50 \leq V0M < 70\%$. In the first line, starting on the left there are the 1D invariant mass spectra for p_{T} intervals [0,1) GeV/c, [1,2) GeV/c, [2,3) GeV/c, in the second line there are the 1D invariant mass spectra for p_{T} intervals [3,4) GeV/c and [4,10) GeV/c.

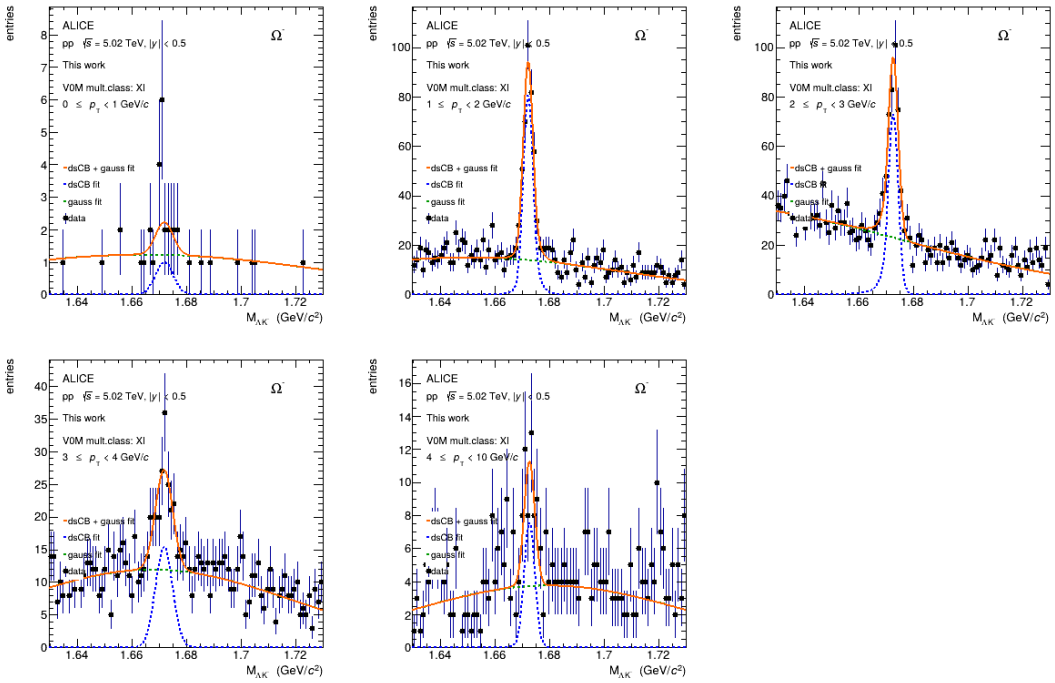

Figure 9.59: Ω^- 1D invariant mass spectra fit for different p_{T} bins in the range [0,10] GeV/c for $70 \leq V0M < 100\%$. In the first line, starting on the left there are the 1D invariant mass spectra for p_{T} intervals [0,1) GeV/c, [1,2) GeV/c, [2,3) GeV/c, in the second line there are the 1D invariant mass spectra for p_{T} intervals [3,4) GeV/c and [4,10) GeV/c. Note that due to the insufficient amount of statistical data, accurate fit cannot be performed in the p_{T} interval [0,1) GeV/c.

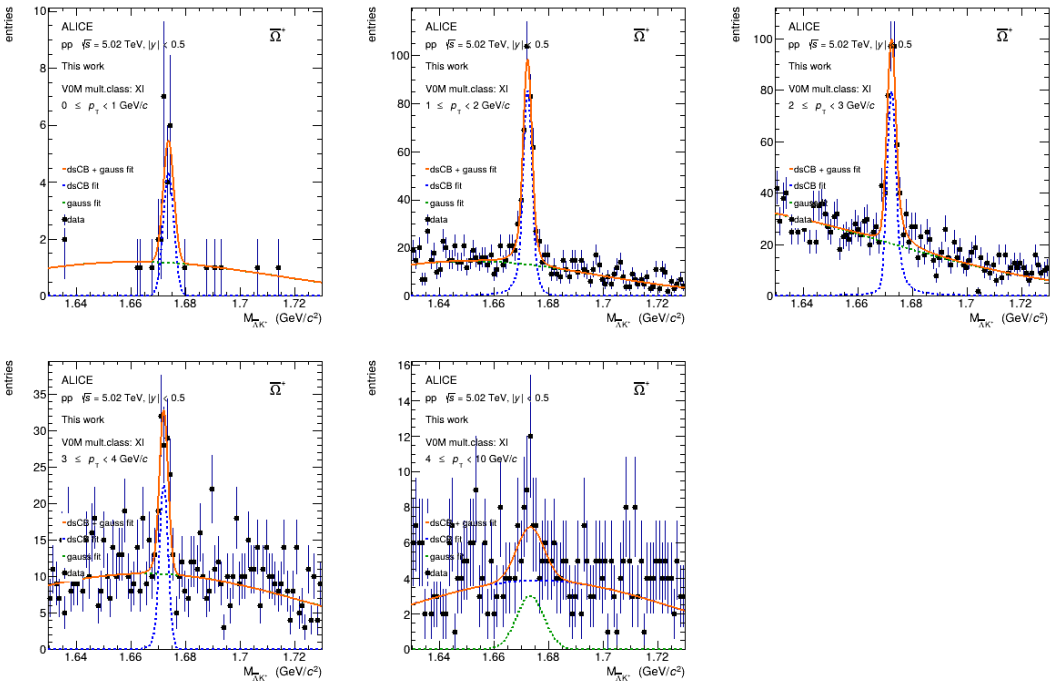

Figure 9.60: $\overline{\Omega}^+$ 1D invariant mass spectra fit for different p_{T} bins in the range [0,10] GeV/c for $70 \leq V0M < 100\%$. In the first line, starting on the left there are the 1D invariant mass spectra for p_{T} intervals [0,1) GeV/c, [1,2) GeV/c, [2,3) GeV/c, in the second line there are the 1D invariant mass spectra for p_{T} intervals [3,4) GeV/c and [4,10) GeV/c.

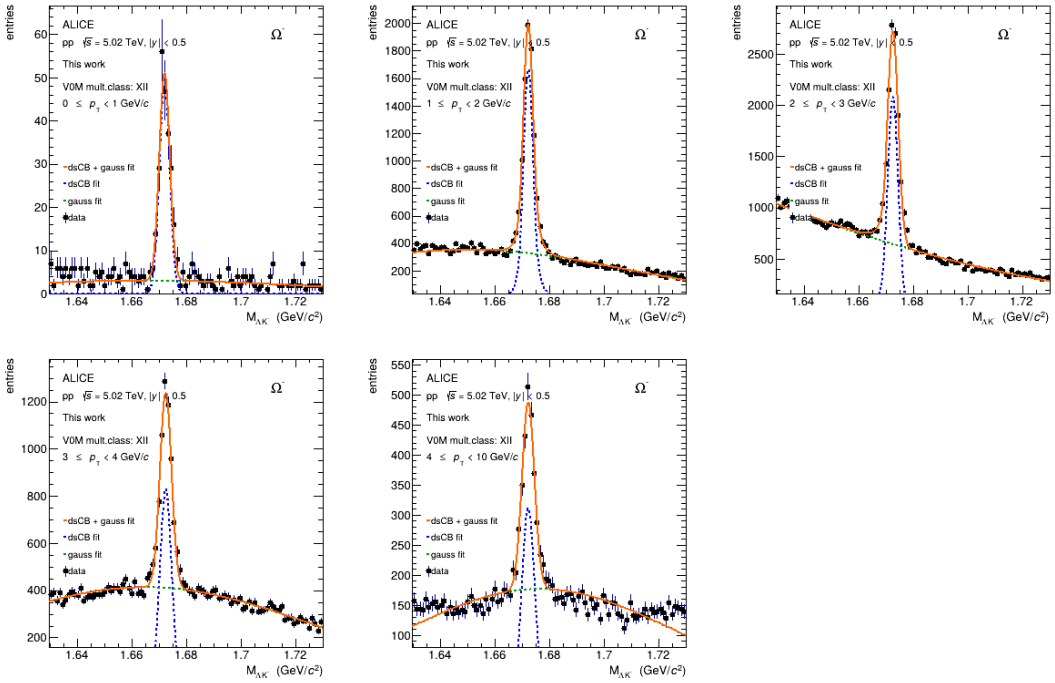

Figure 9.61: Ω^- 1D invariant mass spectra fit for different p_{T} bins in the range [0,10] GeV/c for $0 \leq V0M \geq 100\%$. In the first line, starting on the left there are the 1D invariant mass spectra for p_{T} intervals [0,1) GeV/c, [1,2) GeV/c, [2,3) GeV/c, in the second line there are the 1D invariant mass spectra for p_{T} intervals [3,4) GeV/c and [4,10) GeV/c.

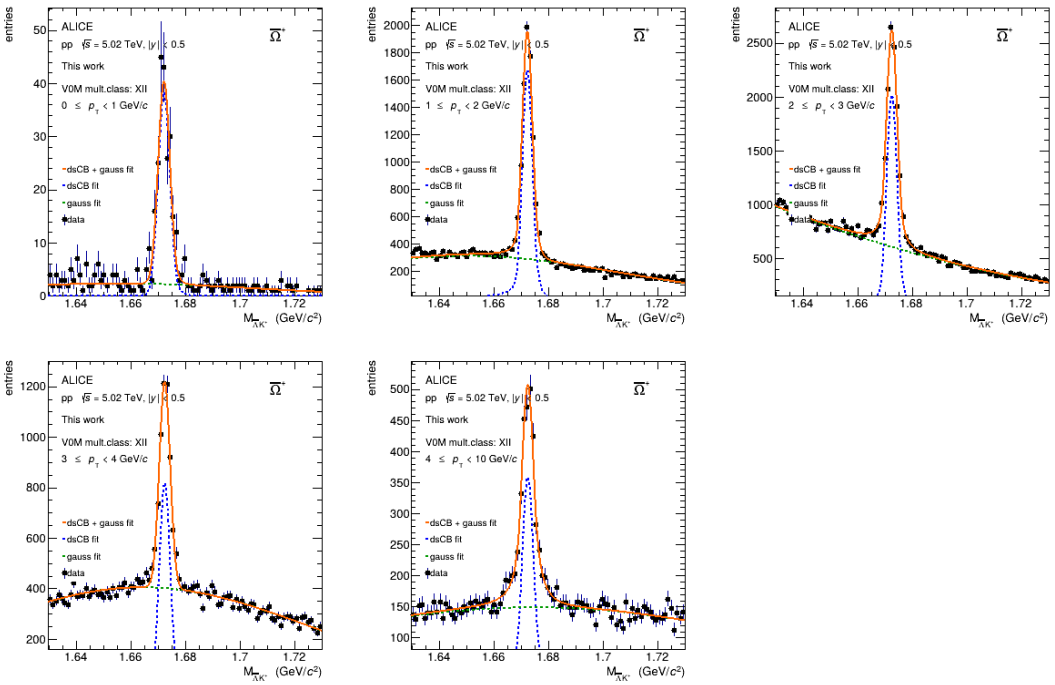

Figure 9.62: $\overline{\Omega}^+$ 1D invariant mass spectra fit for different p_{T} bins in the range [0,10] GeV/c for $0 \leq V0M < 100\%$. In the first line, starting on the left there are the 1D invariant mass spectra for p_{T} intervals [0,1) GeV/c, [1,2) GeV/c, [2,3) GeV/c, in the second line there are the 1D invariant mass spectra for p_{T} intervals [3,4) GeV/c and [4,10) GeV/c.

9.2 Signal probability trends

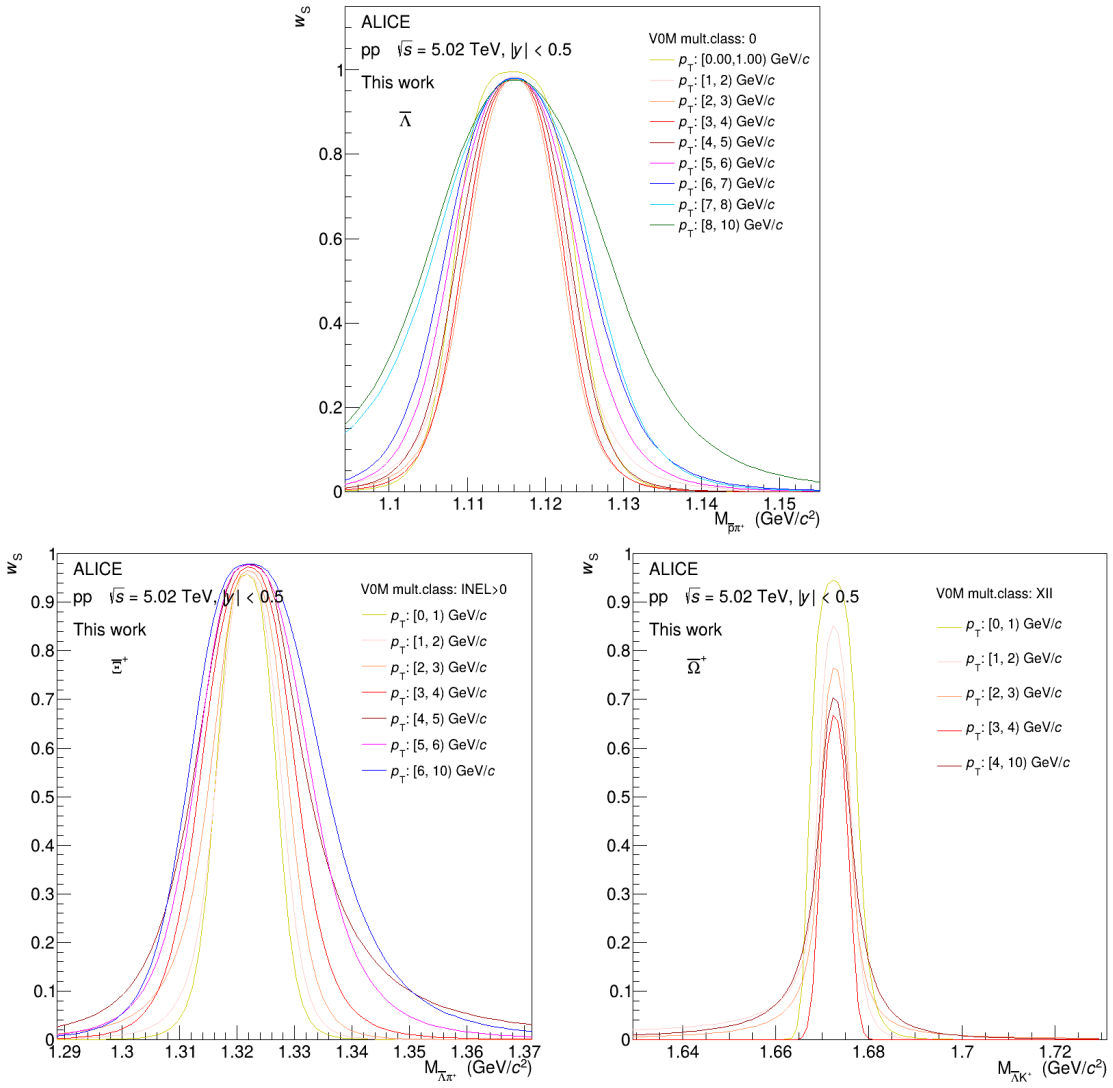

Figure 9.63: Signal probability trend as a function of invariant mass, accounting for the p_{T} dependence for INEL > 0. The first row shows the results for $\overline{\Lambda}$, while the second row presents the results for $\overline{\Xi}^+$ and $\overline{\Omega}^+$.

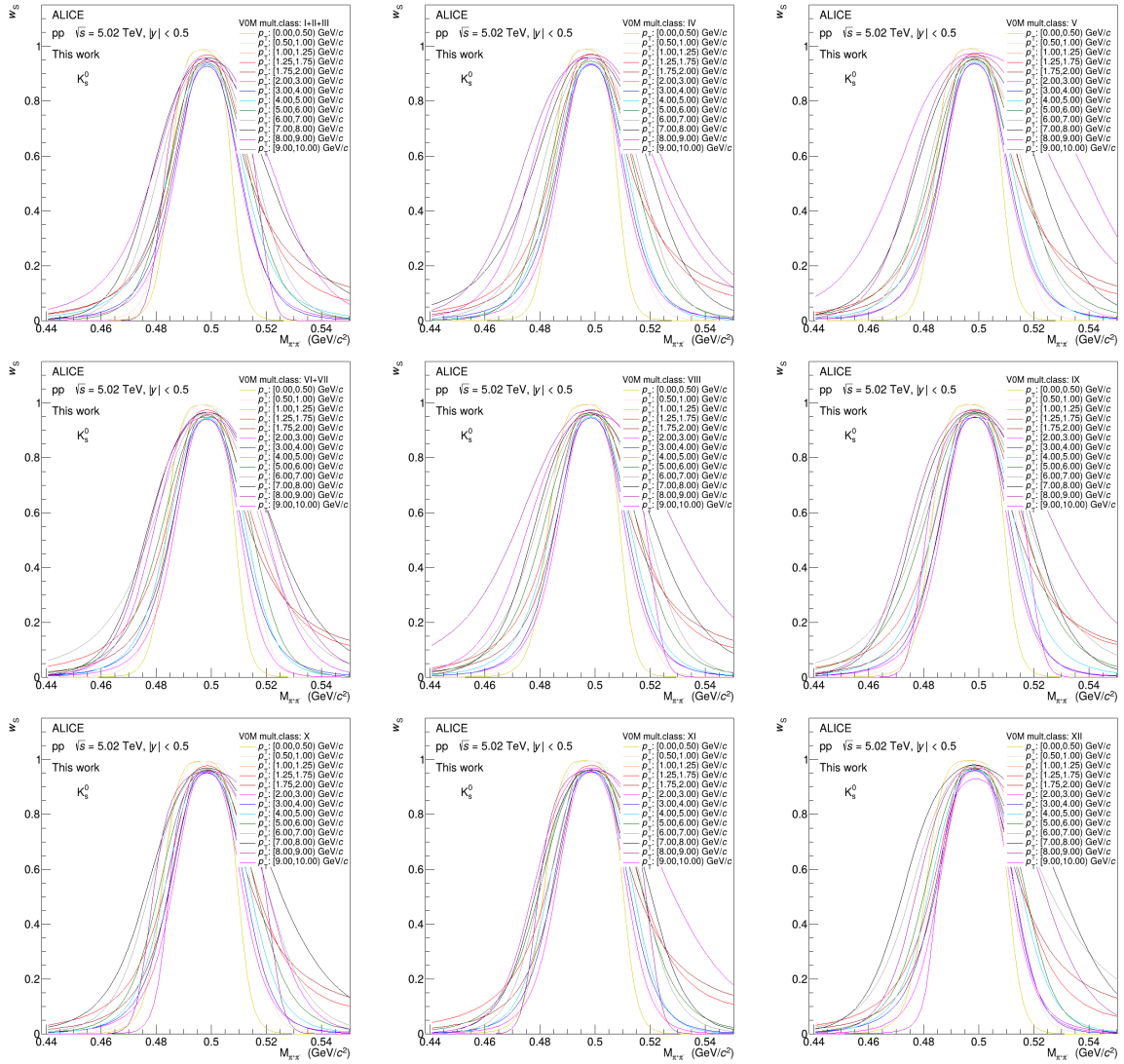

Figure 9.64: K^0_S signal probability trend as a function of the invariant mass, accounting for the p_T dependence for all multiplicity classes.

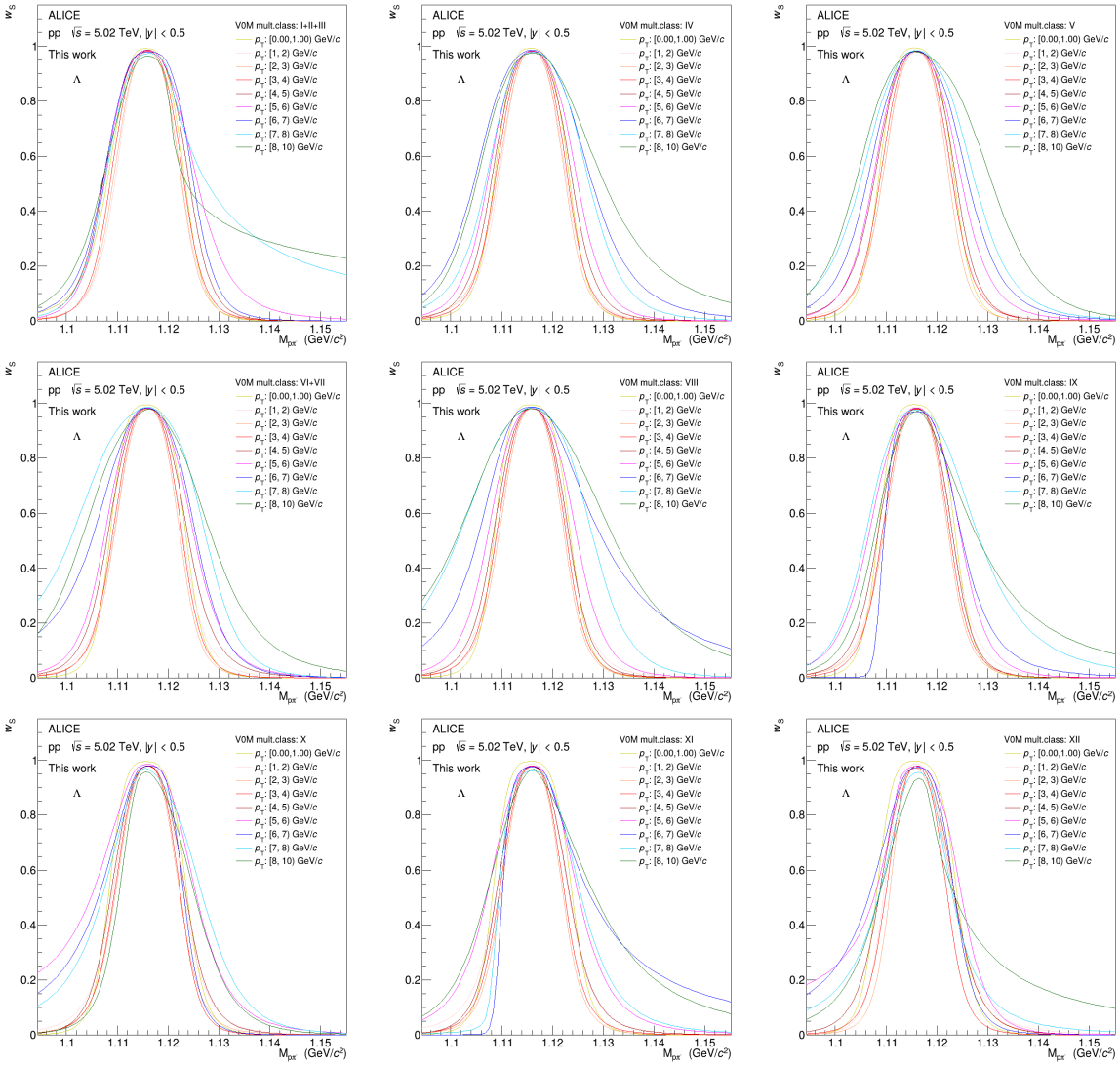

Figure 9.65: Λ signal probability trend as a function of the invariant mass, accounting for the p_{T} dependence for all multiplicity classes.

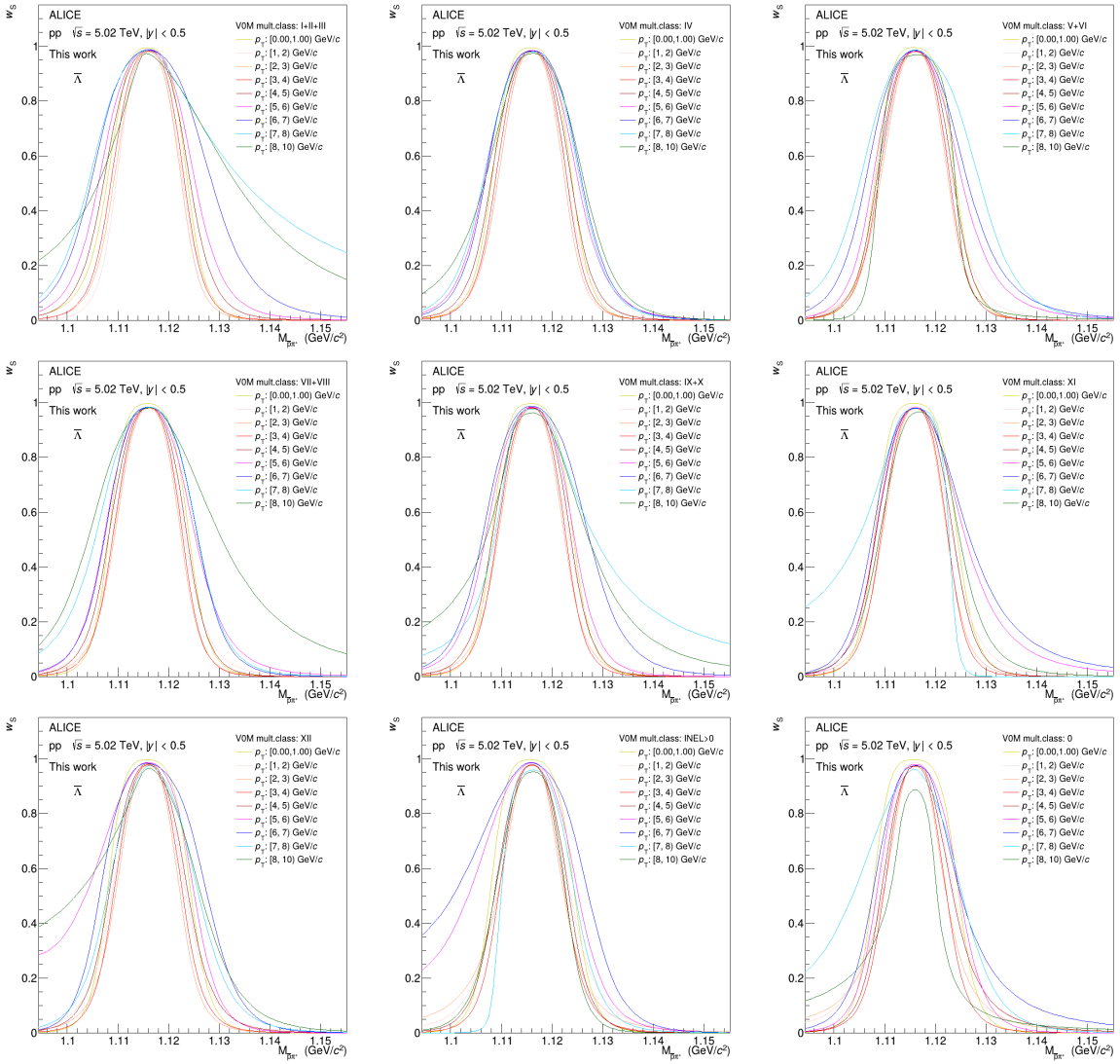

Figure 9.66: $\overline{\Lambda}$ signal probability trend as a function of the invariant mass, accounting for the p_{T} dependence for all multiplicity classes.

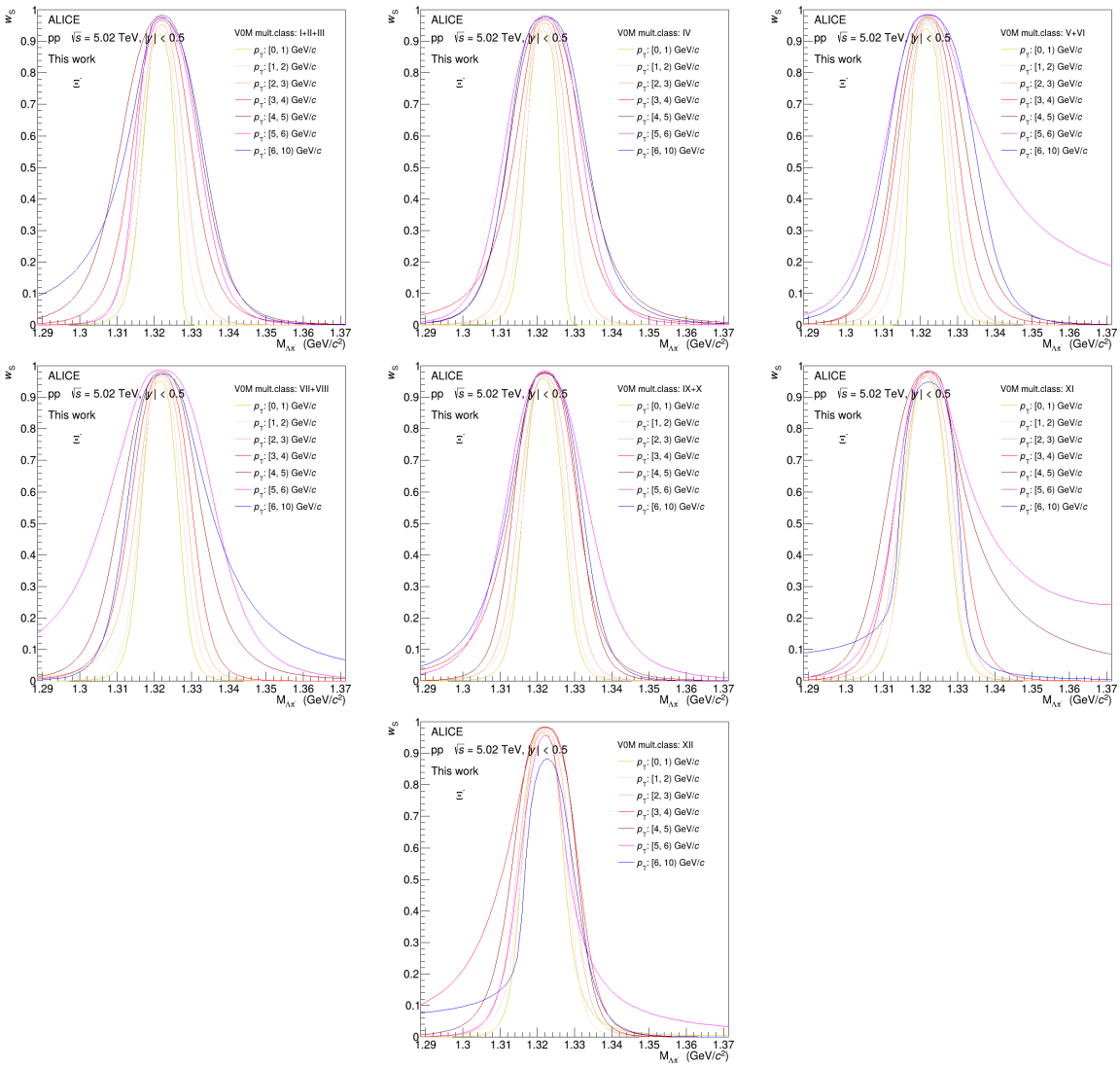

Figure 9.67: Ξ^- signal probability trend as a function of the invariant mass, accounting for the p_{T} dependence for all multiplicity classes.

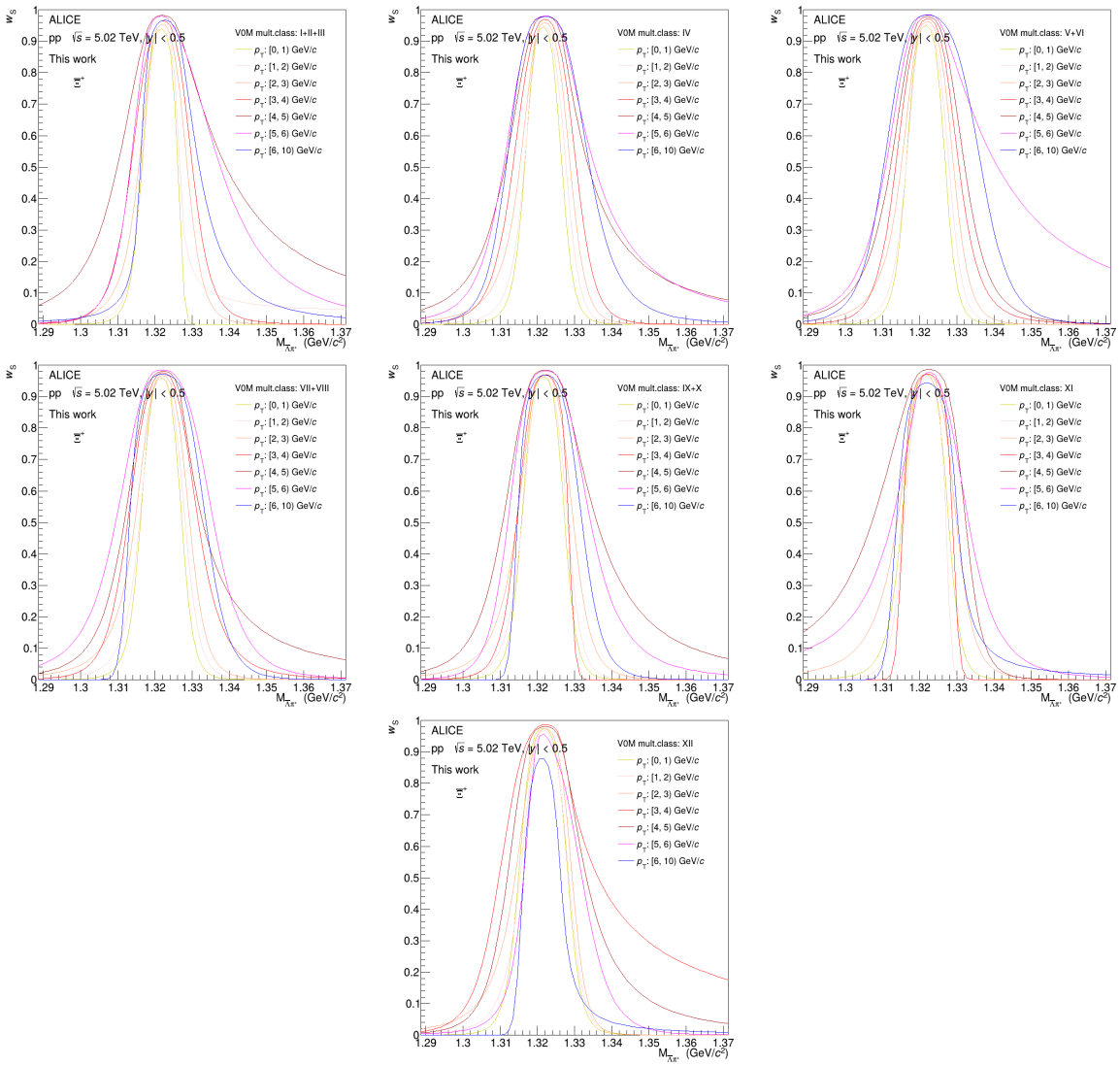

Figure 9.68: $\overline{\Xi}^{+}$ signal probability trend as a function of the invariant mass, accounting for the p_{T} dependence for all multiplicity classes.

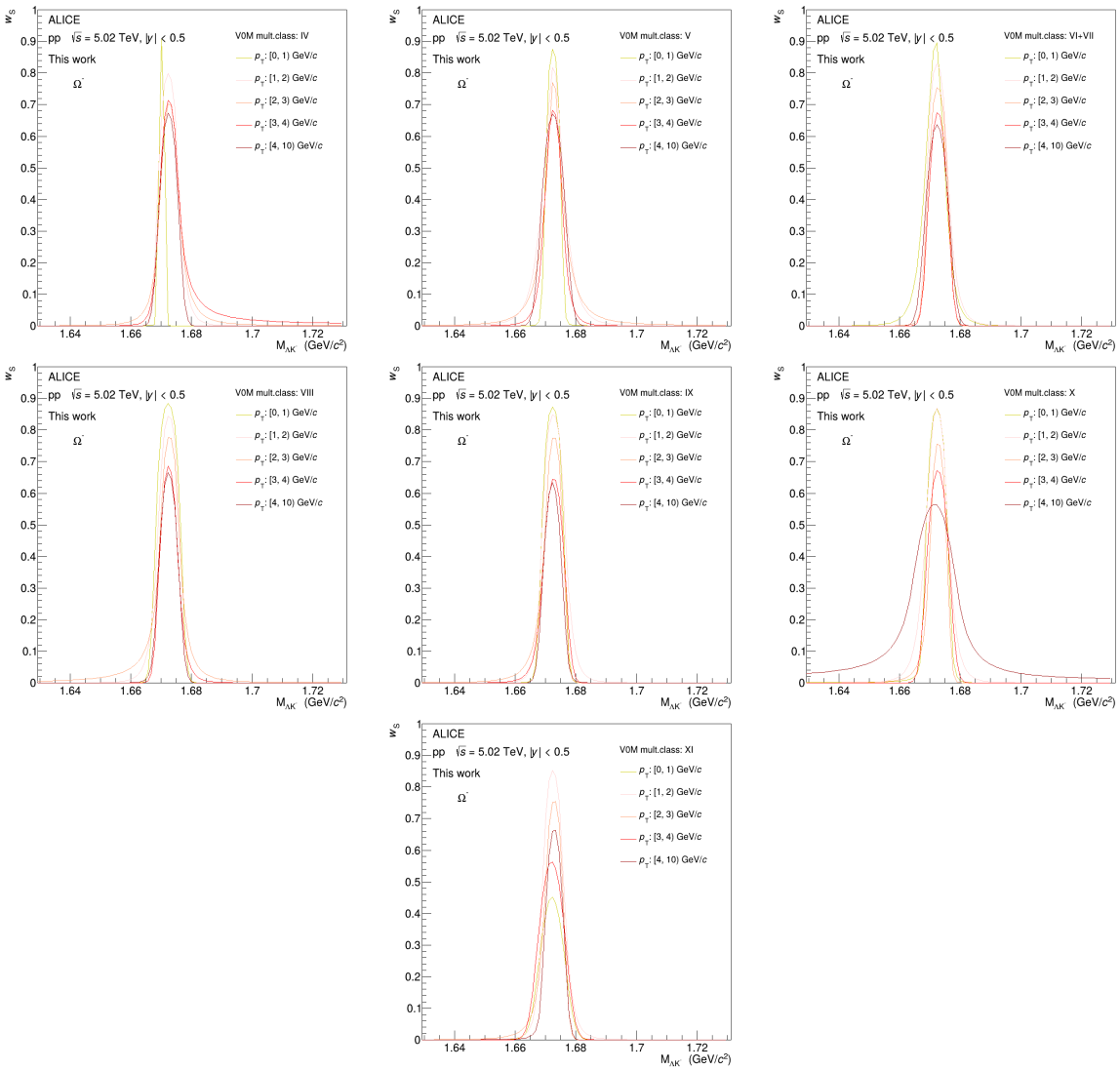

Figure 9.69: Ω^- signal probability trend as a function of the invariant mass, accounting for the p_{T} dependence for all multiplicity classes.

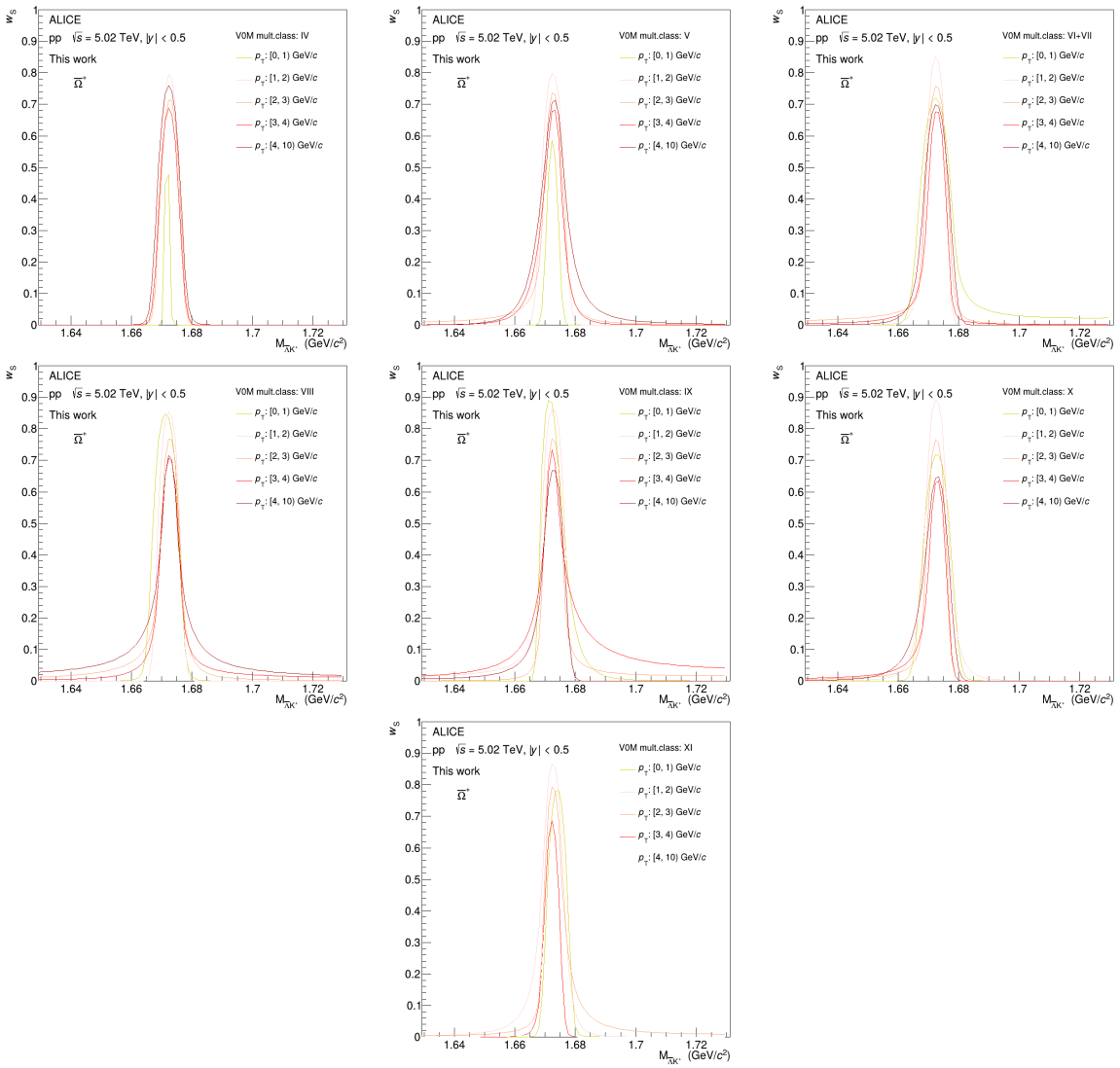

Figure 9.70: $\overline{\Omega}^{+}$ signal probability trend as a function of the invariant mass, accounting for the p_{T} dependence for all multiplicity classes.

9.3 Analysis for different multiplicity classes

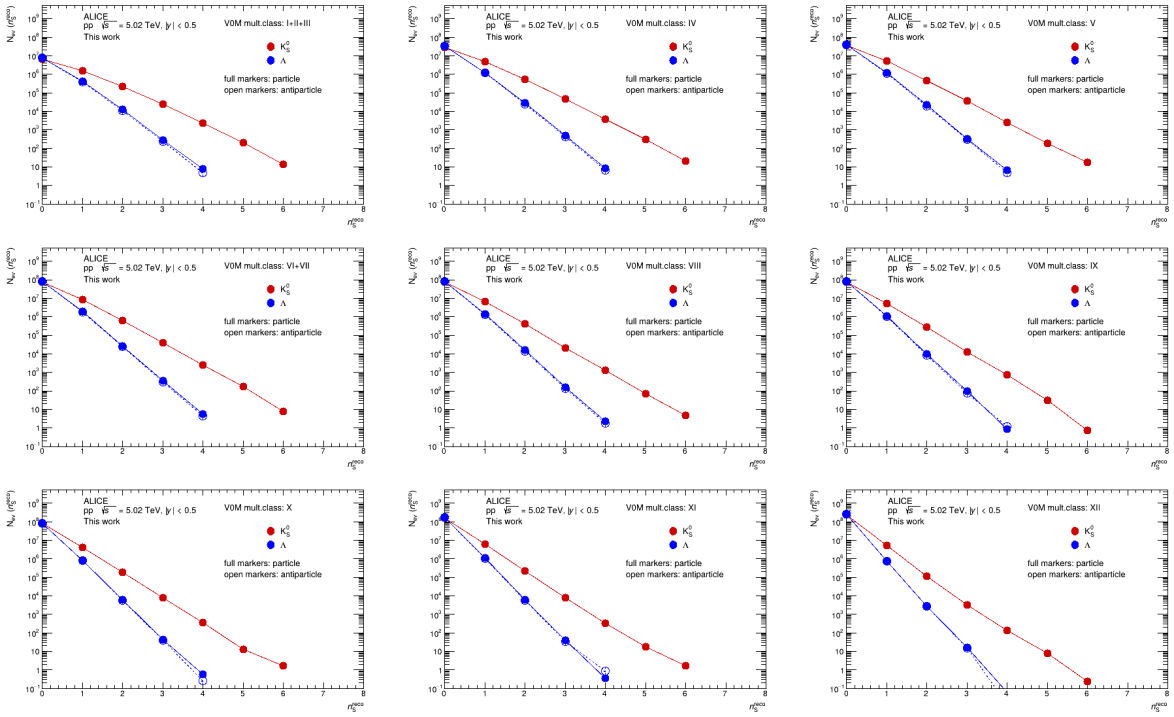

Figure 9.71: Un-corrected multiplicity spectrum for V^0 particles across all the investigated multiplicity classes, arranged from the most central (top-left) to the most peripheral (bottom-right). Particles correspond to full markers, anti-particles to open markers.

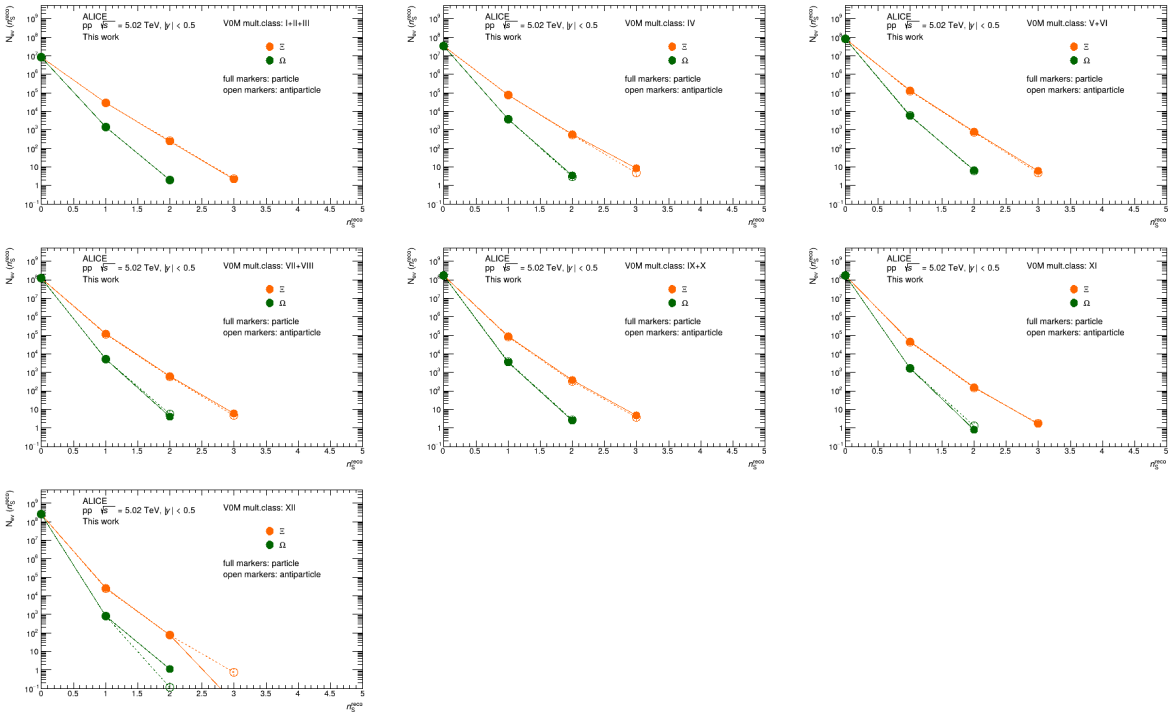

Figure 9.72: Un-corrected multiplicity spectrum for cascade particles across all the investigated multiplicity classes, arranged from the most central (top-left) to the most peripheral (bottom-right). Particles correspond to full markers, anti-particles to open markers.

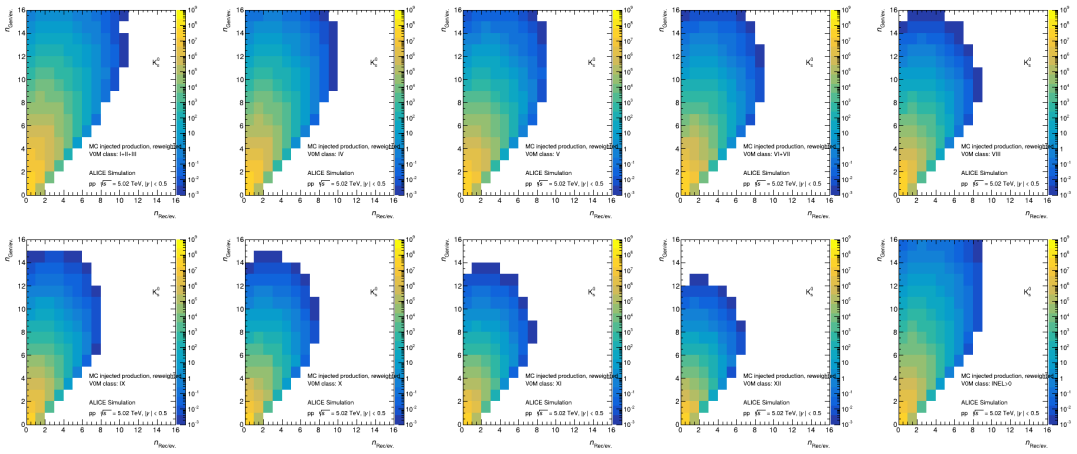

Figure 9.73: Response matrices obtained after the reweighting for K^0_S for all multiplicity classes, starting from high multiplicity moving up to the lowest one. The last response matrix is related to INEL > 0.

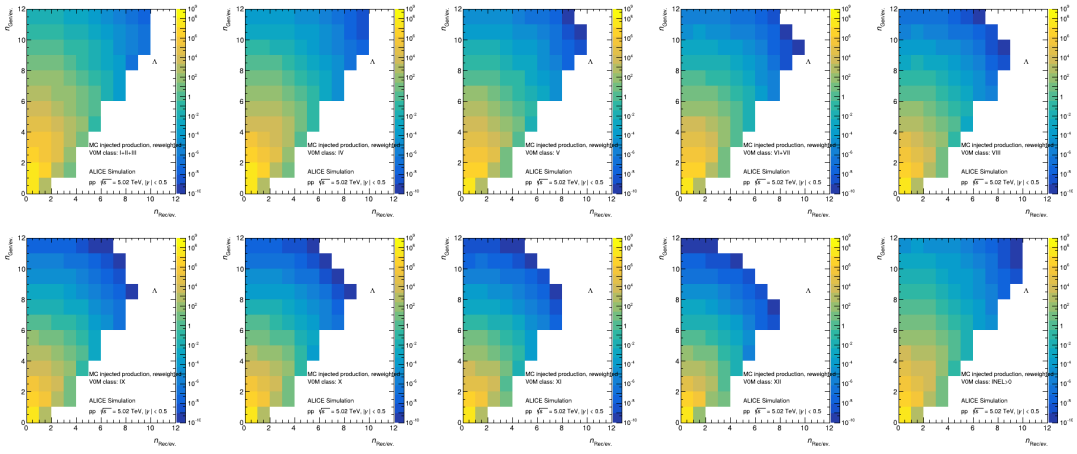

Figure 9.74: Response matrices obtained after the reweighting for Λ for all multiplicity classes, starting from high multiplicity moving up to the lowest one. The last response matrix is related to INEL > 0.

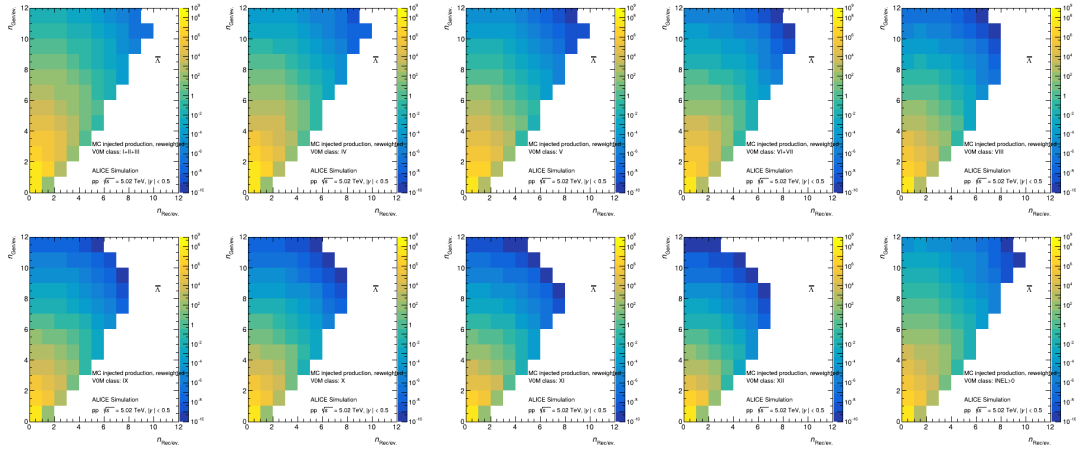

Figure 9.75: Response matrices obtained after the reweighting for $\overline{\Lambda}$ for all multiplicity classes, starting from high multiplicity moving up to the lowest one. The last response matrix is related to INEL > 0.

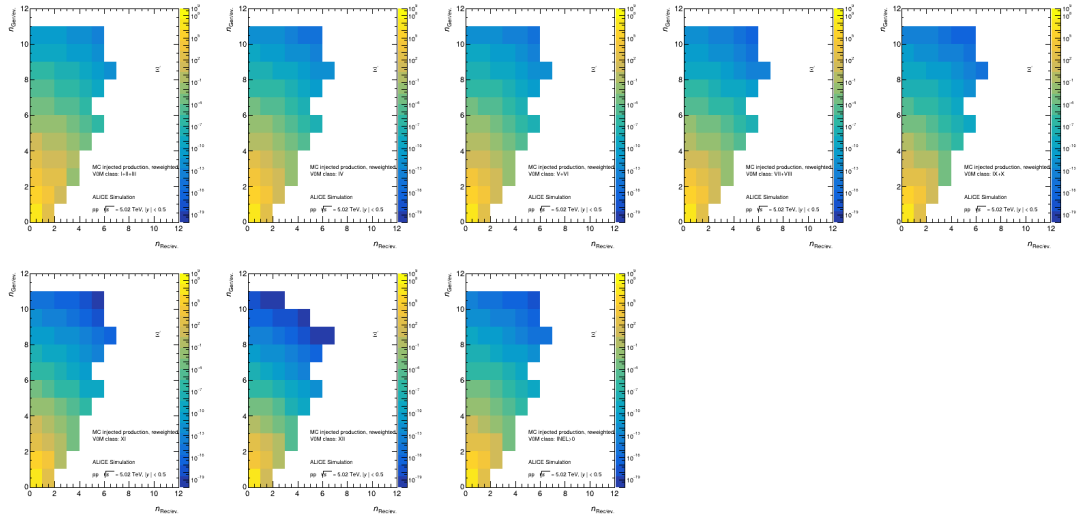

Figure 9.76: Response matrices obtained after the reweighting for Ξ^- for all multiplicity classes, starting from high multiplicity moving up to the lowest one. The last response matrix is related to INEL > 0.

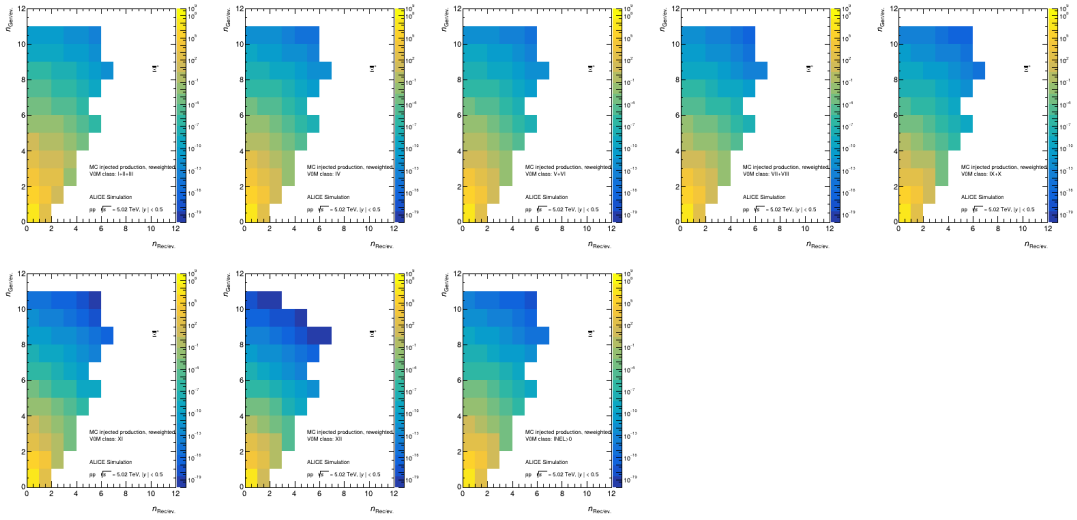

Figure 9.77: Response matrices obtained after the reweighting for $\overline{\Xi}^{+}$ for all multiplicity classes, starting from high multiplicity moving up to the lowest one. The last response matrix is related to INEL > 0.

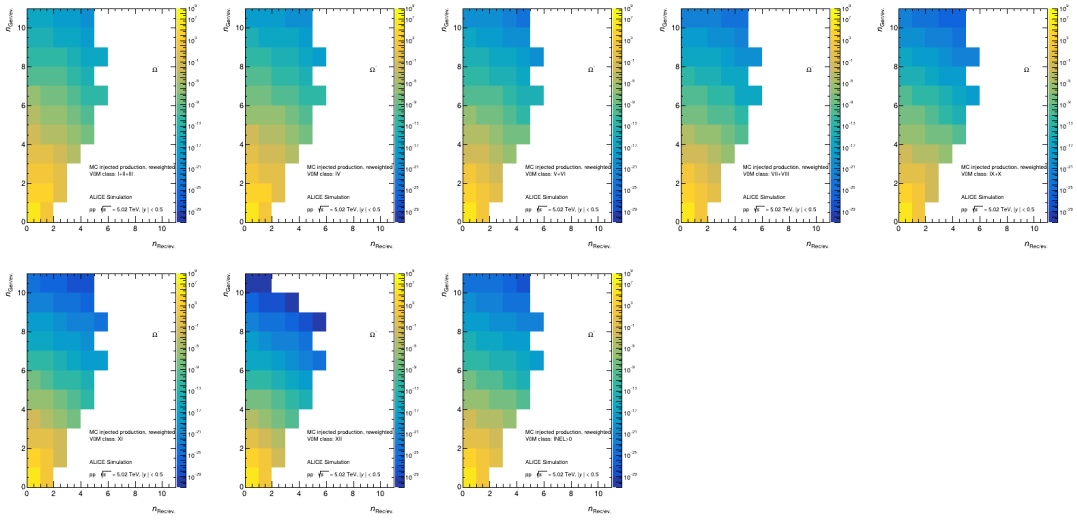

Figure 9.78: Response matrices obtained after the reweighting for Ω^{-} for all multiplicity classes, starting from high multiplicity moving up to the lowest one. The last response matrix is related to INEL > 0.

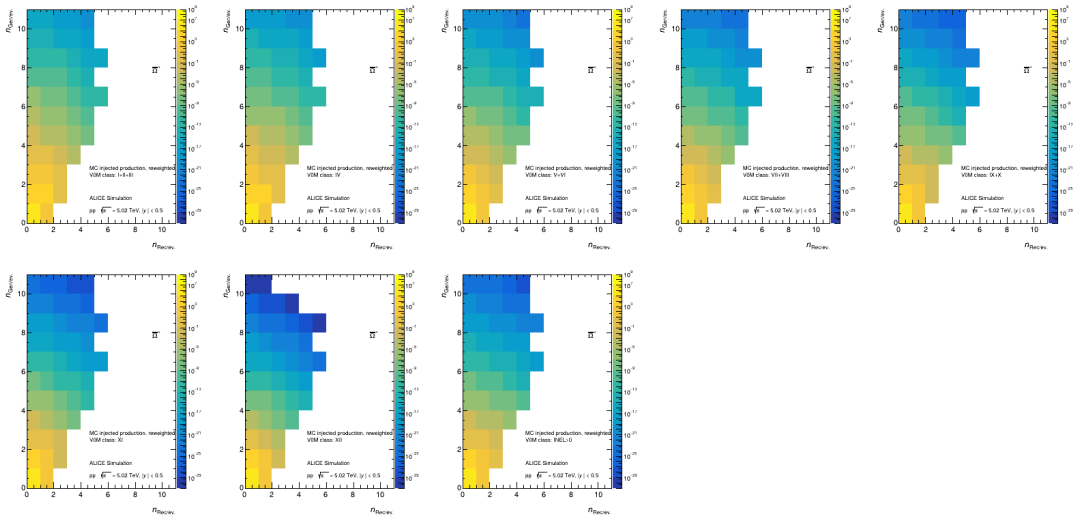

Figure 9.79: Response matrices obtained after the reweighting for $\overline{\Omega}^{+}$ for all multiplicity classes, starting from high multiplicity moving up to the lowest one. The last response matrix is related to INEL > 0.

9.4 Singular systematic source plots

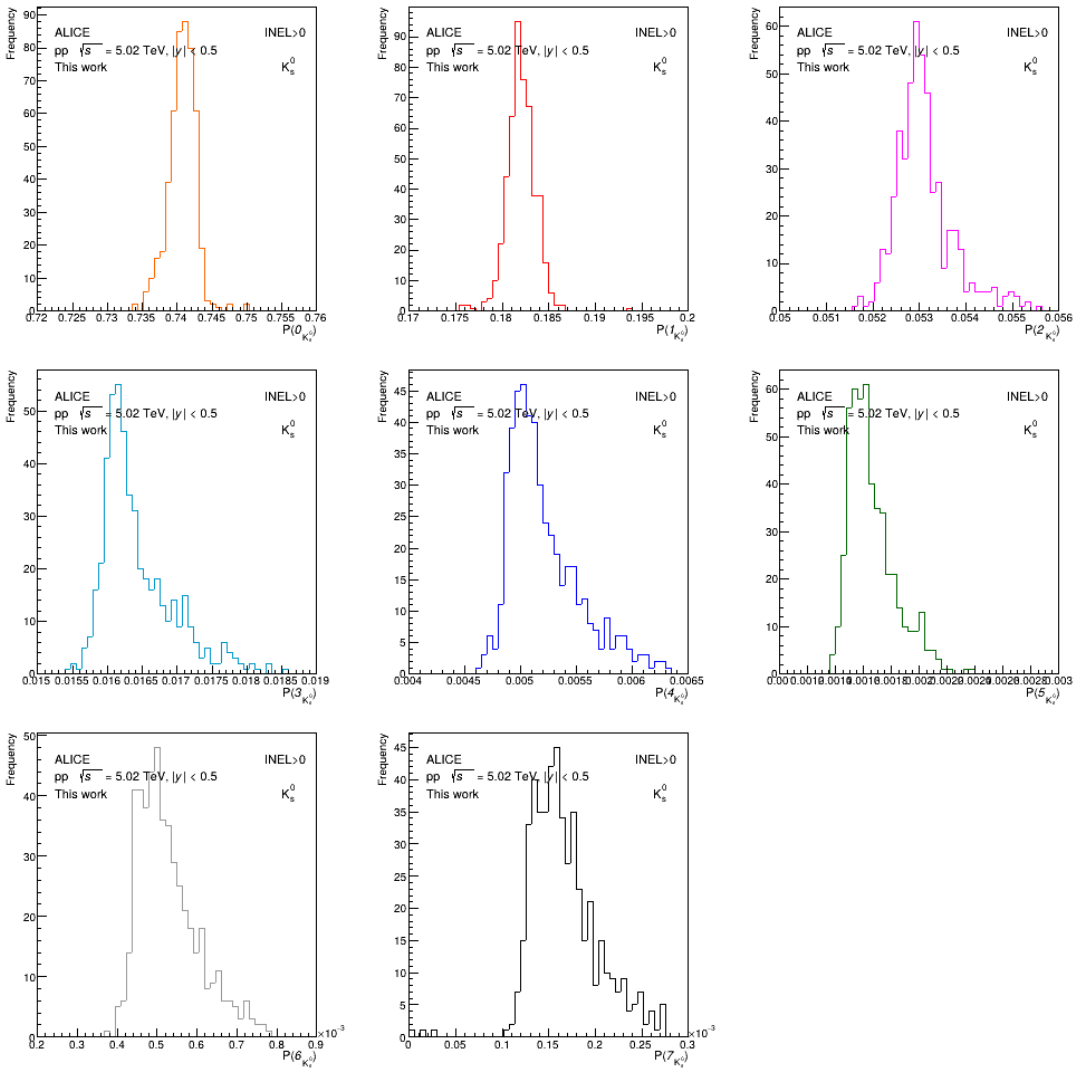

Figure 9.80: The probability of $n-$particles/event for each trial at fixed $n-$particles/event was evaluated and a gaussian dispersion was obtained for K^0_S. In the first line there were the results for 0 particles/event, 1 particles/event and 2 particles/event, in the second line the results for 3 particles/event, 4 particles/event and 5 particles/event and in the third line the results for 6 particles/event and 7 particles/event.

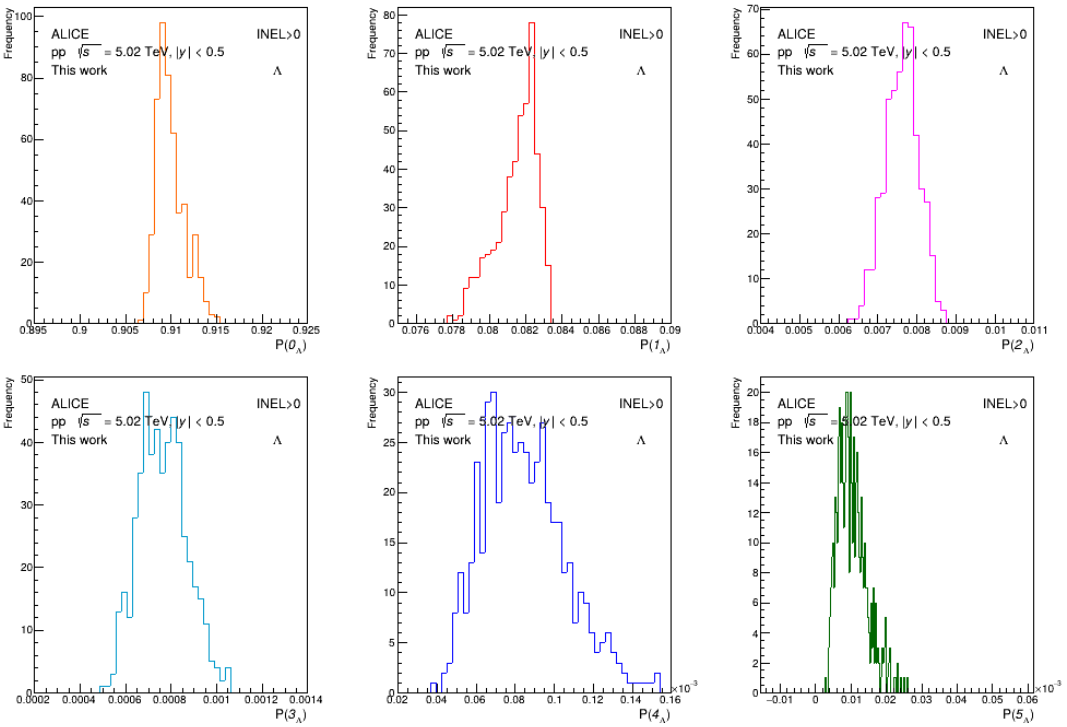

Figure 9.81: The probability of $n-$particles/event for each trial at fixed $n-$particles/event was evaluated and a gaussian dispersion was obtained for Λ. In the first line there were the results for 0 particles/event, 1 particles/event and 2 particles/event and in the second line the results for 3 particles/event, 4 particles/event and 5 particles/event.

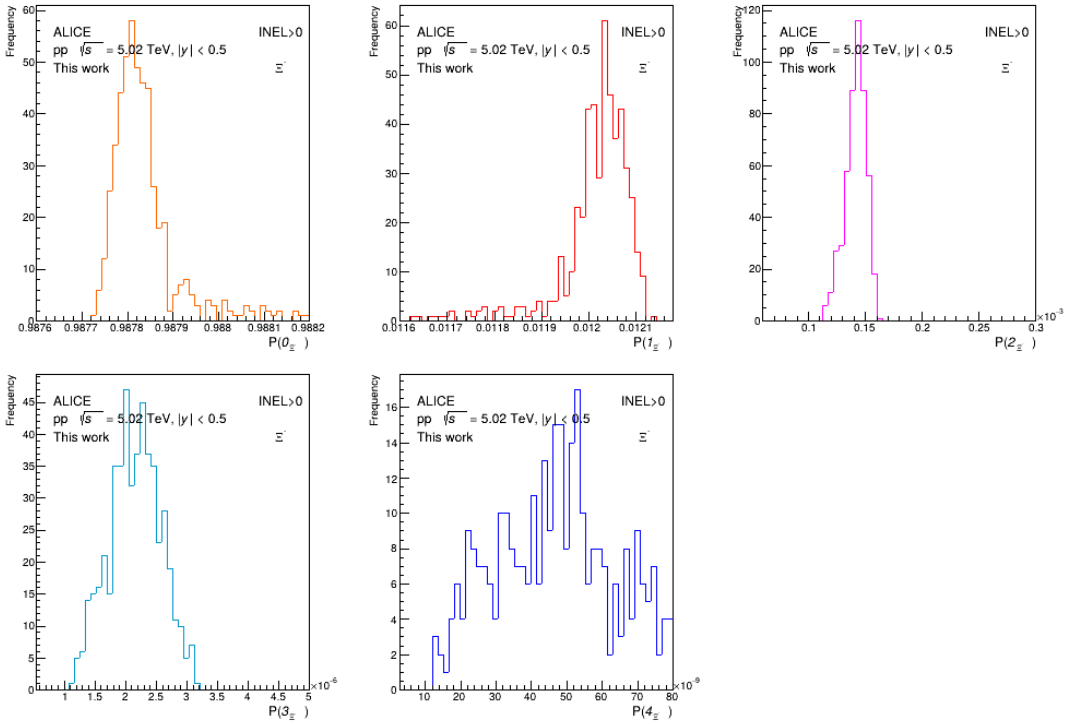

Figure 9.82: The probability of $n-$particles/event for each trial at fixed $n-$particles/event was evaluated and a gaussian dispersion was obtained for Ξ^-. In the first line there were the results for 0 particles/event, 1 particles/event and 2 particles/event and in the second line the results for 3 particles/event and 4 particles/event.

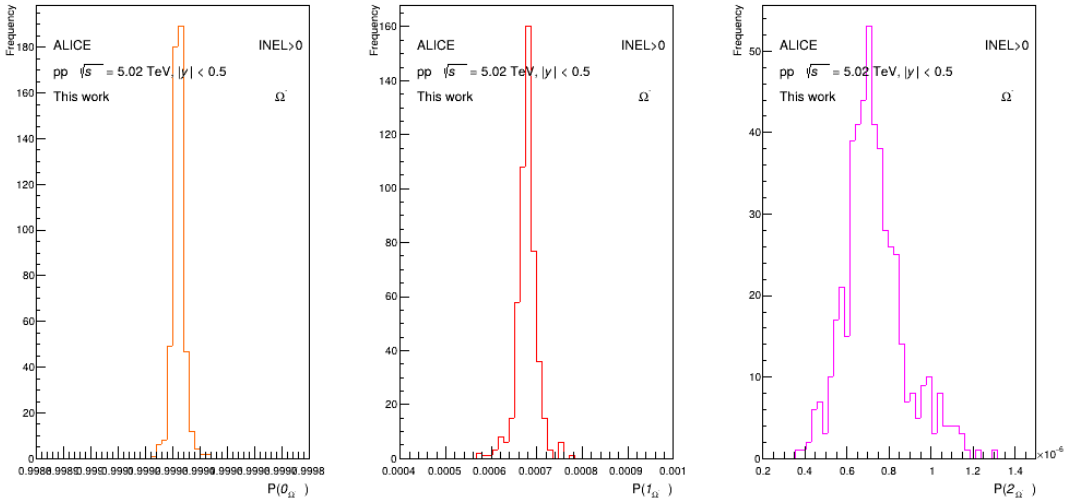

Figure 9.83: The probability of $n-$particles/event for each trial at fixed $n-$particles/event was evaluated and a gaussian dispersion was obtained for Ω^-. There were the results for 0 particles/event, 1 particles/event and 2 particles/event.

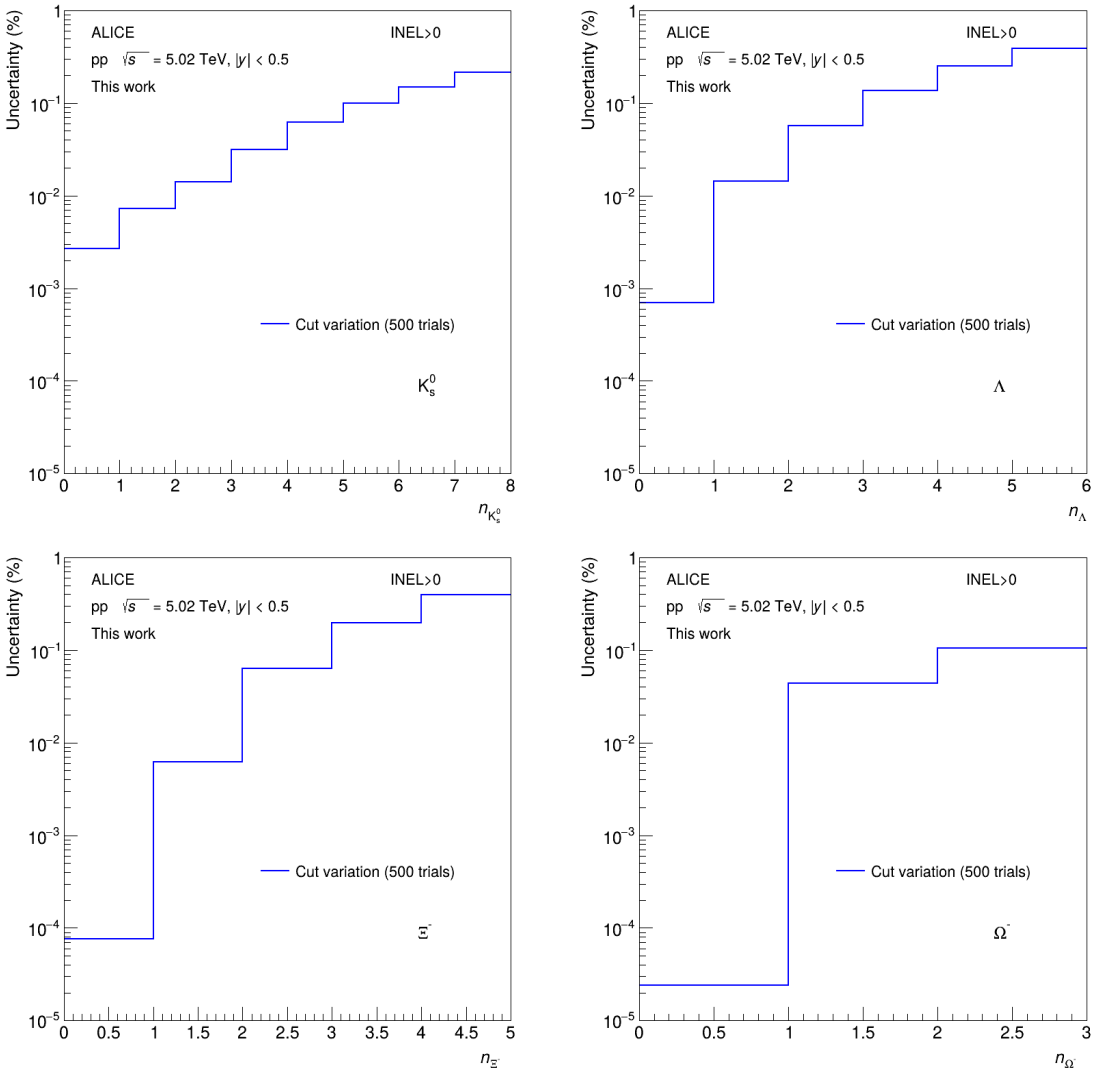

Figure 9.84: The relative systematic errors associated with the cut variation are presented in the first row for K^0_S and Λ, and in the second row for Ξ^- and Ω^-, for INEL > 0.

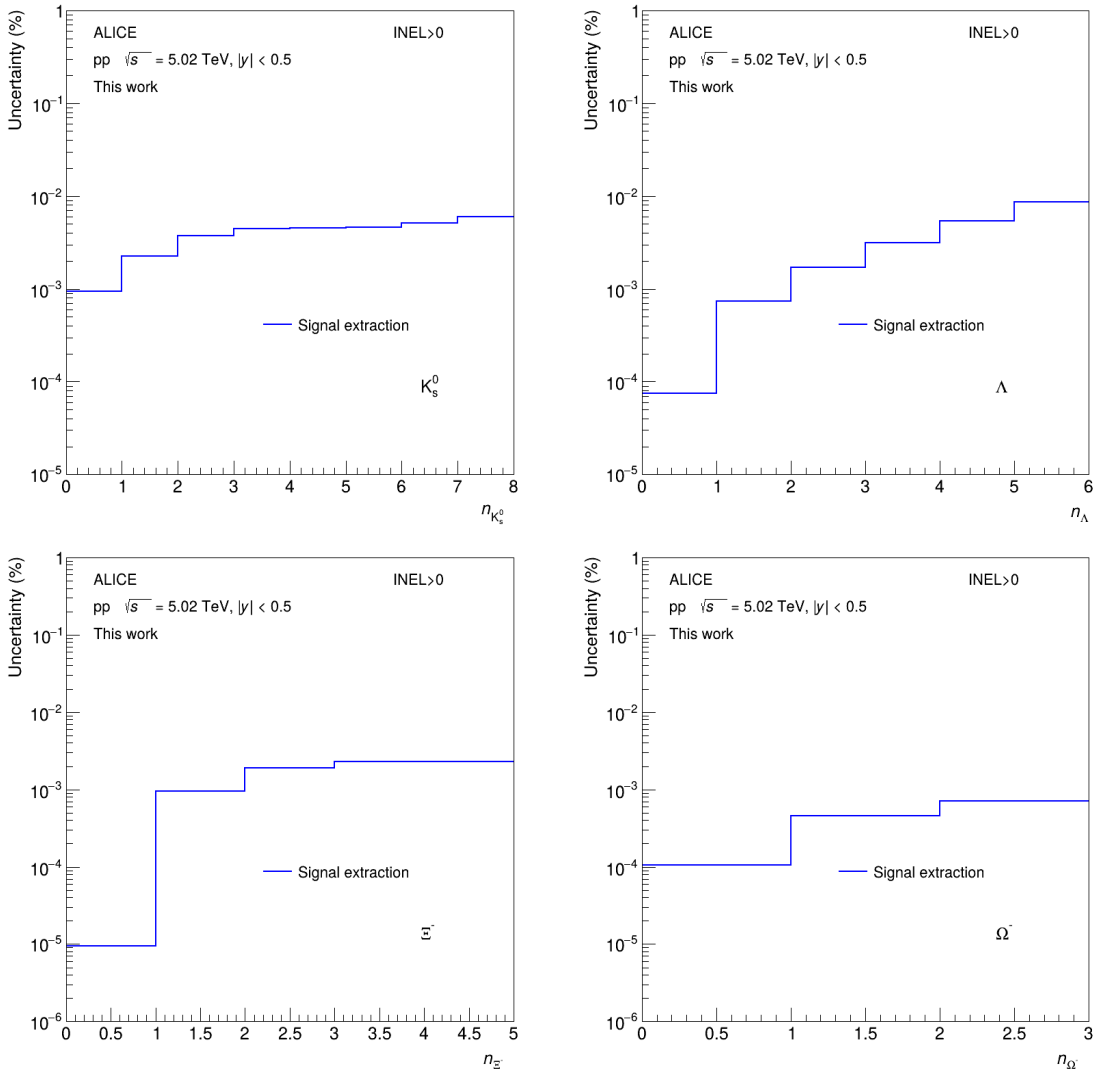

Figure 9.85: The relative systematic errors associated with the signal extraction are presented in the first row for K^0_S and Λ, and in the second row for Ξ^- and Ω^-, for INEL > 0.

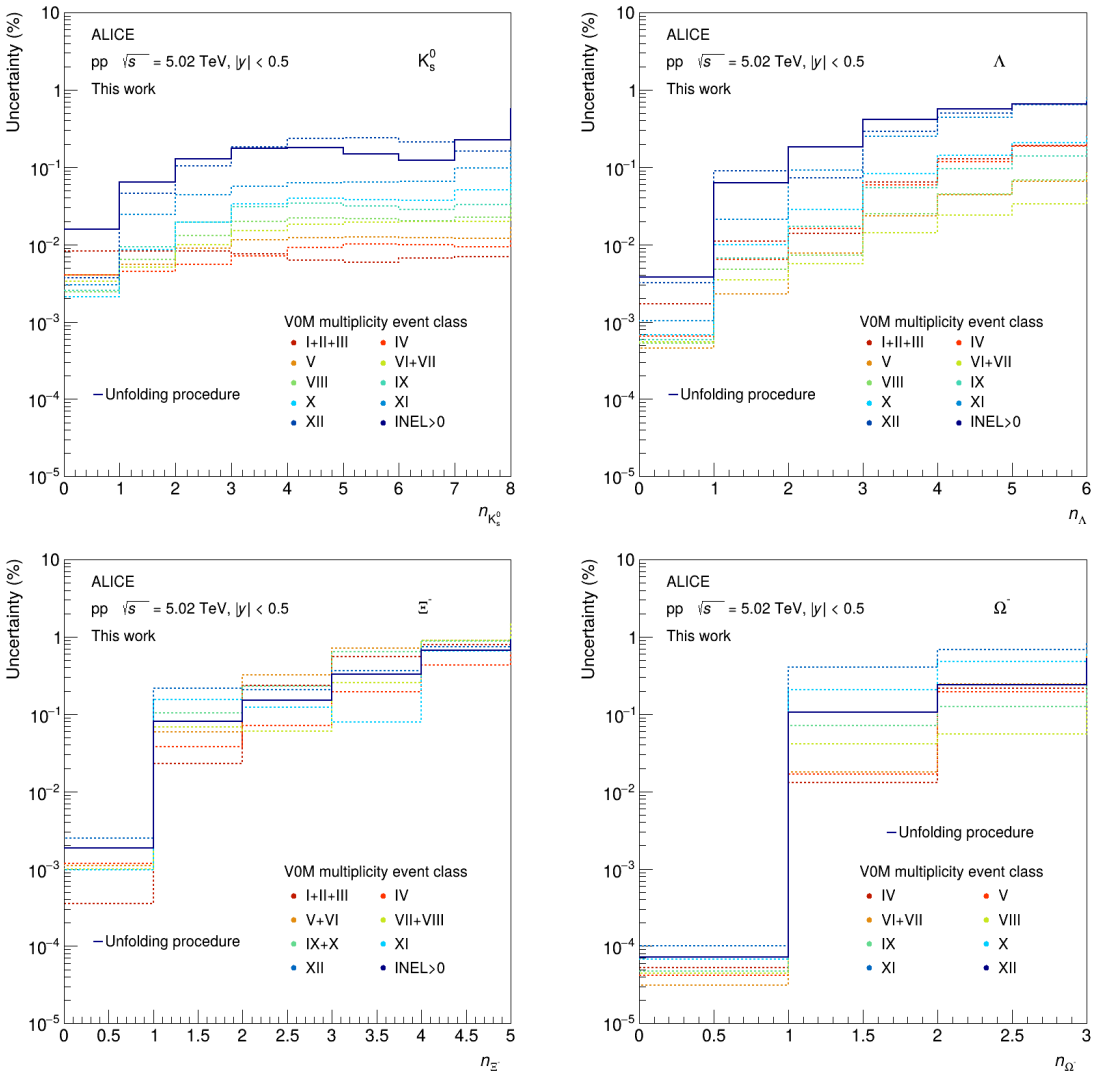

Figure 9.86: The relative systematic errors associated with the unfolding procedure are presented in the first row for K^0_S and Λ, and in the second row for Ξ^- and Ω^-, across all the investigated multiplicity classes.

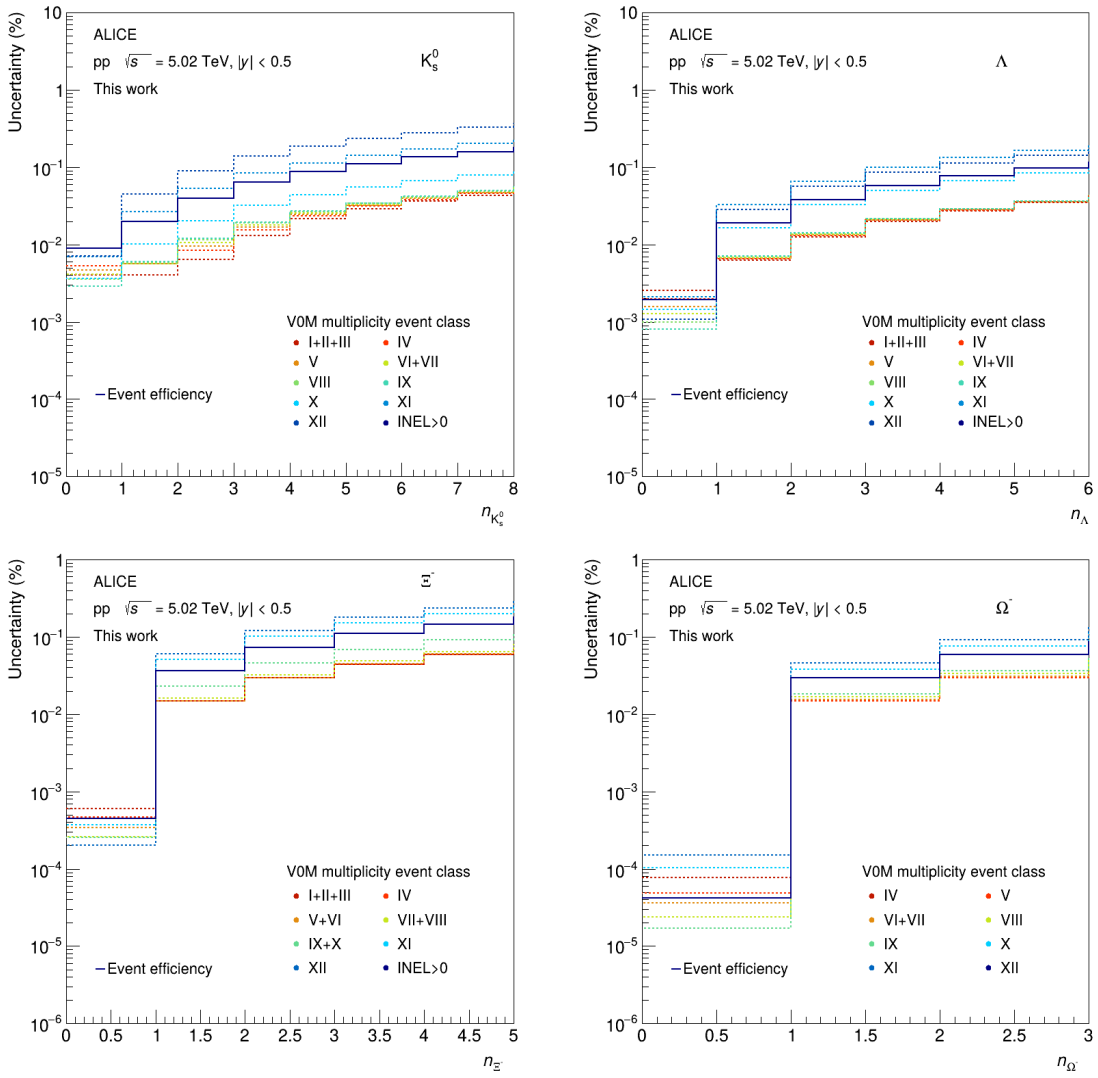

Figure 9.87: The relative systematic errors associated with the trigger inefficiencies are presented in the first row for K^0_S and Λ, and in the second row for Ξ^- and Ω^-, across all the investigated multiplicity classes.

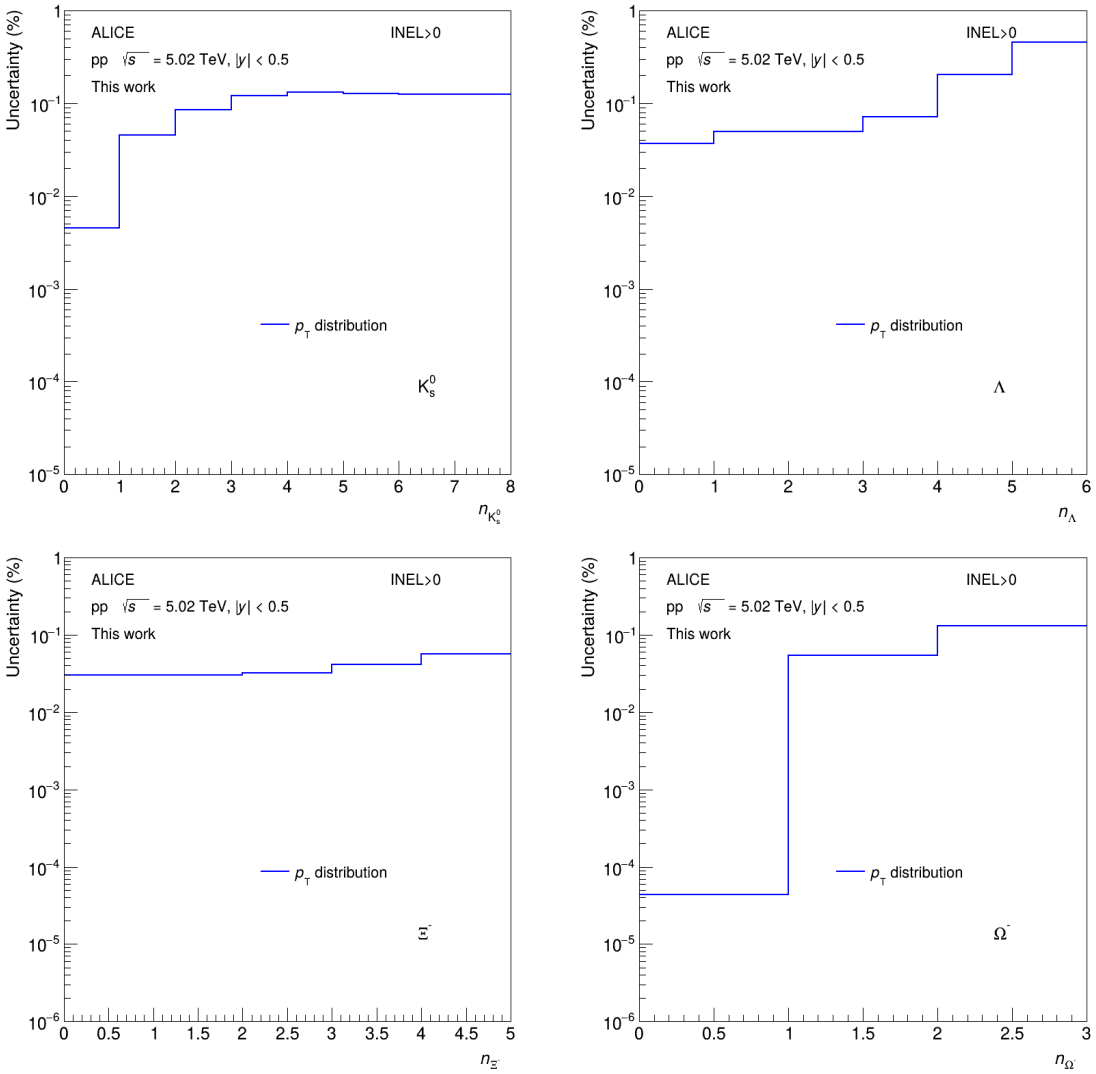

Figure 9.88: The relative systematic errors associated with the knowledge of the p_{T} distribution in MC are presented in the first row for $\mathrm{K}^0_{\mathrm{S}}$ and Λ, and in the second row for Ξ^- and Ω^-, for INEL > 0.

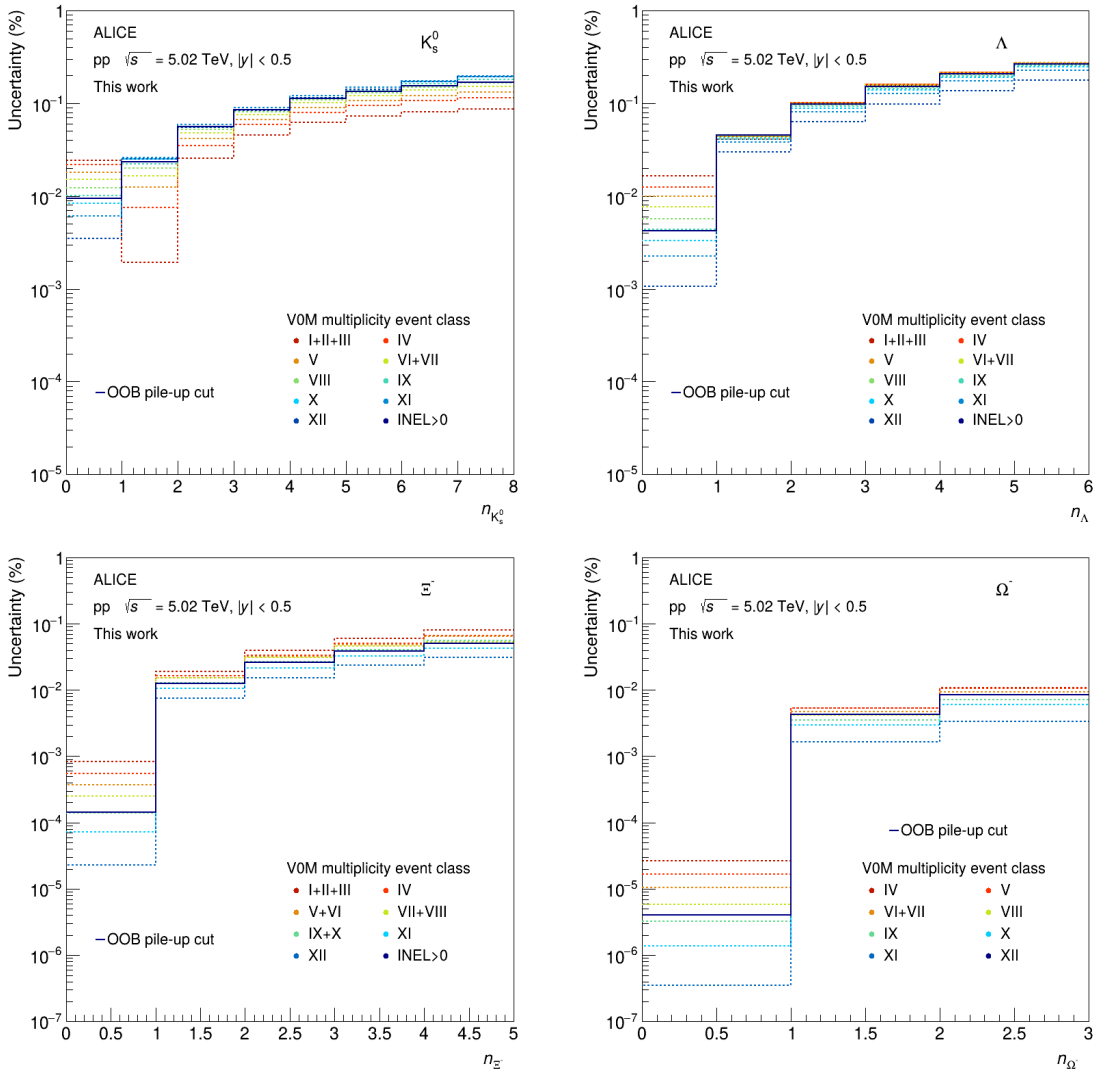

Figure 9.89: The relative systematic errors associated with the effect of the cut on the OOB pile-up are presented in the first row for K^0_S and Λ, and in the second row for Ξ^- and Ω^-, across all the investigated multiplicity classes.

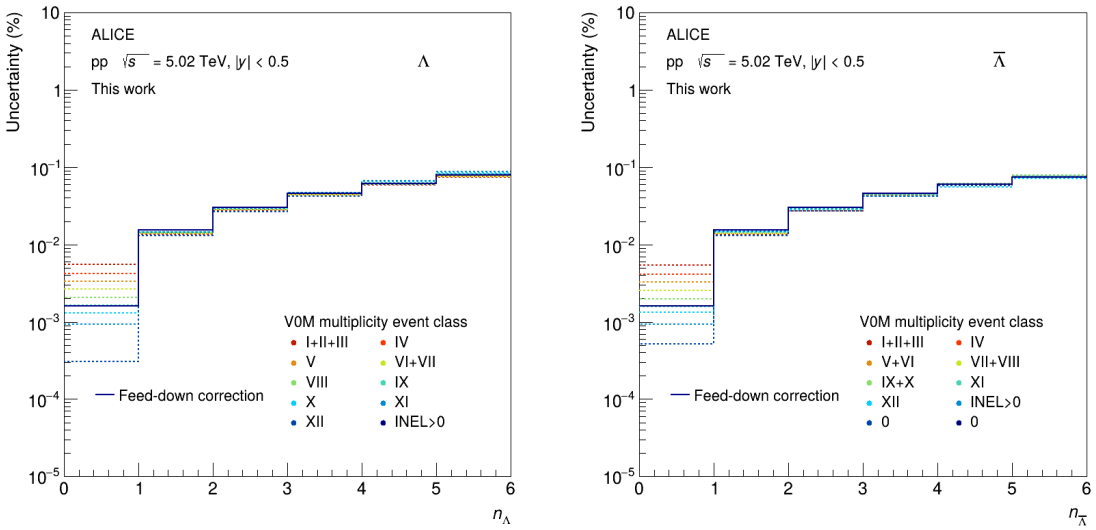

Figure 9.90: The relative systematic errors associated with the feed-down correction are presented for Λ and $\overline{\Lambda}$ respectively on the left and on the right, across all the investigated multiplicity classes.

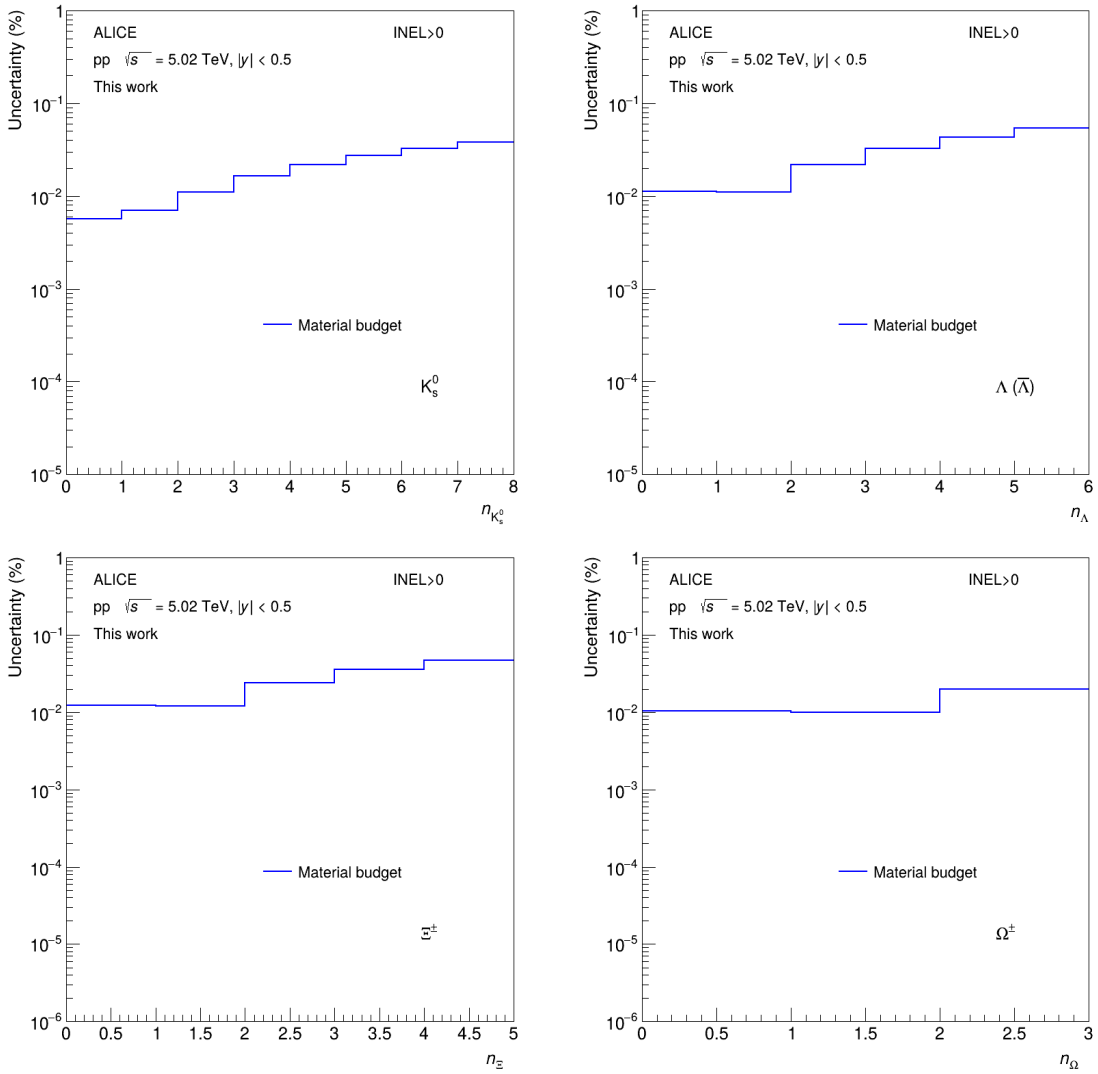

Figure 9.91: The relative systematic errors associated with the material budget are presented in the first row for K^0_S and Λ, and in the second row for Ξ^- and Ω^-, for INEL > 0.

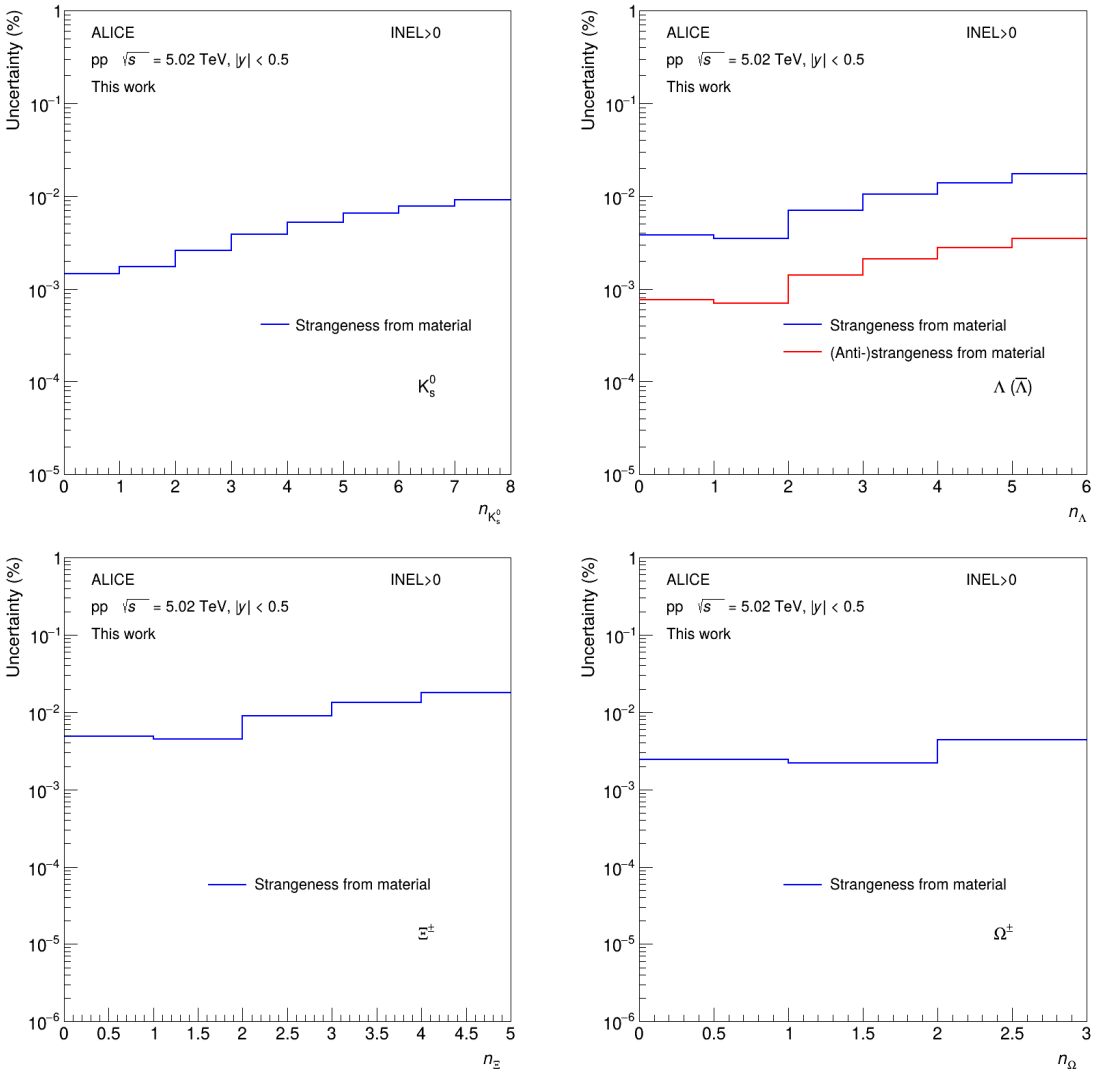

Figure 9.92: The relative systematic errors associated with the strange particle production from hadron-material interactions are presented in the first row for K^0_S and Λ ($\overline{\Lambda}$), and in the second row for Ξ^- and Ω^-, for INEL > 0.

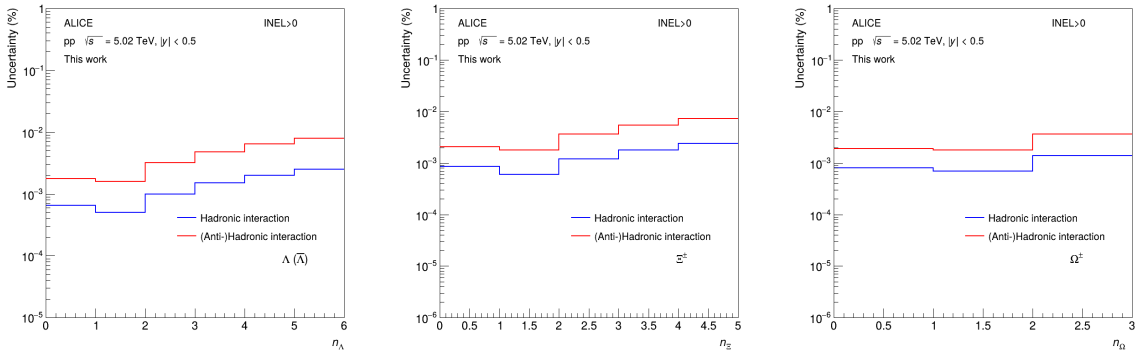

Figure 9.93: The relative systematic errors associated with the the annihilation of strange antiparticles in interactions with the detector material are presented for Λ, Ξ^- and Ω^- (blue) together with the results for the respective anti-particle (red) for INEL > 0.

9.5 Convergence Plots

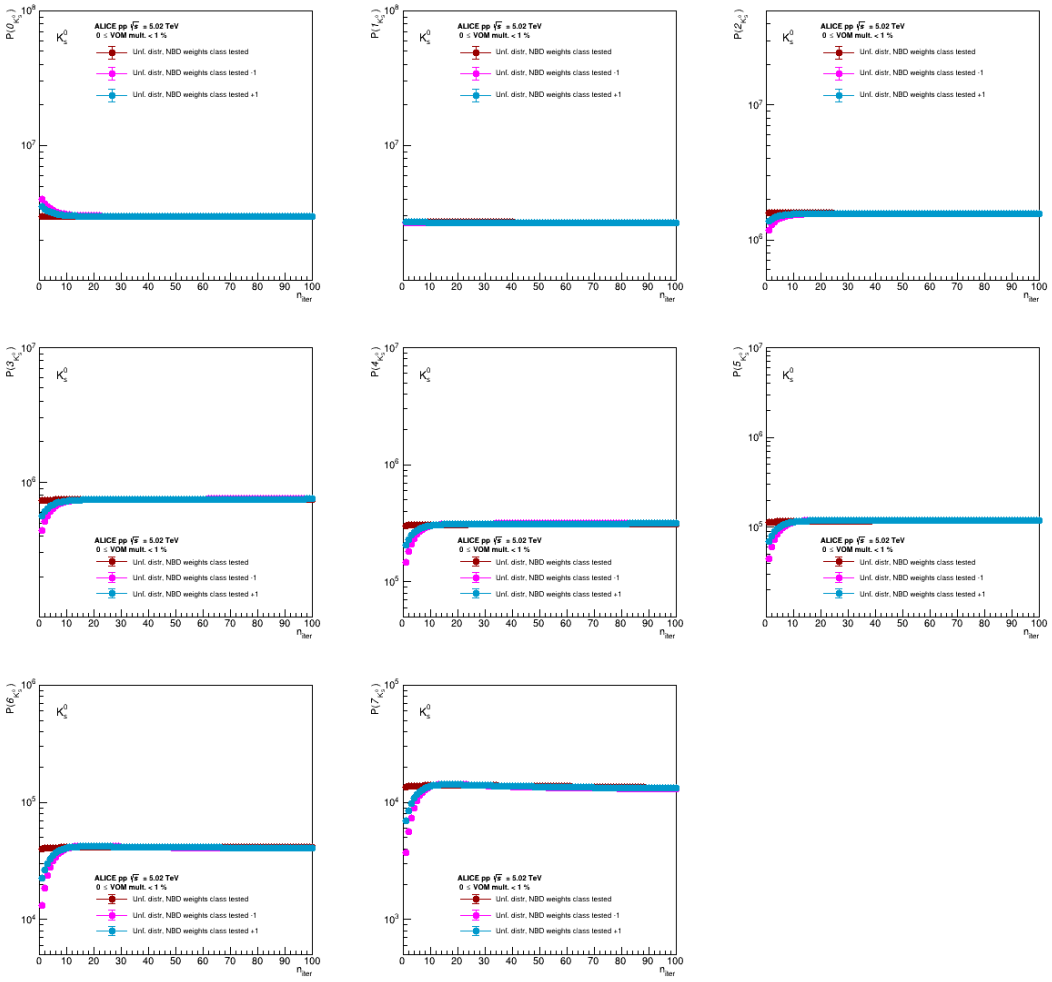

Figure 9.94: Comparison of the unfolded distributions for the $0 \leq V0M < 1\%$ class for K^0_S as a function of the number of iterations: results using NBD-weights specific to the class are shown in dark red, while those obtained using weights from classes $i-1$ (in this case $i+2$) and $i+1$ are depicted in pink and azure, respectively.

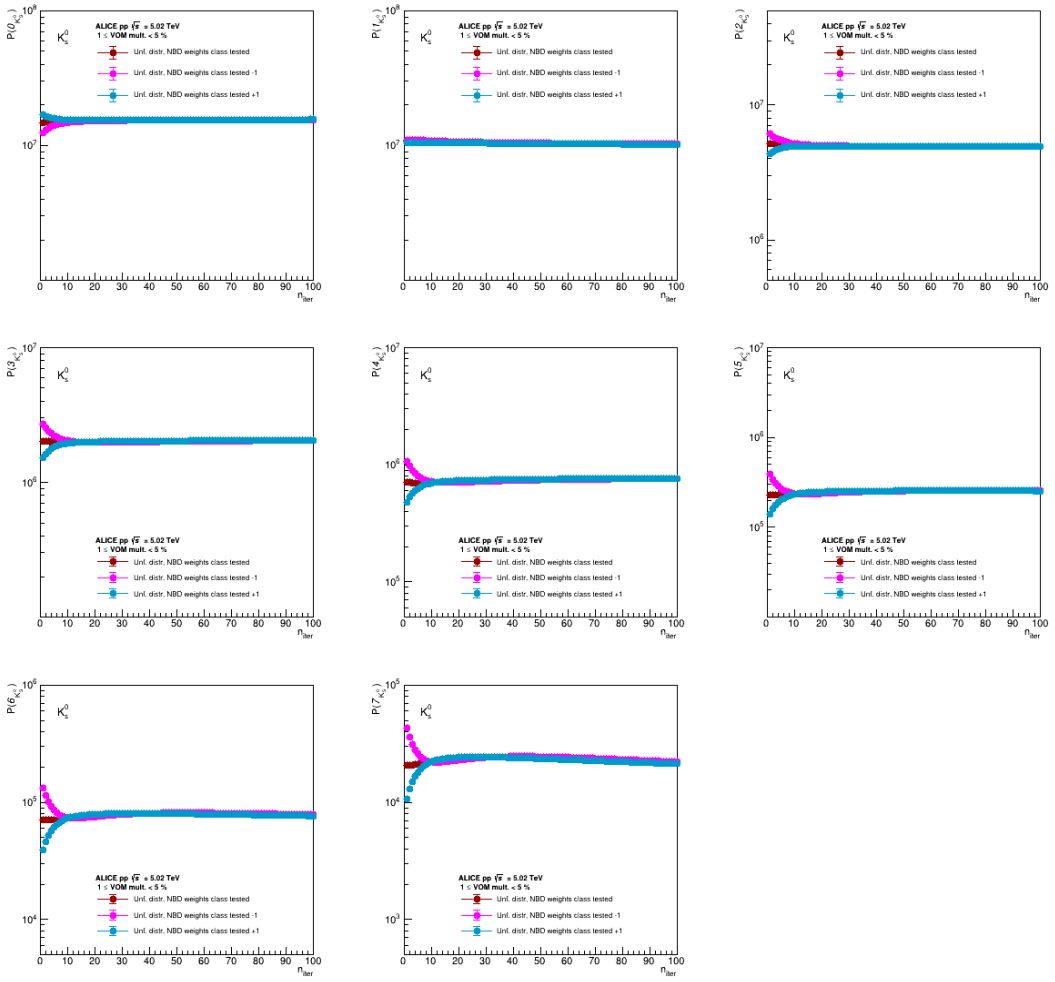

Figure 9.95: Comparison of the unfolded distributions for the $1 \leq V0M < 5\%$ class for K^0_S as a function of the number of iterations: results using NBD-weights specific to the class are shown in dark red, while those obtained using weights from classes $i-1$ and $i+1$ are depicted in pink and azure, respectively.

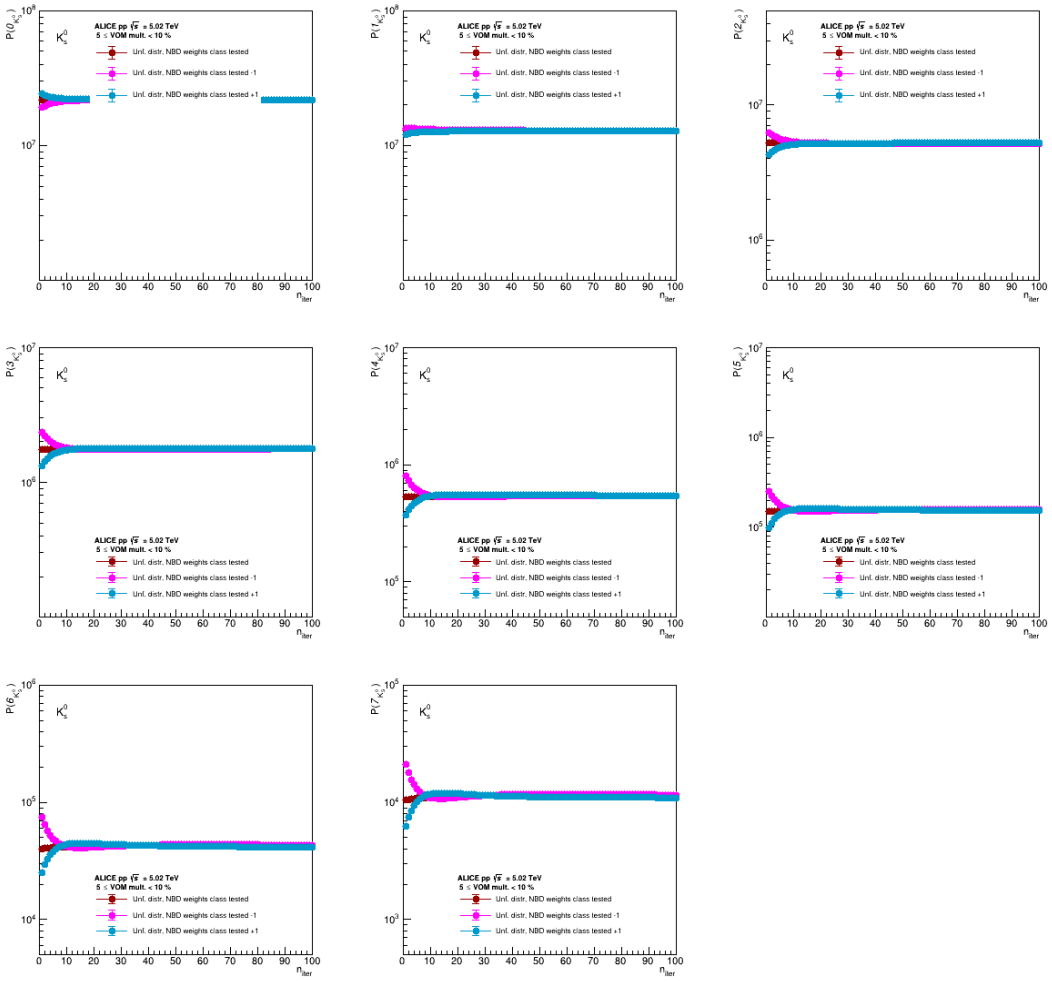

Figure 9.96: Comparison of the unfolded distributions for the $5 \leq V0M < 10\%$ class for K^0_S as a function of the number of iterations: results using NBD-weights specific to the class are shown in dark red, while those obtained using weights from classes $i-1$ and $i+1$ are depicted in pink and azure, respectively.

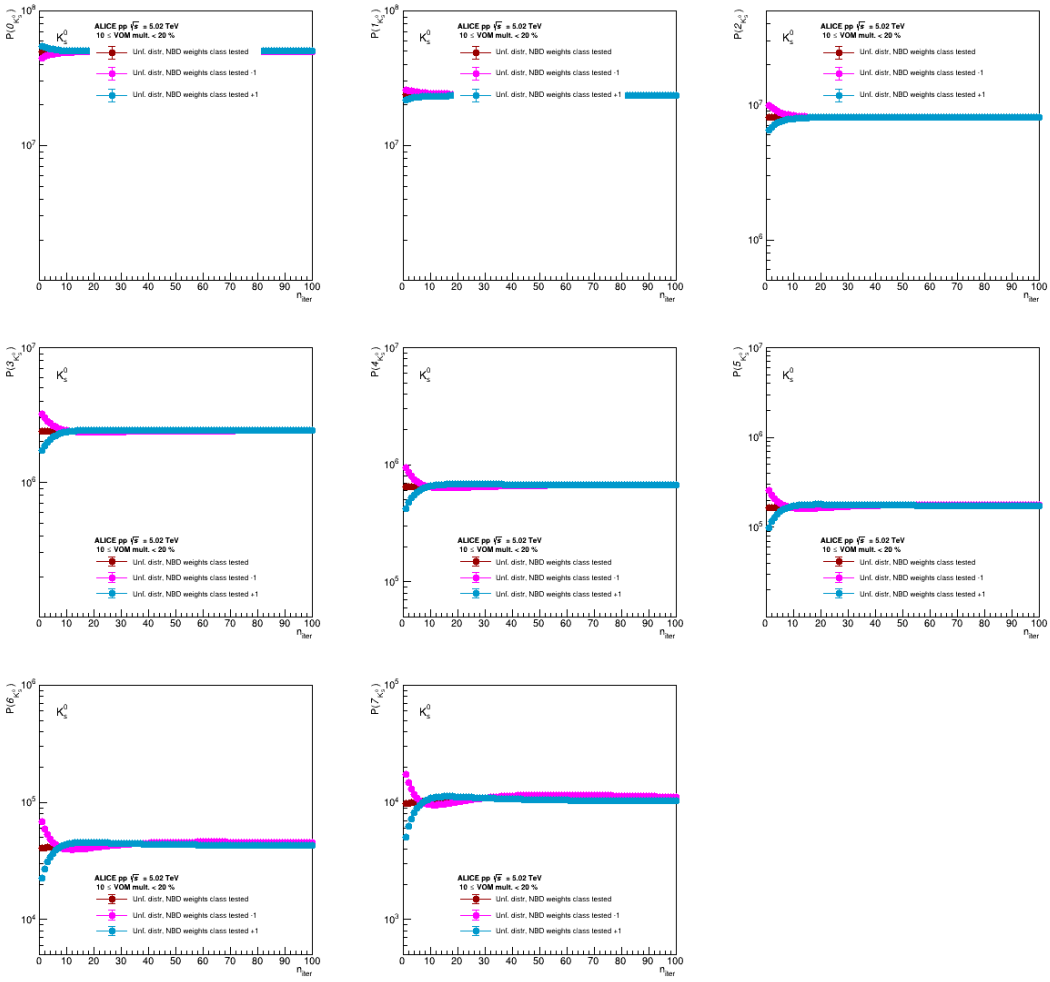

Figure 9.97: Comparison of the unfolded distributions for the $10 \leq V0M < 20\%$ class for K^0_S as a function of the number of iterations: results using NBD-weights specific to the class are shown in dark red, while those obtained using weights from classes $i-1$ and $i+1$ are depicted in pink and azure, respectively.

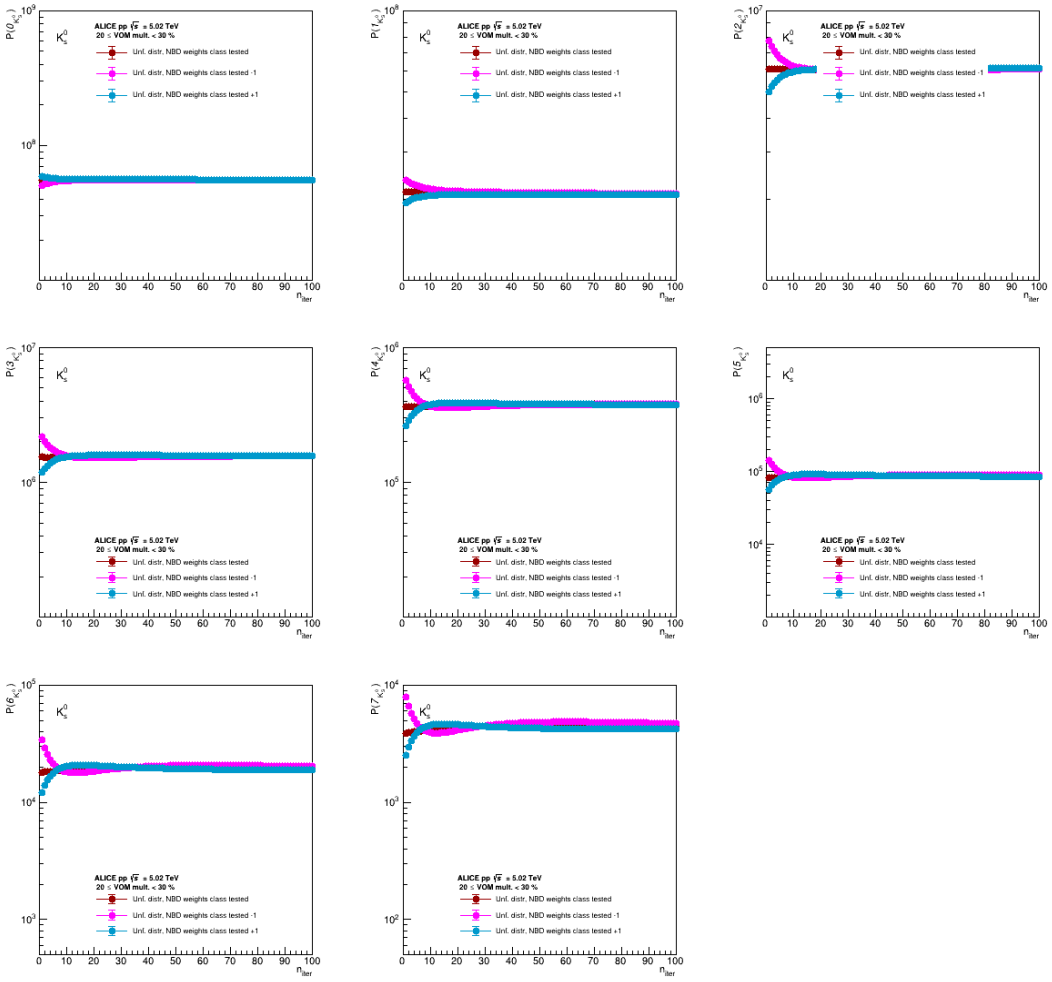

Figure 9.98: Comparison of the unfolded distributions for the $20 \leq V0M < 30\%$ class for K^0_S as a function of the number of iterations: results using NBD-weights specific to the class are shown in dark red, while those obtained using weights from classes $i-1$ and $i+1$ are depicted in pink and azure, respectively.

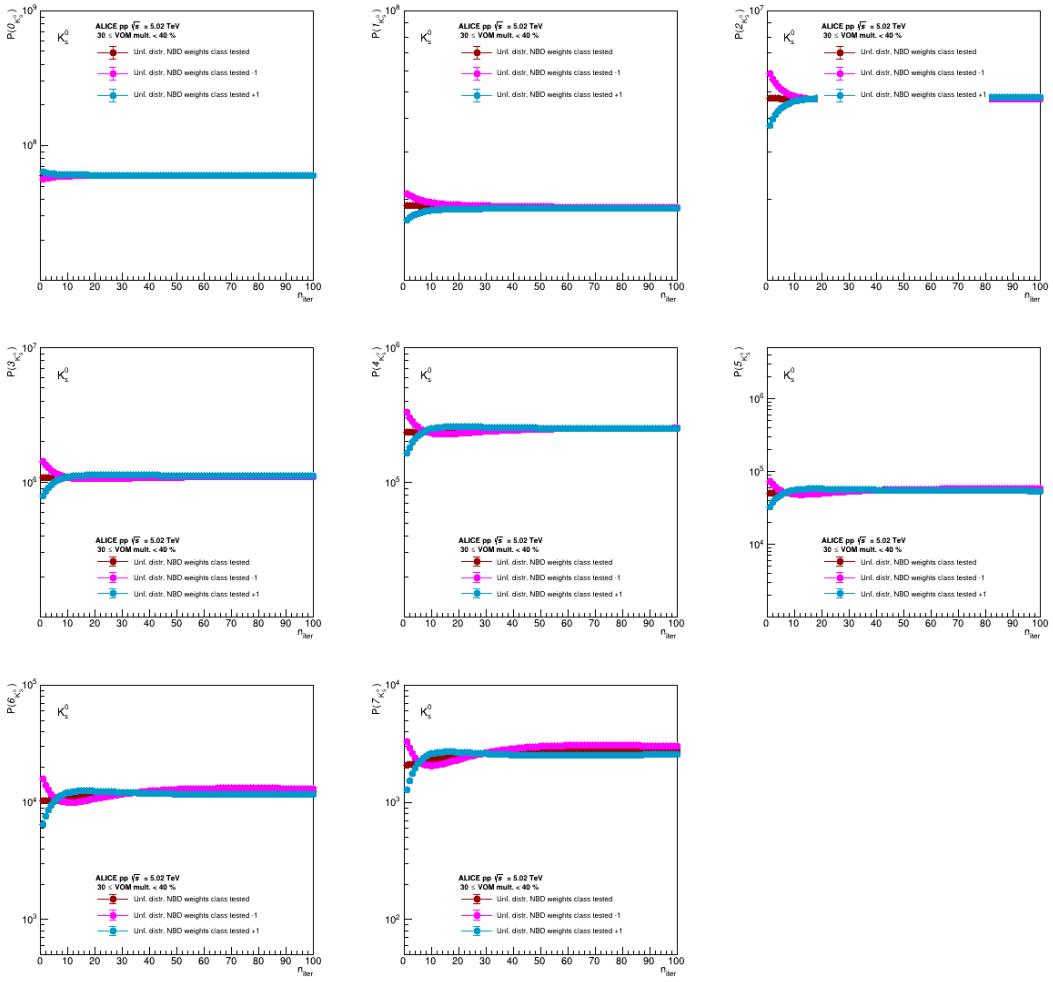

Figure 9.99: Comparison of the unfolded distributions for the $30 \leq V0M < 40\%$ class for K^0_S as a function of the number of iterations: results using NBD-weights specific to the class are shown in dark red, while those obtained using weights from classes $i-1$ and $i+1$ are depicted in pink and azure, respectively.

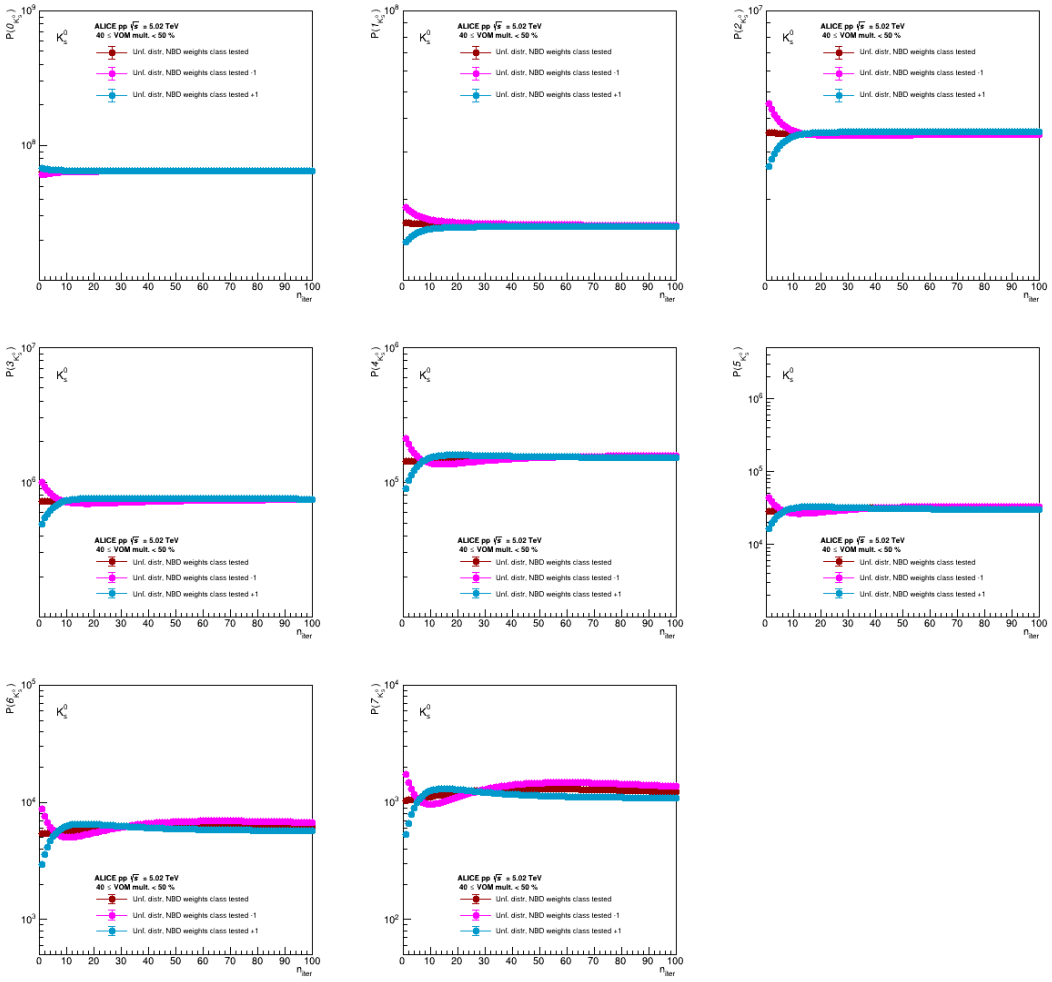

Figure 9.100: Comparison of the unfolded distributions for the $40 \leq V0M < 50\%$ class for K^0_S as a function of the number of iterations: results using NBD-weights specific to the class are shown in dark red, while those obtained using weights from classes $i-1$ and $i+1$ are depicted in pink and azure, respectively.

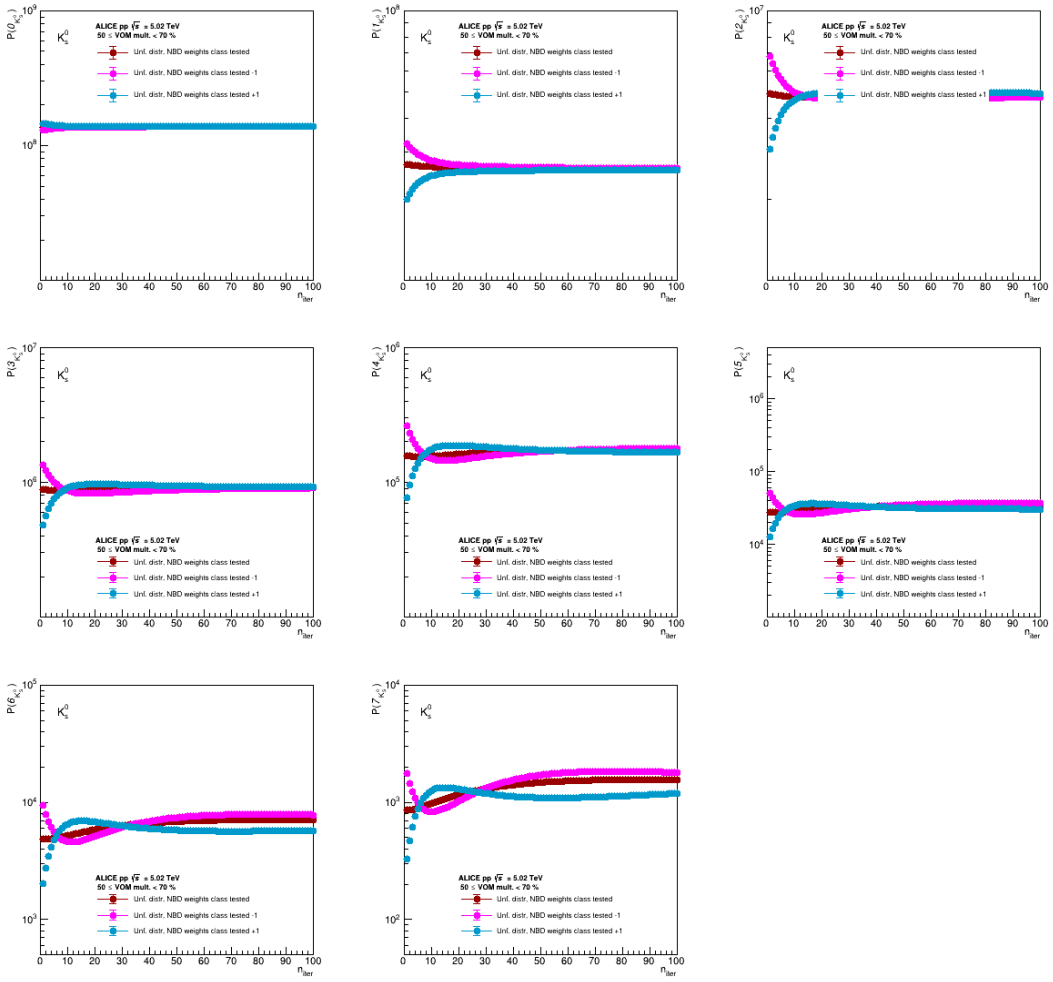

Figure 9.101: Comparison of the unfolded distributions for the $50 \leq V0M < 70\%$ class for K^0_S as a function of the number of iterations: results using NBD-weights specific to the class are shown in dark red, while those obtained using weights from classes $i-1$ and $i+1$ are depicted in pink and azure, respectively.

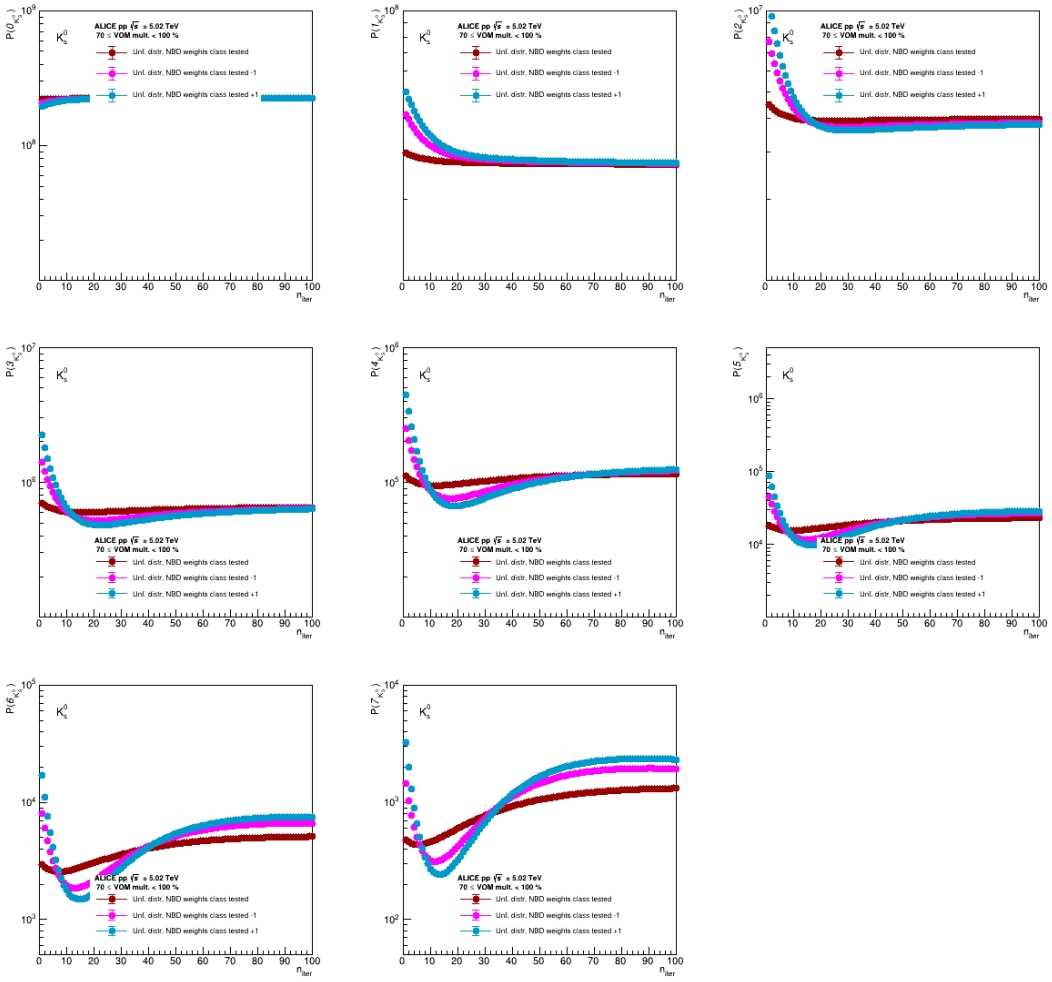

Figure 9.102: Comparison of the unfolded distributions for the $70 \leq V0M < 100\%$ class for K^0_S as a function of the number of iterations: results using NBD-weights specific to the class are shown in dark red, while those obtained using weights from classes $i-1$ and $i+1$ (in this case $i-2$) are depicted in pink and azure, respectively.

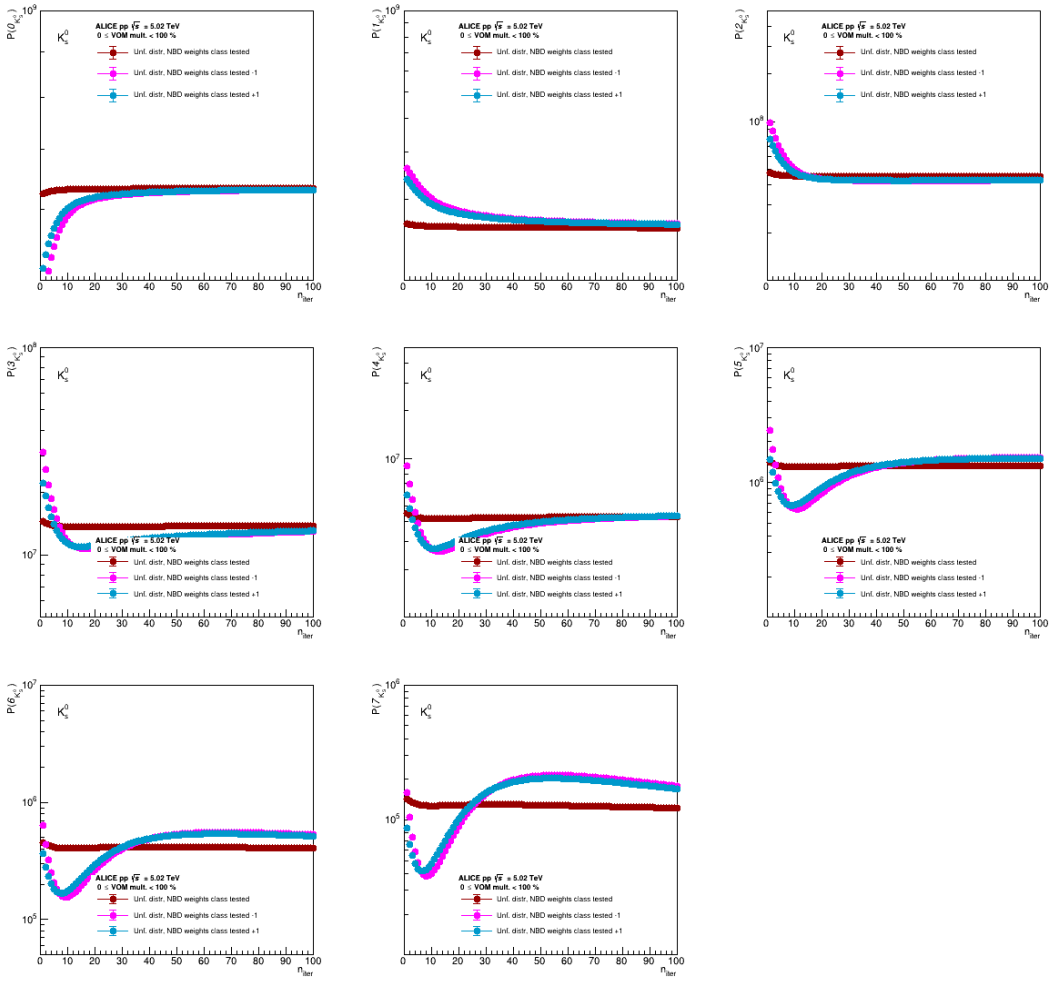

Figure 9.103: Comparison of the unfolded distributions for the INEL > 0 event class for K^0_S as a function of the number of iterations: results using NBD-weights specific to the class are shown in dark red, while those obtained using weights from classes $i-1$ (in this case class V) and $i+1$ (in this case class VI) are depicted in pink and azure, respectively.

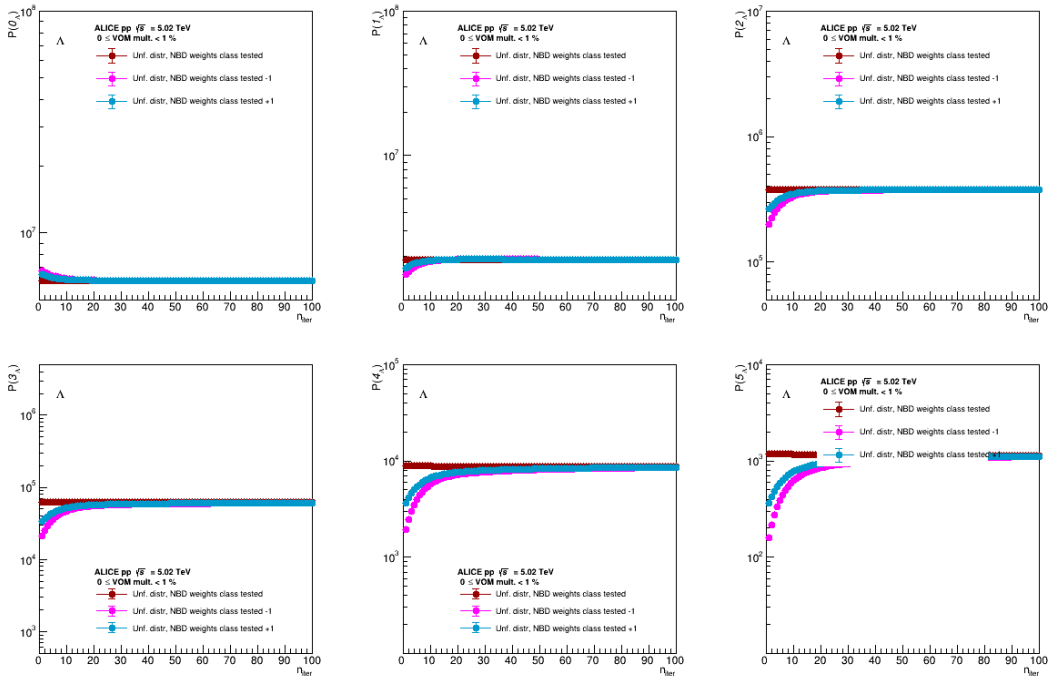

Figure 9.104: Comparison of the unfolded distributions for the $0 \leq V0M < 1\%$ class for Λ as a function of the number of iterations: results using NBD-weights specific to the class are shown in dark red, while those obtained using weights from classes $i-1$ (in this case $i+2$) and $i+1$ are depicted in pink and azure, respectively.

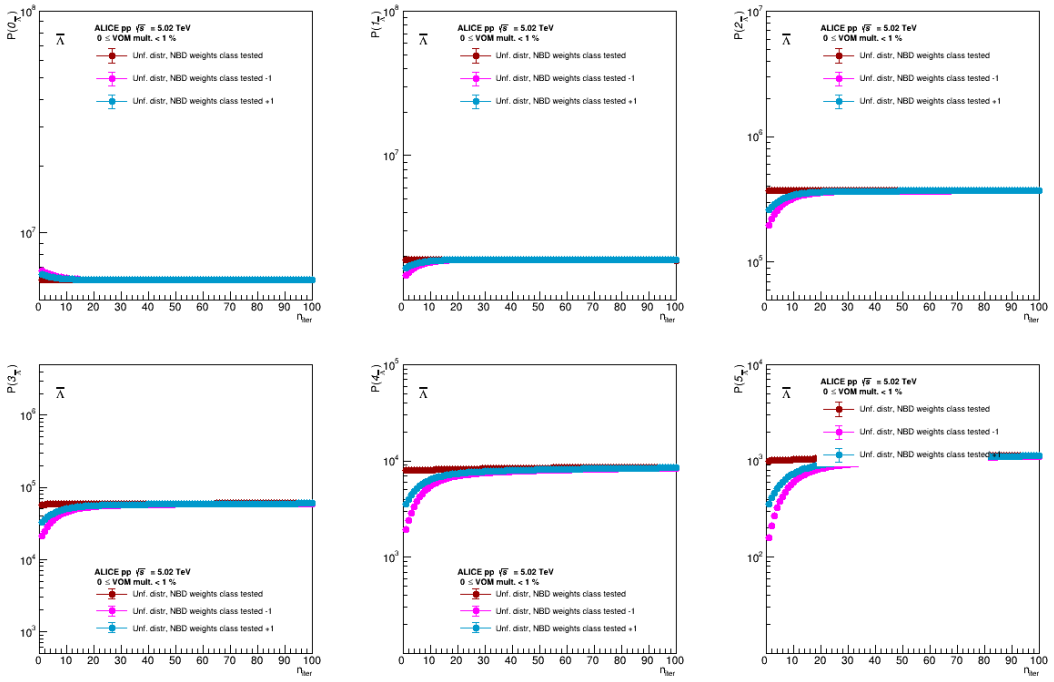

Figure 9.105: Comparison of the unfolded distributions for the $0 \leq V0M < 1\%$ class for $\overline{\Lambda}$ as a function of the number of iterations: results using NBD-weights specific to the class are shown in dark red, while those obtained using weights from classes $i-1$ (in this case $i+2$) and $i+1$ are depicted in pink and azure, respectively.

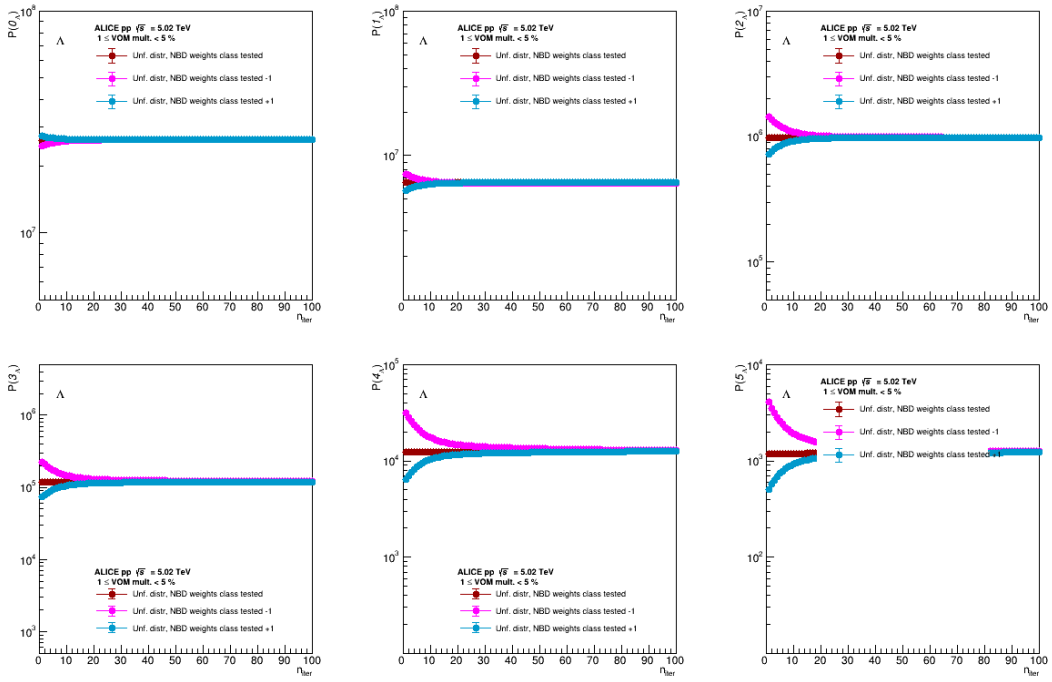

Figure 9.106: Comparison of the unfolded distributions for the $1 \leq V0M < 5\%$ class for Λ as a function of the number of iterations: results using NBD-weights specific to the class are shown in dark red, while those obtained using weights from classes $i-1$ and $i+1$ are depicted in pink and azure, respectively.

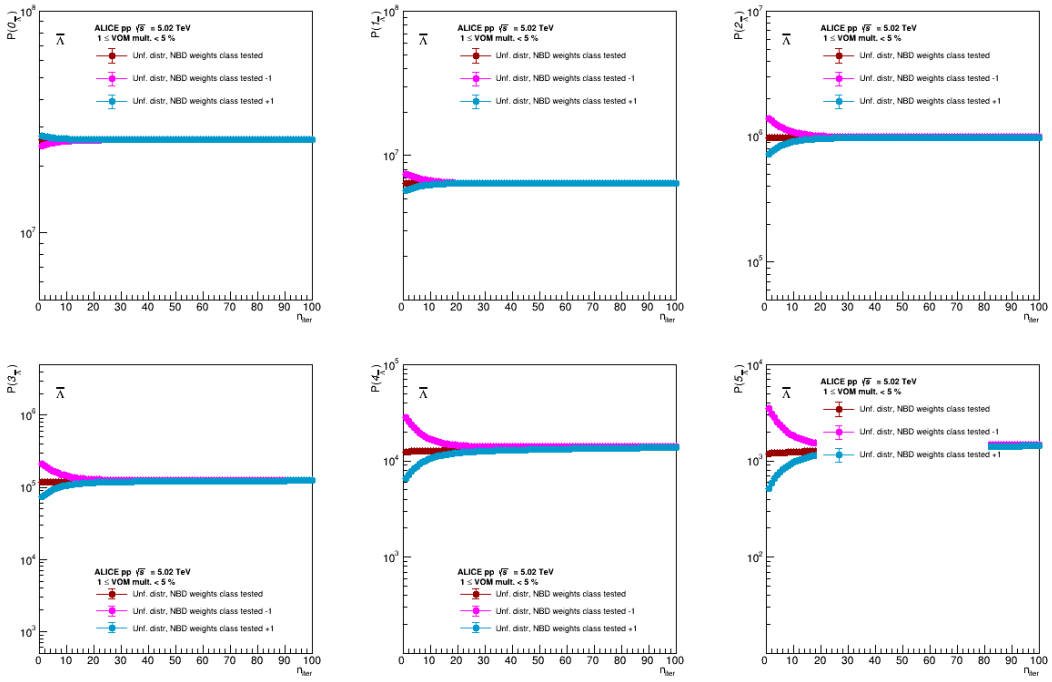

Figure 9.107: Comparison of the unfolded distributions for the $1 \leq V0M < 5\%$ class for $\overline{\Lambda}$ as a function of the number of iterations: results using NBD-weights specific to the class are shown in dark red, while those obtained using weights from classes $i-1$ and $i+1$ are depicted in pink and azure, respectively.

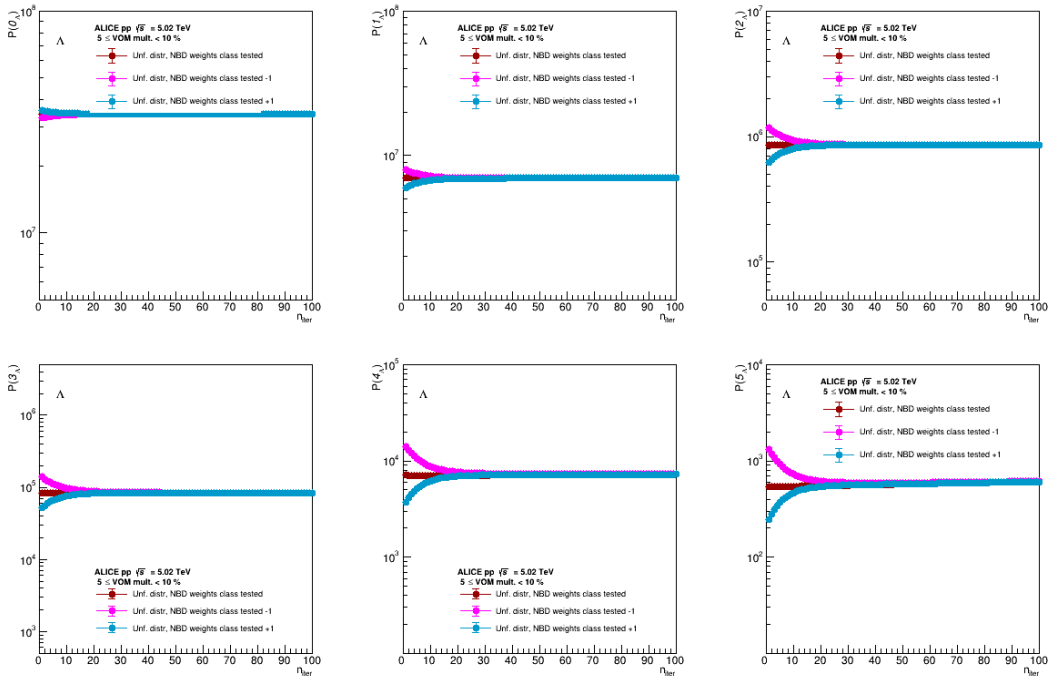

Figure 9.108: Comparison of the unfolded distributions for the $5 \leq V0M < 10\%$ class for Λ as a function of the number of iterations: results using NBD-weights specific to the class are shown in dark red, while those obtained using weights from classes $i-1$ and $i+1$ are depicted in pink and azure, respectively.

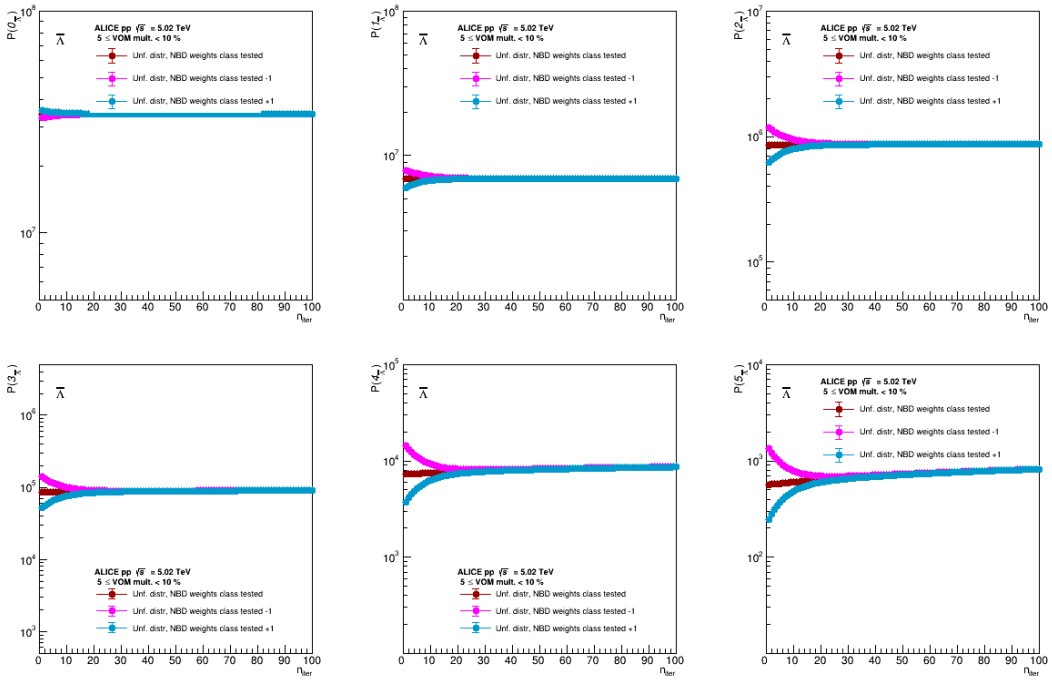

Figure 9.109: Comparison of the unfolded distributions for the $5 \leq V0M < 10\%$ class for $\overline{\Lambda}$ as a function of the number of iterations: results using NBD-weights specific to the class are shown in dark red, while those obtained using weights from classes $i-1$ and $i+1$ are depicted in pink and azure, respectively.

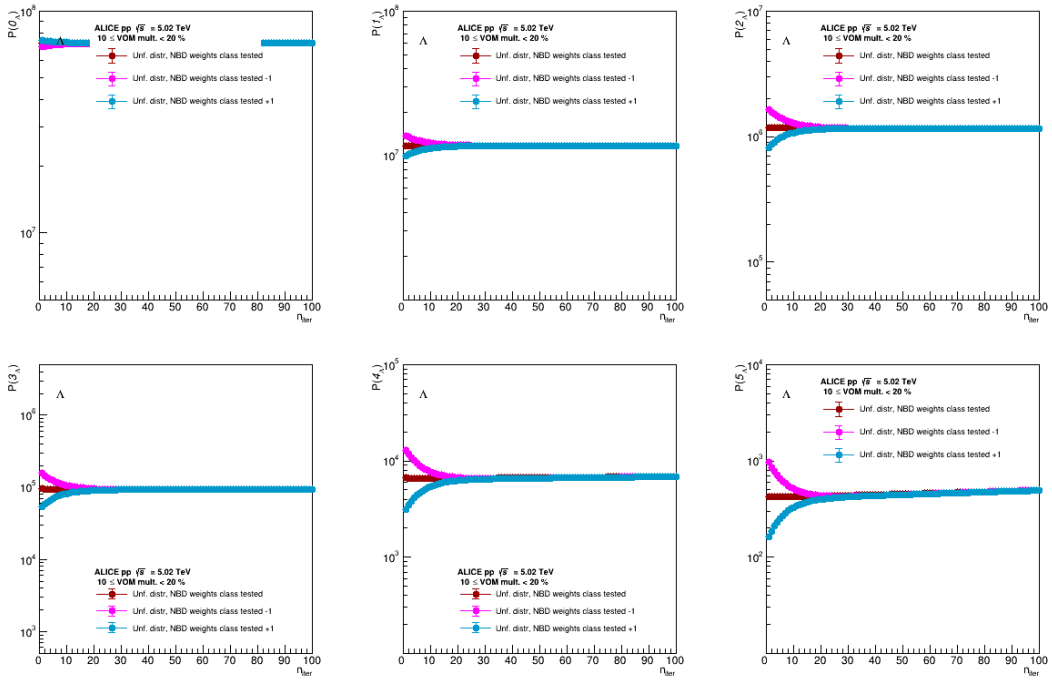

Figure 9.110: Comparison of the unfolded distributions for the $10 \leq V0M < 20\%$ class for Λ as a function of the number of iterations: results using NBD-weights specific to the class are shown in dark red, while those obtained using weights from classes $i-1$ and $i+1$ are depicted in pink and azure, respectively.

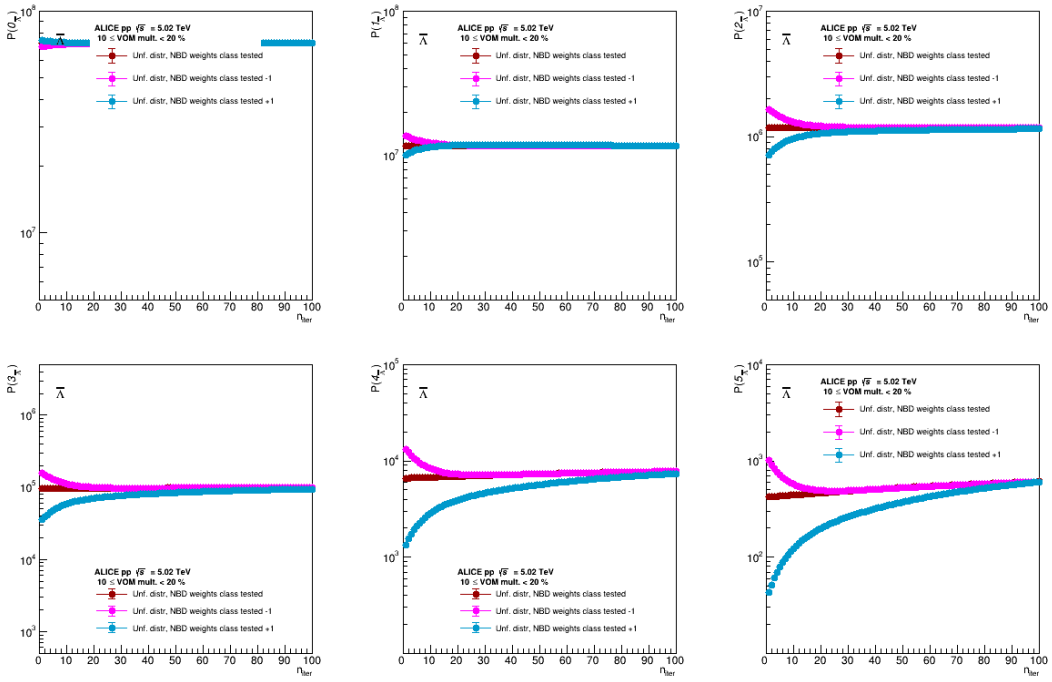

Figure 9.111: Comparison of the unfolded distributions for the $10 \leq V0M < 20\%$ class for $\overline{\Lambda}$ as a function of the number of iterations: results using NBD-weights specific to the class are shown in dark red, while those obtained using weights from classes $i-1$ and $i+1$ are depicted in pink and azure, respectively.

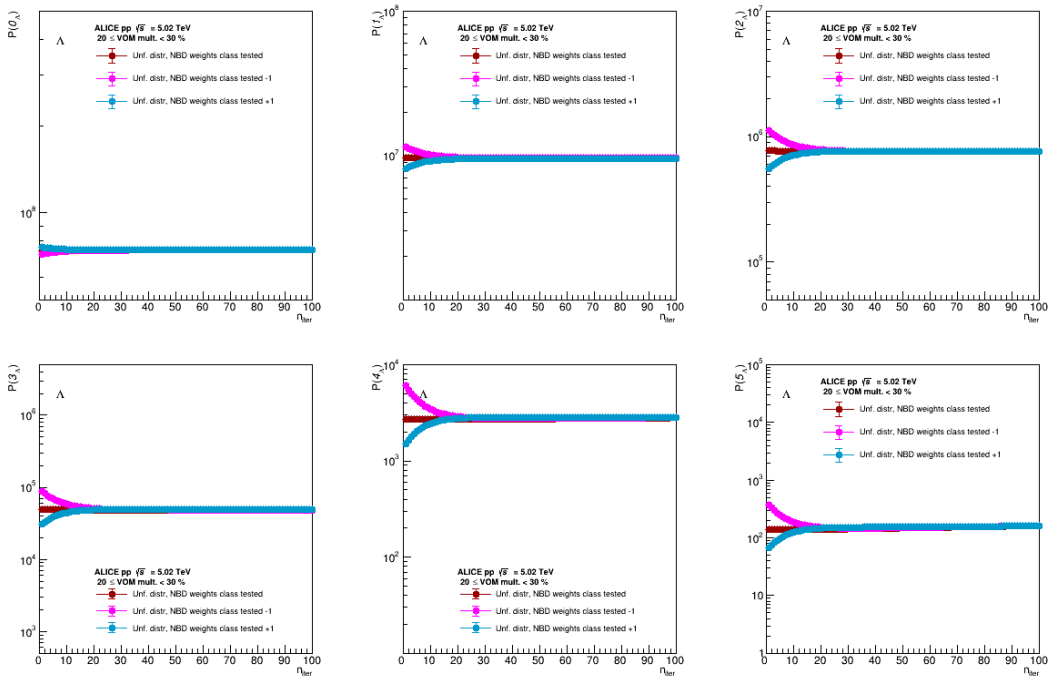

Figure 9.112: Comparison of the unfolded distributions for the $20 \leq V0M < 30\%$ class for Λ as a function of the number of iterations: results using NBD-weights specific to the class are shown in dark red, while those obtained using weights from classes $i-1$ and $i+1$ are depicted in pink and azure, respectively.

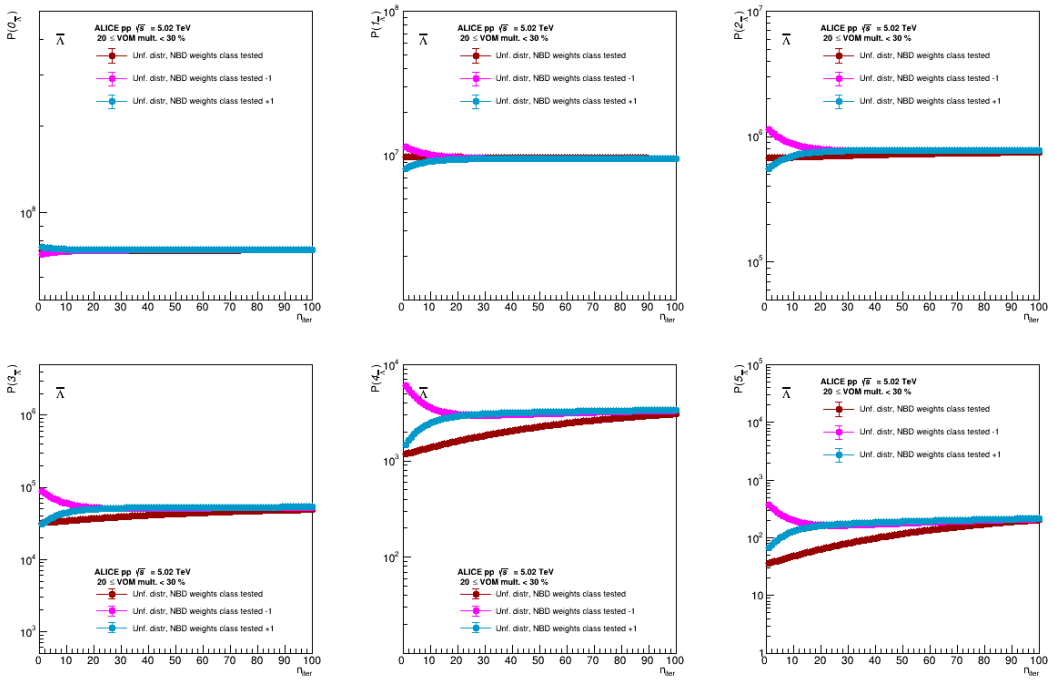

Figure 9.113: Comparison of the unfolded distributions for the $20 \leq V0M < 30\%$ class for $\overline{\Lambda}$ as a function of the number of iterations: results using NBD-weights specific to the class are shown in dark red, while those obtained using weights from classes $i-1$ and $i+1$ are depicted in pink and azure, respectively.

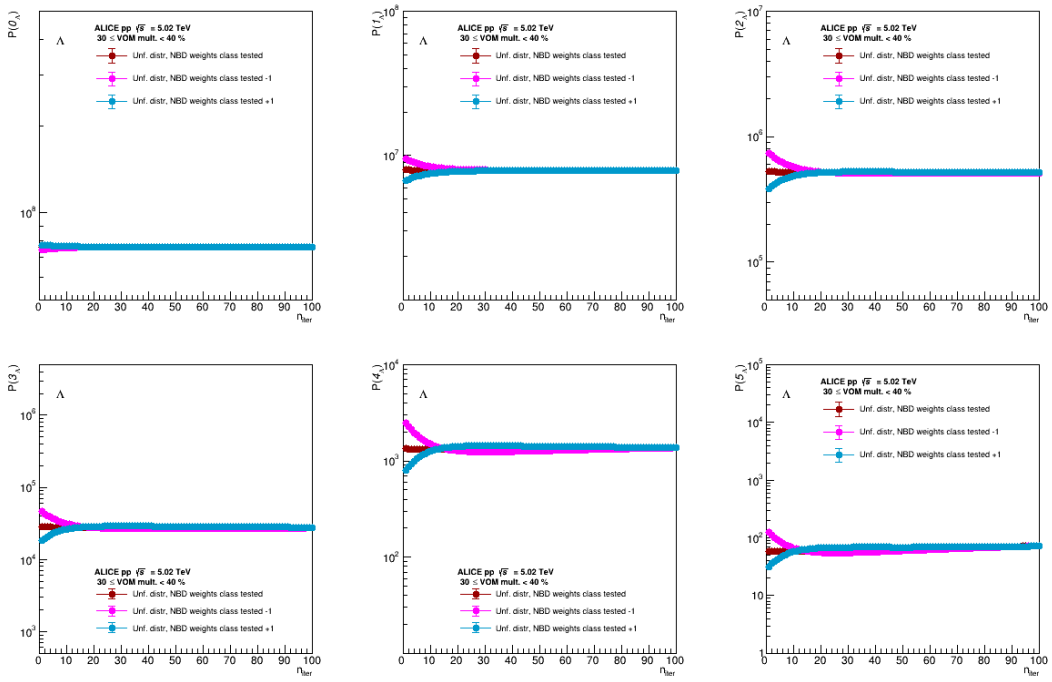

Figure 9.114: Comparison of the unfolded distributions for the $30 \leq V0M < 40\%$ class for Λ as a function of the number of iterations: results using NBD-weights specific to the class are shown in dark red, while those obtained using weights from classes $i-1$ and $i+1$ are depicted in pink and azure, respectively.

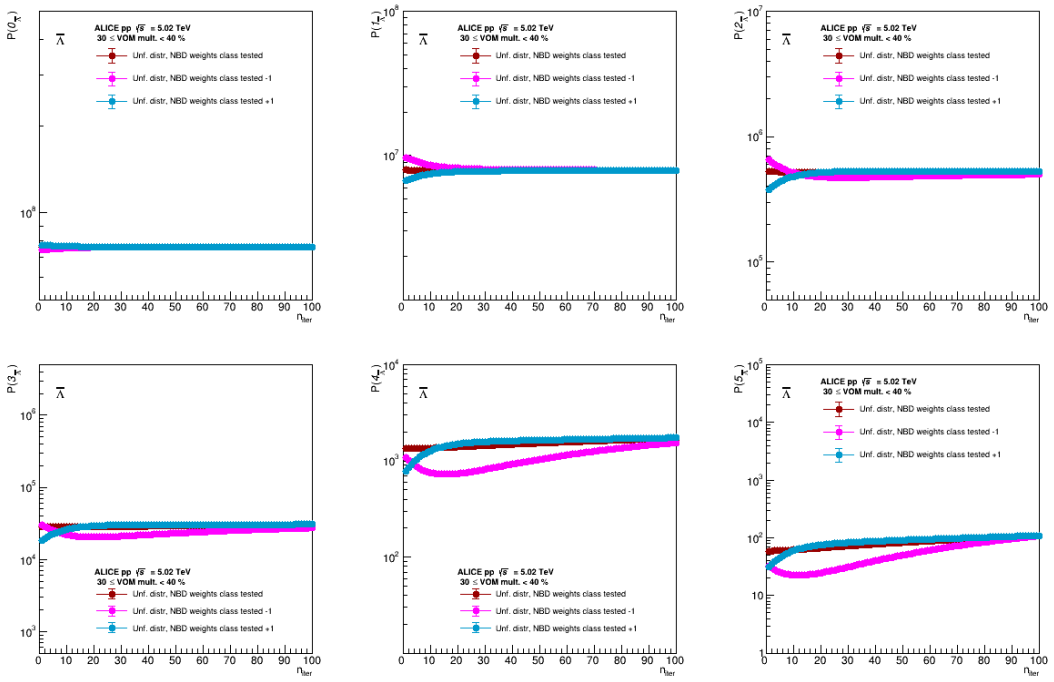

Figure 9.115: Comparison of the unfolded distributions for the $30 \leq V0M < 40\%$ class for $\overline{\Lambda}$ as a function of the number of iterations: results using NBD-weights specific to the class are shown in dark red, while those obtained using weights from classes $i-1$ and $i+1$ are depicted in pink and azure, respectively.

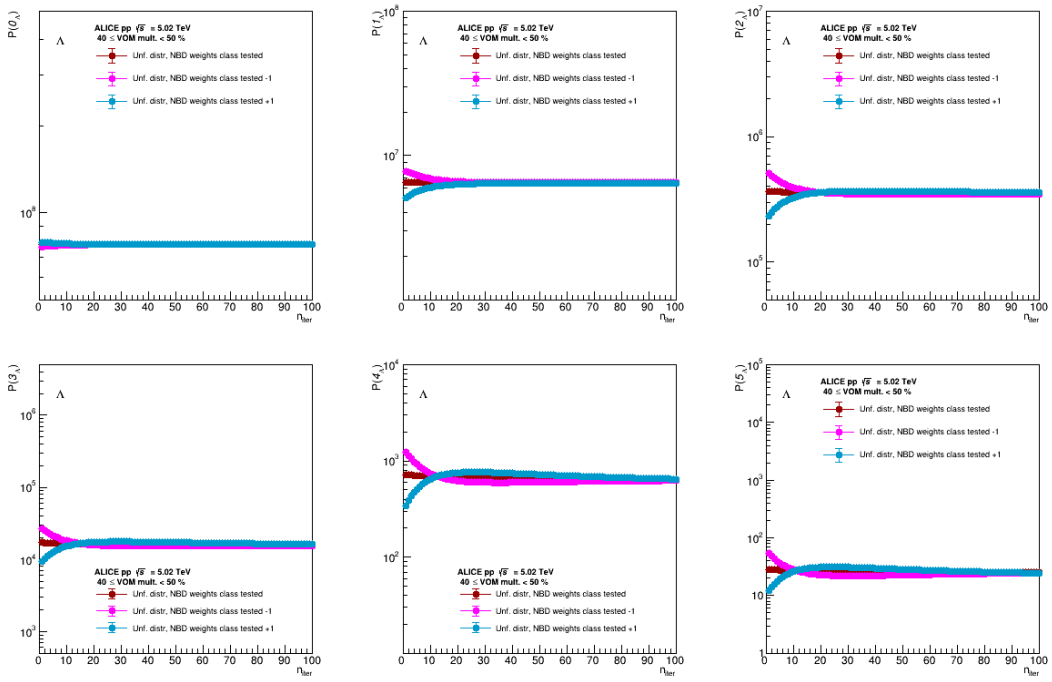

Figure 9.116: Comparison of the unfolded distributions for the $40 \leq V0M < 50\%$ class for Λ as a function of the number of iterations: results using NBD-weights specific to the class are shown in dark red, while those obtained using weights from classes $i-1$ and $i+1$ are depicted in pink and azure, respectively.

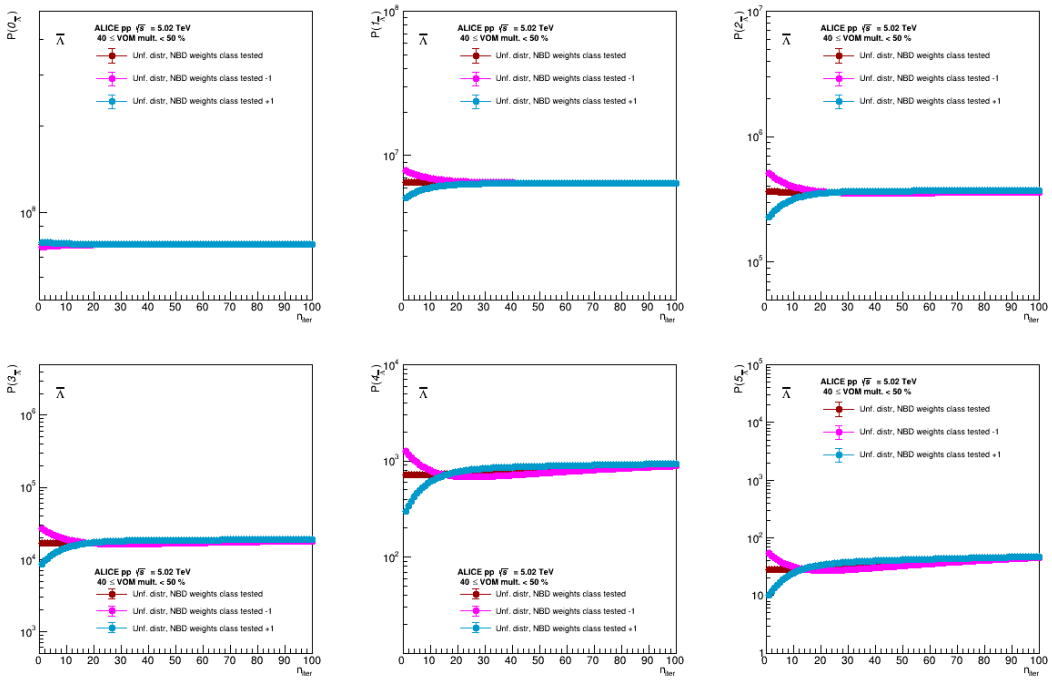

Figure 9.117: Comparison of the unfolded distributions for the $40 \leq V0M < 50\%$ class for $\overline{\Lambda}$ as a function of the number of iterations: results using NBD-weights specific to the class are shown in dark red, while those obtained using weights from classes $i-1$ and $i+1$ are depicted in pink and azure, respectively.

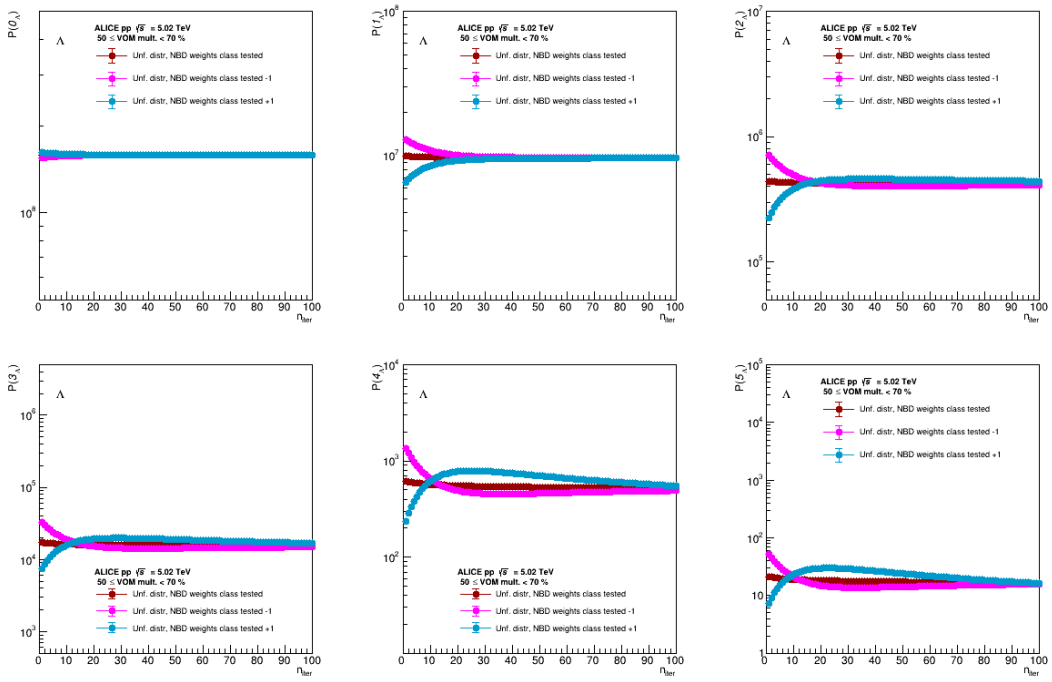

Figure 9.118: Comparison of the unfolded distributions for the $50 \leq V0M < 70\%$ class for Λ as a function of the number of iterations: results using NBD-weights specific to the class are shown in dark red, while those obtained using weights from classes $i-1$ and $i+1$ are depicted in pink and azure, respectively.

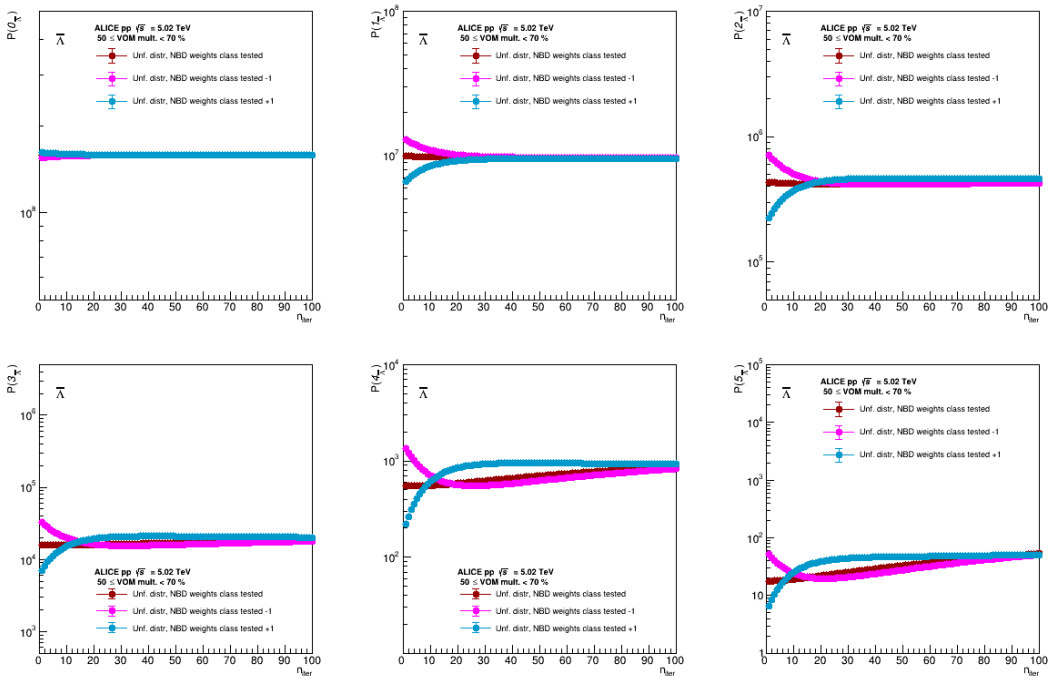

Figure 9.119: Comparison of the unfolded distributions for the $50 \leq V0M < 70\%$ class for $\overline{\Lambda}$ as a function of the number of iterations: results using NBD-weights specific to the class are shown in dark red, while those obtained using weights from classes $i-1$ and $i+1$ are depicted in pink and azure, respectively.

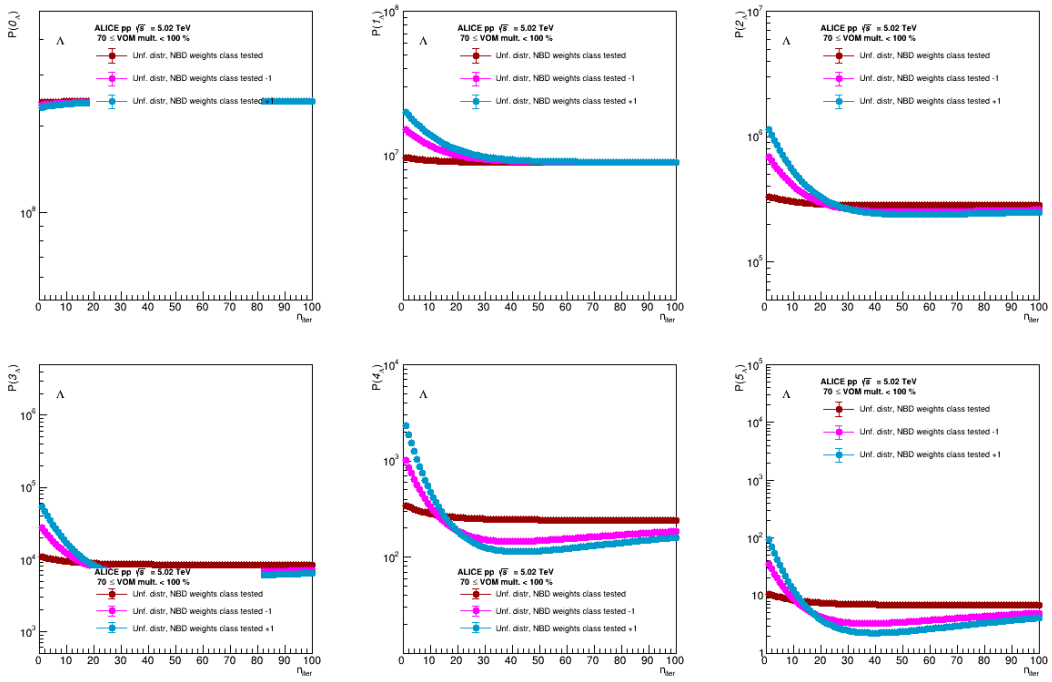

Figure 9.120: Comparison of the unfolded distributions for the $70 \leq V0M < 100\%$ class for Λ as a function of the number of iterations: results using NBD-weights specific to the class are shown in dark red, while those obtained using weights from classes $i-1$ and $i+1$ (in this case $i-2$) are depicted in pink and azure, respectively.

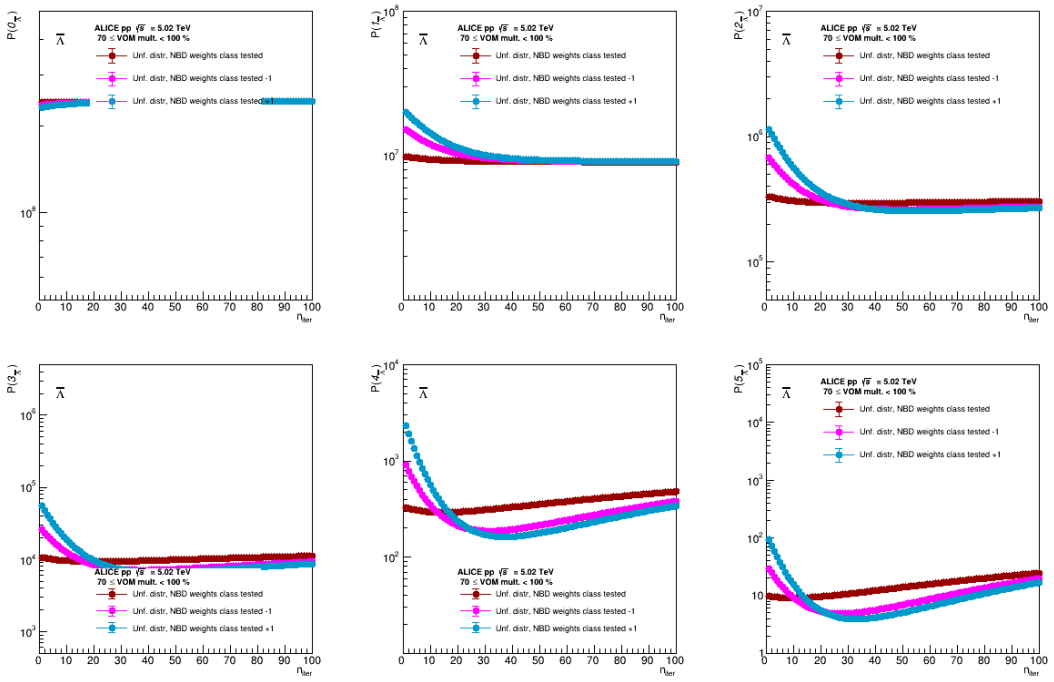

Figure 9.121: Comparison of the unfolded distributions for the $70 \leq V0M < 100\%$ class for $\overline{\Lambda}$ as a function of the number of iterations: results using NBD-weights specific to the class are shown in dark red, while those obtained using weights from classes $i-1$ and $i+1$ (in this case $i-2$) are depicted in pink and azure, respectively.

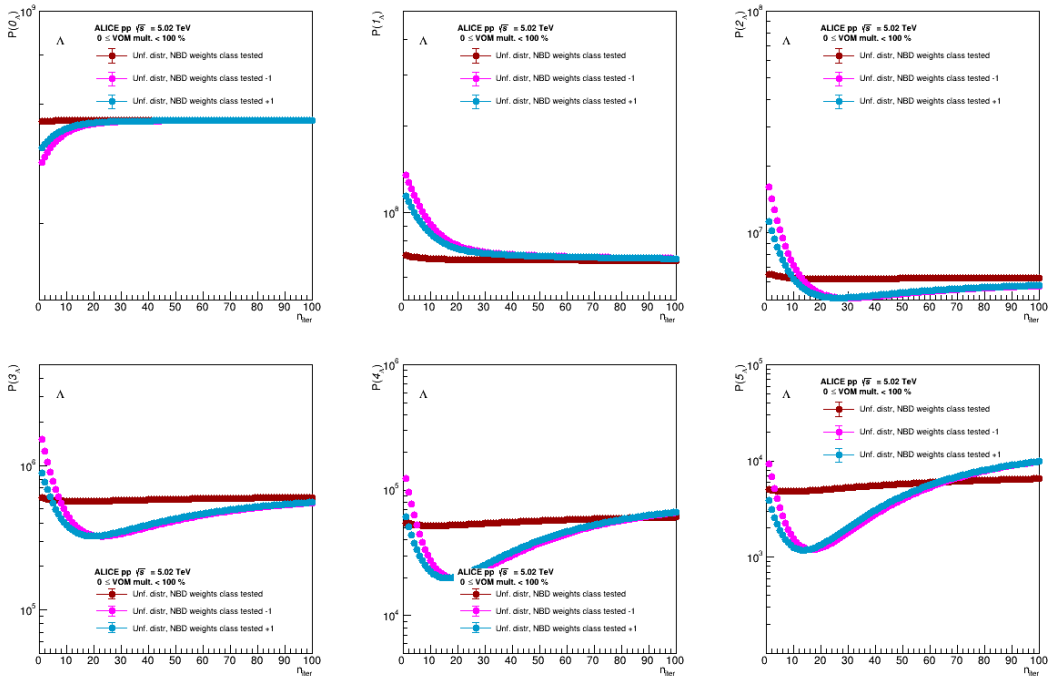

Figure 9.122: Comparison of the unfolded distributions for the INEL > 0 event class for Λ as a function of the number of iterations: results using NBD-weights specific to the class are shown in dark red, while those obtained using weights from classes $i-1$ (in this case class V) and $i+1$ (in this case class VI) are depicted in pink and azure, respectively.

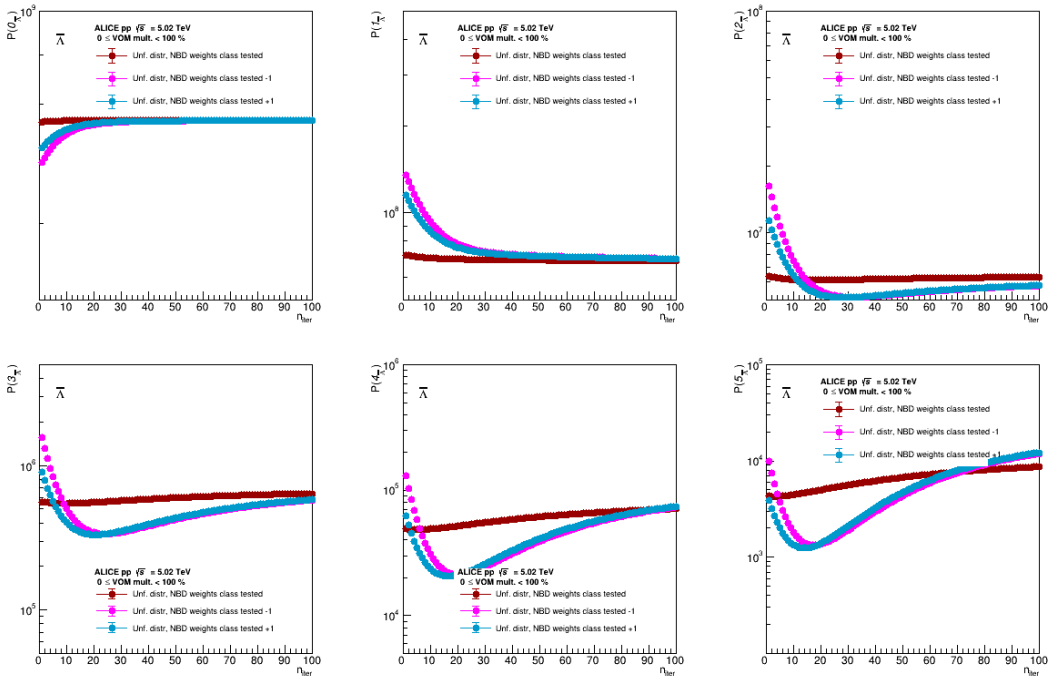

Figure 9.123: Comparison of the unfolded distributions for the INEL > 0 event class for $\overline{\Lambda}$ as a function of the number of iterations: results using NBD-weights specific to the class are shown in dark red, while those obtained using weights from classes $i-1$ (in this case class V) and $i+1$ (in this case class VI) are depicted in pink and azure, respectively.

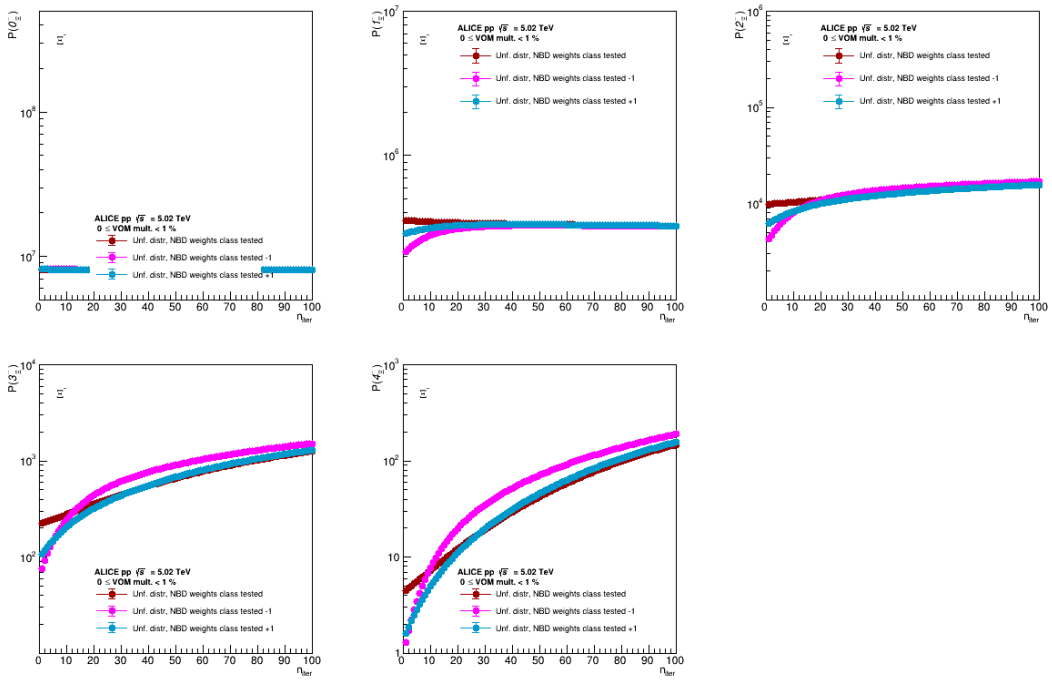

Figure 9.124: Comparison of the unfolded distributions for the $0 \leq V0M < 1\%$ class for Ξ^- as a function of the number of iterations: results using NBD-weights specific to the class are shown in dark red, while those obtained using weights from classes $i-1$ (in this case $i+2$) and $i+1$ are depicted in pink and azure, respectively.

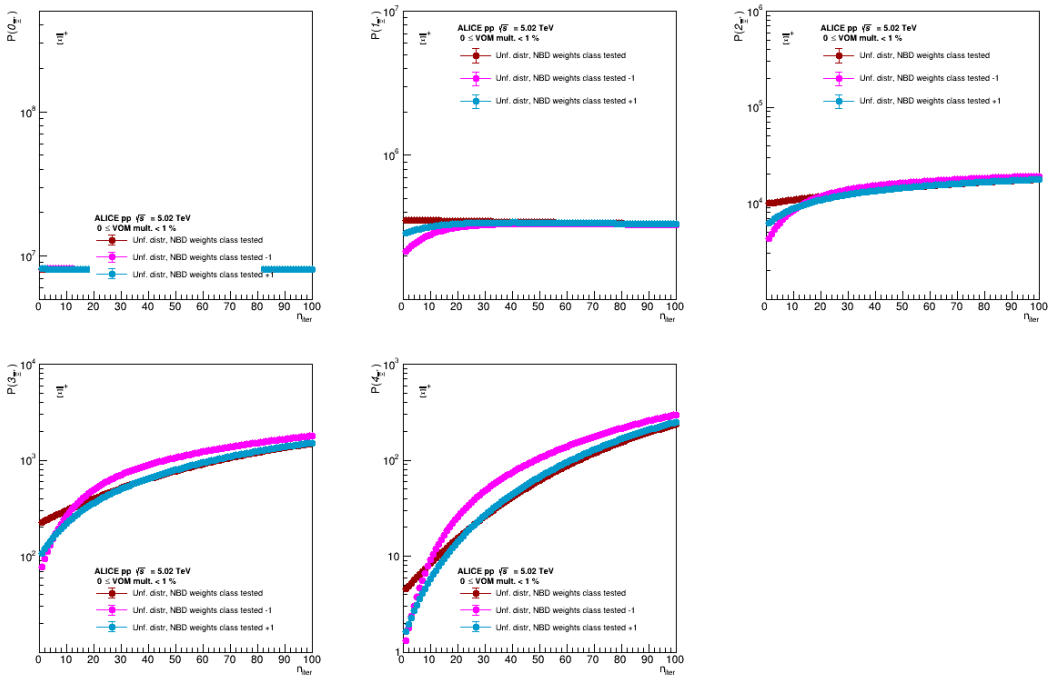

Figure 9.125: Comparison of the unfolded distributions for the $0 \leq V0M < 1\%$ class for $\overline{\Xi}^{+}$ as a function of the number of iterations: results using NBD-weights specific to the class are shown in dark red, while those obtained using weights from classes $i-1$ (in this case $i+2$) and $i+1$ are depicted in pink and azure, respectively.

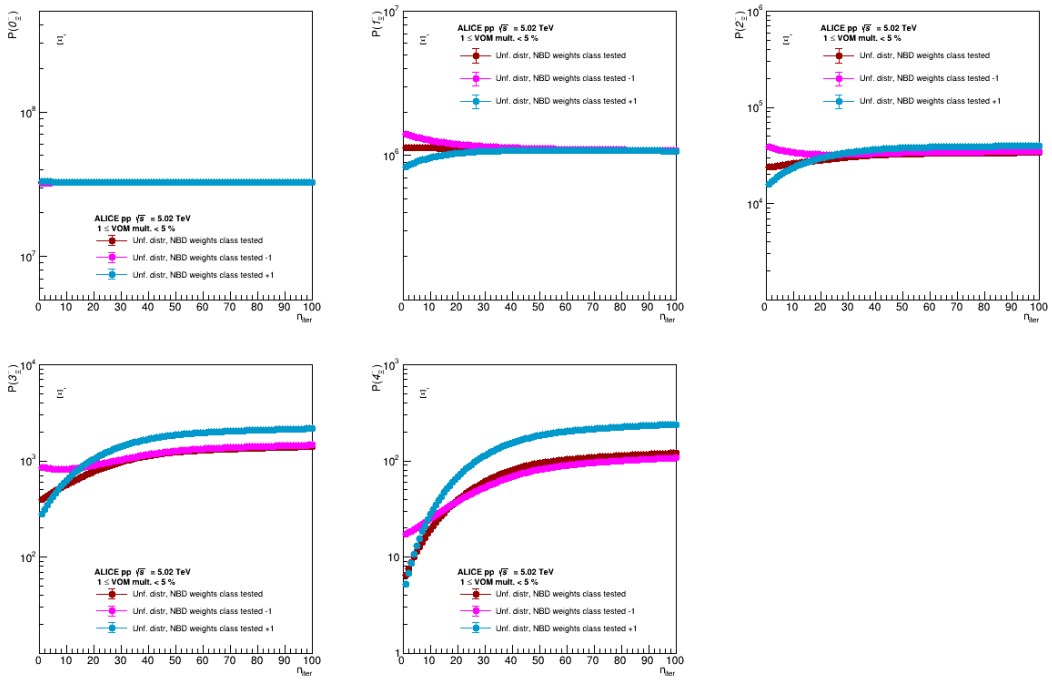

Figure 9.126: Comparison of the unfolded distributions for the $1 \leq V0M < 5\%$ class for Ξ^- as a function of the number of iterations: results using NBD-weights specific to the class are shown in dark red, while those obtained using weights from classes $i-1$ and $i+1$ are depicted in pink and azure, respectively.

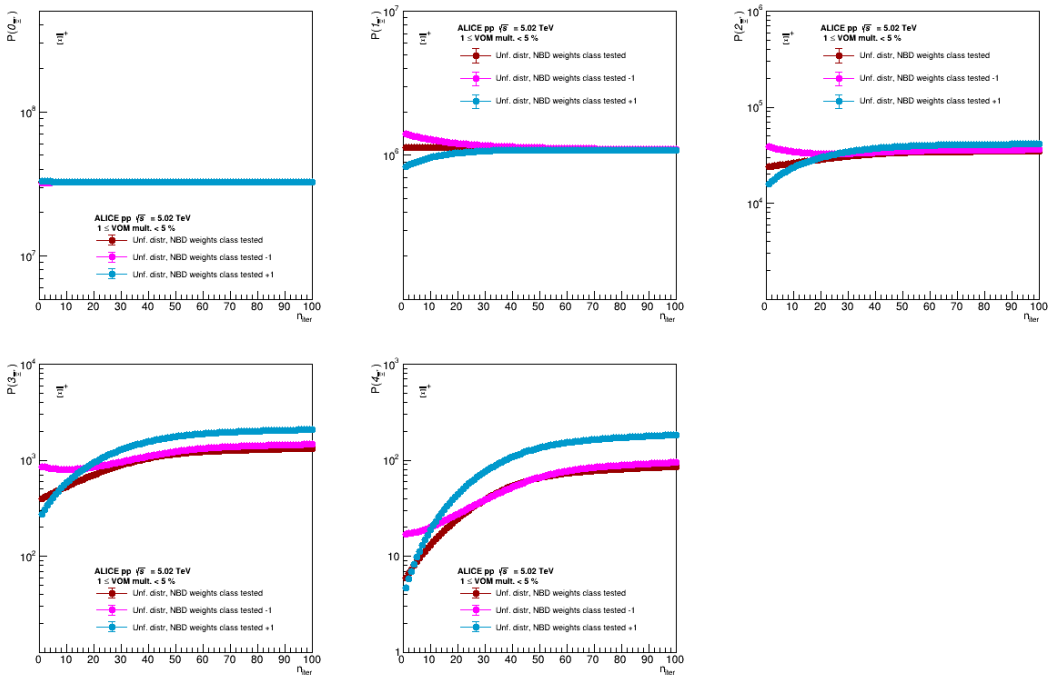

Figure 9.127: Comparison of the unfolded distributions for the $1 \leq V0M < 5\%$ class for $\overline{\Xi}^{+}$ as a function of the number of iterations: results using NBD-weights specific to the class are shown in dark red, while those obtained using weights from classes $i-1$ and $i+1$ are depicted in pink and azure, respectively.

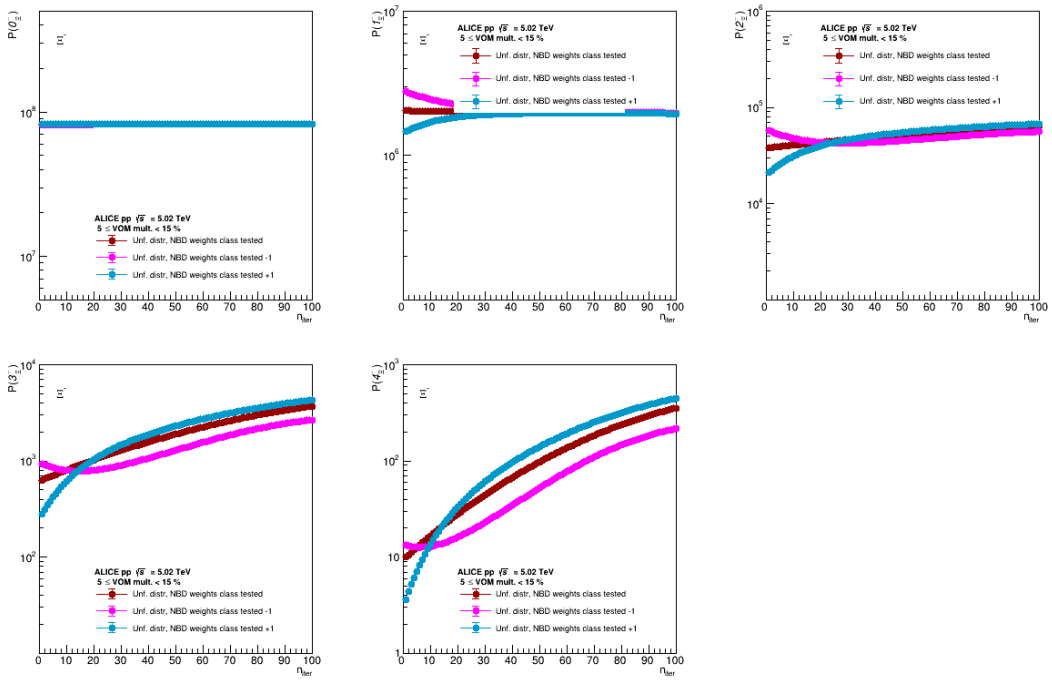

Figure 9.128: Comparison of the unfolded distributions for the $5 \leq V0M < 15\%$ class for Ξ^- as a function of the number of iterations: results using NBD-weights specific to the class are shown in dark red, while those obtained using weights from classes $i-1$ and $i+1$ are depicted in pink and azure, respectively.

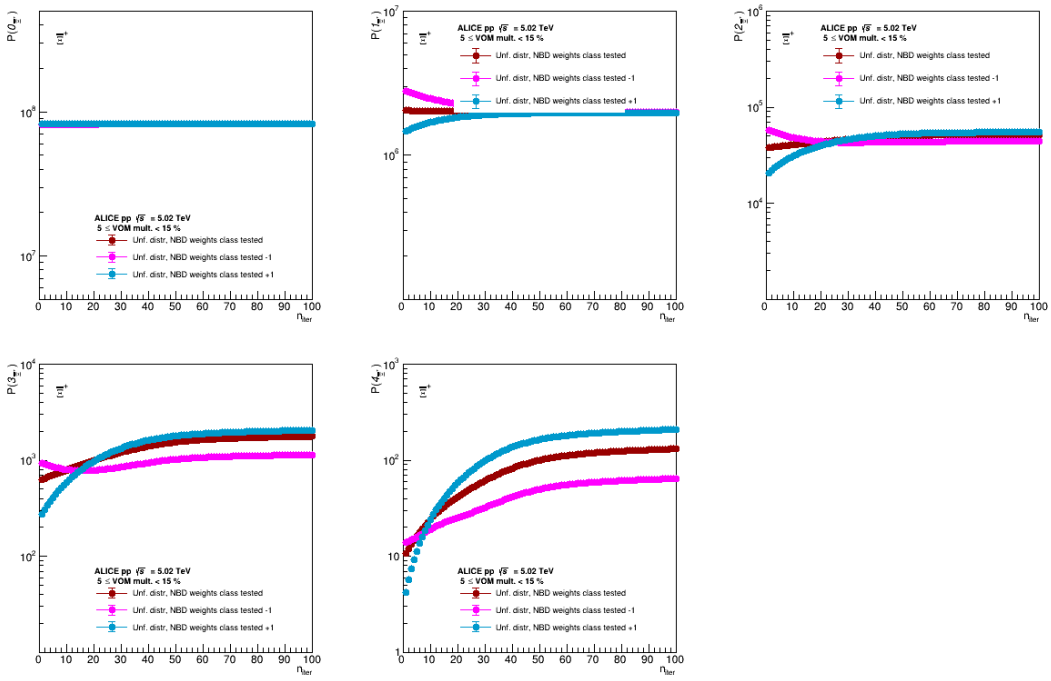

Figure 9.129: Comparison of the unfolded distributions for the $1 \leq V0M < 5\%$ class for $\bar{\Xi}^{+}$ as a function of the number of iterations: results using NBD-weights specific to the class are shown in dark red, while those obtained using weights from classes $i-1$ and $i+1$ are depicted in pink and azure, respectively.

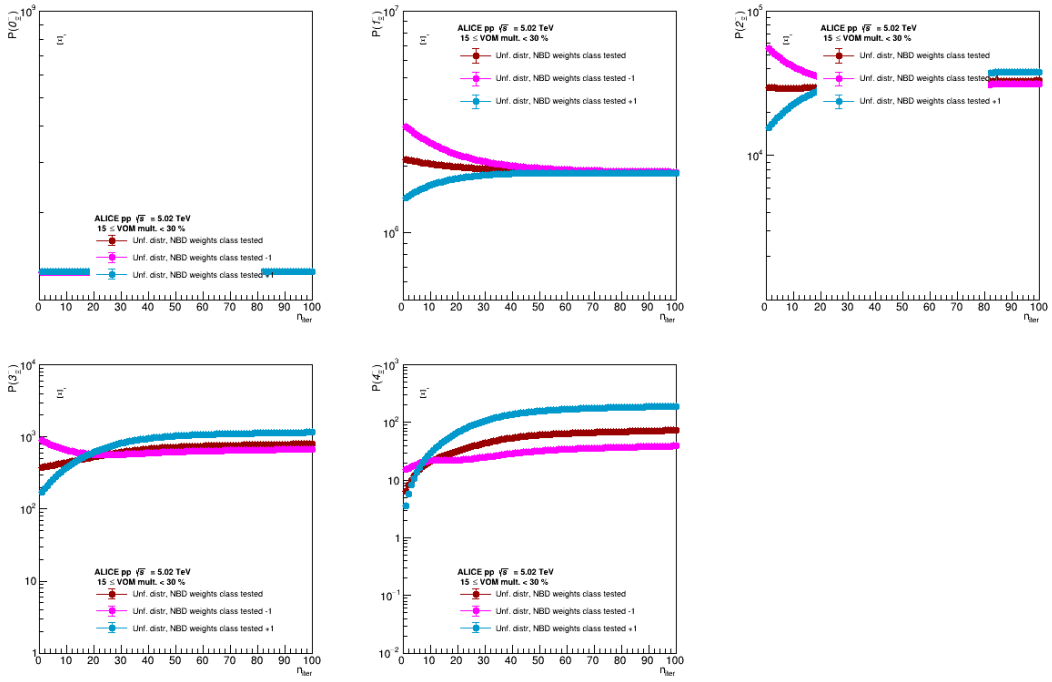

Figure 9.130: Comparison of the unfolded distributions for the $15 \leq V0M < 30\%$ class for Ξ^- as a function of the number of iterations: results using NBD-weights specific to the class are shown in dark red, while those obtained using weights from classes $i-1$ and $i+1$ are depicted in pink and azure, respectively.

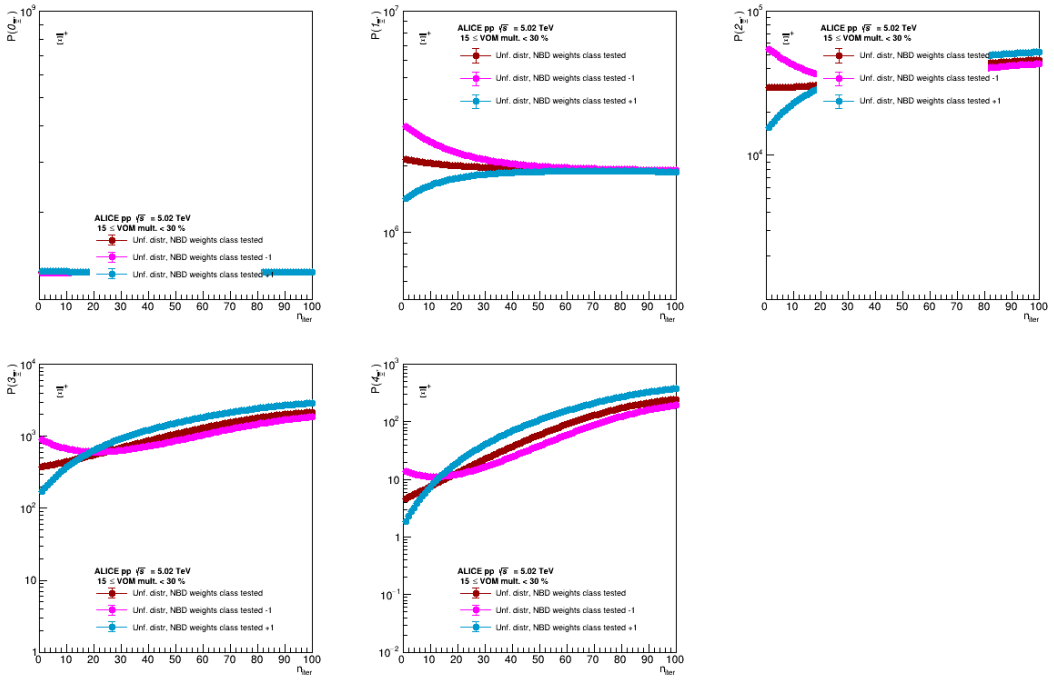

Figure 9.131: Comparison of the unfolded distributions for the $15 \leq V0M < 30\%$ class for $\overline{\Xi}^{+}$ as a function of the number of iterations: results using NBD-weights specific to the class are shown in dark red, while those obtained using weights from classes $i-1$ and $i+1$ are depicted in pink and azure, respectively.

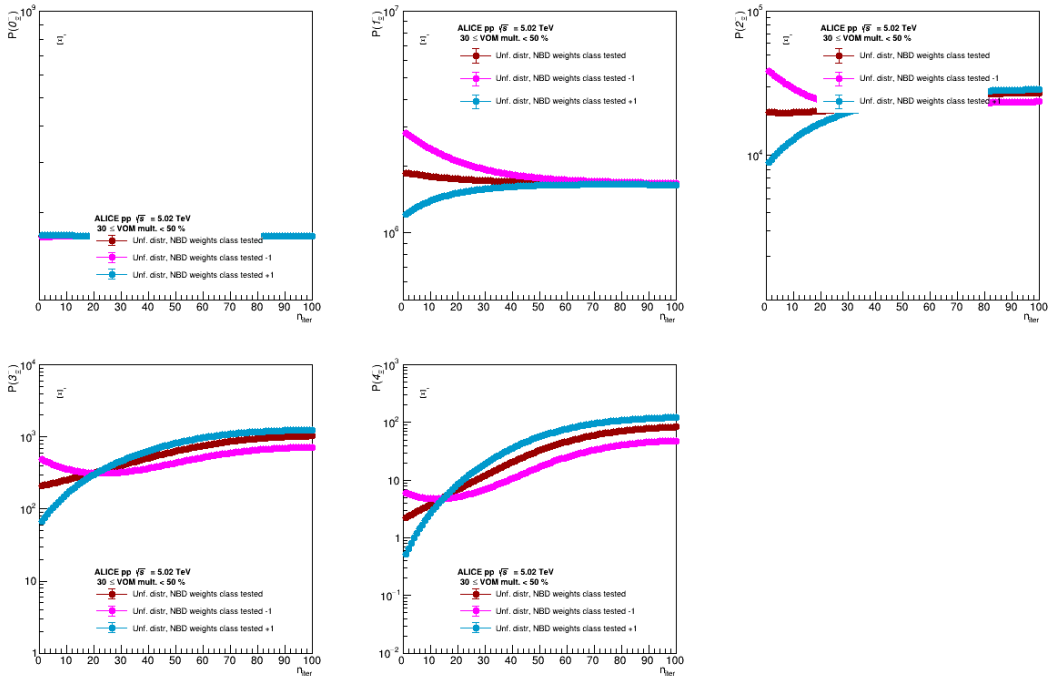

Figure 9.132: Comparison of the unfolded distributions for the $30 \leq V0M < 50\%$ class for Ξ^- as a function of the number of iterations: results using NBD-weights specific to the class are shown in dark red, while those obtained using weights from classes $i-1$ and $i+1$ are depicted in pink and azure, respectively.

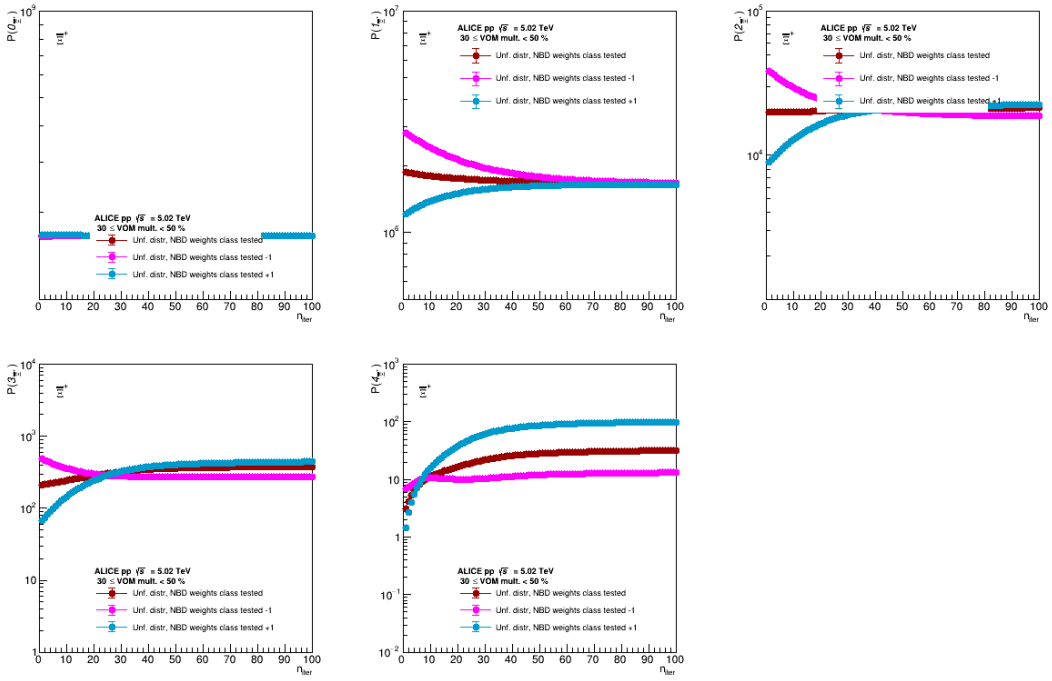

Figure 9.133: Comparison of the unfolded distributions for the $30 \leq V0M < 50\%$ class for $\overline{\Xi}^{+}$ as a function of the number of iterations: results using NBD-weights specific to the class are shown in dark red, while those obtained using weights from classes $i-1$ and $i+1$ are depicted in pink and azure, respectively.

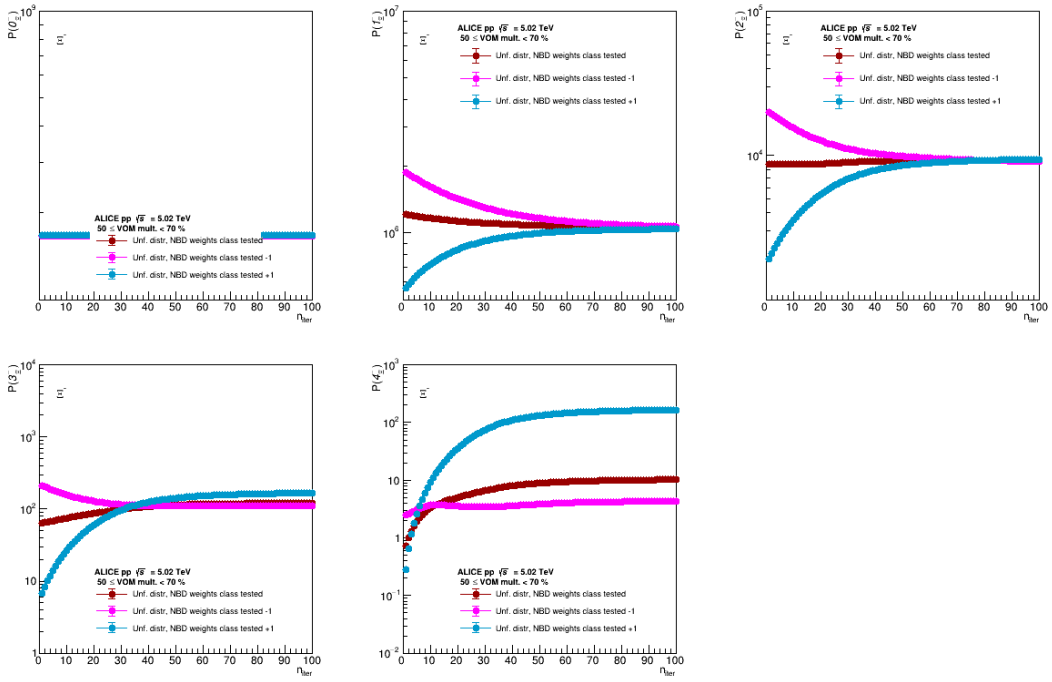

Figure 9.134: Comparison of the unfolded distributions for the $50 \leq V0M < 70\%$ class for Ξ^- as a function of the number of iterations: results using NBD-weights specific to the class are shown in dark red, while those obtained using weights from classes $i-1$ and $i+1$ are depicted in pink and azure, respectively.

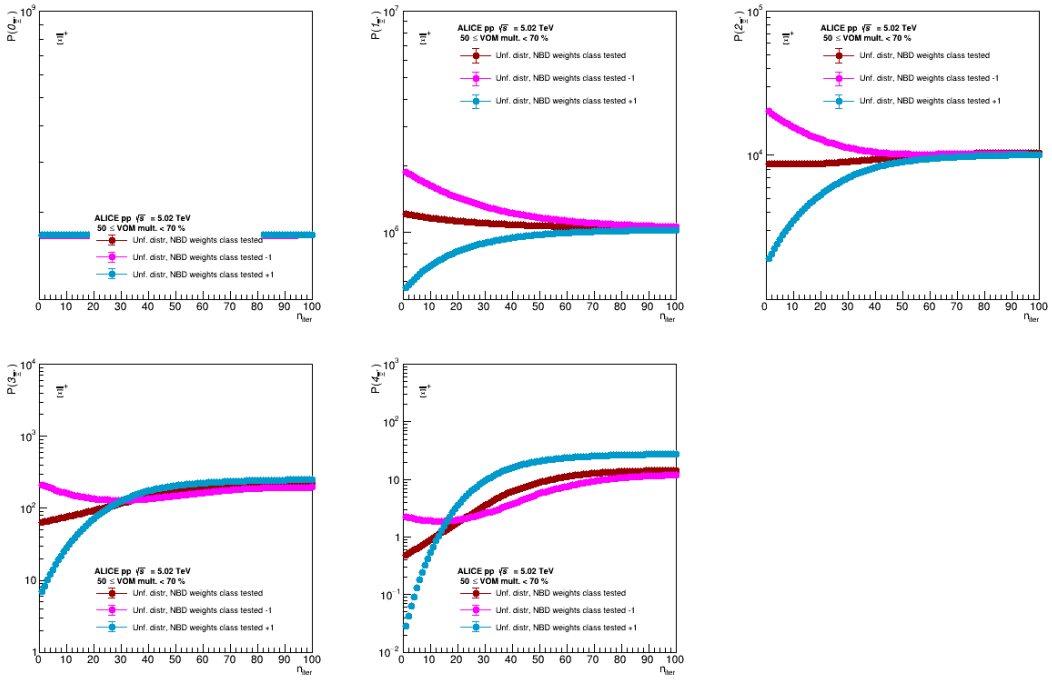

Figure 9.135: Comparison of the unfolded distributions for the $50 \leq V0M < 70\%$ class for $\overline{\Xi}^{+}$ as a function of the number of iterations: results using NBD-weights specific to the class are shown in dark red, while those obtained using weights from classes $i-1$ and $i+1$ are depicted in pink and azure, respectively.

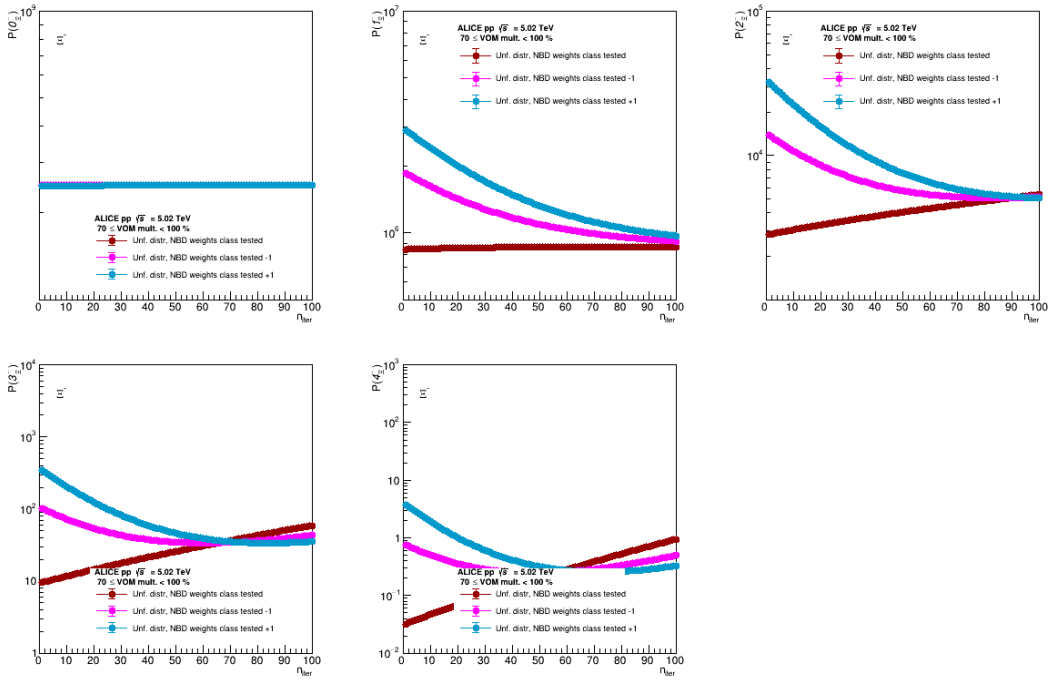

Figure 9.136: Comparison of the unfolded distributions for the $70 \leq V0M < 100\%$ class for Ξ^- as a function of the number of iterations: results using NBD-weights specific to the class are shown in dark red, while those obtained using weights from classes $i-1$ and $i+1$ (in this case $i-2$) are depicted in pink and azure, respectively.

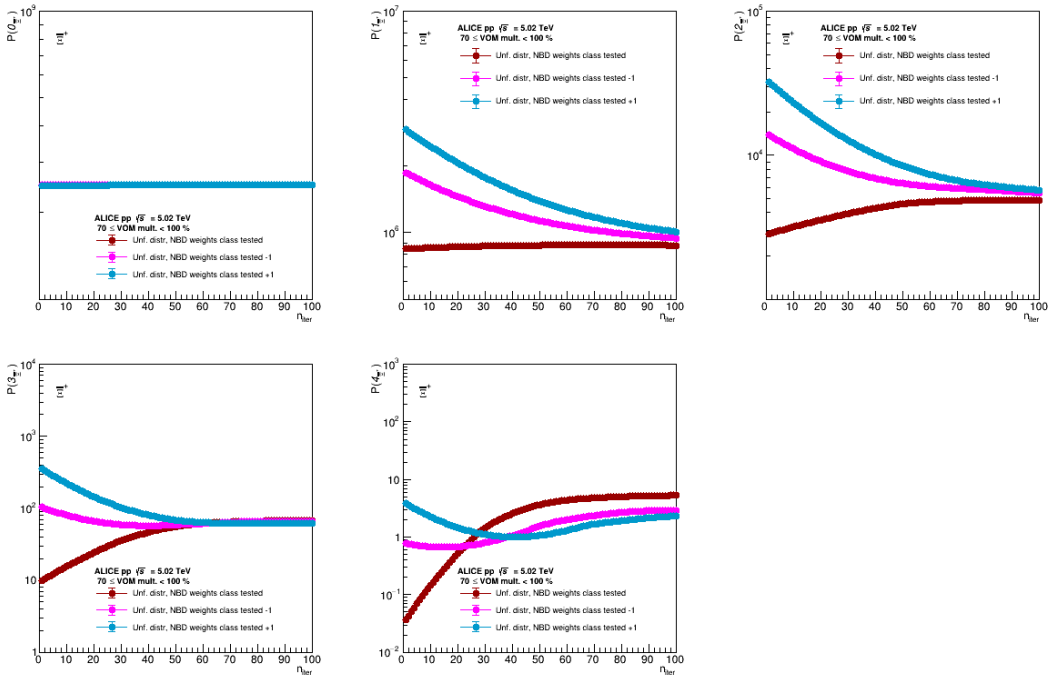

Figure 9.137: Comparison of the unfolded distributions for the $70 \leq V0M < 100\%$ class for $\overline{\Xi}^{+}$ as a function of the number of iterations: results using NBD-weights specific to the class are shown in dark red, while those obtained using weights from classes $i-1$ and $i+1$ (in this case $i-2$) are depicted in pink and azure, respectively.

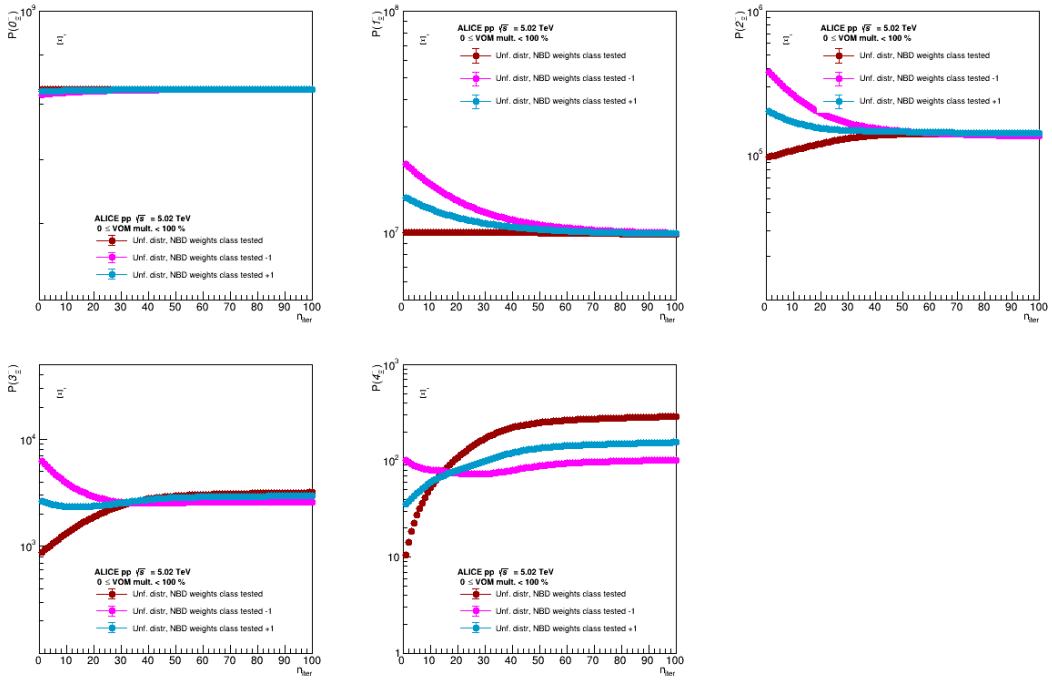

Figure 9.138: Comparison of the unfolded distributions for the INEL > 0 event class for Ξ^- as a function of the number of iterations: results using NBD-weights specific to the class are shown in dark red, while those obtained using weights from classes $i-1$ (in this case class V) and $i+1$ (in this case class VI) are depicted in pink and azure, respectively.

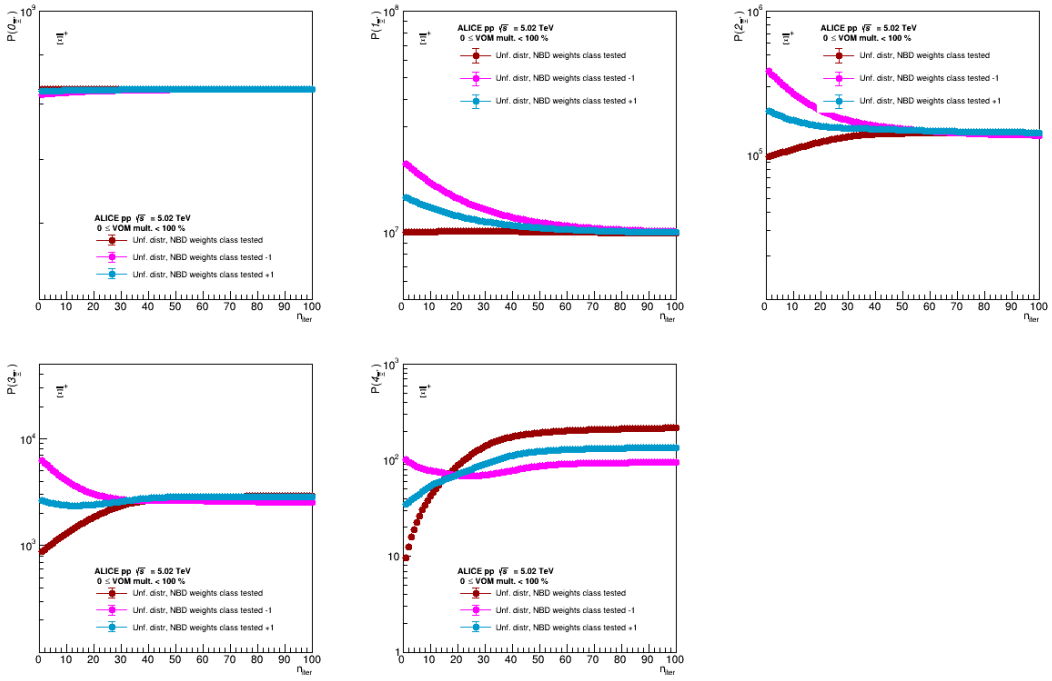

Figure 9.139: Comparison of the unfolded distributions for the INEL > 0 event class for $\overline{\Xi}^{+}$ as a function of the number of iterations: results using NBD-weights specific to the class are shown in dark red, while those obtained using weights from classes $i-1$ (in this case class V) and $i+1$ (in this case class VI) are depicted in pink and azure, respectively.

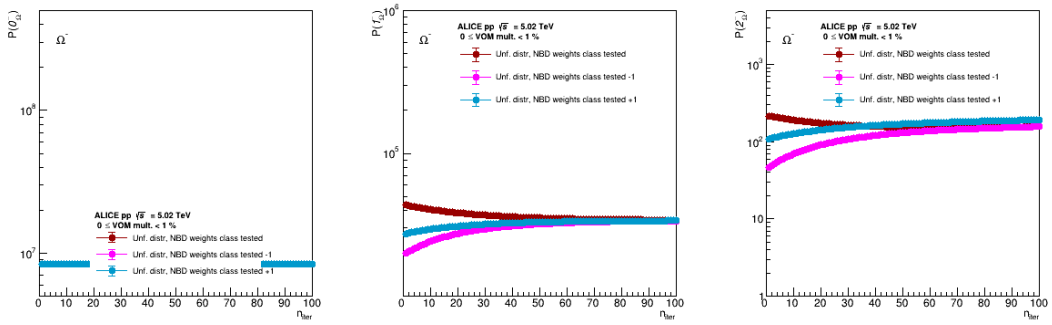

Figure 9.140: Comparison of the unfolded distributions for the $0 \leq V0M < 1\%$ class for Ω^- as a function of the number of iterations: results using NBD-weights specific to the class are shown in dark red, while those obtained using weights from classes $i-1$ (in this case $i+2$) and $i+1$ are depicted in pink and azure, respectively.

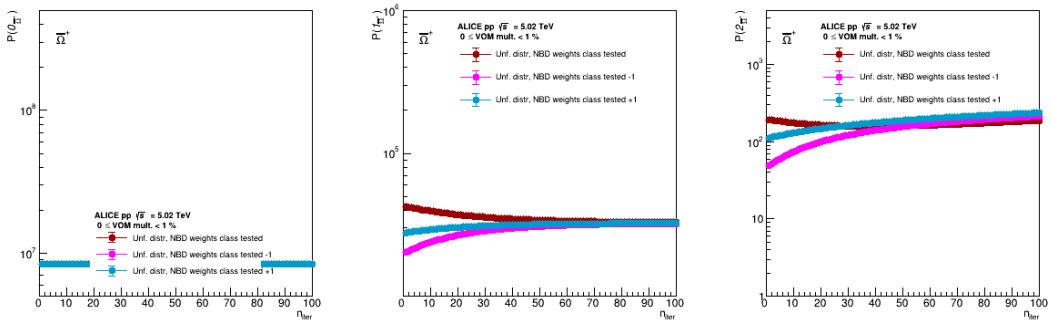

Figure 9.141: Comparison of the unfolded distributions for the $0 \leq V0M < 1\%$ class for $\overline{\Omega}^+$ as a function of the number of iterations: results using NBD-weights specific to the class are shown in dark red, while those obtained using weights from classes $i-1$ (in this case $i+2$) and $i+1$ are depicted in pink and azure, respectively.

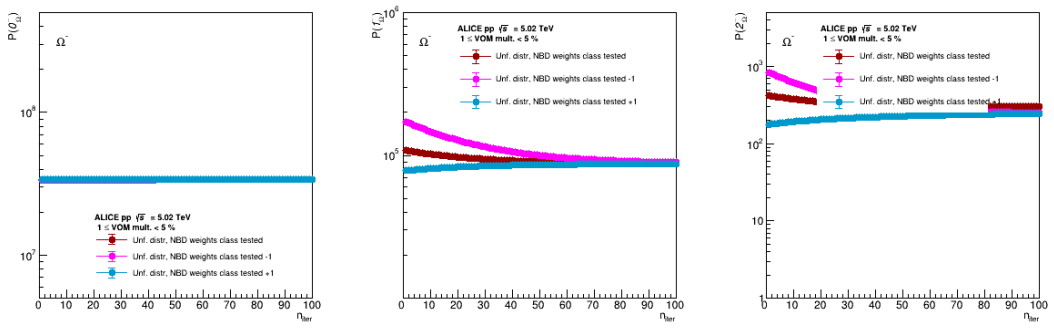

Figure 9.142: Comparison of the unfolded distributions for the $1 \leq V0M < 5\%$ class for Ω^- as a function of the number of iterations: results using NBD-weights specific to the class are shown in dark red, while those obtained using weights from classes $i-1$ and $i+1$ are depicted in pink and azure, respectively.

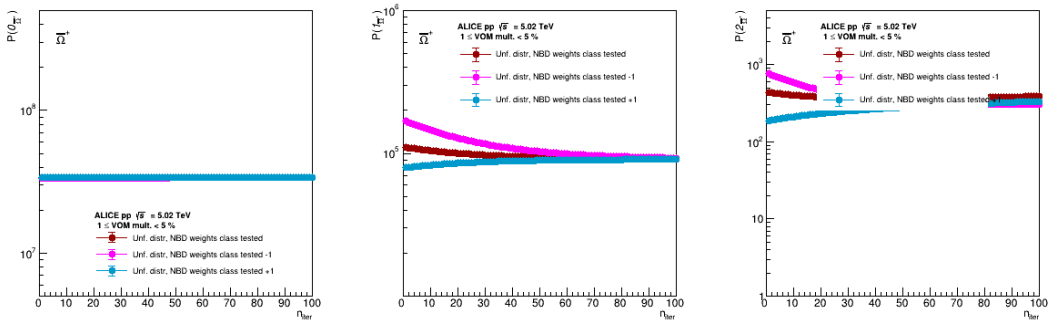

Figure 9.143: Comparison of the unfolded distributions for the $1 \leq V0M < 5\%$ class for $\overline{\Omega}^+$ as a function of the number of iterations: results using NBD-weights specific to the class are shown in dark red, while those obtained using weights from classes $i-1$ and $i+1$ are depicted in pink and azure, respectively.

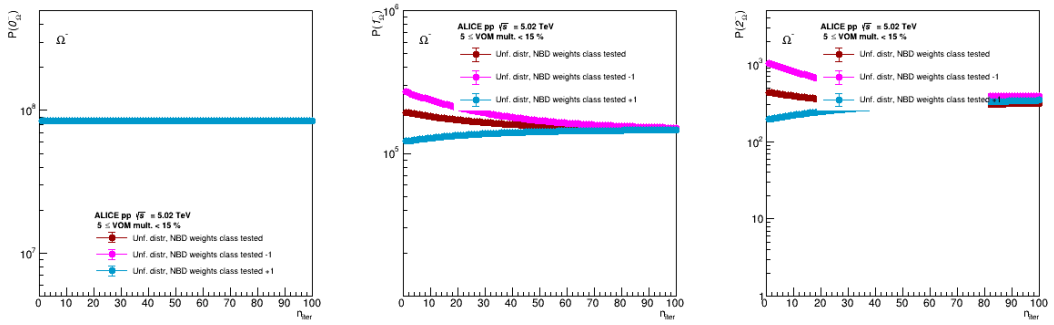

Figure 9.144: Comparison of the unfolded distributions for the $5 \leq V0M < 15\%$ class for Ω^- as a function of the number of iterations: results using NBD-weights specific to the class are shown in dark red, while those obtained using weights from classes $i-1$ and $i+1$ are depicted in pink and azure, respectively.

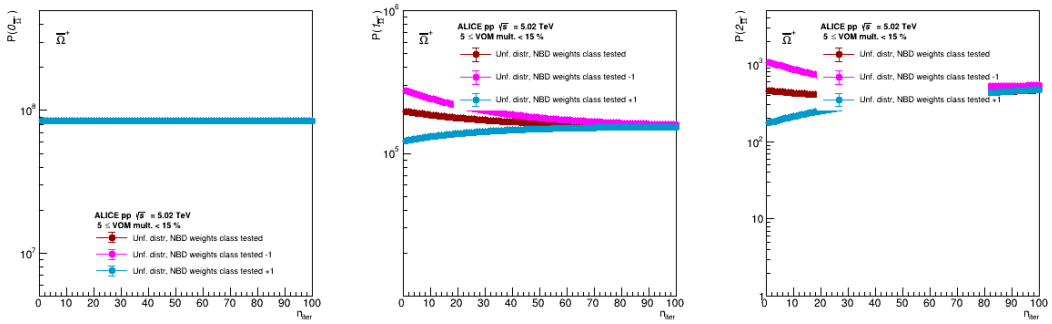

Figure 9.145: Comparison of the unfolded distributions for the $5 \leq V0M < 15\%$ class for $\overline{\Omega}^{+}$ as a function of the number of iterations: results using NBD-weights specific to the class are shown in dark red, while those obtained using weights from classes $i-1$ and $i+1$ are depicted in pink and azure, respectively.

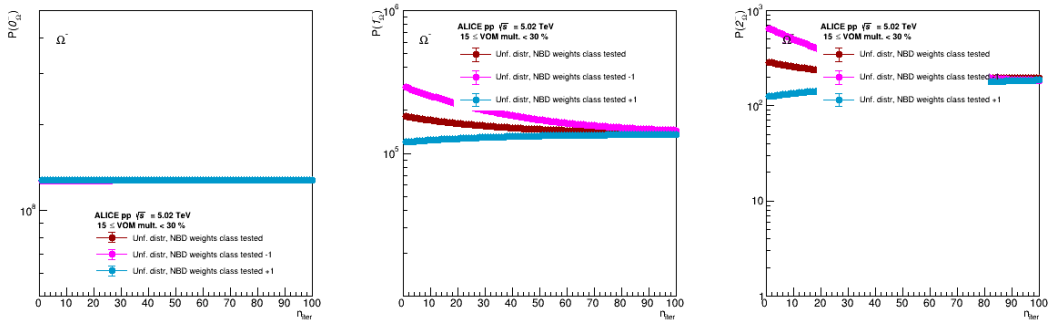

Figure 9.146: Comparison of the unfolded distributions for the $15 \leq V0M < 30\%$ class for Ω^{-} as a function of the number of iterations: results using NBD-weights specific to the class are shown in dark red, while those obtained using weights from classes $i-1$ and $i+1$ are depicted in pink and azure, respectively.

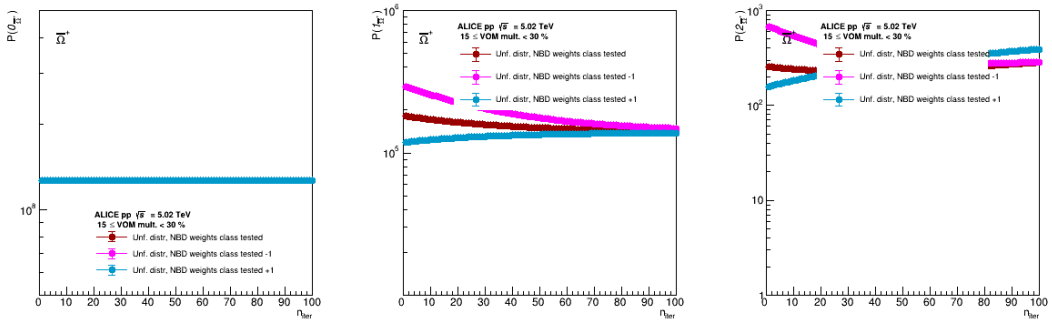

Figure 9.147: Comparison of the unfolded distributions for the $15 \leq V0M < 30\%$ class for $\overline{\Omega}^{+}$ as a function of the number of iterations: results using NBD-weights specific to the class are shown in dark red, while those obtained using weights from classes $i-1$ and $i+1$ are depicted in pink and azure, respectively.

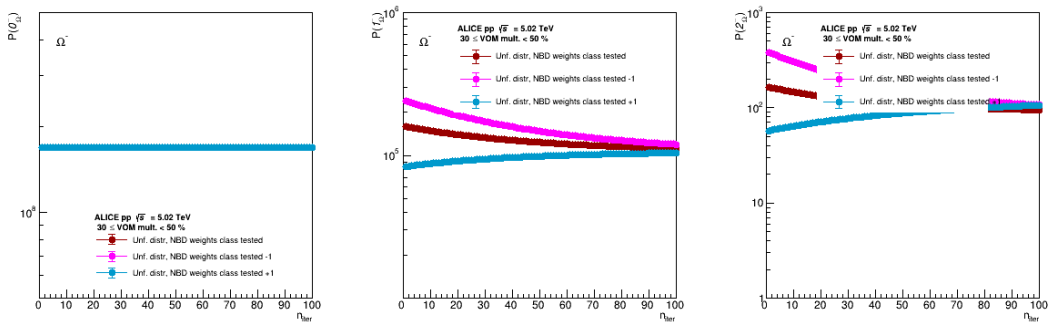

Figure 9.148: Comparison of the unfolded distributions for the $30 \leq V0M < 50\%$ class for Ω^- as a function of the number of iterations: results using NBD-weights specific to the class are shown in dark red, while those obtained using weights from classes $i-1$ and $i+1$ are depicted in pink and azure, respectively.

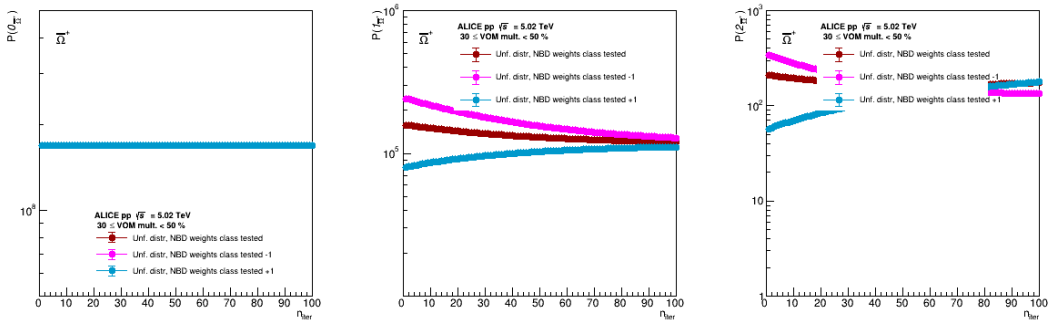

Figure 9.149: Comparison of the unfolded distributions for the $30 \leq V0M < 50\%$ class for $\overline{\Omega}^+$ as a function of the number of iterations: results using NBD-weights specific to the class are shown in dark red, while those obtained using weights from classes $i-1$ and $i+1$ are depicted in pink and azure, respectively.

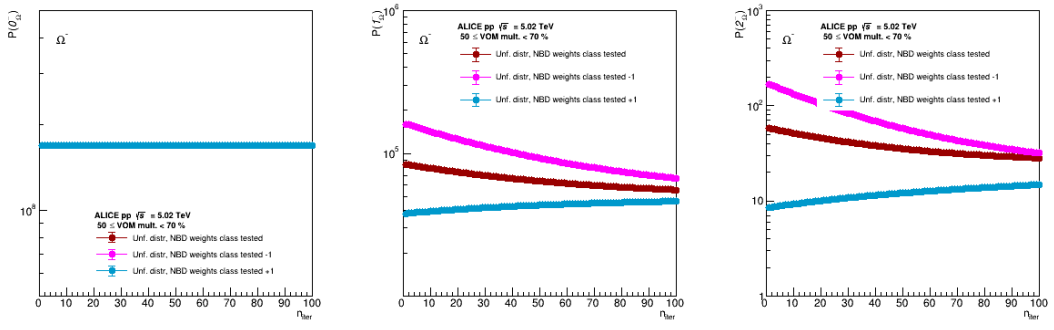

Figure 9.150: Comparison of the unfolded distributions for the $50 \leq V0M < 70\%$ class for Ω^- as a function of the number of iterations: results using NBD-weights specific to the class are shown in dark red, while those obtained using weights from classes $i-1$ and $i+1$ are depicted in pink and azure, respectively.

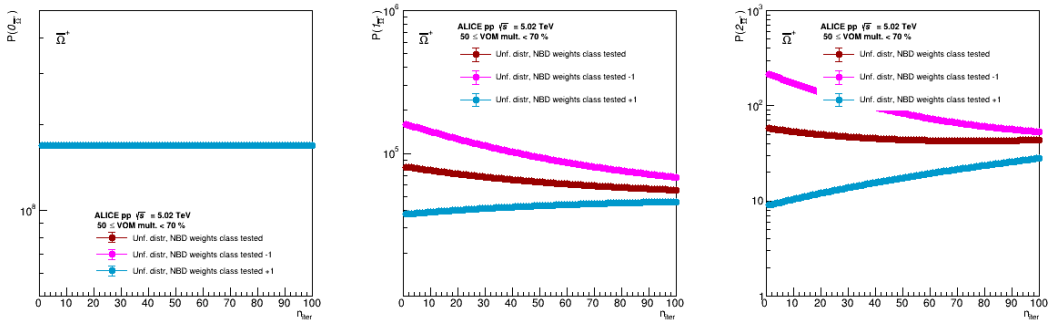

Figure 9.151: Comparison of the unfolded distributions for the $50 \leq V0M < 70\%$ class for $\overline{\Omega}^{+}$ as a function of the number of iterations: results using NBD-weights specific to the class are shown in dark red, while those obtained using weights from classes $i-1$ and $i+1$ are depicted in pink and azure, respectively.

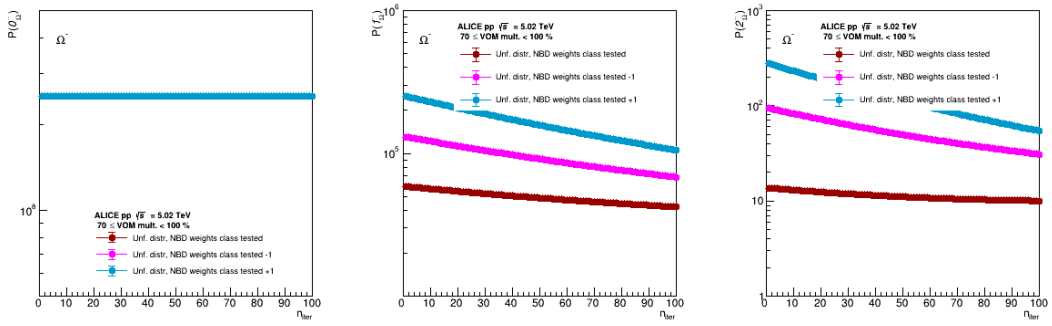

Figure 9.152: Comparison of the unfolded distributions for the $70 \leq V0M < 100\%$ class for Ω^{-} as a function of the number of iterations: results using NBD-weights specific to the class are shown in dark red, while those obtained using weights from classes $i-1$ and $i+1$ (in this case $i-2$) are depicted in pink and azure, respectively.

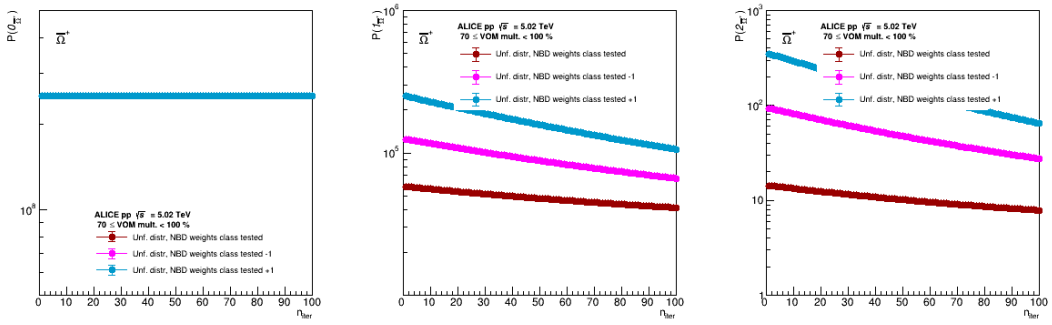

Figure 9.153: Comparison of the unfolded distributions for the $70 \leq V0M < 100\%$ class for $\overline{\Omega}^{+}$ as a function of the number of iterations: results using NBD-weights specific to the class are shown in dark red, while those obtained using weights from classes $i-1$ and $i+1$ (in this case $i-2$) are depicted in pink and azure, respectively.

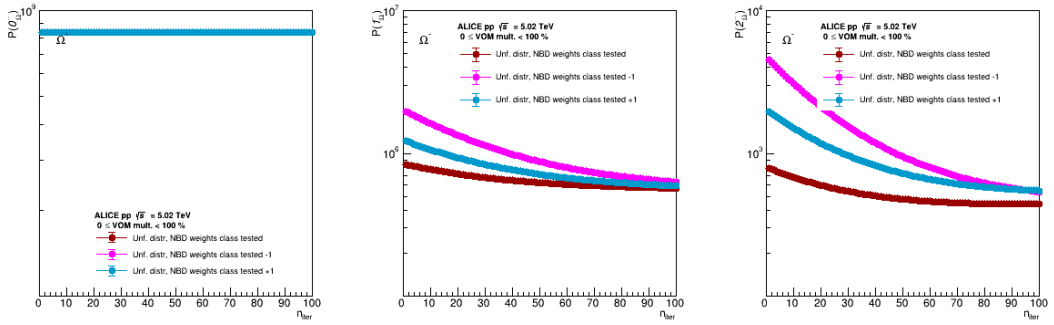

Figure 9.154: Comparison of the unfolded distributions for the INEL > 0 event class for Ω^- as a function of the number of iterations: results using NBD-weights specific to the class are shown in dark red, while those obtained using weights from classes $i-1$ (in this case class V) and $i+1$ (in this case class VI) are depicted in pink and azure, respectively.

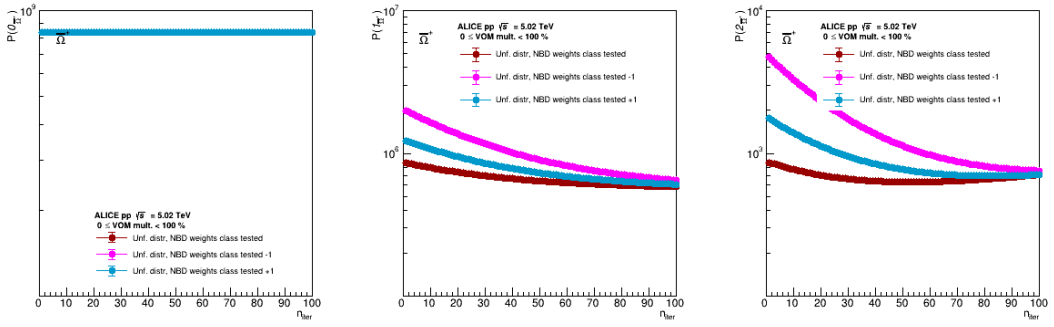

Figure 9.155: Comparison of the unfolded distributions for the INEL > 0 event class for $\overline{\Omega}^+$ as a function of the number of iterations: results using NBD-weights specific to the class are shown in dark red, while those obtained using weights from classes $i-1$ (in this case class V) and $i+1$ (in this case class VI) are depicted in pink and azure, respectively.

9.6 Agreement between particle and anti-particle

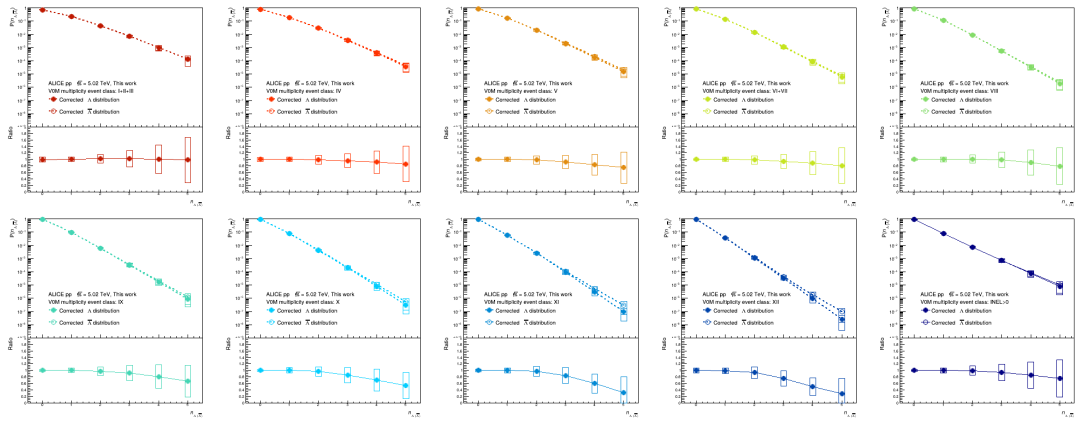

Figure 9.156: Comparison between the particle multiplicity distributions for Λ (full points) and $\overline{\Lambda}$ (open points) across different V0M multiplicity classes. The bottom panels show the ratios of particle to anti-particle distributions, with errors calculated through propagation.

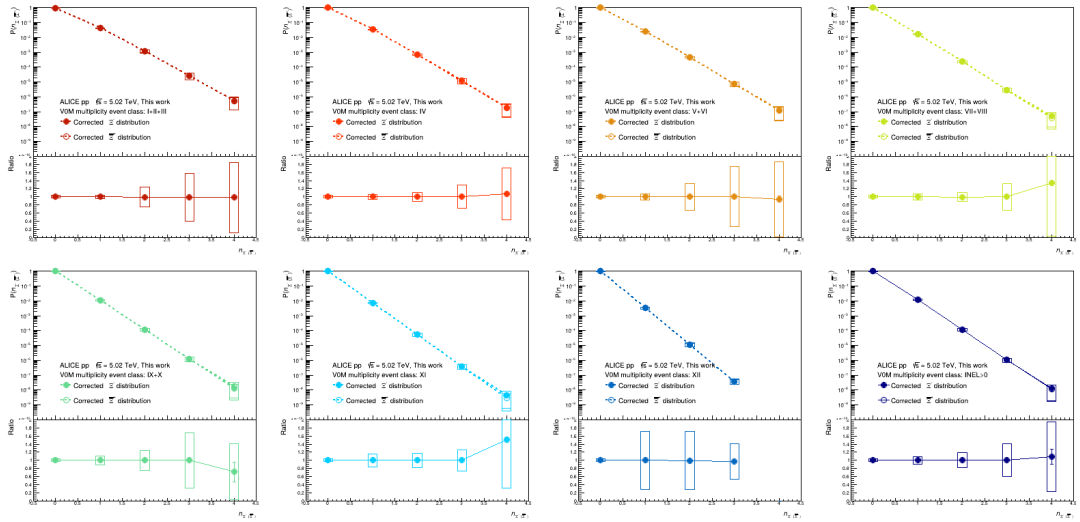

Figure 9.157: Comparison between the particle multiplicity distributions for Ξ^- (full points) and $\overline{\Xi}^+$ (open points) across different V0M multiplicity classes. The bottom panels show the ratios of particle to anti-particle distributions, with errors calculated through propagation.

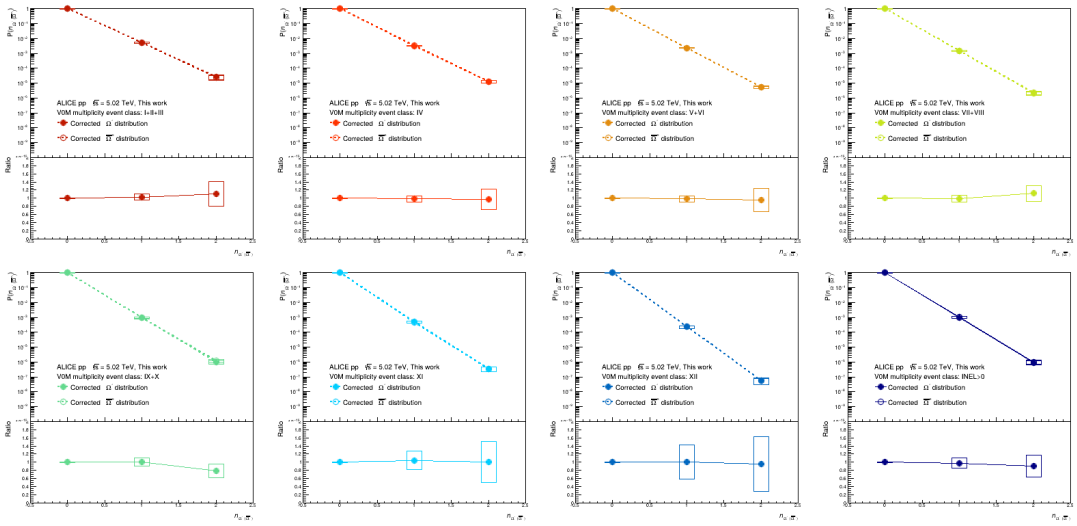

Figure 9.158: Comparison between the particle multiplicity distributions for Ω^- (full points) and $\overline{\Omega}^+$ (open points) across different V0M multiplicity classes. The bottom panels show the ratios of particle to anti-particle distributions, with errors calculated through propagation.

9.7 Fit to the (multi-)strange particle multiplicity distribution

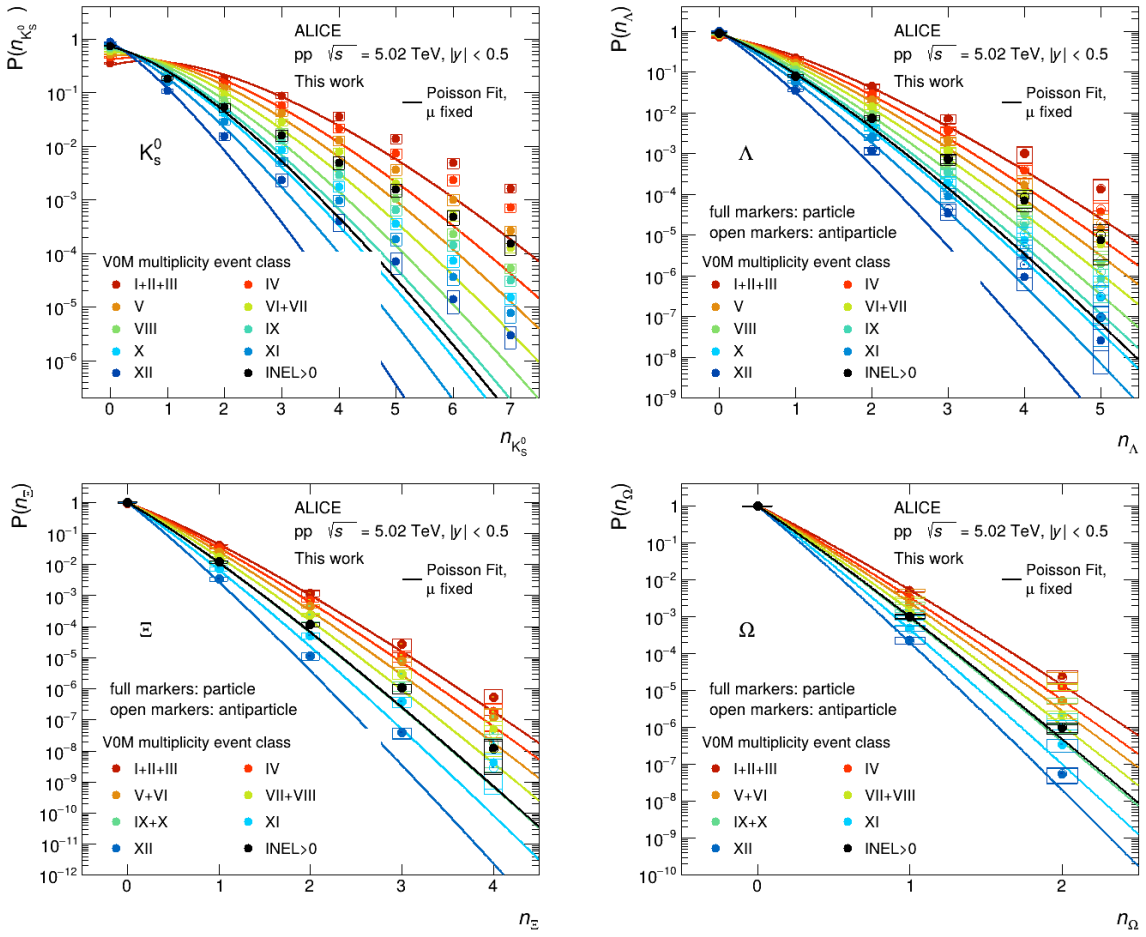

Figure 9.159: (multi-)Strange particle multiplicity distributions for K^0_S (top-left), Λ and $\overline{\Lambda}$ (top-right), Ξ^- and $\overline{\Xi}^+$ (bottom-left) and Ω^- and $\overline{\Omega}^+$ (bottom-right) for several V0M multiplicity classes. Solid lines represent Poisson fits applied to the multiplicity distributions with the mean fixed to the $\mathrm{d}N/\mathrm{d}y$ values ([16]).

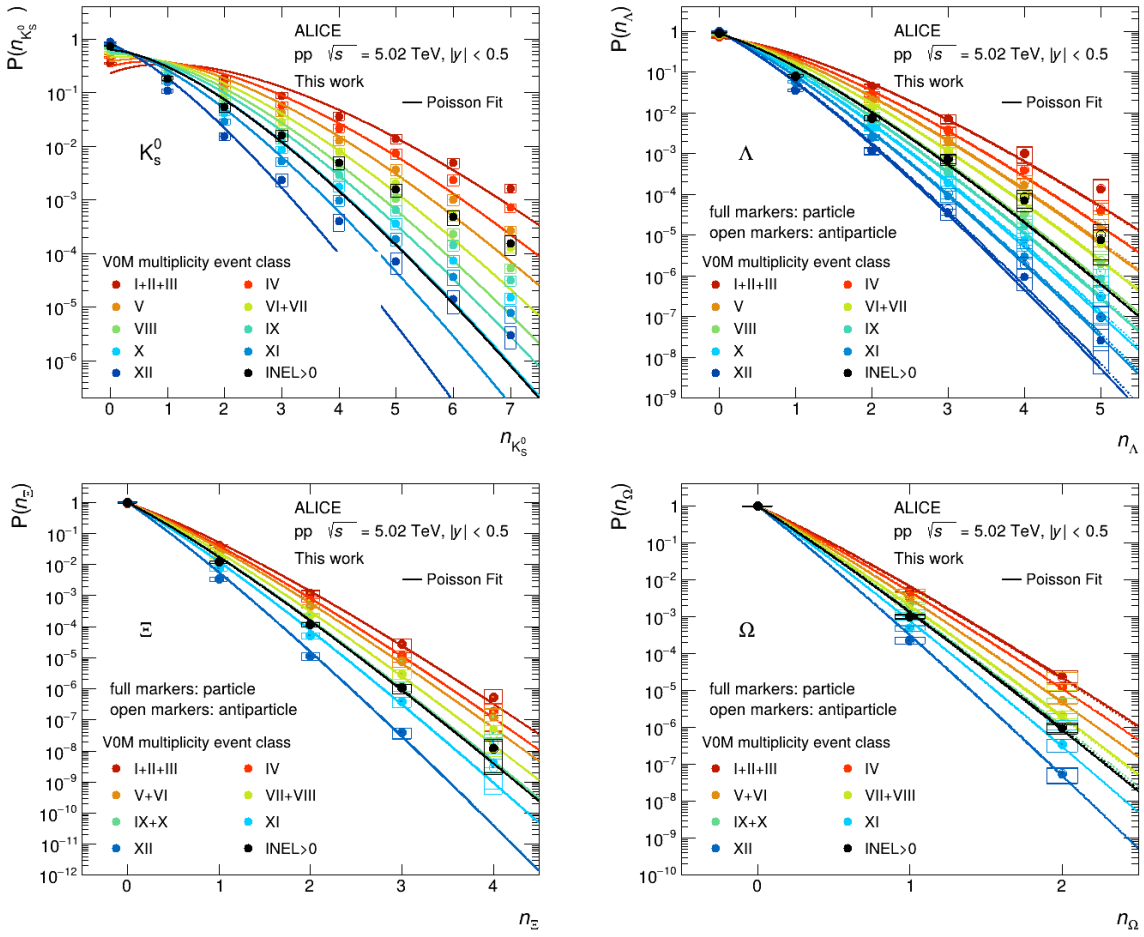

Figure 9.160: (multi-)Strange particle multiplicity distributions for K^0_S (top-left), Λ and $\overline{\Lambda}$ (top-right), Ξ^- and $\overline{\Xi}^+$ (bottom-left) and Ω^- and $\overline{\Omega}^+$ (bottom-right) for several V0M multiplicity classes. Solid (dashed) lines correspond to Poisson fits to the multiplicity distributions.

9.8 Strangeness-driven bias in the charged-particle multiplicity in Pythia 8 Monash and Epos LHC

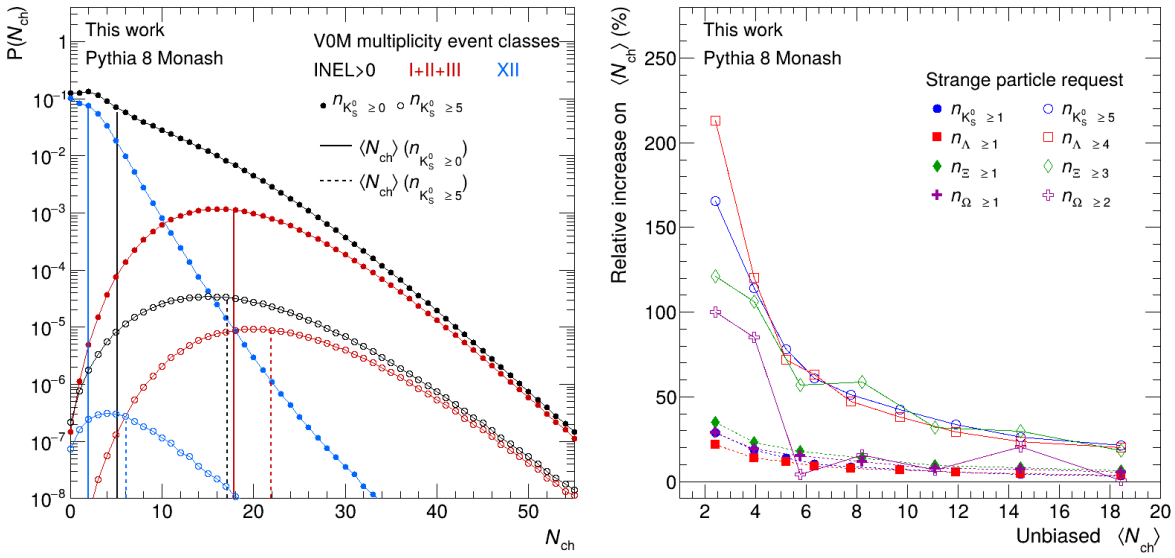

Figure 9.161: Illustration of the strangeness-induced charged-particle multiplicity bias effect observed in Pythia 8 Monash simulations. (*Left.*) The $\mathrm{d}N_{\mathrm{ch}}/\mathrm{d}\eta|_{|\eta| < 0.5}$ distribution is presented for the INEL > 0 (black markers), V0M-(I+II+III) and V0M-XII event classes (red and light blue points, respectively). Open markers indicate the corresponding $\mathrm{d}N_{\mathrm{ch}}/\mathrm{d}\eta|_{|\eta| < 0.5}$ distributions obtained when requiring at least five $\mathrm{K}^0_{\mathrm{S}}$ particles per event. Continuous and dashed lines represent the averages of the unbiased and biased multiplicity distributions, respectively. (*Right.*) The relative shift in $\langle \mathrm{d}N_{\mathrm{ch}}/\mathrm{d}\eta \rangle$ is shown for all V0M event classes, with a requirement of at least one (solid markers) or more than one (open markers) strange particle per event. Lines are included to guide the eye.

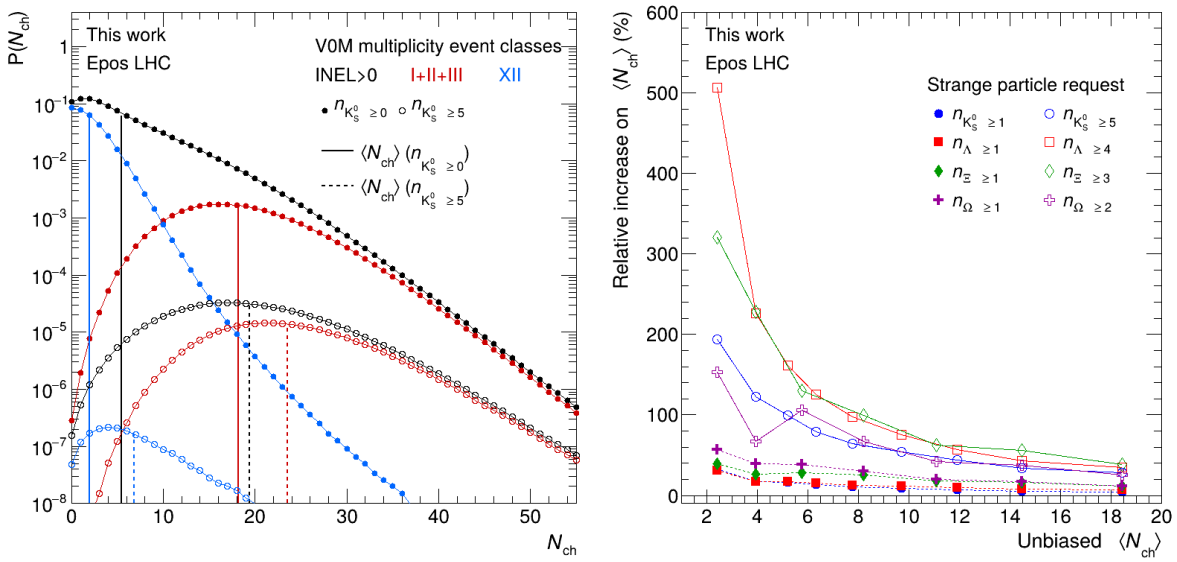

Figure 9.162: Illustration of the strangeness-induced charged-particle multiplicity bias effect observed in Epos LHC simulations. (*Left.*) The $\mathrm{d}N_{\mathrm{ch}}/\mathrm{d}\eta|_{|\eta|<0.5}$ distribution is presented for the INEL > 0 (black markers), V0M-(I+II+III) and V0M-XII event classes (red and light blue points, respectively). Open markers indicate the corresponding $\mathrm{d}N_{\mathrm{ch}}/\mathrm{d}\eta|_{|\eta|<0.5}$ distributions obtained when requiring at least five $\mathrm{K}^0_{\mathrm{S}}$ particles per event. Continuous and dashed lines represent the averages of the unbiased and biased multiplicity distributions, respectively. (*Right.*) The relative shift in $\langle \mathrm{d}N_{\mathrm{ch}}/\mathrm{d}\eta \rangle$ is shown for all V0M event classes, with a requirement of at least one (solid markers) or more than one (open markers) strange particle per event. Lines are included to guide the eye.

Bibliography

[1] ALICE Coll., "Enhanced production of multi-strange hadrons in high-multiplicity proton–proton collisions," *Nature Physics*, (2017). [Online]. Available: https://doi.org/10.1038/nphys4111.

[2] ALICE Coll., "The ALICE experiment at the CERN LHC," *JINST*, vol. 3, (2008). [Online]. Available: https://iopscience.iop.org/article/10.1088/1748-0221/3/08/S08002/meta.

[3] O. S. Brüning *et al.*, *LHC Design Report* (CERN Yellow Reports: Monographs). Geneva: CERN, 2004. DOI: 10.5170/CERN-2004-003-V-1. [Online]. Available: https://cds.cern.ch/record/782076.

[4] J.Rafelski, B.Müller, "Strangeness Production in the Quark-Gluon Plasma," *Phys.Rev.*, vol. 48, no. 16, (1982). [Online]. Available: https://doi.org/10.1103/PhysRevLett.48.1066.

[5] NA57 Coll., "Strangeness enhancements at central rapidity in 40 A GeV/c Pb-Pb collisions," *J.Phys.G:Nucl.Part.Phys*, (2010). [Online]. Available: https://dx.doi.org/10.1088/0954-3899/37/4/045105.

[6] STAR Coll., "Enhanced strange baryon production in Au+Au collisions compared to p+p at $\sqrt{s_{NN}}$ = 200 GeV," *Phys.Rev.*, vol. 77, no. 0449908, (2008). [Online]. Available: https://doi.org/10.1103/PhysRevC.77.044908.

[7] ALICE Coll., "Multi-strange baryon production at mid-rapidity in Pb-Pb collisions at $\sqrt{s_{NN}}$ = 2.76 TeV," *Physics Letters B*, vol. 728, pp. 216–227, Jan. 2014, ISSN: 0370-2693. DOI: 10.1016/j.physletb.2013.11.048. [Online]. Available: http://dx.doi.org/10.1016/j.physletb.2013.11.048.

[8] J.Cleymans, I.Kraus, H.Oeschler, K.Redlich, S.Wheaton, "Statistical Model Predictions for Particle Ratios at $\sqrt{s_{NN}}$ = 5.5 TeV," *Physical Review C*, vol. 74, no. 3, Sep. 2006, ISSN: 1089-490X. DOI: 10.1103/physrevc.74.034903. [Online]. Available: http://dx.doi.org/10.1103/PhysRevC.74.034903.

[9] A.Andronic, P.Braun-Munzinger, J.Stachel, "Thermal hadron production in relativistic nuclear collisions: the hadron mass spectrum, the horn, and the QCD phase transition," *Phys.Rev.Lett.B*, vol. 673, (2009). [Online]. Available: https://doi.org/10.1016/j.physletb.2009.02.014.

[10] A.Andronic, P.Braun-Munzinger, K.Redlich, J.Stachel, "Decoding the phase structure of QCD via particle production at high energy," *arXiv e-prints*, (2017). [Online]. Available: https://doi.org/10.1038/s41586-018-0491-6.

[11] V. Vovchenko and H. Stoecker, "Thermal-FIST: A package for heavy-ion collisions and hadronic equation of state," *Computer Physics Communications*, vol. 244, pp. 295–310, Nov. 2019, ISSN: 0010-4655. DOI: 10.1016/j.cpc.2019.06.024. [Online]. Available: http://dx.doi.org/10.1016/j.cpc.2019.06.024.

[12] A. Tounsi and K. Redlich, "Strangeness enhancement and canonical suppression," Nov. 2001. arXiv: hep-ph/0111159. [Online]. Available: https://arxiv.org/abs/hep-ph/0111159.

[13] F. Becattini, J. Manninen, and M. Ga ździcki, "Energy and system size dependence of chemical freeze-out in relativistic nuclear collisions," *Phys. Rev. C*, vol. 73, p. 044 905, 4 Apr. 2006. DOI: 10.1103/PhysRevC.73.044905. [Online]. Available: https://link.aps.org/doi/10.1103/PhysRevC.73.044905.

[14] ALICE Coll., "Multiplicity dependence of light-flavor hadron production in pp collisions at $\sqrt{s} = 7$ TeV," *Physical Review C*, vol. 99, no. 2, Feb. 2019, ISSN: 2469-9993. DOI: 10.1103/physrevc.99.024906. [Online]. Available: http://dx.doi.org/10.1103/PhysRevC.99.024906.

[15] ALICE Coll., "Multiplicity dependence of (multi-)strange hadron production in proton-proton collisions at $\sqrt{s} = 13$ TeV," *Eur.Phys.J.C*, vol. 80, (2020). [Online]. Available: https://doi.org/10.1140/epjc/s10052-020-7673-8.

[16] ALICE Coll., " Multiplicity dependence of (multi-)strange hadrons production in proton-proton collisions at $\sqrt{s} = 5.02$ TeV," In Publication.

[17] ALICE Coll., "Multiplicity dependence of pion, kaon, proton and lambda production in p-Pb collisions at $\sqrt{s_{NN}} = 5.02$ TeV," *Phys.Rev. B*, vol. 728, (2014). [Online]. Available: https://doi.org/10.1016/j.physletb.2013.11.020.

[18] ALICE Coll., "Multi-strange baryon production in p-Pb collisions at $\sqrt{s_{NN}} = 5.02$ TeV," *Phys.Rev. B*, vol. 758, (2016). [Online]. Available: https://doi.org/10.48550/arXiv.1512.07227.

[19] ALICE Coll., "Centrality dependence of strange hadron production in Pb–Pb collisions at $\sqrt{s_{NN}} = 5.02$ TeV," In Publication.

[20] T.Sjöstrand, S.Mrenna, P.Skands, "A brief Introduction to PYTHIA8.1," *Comput.Phys.Commun*, vol. 178, (2008). [Online]. Available: https://doi.org/10.1016/j.cpc.2008.01.036.

[21] M. Bähr *et al.*, "Herwig++ physics and manual," *The European Physical Journal C*, vol. 58, no. 4, pp. 639–707, Nov. 2008, ISSN: 1434-6052. DOI: 10.1140/epjc/s10052-008-0798-9. [Online]. Available: http://dx.doi.org/10.1140/epjc/s10052-008-0798-9.

[22] J.R.Christiansen, P.Skands, "String Formation Beyond Leading Colour," *arXiv e-prints*, (2015). [Online]. Available: https://arxiv.org/abs/1505.01681.

[23] C. Bierlich, G. Gustafson, L. Lönnblad, and A. Tarasov, "Effects of Overlapping Strings in pp Collisions," *JHEP*, vol. 03, p. 148, 2015. DOI: 10.1007/JHEP03(2015)148. arXiv: 1412.6259 [hep-ph].

[24] C. B. Duncan and P. Kirchgaeßer, "Kinematic strangeness production in cluster hadronization," *The European Physical Journal C*, vol. 79, p. 61, 1 2019. DOI: 10.1140/epjc/s10052-019-6573-2. [Online]. Available: https://doi.org/10.1140/epjc/s10052-019-6573-2.

[25] J. Cleymans, P. M. Lo, K. Redlich, and N. Sharma, "Multiplicity dependence of (multi)strange baryons in the canonical ensemble with phase shift corrections," *Physical Review C*, vol. 103, no. 1, Jan. 2021, ISSN: 2469-9993. DOI: 10.1103/physrevc.103.014904. [Online]. Available: http://dx.doi.org/10.1103/PhysRevC.103.014904.

[26] V. Vovchenko, B. Dönigus, and H. Stoecker, "Canonical statistical model analysis of p-p, p-Pb, and Pb-Pb collisions at energies available at the cern large hadron collider," *Physical Review C*, vol. 100, no. 5, Nov. 2019, ISSN: 2469-9993. DOI: 10.1103/physrevc.100.054906. [Online]. Available: http://dx.doi.org/10.1103/PhysRevC.100.054906.

[27] J. Cleymans, P. M. Lo, K. Redlich, and N. Sharma, "Multiplicity dependence of (multi)strange baryons in the canonical ensemble with phase shift corrections," *Phys. Rev. C*, vol. 103, p. 014 904, 1 Jan. 2021. DOI: 10.1103/PhysRevC.103.014904. [Online]. Available: https://link.aps.org/doi/10.1103/PhysRevC.103.014904.

[28] ALICE Coll., "Production of Λ and K^0_S in p-Pb collisions at $\sqrt{s_{NN}} = 5.02$ TeV and pp collisions at $\sqrt{s} = 7$ TeV," *Physics Letters B*, vol. 827, 2022, ISSN: 0370-2693. DOI: 10.1016/j.physletb.2022.136984. [Online]. Available: http://dx.doi.org/10.1016/j.physletb.2022.136984.

[29] ALICE Coll., "Investigating strangeness enhancement with multiplicity in pp collisions using angular correlations," *Journal of High Energy Physics*, vol. 2024, no. 9, Sep. 2024, ISSN: 1029-8479. DOI: 10.1007/jhep09(2024)204. [Online]. Available: http://dx.doi.org/10.1007/JHEP09(2024)204.

[30] ALICE Coll., "Light-flavor particle production in high-multiplicity pp collisions at $\sqrt{s} = 13$ TeV as a function of transverse spherocity," *Journal of High Energy Physics*, 2024. DOI: 10.1007/JHEP05(2024)184. [Online]. Available: https://doi.org/10.1007/JHEP05(2024)184.

[31] ALICE Coll., "First observation of strange baryon enhancement with effective energy in pp collisions at the LHC," DOI: https://doi.org/10.48550/arXiv.2409.12702. arXiv: 2409.12702 [hep-ex]. [Online]. Available: https://arxiv.org/abs/2409.12702.

[32] ALICE Coll., "Studying strangeness and baryon production mechanisms through angular correlations between charged Ξ baryons and identified hadrons in pp collisions at $\sqrt{s} = 13$ TeV," 2023. DOI: https://doi.org/10.48550/arXiv.2308.16706. arXiv: 2308.16706 [hep-ex]. [Online]. Available: https://arxiv.org/abs/2308.16706.

[33] ALICE Coll., "Probing strangeness hadronization with event-by-event production of multistrange hadrons," DOI: https://doi.org/10.48550/arXiv.2405.19890. arXiv: 2405.19890 [nucl-ex]. [Online]. Available: https://arxiv.org/abs/2405.19890.

[34] F.Halzen, A.D.Martin, *Quarks and Leptons: an introductory course in modern particel physics*. John Wiley & Sons Inc, (1984).

[35] T.-P. Cheng and L.-F. Li, *Gauge theory of elementary particle physics: Problems and solutions*. Oxford university press, 2000.

[36] D. J. Gross and F. Wilczek, "Ultraviolet behavior of non-abelian gauge theories," *Phys. Rev. Lett.*, vol. 30, pp. 1343–1346, 26 Jun. 1973. DOI: 10.1103/PhysRevLett.30.1343. [Online]. Available: https://link.aps.org/doi/10.1103/PhysRevLett.30.1343.

[37] H. D. Politzer, "Reliable perturbative results for strong interactions?" *Phys. Rev. Lett.*, vol. 30, pp. 1346–1349, 26 Jun. 1973. DOI: 10.1103/PhysRevLett.30.1346. [Online]. Available: https://link.aps.org/doi/10.1103/PhysRevLett.30.1346.

[38] S. Navas *et al.*, "Review of particle physics," *Phys. Rev. D*, vol. 110, no. 3, p. 030 001, 2024. DOI: 10.1103/PhysRevD.110.030001.

[39] R.Gupta, "Introduction to Lattice QCD," *arXiv e-prints*, (1998). [Online]. Available: https://arxiv.org/abs/hep-lat/9807028.

[40] K.G.Wilson, "Confinement of quarks," *Phys.Rev.D*, vol. 10, no. 9, (1974). [Online]. Available: https://doi.org/10.1103/PhysRevD.10.2445.

[41] K.Yagi, T.Hatsuda, Y.Miake, *Quark-Gluon Plasma: From big bang to little bagng*. Cambridge University Press, (2008).

[42] [Online]. Available: https://cerncourier.com/a/quark-matter-fireballs-hashed-out-in-protvino/.

[43] M. Baldo, M. Buballa, G. Burgio, F. Neumann, M. Oertel, and H.-J. Schulze, "Neutron stars and the transition to color superconducting quark matter," *Physics Letters B*, vol. 562, no. 3–4, pp. 153–160, Jun. 2003, ISSN: 0370-2693. DOI: 10.1016/s0370-2693(03)00556-2. [Online]. Available: http://dx.doi.org/10.1016/S0370-2693(03)00556-2.

[44] J. Letessier and J. Rafelski, *Hadrons and Quark–Gluon Plasma* (Cambridge Monographs on Particle Physics, Nuclear Physics and Cosmology). Cambridge University Press, 2023.

[45] U. Heinz and M. Jacob, "Evidence for a new state of matter: An assessment of the results from the cern lead beam programme," 2000. arXiv: nucl-th/0002042 [nucl-th]. [Online]. Available: https://arxiv.org/abs/nucl-th/0002042.

[46] C. Ogilvie, "Review of nuclear reactions at the AGS," *Nuclear Physics A*, vol. 698, no. 1, pp. 3–12, 2002, 15th Int. Conf. on Ultra-Relativistic Nucleus-Nucleus Collisions (Quark Matter 2001), ISSN: 0375-9474. DOI: https://doi.org/10.1016/S0375-9474(01)01343-4. [Online]. Available: https://www.sciencedirect.com/science/article/pii/S0375947401013434.

[47] M. Harrison, T. Ludlam, and S. Ozaki, "RHIC project overview," *Nuclear Instruments and Methods in Physics Research Section A: Accelerators, Spectrometers, Detectors and Associated Equipment*, vol. 499, no. 2, pp. 235–244, 2003, The Relativistic Heavy Ion Collider Project: RHIC and its Detectors, ISSN: 0168-9002. DOI: https://doi.org/10.1016/S0168-9002(02)01937-X. [Online]. Available: https://www.sciencedirect.com/science/article/pii/S016890020201937X.

[48] ALICE Coll., "The ALICE experiment: A journey through QCD," *The European Physical Journal C*, vol. 84, no. 8, Aug. 2024, ISSN: 1434-6052. DOI: 10.1140/epjc/s10052-024-12935-y. [Online]. Available: http://dx.doi.org/10.1140/epjc/s10052-024-12935-y.

[49] R. e. a. Aaij, "Centrality determination in heavy-ion collisions with the LHCb detector," *JINST*, vol. 17, no. 05, P05009, 2022, All figures and tables, along with any supplementary material and additional information, are available at https://lhcbproject.web.cern.ch/Publications/p/LHCb-DP-2021-002.html (LHCb public pages). DOI: 10.1088/1748-0221/17/05/P05009. arXiv: 2111.01607. [Online]. Available: https://cds.cern.ch/record/2789548.

[50] C.Gale, S.Jeon, B.Schenke, "Hydrodynamic Modeling of Heavy-Ion Collisions," *Int.J. of Mod.Phys.A*, vol. 28, (2013). [Online]. Available: https://arxiv.org/abs/1301.5893.

[51] G. e. a. Aad, "Measurement of the centrality dependence of the charged particle pseudorapidity distribution in lead–lead collisions at $\sqrt{s_{NN}} = 2.76$ TeV with the ATLAS detector," *Physics Letters B*, vol. 710, no. 3, pp. 363–382, Apr. 2012, ISSN: 0370-2693. DOI: 10.1016/j.physletb.2012.02.045. [Online]. Available: http://dx.doi.org/10.1016/j.physletb.2012.02.045.

[52] Chatrchyan, S. et al., "Dependence on pseudorapidity and on centrality of charged hadron production in Pb-Pb collisions at $\sqrt{s_{\mathrm{NN}}} = 2.76$ TeV," *Journal of High Energy Physics*, vol. 2011, no. 8, Aug. 2011, ISSN: 1029-8479. DOI: 10.1007/jhep08(2011)141. [Online]. Available: http://dx.doi.org/10.1007/JHEP08(2011)141.

[53] NA50 Coll., "Scaling of charged particle multiplicity in Pb–Pb collisions at SPS energies," *Physics Letters B*, vol. 530, no. 1, pp. 43–55, 2002, ISSN: 0370-2693. DOI: https://doi.org/10.1016/S0370-2693(02)01353-9. [Online]. Available: https://www.sciencedirect.com/science/article/pii/S0370269302013539.

[54] Arsene, I. et al., "Transverse-momentum spectra in Au+Au and d+Au collisions at $\sqrt{s_{NN}} = 200$ GeV and the pseudorapidity dependence of high p_T suppression," *Physical Review Letters*, vol. 91, no. 7, Aug. 2003, ISSN: 1079-7114. DOI: 10.1103/physrevlett.91.072305. [Online]. Available: http://dx.doi.org/10.1103/PhysRevLett.91.072305.

[55] Abelev, B. I. et al., "Systematic measurements of identified particle spectra in pp, d+Au and Au+Au collisions from star," *Physical Review C*, vol. 79, no. 3, Mar. 2009, ISSN: 1089-490X. DOI: 10.1103/physrevc.79.034909. [Online]. Available: http://dx.doi.org/10.1103/PhysRevC.79.034909.

[56] Adcox, K. et al., "Centrality dependence of charged particle multiplicity in Au-Au collisions at $\sqrt{s_{NN}}$=130 GeV," *Physical Review Letters*, vol. 86, no. 16, pp. 3500–3505, Apr. 2001, ISSN: 1079-7114. DOI: 10.1103/physrevlett.86.3500. [Online]. Available: http://dx.doi.org/10.1103/PhysRevLett.86.3500.

[57] Alver, B. et al., "Charged-particle multiplicity and pseudorapidity distributions measured with the PHOBOS detector in Au+Au, Cu+Cu, d+Au, and p+p collisions at ultra-relativistic energies," *Physical Review C*, vol. 83, no. 2, Feb. 2011, ISSN: 1089-490X. DOI: 10.1103/physrevc.83.024913. [Online]. Available: http://dx.doi.org/10.1103/PhysRevC.83.024913.

[58] W. C. A. Biallas M. Bleszynski, "Multiplicity distributions in nucleus-nucleus collisions at high energies," *Nuclear Physics B*, vol. 111, no. 3, pp. 461–476, 1976, ISSN: 0550-3213. DOI: https://doi.org/10.1016/0550-3213(76)90329-1. [Online]. Available: https://www.sciencedirect.com/science/article/pii/0550321376903291.

[59] ALICE Coll., "Centrality dependence of the charged-particle multiplicity density at mid-rapidity in Pb-Pb collisions at $\sqrt{s_{NN}} = 5.02$ TeV," *Physical Review Letters*, vol. 116, no. 22, Jun. 2016, ISSN: 1079-7114. DOI: 10.1103/physrevlett.116.222302. [Online]. Available: http://dx.doi.org/10.1103/PhysRevLett.116.222302.

[60] S. Wheaton, J. Cleymans, and M. Hauer, "Thermus," 2011. arXiv: 1108.4588 [hep-ph]. [Online]. Available: https://arxiv.org/abs/1108.4588.

[61] J. Cleymans, I. Kraus, H. Oeschler, K. Redlich, and S. Wheaton, "Statistical model predictions for particle ratios at $\sqrt{s_{NN}} = 5.5$ TeV," *Physical Review C*, vol. 74, no. 3, Sep. 2006, ISSN: 1089-490X. DOI: 10.1103/physrevc.74.034903. [Online]. Available: http://dx.doi.org/10.1103/PhysRevC.74.034903.

[62] G. Torrieri, S. Steinke, W. Broniowski, W. Florkowski, J. Letessier, and J. Rafelski, "SHARE: Statistical hadronization with resonances," *Computer Physics Communications*, vol. 167, no. 3, pp. 229–251, May 2005, ISSN: 0010-4655. DOI: 10.1016/j.cpc.2005.01.004. [Online]. Available: http://dx.doi.org/10.1016/j.cpc.2005.01.004.

[63] G. Torrieri, S. Jeon, J. Letessier, and J. Rafelski, "SHAREv2: Fluctuations and a comprehensive treatment of decay feed-down," *Computer Physics Communications*, vol. 175, no. 10, pp. 635–649, Nov. 2006, ISSN: 0010-4655. DOI: 10.1016/j.cpc.2006.07.010. [Online]. Available: http://dx.doi.org/10.1016/j.cpc.2006.07.010.

[64] M. Petran, J. Letessier, J. Rafelski, and G. Torrieri, "SHARE with CHARM," *Computer Physics Communications*, vol. 185, no. 7, pp. 2056–2079, Jul. 2014, ISSN: 0010-4655. DOI: 10.1016/j.cpc.2014.02.026. [Online]. Available: http://dx.doi.org/10.1016/j.cpc.2014.02.026.

[65] V. Vovchenko, M. I. Gorenstein, and H. Stoecker, "Finite resonance widths influence the thermal-model description of hadron yields," *Physical Review C*, vol. 98, no. 3, Sep. 2018, ISSN: 2469-9993. DOI: 10.1103/physrevc.98.034906. [Online]. Available: http://dx.doi.org/10.1103/PhysRevC.98.034906.

[66] A. Andronic, P. Braun-Munzinger, B. Friman, P. M. Lo, K. Redlich, and J. Stachel, "The thermal proton yield anomaly in Pb-Pb collisions at the LHC and its resolution," *Physics Letters B*, vol. 792, pp. 304–309, May 2019, ISSN: 0370-2693. DOI: 10.1016/j.physletb.2019.03.052. [Online]. Available: http://dx.doi.org/10.1016/j.physletb.2019.03.052.

[67] D. H. Rischke, M. I. Gorenstein, H. Stoecker, and W. Greiner, "Excluded volume effect for the nuclear matter equation of state," *Z. Phys. C*, vol. 51, pp. 485–490, 1991. DOI: 10.1007/BF01548574.

[68] NA57 Coll. [Online]. Available: https://na57.web.cern.ch/NA57/yields.html.

[69] G. Gatoff and C. Y. Wong, "Origin of the soft p_T spectra," *Phys. Rev. D*, vol. 46, pp. 997–1006, 1992. DOI: 10.1103/PhysRevD.46.997.

[70] E. Schnedermann, J. Sollfrank, and U. Heinz, "Thermal phenomenology of hadrons from 200A GeV S+S collisions," *Physical Review C*, vol. 48, no. 5, pp. 2462–2475, Nov. 1993, ISSN: 1089-490X. DOI: 10.1103/physrevc.48.2462. [Online]. Available: http://dx.doi.org/10.1103/PhysRevC.48.2462.

[71] ALICE Coll., "Pion, kaon, and proton production in central Pb-Pb collisions at $\sqrt{s_{NN}}$ = 2.76 TeV," *Physical Review Letters*, vol. 109, no. 25, Dec. 2012, ISSN: 1079-7114. DOI: 10.1103/physrevlett.109.252301. [Online]. Available: http://dx.doi.org/10.1103/PhysRevLett.109.252301.

[72] ALICE Coll., "Production of charged pions, kaons, and (anti-)protons in Pb-Pb and inelastic pp collisions at $\sqrt{s_{NN}}$ = 5.02 TeV," *Physical Review C*, vol. 101, no. 4, Apr. 2020, ISSN: 2469-9993. DOI: 10.1103/physrevc.101.044907. [Online]. Available: http://dx.doi.org/10.1103/PhysRevC.101.044907.

[73] J. L. Nagle and W. A. Zajc, "Small system collectivity in relativistic hadronic and nuclear collisions," *Annual Review of Nuclear and Particle Science*, vol. 68, no. 1, pp. 211–235, Oct. 2018, ISSN: 1545-4134. DOI: 10.1146/annurev-nucl-101916-123209. [Online]. Available: http://dx.doi.org/10.1146/annurev-nucl-101916-123209.

[74] D. Molnár and S. A. Voloshin, "Elliptic flow at large transverse momenta from quark coalescence," *Physical Review Letters*, vol. 91, no. 9, Aug. 2003, ISSN: 1079-7114. DOI: 10.1103/physrevlett.91.092301. [Online]. Available: http://dx.doi.org/10.1103/PhysRevLett.91.092301.

[75] ALICE Coll., "Anisotropic flow of identified particles in Pb-Pb collisions at $\sqrt{s_{NN}}$ =5.02 TeV," *Journal of High Energy Physics*, vol. 2018, no. 9, Sep. 2018, ISSN: 1029-8479. DOI: 10.1007/jhep09(2018)006. [Online]. Available: http://dx.doi.org/10.1007/JHEP09(2018)006.

[76] Adams, J. et al., "Evidence from d+Au measurements for final-state suppression of high p_T hadrons in Au+Au collisions at RHIC," *Physical Review Letters*, vol. 91, no. 7, Aug. 2003, ISSN: 1079-7114. DOI: 10.1103/physrevlett.91.072304. [Online]. Available: http://dx.doi.org/10.1103/PhysRevLett.91.072304.

[77] A. Mocsy and P. Petreczky, "Can quarkonia survive deconfinement?" *Physical Review D*, vol. 77, no. 1, Jan. 2008, ISSN: 1550-2368. DOI: 10.1103/physrevd.77.014501. [Online]. Available: http://dx.doi.org/10.1103/PhysRevD.77.014501.

[78] T. Matsui and H. Satz, "J/ψ suppression by quark-gluon plasma formation," *Physics Letters B*, vol. 178, no. 4, pp. 416–422, 1986, ISSN: 0370-2693. DOI: https://doi.org/10.1016/0370-2693(86)91404-8. [Online]. Available: https://www.sciencedirect.com/science/article/pii/0370269386914048.

[79] ALICE Coll., "$\psi(2S)$ suppression in Pb-Pb collisions at the LHC," *Physical Review Letters*, vol. 132, no. 4, Jan. 2024, ISSN: 1079-7114. DOI: 10.1103/physrevlett.132.042301. [Online]. Available: http://dx.doi.org/10.1103/PhysRevLett.132.042301.

[80] Sirunyan, A. et al., "Relative modification of prompt $\psi(2S)$ and J/ψ yields from pp to Pb-Pb collisions at $\sqrt{s_{NN}} = 5.02$ TeV," *Physical Review Letters*, vol. 118, no. 16, Apr. 2017, ISSN: 1079-7114. DOI: 10.1103/physrevlett.118.162301. [Online]. Available: http://dx.doi.org/10.1103/PhysRevLett.118.162301.

[81] ALICE Coll., "Υ production and nuclear modification at forward rapidity in Pb–Pb collisions at $\sqrt{s_{NN}} = 5.02$ TeV," *Physics Letters B*, vol. 822, p. 136 579, Nov. 2021, ISSN: 0370-2693. DOI: 10.1016/j.physletb.2021.136579. [Online]. Available: http://dx.doi.org/10.1016/j.physletb.2021.136579.

[82] Sirunyan, A.M. et al., "Measurement of nuclear modification factors of $\Upsilon(1S)$, $\Upsilon(2S)$, and $\Upsilon(3S)$ mesons in Pb-Pb collisions at $\sqrt{s_{NN}}$ TeV," *Physics Letters B*, vol. 790, pp. 270–293, Mar. 2019, ISSN: 0370-2693. DOI: 10.1016/j.physletb.2019.01.006. [Online]. Available: http://dx.doi.org/10.1016/j.physletb.2019.01.006.

[83] Tumasyan, A. et al., "Observation of the $\Psi(3S)$ meson and suppression of Υ states in Pb-Pb collisions at $\sqrt{s_{NN}} = 5.02$ TeV," *Physical Review Letters*, vol. 133, no. 2, Jul. 2024, ISSN: 1079-7114. DOI: 10.1103/physrevlett.133.022302. [Online]. Available: http://dx.doi.org/10.1103/PhysRevLett.133.022302.

[84] NA50 Coll., "A new measurement of J/ψ suppression in Pb-Pb collisions at 158 GeV per nucleon," *The European Physical Journal C*, vol. 39, no. 3, pp. 335–345, Feb. 2005, ISSN: 1434-6052. DOI: 10.1140/epjc/s2004-02107-9. [Online]. Available: http://dx.doi.org/10.1140/epjc/s2004-02107-9.

[85] Adam, J. et al., "Measurement of inclusive J/ψ suppression in Au+Au collisions at $\sqrt{s_{NN}} = 200$ GeV through the dimuon channel at star," *Physics Letters B*, vol. 797, p. 134 917, Oct. 2019, ISSN: 0370-2693. DOI: 10.1016/j.physletb.2019.134917. [Online]. Available: http://dx.doi.org/10.1016/j.physletb.2019.134917.

[86] ALICE Coll., "Enhanced production of multi-strange hadrons in high-multiplicity proton–proton collisions," *Nature Physics*, (2017). [Online]. Available: https://arxiv.org/abs/1606.07424.

[87] ALICE Coll., "Multiplicity dependence of π, k, and p production in pp collisions at $\sqrt{s} = 13$ TeV," *The European Physical Journal C*, vol. 80, no. 8, Aug. 2020, ISSN: 1434-6052. DOI: 10.1140/epjc/s10052-020-8125-1. [Online]. Available: http://dx.doi.org/10.1140/epjc/s10052-020-8125-1.

[88] A. Coll., "Investigations of anisotropic flow using multiparticle azimuthal correlations in pp, $p-Pb$, Xe-Xe, and Pb-Pb collisions at the LHC," *Phys. Rev. Lett.*, vol. 123, p. 142 301, 14 Oct. 2019. DOI: 10.1103/PhysRevLett.123.142301. [Online]. Available: https://link.aps.org/doi/10.1103/PhysRevLett.123.142301.

[89] Chatrchyan, S. et al., "Multiplicity and transverse momentum dependence of two- and four-particle correlations in p-Pb and Pb-Pb collisions," *Phys. Lett. B*, vol. 724, pp. 213–240, 2013, Comments: Replaced with published version. Added journal reference and DOI. DOI: 10.1016/j.physletb.2013.06.028. arXiv: 1305.0609. [Online]. Available: https://cds.cern.ch/record/1545429.

[90] Aad, G. et al., "Observation of long-range elliptic azimuthal anisotropies in $\sqrt{s} =$ 13 and 2.76 TeV pp collisions with the ATLAS detector," *Physical Review Letters*, vol. 116, no. 17, Apr. 2016, ISSN: 1079-7114. DOI: 10.1103/physrevlett.116.172301. [Online]. Available: http://dx.doi.org/10.1103/PhysRevLett.116.172301.

[91] ALICE Coll., "Multiplicity dependence of the average transverse momentum in pp, p–pb, and pb–pb collisions at the LHC," *Physics Letters B*, vol. 727, no. 4–5, pp. 371–380, Dec. 2013, ISSN: 0370-2693. DOI: 10.1016/j.physletb.2013.10.054. [Online]. Available: http://dx.doi.org/10.1016/j.physletb.2013.10.054.

[92] J. Rafelski and J. Letessier, "Importance of reaction volume in hadronic collisions: Canonical enhancement," *Journal of Physics G: Nuclear and Particle Physics*, vol. 28, no. 7, pp. 1819–1832, Jun. 2002, ISSN: 0954-3899. DOI: 10.1088/0954-3899/28/7/336. [Online]. Available: http://dx.doi.org/10.1088/0954-3899/28/7/336.

[93] K. Redlich and A. Tounsi, "Strangeness enhancement and energy dependence in heavy ion collisions," *The European Physical Journal C*, vol. 24, no. 4, pp. 589–594, Aug. 2002, ISSN: 1434-6052. DOI: 10.1007/s10052-002-0983-1. [Online]. Available: http://dx.doi.org/10.1007/s10052-002-0983-1.

[94] S. Hamieh, K. Redlich, and A. Tounsi, "Canonical description of strangeness enhancement from p–A to Pb–Pb collisions," *Physics Letters B*, vol. 486, no. 1–2, pp. 61–66, Jul. 2000, ISSN: 0370-2693. DOI: 10.1016/s0370-2693(00)00762-0. [Online]. Available: http://dx.doi.org/10.1016/S0370-2693(00)00762-0.

[95] E. Shuryak and I. Zahed, "High-multiplicity pp and pA collisions: Hydrodynamics at its edge," *Physical Review C*, vol. 88, no. 4, Oct. 2013, ISSN: 1089-490X. DOI: 10.1103/physrevc.88.044915. [Online]. Available: http://dx.doi.org/10.1103/PhysRevC.88.044915.

[96] ALICE Coll., "Centrality dependence of π, k, p production in Pb-Pb collisions at $\sqrt{s_{NN}} = 2.76$ TeV," *Physical Review C*, vol. 88, no. 4, Oct. 2013, ISSN: 1089-490X. DOI: 10.1103/physrevc.88.044910. [Online]. Available: http://dx.doi.org/10.1103/PhysRevC.88.044910.

[97] P.Skands, S.Carrazza, J.Rojo, "Tuning PYTHIA 8.1: the Monash 2013 Tune," *arXiv e-prints*, (2014). [Online]. Available: https://arxiv.org/abs/1404.5630.

[98] T. Sjöstrand *et al.*, "An introduction to PYTHIA 8.2," *Computer Physics Communications*, vol. 191, pp. 159–177, Jun. 2015, ISSN: 0010-4655. DOI: 10.1016/j.cpc.2015.01.024. [Online]. Available: http://dx.doi.org/10.1016/j.cpc.2015.01.024.

[99] B. Andersson, *The Lund Model* (Cambridge Monographs on Particle Physics, Nuclear Physics and Cosmology). Cambridge University Press, Jul. 2023, vol. 7, ISBN: 978-1-009-40129-6, 978-1-009-40125-8, 978-1-009-40128-9, 978-0-521-01734-3, 978-0-521-42094-5, 978-0-511-88149-7. DOI: 10.1017/9781009401296.

[100] J. Bellm *et al.*, "Herwig 7.0/Herwig++ 3.0 release note," *The European Physical Journal C*, vol. 76, no. 4, Apr. 2016, ISSN: 1434-6052. DOI: 10.1140/epjc/s10052-016-4018-8. [Online]. Available: http://dx.doi.org/10.1140/epjc/s10052-016-4018-8.

[101] K. Werner, "Core-corona separation in ultrarelativistic heavy ion collisions," *Physical Review Letters*, vol. 98, no. 15, Apr. 2007, ISSN: 1079-7114. DOI: 10.1103/physrevlett.98.152301. [Online]. Available: http://dx.doi.org/10.1103/PhysRevLett.98.152301.

[102] T.Pierog, Iu.Karpenko, J.M.Katzy, E.Yatsenko, K.Werner, "EPOS LHC: test of collective hadronization with LHC data," *Phys.Rev.C*, vol. 92, (2015). [Online]. Available: https://arxiv.org/abs/1306.0121.

[103] Y. Kanakubo, Y. Tachibana, and T. Hirano, "Unified description of hadron yield ratios from dynamical core-corona initialization," *Physical Review C*, vol. 101, no. 2, Feb. 2020, ISSN: 2469-9993. DOI: 10.1103/physrevc.101.024912. [Online]. Available: http://dx.doi.org/10.1103/PhysRevC.101.024912.

[104] Y. Kanakubo, Y. Tachibana, and T. Hirano, "Interplay between core and corona components in high-energy nuclear collisions," *Physical Review C*, vol. 105, no. 2, Feb. 2022, ISSN: 2469-9993. DOI: 10.1103/physrevc.105.024905. [Online]. Available: http://dx.doi.org/10.1103/PhysRevC.105.024905.

[105] C. Bierlich, G. Gustafson, L. Lönnblad, and H. Shah, "The Angantyr model for heavy-ion collisions in Pythia8," *Journal of High Energy Physics*, vol. 2018, no. 10, Oct. 2018, ISSN: 1029-8479. DOI: 10.1007/jhep10(2018)134. [Online]. Available: http://dx.doi.org/10.1007/JHEP10(2018)134.

[106] C.Blume, C.Markert, "Strange hadron production in heavy-ion collisions from SPS to RHIC," *arXiv e-prints*, (2011). [Online]. Available: https://arxiv.org/abs/1105.2798.

[107] P.Koch, B.Müller, J.Rafelski, "Strangeness in relativistic heavy-ion collisions," *Physics Reports*, vol. 142, no. 4, (1986). [Online]. Available: https://doi.org/10.1016/0370-1573(86)90096-7.

[108] J. S. A. Andronic P. Braun-Munzinger, "Thermal hadron production in relativistic nuclear collisions: The hadron mass spectrum, the horn, and the QCD phase transition," *Phys.Lett.B 673*, 2008. DOI: arXiv:0812.1186. [Online]. Available: https://doi.org/10.48550/arXiv.0812.1186.

[109] J. Cleymans, I. Kraus, H. Oeschler, K. Redlich, and S. Wheaton, "Statistical model predictions for particle ratios at $\sqrt{s_{NN}} = 5.5$ TeV," *Physical Review C*, vol. 74, no. 3, 2006, ISSN: 1089-490X. DOI: 10.1103/physrevc.74.034903. [Online]. Available: http://dx.doi.org/10.1103/PhysRevC.74.034903.

[110] ALICE Coll. [Online]. Available: https://alice-figure.web.cern.ch/node/15504.

[111] ALICE Coll., "Production of K^0_S, Λ ($\overline{\Lambda}$), $\Xi^{\pm}$ and $\Omega^{\pm}$ in jets and in underlying event in pp and p-Pb collisions," *Journal of High Energy Physics*, vol. 2023, no. 7, Jul. 2023, ISSN: 1029-8479. DOI: 10.1007/jhep07(2023)136. [Online]. Available: http://dx.doi.org/10.1007/JHEP07(2023)136.

[112] M. Cacciari, G. P. Salam, and G. Soyez, "The anti-ktjet clustering algorithm," *Journal of High Energy Physics*, vol. 2008, no. 04, pp. 063–063, Apr. 2008, ISSN: 1029-8479. DOI: 10.1088/1126-6708/2008/04/063. [Online]. Available: http://dx.doi.org/10.1088/1126-6708/2008/04/063.

[113] M. Cacciari, G. P. Salam, and G. Soyez, "FastJet user manual: (for version 3.0.2)," *The European Physical Journal C*, vol. 72, no. 3, Mar. 2012, ISSN: 1434-6052. DOI: 10.1140/epjc/s10052-012-1896-2. [Online]. Available: http://dx.doi.org/10.1140/epjc/s10052-012-1896-2.

[114] ALICE Coll., "Charged-particle production as a function of multiplicity and transverse spherocity in pp collisions at $\sqrt{s} = 5.02$ and 13 TeV," *The European Physical Journal C*, vol. 79, no. 10, 2019, ISSN: 1434-6052. DOI: 10.1140/epjc/s10052-019-7350-y. [Online]. Available: http://dx.doi.org/10.1140/epjc/s10052-019-7350-y.

[115] ALICE Coll., "Performance of the ALICE Experiment at the CERN LHC," *Int.J.Mod.Phys.A*, vol. 29, (2014). [Online]. Available: https://arxiv.org/abs/1402.4476.

[116] Vretenar, Ma. et al., *Linac4 design report* (CERN Yellow Reports: Monographs). Geneva: CERN, 2020, vol. 6. DOI: 10.23731/CYRM-2020-006. [Online]. Available: https://cds.cern.ch/record/2736208.

[117] E. Regenstreif, *The CERN Proton Synchrotron* (CERN Yellow Reports: Monographs). Geneva: CERN, 1962, French version published as CERN 61-09. DOI: 10.5170/CERN-1962-003. [Online]. Available: https://cds.cern.ch/record/278715.

[118] *The Super Proton Synchrotron*, 2012. [Online]. Available: https://cds.cern.ch/record/1997188.

[119] E. Lopienska, "The CERN accelerator complex, layout in 2022. Complexe des accélérateurs du CERN en janvier 2022," *General Photo*, 2022. [Online]. Available: https://cds.cern.ch/record/2800984.

[120] ALICE Coll., *ALICE Inner Tracking System (ITS): Technical Design Report* (Technical design report. ALICE). Geneva: CERN, 1999. [Online]. Available: https://cds.cern.ch/record/391175.

[121] ALICE Coll., "Alignment of the alice inner tracking system with cosmic-ray tracks," *Journal of Instrumentation*, vol. 5, no. 03, P03003–P03003, Mar. 2010, ISSN: 1748-0221. DOI: 10.1088/1748-0221/5/03/p03003. [Online]. Available: http://dx.doi.org/10.1088/1748-0221/5/03/P03003.

[122] D.Colella, "ALICE ITS: the Run 1 to Run 2 transition and recent operational experience," *CERN Document Server*, (2016). [Online]. Available: http://dx.doi.org/10.22323/1.254.0003.

[123] ALICE Coll., "Upgrade of the ALICE Time Projection Chamber," CERN, Tech. Rep., 2013. [Online]. Available: https://cds.cern.ch/record/1622286.

[124] ALICE Coll., "Technical Design Report for the Upgrade of the ALICE Time Projection Chamber," *CERN Document Server*, (2019). [Online]. Available: http://cds.cern.ch/record/1622286/files/ALICE-TDR-016.pdf.

[125] ALICE Coll., "Performance of the ALICE VZERO system," *Journal of Instrumentation*, vol. 8, (2013). [Online]. Available: https://iopscience.iop.org/article/10.1088/1748-0221/8/10/P10016/pdf.

[126] ALICE Coll. [Online]. Available: https://alice-figure.web.cern.ch/node/11517.

[127] Bos, K. et al., *LHC computing Grid: Technical Design Report. Version 1.06 (20 Jun 2005)* (Technical design report. LCG). Geneva: CERN, 2005. [Online]. Available: https://cds.cern.ch/record/840543.

[128] Bagnasco, S. et al., "Alien: ALICE environment on the GRID," *Journal of Physics: Conference Series*, vol. 119, no. 6, p. 062 012, Jul. 2008. DOI: 10.1088/1742-6596/119/6/062012. [Online]. Available: https://dx.doi.org/10.1088/1742-6596/119/6/062012.

[129] Cortese, P. et al, *ALICE computing: Technical Design Report* (Technical design report. ALICE). Geneva: CERN, 2005, Submitted on 15 Jun 2005. [Online]. Available: https://cds.cern.ch/record/832753.

[130] [Online]. Available: https://github.com/alisw/AliPhysics.

[131] X.-N. Wang and M. Gyulassy, "Hijing: A Monte Carlo model for multiple jet production in pp, pA, and AA collisions," *Phys. Rev. D*, vol. 44, pp. 3501–3516, 11 Dec. 1991. DOI: 10.1103/PhysRevD.44.3501. [Online]. Available: https://link.aps.org/doi/10.1103/PhysRevD.44.3501.

[132] Brun, R. et al., *GEANT 3: user's guide Geant 3.10, Geant 3.11; rev. version.* Geneva: CERN, 1987. [Online]. Available: https://cds.cern.ch/record/1119728.

[133] S. Agostinelli *et al.*, "GEANT4–a simulation toolkit," *Nucl. Instrum. Meth. A*, vol. 506, pp. 250–303, 2003. DOI: 10.1016/S0168-9002(03)01368-8.

[134] P. Billoir, "Progressive track recognition with a kalman-like fitting procedure," *Computer Physics Communications*, vol. 57, no. 1, pp. 390–394, 1989, ISSN: 0010-4655. DOI: https://doi.org/10.1016/0010-4655(89)90249-X. [Online]. Available: https://www.sciencedirect.com/science/article/pii/001046558990249X.

[135] A. Maire, "Track reconstruction principle in ALICE for LHC run I and run II. Principes de reconstruction de traces dans ALICE pour les runs I et II du LHC," General Photo, 2011. [Online]. Available: https://cds.cern.ch/record/1984041.

[136] ALICE Coll., "Upgrade of the ALICE Experiment: Letter of Intent," CERN, Geneva, Tech. Rep., 2014. DOI: 10.1088/0954-3899/41/8/087001. [Online]. Available: https://cds.cern.ch/record/1475243.

[137] P. Buncic, M. Krzewicki, and P. Vande Vyvre, "Technical design report for the upgrade of the online-offline computing system," CERN, Tech. Rep., 2015. [Online]. Available: https://cds.cern.ch/record/2011297.

[138] ALICE Coll., "Future high-energy pp programme with ALICE," 2020. [Online]. Available: https://cds.cern.ch/record/2724925.

[139] G.D'Agostini, "Improved iterative Bayesian unfolding," *arXiv e-prints*, (2010). [Online]. Available: https://arxiv.org/abs/1010.0632.

[140] B. Salvachua *et al.*, "LHC Operational Scenarios During 2017 Run," in *Proc. 9th International Particle Accelerator Conference (IPAC'18), Vancouver, BC, Canada, April 29-May 4, 2018*, (Vancouver, BC, Canada), ser. International Particle Accelerator Conference, JACoW Publishing, Jun. 2018, pp. 220–223, ISBN: 978-3-95450-184-7. DOI: doi:10.18429/JACoW-IPAC2018-MOPMF051. [Online]. Available: http://jacow.org/ipac2018/papers/mopmf051.pdf.

[141] ALICE Coll., "Pseudorapidity distributions of charged particles as a function of mid- and forward rapidity multiplicities in pp collisions at $\sqrt{s} = 5.02$, 7 and 13 TeV," *Eur. Phys. J. C*, vol. 81, p. 630, 2021. DOI: 10.1140/epjc/s10052-021-09349-5. arXiv: 2009.09434 [nucl-ex]. [Online]. Available: https://arxiv.org/abs/2009.09434.

[142] [Online]. Available: https://pdg.lbl.gov/.

[143] ALICE Coll., "Strange particle production in proton-proton collisions at $\sqrt{s} = 0.9$ TeV with ALICE at the LHC," *Eur.Phys.J.C*, vol. 71, (2011). [Online]. Available: https://arxiv.org/abs/1012.3257.

[144] ALICE Coll., "Strange particle production in proton–proton collisions at $\sqrt{s}$= 0.9 TeV with ALICE at the LHC," *Eur. Phys. J. C*, vol. 71, p. 1594, 3 2011. DOI: 10.1140/epjc/s10052-011-1594-5. arXiv: 1012.3257 [hep-ex]. [Online]. Available: https://arxiv.org/abs/1012.3257.

[145] J. E. Gaiser, "Charmonium Spectroscopy From Radiative Decays of the J/ψ and ψ'," Other thesis, Aug. 1982. [Online]. Available: https://www.osti.gov/biblio/5211117.

[146] S.Schmitt, "TUnfold: an algorithm for correcting migration effects in high energy physics," *arXiv e-prints*, (2012). [Online]. Available: https://arxiv.org/abs/1205.6201.

[147] ALICE Coll., "Charged-particle multiplicity distributions over a wide pseudorapidity range in proton-proton collisions at $\sqrt{\mathrm{s}} = 0.9$, 7 and 8 TeV," 2017. arXiv: 1708.01435 [hep-ex]. [Online]. Available: https://arxiv.org/abs/1708.01435.

[148] [Online]. Available: https://root.cern.ch/.

[149] T.Adye, "Unfolding algorithms and tests using RooUnfold," *Geneva : CERN*, (2011). [Online]. Available: https://arxiv.org/abs/1105.1160.

[150] G. Alner *et al.*, "An investigation of multiplicity distributions in different pseudorapidity intervals in $\overline{p}$p reactions at a CMS energy of 540 GeV.," *Phys. Lett. B*, vol. 160, pp. 193–198, 1985. DOI: 10.1016/0370-2693(85)91491-1. [Online]. Available: https://cds.cern.ch/record/159457.

[151] A. Pandav, D. Mallick, and B. Mohanty, "Effect of limited statistics on higher order cumulants measurement in heavy-ion collision experiments," *Nuclear Physics A*, vol. 991, p. 121 608, Nov. 2019, ISSN: 0375-9474. DOI: 10.1016/j.nuclphysa.2019.08.002. [Online]. Available: http://dx.doi.org/10.1016/j.nuclphysa.2019.08.002.

[152] ALICE Coll., "Systematic uncertainties on (anti)(hyper)nuclei absorption," In Publication.

[153] Sara Pucillo on behalf of the ALICE Collaboration, "Insights on strange quark hadronization in small collision system with ALICE: Multiple strange hadrons and $\Sigma\pm$ baryons," *EPJ Web Conf.*, vol. 296, p. 15 005, 2024. DOI: 10.1051/epjconf/202429615005. arXiv: 2312.14892 [hep-ex].

[154] Sara Pucillo on behalf of the ALICE Collaboration, "New insights into strange-quark hadronization measuring multiple (multi-)strange hadron production in small collision systems with ALICE," in *21st International Conference on Strangeness in Quark Matter 2024*, Sep. 2024. arXiv: 2409.12987 [hep-ex].

[155] ALICE Coll., "Strangeness enhancement at its extremes: multiple (multi-)strange hadron production in pp collisions at $\sqrt{s} = 5.02$ TeV," In Publication.

[156] ALICE Coll., "Charged-particle multiplicity measurement in proton–proton collisions at $\sqrt{s} = 0.9$ and 2.36 TeV with ALICE at LHC," *Eur. Phys. J. C*, vol. 68, pp. 89–108, 2010. DOI: 10.1140/epjc/s10052-010-1339-x. arXiv: 1004.3034 [hep-ex].

[157] ALICE Coll., "Multiplicity dependence of charged-particle production in pp, p–pb, xe–xe and pb–pb collisions at the LHC," *Physics Letters B*, vol. 845, p. 138 110, Oct. 2023, ISSN: 0370-2693. DOI: 10.1016/j.physletb.2023.138110. [Online]. Available: http://dx.doi.org/10.1016/j.physletb.2023.138110.

[158] C. Loizides and A. Morsch, "Apparent strangeness enhancement from multiplicity selection in high energy proton-proton collisions," 2021. arXiv: 2109.05181 [hep-ph]. [Online]. Available: https://arxiv.org/abs/2109.05181.

[159] ALICE Coll., "Upgrade of the ALICE Experiment: Letter of Intent," *J.Phys.G:Nucl.Part.Phys*, vol. 41, (2014). [Online]. Available: http://dx.doi.org/10.1088/0954-3899/41/8/087001.

[160] Francesco Noferini on behalf of the ALICE Collaboration, "ALICE results from Run-1 and Run-2 and perspectives for Run-3 and Run-4," *J.Phys.:Conf.Ser.*, vol. 1014, no. 012010, (2018). [Online]. Available: http://dx.doi.org/10.1088/1742-6596/1014/1/012010.

[161] Andrea Ferrero on behalf of the ALICE Collaboration, "Alice status report," 2024. [Online]. Available: https://indico.cern.ch/event/1470570/contributions/6191108/attachments/2969381/5226120/ALICE-STATUS-20241118.pdf.

[162] D. Dobrigkeit Chinellato, "Charm and multi-charm baryon measurements via strangeness tracking with the upgraded ALICE detector," *EPJ Web of Conferences*, vol. 259, G. David *et al.*, Eds., p. 09 004, 2022, ISSN: 2100-014X. DOI: 10.1051/epjconf/202225909004. [Online]. Available: http://dx.doi.org/10.1051/epjconf/202225909004.

[163] J. Ahn *et al.*, "Measurement of the Ξ-p scattering cross sections at low energy," *Physics Letters B*, vol. 633, no. 2–3, pp. 214–218, Feb. 2006, ISSN: 0370-2693. DOI: 10.1016/j.physletb.2005.12.057. [Online]. Available: http://dx.doi.org/10.1016/j.physletb.2005.12.057.

[164] [Online]. Available: https://twiki.cern.ch/twiki/bin/viewauth/ALICE/PWGLFPAGSTRANGENESS.

[165] ALICE Coll., *ALICE dimuon forward spectrometer: addendum to the Technical Design Report* (Technical design report. ALICE). Geneva: CERN, 2000. [Online]. Available: https://cds.cern.ch/record/494265.

[166] A. Coll., "Technical Design Report for the Muon Forward Tracker," CERN, Tech. Rep., 2015. [Online]. Available: https://cds.cern.ch/record/1981898.

[167] F. Bossù, "The trigger system of the muon spectrometer of the ALICE experiment at the LHC," *Nuclear Physics B - Proceedings Supplements*, vol. 215, no. 1, pp. 204–207, 2011, Proceedings of the 12th Topical Seminar on Innovative Particle and Radiation Detectors (IPRD10), ISSN: 0920-5632. DOI: https://doi.org/10.1016/j.nuclphysbps.2011.04.009. [Online]. Available: https://www.sciencedirect.com/science/article/pii/S0920563211002489.

[168] G. Aglieri Rinella, "The alpide pixel sensor chip for the upgrade of the alice inner tracking system," *Nuclear Instruments and Methods in Physics Research Section A: Accelerators, Spectrometers, Detectors and Associated Equipment*, vol. 845, pp. 583–587, 2017, Proceedings of the Vienna Conference on Instrumentation 2016, ISSN: 0168-9002. DOI: https://doi.org/10.1016/j.nima.2016.05.016. [Online]. Available: https://www.sciencedirect.com/science/article/pii/S0168900216303825.

[169] ALICE Coll., *ALICE dimuon forward spectrometer: addendum to the Technical Design Report* (Technical design report. ALICE). Geneva: CERN, 2000. [Online]. Available: https://cds.cern.ch/record/494265.

[170] ALICE Coll., *ALICE dimuon forward spectrometer: Technical Design Report* (Technical design report. ALICE). Geneva: CERN, 1999. [Online]. Available: https://cds.cern.ch/record/401974.

[171] ALICE Coll., "Upgrade of the ALICE Readout & Trigger System," Tech. Rep., 2013. [Online]. Available: https://cds.cern.ch/record/1603472.

[172] [Online]. Available: https://github.com/AliceO2Group/QualityControl/tree/master/doc.

[173] [Online]. Available: https://ali-bookkeeping.cern.ch/?page=lhc-period-overview.

[174] [Online]. Available: https://ali-bookkeeping.cern.ch/?page=qc-flag-types-overview.

[175] [Online]. Available: https://twiki.cern.ch/twiki/bin/viewauth/ALICE/AliDPGRCT$_$3.

[176] [Online]. Available: https://ali-qcg.cern.ch/?page=layoutShow&layoutId=650db741c5e1b41e6538a984&tab=Digits.

[177] [Online]. Available: https://ali-qcg.cern.ch/?page=layoutShow&layoutId=650db741c5e1b41e6538a984&tab=Tracks.

[178] [Online]. Available: https://ali-qcg.cern.ch/?page=layoutShow&layoutId=62bdc28f8a2809e8a2b0ee08&tab=Ratio44.

[179] [Online]. Available: https://ali-qcg.cern.ch/?page=layoutShow&layoutId=6449181246a87f6084cb265b&tab=main.